



energies

Biomass Chars Elaboration, Characterization and Applications II

Edited by
Mejdi Jeguirim and Lionel Limousy
Printed Edition of the Special Issue Published in *Energies*

Biomass Chars

Biomass Chars: Elaboration, Characterization and Applications II

Special Issue Editors

Mejdi Jeguirim

Lionel Limousy

MDPI • Basel • Beijing • Wuhan • Barcelona • Belgrade



Special Issue Editors

Mejdi Jeguirim

Institut de Sciences des Matériaux de Mulhouse
France

Lionel Limousy

Institut de Sciences des Matériaux de Mulhouse
France

Editorial Office

MDPI

St. Alban-Anlage 66
4052 Basel, Switzerland

This is a reprint of articles from the Special Issue published online in the open access journal *Energies* (ISSN 1996-1073) from 2017 to 2019 (available at: https://www.mdpi.com/journal/energies/special-issues/biomass_chars_2017).

For citation purposes, cite each article independently as indicated on the article page online and as indicated below:

LastName, A.A.; LastName, B.B.; LastName, C.C. Article Title. *Journal Name Year, Article Number*, Page Range.

ISBN 978-3-03921-662-8 (Pbk)

ISBN 978-3-03921-663-5 (PDF)

© 2019 by the authors. Articles in this book are Open Access and distributed under the Creative Commons Attribution (CC BY) license, which allows users to download, copy and build upon published articles, as long as the author and publisher are properly credited, which ensures maximum dissemination and a wider impact of our publications.

The book as a whole is distributed by MDPI under the terms and conditions of the Creative Commons license CC BY-NC-ND.

Contents

About the Special Issue Editors	ix
Preface to "Biomass Chars: Elaboration, Characterization and Applications II"	xi
Mejdi Jeguirim and Lionel Limousy	
Biomass Chars: Elaboration, Characterization and Applications II	1
Reprinted from: <i>Energies</i> 2019, 12, 384, doi:10.3390/en12030384	
Deneb Peredo-Mancilla, Cecile Hort, Camelia Matei Ghimbeu, Mejdi Jeguirim, Imen Ghouma and David Bessieres	
CO ₂ and CH ₄ Adsorption Behavior of Biomass-Based Activated Carbons	
Reprinted from: <i>Energies</i> 2018, 11, 3136, doi:10.3390/en1113136	7
Bogdan Saletnik, Grzegorz Zagula, Marcin Bajcar, Maria Czernicka and Czeslaw Puchalski	
Biochar and Biomass Ash as a Soil Ameliorant: The Effect on Selected Soil Properties and Yield of Giant Miscanthus (<i>Miscanthus x giganteus</i>)	
Reprinted from: <i>Energies</i> 2018, 11, 2535, doi:10.3390/en1102535	20
Ye-Eun Lee, Jun-Ho Jo, I-Tae Kim and Yeong-Seok Yoo	
Influence of NaCl Concentration on Food-Waste Biochar Structure and Templating Effects	
Reprinted from: <i>Energies</i> 2018, 11, 2341, doi:10.3390/en11092341	44
Nourelhouda Boukaous, Lokmane Abdelouahed, Mustapha Chikhi, Abdeslam-Hassen Meniai, Chetna Mohabeer and Taouk Bechara	
Combustion of Flax Shives, Beech Wood, Pure Woody Pseudo-Components and Their Chars: A Thermal and Kinetic Study	
Reprinted from: <i>Energies</i> 2018, 11, 2146, doi:10.3390/en11082146	60
Tilia Dahou, Françoise Defoort, Sébastien Thiéry, Maguelone Grateau, Matthieu Campargue, Simona Bennici, Mejdi Jeguirim and Capucine Dupont	
The Influence of Char Preparation and Biomass Type on Char Steam Gasification Kinetics	
Reprinted from: <i>Energies</i> 2018, 11, 2126, doi:10.3390/en11082126	76
Shurooq Badri Al-Badri, Ying Jiang and Stuart Thomas Wagland	
Possible Interactions and Interferences of Copper, Chromium, and Arsenic during the Gasification of Contaminated Waste Wood †	
Reprinted from: <i>Energies</i> 2018, 11, 1966, doi:10.3390/en11081966	91
Mohamed Ali Mami, Hartmut Mätzing, Hans-Joachim Gehrmann, Dieter Stapf, Rainer Bolduan and Marzouk Lajili	
Investigation of the Olive Mill Solid Wastes Pellets Combustion in a Counter-Current Fixed Bed Reactor	
Reprinted from: <i>Energies</i> 2018, 11, 1965, doi:10.3390/en11081965	108
Amna Abdeljaoued, Nausika Querejeta, Inés Durán, Noelia Álvarez-Gutiérrez, Covadonga Pevida and Mohamed Hachemi Chahbani	
Preparation and Evaluation of a Coconut Shell-Based Activated Carbon for CO ₂ /CH ₄ Separation	
Reprinted from: <i>Energies</i> 2018, 11, 1748, doi:10.3390/en11071748	129

Ye-Eun Lee, Jun-Ho Jo, I-Tae Kim and Yeong-Seok Yoo Value-Added Performance and Thermal Decomposition Characteristics of Dumped Food Waste Compost by Pyrolysis Reprinted from: <i>Energies</i> 2018, 11, 1061, doi:10.3390/en11051061	143
Jinsu Kim, Hyunmin Oh, Seokyoung Lee and Young-Seek Yoon Advanced One-Dimensional Entrained-Flow Gasifier Model Considering Melting Phenomenon of Ash Reprinted from: <i>Energies</i> 2018, 11, 1015, doi:10.3390/en11041015	157
Besma Khiari and Mejdi Jeguirim Pyrolysis of Grape Marc from Tunisian Wine Industry: Feedstock Characterization, Thermal Degradation and Kinetic Analysis Reprinted from: <i>Energies</i> 2018, 11, 730, doi:10.3390/en11040730	171
Xiaorui Liu, Zhongyang Luo, Chunjiang Yu, Bitao Jin and Hanchao Tu Release Mechanism of Fuel-N into NO _x and N ₂ O Precursors during Pyrolysis of Rice Straw Reprinted from: <i>Energies</i> 2018, 11, 520, doi:10.3390/en11030520	185
Alba Dieguez-Alonso, Axel Funke, Andrés Anca-Couce, Alessandro Girolamo Rombolà, Gerardo Ojeda, Jörg Bachmann and Frank Behrendt Towards Biochar and Hydrochar Engineering—Influence of Process Conditions on Surface Physical and Chemical Properties, Thermal Stability, Nutrient Availability, Toxicity and Wettability Reprinted from: <i>Energies</i> 2018, 11, 496, doi:10.3390/en11030496	198
Xi Lin, Qingya Liu and Zhenyu Liu Estimation of Effective Diffusion Coefficient of O ₂ in Ash Layer in Underground Coal Gasification by Thermogravimetric Apparatus Reprinted from: <i>Energies</i> 2018, 11, 460, doi:10.3390/en11020460	224
Dongdong Feng, Yijun Zhao, Yu Zhang, Shaozeng Sun and Jianmin Gao Steam Gasification of Sawdust Biochar Influenced by Chemical Speciation of Alkali and Alkaline Earth Metallic Species Reprinted from: <i>Energies</i> 2018, 11, 205, doi:10.3390/en11010205	238
Chang Liu, Xin Huang and Lingzhao Kong Efficient Low Temperature Hydrothermal Carbonization of Chinese Reed for Biochar with High Energy Density Reprinted from: <i>Energies</i> 2017, 10, 2094, doi:10.3390/en10122094	254
Xia Liu, Juntao Wei, Wei Huo and Guangsuo Yu Gasification under CO ₂ -Steam Mixture: Kinetic Model Study Based on Shared Active Sites Reprinted from: <i>Energies</i> 2017, 10, 1890, doi:10.3390/en10111890	264
Seung-Yong Oh and Young-Man Yoon Energy Recovery Efficiency of Poultry Slaughterhouse Sludge Cake by Hydrothermal Carbonization Reprinted from: <i>Energies</i> 2017, 10, 1876, doi:10.3390/en10111876	274
Ye-Eun Lee, Jun-Ho Jo, I-Tae Kim and Yeong-Seok Yoo Chemical Characteristics and NaCl Component Behavior of Biochar Derived from the Salty Food Waste by Water Flushing Reprinted from: <i>Energies</i> 2017, 10, 1555, doi:10.3390/en10101555	287

Gyeong-Min Kim, Jong-Pil Kim, Kevin Yohanes Lisandy and Chung-Hwan Jeon	
Experimental Model Development of Oxygen-Enriched Combustion Kinetics on Porous Coal	
Char and Non-Porous Graphite	
Reprinted from: <i>Energies</i> 2017, 10, 1436, doi:10.3390/en10091436	302
Christina Moulogianni and Thomas Bournaris	
Biomass Production from Crops Residues: Ranking of Agro-Energy Regions	
Reprinted from: <i>Energies</i> 2017, 10, 1061, doi:10.3390/en10071061	316

About the Special Issue Editors

Mejdi Jeguirim has been Associate Professor at the University of Haute Alsace (France) since 2005 in the field of energy and process engineering. Most of his research is dedicated to the study of biomass valorization through thermochemical conversion and char elaboration for energy and syngas production, pollutant removal, and soil amendment. This research has been conducted in the framework of international collaborations and industrial contracts. He has served as PhD advisor for 10 students and co-authored 85 referred publications in international journals. He is on the Editorial Board of numerous international scientific journals (*Energy*, *Energy for Sustainable Development*, *Energies*) and has organized several Special Issues as Guest Editor. He belongs to the scientific committee of numerous international congresses and is involved as a scientific expert for several national and international research programs. He has received the French National Research Excellence Award as a researcher with a high level of scientific activity for the periods 2009–2012, 2013–2016, and 2017–2020.

Lionel Limousy has been Associate Professor at the University of Haute Alsace since 2010. He teaches in chemical and environmental engineering as well as risk management and assessment. He was recruited to the University of South Brittany in 2000 where he was Head of the Chemical Engineering and Process department from 2003 and 2005. He founded the Prodiabio platform in 2005, where he was Director until 2010. In 2013, he joined the Institute of Material Science of Mulhouse where he became responsible for the industrial research partnership. He has experience in the biological and chemical treatment of wastewater, membrane filtration, biomass valorization, and materials characterization. He is involved in several national and international academic and industrial projects. He has 89 scientific publications and collaborated in the organization of Special Issues. He has received the French National Research Excellence Award as a researcher with a high level of scientific activity for the periods 2013–2016 and 2017–2020.

Preface to "Biomass Chars: Elaboration, Characterization and Applications II"

Biomass Chars: Elaboration, Characterization and Applications II is a continuation of the previous and successful Special Issue "Biomass Chars: Elaboration, Characterization and Applications". This SI contains 22 original articles that were selected and evaluated for this Special Issue and provide an overview of the properties of biomass chars as well as methods for their production, characterization techniques, as well as suitable recovery processes.

Mejdi Jeguirim, Lionel Limousy

Special Issue Editors

Editorial

Biomass Chars: Elaboration, Characterization and Applications II

Mejdi Jeguirim * and Lionel Limousy

Université de Strasbourg, Université de Haute Alsace, Institut de Science des Matériaux de Mulhouse (IS2M) UMR CNRS 7361, 68093 Mulhouse, France; lionel.limousy@uha.fr

* Correspondence: mejdi.jeguirim@uha.fr

Received: 14 November 2018; Accepted: 23 January 2019; Published: 25 January 2019

This Special Issue of *Energies* contains the successful invited submissions [1–21] on the subject area of “Biomass Chars: Elaboration, Characterization and Applications”. After the organization of a first edition, the guest editors have decided to continue focusing on char production from biomass and their applications various applications. In response to our call for papers we received 27 submissions, of which 21 have been published and six rejected during the peer review process. The geographical distribution of the authors of the published papers is as follows:

- China (5)
- UK (1)
- France (4)
- Greece (1)
- Spain (1)
- Korea (6)
- Germany (1)
- Tunisia (1)
- Poland (1)

Published submissions are related to biomass char production methods, including pyrolysis, and hydrothermal carbonization. In addition, various characterization techniques were used to identify the physico-chemical, morphological, textural, surface chemistry and structural properties of the products. The main applied techniques were thermogravimetric analysis (TGA), calorimetry, pH measurements, scanning electron microscopy (SEM)–energy dispersive X-ray (EDX) analyses, X-ray diffraction (XRD), nitrogen gas adsorption, Fourier transform infrared spectroscopy (FTIR), etc. The different recovery routes of biomass-derived chars were also addressed. Particular attention was paid to char gasification and combustion as well as to the applications of chars for gas storage and soil amendment. The main results are described below. New developments are still under progress, encouraging the organization of a third edition of this special issue.

Moulogianni and Bouraris have ranked the agro-energy regions in the Region of Central Macedonia (RCM) according to their biomass production potential [1]. In this context, the authors have developed a Multi-Criteria Analysis (MCDA) model using the ELimination and Et Choix Traduisant la REalité (ELECTRE) III method through the construction of outranking relations. The authors concluded that agro-energy regions with cereals and arable crops will have better results than regions with fruit trees and other crops.

Khiari and Jeguirim have attempted to identify an environmentally friendly valorization method for the huge amounts of grape marc generated in Tunisia by the wine industry [2]. Hence, the authors have determined physico-chemical and energy characteristics of grape marc according to international standards. Based on these characteristics, they proposed a pyrolysis process as a recovery route for the

grape marc due to its high minerals content and the ability to create high added value derived products. During the thermogravimetric analysis the biochar yield was about 40%, a value never previously reported in the literature for an agricultural biomass subjected to slow pyrolysis. Such behavior may be attributed to the high lignin and high minerals contents in grape marc, confirming its potential for agricultural applications.

Lee et al. have studied an alternative for the recovery of food waste compost since the amount generated every day is higher than the amount consumed in farms [3]. Hence, authors have suggested producing biochar from food waste compost using pyrolysis processes. In this context, they have analyzed the thermal degradation behavior, calorific value, and char composition (using gas chromatography) during the pyrolysis of food waste compost. The authors showed that biochar from the pyrolysis of food waste compost had a high carbon content of 51% at 300 °C. Hence, it seems that food waste compost can be used as a promising alternative fuel at a low pyrolysis temperature, like other lignocellulosic refuse-derived fuels (RDF).

Liu et al. have studied the pyrolysis of rice straw in a horizontal tube reactor at temperatures ranging from 500 to 900 °C [4]. The authors have monitored the gaseous nitrogen components emitted during rice straw pyrolysis in order to identify the release mechanism of fuel-N into NO_x and N₂O precursors. A high dependency between the gaseous products and temperature was found. NH₃ and HNCO were preferentially formed at lower temperatures and HCN tended to form at higher temperatures. The authors have also noted that NO was also an important product and its formation during the pyrolysis of rice straw was due to the direct oxidization reaction of -NH and -OH, the latter being abundant in the raw material.

Hydrothermal carbonization (HTC) is an emerging technology used for bioenergy conversion from bio-wastes such as sewage sludge, livestock manure, and food waste. Oh and Yoon have studied the hydrothermal carbonization of poultry slaughterhouse sludge cake in a pilot-scale HTC reactor at temperatures from 170 to 220 °C [5]. The authors have analyzed the gross energy recovery efficiency based on the calorific value of the HTC-biochar and the ultimate methane potential of the HTC-hydrolysate, indicating that poultry slaughterhouse sludge cake is a useful source for bioenergy conversion with a total gross energy recovery (GER_{total}) of 4318 MJ/kg attained at 180 °C.

Similar analysis were performed by Liu et al. during the hydrothermal carbonization of a major energy crop, reeds [6]. The HTC experiments were performed in a batch reactor at 200–280 °C for 0.5 to 4 h. The authors indicated that the hydrochar mass yield changed from 66.7% to 19.2% and high heating value (HHV) from 20.0 kJ/g to 28.3 kJ/g, respectively, by increasing the carbonization temperature from 200 °C to 280 °C and decreasing the residence time from 2 h to 1 h.

The operating conditions in pyrolysis and hydrothermal carbonization strongly impact the properties of biochars and hydrochars. Dieguez-Alonso et al. have used pine wood (PW) and corn digestate (CD) as feedstocks for biochar and hydrochar production [7]. CD biochars showed lower H/C ratios, thermal recalcitrance and total specific surface area than PW biochars, but higher mesoporosity. CD and PW biochars presented higher naphthalene and phenanthrene contents, respectively, which may indicate different reaction pathways. High temperatures (>500 °C) lead to lower polycyclic aromatic hydrocarbon (PAH) content (<12 mg/kg) and higher specific surface area. In hydrochars the high inorganic content favors decarboxylation over dehydration reactions. Hydrochars showed mainly mesoporosity, with a higher pore volume but generally lower specific surface area than biochars. Biochars presented negligible availability of NO₃⁻ and NH₄⁺, irrespective of the nitrogen content of the feedstock. For hydrochars, a potential increase in availability of NO₃⁻, NH₄⁺, PO₄³⁻, and K⁺ with respect to the feedstock is possible.

The char characterization is a crucial step to identify the suitable recovery route for biochar. Lee et al. have analyzed the chemical characteristics of biochar produced using food waste containing low- and high-concentration salt and biochar flushed with water to remove the concentrated salt [8]. Peak analysis of XRD confirmed that it is difficult to find salt crystals in flushed char since salt remains in the form of crystals when salty food waste was pyrolyzed was washed away after water flushing.

In addition, the Cl content significantly decreased to 1–2% after flushing, similar to that of Cl content in the standard, non-salted food waste char. On the other hand, a significant amount of Na was found in pyrolyzed char even after flushing resulting from a phenomenon in which salt is dissolved in water while flushing and Na ions are adsorbed. FT-IR analysis showed that salt in waste affects the binding of aromatic carbons to compounds in the pyrolysis process. NMR spectroscopy experiments demonstrated that the aromatic carbon content, which is an indicator of the stability of a biochar, is not influenced by the salt content and increases with increasing pyrolysis temperature.

Lee et al. have followed up on their investigation by analyzing food-waste-derived biochar structures obtained through pyrolysis and with different NaCl concentrations [9]. The authors indicate that increased NaCl concentration in the samples inhibited cellulose and lignin decomposition, ultimately increasing the biochar yield by 2.7% for 20%-NaCl concentration. NaCl added in solution state exhibited templating effects, with maximum increase in the Brunauer–Emmett–Teller (BET) surface area and pore volume of 1.23 to $3.50 \text{ m}^2 \cdot \text{g}^{-1}$ and 0.002 to $0.007 \text{ cm}^3 \cdot \text{g}^{-1}$, respectively, after washing. Adding a high concentration (20%) of NaCl reduced the BET surface area. In contrast, the mean pore diameter increased owing to the increased NaCl clustering area.

Different recovery routes for biomass-derived chars were examined in the literature such as combustion, gasification, pollutants adsorption, soil amendments. Boukaous et al. have examined the combustion characteristics of flax shives, beech wood, hemicellulose, cellulose, lignin, and their chars prepared in a fixed-bed reactor at 850°C [10]. The authors have assessed the thermal behavior based on characteristic temperatures (ignition, maximum, and final temperatures), burnout time and maximum rate. The results revealed that the combustion of pure pseudo-components behaved differently from that of biomass. In contrast, the combustion of the hemicellulose and cellulose chars showed that they have almost the same structure. Their overall thermal and kinetic behavior remained between that of biomass and lignin.

Mami et al. have carried out combustion tests of olive mill solid wastes pellets (olive pomace (OP), and olive pits (OPI)) in an updraft counter-current fixed bed reactor [11]. The authors have found that the exhaust gases were emitted in acceptable concentrations compared to the combustion of standard wood pellets reported in the literature (EN 303-5). Furthermore, it was shown that the bed temperature increased from the ambient value to a maximum value ranging from 750 to 1000°C as previously reported in the literature. The results demonstrated the interest of using olive mill solid waste pellets as an alternative biofuel for heat and/or electricity production

Kim et al. have examined experimentally the effect of oxygen-enriched air on char combustion [12]. During their investigation, a coal-heating reactor equipped with a platinum wire mesh in the reaction chamber was used to analyze the combustion temperature, reaction time, and reaction kinetics. The authors have found that increasing the oxygen content of the primary combustion air increased the combustion temperature and decreased the reaction time. As the oxygen content increased from 21% to 30%, the average temperature increased by 47.72 K at a setup temperature of 1673 K , and the reaction time decreased by 30.22% at the same temperature. The graphite sample exhibited similar trends in temperature and reaction time, although the degree of change was smaller because the pores produced during char devolatilization expanded the active surface available for oxidation of the char sample. A mathematical model was used to define the intrinsic kinetics of the reaction. As the oxygen content increased from 21% to 30%, the reaction rate of the low-rank coal char increased. These results were also compared with those of the graphite sample

Char gasification is attracting nowadays growing interest. Liu et al. have studied the char gasification of two coals (i.e., Shenshu bituminous coal and Zunyi anthracite) and a petroleum coke under a steam and CO₂ mixture (steam/CO₂ partial pressures, 0.025–0.075 MPa; total pressures, 0.100 MPa) and CO₂/steam chemisorption of char samples using a Thermogravimetric Analyzer (TGA) [13]. As a result a modified model based on Langmuir–Hinshelwood model and assuming that char–CO₂ and char–steam reactions partially shared active sites was proposed and had indicated high accuracy for estimating the interactions in char–steam–CO₂ reaction. Moreover, it was found that

two new model parameters (respectively characterized as the amount ratio of shared active sites to total active sites in char–CO₂ and char–steam reactions) in the modified model hardly varied with gasification conditions, and the results of chemisorption indicate that these two new model parameters mainly depended on the carbon active sites in char samples.

The char gasification reactivity is strongly affected by the presence of inorganic elements in the raw biomass. Feng et al. have examined the effect of chemical speciation (H₂O/NH₄Ac/HCl-soluble and insoluble) of alkali and alkaline earth metallic species on the steam gasification of sawdust biochar in a lab-scale, fixed-bed reactor, with the method of chemical fractionation analysis [14]. The results indicated that H₂O/NH₄Ac/HCl-soluble AAEMs have a significant effect on biochar gasification rates. The release of K occurs mainly in the form of inorganic salts and hydrated ions, while that of Ca occurs mainly as organic ones. The sp³-rich or sp²–sp³ structures and different chemical-speciation AAEMs function together as the preferred active sites during steam gasification. H₂O/HCl-soluble AAEMs could promote the transformation of biochar surface functional groups, from ether/alkene C–O–C to carboxylate COO[–] in biochar, while they may both be improved by NH₄Ac-soluble AAEMs. H₂O-soluble AAEMs play a crucial catalytic role in biochar reactivity.

In addition to the inorganic elements, char preparation methods may influence the gasification reactivity. Dahou et al. conducted a study to investigate the parameters that influence the steam gasification kinetics according to the biomass type and char preparation method [15]. Chars were prepared using three different sets of low heating rate (LHR) pyrolysis conditions including different temperatures and biomass bed geometry. The authors have shown by a characteristic time analysis that these pyrolysis conditions were not associated with a chemical regime in a large amount of devices. However, they have shown that conditions used to prepare the char had a much lower influence on steam gasification kinetics than the biomass type.

The presence of heavy metals in waste wood may have negative effects during the gasification process through toxicity emissions and facility damaging. Therefore, Al-Badri et al. have performed thermodynamic equilibrium calculations for the Boudouard reaction (BR) and partial combustion reaction (PCR) to explore the possible interactions and interferences among CCA-elements themselves and with Ca, Na, S, Cl, Fe, and Ni during the gasification of contaminated waste wood [16]. The results revealed that Ni–As interactions generate dominant species As₂Ni₅ and As₈Ni₁₁, which increase the solid–gaseous transformation temperature of As. Moreover, the interactions between Ca and Cr predominantly form C₃Cr₇; whereas the absence of Ca leads to Cr₂Na₂O₄ causing instability in the Cr phase transformation.

During the char gasification, an ash layer is accumulated on the char surface. The ash layer increases the mass transfer resistance of O₂ to the gasification surface, which may become the limiting step of whole process. In this context, Lin et al. studied O₂ diffusion in the ash layer formed on cylindrical char samples using a specially designed one-dimension setup in a thermogravimetric apparatus (TGA) [17]. The effective internal diffusion coefficient (D_e) was found to increase with an increase in ash layer thickness, due to an increase in median pore diameter. Methods were established to correlate D_e with operating conditions and to estimate the role of internal diffusion resistance in overall mass transfer resistance.

The effect of ash melting phenomena was also assessed by Kim et al. through the development of a one-dimensional (1-D) entrained-flow gasifier model [18]. The authors have included sensible heat of slag and the fusion heat of ash in the heat balance equation in their model. To consider the melting of ash, they have proposed an algorithm that calculates the energy balance for three scenarios based on temperature. Based on the Texaco pilot plant gasifier, the model was validated. The obtained results showed good agreement with previous experimental data. Kim et al. have concluded that the sensible heat of slag and the fusion heat of ash must be included in the entrained flow gasifier model.

In addition to the thermal conversion, biomass chars could be physically or chemically activated in order to elaborate efficient adsorbents. In this sense, Abdeljaoued et al. have produced an activated carbon from coconut shells with suitable characteristics to separate CO₂ from biogas [19]. The textural

characterization of the adsorbent has been determined. Pure component adsorption isotherms of CO₂ and CH₄ at 30–70 °C have been measured. The obtained results revealed that the activated carbon had high CO₂ adsorption capacity. Equilibrium of adsorption of CO₂ and CH₄ adsorption on the produced activated carbon reached 8.36 mmol/g and 4.63 mmol/g, respectively, at 30 °C and 10 bar.

Peredo-Mancilla et al. have compared the performance of different biomass-based activated carbons for CO₂ and CH₄ adsorption [20]. In particular, authors have studied the influence of the activation method on the adsorption uptake using three activated carbons obtained by different activation methods (H₃PO₄ chemical activation and H₂O and CO₂ physical activation) of olive stones. For the three adsorbents, the CO₂ adsorption was more important than that of CH₄. The chemically-activated carbon presented a higher specific surface area and micropore volume, which led to a higher adsorption capacity of both CO₂ and CH₄. For methane adsorption, the presence of mesopores facilitated the diffusion of the gas molecules into the micropores. In the case of carbon dioxide adsorption, the presence of more oxygen groups on the water vapor-activated carbon enhanced its adsorption capacity.

Energy crops such as *Miscanthus* have attracted growing interest during the last decade. Saletnik et al. have assessed the possibility of using biochar and ash from plant biomass to fertilise giant miscanthus (*Miscanthus x giganteus*). Authors have examined the optimisation of the combination of fertiliser applications of the aforementioned materials in the context of the plant yield obtained. There was an increase in yield of 8–68% over the two years of research when compared with the control plots. It was found that the application of biochar, ash from biomass and a combination of the two at appropriate rates as a soil additive can substitute for classic mineral fertilisers and strengthen the ecological aspects of energy crop cultivation.

We found the edition and selections of papers for this Special Issue very inspiring and rewarding. We also thank the editorial staff and reviewers for their efforts and help during the process.

References

1. Moulogianni, C.; Bournaris, T. Biomass Production from Crops Residues: Ranking of Agro-Energy Regions. *Energies* **2017**, *10*, 1061. [[CrossRef](#)]
2. Khiari, B.; Jeguirim, M. Pyrolysis of Grape Marc from Tunisian Wine Industry: Feedstock Characterization, Thermal Degradation and Kinetic Analysis. *Energies* **2018**, *11*, 730. [[CrossRef](#)]
3. Lee, Y.; Jo, J.; Kim, I.; Yoo, Y. Value-Added Performance and Thermal Decomposition Characteristics of Dumped Food Waste Compost by Pyrolysis. *Energies* **2018**, *11*, 1061. [[CrossRef](#)]
4. Liu, X.; Luo, Z.; Yu, C.; Jin, B.; Tu, H. Release Mechanism of Fuel-N into NOx and N₂O Precursors during Pyrolysis of Rice Straw. *Energies* **2018**, *11*, 520. [[CrossRef](#)]
5. Oh, S.; Yoon, Y. Energy Recovery Efficiency of Poultry Slaughterhouse Sludge Cake by Hydrothermal Carbonization. *Energies* **2017**, *10*, 1876. [[CrossRef](#)]
6. Liu, C.; Huang, X.; Kong, L. Efficient Low Temperature Hydrothermal Carbonization of Chinese Reed for Biochar with High Energy Density. *Energies* **2017**, *10*, 2094. [[CrossRef](#)]
7. Dieguez-Alonso, A.; Funke, A.; Anca-Couce, A.; Rombolà, A.; Ojeda, G.; Bachmann, J.; Behrendt, F. Towards Biochar and Hydrochar Engineering—Influence of Process Conditions on Surface Physical and Chemical Properties, Thermal Stability, Nutrient Availability, Toxicity and Wettability. *Energies* **2018**, *11*, 496. [[CrossRef](#)]
8. Lee, Y.; Jo, J.; Kim, I.; Yoo, Y. Chemical Characteristics and NaCl Component Behavior of Biochar Derived from the Salty Food Waste by Water Flushing. *Energies* **2017**, *10*, 1555. [[CrossRef](#)]
9. Lee, Y.; Jo, J.; Kim, I.; Yoo, Y. Influence of NaCl Concentration on Food-Waste Biochar Structure and Templating Effects. *Energies* **2018**, *11*, 2341. [[CrossRef](#)]
10. Boukaous, N.; Abdelouahed, L.; Chikhi, M.; Meniai, A.; Mohabeer, C.; Bechara, T. Combustion of Flax Shives, Beech Wood, Pure Woody Pseudo-Components and Their Chars: A Thermal and Kinetic Study. *Energies* **2018**, *11*, 2146. [[CrossRef](#)]
11. Mami, M.; Mätzing, H.; Gehrmann, H.; Stapf, D.; Bolduan, R.; Lajili, M. Investigation of the Olive Mill Solid Wastes Pellets Combustion in a Counter-Current Fixed Bed Reactor. *Energies* **2018**, *11*, 1965. [[CrossRef](#)]

12. Kim, G.; Kim, J.; Lisandy, K.; Jeon, C. Experimental Model Development of Oxygen-Enriched Combustion Kinetics on Porous Coal Char and Non-Porous Graphite. *Energies* **2017**, *10*, 1436. [[CrossRef](#)]
13. Liu, X.; Wei, J.; Huo, W.; Yu, G. Gasification under CO₂-Steam Mixture: Kinetic Model Study Based on Shared Active Sites. *Energies* **2017**, *10*, 1890. [[CrossRef](#)]
14. Feng, D.; Zhao, Y.; Zhang, Y.; Sun, S.; Gao, J. Steam Gasification of Sawdust Biochar Influenced by Chemical Speciation of Alkali and Alkaline Earth Metallic Species. *Energies* **2018**, *11*, 205. [[CrossRef](#)]
15. Dahou, T.; Defoort, F.; Thiéry, S.; Grateau, M.; Campargue, M.; Bennici, S.; Jeguirim, M.; Dupont, C. The Influence of Char Preparation and Biomass Type on Char Steam Gasification Kinetics. *Energies* **2018**, *11*, 2126. [[CrossRef](#)]
16. Al-Badri, S.; Jiang, Y.; Wagland, S. Possible Interactions and Interferences of Copper, Chromium, and Arsenic during the Gasification of Contaminated Waste Wood. *Energies* **2018**, *11*, 1966. [[CrossRef](#)]
17. Lin, X.; Liu, Q.; Liu, Z. Estimation of Effective Diffusion Coefficient of O₂ in Ash Layer in Underground Coal Gasification by Thermogravimetric Apparatus. *Energies* **2018**, *11*, 460. [[CrossRef](#)]
18. Kim, J.; Oh, H.; Lee, S.; Yoon, Y. Advanced One-Dimensional Entrained-Flow Gasifier Model Considering Melting Phenomenon of Ash. *Energies* **2018**, *11*, 1015. [[CrossRef](#)]
19. Abdeljaoued, A.; Querejeta, N.; Durán, I.; Álvarez-Gutiérrez, N.; Pevida, C.; Chahbani, M. Preparation and Evaluation of a Coconut Shell-Based Activated Carbon for CO₂/CH₄ Separation. *Energies* **2018**, *11*, 1748. [[CrossRef](#)]
20. Peredo-Mancilla, D.; Ghouma, I.; Hort, C.; Matei Ghimbeu, C.; Jeguirim, M.; Bessieres, D. CO₂ and CH₄ Adsorption Behavior of Biomass-Based Activated Carbons. *Energies* **2018**, *11*, 3136. [[CrossRef](#)]
21. Saletník, B.; Zagula, G.; Bajcar, M.; Czernicka, M.; Puchalski, C. Biochar and Biomass Ash as a Soil Ameliorant: The Effect on Selected Soil Properties and Yield of Giant Miscanthus (*Miscanthus x giganteus*). *Energies* **2018**, *11*, 2535. [[CrossRef](#)]



© 2019 by the authors. Licensee MDPI, Basel, Switzerland. This article is an open access article distributed under the terms and conditions of the Creative Commons Attribution (CC BY) license (<http://creativecommons.org/licenses/by/4.0/>).

Article

CO₂ and CH₄ Adsorption Behavior of Biomass-Based Activated Carbons

Deneb Peredo-Mancilla ^{1,2,*}, Imen Ghouma ³, Cecile Hort ², Camelia Matei Ghimbeu ³, Mejdi Jeguirim ³ and David Bessieres ¹

¹ CNRS/Total/Univ Pau & Pays Adour/ E2S UPPA, Laboratoire des Fluides Complexes et Leurs Reservoirs-IPRA, UMRS5150, 64000 Pau, France; david.bessieres@univ-pau.fr

² Univ Pau & Pays Adour/ E2S UPPA, Laboratoire de Thermique, Energetique et Procedes-IPRA, EA1932, 64000 Pau, France; cecile.hort@univ-pau.fr

³ Institut de Sciences des Matériaux de Mulhouse, UMR 7661 CNRS, 15 rue Jean Starcky, 68057 Mulhouse, France; imenghouma83@gmail.com (I.G.); camelia.ghimbeu@uha.fr (C.M.G.); mejdi.jeguirim@uha.fr (M.J.)

* Correspondence: peredo-mancilla.jd@univ-pau.fr

Received: 25 July 2018; Accepted: 8 November 2018; Published: 13 November 2018

Abstract: The aim of the present work is to study the effect of different activation methods for the production of a biomass-based activated carbon on the CO₂ and CH₄ adsorption. The influence of the activation method on the adsorption uptake was studied using three activated carbons obtained by different activation methods (H₃PO₄ chemical activation and H₂O and CO₂ physical activation) of olive stones. Methane and carbon dioxide pure gas adsorption experiments were carried out at two working temperatures (303.15 and 323.15 K). The influence of the activation method on the adsorption uptake was studied in terms of both textural properties and surface chemistry. For the three adsorbents, the CO₂ adsorption was more important than that of CH₄. The chemically-activated carbon presented a higher specific surface area and micropore volume, which led to a higher adsorption capacity of both CO₂ and CH₄. For methane adsorption, the presence of mesopores facilitated the diffusion of the gas molecules into the micropores. In the case of carbon dioxide adsorption, the presence of more oxygen groups on the water vapor-activated carbon enhanced its adsorption capacity.

Keywords: CO₂ adsorption; CH₄ adsorption; biomass; activated carbon

1. Introduction

As part of the efforts being made to fight climate change, governments of 195 countries signed the Paris Agreement, in which they agreed to keep the increase of the global average temperature well below 2 °C from the preindustrial temperatures [1]. In order to meet this target, the EU set a 20-20-20 goal: 20% increase of energy efficiency, 20% reduction of greenhouse gas (GHG) emissions and 20% of EU energy from renewables by 2020. Furthermore, 10% of transportation fuels have to come from renewable sources such as biofuels [2].

Biogas is a gaseous mixture produced when organic matter is degraded by micro-organisms under anaerobic conditions in a process known as anaerobic digestion (AD); its main components are methane (CH₄) in a concentration of 50–70 vol% and carbon dioxide (CO₂) ranging from 30–45 vol%. Collected biogas can be directly burned to produce electricity with an efficiency of roughly 38% [3]. Alternatively, the energy density of biogas can be increased by an upgrading process in which the non-combustible gas (CO₂) and other impurities are separated to produce biomethane, a highly-purified methane stream (around 98% purity), which can function as a vehicle fuel or can also be injected into the natural gas grid.

The use of biogas and biomethane as alternative energy sources has gained attention, because it results in the reduction of greenhouse gases from both the burning of fossil fuels and from the landfill of organic wastes, which accounts for 3.2% of the total GHG emissions of the EU. Consequently, in Europe, more than 90% of the produced biogas is already being used for electricity generation, and the upgrading of biogas is being promoted more and more [4]. EU energy production from biomethane rose from 752 GWh in 2011 to 17.264 GWh in 2016 (+16.512 GWh). Moreover, in 2016, biomethane production in Europe increased by 4.971 GWh (+40%), proving an accelerated development in the sector [5].

Adsorption-based processes have been widely explored for the upgrading of biogas. They present several advantages such as relatively low energy requirements and low capital investment costs, flexibility of design, safety and simplicity of operation, as well as a high separation efficiency [6]. In this type of separation technology, the components of a gas mixture are separated by their molecular characteristics and affinity to an adsorbent material. For this purpose, a variety of materials have been studied including zeolites [7–9], carbon molecular sieves (CMS) [10–12], metal organic frameworks (MOFs) [13–15] and activated carbons (ACs) [16–18]. Among these materials, activated carbons present advantages in terms of: (i) hydrophobicity; thus, there is no need for a drying step before upgrading; (ii) low heat of adsorption, therefore a low energy of regeneration; (iii) the possibility of heteroatoms' functionalization to modify their adsorption behavior; and (iv) high CO₂ adsorption capacity at ambient pressure [19]. Furthermore, activated carbons can be produced with a lower cost than other adsorbents, with a wide range of available precursor materials. In fact, any carbonaceous material can be used as a precursor for activated carbon production as long as it has a low ash content and a high proportion of carbon [20]. In this sense, the use of agro-industrial wastes as an alternative to coal and wood as precursors for activated carbon production has been widely studied [21–23]. This waste-valorization process reduces the environmental and economic costs associated with the precursors while eliminating the need for disposal or incineration of unwanted agricultural by-products [24]. Materials such as corn cobs, palm shells, starch, coconut shells, durian shell, olive stones and bamboo have already been studied for activated carbon production [19,25–32]. In particular, olive stones are seen as suitable precursors, giving activated carbon with high adsorption capacities, important mechanical strength and low ash content [29,33]. A complete review of precursors, activation methods and applications of biomass-based activated carbons is available elsewhere [34].

Depending on the activation conditions, ACs can present surface areas as high as 3000 m² g⁻¹. Activated carbons can be produced in two ways: physical activation and chemical activation. Physical activation is a two-step process that begins with the carbonization of the precursor at high temperatures (up to 1073 K), a process in which the volatile compounds present in the precursor are removed under an inert atmosphere (i.e., nitrogen atmosphere) producing a carbon-rich material. Carbonization is followed by the activation step: the material is exposed to an oxidizing gas current (such as air, CO₂ and water vapor) at a temperature between 1073 and 1273 K. On the other hand, chemical activation consists of the immersion of the raw material into a dehydrating agent followed by a heat treatment step. Examples of dehydrating agents are sodium and potassium hydroxide (KOH and NaOH), zinc chloride (ZnCl₂) and phosphoric acid (H₃PO₄). Chemical activation with KOH results in activated carbons with a high micropore volume, a key factor for CH₄ and CO₂ adsorption; nevertheless, this activation agent presents the disadvantage of low production yields due to the presence of potassium atoms on the resulting structure, which lowers the activated carbon yield; thus, the carbon content of the obtained activated carbon is lower than that of the precursor material. The use of ZnCl as the activation agent has environmental disadvantages due to zinc chloride's high corrosivity. Therefore, H₃PO₄ has become the most used impregnation agent for AC production [35].

Different activation methods and activation conditions (i.e., temperature and time of activation) result in differences in the textural properties such as surface area, pore size distribution and micropore volume, as well as in the chemical properties of the obtained activated carbons. The textural properties are the most determining factor of the adsorption behavior in a physical adsorption process.

However, specific interactions between the adsorbed gas and the adsorbent may also play a role in the adsorption process, and they are unique for each adsorbent/adsorbate pair [36]. Therefore, it is necessary to establish the best activation method for each particular adsorption process.

Several studies have been published on the CH₄ and CO₂ adsorption capacity of CO₂ physically-activated carbon, as well as KOH chemically-activated carbons, but a less important number of works report H₃PO₄ activation [19,25,31,35,37–42]. The literature review shows that the use of olive stones as precursor materials for activated carbon production is a promising alternative for biogas upgrading with the additional advantage of waste valorization. In this context, the present work provides a novel systematic analysis of the influence of both the textural properties and surface chemistry of olive stone activated carbons on the methane and carbon dioxide adsorption. The effect of the activation method (physical versus chemical activation) on the properties of the obtained activated carbons is also discussed. To this end, the adsorption capacity of both methane and carbon dioxide is determined for three activated carbons produced from olive stones by different activation methods: CO₂ physical activation, H₂O physical activation and H₃PO₄ chemical activation. The factors influencing the gas adsorption capacity are discussed in terms of the effect of the activation method on both the textural and chemical properties of the obtained activated carbon.

2. Materials

2.1. Sample Preparation

Three activated carbons were prepared using olive stones provided by an olive oil factory located in Zarzis (Tunisia); two of them were obtained by physical activation and the other one by chemical activation. Prior to the activation procedures, the raw materials, were thoroughly washed with hot distilled water, dried under ambient conditions for 24 h and crushed to form particles with a diameter between 1 and 3 mm. The activated carbon preparation methods are summarized in this section. A detailed description of the selection procedure of the optimal activation conditions and sample characterization can be found in [43–45].

2.1.1. Physical Activation

Two physical activation methods were carried out: activation with water vapor and activation with carbon dioxide. Both methods followed a two-step scheme in which the first step was the carbonization of the precursor under a continuous flow of purified nitrogen with a flow rate of 10 NL/h. Using a heating velocity of 5 K/min, the precursor was heated from room temperature to a temperature of 873 K and kept at this final temperature for 60 min. Nitrogen flow was used in order to evacuate the residual oxygen from the system. The second step was the activation of the samples consisting of placing the sample under a gas flow of the activation agent at a flow velocity of 10 NL/h and a temperature of 1023 K for 360 min (temperature ramp of 15 K/min). For the water vapor activated carbon (AC-H₂O), the activation agent was water 70 vol. % in N₂. Meanwhile, for CO₂ activation, a flow of pure carbon dioxide was employed.

2.1.2. Chemical Activation

The olive stones were immersed in an orthophosphoric acid aqueous solution (50% *w/w*) at a weight ratio of 1:3. The mixture was kept under stirring for 9 h at 383 K. Consecutively, the solution was filtrated, dried and flushed by a stream of nitrogen at a temperature of 443 K for 30 min and an extra 150 min at 683 K. The heating velocity during this whole procedure was 5 K/min. The sample, referred to as AC-H₃PO₄, had a chemical activation yield of 33 wt%.

2.2. Samples Properties

The characterization of the activated carbons was done by means of textural properties (such as surface area and pore volume) and surface chemistry. The specific surface area was calculated by means

of the Brunauer–Emmett–Teller (BET) method [46] from the linear plot of the nitrogen adsorption isotherm at 77 K in the relative pressure range of 0.05–0.15 (Figure S1 of the Supplementary Materials). Total pore volume was determined by the amount of nitrogen adsorbed by each material at a relative pressure $P/P^\circ = 0.99$. The t -plot method was used for the calculation of the micropore volume. The mesopore volume was defined as the difference between the total pore volume and the micropore volume. Finally, the pore size distribution (PSD) (Figure S2 of the Supplementary Materials) was obtained by non-local density functional theory (NLDFT) using a model for slit carbon pores. The textural properties of the three activated carbons are summarized in Table 1 and can also be found in the literature [43]. The three activated carbons are mainly microporous. The water vapor activated carbon has a higher total pore volume V_{TOT} due to the presence of an important volume of mesopores ($V_{meso} = 0.30 \text{ cm}^3 \text{ g}^{-1}$). The presence of mesopores on water vapor-activated carbons due to a higher gasification of the carbon source of the precursor has been previously reported [43,47]. On the other hand, the chemically-activated carbon AC-H₃PO₄ has significantly higher specific surface area (SSA) and micropore volume V_μ than the physically-activated ones, in agreement with the literature [48].

Table 1. Textural properties of carbon materials. SSA, specific surface area; AC, activated carbon.

Sample	SSA ($\text{m}^2 \text{ g}^{-1}$)	$V_\mu (\text{cm}^3 \text{ g}^{-1})$	$V_{TOT} (\text{cm}^3 \text{ g}^{-1})$	$V_{meso} (\text{cm}^3 \text{ g}^{-1})$
AC-H ₃ PO ₄	1178	0.45	0.49	0.04
AC-CO ₂	757	0.30	0.32	0.02
AC-H ₂ O	754	0.28	0.58	0.30

The surface chemistry of the adsorbent can be of great importance for the adsorption process; for this reason, the type and quantity of surface oxygenated groups were determined by means of a home-made temperature programmed desorption device coupled with a mass spectrometer (TPD-MS). In the TPD-MS experiments, a sample weighting 10 mg of each activated carbon was placed in a quartz tube that was introduced to an oven. The temperature of the oven was then increased at a rate of 5 K per minute under vacuum conditions. The surface properties of the sample were analyzed in the temperature range 298–1173 K. During the heating process, the quantitative evolution of gases was analyzed by mass spectrometry. The total amount of emitted CO and CO₂ during the TPD-MS analysis was obtained by integration of the desorption peaks (see Table 2). With the increase of temperature, oxygenated groups decomposed into CO₂ and CO. The desorption temperature gives information about the nature of oxygenated groups present on the carbon surface. Furthermore, by correlation between diffuse reflectance infrared Fourier transform spectroscopy (DRIFTS) spectra of different activated carbons and their TPD-MS profiles, it has been established that the emission of carbon dioxide results from the decomposition of lactones, carboxylic acids and anhydrides, while carbon monoxide is emitted by the decomposition of groups such as phenols, ethers and quinones [49].

Table 2. Cumulated amounts of the emitted CO and CO₂ during the temperature programmed desorption (TPD-MS) analysis of carbon materials.

Sample	CO (mmol g^{-1})	CO ₂ (mmol g^{-1})
AC-H ₃ PO ₄	3.43	0.72
AC-CO ₂	1.06	0.38
AC-H ₂ O	1.25	0.39

In this context, the chemically-activated carbon (AC-H₃PO₄) presented higher amounts of oxygenated groups, mainly carboxylic acids, quinones and anhydrides. Among the physically-activated carbons, the water vapor activation resulted in more surface oxygen in the form of phenol and carboxylic acids. Meanwhile, carbon dioxide activation resulted in the formation of quinones, lactones and carboxylic acids on the activated carbon surface [43].

3. Experimental Methodology

3.1. High Pressure Manometric Adsorption Setup

The instrument used in the present study was a high pressure (HP) manometric device. A schematic view of this “homemade” apparatus is provided in Figure 1. The fundamental elements of this apparatus are the dosing cell (V_{dos}) and the adsorption cell (V_{ads}). The pressure was measured by a MKS pressure transducer Baratron Type 121 A (MKS Instruments, München, Deutschland). (0.01% uncertainty in the full scale from vacuum to 3.3 MPa) connected to the dosing cell. The two cells were isolated by spherical valves, thus limiting the “dead space” volume. During the adsorption experiments, the isothermal condition of the system was ensured by a heating wire controlled by a Eurotherm 3208 PID. (Schneider Electric, Worthing, United Kingdom). Thermocouples located at several points of the instrument allowed verifying the non-appearance of temperature gradients within the system. This setup was designed to operate over wide a range of pressure (0–3.3 MPa) and temperature up to 373.15 K [50,51].

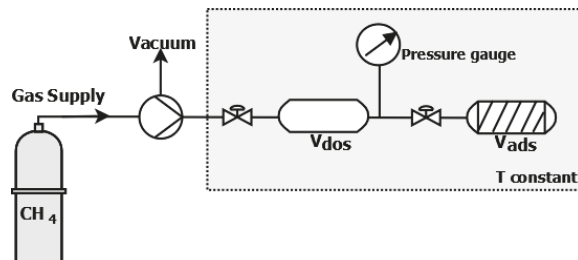


Figure 1. Schematic diagram of the high pressure and high temperature (HP/HT) manometric adsorption setup.

3.2. Determination of Excess Adsorption

Prior to the adsorption experiments, both the dosing cell volume and adsorption cell volume need to be calculated. The volume of the dosing cell was measured by a gravimetric scheme in which the pressure change at a given temperature due to a known quantity of carbon dioxide (CO_2) was recorded, using the NIST isothermal properties of carbon dioxide, the corresponding volume was calculated [52]. The adsorption cell accessible volume, also known as void volume, in the presence of the sample of activated carbon was calculated by helium (He) expansions from the dosing cell to the adsorption cell (helium is considered as a non-sorbing gas). The experimental methodology applied for the adsorption isotherms’ measurement was based on a mass balance principle. The uncertainty in the calculations of the void and adsorption cell volume was always less than 0.5%. In all cases, an out-gassing process consisting of keeping the sample under vacuum conditions at 473 K for 10 h was performed before any experiment. The adsorption isotherms were obtained by an accumulative process: successive doses (≈ 3 bar) of the adsorbate (CH_4 or CO_2) were introduced into the dosing cell and expanded into the adsorption cell. The stability of the pressure was the chosen indicator of equilibrium conditions. The reproducibility of the experiment was tested by repeating one of the adsorption isotherm 3 times, and the absolute standard deviation was found to be less than 1%.

3.3. Parametrization of Excess Adsorption Isotherms

The excess adsorption isotherms were fitted to a modified Langmuir model:

$$n_{exc} = n_L \frac{p}{p + p_L} \left(1 - \frac{\rho_g(p, T)}{\rho_{ads}} \right) \quad (1)$$

In this expression, n_{exc} represents the adsorbed amount of gas (mol kg^{-1}) at a pressure p (MPa); p_L is the pressure at which half of the adsorption sites are occupied (monolayer), also known as the Langmuir pressure; n_L is the maximum Langmuir capacity, which corresponds to the adsorbed amount in which the monolayer is filled; ρ_g is the gas density (kg m^{-3}) at pressure p and temperature T . Meanwhile, ρ_{ads} (kg m^{-3}) stands for the adsorbed phase density; in this work, it was fixed to the inverse of the van der Waals volume of each gas (373 kg m^{-3} for methane and 1027 kg m^{-3} for carbon dioxide) [53]. The Langmuir model has the advantage of taking into account the volume of the adsorbed phase. It has a theoretical basis, whilst other models such as Toth (1995) [54] and Sips (1948) [55] are empirical. This model was initially developed for the low pressure region; nevertheless, it provides a reasonable estimation of the excess adsorption isotherms at higher pressures [17].

The best fit of the Langmuir model for each adsorption isotherm was obtained by minimizing the root mean square error (RMSE) provided by Equation (2) [7]:

$$RMSE = \frac{1}{k} \cdot \sqrt{\sum_1^k (n_{exp} - n_{calc})^2} \quad (2)$$

where n_{exp} and n_{calc} are the experimental and calculated adsorption amounts in mol kg^{-1} at a pressure p for a number k of data points in the adsorption isotherm.

4. Results

CH_4 and CO_2 adsorption isotherms were obtained for the set of three olive stone-based activated carbons (Figures 2 and 3) up to a pressure of 3.2 MPa at two working temperatures: 303.15 and 323.15 K, with a reproducibility superior to 99% (average absolute deviation of less than 1%). All the isotherms were fitted by the Langmuir two-parameter model (see Equation (1)), and the obtained fitting parameters and root mean square error (RMSE) are presented in Table 3 (CH_4 adsorption) and Table 4 (CO_2 adsorption). The goodness of the fitting process is depicted by the RMSE values; values under 0.09 were obtained for the fitting of all the isotherms.

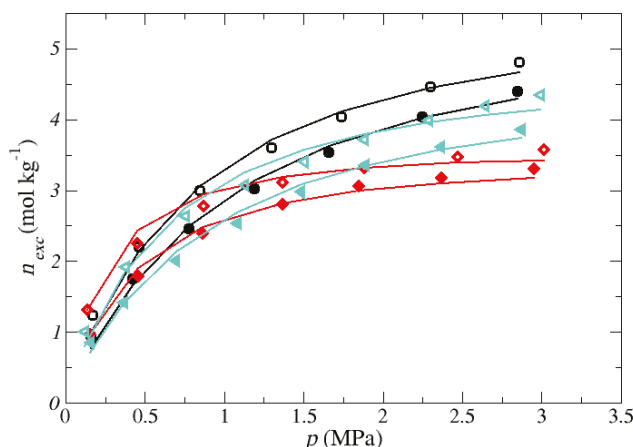


Figure 2. CH_4 adsorption isotherms for the three olive stone-based activated carbons: AC- H_3PO_4 (black circles), AC- CO_2 (red diamonds) and AC- H_2O (turquoise triangles). Open symbols represent the adsorption data at 303.15 K, while the data at 323.15 are shown by the filled symbols. Uncertainties: $\Delta p = 0.01$ MPa, $\Delta T = 0.2$ K. The obtained Langmuir fitting isotherms are shown by the solid lines.

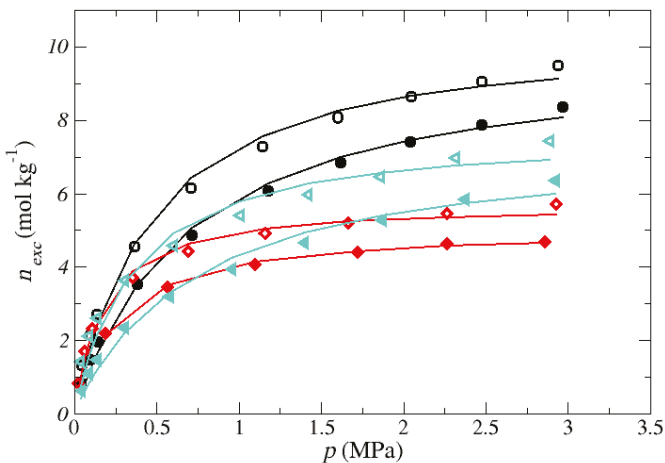


Figure 3. CO_2 adsorption isotherms for the three olive stone-based activated carbons: AC- H_3PO_4 (black circles), AC- CO_2 (red diamonds) and AC- H_2O (turquoise triangles). Open symbols represent the adsorption data at 303.15 K, while the data at 323.15 are shown by the filled symbols. Uncertainties: $\Delta p = 0.01 \text{ MPa}$, $\Delta T = 0.2 \text{ K}$. The obtained Langmuir fitting isotherms are shown by the solid lines.

A higher adsorption of carbon dioxide than methane can be noticed for the three ACs (Figures 2 and 3). This is a typical behavior of activated carbon adsorption that can be explained by the presence of a quadrupole moment on the molecule of carbon dioxide that leads to stronger adsorptive/adsorbent interactions. Another possible explanation can be given in terms of the critical point of the gases: the critical temperature (190 K) and critical pressure (4.59 MPa) of methane were much lower than those of carbon dioxide (304.45 K and 7.38 MPa), which means that carbon dioxide was in the form of a condensable vapor, while methane acted as a supercritical gas at the adsorption conditions. A lower adsorption and lower maximum Langmuir capacity (n_L) upon an increase in the adsorand Tables 3 and 4, indicating a physical adsorption process. Furthermore, for both adsorptives, the chemically-activated carbon AC- H_3PO_4 showed a higher adsorption capacity; the adsorption tendency varied in the following order: AC- H_3PO_4 > AC- H_2O > AC- CO_2 .

Table 3. Langmuir fitting parameters for the CH_4 adsorption isotherms.

CH ₄ Adsorption				
Sample	Temperature (K)	n_L (mol kg ⁻¹)	ρ_L (MPa)	RMSE
AC- H_3PO_4	303.15	6.518	0.932	0.042
	323.15	6.369	1.182	0.037
AC- CO_2	303.15	3.913	0.273	0.043
	323.15	3.830	0.076	0.031
AC- H_2O	303.15	5.417	0.714	0.067
	323.15	5.301	1.011	0.056

The superior adsorption of AC- H_3PO_4 can be explained in regards to the textural properties of the samples (see Table 1); the chemically-activated carbon had the highest specific surface area and micropore volume, both adsorption-enhancing factors. A higher surface area means more available physisorption sites, while a linear relationship between the micropore volume and the adsorption of both methane and carbon dioxide has been reported [21,56]. Concerning the difference in the methane adsorption capacity of the two physically-activated carbons, the presence of the

mesoporosity of the structure of the water vapor-activated carbon AC-H₂O is thought to be the determining factor. Both physically-activated carbons had similar SSA and micropore volume, with the only difference being the mesopore volume. In fact, it has been shown that activated carbons that combine both micropores and mesopores can adsorb a significantly higher amount of CH₄ than their totally microporous counterparts [57].

Table 4. Langmuir fitting parameters for the CO₂ adsorption isotherms.

CO ₂ Adsorption				
Sample	Temperature (K)	n_L (mol kg ⁻¹)	ρ_L (MPa)	RMSE
AC-H ₃ PO ₄	303.15	10.873	0.488	0.080
	323.15	10.254	0.733	0.065
AC-CO ₂	303.15	5.878	0.181	0.059
	323.15	5.191	0.273	0.020
AC-H ₂ O	303.15	7.968	0.371	0.073
	323.15	7.721	0.772	0.087

While methane adsorption by activated carbons is only influenced by the textural properties of the adsorbent, the carbon dioxide adsorption is also thought to be related to the surface chemistry. In the present work, the influence of the surface chemistry was depicted by normalizing the CO₂ adsorption isotherms by the surface area (Figure 4). One could expect that by doing this, the adsorption of the chemically-activated carbon would still be the most important due to a higher micropore volume. In reality, the AC-H₂O showed a higher adsorption. Chemical activation with phosphoric acid (H₃PO₄) was reported to produce acid activated carbon surfaces [58], which seems to reduce the interactions between the basic surface groups and the carbon dioxide molecules, explaining its lower adsorption when the textural effect is eliminated by normalizing the adsorption isotherms by the specific surface area. However, the negative influence of acid surface groups on the AC-H₃PO₄ was small compared to the effect of its higher surface area, thus showing a higher adsorption capacity when no normalization of the isotherms was done (Table 4).

Among the two physically-activated carbons, AC-H₂O had the highest quantity of oxygenated surface groups (Table 2), which explains its dominant adsorption when SSA normalized. An increase in the CO₂ adsorption capacity in the presence of oxygen-containing surface functionalities by means of acid-base interactions and hydrogen bond formation between the adsorbate and the activated carbons surface was shown [59,60]. The high electronic density of oxygen on the oxygenated surface groups, due to electron gain from the carbon surface atoms, allowed them to act as electron-donors, in which case the CO₂ adsorbate molecules behaved as basic groups.

Table 5 shows the comparison of the adsorption capacities of the activated carbons studied in this work with other biomass-based activated carbons of the literature. It can be seen that the adsorption values were well in the range reported in the literature for both carbon dioxide and methane. Their competitive adsorption capacities and higher carbon dioxide adsorption capacity over methane made the olive stone activated carbons a suitable material for further studies on the CH₄ and CO₂ storage and separation.

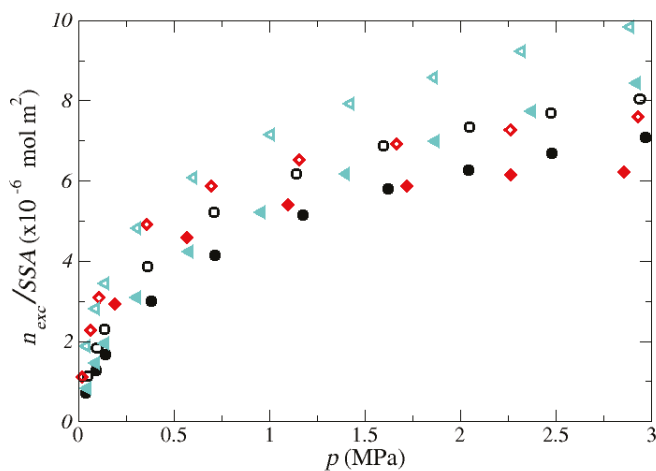


Figure 4. SSA normalized CO₂ adsorption isotherms of the activated carbons: AC-H₃PO₄ (black circles), AC-CO₂ (red diamonds) and AC-H₂O (turquoise triangles). Open symbols represent the adsorption data at 303.15 K, while the data at 323.15 are shown by the filled symbols 323.15 K.

Table 5. Adsorption capacities of different biomass-based adsorbents.

CO ₂ and CH ₄ Adsorption Capacity					
Sample	Precursor	Activation Agent	Temperature (K)	CH ₄ Adsorption Capacity (mol kg ⁻¹)	CO ₂ Adsorption Capacity (mol kg ⁻¹)
AC-H ₃ PO ₄ *	Olive stones	H ₃ PO ₄	303.15	6.518	10.873
AC-CO ₂ *	Olive stones	CO ₂	303.15	3.913	5.878
AC-H ₂ O *	Olive stones	H ₂ O *	303.15	5.417	7.968
BC [19]	Babassu coconut	CO ₂	293	5.343	10.49
CS [19]	Coconut shell	CO ₂	293	7.259	14.67
Pinpel20 [61]	Wood pellets	CO ₂	303	3.36	6.66
MSS-AC [62]	Mango Seeds	H ₃ PO ₄	303	0.858	8.788
CS-H ₂ O [39]	Cherry stones	H ₂ O	303	8.36	14.45

* This work.

5. Conclusions

In this work, the effects of the textural and chemical properties of three activated carbons on the adsorption behavior of carbon dioxide and methane were studied. For this purpose, three activated carbons produced from olive stones by CO₂ physical activation, H₂O physical activation and H₃PO₄ chemical activation were employed. The activated carbons were mainly microporous. The activated carbon obtained by chemical activation with phosphoric acid of the precursor material presents a higher surface area, total pore volume and micropore volume, which led to a higher adsorption capacity for both methane and carbon dioxide. Even though the two physically-activated carbons had similar surface areas and micropore volume, the water vapor-activated carbon had also an important volume of mesopores that facilitated the diffusion of the methane molecules into the micropores; thus, its methane adsorption capacity was higher. In the case of carbon dioxide, adsorption-specific interactions between the adsorptive and adsorbent were also found to participate in the adsorption process. Amongst the two physically-activated carbons, H₂O-activated carbon had the highest content of oxygen surface group and therefore a higher CO₂ adsorption capacity. Nevertheless, even if the surface chemistry of the adsorbents can influence the adsorption of carbon dioxide, textural properties are still the main governing parameters. Finally, the three activated carbons from olive stones had a higher adsorption of carbon dioxide than methane, meaning a higher selectivity towards carbon dioxide than methane. Furthermore, their carbon dioxide and methane adsorption capacities were

found to be in the range of other biomass-based activated carbons reported in the literature, making them suitable candidates for the upgrading of biogas.

Supplementary Materials: The following are available online at <http://www.mdpi.com/1996-1073/11/11/3136/s1>. Figure S1: Adsorption and desorption of nitrogen (N₂) at 77 K on the olive stone activated carbons. Figure S2: Pore size distribution (PSD) of the olive stone activated carbons obtained by means of density functional theory (DFT). Figure S3: Emited CO₂ during temperature programmed desorption-mass spectroscopy (TPD-MS) of the olive stone activated carbons. Figure S4: Emited CO during temperature programmed desorption-mass spectroscopy (TPD-MS) of the olive stone activated carbons.

Author Contributions: Sample preparation and characterization: I.G., C.M.G. and M.J. Adsorption isotherms: D.P.-M., C.H. and D.B. Writing of the article: D.P.-M. Revision of the article content: All of the authors.

Funding: This research received no external funding

Acknowledgments: Deneb Peredo is grateful to CONACyT for the fellowship 293897 to pursue her PhD degree.

Conflicts of Interest: The authors declare no conflict of interest.

References

- European Comission. Paris Agreement. Available online: https://ec.europa.eu/clima/policies/international/negotiations/paris_en (accessed on 12 November 2018)
- European Comission. Renewable Energy. Moving towards a low carbon economy. Available online: <https://ec.europa.eu/energy/en/topics/renewable-energy> (accessed on 12 November 2018)
- Starr, K.; Villalba, G.; Gabarrell, X. Upgraded biogas from municipal solid waste for natural gas substitution and CO₂ reduction—A case study of Austria, Italy, and Spain. *Waste Manag.* **2015**, *38*, 105–116, doi:10.1016/j.wasman.2015.01.001. [CrossRef] [PubMed]
- Sahota, S.; Shah, G.; Ghosh, P.; Kapoor, R.; Sengupta, S.; Singh, P.; Vijay, V.; Sahay, A.; Vijay, V.K.; Thakur, I.S. Review of trends in biogas upgradation technologies and future perspectives. *Bioresour. Technol. Rep.* **2018**, *1*, 79–88, doi:10.1016/j.biteb.2018.01.002. [CrossRef]
- EBA European Biogas Association. EBA Statistical Report 2017 Published Soon. Available online: <http://european-biogas.eu/2017/12/14/eba-statistical-report-2017-published-soon/> (accessed on 12 November 2018)
- Angelidaki, I.; Treu, L.; Tsapekos, P.; Luo, G.; Campanaro, S.; Wenzel, H.; Kougias, P.G. Biogas upgrading and utilization: Current status and perspectives. *Biotechnol. Adv.* **2018**, *36*, 452–466, doi:10.1016/j.biotechadv.2018.01.011. [CrossRef] [PubMed]
- Jiang, Y.; Ling, J.; Xiao, P.; He, Y.; Zhao, Q.; Chu, Z.; Liu, Y.; Li, Z.; Webley, P.A. Simultaneous biogas purification and CO₂ capture by vacuum swing adsorption using zeolite NaUSY. *Chem. Eng. J.* **2018**, *334*, 2593–2602, doi:10.1016/j.cej.2017.11.090. [CrossRef]
- Gong, H.; Lee, S.S.; Bae, T.H. Mixed-matrix membranes containing inorganically surface-modified 5A zeolite for enhanced CO₂/CH₄ separation. *Microporous Mesoporous Mater.* **2017**, *237*, 82–89, doi:10.1016/j.micromeso.2016.09.017. [CrossRef]
- Kennedy, D.A.; Tezel, F.H. Cation exchange modification of clinoptilolite—Screening analysis for potential equilibrium and kinetic adsorption separations involving methane, nitrogen, and carbon dioxide. *Microporous Mesoporous Mater.* **2018**, *262*, 235–250, doi:10.1016/j.micromeso.2017.11.054. [CrossRef]
- Son, S.J.; Choi, J.S.; Choo, K.Y.; Song, S.D.; Vijayalakshmi, S.; Kim, T.H. Development of carbon dioxide adsorbents using carbon materials prepared from coconut shell. *Korean J. Chem. Eng.* **2005**, *22*, 291–297, doi:10.1007/BF02701500. [CrossRef]
- Rocha, L.A.; Andreassen, K.A.; Grande, C.A. Separation of CO₂/CH₄ using carbon molecular sieve (CMS) at low and high pressure. *Chem. Eng. Sci.* **2017**, *164*, 148–157, doi:10.1016/j.ces.2017.01.071. [CrossRef]
- Arya, A.; Divekar, S.; Rawat, R.; Gupta, P.; Garg, M.O.; Dasgupta, S.; Nanoti, A.; Singh, R.; Xiao, P.; Webley, P.A. Upgrading biogas at low pressure by vacuum swing adsorption. *Ind. Eng. Chem. Res.* **2015**, *54*, 404–413, doi:10.1021/ie503243f. [CrossRef]
- Samarasinghe, S.A.; Chuah, C.Y.; Yang, Y.; Bae, T.H. Tailoring CO₂/CH₄ separation properties of mixed-matrix membranes via combined use of two- and three-dimensional metal-organic frameworks. *J. Membr. Sci.* **2018**, *557*, 30–37, doi:10.1016/j.memsci.2018.04.025. [CrossRef]

14. Zacharia, R.; Gomez, L.F.; Chahine, R.; Cossement, D.; Benard, P. Thermodynamics and kinetics of CH₄/CO₂ binary mixture separation by metal-organic frameworks from isotope exchange and adsorption breakthrough. *Microporous Mesoporous Mater.* **2018**, *263*, 165–172, doi:10.1016/j.micromeso.2017.12.011. [CrossRef]
15. Cheng, Y.; Wang, X.; Jia, C.; Wang, Y.; Zhai, L.; Wang, Q.; Zhao, D. Ultrathin mixed matrix membranes containing two-dimensional metal-organic framework nanosheets for efficient CO₂/CH₄ separation. *J. Membr. Sci.* **2017**, *539*, 213–223, doi:10.1016/j.memsci.2017.06.011. [CrossRef]
16. Yao, K.X.; Chen, Y.; Lu, Y.; Zhao, Y.; Ding, Y. Ultramicroporous carbon with extremely narrow pore distribution and very high nitrogen doping for efficient methane mixture gases upgrading. *Carbon* **2017**, *122*, 258–265, doi:10.1016/j.carbon.2017.06.073. [CrossRef]
17. Koonaphapdeelert, S.; Moran, J.; Aggarangsi, P.; Bunkham, A. Low pressure biomethane gas adsorption by activated carbon. *Energy Sustain. Dev.* **2018**, *43*, 196–202, doi:10.1016/j.esd.2018.01.010. [CrossRef]
18. Saha, D.; Nelson, K.; Chen, J.; Lu, Y.; Ozcan, S. Adsorption of CO₂, CH₄, and N₂ in Micro-Mesoporous Nanographene: A Comparative Study. *J. Chem. Eng. Data* **2015**, *60*, 2636–2645, doi:10.1021/acs.jcd.5b00291. [CrossRef]
19. Vilella, P.C.; Lira, J.A.; Azevedo, D.C.; Bastos-Neto, M.; Stefanutti, R. Preparation of biomass-based activated carbons and their evaluation for biogas upgrading purposes. *Ind. Crops Prod.* **2017**, *109*, 134–140, doi:10.1016/j.indcrop.2017.08.017. [CrossRef]
20. Rashidi, N.A.; Yusup, S. An overview of activated carbons utilization for the post-combustion carbon dioxide capture. *J. CO₂ Util.* **2016**, *13*, 1–16, doi:10.1016/j.jcou.2015.11.002. [CrossRef]
21. Serafin, J.; Narkiewicz, U.; Morawski, A.W.; Wróbel, R.J.; Michalkiewicz, B. Highly microporous activated carbons from biomass for CO₂ capture and effective micropores at different conditions. *J. CO₂ Util.* **2017**, *18*, 73–79, doi:10.1016/j.jcou.2017.01.006. [CrossRef]
22. Yadavalli, G.; Lei, H.; Wei, Y.; Zhu, L.; Zhang, X.; Liu, Y.; Yan, D. Carbon dioxide capture using ammonium sulfate surface modified activated biomass carbon. *Biomass Bioenergy* **2017**, *98*, 53–60, doi:10.1016/j.biombioe.2017.01.015. [CrossRef]
23. Hao, W.; Björkman, E.; Lilliestråle, M.; Hedin, N. Activated carbons prepared from hydrothermally carbonized waste biomass used as adsorbents for CO₂. *Appl. Energy* **2013**, *112*, 526–532, doi:10.1016/j.apenergy.2013.02.028. [CrossRef]
24. Gil, R.R.; Ruiz, B.; Lozano, M.S.; Fuente, E. Influence of the pyrolysis step and the tanning process on KOH-activated carbons from biocollagenic wastes. Prospects as adsorbent for CO₂ capture. *J. Anal. Appl. Pyrolysis* **2014**, *110*, 194–204, doi:10.1016/j.jaat.2014.09.001. [CrossRef]
25. Bagheri, N.; Abedi, J. Adsorption of methane on corn cobs based activated carbon. *Chem. Eng. Res. Des.* **2011**, *89*, 2038–2043, doi:10.1016/j.cherd.2011.02.002. [CrossRef]
26. Arami-Niya, A.; Daud, W.M.A.W.; Mjalli, F.S. Comparative study of the textural characteristics of oil palm shell activated carbon produced by chemical and physical activation for methane adsorption. *Chem. Eng. Res. Des.* **2011**, *89*, 657–664, doi:10.1016/j.cherd.2010.10.003. [CrossRef]
27. Alabadi, A.; Razzaque, S.; Yang, Y.; Chen, S.; Tan, B. Highly porous activated carbon materials from carbonized biomass with high CO₂ capturing capacity. *Chem. Eng. J.* **2015**, *281*, 606–612, doi:10.1016/j.cej.2015.06.032. [CrossRef]
28. Chen, Y.; Zhou, L.J.; Hong, Y.Z.; Cao, F.; Li, L.; Li, J.b. Preparation of high-surface-area activated carbon from coconut shell fibers. *Carbon* **2010**, *48*, 3005, doi:10.1016/j.carbon.2010.03.059. [CrossRef]
29. Iley, M.; Marsh, H.; Rodriguez-Reinoso, F. The Adsorptive Properties of Carbonised Olive Stones. *Carbon* **1973**, *11*, 633–636, doi:10.1016/0008-6223(73)90330-8. [CrossRef]
30. Zhao, G.; Zou, G.; Hou, H.; Ge, P.; Cao, X.; Ji, X. Sulfur-doped carbon employing biomass-activated carbon as a carrier with enhanced sodium storage behavior. *J. Mater. Chem. A* **2017**, *5*, 24353–24360, doi:10.1039/C7TA07860A. [CrossRef]
31. Yakout, S.M.; Sharaf El-Deen, G. Characterization of activated carbon prepared by phosphoric acid activation of olive stones. *Arab. J. Chem.* **2016**, *9*, S1155–S1162, doi:10.1016/j.arabjc.2011.12.002. [CrossRef]
32. Wei, H.; Deng, S.; Hu, B.; Chen, Z.; Wang, B.; Huang, J.; Yu, G. Granular Bamboo-Derived Activated Carbon for High CO₂ Adsorption: The Dominant Role of Narrow Micropores. *ChemSusChem* **2012**, *5*, 2354–2360, doi:10.1002/cssc.201200570. [CrossRef] [PubMed]

33. Álvarez-Gutiérrez, N.; García, S.; Gil, M.V.; Rubiera, F.; Pevida, C. Towards bio-upgrading of biogas: Biomass waste-based adsorbents. *Energy Procedia* **2014**, *63*, 6527–6533, doi:10.1016/j.egypro.2014.11.688. [CrossRef]
34. González-García, P. Activated carbon from lignocellulosics precursors: A review of the synthesis methods, characterization techniques and applications. *Renew. Sust. Energy Rev.* **2018**, *82*, 1393–1414, doi:10.1016/j.rser.2017.04.117. [CrossRef]
35. Gil, M.V.; Martínez, M.; García, S.; Rubiera, F.; Pis, J.J.; Pevida, C. Response surface methodology as an efficient tool for optimizing carbon adsorbents for CO₂ capture. *Fuel Process. Technol.* **2013**, *106*, 55–61, doi:10.1016/j.fuproc.2012.06.018. [CrossRef]
36. Djeridi, W.; Ben Mansour, N.; Ouederni, A.; Llewellyn, P.L.; El Mir, L. Influence of the raw material and nickel oxide on the CH₄ capture capacity behaviors of microporous carbon. *Int. J. Hydrogen Energy* **2015**, *40*, 13690–13701, doi:10.1016/j.ijhydene.2015.05.010. [CrossRef]
37. Soudani, N.; Najar-Souissi, S.; Abderkader-Fernandez, V.; Ouederni, A. Effects of nitrogen plasma treatment on the surface characteristics of olive stone-based activated carbon. *Environ. Technol.* **2017**, *38*, 956–966, doi:10.1080/09593330.2016.1214626. [CrossRef] [PubMed]
38. Balsamo, M.; Tsintsarski, B.; Erto, A.; Budinova, T.; Petrova, B.; Petrov, N.; Lancia, A. Dynamic studies on carbon dioxide capture using lignocellulosic based activated carbons. *Adsorption* **2015**, *21*, 633–643, doi:10.1007/s10450-015-9711-7. [CrossRef]
39. Álvarez-Gutiérrez, N.; García, S.; Gil, M.V.; Rubiera, F.; Pevida, C. Dynamic Performance of Biomass-Based Carbons for CO₂/CH₄ Separation. Approximation to a Pressure Swing Adsorption Process for Biogas Upgrading. *Energy Fuels* **2016**, *30*, 5005–5015, doi:10.1021/acs.energyfuels.6b00664. [CrossRef]
40. Erto, A.; Tsintsarski, B.; Balsamo, M.; Budinova, T.; Lancia, A.; Petrova, B.; Petrov, N. Synthesis of Activated Carbons by Thermal Treatments of Agricultural Wastes for CO₂ Capture from Flue Gas. *Combust. Sci. Technol.* **2016**, *188*, 581–593, doi:10.1080/00102202.2016.1138809. [CrossRef]
41. Moussa, M.; Bader, N.; Querejeta, N.; Durán, I.; Pevida, C.; Ouederni, A. Toward sustainable hydrogen storage and carbon dioxide capture in post-combustion conditions. *J. Environ. Chem. Eng.* **2017**, *5*, 1628–1637, doi:10.1016/j.jece.2017.03.003. [CrossRef]
42. Balsamo, M.; Silvestre-Albero, A.; Silvestre-Albero, J.; Erto, A.; Rodríguez-Reinoso, F.; Lancia, A. Assessment of CO₂ adsorption capacity on activated carbons by a combination of batch and dynamic tests. *Langmuir* **2014**, *30*, 5840–5848, doi:10.1021/la500780h. [CrossRef] [PubMed]
43. Ghouma, I.; Jeguirim, M.; Sager, U.; Limousy, L.; Bennici, S.; Däuber, E.; Asbach, C.; Ligotski, R.; Schmidt, F.; Ouederni, A. The potential of activated carbon made of agro-industrial residues in NO_x immissions abatement. *Energies* **2017**, *10*, 508, doi:10.3390/en10101508. [CrossRef]
44. Ghouma, I.; Jeguirim, M.; Dorge, S.; Limousy, L.; Matei Ghimbeu, C.; Ouederni, A. Activated carbon prepared by physical activation of olive stones for the removal of NO₂ at ambient temperature. *Comptes Rendus Chimie* **2015**, *18*, 63–74, doi:10.1016/j.crci.2014.05.006. [CrossRef]
45. Limousy, L.; Ghouma, I.; Ouederni, A.; Jeguirim, M. Amoxicillin removal from aqueous solution using activated carbon prepared by chemical activation of olive stone. *Environ. Sci. Pollut. R.* **2017**, *24*, 9993–10004, doi:10.1007/s11356-016-7404-8. [CrossRef] [PubMed]
46. Brunauer, S.; Emmett, P.H.; Teller, E. Adsorption of Gases in Multimolecular Layers. *J. Am. Chem. Soc.* **1938**, *60*, 309–319. [CrossRef]
47. Román, S.; Ledesma, B.; Álvarez-Murillo, A.; Al-Kassir, A.; Yusaf, T. Dependence of the microporosity of activated carbons on the lignocellulosic composition of the precursors. *Energies* **2017**, *10*, 542, doi:10.3390/en10040542. [CrossRef]
48. Song, T.; Liao, J.M.; Xiao, J.; Shen, L.H. Effect of micropore and mesopore structure on CO₂ adsorption by activated carbons from biomass. *Xinxing Tan Cailiao/New Carbon Mater.* **2015**, *30*, 156–166, doi:10.1016/S1872-5805(15)60181-0. [CrossRef]
49. Figueiredo, J.; Pereira, M.; Freitas, M.; Órfão, J. Modification of the surface chemistry of activated carbons. *Carbon* **1999**, *37*, 1379–1389, doi:10.1016/S0008-6223(98)00333-9. [CrossRef]
50. Ortiz Cancino, O.P.; Peredo Mancilla, D.; Pozo, M.; Pérez, E.; Bessieres, D. Effect of Organic Matter and Thermal Maturity on Methane Adsorption Capacity on Shales from the Middle Magdalena Valley Basin in Colombia. *Energy Fuels* **2017**, *31*, 11698–11709, doi:10.1021/acs.energyfuels.7b01849. [CrossRef]

51. Peredo-Mancilla, D.; Hort, C.; Jeguirim, M.; Ghimbeu, C.M.; Limousy, L.; Bessieres, D. Experimental Determination of the CH₄ and CO₂ Pure Gas Adsorption Isotherms on Different Activated Carbons. *J. Chem. Eng. Data* **2018**, doi:10.1021/acs.jced.8b00297. [CrossRef]
52. National Institute of Standards and Technology NIST, U.S. Secretary of Commerce. Isothermal Properties for Carbon Dioxide. Available online: <https://webbook.nist.gov/cgi/cbook.cgi?Name=carbon+dioxide&Units=SI> (accessed on 12 November 2018).
53. Gensterblum, Y.; Merkel, A.; Busch, A.; Krooss, B.M. High-pressure CH₄ and CO₂ sorption isotherms as a function of coal maturity and the influence of moisture. *Int. J. Coal Geol.* **2013**, *118*, 45–57, doi:10.1016/j.coal.2013.07.024. [CrossRef]
54. Tóth, J. Uniform interpretation of gas/solid adsorption. *Adv. Colloid Interface Sci.* **1995**, *55*, 1–239, doi:10.1016/0001-8686(94)00226-3. [CrossRef]
55. Sips, R. On the Structure of a Catalyst Surface. *J. Chem. Phys.* **1948**, *16*, 490–495, doi:10.1063/1.1746922. [CrossRef]
56. Lozano-Castelló, D.; Cazorla-Amorós, D.; Linares-Solano, A.; Quinn, D.F. Influence of pore size distribution on methane storage at relatively low pressure: Preparation of activated carbon with optimum pore size. *Carbon* **2002**, *40*, 989–1002, doi:10.1016/S0008-6223(01)00235-4. [CrossRef]
57. Casco, M.E.; Martínez-Escandell, M.; Gadea-Ramos, E.; Kaneko, K.; Silvestre-Albero, J.; Rodríguez-Reinoso, F. High-pressure methane storage in porous materials: Are carbon materials in the pole position? *Chem. Mater.* **2015**, *27*, 959–964, doi:10.1021/cm5042524. [CrossRef]
58. Nowicki, P.; Wachowska, H.; Pietrzak, R. Active carbons prepared by chemical activation of plum stones and their application in removal of NO₂. *J. Hazard. Mater.* **2010**, *181*, 1088–1094, doi:10.1016/j.jhazmat.2010.05.126. [CrossRef] [PubMed]
59. Liu, Y.; Wilcox, J. Molecular Simulation Studies of CO₂ Adsorption by Carbon Model Compounds for Carbon Capture and Sequestration Applications. *Environ. Sci. Technol.* **2013**, *47*, 95–101, doi:10.1021/es3012029. [CrossRef] [PubMed]
60. Xing, W.; Liu, C.; Zhou, Z.; Zhou, J.; Wang, G.; Zhuo, S.; Xue, Q.; Song, L.; Yan, Z. Oxygen-containing functional group-facilitated CO₂ capture by carbide-derived carbons. *Nanoscale Res. Lett.* **2014**, *9*, 1–8, doi:10.1186/1556-276X-9-189. [CrossRef] [PubMed]
61. Vivo-Vilches, J.F.; Pérez-Cadenas, A.F.; Maldonado-Hódar, F.J.; Carrasco-Marín, F.; Faria, R.P.V.; Ribeiro, A.M.; Ferreira, A.F.P.; Rodrigues, A.E. Biogas upgrading by selective adsorption onto CO₂ activated carbon from wood pellets. *J. Environ. Chem. Eng.* **2017**, *5*, 1386–1393, doi:10.1016/j.jece.2017.02.015. [CrossRef]
62. Munusamy, K.; Somani, R.S.; Bajaj, H.C. Breakthrough adsorption studies of mixed gases on mango (*Mangifera indica* L.) seed shell derived activated carbon extrudates. *J. Environ. Chem. Eng.* **2015**, *3*, 2750–2759, doi:10.1016/j.jece.2015.05.010. [CrossRef]



© 2018 by the authors. Licensee MDPI, Basel, Switzerland. This article is an open access article distributed under the terms and conditions of the Creative Commons Attribution (CC BY) license (<http://creativecommons.org/licenses/by/4.0/>).

Article

Biochar and Biomass Ash as a Soil Ameliorant: The Effect on Selected Soil Properties and Yield of Giant Miscanthus (*Miscanthus x giganteus*)

Bogdan Saletnik *, Grzegorz Zagula, Marcin Bajcar, Maria Czernicka and Czeslaw Puchalski

Department of Bioenergetics and Food Analysis, Faculty of Biology and Agriculture, Rzeszow University, Cwiklinskiej 2D, 35-601 Rzeszow, Poland; g_zagula@ur.edu.pl (G.Z.); mbajcar@ur.edu.pl (M.B.); czernicka.maria@gmail.com (M.C.); cpuchal@ur.edu.pl (C.P.)

* Correspondence: bogdan.saletnik@urz.pl; Tel.: +48-177-854-965

Received: 15 August 2018; Accepted: 20 September 2018; Published: 22 September 2018

Abstract: We assess the possibility of using biochar and ash from plant biomass to fertilise giant miscanthus (*Miscanthus x giganteus*). The paper concerns the optimisation of the combination of fertiliser applications of the aforementioned materials in the context of the plant yield obtained. There was an increase in yield of 8–68% over the two years of research when compared with the control plots. It was found that the application of biochar, ash from biomass and a combination of the two at appropriate rates as a soil additive can substitute for classic mineral fertilisers and strengthen the ecological aspects of energy crop cultivation. The interpretation of the results obtained enabled the selection of optimum fertiliser applications, resulting in a significant increase in the yield of plants and an improvement in soil chemical properties. It was found that the highest yield of dry matter of giant miscanthus plants, after both the first and second year of cultivation, was obtained by applying the fertiliser containing ash at a rate of 1.5 t ha^{-1} , together with biocarbon and the combination of biochar and ash at a rate of 1.5 t ha^{-1} .

Keywords: biochar; ash from biomass; giant miscanthus; fertilisation

1. Introduction

Plant biomass, due to its specific chemical structure and high calorific value, can be used in numerous conversion processes aimed at the production of solid, liquid and gaseous fuels [1]. The acquisition of energy from biomass is possible through its conversion in the form of direct combustion, co-incineration with coal, gasification, pyrolysis, and fermentation [2].

The factors determining the growth performance of biomass in energy crops are the choice of plant species and production cycle, including the location of the plantation and appropriate fertilisation. In turn, the proper preparation of the material and the optimisation of the technological process, including the management of waste products, i.e., ashes generated during combustion, affect the efficiency of using biomass as an energy source. Both the cultivation of energy crops and the utilisation of the ash from biomass are part of sustainable energy management and have a huge impact on the environment. Agroenergy is also recommended from an environmental protection point of view to carry out agrotechnical sanitation in contaminated areas, especially those with toxic metals [3]. Ash from biomass, according to data available in the literature, can favourably affect the physicochemical properties of soils to a comparable or even greater degree than mineral fertiliser [4]. According to the latest research, the effective improvement of the physicochemical properties of soils and the increase in fertility of less fertile soils can be obtained by using biochar. Biochar is a material formed in the process of thermal conversion of biomass under conditions of limited access of oxygen, which results in the formation of a product with a high carbon content and very good

sorption properties [5]. In addition, it was proven that biochar has high chemical reactivity to organic and inorganic compounds present in the soil environment, and therefore its potential use in the reclamation of chemically degraded soils is more and more frequently discussed. From an agricultural point of view, the introduction of biochar into soils provides many benefits by improving physical, chemical and biological properties, which in turn contributes to an increase in crop yield [6,7].

From an agricultural point of view, the introduction of biochars into soils as agents that improve their properties seems to be beneficial due to the possibility of improving the conditions for the growth, development and increased yield of crops [7]. In addition, in view of the rapid effects and relatively low costs of using them, biochar compounds are more and more often used in the remediation and soil protection process [8]. The performance of biochar introduced into the soil environment mainly depends on the raw materials used for its production, as well as the parameters of the pyrolysis process. They determine the contents of macro- and microelements, as well as harmful substances such as heavy metals. The heterogenous chemical composition of biochars allows their interaction with a large group of inorganic and organic compounds present in the soil [9]. Various properties of these materials allow reactions with mineral and organic particles in the soil, as well as the formation of mineral–organic complexes [10]. Biochars introduced into the soil are characterised by high stability and resistance to biological decomposition, which is why they are considered a highly effective agent of carbon dioxide sequestration in the soil [11]. In addition, the application of biochars not only allows the soil to increase its carbon content, but also other biogenic compounds, such as phosphorus, potassium, magnesium and nitrogen [12,14]. The high ion-exchange capacity and the specific surface of biochars contribute to the reduction of leaching of biogenic elements from the soil environment and reduce the emission of nitrogen oxide [14]. Biochars introduced into the soil as fertiliser materials also affect the increase in soil pH [15]. The research conducted so far has shown that biochars contain numerous alkaline substances, such as calcium carbonate, which may affect the soil pH, and the best results in the form of pH increase can be obtained in heavily acidified soils [16,17]. Biochar added to the soil also affects its physical properties by increasing the ability to form soil aggregates and resistance to erosion or improvement in water retention [18]. The improvement of physical properties of soils after the application of the biochar additive mainly depends on its properties, which are predominantly determined by the technology used in its production [19,20]. The highly porous structure of biochars can also create a favourable environment for the existence of microorganisms, which results in increased fertility and soil productivity [21].

Giant miscanthus (*Miscanthus x giganteus*) is a long-term energy crop, characterised by high yield potential. This impressive grass originates from tropical, subtropical and more temperate areas of Southeast Asia. In its natural environment it can reach 6 meters in height, and the diameter of stiff sprouts can be 20 mm. It has been known in Europe for about 50 years; it was originally treated as an ornamental plant, and then started to be used for energy purposes. This plant is a natural hybrid that was created by crossing *Miscanthus sinensis* and *Miscanthus sacchariflorus*. This interspecific hybrid belongs to the group of plants with the C-4 photosynthetic cycle, which is an efficient process of photosynthesis. In the first year of cultivation, the miscanthus can reach a height of about 2 meters and the yield is at the level of 2–5 t ha⁻¹ dry matter. In the second year of cultivation, the plants can reach a height of more than 3 meters and the obtained yield can be at the level of 8–10 t ha⁻¹ dry matter. In order to ensure the correct rate of plant growth, it is important to apply an appropriate fertilizer dose in the initial growing period. The maximum potential harvesting of miscanthus starts from the third year of cultivation. High biomass yields, which can reach over 20 t ha⁻¹ of dry matter, can keep to 10 years during harvesting. Biomass from the giant miscanthus is a very high-quality form of 'fuel' intended for direct combustion. It also has high potential as a substrate in bio-oil production, gasification and charring processes [22,23].

The purpose of the paper is to assess the possibility of using biochar and ash formed through the plant biomass combustion process as a fertiliser used in the cultivation of giant miscanthus (*Miscanthus x giganteus*) and the optimisation of the combination of fertiliser applications. Prior to the

studies, the following research problem was formulated: if biochar and ash from plant biomass can be used as a fertiliser in the cultivation of energy crops, which has a positive effect on soil properties and increases crop yields?

2. Results

2.1. Names of Tests

The tests used for further identification are described by symbols, due to the type and application rate of the fertiliser used:

- B1/P1 (control test—no fertiliser),
- P2 (fertilised with ash at a dose of 1.5 t ha^{-1}),
- P3 (fertilised with ash at a dose of 3.0 t ha^{-1}),
- P4 (fertilised with ash at a dose of 4.5 t ha^{-1}),
- B2/P1 (fertilised with biochar at a dose of 11.5 t ha^{-1}),
- B2/P2 (fertilised with biochar and ash at doses of 11.5 and 1.5 t ha^{-1} , respectively),
- B2/P3 (fertilised with biochar and ash at doses of 11.5 and 3.0 t ha^{-1} , respectively),
- B2/P4 (fertilised with biochar and ash at doses of 11.5 and 4.5 t ha^{-1} , respectively).

2.2. Biochar and Biomass Ash

Tables 1 and 2 present the results of the pH value, total carbon and total nitrogen content, ash and water content, volatile substances and contents of available forms of the chosen minerals in biochar and biomass ash used as fertilisers.

Table 1. pH value, contents of absorbable forms of macroelements and percentage content of carbon and nitrogen in biochar and ash from biomass.

pH (KCl)	Carbon	Nitrogen	P ₂ O ₅	K ₂ O	Mg
	% $\text{x} \pm \text{SD}$				
	$\text{x} \pm \text{SD}$				
Biochar	6.59 ± 0.21	74.35 ± 0.24	0.93 ± 0.07	1382 ± 41	5752 ± 63
Ash	12.89 ± 0.32	1.22 ± 0.22	0.17 ± 0.01	6394 ± 52	91133 ± 4

x—average, SD—standard deviation.

Table 2. Contents of water, ash and volatile substances in biochar and ash from biomass.

	Water	Ash	Volatile Substances
	% $\text{x} \pm \text{SD}$		
	$\text{x} \pm \text{SD}$		
Biochar	9.11 ± 0.03	11.57 ± 0.21	66.42 ± 0.18
Ash	-	-	94.42 ± 0.27

x—average, SD—standard deviation.

Table 3 presents the contents of selected macro- and microelements in biochar and ash from biomass. Ash from biomass was characterised by a higher content of all the ingredients studied than that found in biochar. Bearing in mind that fertilisers used in agriculture may contain toxic metals, the fertiliser material applied was examined. Aluminium, arsenic, cadmium and lead were not present in the materials analysed.

Table 3. Contents of selected macro- and microelements in biochar and ash from biomass.

	Al	As	Ca	Cd	Cr	Cu	Mn
mg kg^{-1}							
$\bar{x} \pm \text{SD}$							
Biochar	< 0.01	< 0.01	18,520 ± 21	< 0.01	< 0.01	10 ± 0.8	240 ± 2.5
Ash	< 0.01	< 0.01	131,220 ± 35	< 0.01	50 ± 0.9	110 ± 0.7	1930 ± 9.5
	Mo	Na	Ni	Pb	S	Sr	Zn
mg kg^{-1}							
$\bar{x} \pm \text{SD}$							
Biochar	< 0.01	< 0.01	< 0.01	< 0.01	880 ± 12	< 0.01	130 ± 11.5
Ash	< 0.01	< 0.01	40 ± 2.5	< 0.01	19,710 ± 23	< 0.01	710 ± 8.2

\bar{x} —average, SD—standard deviation.

2.3. Soil

Figure 1 shows the pH value of the soil before the experiment (2015) and after the first and second year of cultivation, depending on the fertiliser used. The soil taken from the area on which the field experiment was carried out was, as in the previous experiment, characterised by an acid reaction (pH in 1M KCl—4.98). The pH value of the soil determined for the control plots (no fertilisation) was 5.13, after both the first and second year of cultivation. There were no statistically significant differences for this variant when compared to the results obtained prior to the experiment. The addition of biochar, ash and their mixture in the soil influenced the increase in the pH value of the soil to a statistically significant extent when compared to the results obtained in 2015 (in 13 cases out of the 16 analysed). Depending on the type of fertiliser used and its application rate, there was an increase in the study parameter by a value in the range from 0.19 to 1.29 after the first year and from 0.04 to 1.13 after the second year of cultivation when compared to the control group. The highest concentrations of hydrogen ions in the soil, after both the first and second year of cultivation of giant miscanthus were determined in the case of fertilisation with ash at an application rate of 4.5 t ha^{-1} and a combination of biochar and ash at an application rate of 3.0 and 4.5 t ha^{-1} .

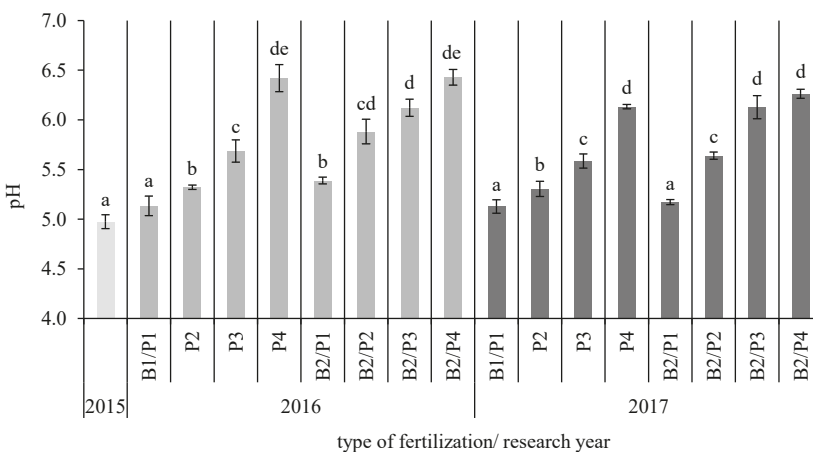


Figure 1. pH value of the soil before the experiment (2015) and after the first and second year of cultivation, depending on the fertiliser used. Differences between average values marked with the same Arabic letters are not statistically significant at the level of $\alpha \leq 0.05$ according to the Bonferroni test.

Figure 2 presents the contents of absorbable forms of phosphorus, potassium and magnesium in the soil before the experiment (2015) and after the first and second year of cultivation, depending on the fertilisers used. The analyses performed before the field experiment showed the contents of absorbable forms of phosphorus, potassium and magnesium in the soil at a level of 48, 90 and 95 mg kg⁻¹ respectively. The contents of the study elements in the fertiliser variants showed, in most cases, statistically significant differences in comparison with the control plots and the year 2015 (before the experiment). After the second year of cultivation of giant miscanthus (2017), the contents of the form of phosphorus, potassium and magnesium available to plants in the soil on plots without the use of fertilisers amounted to 58.75, 104.00 and 95.25 mg kg⁻¹, respectively. Thus, a slight decrease in the potassium content and an increase in the content of phosphorus and magnesium was noted in relation to the previous season.

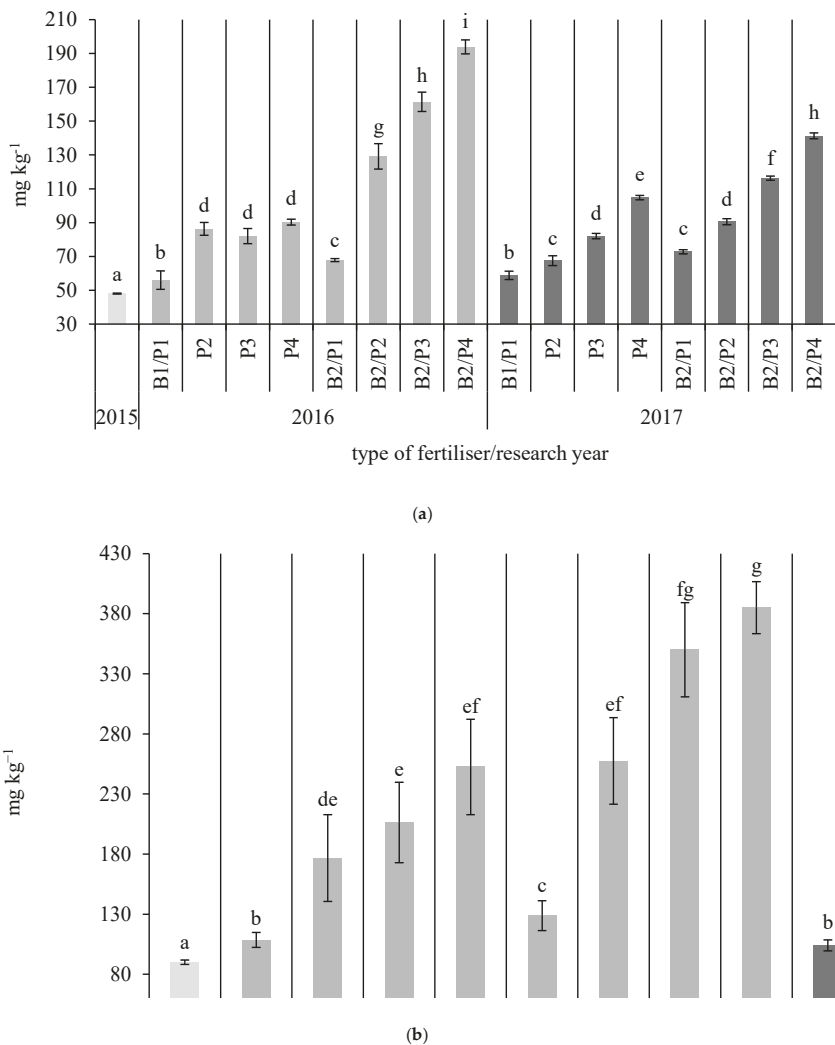


Figure 2. Cont.

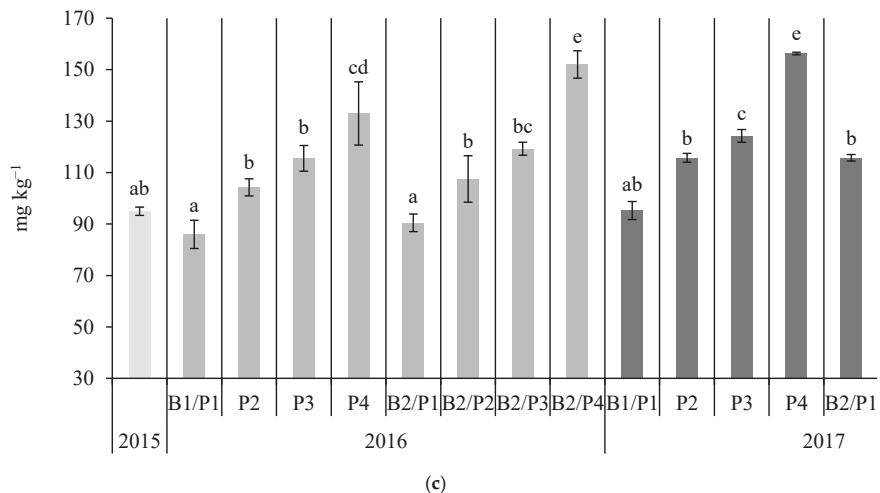


Figure 2. Contents of absorbable forms of phosphorus P_2O_5 (a), potassium K_2O (b), and magnesium Mg (c) in the soil before the experiment (2015) and after the first and second year of cultivation, depending on the fertiliser used. Differences between average values marked with the same Arabic letters are not statistically significant at the level of $\alpha \leq 0.05$ according to the Bonferroni test.

Figure 3 presents the percentage of total carbon and total nitrogen before the experiment (2015) and after the first and second year of cultivation, depending on the fertiliser used. The content of carbon in the soil in the area selected for the field experiment was 0.64%. After the first year of cultivation of giant miscanthus (2016), an increase of 3.13% (control plots) was noted in the carbon content in the soil. In 2017, this content increased to 3.17%; however, it was not a statistically significant change. The experimental factors in the form of fertilisation with ash did not significantly change this parameter in relation to the control plots after the first and second year of cultivation. Only fertilising with biochar and the combination of biochar with ash contributed to an increase in the concentration of total carbon in the soil when compared to the control plots. The highest carbon content determined in the soil samples collected was 4.41% after the first year and 4.34% after the second year of the experiment.

The content of carbon in the soil before the experiment was 0.63% and it increased to 1.16% after the first year of cultivation (control plots). In 2017, there was a statistically insignificant decrease in the content of this parameter to the value of 1.06%. The fertilisers used in the experiment did not have a significant impact on the change in the carbon content when compared to the control plots after the first year of cultivation (carbon content in the range from 1.15 to 1.27%). After the second year, small fluctuations in these parameters were noted; however, in most cases they were not statistically significant. The carbon content in the soil, after the use of fertilisers, was in the range 1.13–1.26%.

The content of nitrogen in the arable land studied was 0.26% before the field experiment. The content of this element in the control plots dropped to 0.02% and 0.07%, respectively, after the first and second year of cultivation. The concentration of nitrogen in the soil, after the use of fertilisers, was in the range 0.002–0.07% after the second year of the experiment. The following was observed.

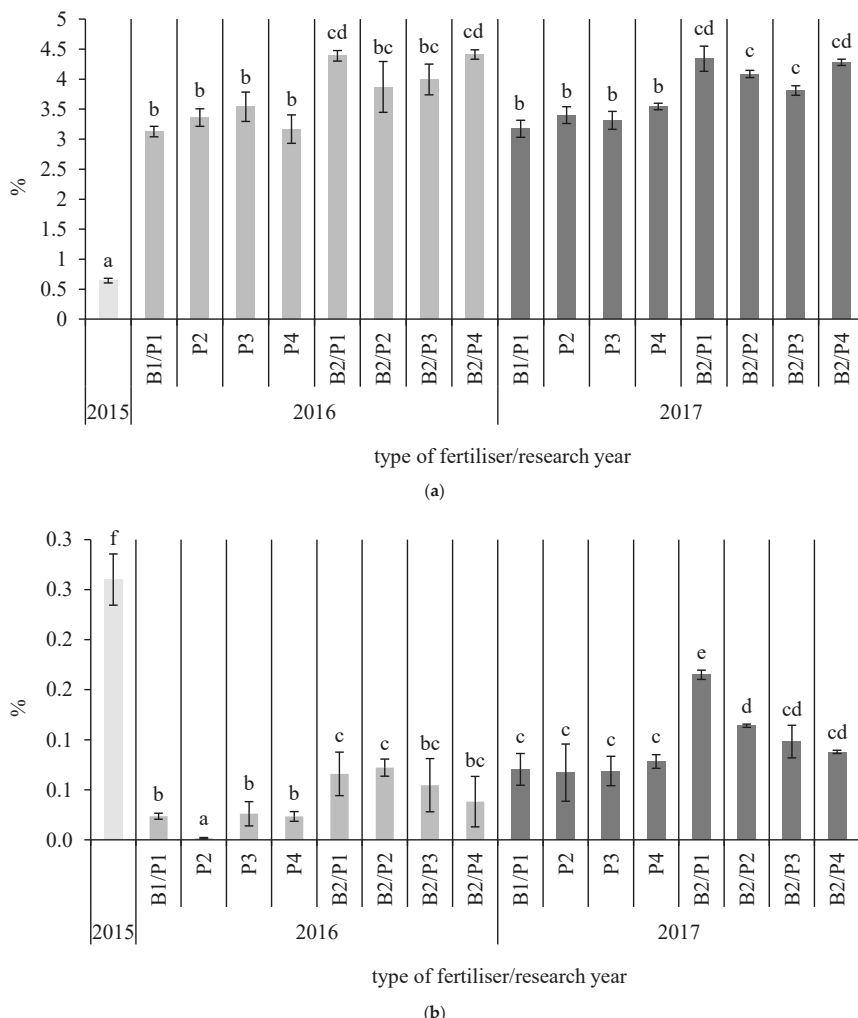


Figure 3. Content of carbon (a) and nitrogen (b) in the soil before the experiment (2015) and after the first and second year of cultivation, depending on the fertiliser used. Differences between average values marked with the same Arabic letters are not statistically significant at the level of $\alpha \leq 0.05$ according to the Bonferroni test.

Table 4 presents the total contents of selected macro- and microelements and heavy metals in the soil before the experiment (2015) and after the first and second year of cultivation, depending on the fertiliser used. The highest concentration of the macroelements examined (total contents of calcium, sodium and sulphur) in both 2016 and 2017 was recorded after the use of fertiliser in the form of a combination of biochar and ash at an application rate of 1.5 t ha^{-1} . The largest increase in the totals of the soil macroelements examined after the first and second year of the experiment when compared to the year 2015 was 50% and 31%, respectively. The lowest total contents of Ca, Na and S in 2016 and 2017 were recorded in the case of fertilising with ash (all fertiliser application rates).

Table 4. Contents of selected macro- and microelements and heavy metals in the soil before the experiment and after the first and second year of cultivation, depending on the fertiliser used.

Year	Fertiliser/Seed	Macro- and Microelements									
		As	Ca	Cd	Cu	Mn	Na	Ni	Pb	S	Zn
$\bar{x} \pm SD$											
2015	-	<0.01	2,300 ^b ± 19	<0.01	20,00 ^a ± 0.41	624 ^c ± 5	174,75 ^h ± 1.50	<0.01	12,40 ^a ± 0.41	113 ^a ± 0.87	50,03 ^d ± 2.41
2016	B1/P1	<0.01	2,646 ^c ± 19	<0.01	53,75 ^c ± 0.50	520 ^b ± 18	91,09 ^e ± 26.25	<0.01	13,91 ^b ± 0.69	160 ^c ± 13	25,95 ^a ± 10.70
	P2	<0.01	2,352 ^b ± 158	<0.01	50,93 ^c ± 1.57	505 ^b ± 2	93,88 ^e ± 40.23	<0.01	13,65 ^b ± 0.82	131 ^c ± 18	30,49 ^{ab} ± 12.37
	P3	<0.01	2,338 ^b ± 20	<0.01	46,32 ^b ± 3.12	507 ^b ± 27	19,17 ^a ± 8.47	<0.01	13,89 ^b ± 0.22	139 ^c ± 19	25,49 ^a ± 10.24
	P4	<0.01	2,436 ^{bc} ± 93	<0.01	51,54 ^c ± 2.44	527 ^b ± 12	11,48 ^a ± 0.85	<0.01	16,10 ^e ± 0.60	125 ^b ± 3	33,72 ^b ± 4.80
2017	B2/P1	<0.01	2,848 ^c ± 139	<0.01	53,97 ^c ± 2.17	505 ^b ± 11	109,59 ^f ± 18.75	<0.01	13,70 ^c ± 0.82	196 ^e ± 6	37,07 ^b ± 3.30
	B2/P2	<0.01	3,690 ^f ± 350	<0.01	54,78 ^c ± 0.66	516 ^b ± 2	125,25 ^g ± 4.70	<0.01	16,97 ^e ± 0.73	210 ^f ± 6	56,99 ^d ± 10.02
	B2/P3	<0.01	2,893 ^c ± 150	<0.01	44,89 ^b ± 3.40	484 ^a ± 3	51,71 ^c ± 20.58	<0.01	13,60 ^c ± 0.84	197 ^e ± 2	26,67 ^a ± 10.23
	B2/P4	<0.01	3,038 ^d ± 65	<0.01	47,15 ^b ± 3.55	521 ^b ± 5	79,68 ^d ± 25.23	<0.01	15,29 ^d ± 0.78	213 ^f ± 8	44,69 ^c ± 0.81
2015	B1/P1	<0.01	1,959 ^a ± 7	<0.01	42,35 ^b ± 0.96	460 ^a ± 5	33,60 ^b ± 1.82	<0.01	13,24 ^b ± 0.38	154 ^c ± 5	25,51 ^a ± 0.76
	P2	<0.01	2,303 ^b ± 105	<0.01	47,89 ^b ± 1.10	478 ^a ± 4	52,93 ^c ± 6.01	<0.01	13,26 ^c ± 0.15	169 ^{cd} ± 2	27,67 ^a ± 0.27
	P3	<0.01	2,137 ^b ± 138	<0.01	44,63 ^b ± 3.50	453 ^a ± 6	52,66 ^c ± 37.08	<0.01	13,89 ^b ± 0.42	173 ^d ± 7	27,26 ^a ± 0.21
	P4	<0.01	3,303 ^e ± 858	<0.01	57,96 ^d ± 3.77	495 ^{ab} ± 12	158,34 ^g ± 35.16	<0.01	15,97 ^d ± 0.93	189 ^d ± 10	34,33 ^b ± 1.95
	B2/P1	<0.01	2,306 ^b ± 33	<0.01	44,61 ^b ± 1.61	481 ^a ± 8	55,21 ^c ± 1.96	<0.01	15,05 ^c ± 0.11	190 ^d ± 4	29,27 ^{ab} ± 0.39
	B2/P2	<0.01	3,137 ^d ± 297	<0.01	57,80 ^d ± 2.28	511 ^b ± 17	184,87 ^h ± 37.12	<0.01	13,63 ^c ± 0.50	189 ^d ± 4	32,23 ^b ± 1.47
	B2/P3	<0.01	2,684 ^c ± 167	<0.01	51,37 ^c ± 2.67	505 ^b ± 8	82,10 ^d ± 13.94	<0.01	15,29 ^d ± 0.74	187 ^d ± 5	33,32 ^b ± 2.08
	B2/P4	<0.01	2,747 ^c ± 48	<0.01	48,65 ^b ± 0.20	535 ^b ± 17	48,89 ^c ± 4.07	<0.01	16,94 ^e ± 0.57	199 ^e ± 9	35,03 ^b ± 11.9

\bar{x} —average; SD—standard deviation. Differences between average values marked with the same Arabic letters (a–f) are not statistically significant at the level of $\alpha \leq 0.05$ according to the Bonferroni test.

The highest total contents recorded for the microelements examined in soil samples collected after the first and second year of cultivation of giant miscanthus, respectively, were found in plots that were fertilised with biochar and biochar with ash at an application rate of 4.5 t ha^{-1} . The decrease in the totals of the soil microelements after the first and second year of the experiment was determined to be 15% and 13%, respectively, in comparison with the initial values obtained, i.e., before the experiment was carried out for all the aforementioned variants of fertiliser dosage. The lowest total value found during analysis of microelements in the soil in 2016 and 2017 was recorded in the case of fertilising with biochar and ash at an application rate of 3.0 t ha^{-1} and ash alone at this application rate. In the soil samples studied, no arsenic, cadmium or nickel was found in the material collected before the experiment or after the first and second year of the experiment—values were below the detection limit (0.01 mg kg^{-1}) of the analytical method used. The marked concentration of lead changed slightly depending on factors and the year of research, but it should be emphasised that, again, in no case did it exceed the permissible contents for soil used for agricultural purposes.

Principal component analysis of variables (elements) for the soil after the first and second year of cultivation of giant miscanthus identified two factors describing the level of variation in the group with values for the first year for factor 1 (70%) and factor 2 (18.7%), as well as for the second year for factor 1 (46.6%) and factor 2 (24.4%), respectively. The selection of the number of main components was made using the scree test and the Kaiser criterion. The first factor included the following variables: calcium, copper, manganese, sodium, lead, sulphur, zinc (first year) and calcium, sodium, sulphur, zinc (second year). The second factor was represented by the following variables: sodium (first year), and copper and manganese (second year). It was noted that factor 1 is most strongly associated with the variable Ca, while factor 2 with the variable Mn (first year). In the second year of research it was found that factor 1 is mainly associated with the variable Zn, while factor 2 is most strongly associated with the variable Na. The projection of variables on the factor plane is presented in Figure 4.

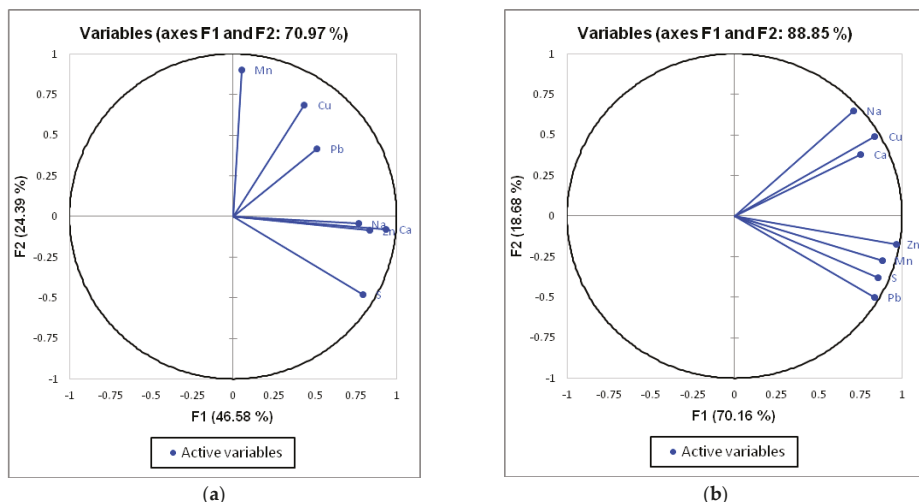


Figure 4. Variable plot in the system of the first two factor axes for the soil after the first (a) and second (b) year of cultivation of giant miscanthus.

2.4. Biomass of Giant Miscanthus

Figure 5 presents the yield of biomass of giant miscanthus (dry matter—d.m.) after the first year of cultivation, depending on the fertiliser used. The average yield of biomass obtained from the control plots (no fertiliser) was 1.04 t ha^{-1} of d.m. The largest values of the parameter studied of 1.22, 1.22 and 1.75 t ha^{-1} , respectively, were recorded in the case of fertilising with ash at an application

rate of 1.5 t ha^{-1} , with biochar and with the combination of biochar and ash at an application rate of 1.5 t ha^{-1} . The highest yield of biomass of plants in 2016 was obtained by introducing the fertilisation factor in the form of the combination of biochar and ash at an application rate of 1.5 t ha^{-1} . Fertilisation with ash at doses of 3.0 and 4.5 t ha^{-1} and its combinations with biochar affected yield, with values of 0.75 , 0.57 , 0.90 and 0.86 t ha^{-1} of d.m., respectively.

After the second year of cultivation of giant miscanthus, the average yield of biomass in the control plots was 8.82 t ha^{-1} of d.m. As in the previous year, the highest values of average yield of dry matter of 9.50 , 13.04 , and 9.80 t ha^{-1} , respectively, were recorded for the plots fertilised with the lowest application rate of ash, biochar alone, and the combination of biochar and ash at a dose of 1.5 t ha^{-1} . The highest yield of dry matter of plants in 2017 was recorded on plots fertilised only with biochar before the experiment. Fertiliser application rates of ash of 3.0 and 4.5 t ha^{-1} and its combination with biochar negatively influenced crop yield—there was a decrease in the average yield of dry matter of plants when compared with the control plots of 1.43 , 2.56 , 0.23 , and 0.38 t ha^{-1} , respectively (Figure 5).

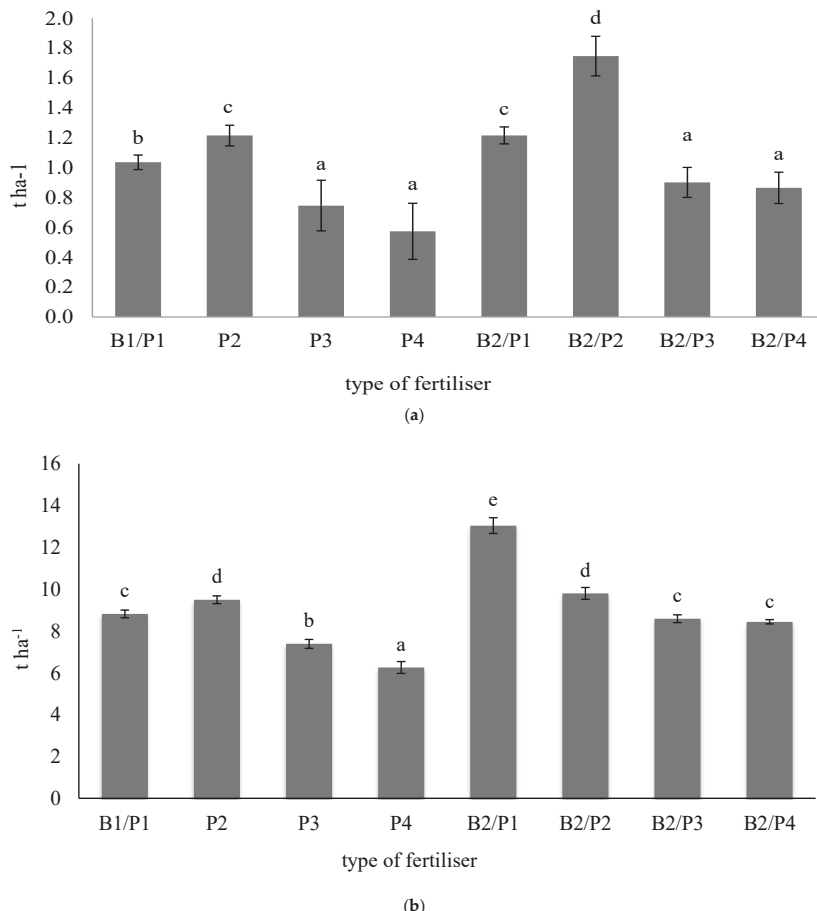


Figure 5. Biomass yield of giant miscanthus after the first (a) and second (b) year of cultivation, depending on the fertilisation used. Differences between average values marked with the same Arabic letters are not statistically significant at the level of $\alpha \leq 0.05$ according to the Bonferroni test.

Figure 6 presents the calorific value of biomass of giant miscanthus, depending on the fertiliser used and the year of research. The calorific value of biomass after the first year of cultivation ranged from 17.54 to 17.75 MJ kg⁻¹ of d.m., while after the second year of cultivation it ranged from 17.65 to 17.72 MJ kg⁻¹ of d.m. There were no statistically significant differences between the values measured. When assessing the calorific value of the biomass of giant miscanthus in laboratory tests, both after the first and second year of cultivation, no effects were found on changes in the parameters analysed in relation to the use of fertilisers.

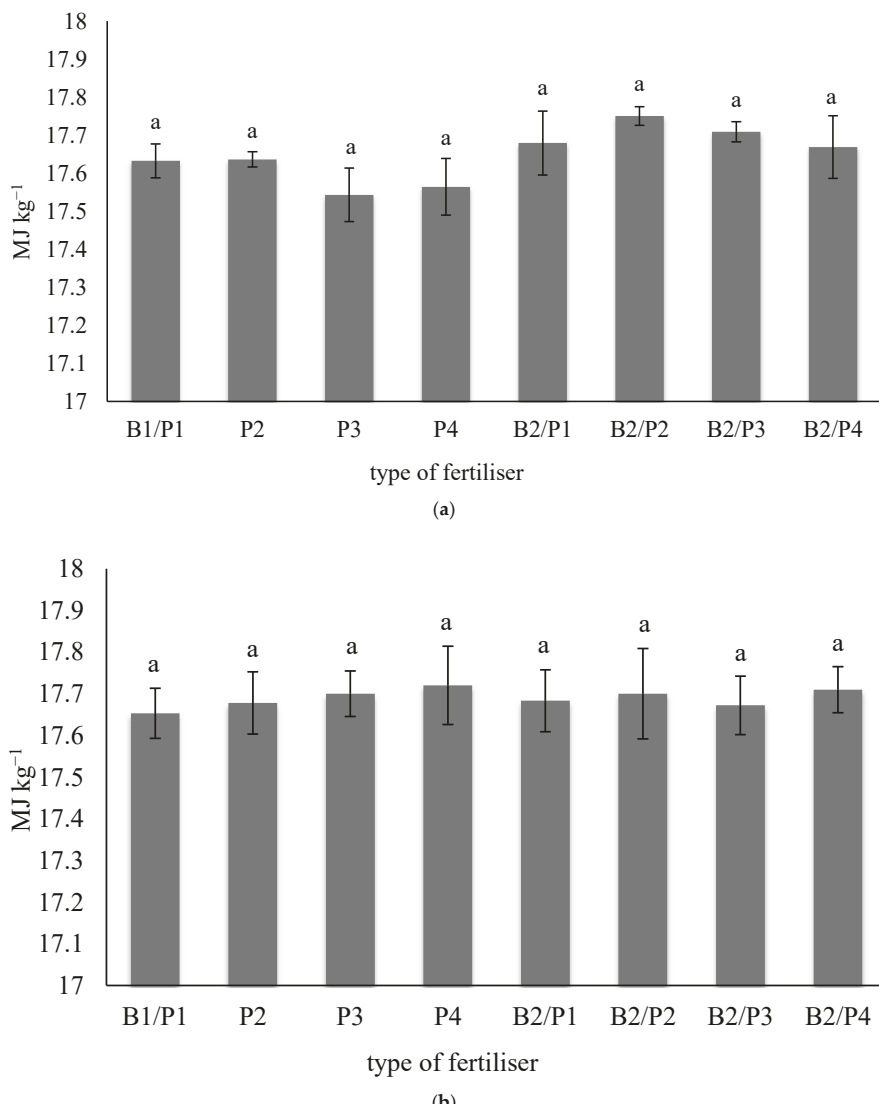


Figure 6. Calorific value of giant miscanthus after the first (a) and second (b) year of cultivation, depending on the fertiliser used. Differences between average values marked with the same Arabic letters are not statistically significant at the level of $\alpha \leq 0.05$ according to the Bonferroni test.

Table 5 presents the total contents of selected macroelements in the biomass of giant miscanthus, depending on the fertiliser used and year of research. The highest concentration of the macroelements studied in the above ground parts of plants in 2016 and 2017, respectively, was recorded after the use of fertiliser in the form of ash at the lowest application rate and ash at an application rate of 3.0 t ha^{-1} . The greatest increase in the total of the macroelements studied in the biomass of plants was recorded after the first and second year of the experiment in the control plots, with increases of 13% and 7%, respectively. The lowest total content of the elements studied in 2016 and 2017, respectively, was recorded for the fertiliser in the form of biochar and the combination of biochar and ash at a dose of 1.5 t ha^{-1} . Among the ions analysed, the highest concentration in the biomass of giant miscanthus was found for potassium—after both the first and second year of cultivation. There was a change in the content of this element, depending on the combination of factors used in the experiment; however, not all changes were statistically significant. When analysing the results of the total contents of selected macroelements, it was found that aboveground parts of plants of giant miscanthus contained the least sodium and iron. The fertiliser did not produce statistically significant changes in the contents of these elements in the biomass after the first and second year of cultivation when compared to control tests.

Table 6 presents the total contents of selected microelements and heavy metals in the biomass of giant miscanthus, depending on the fertiliser used and the year of research. In the aboveground parts of the plants analysed after the first year of cultivation, manganese, strontium, zinc and aluminium were found. No strontium was recorded in samples obtained after the second year of cultivation. The concentration of these elements was determined to be at a very low level and did not show statistically significant variability between the experimental plots. Plant biomass obtained after the second year of research was characterised by a lower content of the elements analysed when compared to the previous year. In the plant samples studied, no arsenic, cadmium, chromium, copper, molybdenum, nickel or lead was found after both the first and second year of the experiment—values were below the detection limit (0.01 mg kg^{-1}) in the analytical method used.

Table 5. Contents of selected macroelements in the biomass of giant miscanthus after the first (2016) and second (2017) year of cultivation, depending on the fertiliser used.

Year	Fertiliser Used	Macroelements					
		Ca	Fe	K	Mg	Na	P
		mg kg^{-1}					
2016	B1/P1	2.29 ^a ± 0.16	0.20 ^a ± 0.05	6.66 ^b ± 0.32	0.82 ^{ab} ± 0.04	0.13 ^a ± 0.02	1.28 ^b ± 0.08
	P2	2.58 ^b ± 0.09	0.20 ^a ± 0.03	7.71 ^c ± 0.22	0.89 ^{bc} ± 0.10	0.13 ^a ± 0.02	1.43 ^c ± 0.11
	P3	2.23 ^a ± 0.21	0.19 ^a ± 0.03	6.03 ^a ± 0.19	0.74 ^a ± 0.11	0.13 ^a ± 0.01	1.11 ^a ± 0.04
	P4	2.38 ^a ± 0.09	0.20 ^a ± 0.02	6.93 ^b ± 0.29	0.91 ^b ± 0.09	0.13 ^a ± 0.01	1.49 ^c ± 0.03
	B2/P1	2.31 ^a ± 0.17	0.19 ^a ± 0.09	5.75 ^a ± 0.23	0.74 ^a ± 0.03	0.12 ^a ± 0.01	1.25 ^b ± 0.06
	B2/P2	2.31 ^a ± 0.15	0.10 ^a ± 0.05	7.13 ^b ± 0.24	0.83 ^{ab} ± 0.04	0.12 ^a ± 0.02	1.29 ^b ± 0.10
	B2/P3	2.23 ^a ± 0.18	0.19 ^a ± 0.12	7.05 ^b ± 0.34	0.99 ^c ± 0.08	0.12 ^a ± 0.02	1.29 ^b ± 0.09
	B2/P4	2.33 ^a ± 0.18	0.15 ^a ± 0.05	6.84 ^b ± 0.42	1.03 ^c ± 0.07	0.12 ^a ± 0.03	1.31 ^b ± 0.11
2017	B1/P1	1.06 ^a ± 0.12	0.04 ^a ± 0.01	5.59 ^c ± 0.12	0.31 ^a ± 0.03	0.09 ^a ± 0.00	1.13 ^c ± 0.09
	P2	1.13 ^a ± 0.15	0.06 ^a ± 0.02	4.90 ^b ± 0.07	0.34 ^b ± 0.06	0.08 ^a ± 0.00	0.97 ^b ± 0.07
	P3	1.60 ^c ± 0.06	0.06 ^a ± 0.01	5.37 ^c ± 0.09	0.37 ^b ± 0.04	0.09 ^a ± 0.01	1.25 ^d ± 0.07
	P4	1.26 ^a ± 0.08	0.05 ^a ± 0.02	4.58 ^a ± 0.12	0.36 ^b ± 0.01	0.09 ^a ± 0.01	1.06 ^c ± 0.04
	B2/P1	1.17 ^a ± 0.12	0.05 ^a ± 0.02	4.74 ^b ± 0.10	0.28 ^a ± 0.03	0.08 ^a ± 0.01	0.95 ^b ± 0.01
	B2/P2	1.22 ^a ± 0.19	0.05 ^a ± 0.03	4.34 ^a ± 0.08	0.29 ^a ± 0.05	0.07 ^a ± 0.01	0.81 ^a ± 0.09
	B2/P3	1.15 ^a ± 0.03	0.04 ^a ± 0.02	4.78 ^b ± 0.11	0.39 ^b ± 0.10	0.07 ^a ± 0.01	0.79 ^a ± 0.08
	B2/P4	1.44 ^b ± 0.07	0.05 ^a ± 0.01	4.66 ^a ± 0.12	0.40 ^b ± 0.05	0.09 ^a ± 0.00	1.09 ^c ± 0.07

x—average, SD—standard deviation. Differences between average values marked with the same Arabic letters (a–d) are not statistically significant at the level of $\alpha \leq 0.05$ according to the Bonferroni test, for each years.

Table 6. Contents of selected microelements and heavy metals in the biomass of giant miscanthus after the first (2016) and second (2017) year of cultivation, depending on the fertiliser used.

Year	Fertiliser Used	Microelements						Zn			
		Al	As	Cd	Cr	Cu	Mo	Ni	Pb	Mn	Sr
		mg kg^{-1}						$\bar{x} \pm \text{SD}$			
2016	B1/P1	0.14 ^a ± 0.04	<0.01	<0.01	<0.01	<0.01	<0.01	0.14 ^a ± 0.00	0.01 ^a ± 0.00	0.07 ^a ± 0.03	
	P2	0.18 ^a ± 0.06	<0.01	<0.01	<0.01	<0.01	<0.01	0.14 ^a ± 0.02	0.02 ^a ± 0.00	0.07 ^a ± 0.02	
	P3	0.14 ^a ± 0.05	<0.01	<0.01	<0.01	<0.01	<0.01	0.13 ^a ± 0.01	0.01 ^a ± 0.00	0.06 ^a ± 0.02	
	P4	0.19 ^a ± 0.03	<0.01	<0.01	<0.01	<0.01	<0.01	0.13 ^a ± 0.01	0.01 ^a ± 0.00	0.07 ^a ± 0.04	
	B2/P1	0.16 ^a ± 0.03	<0.01	<0.01	<0.01	<0.01	<0.01	0.12 ^a ± 0.01	0.01 ^a ± 0.00	0.03 ^a ± 0.02	
	B2/P2	0.13 ^a ± 0.03	<0.01	<0.01	<0.01	<0.01	<0.01	0.12 ^a ± 0.02	0.03 ^a ± 0.04	0.06 ^a ± 0.05	
	B2/P3	0.17 ^a ± 0.02	<0.01	<0.01	<0.01	<0.01	<0.01	0.12 ^a ± 0.02	0.01 ^a ± 0.00	0.05 ^a ± 0.03	
	B2/P4	0.16 ^a ± 0.03	<0.01	<0.01	<0.01	<0.01	<0.01	0.12 ^a ± 0.01	0.01 ^a ± 0.00	0.05 ^a ± 0.02	
	B1/P1	0.02 ^a ± 0.00	<0.01	<0.01	<0.01	<0.01	<0.01	0.09 ^a ± 0.02	<0.001	0.03 ^a ± 0.01	
	P2	0.03 ^a ± 0.00	<0.01	<0.01	<0.01	<0.01	<0.01	0.08 ^a ± 0.03	<0.001	0.02 ^a ± 0.00	
2017	P3	0.05 ^a ± 0.00	<0.01	<0.01	<0.01	<0.01	<0.01	0.09 ^a ± 0.01	<0.001	0.03 ^a ± 0.01	
	P4	0.04 ^a ± 0.02	<0.01	<0.01	<0.01	<0.01	<0.01	0.09 ^a ± 0.01	<0.001	0.02 ^a ± 0.01	
	B2/P1	0.02 ^a ± 0.01	<0.01	<0.01	<0.01	<0.01	<0.01	0.08 ^a ± 0.03	<0.001	0.02 ^a ± 0.00	
	B2/P2	0.03 ^a ± 0.01	<0.01	<0.01	<0.01	<0.01	<0.01	0.07 ^a ± 0.02	<0.001	0.01 ^a ± 0.00	
	B2/P3	0.03 ^a ± 0.01	<0.01	<0.01	<0.01	<0.01	<0.01	0.07 ^a ± 0.02	<0.001	0.02 ^a ± 0.01	
	B2/P4	0.03 ^a ± 0.00	<0.01	<0.01	<0.01	<0.01	<0.01	0.09 ^a ± 0.01	<0.001	0.02 ^a ± 0.01	

\bar{x} —average, SD—standard deviation. Differences between average values marked with the same Arabic letter are not statistically significant at the level of $\alpha \leq 0.05$ according to the Bonferroni test, for each years.

Principal component analysis of variables (elements) for the biomass of giant miscanthus after the first and second year of cultivation selected two factors describing the level of variability in the group with values, respectively, for the first year: factor 1 (27.7%) and factor 2 (21.7%), and for the second year: factor 1 (33.9%) and factor 2 (24.4%). The selection of the number of main components was made using the scree test and the Kaiser criterion. The first factor included variables such as aluminium, potassium, magnesium, sodium, sulphur (first year) and aluminium, manganese, phosphorus, sulphur (second year). The second factor was represented by variables such as iron, manganese, phosphorus (first year) and calcium, potassium, magnesium (second year). It was noted that factor 1 is most strongly associated with variables K and S, while factor 2 is associated with variables Fe and Mn (first year). In the second year of research, it was found that factor 1 is mainly associated with variables S and Sr, while factor 2 is most strongly associated with variable K. The projection of variables on the factor plane is presented in Figure 7.

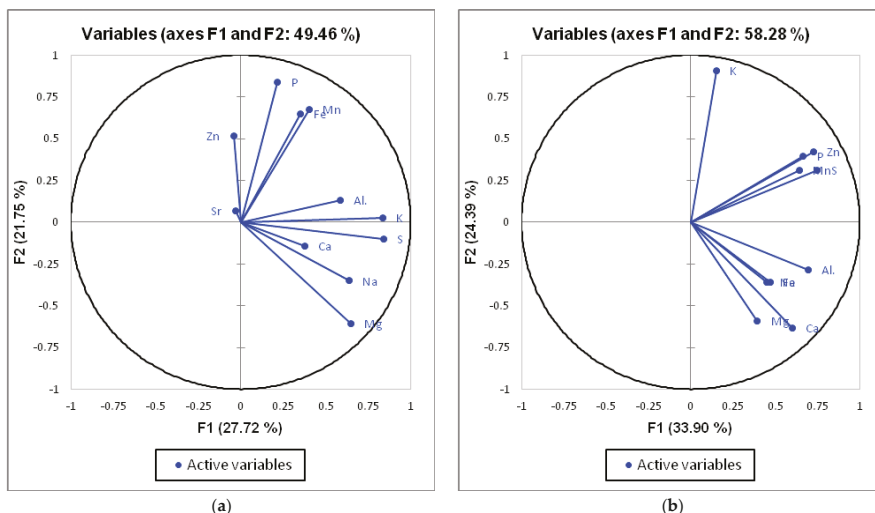


Figure 7. Variable plot in the system of the first two factor axes for the biomass of giant miscanthus after the first (a) and second (b) year of cultivation.

3. Discussion

The cultivation of plants is becoming more and more effective due to the use of numerous means of support, including different types of fertilisers. The agents most commonly used in modern agriculture, which contain easily absorbable mineral components, are fertilisers [24].

Recent years have seen the intensive development of research on the use of unconventional materials as plant fertilisers and for soil reclamation. This research concerns the use of, among other materials, sewage sludge, ash from biomass, brown coal or biochar. In addition, the literature presents only rudimentary information on the use of biochar and ash from biomass as a fertiliser material in the cultivation of perennial energy crops.

The soil reaction plays an important role in many processes occurring in the soil environment. It is important in the uptake of nutrients by plants and affects the mobility of heavy metals, such as cadmium, lead or nickel [5,16]. The alkalizing effect associated with the application of biochar to the soil environment relates to the alkaline compound content and the application rate. The clearest changes can be obtained in the case of heavily acidified soils, where a significant decrease is visible in the share of H^+ and Al^{3+} [17]. Much of the research conducted so far indicates that the addition of biochar produces an increase in soil pH [25–28]. Research conducted by Nigussie et al. [29] showed

that biochar produced from corn stalks and applied to soils contaminated with chromium produced an increase in pH and ion exchange in the soils analysed. Clear effects on the soil pH after the application of ashes can be obtained by the application of fertiliser doses at the level of $10\text{--}20 \text{ t ha}^{-1}$ [30]. However, the use of such high doses of ash could result in the introduction of too large quantities of nutrients or heavy metals into the soil.

According to the analyses performed, the use of fertiliser in the form of a combination of biochar and ash at an application rate of 4.5 t ha^{-1} produced the greatest increase in the content of absorbable forms of phosphorus (P_2O_5), potassium (K_2O) and magnesium (Mg) in the soil on which perennial energy crops were grown.

The high potential of biochars for exchangeable ion sorption affects the increase in the concentration of macro- and microelements in the soil profile, which is why it modulates their effective uptake by plants, as well as reduces the risk of their leaching and being displaced to surface and underground waters [12]. The introduction of biochar into the soil may have a positive effect, including on the increase in the phosphorus content in the soil environment. As emphasised by Chan et al. [14], the use of biochar in the soil at a fertiliser dose of more than 50 t ha^{-1} significantly increases the concentration of phosphorus in the soil. The increase in the phosphorus content in the soil after the application of biochar results from the content of easily absorbable forms of this element in biochars, as well as from its ability to react on the soil reaction, thus producing changes in the solubility of phosphorus forms [31,32]. Numerous authors report that the addition of biochars to the soil affects the intensive growth of soluble forms of potassium in the soil solution [33,34]. Liu et al. [35] note an increase in the contents of macroelements in the soil compared to the control following the application of biochar from the vegetative parts of bamboo and rice straw. In their paper, the authors used biochars obtained from the pyrolysis process with parameters of $500 \text{ }^{\circ}\text{C}$ and $600 \text{ }^{\circ}\text{C}$ and a process duration of 60 min. Fertiliser doses of biochar from bamboo and rice straw amounted to 5, 18, and 10.5 t ha^{-1} , respectively. According to many authors, ash from plant biomass is characterized by a high amount of the biogenic elements necessary for the proper growth of plants, thanks to which it can supplement deficiencies of macro- and microelements in the soil [36]. Piekarczyk [25] states that the use of ash from wheat straw (1.0 t ha^{-1}) as a fertiliser material produced an increase in absorbable forms of macroelements in the soil, at the same time indicating that these changes were not statistically significant. The author explains this result by the relatively low content of nutrients in the ash used. It should be noted that changes in soil fertility resulting from the introduction of ash depend on the ash source, its elemental composition and the size of the dose applied [37]. In research on the long-term effects of the use of wood ash agents, Klavina et al. [38] note an increase in the concentration of magnesium and phosphorus in peat soils. The authors also inform us about the positive impact of ash on the calcium content and the formation of soil pH.

Biochar and ash from biomass used in field experiments were characterised by total carbon contents of 74.35% and 1.22%, respectively. This was reflected in the results obtained, which indicate the lack of a fertilising effect of ash itself on changes in the total carbon concentration in the soil. Fertilisers in the form of biochar and its combination with ash produced an increase in the concentration of carbon in the soil, in comparison with the control plot (statistically significant changes in most cases). Similar results were obtained by Doan et al. [39], who reported that the use of biochar from cattle manure in the corn cultivation slightly increased the C content of the soil. In research on the impact of biochar and compost on soil properties in a tropical climate, Ghosh et al. [40] determined that the organic carbon content in the soil after the application of biochar was almost twice as high as in the control plot (an increase from 1.18 to 2.13%). It should also be emphasised that stable forms of carbon are characterised by high resistance to biological decomposition, which is why biochar can be treated as an effective agent for carbon sequestration in the soil [11,41,42].

Research conducted as part of the cultivation of giant miscanthus showed that fertilising with a combination of biochar and ash at a dose of 1.5 t ha^{-1} produced the greatest increase in the total calcium, sodium and sulphur contents after the first and second year of cultivation, when compared to 2015.

For the aforementioned fertiliser, a decrease was noted in the total concentration of the microelements in 2016 and 2017 when compared to their concentration before the experiment. Many researchers point to biochar's great potential as a material that can be used to reduce the mobility of heavy metals in the soil [43,44]. According to Bielinska et al. [45], ash from fluidised bed combustion of hard coal used for agricultural purposes did not produce an increase in the amount of zinc, copper and cadmium in the soil. One of the key features of energy crops should be the high level of biomass productivity. On the basis of the research conducted, it was found that the highest yield of dry matter of giant miscanthus plants, both after the first and second year of cultivation, was obtained by fertilising with ash at an application rate of 1.5 t ha^{-1} , with biochar, and the combination of biochar and ash at a dose of 1.5 t ha^{-1} . The aforementioned fertilisers produced an increase in yield in 2016 compared to the control plots by 17%, 17% and 68%, respectively. The dry matter yield of plants recorded in 2017 was several times higher than in the previous year, and the recorded changes for the aforementioned factors in relation to the control plots were 8%, 48% and 11%, respectively. In research on the yield of osier cultivated using the Eko-Salix system (five-year rotation), Szczukowski et al. [46] determined the dry matter yield of plants to be on average 7.46 t ha^{-1} per year. Kwasniewski [47] states that the average yield of fresh biomass of energy willow obtained from 30 selected plantations located in Poland was 7.0 t ha^{-1} (first year of cultivation). Field experiments carried out so far in Poland have shown that the average yield of willow cultivated using the short rotation system ranged from 10 to 15 t ha^{-1} of dry matter [48,49]. Kobylinski and Olszewska [50], conducting research on energy efficiency in the production of giant miscanthus, recorded a dry matter yield of plants of 1.5 t ha^{-1} in the first year of cultivation and 9 t ha^{-1} in the second year of cultivation. These values increased to the level of 15 t ha^{-1} in the third year of cultivation. The authors claim that the slow rate of plant development in the early period of cultivation, environmental conditions and the small doses of mineral fertilisers affected the low biomass yield obtained in the first year. It should also be emphasised that the full yield of perennial energy crops may be obtained after 3–4 years of cultivation.

Research conducted by Puchalski et al. [51] confirms the positive effect of the use of plant biomass ash on the yield of two varieties of topinambour (*Helianthus tuberosus* L.). The fertiliser dose used was 12.8 t ha^{-1} , which produced an increase in the dry matter yield of plants after the first year of cultivation compared to the control plot of 7% for the Albik variety and 21% for the Gigant variety. However, it should be noted that the lower doses of ash used in the experiment did not produce statistically significant changes in the yield. In our own research, a significant increase in the yield of osier and giant miscanthus was obtained after the application of ash at a dose of 1.5 t ha^{-1} . The majority of research conducted so far on the response of giant miscanthus to the fertiliser applied concerned the use of inorganic nitrogen. However, the results obtained were contradictory and did not give a definite answer concerning the positive effect that fertilising with nitrogen has on plants. Many authors state that fertilising with nitrogen did not affect the growth and yield of various types of miscanthus [52–55].

Research conducted so far on the use of biochar in plant production has concentrated in the area of cultivation of such plants as corn, radish, rape, rice and potatoes [14,43,56–58]. According to Liu et al. [59], the use of biochar at doses below 30 t ha^{-1} (field conditions) produced, to varying degrees, an increase in the yield depending on the type of cultivation. The authors note a growth in crop yield of 30%, 29%, 13%, 11%, 8% and 7%, respectively, for legumes, vegetables, grasses, wheat, corn and rice. The literature also states that biochars from sewage sludge can be used for the fertilisation of plants. Hossain et al. [60], following the use of 10 t ha^{-1} of biochar from sewage sludge in the cultivation of cherry tomatoes, obtained a 64% increase in production, compared to the control plot. However, it should be noted that there is an upper limit to the amount of biochar that should be applied with respect to crop productivity. Lehmann et al. [61] note that plants respond positively to the addition of biochar to the soil at doses of up to 55 t ha^{-1} . The authors report that the use of higher doses does not produce a statistically significant impact on the increase in plant yield. Increased plant production due to the use of biochar as a fertiliser material can be observed as changes in plant growth, nutrient uptake and yield [62]. It should be noted that the research conducted so far has been

of a short-term character; therefore, the assessment of the long-term impact of biochar on the soil and plants seems to be justified.

The calorific value of the biomass of giant miscanthus harvested after two years of research ranged from 17.54 to 17.75 MJ kg⁻¹ of d.m. There were no statistically significant changes in the parameters investigated after the use of fertilisation factors. The results obtained are consistent with the data contained in the available literature [63–65].

The average total contents of the elements studied in the biomass of giant miscanthus after the first and second year of cultivation were determined to be a series of decreasing values of K > Ca > P > S > Mg > Al > Fe > Mn > Zn > Na > Sr and K > Ca > P > S > Mg > Mn > Fe > Al > Zn > Na. In 2017, there was a decrease in the average total contents of the macroelements analysed in the biomass obtained from experiments in relation to the previous year. Similar results were obtained by Borkowska and Lipinski [66] in research on the contents of selected elements in the biomass of energy crops. These authors recorded a high concentration of calcium and potassium in comparison with other elements for giant miscanthus, sugar miscanthus and two clones of osier. According to Szyszak-Barglowicz [67], various levels of mineral fertilisation did not significantly affect the contents of macroelements studied in the biomass of Virginia fanpetals. The analysis of the concentration of N, P, K, Ca and Mg in the stems and leaves of the study plants showed the highest content of potassium and calcium.

No harmful compounds such as arsenic, cadmium, chromium and lead were found in the biomass of the aboveground parts of plants collected from experimental plots. Academic literature states that with the increase in concentration of heavy metals in the substrate, we should expect an increase in the contents of metals in the biomass of miscanthus. Experiments confirm this relationship with respect to cadmium and copper. In the case of the cultivation of miscanthus on a substrate contaminated with lead, there were no significant changes in the content of this element in plants [68]. In research on the impact of fertilisation with sewage sludge on the contents of heavy metals in osier, Kalembasa et al. [69] note the lack of a significant dependence between the lead content in leafless plant shoots as controls and items with fertiliser treatments. However, the authors note that plants from plots on which the highest fertiliser dose was applied contained more heavy metals than those fertilised with a smaller amount of sewage sludge. Bearing in mind the environmental aspects, particular attention should be paid to the potential presence of heavy metals in plant biomass for energy purposes, and one should conduct in-depth qualitative characteristics [70].

4. Materials and Methods

4.1. Site Description

Two-year field trials were conducted in Krasne (Subcarpathian Voivodship, Poland, 50°04'16.1" N 22°04'37.6" E) over 2015–2017. They were located on arable land of the IVb land quality class in split-block system in four repetitions. The total number of plots in the field experiment was 32; the area of each was 35 m² (7 m length, 5 m width) and to the harvest 24 m² (6 m length, 4 m width).

4.2. Experimental Design

The area covered by the research was agricultural fallow left without any intervention for more than 10 years. In order to prepare the soil for cultivation (autumn 2013), mulching was performed with a bush cutter, followed by weeding in the form of a Roundup 360 SL spray (dose: 6 l ha⁻¹); after two weeks, disc ploughs and deep ploughing were performed using a mouldboard plough. In the spring of 2015, treatments for improving the soil (levelling the land surface, breaking up the soil lumps and destroying emerging weeds) were performed in the form of harrowing, with the use of a passive pneumatic seed drill. Based on the results of analyses performed before the experiment and the nutritional needs of plants, recommendations for fertiliser application were developed. Fertiliser treatments with biochar at a dose of 11.5 t ha⁻¹, ash from biomass at doses of 1.5, 3.0, 4.5 t ha⁻¹ and a

combination of these were used. In April 2015, fertilizers were sown manually, and then mixed with the soil to a depth of approximately 20 cm by means of a rototiller. Seedlings of giant miscanthus were obtained from a private supplier (Lublin Voivodship, Poland). On 16 April 2015, seedlings were manually planted on the experimental plots: planting depth: 10–15 cm; spacing of seedlings: 1 m; spacing of rows: 0.8 m; density: 13,000 plants ha^{-1} . The biomass harvest from the plots was performed in February 2016 and 2017 using a brushcutter with a cutting disc, rejecting extreme rows (height of the cut above the soil surface—10 cm). In the second year of the experiment, no re-application of fertiliser in the form of biochar and ash from biomass was carried out.

4.3. Fertiliser Material

The biochar, in the form of coal scales, originated from the processing of biomass from energy crops (commercially available, Poland). The fertiliser material in the form of ash from the combustion of a mixture of biomass from energy crops and plant biomass of agricultural origin was obtained from the Tauron power station (Stalowa Wola, Poland). Biochar was subjected to a grinding process with the use of the Laarmann CM-1000 high-speed cutting mill. The grinding process was performed using a sieve with a mesh size of 10 mm. Ash generated from the combustion of plant biomass did not require additional treatment before its application.

4.4. Biomass Production

The yield of plants was assessed at the end of each growing season. The plant material collected was dried at 70 °C, weighed and the biomass yield of dry matter in t ha^{-1} was calculated.

4.5. Examination of Samples

Samples of soil, biochar, ash from biomass and the aboveground parts of giant miscanthus plants were subjected to laboratory analyses using current analytical standards (Table 7).

Table 7. Parameters analysed with research methods.

Item	Parameter	Research Method
1	pH w KCl	PN-ISO 10390:1997 [71]
2	Content of absorbable forms of phosphorus (P_2O_5)	PN-R-04023:1996 [72]
3	Content of absorbable forms of potassium (K_2O)	PN-R-04022:1996/Az1:2002 [73]
4	Content of absorbable form of magnesium (Mg)	PN-R-04020:1996/Az1:2004 [74]
5	Content of carbon, nitrogen and hydrogen	PN-EN 15104:2011 [75]
6	Ash content	PN-EN 13775:2010 [76]
7	Content of volatile substances	PN-EN 15138:2011 [77]
8	Calorific value	PN-EN 13918:2010 [78]
9	Total content of selected macro- and microelements	Method using atomic emission spectrometry with excitation in argon plasma (ICP-OES)

The determination of the pH of the study materials was performed by measuring the concentration of hydrogen ions, i.e., the activity of hydrogen ions (H^+) with the use of the potentiometric method. The analysis was performed in KCl solution with a concentration of 1 mol dm^{-3} , assuming a mass ratio of the study sample to solution volume of 1:2.5. Measurements were performed using the Nahita pH meter, model 907 (AUXILAB, Beriáin, Spain).

Analyses of the contents of ash and volatile substances in the study materials using thermogravimetric methods were performed using the TGA 701 apparatus by LECO (LECO Corporation, Saint Joseph, MI, USA). The content of total carbon and nitrogen was tested using the TrueSpec CHN analyser by LECO (LECO Corporation, Saint Joseph, MI, USA). The AC500 calorimeter

by LECO (LECO Corporation, Saint Joseph, MI, USA) was used to determine the calorific value of the materials analysed.

The mineralisation of the study material was performed in three repetitions. Contents of elements in samples were determined using a method based on inductively coupled plasma atomic emission spectroscopy (ICP-OES), with the use of the iCAP Dual 6500 analyser (Thermo Fisher Scientific, Schaumburg, IL, USA). The mineralisation of the study samples was performed in Teflon containers using a mixture of acids under specific conditions (Table 8). In each case, a 0.2-g sample was mineralised. The sample obtained in this way was supplemented with mineralised water to make a volume of 50 mL. In the calibration step, standard solutions for all elements were prepared from the spectroscopic grade reagent (Thermo) with a three-step curve. The curve fit factor for all elements was over 0.99. Selection of a measuring line of appropriate length was validated by the method of standard additions. The recovery on selected lines was above 98.5% for each of the elements. Each time, the CRM 1515 (Certified Reference Material) was used and the selection of appropriate lines was implemented using the standard addition method. Each time we also used internal standards for matrix curve correction; these were Yttrium (Y) and Ytterbium (Yb), two elements not detected in the samples. The detection limit of the analytical method used for the elements studied was no worse than 0.01 mg kg⁻¹ [79].

Table 8. Parameters of the mineralisation process.

Material	Acid	Temperature and Time	Power	Application Note
Soil	8 mL HNO ₃ 65% 5 mL HCl 37% 1 mL HF 40% 5 mL H ₃ BO ₃ 5%	- temperature increase to 200 °C, time: 15 min; - maintaining at temperature of 200 °C, time: 15 min	1500 W	HPR-EN-13 [80]
Biochar	7 mL HNO ₃ 65% 1 mL H ₂ O ₂ 30%			HPR-PE-19 [81]
Plant biomass	6 mL HNO ₃ 65% 2 mL H ₂ O ₂ 30%			HPR-AG-02 [82]
Ash from biomass	7 mL HNO ₃ 65% 1 mL HCl 37% 1.5 mL HF 40%	- temperature increase to 220 °C, time: 20 min; - maintaining at temperature of 220 °C, time: 15 min		HPR-EN-04 [83]

4.6. Statistical Analyses

The verification of the influence of the experimental factors used on the parameters analysed and existing dependencies was performed using ANOVA statistical analysis by means of the Bonferroni post hoc test. A materiality level of $\alpha \leq 0.05$ was applied. Principal component analysis (PCA) was also applied. This indirect ordination technique allows one to analyse a large number of variables to detect structure and regularity in relationships between them. Statistical analyses were performed using Statistica 12 software (StatSoft Polska, Krakow, Poland).

5. Conclusions

While verifying the research hypothesis, it should be stated that biochar and ash from plant biomass can be used as a fertiliser in the cultivation of energy crops. The results of research presented in this paper confirm that biochar and ash from biomass used at an appropriate dose have a positive effect on the chemical properties of the soil and increase the yield of giant miscanthus. The result of the research indicates that biochar is a better fertiliser than biomass ash due to the wider spectrum of activity. However, the research conducted needs to be continued in order to monitor soil properties and assess the crop yield to be obtained in the following years. Deepening knowledge in this area is an attempt to direct the circulation of inorganic matter in the environment, and at the same time forms an important support for environmental protection, with particular emphasis on phytoremediation and the utilitarian dimension of sustainable energy management. The introduction of biochar into the soil

in combination with ash from biomass may be an alternative to traditional forms of mineral fertiliser, as well as a means to strengthen the ecological aspect of agro-energy.

Author Contributions: Conceptualization, B.S.; Data curation, B.S. and G.Z.; Formal analysis, B.S., G.Z., M.B. and M.C.; Methodology, B.S., G.Z., M.B. and M.C.; Project administration, C.P.; Supervision, C.P.; Writing—original draft, B.S. and G.Z.; Writing—review & editing, C.P.

Funding: This research received no external funding.

Conflicts of Interest: The authors declare no conflict of interest.

References

- Kumar, P.; Barret, D.M.; Delwiche, M.J.; Stroeve, P. Methods for pretreatment of lignocellulosic biomass for efficient hydrolysis and biofuel production. *Ind. Eng. Chem. Res.* **2009**, *48*, 3713–3729. [[CrossRef](#)]
- Tripathi, M.; Sahu, J.N.; Ganesan, P. Effect of process parameters on production of biochar from biomass waste through pyrolysis: A review. *Renew. Sustain. Energy Rev.* **2016**, *55*, 467–481. [[CrossRef](#)]
- Kalembasa, D. Amount and chemical composition of ash from biomass of energy crops. *Acta Agrophys.* **2006**, *7*, 909–913.
- Pels, J.R.; Nie, D.S.; Kiel, J.H.A. Utilization of ashes from biomass combustion and gasification. In Proceedings of the 13th European Biomass Conference & Exhibition, Paris, France, 17–21 October 2005.
- Medyńska-Juraszek, A. Biochar as an addition to soils. *Soil Sci. Annu.* **2016**, *67*, 151–157. [[CrossRef](#)]
- Laird, D.; Fleming, P.; Davis, D.; Horton, R.; Wang, B.; Karlen, D. Impact of biochar amendments on the quality of a typical Midwestern agricultural soil. *Geoderma* **2010**, *158*, 443–449. [[CrossRef](#)]
- Macdonald, L.; Farrell, M.; Van Zwieten, L.; Krull, E. Plant growth responses to biochar addition: An Australian soils perspective. *Biol. Fertil. Soils* **2013**, *50*, 1035–1045. [[CrossRef](#)]
- Beesley, L.; Moreno-Jiménez, E.; Gomez-Eyles, J.; Harris, E.; Robinson, B.; Sizmur, T. A review of biochars' potential role in the remediation, revegetation and restoration of contaminated soils. *Environ. Pollut.* **2011**, *159*, 3269–3282. [[CrossRef](#)] [[PubMed](#)]
- Cross, A.; Sohi, S. The priming potential of biochar products in relation to labile carbon contents and soil organic matter status. *Soil Biol. Biochem.* **2011**, *43*, 2127–2134. [[CrossRef](#)]
- Zhang, Q.; Du, Z.; Lou, Y.; He, X. A one-year short-term biochar application improved carbon accumulation in large macro aggregate fractions. *Catena* **2015**, *127*, 26–31. [[CrossRef](#)]
- Lehmann, J.; Rilling, M.C.; Thies, J.; Masiello, C.A.; Hockaday, W.C.; Crowley, D. Biochar effects on soil biota—A review. *Soil Biol. Biochem.* **2011**, *43*, 1812–1836. [[CrossRef](#)]
- Laird, D.A. The charcoal vision: A win-win-win scenario for simultaneously producing bioenergy, permanently sequestering carbon, while improving soil and water quality. *Agron. J.* **2008**, *100*, 178–181. [[CrossRef](#)]
- Chan, K.Y.; Van Zwieten, L.; Meszaros, I.; Downie, A.; Joseph, S. Agronomic values of green waste biochar as a soil amendment. *Aust. J. Soil Res.* **2007**, *45*, 629–634. [[CrossRef](#)]
- Woolf, D.; Amonet, J.E.; Street-Perrott, F.A.; Lehmann, J.; Joseph, S. Sustainable biochar to mitigate global climate change. *Nat. Commun.* **2010**, *1*, 56. [[CrossRef](#)] [[PubMed](#)]
- Yuan, J.; Xu, R.; Zhang, H. The forms of alkalins in the biochar produced from crop residues at different temperatures. *Bioresour. Technol.* **2011**, *102*, 3488–3497. [[CrossRef](#)] [[PubMed](#)]
- Novak, J.M.; Busscher, W.J.; Laird, D.L.; Ahmedna, M.; Watts, D.W.; Niandou, M.A.S. Impact of biochar amendment on fertility of a Southeastern coastal plain soil. *Soil Sci.* **2009**, *174*, 105–112. [[CrossRef](#)]
- Zong, Y.; Xiao, Q.; Lu, S. Acidity, water retention, and mechanical physical quality of a strongly acidic Ultisol amended with biochars derived from different feedstocks. *J. Soil Sediment* **2006**, *16*, 177–190. [[CrossRef](#)]
- Jien, S.; Wang, C. Effects of biochar on soil properties and erosion potential in a highly weathered soil. *Catena* **2013**, *110*, 225–233. [[CrossRef](#)]
- Agegnehu, G.; Bass, A.; Nelson, P.; Bird, M. Benefits of biochar, compost and biochar-compost for soil quality, maize yield and greenhouse gas emissions in a tropical agricultural soil. *Sci. Total Environ.* **2016**, *543*, 295–306. [[CrossRef](#)] [[PubMed](#)]
- Das, O.; Sarmah, A. The love-hate relationship of pyrolysis biochar and water: A perspective. *Sci. Total Environ.* **2015**, *512/513*, 682–685. [[CrossRef](#)] [[PubMed](#)]

21. Cayuela, M.; Van Zwieten, L.; Singh, B.; Jeffery, S.; Roig, A.; Sanchez-Monedero, M.A. Biochar’s role in mitigating soil nitrous oxide emissions: A review and meta-analysis. *Agric. Ecosyst. Environ.* **2013**, *191*, 5–16. [[CrossRef](#)]
22. Cadoux, S.; Riche, A.B.; Yates, N.E.; Machet, J.M. Nutrient requirements of *Miscanthus × giganteus*: Conclusions from a review of published studies. *Biomass Bioenergy* **2012**, *38*, 13–22. [[CrossRef](#)]
23. Lewandowski, I.; Scurlock, J.M.O.; Lindvall, E.; Christou, M. The development and current status of perennial rhizomatous grasses as energy crops in the US and Europe. *Biomass Bioenergy* **2003**, *25*, 335–361. [[CrossRef](#)]
24. Landrat, M.; Waluda, T. Possibilities of fertilizer using of rabbit manure. *Arch. Waste Manag. Environ. Prot.* **2016**, *18*, 25–32.
25. Piekarczyk, M. Content of absorbable forms of some macro- and microelements in light soil fertilized with ash from winter wheat straw. *Fragm. Agron.* **2013**, *30*, 92–98.
26. Butnan, S.; Deenik, J.L.; Toomsan, B.; Antal, M.J.; Vityakon, P. Biochar characteristics and application rates affecting corn growth and properties of soils contrasting in texture and mineralogy. *Geoderma* **2015**, *237*, 105–116. [[CrossRef](#)]
27. Case, S.D.C.; McNamara, N.P.; Reay, D.S.; Whitaker, J. The effect of biochar addition on N₂O and CO₂ emissions from a sandy loam soil—The role of soil aeration. *Soil Biol. Biochem.* **2012**, *51*, 125–134. [[CrossRef](#)]
28. Lai, W.Y.; Lai, C.M.; Ke, G.R.; Chung, R.S.; Chen, C.T.; Cheng, C.H.; Pai, C.W.; Chen, S.Y.; Chen, C. The effects of woodchip biochar application on crop yield, carbon sequestration and greenhouse gas emissions from soils planted with rice or leaf beet. *J. Taiwan Inst. Chem. Eng.* **2013**, *44*, 1039–1044. [[CrossRef](#)]
29. Nigussie, A.; Kissi, E.; Misganaw, M.; Ambaw, G. Effect of biochar application on soil properties and nutrient uptake of lettuces (*Lactuca sativa*) grown in chromium polluted soils. *Am.-Eurasian. J. Agric. Environ. Sci.* **2012**, *12*, 369–376.
30. Park, B.B.; Yanai, R.D.; Sahm, J.M.; Lee, D.K.; Abrahamson, L.P. Wood ash effects on plant and soil in a willow bioenergy plantation. *Biomass Bioenergy* **2005**, *28*, 355–365. [[CrossRef](#)]
31. Turner, B.L.; Frossard, E.; Oberson, A. *Biological Approaches to Sustainable Soil Systems*; Enhancing phosphorus availability in low-fertility soils; Taylor & Francis: Abingdon, UK, 2006; pp. 191–205.
32. Chintala, R.; Schumacher, T.; McDonald, L.; Clay, D.; Malo, D.; Papiernik, S.; Clay, S.; Julson, J. Phosphorus sorption and availability from biochars and soil/biochar mixtures. *Clean-Soil Air Water* **2013**, *42*, 626–634. [[CrossRef](#)]
33. Oram, N.; van de Voorde, T.; Ouwehand, G.; Bezemer, T.; Mommer, L.; Jeffery, S.; van Groenigen, J. Soil amendment with biochar increases the competitive ability of legumes via increased potassium availability. *Agric. Ecosyst. Environ.* **2013**, *191*, 92–98. [[CrossRef](#)]
34. Widowati, W.; Asnah, A. Biochar can enhance potassium fertilization efficiency and economic feasibility of maize cultivation. *J. Agric. Sci.* **2013**, *6*, 24–32. [[CrossRef](#)]
35. Liu, Y.; Lu, H.; Yang, S.; Wang, Y. Impacts of biochar addition on rice yield and soil properties in a cold waterlogged paddy for two crop seasons. *Field Crops Res.* **2016**, *191*, 161–167. [[CrossRef](#)]
36. James, A.K.; Thring, R.W.; Helle, S.; Ghuman, H.S. Ash management review—Applications of biomass bottom ash. *Energies* **2012**, *5*, 3856–3873. [[CrossRef](#)]
37. Bakisgan, C.; Dumanli, A.G.; Yürüm, Y. Trace elements in Turkish biomass fuels: Ashes of wheat straw, olive bagasse and hazelnut shell. *Fuel* **2009**, *88*, 1842–1851. [[CrossRef](#)]
38. Klavina, D.; Pennanen, T.; Gaitnieks, T.; Velmala, S.; Lazdins, A.; Lazdina, D.; Menkis, A. The ectomycorrhizal community of conifer stands on peat soils 12 years after fertilization with wood ash. *Mycorrhiza* **2016**, *26*, 153–160. [[CrossRef](#)] [[PubMed](#)]
39. Doan, T.T.; Henry-des-Tureaux, T.; Rumpel, C.; Janeau, J.L.; Jouquet, P. Impact of compost, vermicompost and biochar on soil fertility, maize yield and soil erosion in northern Vietnam: A three-year mesocosm experiment. *Sci. Total Environ.* **2015**, *513*, 137–154. [[CrossRef](#)] [[PubMed](#)]
40. Ghosh, S.; Ow, L.F.; Wilson, B. Influence of biochar and compost on soil properties and tree growth in a tropical urban environment. *Int. J. Environ. Sci. Technol.* **2015**, *12*, 1303–1310. [[CrossRef](#)]
41. Spokas, K.A.; Cantrell, K.B.; Novak, J.M.; Archer, D.A.; Ippolito, J.A.; Collins, H.P.; Boateng, A.A.; Lima, I.M.; Lamb, M.C.; McAloon, A.J.; et al. Biochar: A synthesis of its agronomic impact beyond carbon sequestration. *J. Environ. Qual.* **2012**, *41*, 973–989. [[CrossRef](#)] [[PubMed](#)]
42. Kuzyakov, Y.; Subbotina, I.; Chen, H.; Bogomolova, I.; Xu, X. Black carbon decomposition and incorporation into soil microbial biomass estimated by ¹³C labeling. *Soil Biol. Biochem.* **2009**, *41*, 210–219. [[CrossRef](#)]

43. Liu, Z.; Chen, X.; Jing, Y.; Li, Q.; Zhang, J.; Huang, Q. Effects of biochar amendment on rapeseed and sweet potato yields and water stable aggregate in upland red soil. *Catena* **2013**, *123*, 45–51. [[CrossRef](#)]
44. Puga, A.P.; Abreu, C.A.; Melo, L.C.A.; Paz-Ferreiro, J.; Beesley, L. Cadmium, lead and zinc mobility and plant uptake in a mine soil amended with sugarcane straw biochar. *Environ. Sci. Pollut. Res.* **2015**, *22*, 17606–17613. [[CrossRef](#)] [[PubMed](#)]
45. Bielińska, E.J.; Baran, S.; Stankowski, S. Assessment of the suitability of fluidized ashes from hard coal for agricultural purposes. *Agric. Eng.* **2009**, *6*, 7–13.
46. Szczukowski, S.; Stolarski, M.; Tworkowski, J. Yield of willow biomass manufactured with the eco-salix system. *Fragm. Agron.* **2011**, *28*, 104–115.
47. Kwaśniewski, D. Energy efficiency of biomass production from the annual willow. *Agric. Eng.* **2010**, *1*, 289–295.
48. Szczukowski, S.; Stolarski, M.; Tworkowski, J.; Rutkowski, P.; Goliński, P.; Mleczek, M.; Szentner, K. Yield and quality of biomass of selected willow species in the four-year harvest rotation. *Fragm. Agron.* **2013**, *31*, 107–113.
49. Jeżowski, S.; Głowiak, K.; Kaczmarek, Z.; Szczukowski, S. Field traits of eight common osier clones in the first three years following planting in Poland. *Biomass Bioenergy* **2011**, *35*, 1205–1210.
50. Kobyliński, A.; Olszewska, M. Energy efficiency of biomass production *Miscanthus giganteus*. *Grassl. Sci. Pol.* **2013**, *16*, 19–28.
51. Puchalski, C.; Zapałowska, A.; Hury, G. The impact of sewage sludge and biomass ash fertilization on the yield, including biometric features and physiological parameters of plants of two jerusalem artichoke (*Helianthus tuberosus* L.) cultivars. *Folia Pomer. Univ. Technol. Stetin. Agric. Aliment Pisc. Zootech.* **2017**, *332*, 37–52.
52. Boehmel, C.; Claupein, W. Contribution to bioenergy production by different annual and perennial cropping systems. In Proceedings of the 15th European Biomass Conference, Berlin, Germany, 7–11 May 2007.
53. Christou, M.; Mardikis, M.; Alexopoulou, E. Research on the effect of irrigation and nitrogen upon growth and yields of *Arundo donax* L. in Greece. *Asp. Appl. Biol.* **2001**, *65*, 47–55.
54. Danalatos, N.; Archontoulis, S.; Mitsios, I. Potential growth and biomass productivity of *Miscanthus × giganteus* as affected by plant density and N-fertilization in central Greece. *Biomass Bioenergy* **2007**, *31*, 31–152. [[CrossRef](#)]
55. Smith, R.; Slater, F.M. The effects of organic and inorganic fertilizer applications to *Miscanthus × giganteus*, *Arundo donax* and *Phalaris arundinacea*, when grown as energy crops in Wales, UK. *GCB Bioenergy* **2010**, *2*, 169–179. [[CrossRef](#)]
56. Chan, K.Y.; Van Zwieten, L.; Meszaros, I.; Downie, A.; Joseph, S. Using poultry litter biochars as soil amendments. *Aust. J. Soil Res.* **2008**, *46*, 437–444. [[CrossRef](#)]
57. Glaser, B.; Lehmann, J.; Zech, W. Ameliorating physical and chemical properties of highly weathered soils in the tropics with charcoal—Review. *Biol. Fertil. Soils* **2002**, *35*, 1719–1730. [[CrossRef](#)]
58. Uzoma, K.C.; Inoue, M.; Andry, H.; Fujimaki, H.; Zahoor, A.; Nishihara, E. Effect of cow manure biochar on maize productivity under sandy soil condition. *Soil Use Manag.* **2011**, *27*, 205–212. [[CrossRef](#)]
59. Liu, X.; Zhang, A.; Ji, C.; Joseph, S.; Bian, R.; Li, L.; Pan, G.; Paz-Ferreiro, J. Biochar's effect on crop productivity and the dependence on experimental conditions—A meta-analysis of literature data. *Plant Soil* **2013**, *373*, 583–594. [[CrossRef](#)]
60. Hossain, M.K.; Strezov, V.; Chan, K.Y.; Nelson, P.F. Agronomic properties of wastewater sludge biochar and bioavailability of metals in production of cherry tomato (*Lycopersicon esculentum*). *Chemosphere* **2010**, *78*, 1167–1171. [[CrossRef](#)] [[PubMed](#)]
61. Lehmann, J.; Gaunt, J.; Rondon, M. Biochar sequestration in terrestrial ecosystems—A review. *Mitig. Adapt. Strateg. Glob. Chang.* **2006**, *11*, 395–419. [[CrossRef](#)]
62. Gao, S.; DeLuca, T.H. Influence of biochar on soil nutrient transformations, nutrient leaching and crop yield. *Adv. Plants Agric. Res.* **2016**, *4*, 00150.
63. Klašnja, B.; Orlović, S.; Galić, Z. Comparison of different wood species as raw materials for bioenergy. *South-East Eur. For.* **2013**, *4*, 81–88. [[CrossRef](#)]
64. Kołodziej, B.; Antonkiewicz, J.; Sugier, D. *Miscanthus × giganteus* as a biomass feedstock grown on municipal sewage sludge. *Ind. Crops Prod.* **2016**, *81*, 72–82. [[CrossRef](#)]

65. Szyszak-Bargłowicz, J.; Zająć, G.; Piekarski, W. Energy biomass characteristics of chosen plants. *Int. Agrophys.* **2012**, *26*, 175–179. [[CrossRef](#)]
66. Borkowska, H.; Lipiński, W. Content of selected elements in biomass of several species of energy crops. *Acta Agrophys.* **2007**, *10*, 287–292.
67. Szyszak-Bargłowicz, J. Content of chosen macroelements in biomass of Virginia mallow (*Sida hermaphrodita* Rusby). *J. Cent. Eur. Agric.* **2013**, *15*, 263–271. [[CrossRef](#)]
68. Kalembasa, D.; Malinowska, E. Follow-up activities of sewage sludge applied to the soil in the pot experiment on the content of heavy metals in grass *Miscanthus sacchariflorus*. *Acta Agrophys.* **2009**, *13*, 377–384.
69. Kalembasa, S.; Wysokiński, A.; Cichuta, R. Content of heavy metals in willow (*Salix viminalis*) with different nitrogen fertilization. *Acta Agrophys.* **2009**, *13*, 385–392.
70. Szwalec, A.; Mundała, P.; Kędzior, R.; Telk, M.; Gawroński, P. Differentiation of Cd, Pb, Zn and Cu contents in biomass used for energy production. *Acta Sci. Pol. Formatio Circumiectus* **2016**, *15*, 343–351.
71. Polish Committee for Standardization. *Soil Quality—Determination of pH*; Polish Committee for Standardization: Warsaw, Poland, 1997.
72. Polish Committee for Standardization. *Chemical and Agricultural Analysis of the Soil—Determination of the Content of Absorbable Phosphorus in Mineral Soils*; Polish Committee for Standardization: Warsaw, Poland, 1996.
73. Polish Committee for Standardization. *Chemical and Agricultural Analysis of the Soil—Determination of the Content of Potassium in Mineral Soils*; Polish Committee for Standardization: Warsaw, Poland, 2002.
74. Polish Committee for Standardization. *Chemical and Agricultural Analysis of the Soil—Determination of the Content of Potassium in Mineral Soils*; Polish Committee for Standardization: Warsaw, Poland, 2004.
75. British Standards Institution. *Solid Biofuels—Determination of Total Carbon, Hydrogen and Nitrogen Content—Instrumental Methods*; British Standards Institution: London, UK, 2011.
76. British Standards Institution. *Solid Biofuels—Determination of Volatile Part Content*; British Standards Institution: London, UK, 2010.
77. British Standards Institution. *Solid Biofuels—Determination of Calorific Value*; British Standards Institution: London, UK, 2011.
78. British Standards Institution. *Solid Biofuels—Determination of Calorific Value*; British Standards Institution: London, UK, 2010.
79. Saletnik, B.; Zagula, G.; Grabek-Lejko, D.; Kasprzyk, I.; Bajcar, M.; Czernicka, M.; Puchalski, Cz. Biosorption of cadmium (II), lead (II) and cobalt (II) from aqueous solution by biochar from cones of larch (*Larix decidua* Mill. *subsp. decidua*) and spruce (*Picea abies* L. H. Karst.). *Environ. Earth Sci.* **2017**, *76*, 574. [[CrossRef](#)]
80. Milestone. *SK-10 High Pressure Rotor*; HPR-EN-13 Soil Total Digestion; Milestone: Shelton, CT, USA; Available online: <http://subitam.sinop.edu.tr/fileman/Uploads/Subitam/Mikrodalga.pdf> (accessed on 16 January 2018).
81. Milestone. *SK-10 High Pressure Rotor*; HPR-PE-19 Carbon Black; Milestone: Shelton, CT, USA; Available online: <http://subitam.sinop.edu.tr/fileman/Uploads/Subitam/Mikrodalga.pdf> (accessed on 16 January 2018).
82. Milestone. *SK-10 High Pressure Rotor*; HPR-AG-02 Dried Plant Tissue; Milestone: Shelton, CT, USA; Available online: <http://subitam.sinop.edu.tr/fileman/Uploads/Subitam/Mikrodalga.pdf> (accessed on 16 January 2018).
83. Milestone. *SK-10 High Pressure Rotor*; HPR-EN-04 Fly Ash; Milestone: Shelton, CT, USA; Available online: <http://subitam.sinop.edu.tr/fileman/Uploads/Subitam/Mikrodalga.pdf> (accessed on 16 January 2018).



© 2018 by the authors. Licensee MDPI, Basel, Switzerland. This article is an open access article distributed under the terms and conditions of the Creative Commons Attribution (CC BY) license (<http://creativecommons.org/licenses/by/4.0/>).

Article

Influence of NaCl Concentration on Food-Waste Biochar Structure and Templating Effects

Ye-Eun Lee ^{1,2}, Jun-Ho Jo ¹, I-Tae Kim ¹ and Yeong-Seok Yoo ^{1,2,*}

¹ Division of Environment and Plant Engineering, Korea Institute of Civil Engineering and Building Technology, 283 Goyang-daero, Ilsanseo-gu Goyang-si, Gyeonggi-do 10223, Korea; yeueunlee@kict.re.kr (Y.-E.L.); junkr@kict.re.kr (J.-H.J.); itkim@kict.re.kr (I.-T.K.)

² Department of Construction Environment Engineering, University of Science and Technology, 217 Gajeong-ro, Yuseong-gu, Daejeon 34113, Korea

* Correspondence: ysyoo@kict.re.kr; Tel.: +82-31-910-0298; Fax: +82-31-910-0288

Received: 3 August 2018; Accepted: 31 August 2018; Published: 5 September 2018

Abstract: Food-waste-derived biochar structures obtained through pyrolysis and with different NaCl concentrations were investigated. Increased NaCl concentration in the samples inhibited cellulose and lignin decomposition, ultimately increasing the biochar yield by 2.7% for 20%-NaCl concentration. NaCl added in solution state exhibited templating effects, with maximum increases in the Brunauer–Emmett–Teller (BET) surface area and pore volume of 1.23 to 3.50 $\text{m}^2 \cdot \text{g}^{-1}$ and 0.002 to 0.007 $\text{cm}^3 \cdot \text{g}^{-1}$, respectively, after washing. Adding a high concentration (20%) of NaCl reduced the BET surface area. In contrast, the mean pore diameter increased owing to the increased NaCl clustering area. Increased NaCl clustering with increased added NaCl was shown to have positive effects on NaCl removal by washing. Furthermore, as the NaCl adhered to the KCl scattered in the food waste, a high NaCl concentration also had positive effects on KCl removal. This study reports on an investigation on the effects of varying NaCl concentrations injected in solution form on the structure of food-waste biochar during pyrolysis. The templating effect was considered using both added NaCl and NaCl already contained in the food waste, with implementation of a desalination process essential for food-waste treatment for recycling.

Keywords: food waste; food-waste biochar; pyrolysis; NaCl template; desalination

1. Introduction

Carbon-negative biochar can be obtained from biomass via pyrolysis in an oxygen-limited environment [1]. Following the recent 2015 Paris Agreement, which expanded responsibility for greenhouse gas emissions mitigation to both developing and advanced countries, biochar production based on biowaste pyrolysis has become a novel alternative for biomass treatment [2–4].

The two main factors determining biochar characteristics are the physical properties of the raw material and the pyrolytic conditions (e.g., temperature, heating rate, and retention time) [5]. Pyrolysis methods can be broadly categorized into fast or slow techniques, respectively featuring a high heating rate of 100–1000 $^\circ\text{C} \cdot \text{s}^{-1}$ to produce gas or oil or a low heating rate of 20–100 $^\circ\text{C} \cdot \text{min}^{-1}$, which is more effective for biochar production [6,7].

The feedstocks most commonly used in commercial-scale or academic research are green waste materials, such as wood chips, crop residue, switch grass, and sugarcane, and organic wastes, such as sewage sludge and dairy manure [8]. For example, Van Zwieten et al. [9] reported the characteristics of biochar produced from papermill waste via slow pyrolysis at 550 $^\circ\text{C}$, and Kloss et al. [10] analyzed the characteristics of slow pyrolysis for different sources (wheat straw, poplar wood, and spruce wood) at different temperatures (400, 460, and 525 $^\circ\text{C}$). Furthermore, Ronsse et al. [11] compared different feedstocks, including pine wood, wheat straw, green waste, and dried algae, to analyze

the corresponding characteristics of the resultant biochar obtained via slow pyrolysis. However, although various feedstocks were comparatively analyzed in previous studies, the feedstocks themselves were mostly limited to the waste of a single organic crop.

Food is the largest waste source containing a blend of various organics and can be a good energy source with high energy content [12]. However, establishing an appropriate recycling method is challenging, as the NaCl content of food waste necessitates specific treatments. At present, composting is the main treatment method for food waste. However, the presence of NaCl continues to affect the compost quality. According to a recent review on food-waste usage by Pham et al. [13], conversion into biochar may be a promising alternative for food-waste treatment, but there is a lack of research on pyrolysis compared to anaerobic digestion and hydrothermal carbonization. Lee et al. [14] verified the potential application of food-waste pyrolysis at 300–500 °C and desalination to biochar production. Nonetheless, the biochar characteristic dependence on the different food source must be investigated.

In Korea, despite seasonal and source differences due to unique food cultures, the average NaCl content of dried food-waste biomass is 3.45% [15]. This implies that desalination is a prerequisite to food-waste recycling, which may increase the value of biochar. Recently, studies using molten NaCl as a template for increasing porosity have been reported. Among them, Fechler et al. [16] generated a porous material by mixing eutectic NaCl with C material and washing the resulting substance with water, and Liu and Antonietti [17] used molten NaCl and glucose to generate a porous C structure. These reports suggest the possibility of a desalination technique that removes the NaCl already present in the food waste, similar to the activation process for activated carbon.

In this context, the present study investigated whether the same activation effects as those obtained for molten NaCl can be achieved by adding NaCl in solution form to food waste. The corresponding changes in biochar structure, Brunauer–Emmett–Teller (BET) surface area, and pore size were examined for varying NaCl concentrations.

2. Materials and Methods

2.1. Materials

Food-waste samples were prepared using data from the Korean Ministry of the Environment (Table 1) [18]. The food waste was broadly classified into grains, vegetables, fruits, and meat, consisting of 10 ingredients with weight percent (wt %) values of 16, 51, 14, and 19, respectively. Whole ingredients of food waste sample were raw except the cooked rice. And the weight measurements were made at room temperature (25 °C). The prepared samples were dried at 105 °C for 24 h and ground into powder.

Table 1. Standard Food-Waste Samples.

Classification	Composition Ratio (wt %)	Food-Ingredient Processing Methods	
		Food Ingredients	Processing Method
Grains	16	Rice (16) Napa cabbage (9)	Cutting width: <100 mm
Vegetables	51	Potato (20) Onion (20) Daikon (2)	Chopped into 5 mm pieces
Fruits	14	Apple (7) Mandarin/orange (7)	Split lengthwise into 8 pieces
Meat	19	Meat (19)	
Total	100	100	Cutting width: ~3 cm.

2.2. Experimental Methods

The experiment had four steps: sample preparation, NaCl injection and drying, pyrolysis, and washing. Each independent experiment was repeated twice, and the results were presented as mean values. Solutions of 5, 10, and 20% NaCl were added to 120 g dried food-waste

samples, corresponding to 6.32, 13.34, and 15.00 g of NaCl dissolved in distilled water, respectively. The NaCl-free and 5, 10, and 20% NaCl-containing samples are referred to as the 0, 5, 10, and 20%-NaCl samples hereafter. The resulting mixtures were dried at 105 °C for 24 h. Next, the 0%-NaCl dried food samples and those impregnated with NaCl were placed in an electric furnace. The temperature was increased to 500 °C at 20 °C/min (the lowest speed of slow pyrolysis), and the pyrolysis was maintained for 1 h. To prevent sample oxidation, 99.99% N₂ gas (SJGAS, Incheon, Korea) was continuously injected into the furnace at 10 L/min through the flowmeter. The samples were subsequently removed from the furnace and cooled at room temperature until the ambient temperature was reached, after which the produced char was weighed. Figure 1 is a schematic of the pyrolysis reactor used in the experiment.

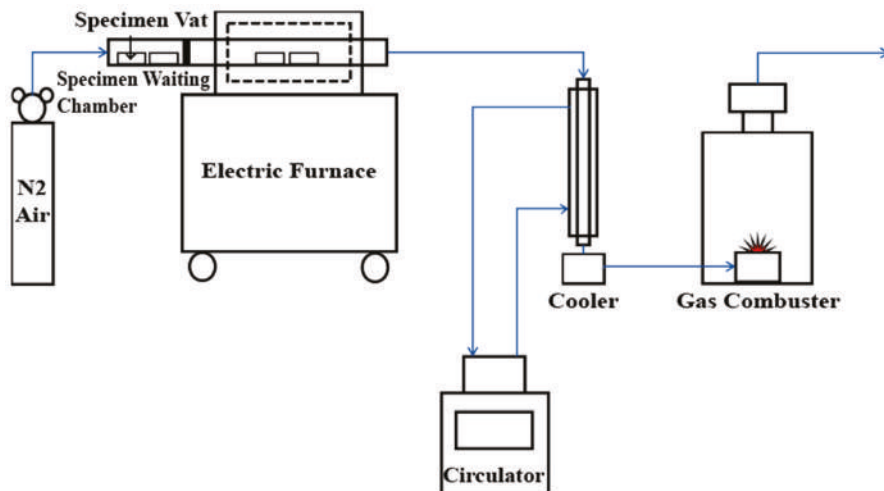


Figure 1. Schematic of the pyrolysis reactor used in this study.

To analyze and compare the differences in BET surface area among the samples, activated C was prepared as follows to be used as a control: For activation, 1 M sodium hydroxide (NaOH) solution was injected into a 0%-NaCl dried food sample at a 1:2 ratio. The sample was then dried at 105 °C before being subjected to pyrolysis under identical conditions as described above. Then, it was washed until the washing water reached pH 7 and dried.

2.3. Analysis Methods

2.3.1. Characterization Analysis Methods

When pyrolysis was complete, a CHNS analyzer (2400SeriesIICHNS/O, Perkin Elmer, Boston, MA, USA) was used to estimate the biochar elemental composition. Under the assumption that C + nitrogen (N) + O + sulfur (S) + hydrogen (H) + sodium (Na) + chlorine (Cl) = 100%, the O content was calculated using the equation 100 (%) – (C + N + S + H + Na + Cl) = O. To estimate the Cl content of the food-waste biochar, combustion ion chromatography (CIC; AQP-2100H, Mitsubishi Chemical Analytech, Chigasaki, Japan) was used. Note that, although CIC was found to be suitable for quantifying the 0%-NaCl biochar and the washed biochar from which the NaCl had been removed, the unwashed 5, 10, and 20%-NaCl biochar samples exceeded the CIC quantifiable range. This was

because the NaCl concentrated during pyrolysis. Thus, the following Equation (1) was used, based on the quantified Na content:

$$\frac{(\text{Na content of sample} \%) - \text{Na content of } 0\% \text{ biochar} (\%)}{22.98 \text{ (Atomic mass of Na)}} \times 35.45 \text{ (Atomic mass of Cl)} = \text{Cl content of sample} (\%) \quad (1)$$

To quantify the Na content of the biochar, atomic absorption spectroscopy (AAnalyst400, Perkin Elmer, Boston, MA, USA) was used.

2.3.2. Structural Analysis

BET and scanning electron microscopy (SEM)-energy dispersive X-ray (EDX) analyses were conducted to study the influence of the NaCl in the food waste on the biochar. The biochar microstructures were observed using SEM (Hitachi Ltd. S-4800 Ibaraki, Japan) with EDX (Oxford, EDX S-10, Abingdon, UK), and the BET surface areas were measured to check the templating effect before and after washing. The BET surface area was estimated based on N₂ gas sorption analysis at 77 K using a specific surface analyzer (BELSORP-MAX, BEL Japan Inc, Osaka, Japan).

To investigate the structural changes in the food-waste-derived biochar according to NaCl concentration, X-ray diffraction (XRD; DMAX 2500, Rigaku, Tokyo, Japan; 18 kW, 60 kV/300 mA) was employed. The 2θ range recorded for the samples was 10–90 °C. To investigate the presence of NaCl in the biochar as well as its influence, the value for 99%-NaCl powder was estimated, which was compared with the Joint Committee on Powder Diffraction and Standards (JCPDS) entry for NaCl (5–628) to establish the standard value. Fourier transform infrared spectroscopy (FT-IR; VERTEX 80V, Bruker Optics, Billerica, MA, USA) was performed and the KBr pellet method was used, in which a 1 mg sample was mixed with KBr powder and pressurized into a thin film. The structure was analyzed by transmitting 400–4000 nm infrared waves. All biochar samples used in the experiment were analyzed without prior treatment.

3. Results and Discussion

3.1. Biochar Characterization

Table 2 lists the chemical compositions of the food-waste-derived biochar for each NaCl concentration. As the NaCl in biochar can be removed by washing, the biochar samples before and after washing were analyzed to study the changes. The biochars before washing were compared with the 0%-NaCl food-waste-derived biochar as a control. Increased NaCl content was found to be accompanied by decreased C, H, and N contents, whereas the Na and Cl were condensed to crystal form. This indicates that the NaCl injected in an ionized state in the solution formed NaCl crystals during the drying and pyrolysis processes, thereby concentrating the NaCl in the biochar and preventing evaporation during pyrolysis. Regarding the post-wash compositions, the C, H, and N contents increased again in a trend similar to that in the control, whereas the Na and Cl contents decreased. This indicates that, although the increased NaCl content per unit weight made it seem as if the relative C, H, and N contents had decreased, the atomic content per unit weight of these materials was recovered as the washing removed the NaCl.

Table 2. Chemical composition of food-waste-derived biochar with different NaCl contents. (A: washed biochar; B: unwashed biochar; -: Not detected.).

(wt %)	C	H	N	S	O	Na	Cl
B_0%	76.29 ± 0.05	2.94 ± 0.02	6.04 ± 0.15	-	14.13 ± 0.10	0.24 ± 0.03	0.38 ± 0.01
B_5%	62.47 ± 0.23	2.39 ± 0.10	5.05 ± 0.01	-	12.62 ± 0.15	7.02 ± 0.01	10.47 ± 0.02
A_5%	75.90 ± 0.13	2.90 ± 0.07	6.03 ± 0.09	-	12.16 ± 0.04	2.20 ± 0.10	0.82 ± 0.10
B_10%	52.43 ± 0.54	2.06 ± 0.05	4.04 ± 0.02	-	10.59 ± 0.35	12.29 ± 0.09	18.60 ± 0.14
A_10%	76.21 ± 0.11	3.00 ± 0.01	5.91 ± 0.19	-	12.04 ± 0.01	2.09 ± 0.14	0.77 ± 0.16
B_20%	38.95 ± 0.89	1.98 ± 0.50	3.41 ± 0.05	-	8.63 ± 1.08	18.64 ± 0.99	28.40 ± 1.53
A_20%	74.92 ± 1.36	3.97 ± 0.72	6.21 ± 0.01	-	12.30 ± 1.09	2.27 ± 0.30	0.34 ± 0.15

Comparison of the Na and Cl contents before and after washing showed that the washing removed most of the NaCl. The post-wash Na content in the 5, 10, and 20%-NaCl biochar was higher than that in the 0%-NaCl control. This may be attributed to the influence of the biochar cation exchange capacity, under which a proportion of the Na^+ ions generated during washing adsorbed to the biochar [14]. Higher Cl content values were obtained for the 5 and 10%-NaCl biochar samples after washing compared to those of the 0%-NaCl biochar. However, the 20%-NaCl biochar exhibited similar contents to that of the control as the content decreased following washing. This similarity was due to the increased NaCl content of that specimen, which caused the NaCl to cluster rather than disperse. The SEM analysis (Section 3.2.2.) also confirmed that clustered NaCl crystals were scattered throughout the biochar for the 20%-NaCl biochar, whereas relatively small, scattered crystals were observed in the 5 and 10%-NaCl biochar samples. In other words, for 5 and 10%-NaCl content, the crystals were bound to the biochar in a scattered state, and complete NaCl removal through washing was difficult. However, for 20%-NaCl content, a large number of clustered NaCl crystals was obtained. Thus, complete removal is possible. The biochar yield, calculated as follows Equation (2):

$$\frac{\text{Weight after pyrolysis (g)} - \text{Impregnated NaCl content (g)}}{\text{Amount of Food waste (g)}} \times 100 = \text{Char Yield (\%)} \quad (2)$$

As Table 3 indicates, the food-waste biochar yield after NaCl injection was higher than that for NaCl-free food waste in general. Further, as the impregnated NaCl content increased, the char yield increased. In other words, the NaCl injection influenced the pyrolysis, thereby affecting the char yield.

Table 3. Effect of NaCl Concentrations on Food Waste Biochar Yield.

Added NaCl	Food Waste (g)	NaCl Content (g)	Weight after Pyrolysis (g)	Char Yield (wt %)
0%	120.00	-	27.29 ± 0.18	22.77 ± 0.15
5%	120.00	6.32	34.79 ± 0.28	23.73 ± 0.23
10%	120.00	13.34	42.04 ± 0.41	23.92 ± 0.34
20%	120.00	30.00	60.59 ± 2.40	25.49 ± 2.01

3.2. Structural Analysis

3.2.1. Brunauer–Emmett–Teller Analysis and Pore Size Distribution

Table 4 lists the BET surface area and pore analysis results for the biochar. For the NaCl-free (0%) biochar, the BET surface area was $1.226 \text{ m}^2 \cdot \text{g}^{-1}$. For the NaCl-containing biochar, increases in both BET surface area and pore volume after washing were observed, with differences according to NaCl content. This phenomenon was due to the empty spaces following NaCl removal by washing. Note that the SEM results discussed below (Section 3.2.2.) provide additional support for these findings.

When the total pore and mesopore volumes were compared, almost identical values were obtained; thus, most pores were mesopores. The approximately two-fold increase in mesopore volume after

washing also indicated that the mesopores were likely to have been caused by NaCl. The average pore diameter of washed sample is lower than unwashed sample. The average pore diameter before washing is not induced by NaCl but generated by the volatilization of organic matter. On the other hand, the pore diameter after washing is contained the pore induced by NaCl templating effect. In Section 3.2.2, showed that a single NaCl crystal size is about 2 nm. Therefore the average pore diameter is decreased after washing since the relatively small pore created by NaCl templating effect.

In contrast to the increase in total pore and mesopore volumes with increased NaCl content, the BET surface area exhibited a decreasing trend. An initial increase accompanied the NaCl content increase from 5 to 10%, but this was followed by a decrease when 20%-NaCl content was reached. This is thought to have been due to the excess NaCl allowing the clustered NaCl to exceed the large dispersion of NaCl. In other words, the higher the NaCl content was, the larger the NaCl crystals were; this yielded pores with a larger diameter and volume when the NaCl was removed. In contrast, the BET surface area decreased because of the growth of large mesopores instead of the even dispersion of relatively small mesopores.

There are other studies using NaCl as a template and washing as an activation process. Liu and Antonietti [17] used molten NaCl injected into a single source type, and Lu et al. [19] injected small-particle NaCl powder. But, these approaches differ from that of the present study. The findings of this study suggest that NaCl in solution form can have templating effects, and that the washing process induced activation effects.

In terms of competence, the BET surface areas and pore volumes observed in this study are not comparable to those of activated carbon. To explain this difference, the same sources were used in an experiment in which the activation method was implemented; the results are listed in the bottom row of Table 4. NaOH samples were prepared for activation by NaOH injection, followed by drying and pyrolysis at 500 °C, as in the main experiment. Washing was subsequently performed for neutralization. Between the biochar samples activated using 10%-NaCl and NaOH, the NaOH-treated biochar had a larger pore diameter. However, the difference in BET surface area was not substantial ($0.414 \text{ m}^2 \cdot \text{g}^{-1}$). Despite the increased pore diameter, the small increase in BET surface area for NaOH activation may indicate increased pore depth compared to activation based on NaCl crystals.

Studies investigating NaOH activation have reported high BET values for a single organic crop waste source, e.g., fir wood ($380 (\text{m}^2/\text{g})$) [20], coconut shell ($1842 (\text{m}^2/\text{g})$) [21], and flamboyant pods ($1076 (\text{m}^2/\text{g})$) [22]. However, Dai et al. [23] obtained low BET surface area values (12.73 and $12.99 (\text{m}^2 \cdot \text{g}^{-1})$) for livestock excretion as a source. This indicates that the BET surface area deviates significantly according to the source, and a lower BET surface area is generally produced when a mixed source is employed. The results of NaCl activation in this study indicate lower BET values than those of the abovementioned studies. However, the overall BET surface area reduction is likely to have resulted from the raw material and not the activation method, based on the comparison with NaOH activation.

Table 4. Brunauer–Emmett–Teller (BET) Surface Area and Pore Volume Analysis of Food-Waste-Derived Biochar with Different NaCl Contents.

Sample	BET Specific Surface Area ($\text{m}^2 \cdot \text{g}^{-1}$)	Total Pore Volume ($p/p_0 = 0.990$) ($\text{cm}^3 \cdot \text{g}^{-1}$)	Average Pore Diameter (nm)	Mesopore Surface Area ($\text{m}^2 \cdot \text{g}^{-1}$)	Mesopore Volume ($\text{cm}^3 \cdot \text{g}^{-1}$)
B_0%	1.226	0.00201	6.552	0.672	0.00176
B_5%	0.824	0.00193	9.475	0.465	0.00177
A_5%	2.946	0.00458	7.556	1.158	0.00377
B_10%	1.184	0.00341	11.505	0.902	0.00329
A_10%	3.500	0.00623	8.501	1.686	0.00537
B_20%	0.795	0.00256	14.119	0.651	0.00248
A_20%	2.485	0.00653	12.610	1.623	0.00613
NaOH	3.914	0.01746	17.845	2.452	0.01675

3.2.2. Scanning Electron Microscopy Analysis

Figure 2 presents images at different magnifications taken before and after biochar washing according to NaCl content. The NaCl crystals are embedded in the biochar surface. In the pre-wash images, the NaCl crystals are clustered together, except for the 20%-NaCl case, in which they are scattered. When crystals cluster, larger pores remain when they are removed through washing. The post-wash images show square-shaped pores identical to the NaCl crystals on the biochar surface. The pore diameter increased from 1.4 to 1.77 and then to 2.3 nm for NaCl contents of 5, 10, and 20%, respectively. In other words, the NaCl injected into the food waste occupied the interparticle spaces, thereby exerting a templating effect that created pores as it left the spaces upon washing. Higher NaCl content corresponded to larger crystals; hence, larger pores were created. The results also suggest that templating effects can be produced using NaCl in solution in addition to molten NaCl.

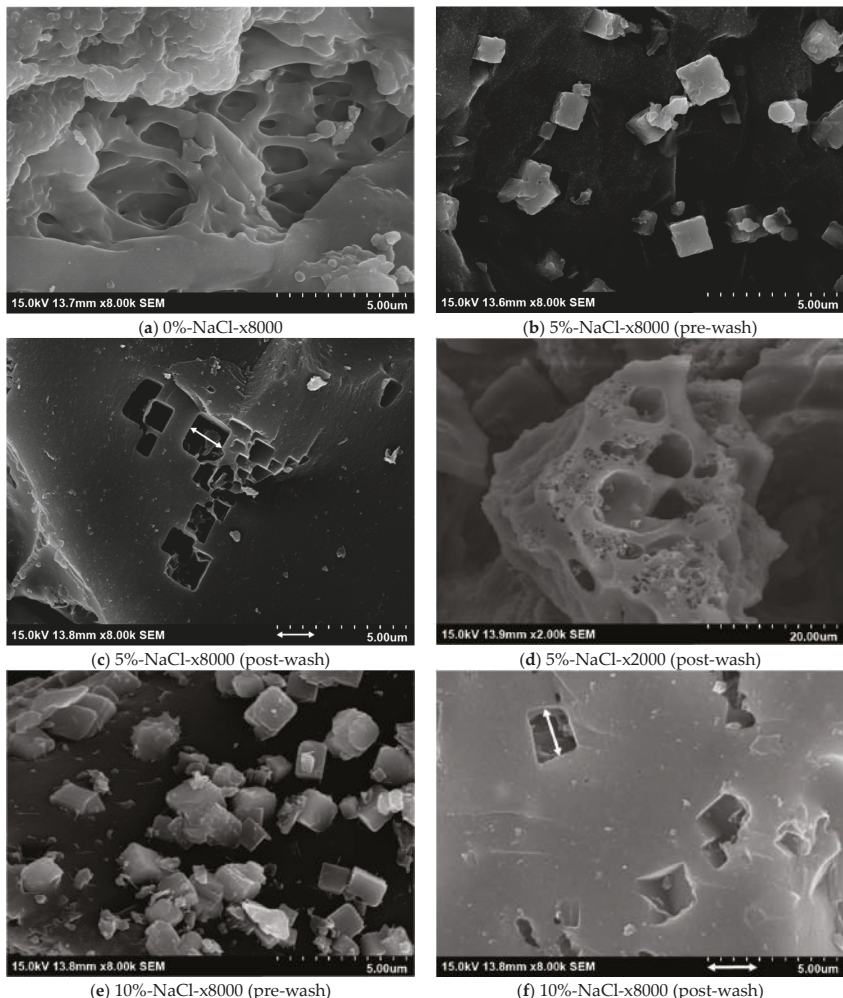


Figure 2. Cont.

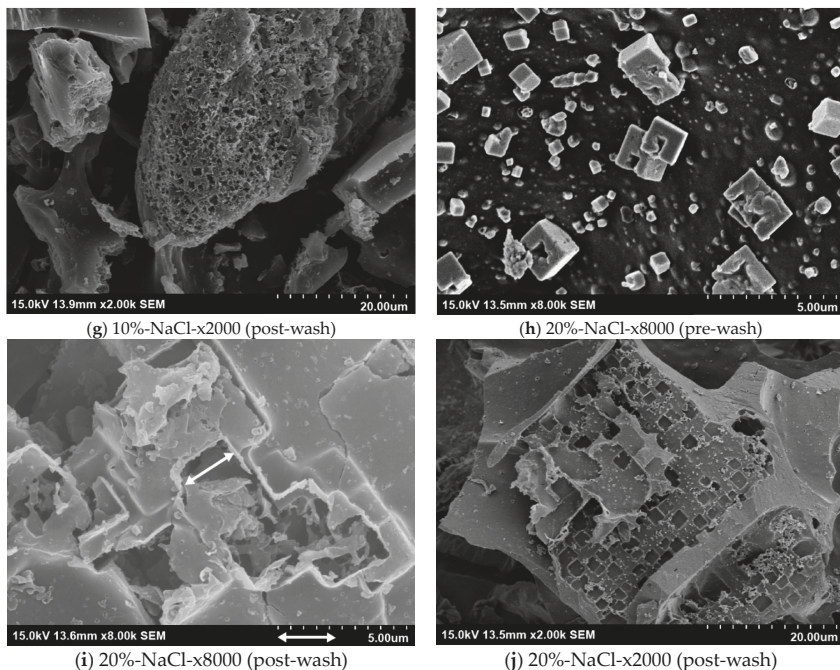


Figure 2. (a–j) scanning electron microscopy (SEM) images of biochar samples with different NaCl contents before and after washing: (a) 0%-NaCl-x8000; (b) 5%-NaCl-x8000 (pre-wash); (c) 5%-NaCl-x8000 (post-wash); (d) 5%-NaCl-x2000 (post-wash); (e) 10%-NaCl-x8000 (pre-wash); (f) 10%-NaCl-x8000 (post-wash); (g) 10%-NaCl-x2000 (post-wash); (h) 20%-NaCl-x8000 (pre-wash); (i) 20%-NaCl-x8000 (post-wash); (j) 20%-NaCl-x2000 (post-wash).

The EDX results of a marked range of figures (a), (c), and (e) in Figure 3 are shown in (b), (d), and (f) in Figure 3, respectively. The EDX results in Figure 3 indicate the places where intercrystal fusion or binding occurred; peaks corresponding to Na, K, and Cl can be seen together. One possible explanation for this phenomenon is the formation of a novel crystal shape upon binding. This may occur through the reformation of some crystals during sintering, as the melting point decreases when sylvite (KCl) and NaCl coexist [24] or through fusion of the injected NaCl and KCl already present in the food sample.

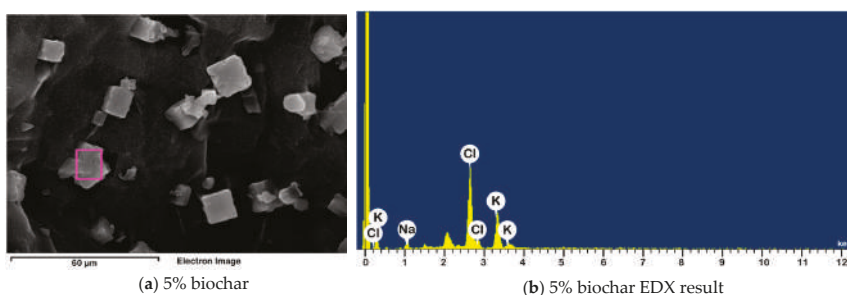


Figure 3. Cont.

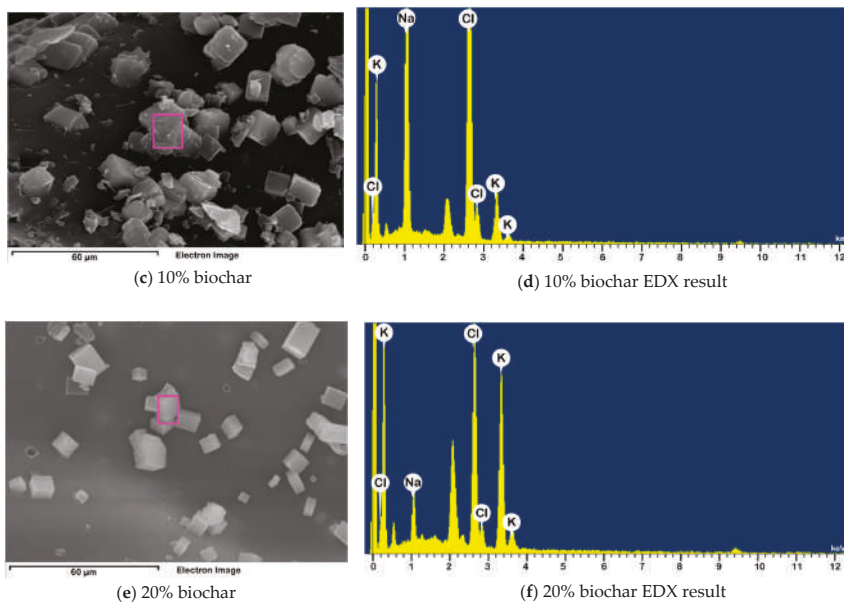


Figure 3. (a-f) NaCl crystal shape deformations and EDX results for biochar samples with different NaCl contents. (a) 5% biochar; (b) 5% biochar EDX result; (c) 10% biochar; (d) 10% biochar EDX result; (e) 20% biochar; (f) 20% biochar EDX result.

3.2.3. Fourier Transform Infrared Analysis

The results of the FT-IR analysis of the biochar according to NaCl content are presented in Figure 4. For the 0%-NaCl biochar sample, a peak appeared at 550 cm^{-1} . For the biochar samples containing NaCl that underwent pyrolysis, a peak appeared at 570 cm^{-1} , as if the peak at 550 cm^{-1} had shifted to the right. Vandecandelaere et al. [25] reported that peaks at 550 cm^{-1} indicate the presence of HPO_4^{2-} ions, whereas peaks at 575 cm^{-1} are related to PO_4^{3-} ions. Furthermore, Bekiaris et al. [26] showed that P=O stretching in hydroxyl apatite, apatite, and amorphous calcium phosphate dibasic in biochar yields 570-cm^{-1} peaks. In other words, if NaCl is present in the biomass during pyrolysis, phosphorus-compound decomposition to PO_4^{3-} rather than HPO_4^{2-} is induced. The peak at 520 cm^{-1} representing C-Cl bonding [27] and that at 646 cm^{-1} corresponding to C-Cl bending vibration [28] were not detected in the samples examined in this study. Therefore, the NaCl injection did not induce bonding with C.

The broad peak over the 700–1600 cm⁻¹ range in Figure 4 indicates the presence of cellulosic and ligneous constituents. For the NaCl-free (0%) biochar, peaks appeared at 1030, 1070, and 1120 cm⁻¹. With increased NaCl content, the peak at 1030 cm⁻¹ shifted to the right, whereas that at 1120 cm⁻¹ moved to 1130–1150 cm⁻¹. The peaks at 1030 and 1120 cm⁻¹ represent symmetric C-O stretching (cellulose, hemicellulose, and methoxy groups of lignin) and the symmetric C-O stretching characteristic of aliphatic C-O-C in the cellulose group, respectively [29,30]. The shifting of these peaks to the right indicated changes in cellulose from aliphatic C-O-C to alcohol C-O stretching or antisymmetric stretching of C-O-C (glycosyl), as the NaCl in the biochar induces hemolytic cleavage in cellulose [31]. During pyrolysis, cellulose generates levoglucosan production due to heterocyclic cleavage of the glycosidic linkage [31]. However, when NaCl is present, the glycosidic bond breaking is inhibited [31]. Thus, a peak representing the glycosidic linkage appears at 1130–1150 cm⁻¹ for the NaCl-containing biochar.

Although the 0, 5, and 10%-NaCl biochar samples mostly displayed similar peaks, the 20%-NaCl biochar exhibited a phase that could be clearly distinguished. These peaks appeared more prominent at 1230 and 1370–1430 cm^{-1} , positions respectively corresponding to the C-H and O-H bending frequencies in lignin [28,32,33]. The peaks at 2918 and 2850 cm^{-1} and 3000–3100 cm^{-1} became more distinct, respectively representing alkanes/aliphatic C-H stretching [34–37] and C-H stretching in aromatic compounds [38,39]. The peaks at 2918 and 2850 cm^{-1} are caused by alkyl adsorption and are strongest in the FT-IR spectra of lignin [40]. The peak at 3000–3100 cm^{-1} , which corresponds to aromatic C-H stretching, is another peak appearing in the spectra of macromolecule units such as lignin [38]. In the present study, the finding that food-waste biochar with 20%-NaCl content produced more distinct peaks for lignin than biochar containing 5 or 10%-NaCl did can be taken to indicate that high NaCl content inhibits lignin degradation during pyrolysis. This is further supported by the fact that the peak at 1700 cm^{-1} corresponding to the carbonyl C=O stretching vibration in cellulose and lignin showed a minor increase for the 5 and 10%-NaCl biochar, whereas a marked increase was detected for the 20%-NaCl biochar. The high NaCl content of the latter probably inhibited the lignin degradation.

The presence of Na during pyrolysis acts as an inhibitor to the conversion of cellulose and lignin into levoglucosan [31,41]. As mentioned above, hemolytic cleavage is induced for cellulose, so that conversion into glycolaldehyde and formic acid, rather than levoglucosan, occurs [31]. For lignin, degradation producing a guaiacol group is induced [41]. Thus, for food waste with high NaCl content, a competitive pathway is induced to replace the original degradation pathway, thereby inhibiting fast degradation of lignin and cellulose, and a proportion of these materials is left behind in the biochar. This increase in the residual lignin and cellulose may be interpreted as the cause of the increase in biochar yield reported in Section 3.1 and the increase in H content that accompanied the increase in NaCl content.

The peak at approximately 1560 cm^{-1} indicates C-N stretching and N-H bending [35,42,43]. The peaks in this region are especially strong for 20%-NaCl biochar, suggesting that high NaCl content may enhance N capture during pyrolysis. The peak representing a nitrile group at 2350 cm^{-1} is also absent from the 0%-NaCl biochar [28], but gains intensity as the NaCl content increases. This provides additional support for the positive effect of NaCl content on N capture. A possible explanation may lie in the protein coagulation caused by inorganic NaCl, although further research is required to determine the precise cause [44].

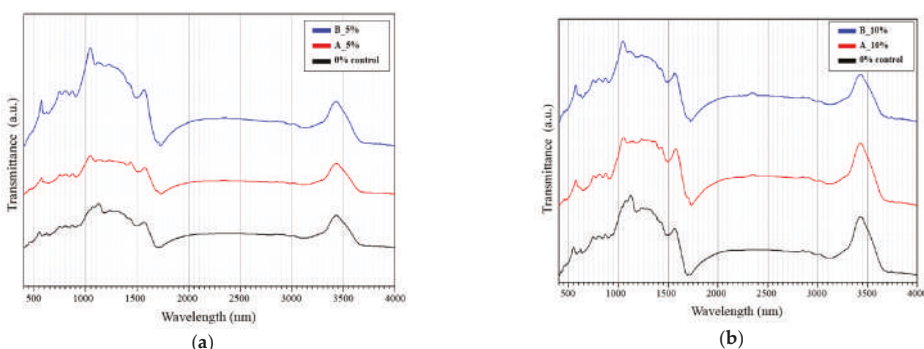


Figure 4. Cont.

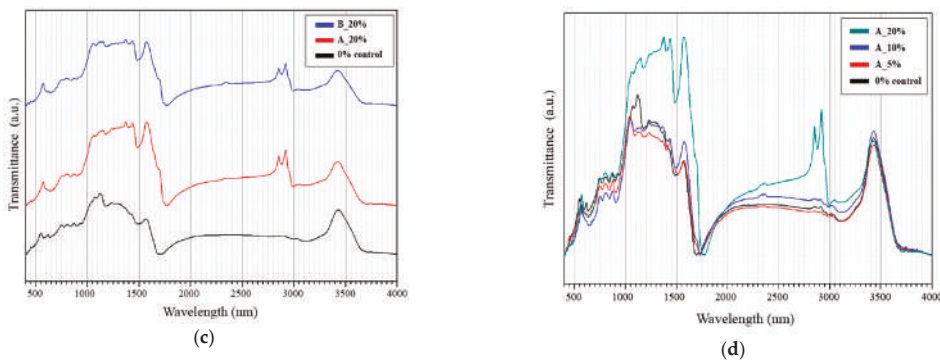


Figure 4. FT-IR results for (a) 5%, (b) 10%, and (c) 20%-NaCl biochar after and before washing, with the results for 0%-NaCl biochar. (d) FT-IR results for 0%, 5%, 10%, and 20%-NaCl biochar after washing.

3.2.4. X-ray Diffraction Analysis

The results of the XRD analysis of the NaCl powder are presented in Figure 5e. The NaCl peaks appear at 27.4, 31.5, 45.5, 56.5, 65.5, 75.5, and 84°. In Figure 5, the XRD result for the 0%-NaCl food-waste biochar indicates peaks at 18.5, 28.4, 30.1, 40.5, 50.3, 66.5, and 74°, with a broad peak in the vicinity of 25°. To analyze the influence of the NaCl content on the biochar structure, the results shown in Figure 5a–d for the biochar samples with varying NaCl concentrations before and after washing were compared with those for the control 0%-NaCl biochar shown in Figure 5e.

Table 5 summarizes the XRD peaks for each sample. The pre-wash biochar samples clearly display NaCl peaks. For the post-wash biochar samples, the NaCl peaks either disappear or lose intensity, indicating that the washing removed most of the NaCl content. The pre-wash results indicate that increased NaCl content in the samples generally shifted the NaCl peak from 31.2 to 31.4 and 31.7°, i.e., from left to right, for 5, 10, and 20%-NaCl content, respectively. This shifting of the peak to a lower angle indicates expansion of the space lattice [45,46]. In the BET surface area analysis discussed above (Section 3.2.1.), the average post-wash pore diameter was found to increase with the NaCl content. The increased pore diameter following the NaCl removal indicates that the increase in NaCl content in turn increased the NaCl crystal size. In other words, the peak shifting from left to right may have been due to the increased crystal size reducing the expansion when the imparted energy was the same, so that a larger expansion occurred in the biochar with lower NaCl content because of the small crystal size.

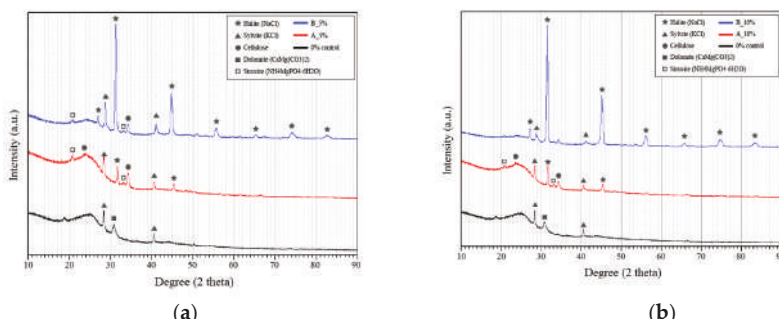


Figure 5. Cont.

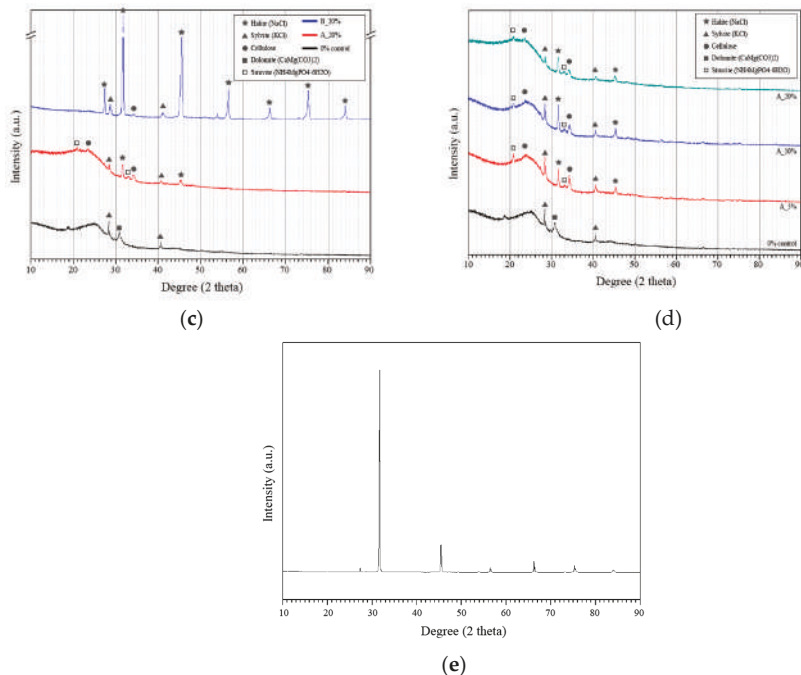


Figure 5. XRD results for (a) 5%, (b) 10%, and (c) 20%-NaCl biochar samples after and before washing, with 0%-NaCl biochar result. (d) XRD results for 0%, 5%, 10%, and 20%-NaCl samples after washing. (e) XRD result for NaCl powder.

The peaks at 3.14, 2.22, and 1.81 Å correspond to KCl (JCPDS #41–1476) [34,47]. Regardless of NaCl concentration, the peaks for the pre-wash biochar shifted to the right and then shifted back to the left after washing, being detected at 28.4° and 40.5°, i.e., the same positions as the KCl in the control. The peaks detected in the pre-wash biochar appeared in the position between standard KCl and halite. Note that, when KCl and NaCl are present together, the melting point decreases and reformation occurs during sintering [24]. As shown in Figure 3, the crystal cube shape was deformed for the K, Na, and Cl bindings.

According to Broström et al. [24], XRD analysis of a mixture of NaCl and KCl showed the KCl peaks shifting to the right compared to the standard, i.e., to 29 and 41°. This could be explained by partial binding between the NaCl injected into the food waste during pyrolysis and the KCl already present in the food waste, which caused the KCl peak to shift to the right (to 28.8 and 41°). This was followed by the emergence of peaks at 28.4 and 40.5° due to the independent KCl content remaining after washing, which removed only the KCl bound to NaCl. As Figure 5d shows, the larger the NaCl injection volume was, the smaller the KCl peak intensity was. The peak intensities at 28.4 and 40.5° were 3872 and 1827, 3831 and 1849, 3582 and 1741, and 3248 and 1560 for the 0, 5, 10, and 20%-NaCl samples, respectively. This indicates a decrease in peak intensity with increased NaCl content. As the NaCl content was increased, a higher proportion of the KCl dispersed in the food waste could combine with the injected NaCl. Thus, the amount of residual KCl decreased as the larger amount of KCl bound to the NaCl was removed by washing.

Peaks at 3.78 and 2.61 Å were not detected in the 0%-NaCl biochar but did appear in the NaCl-containing biochar. The peaks at these positions indicate the presence of cellulose [48,49]. As mentioned in Section 3.2.3., when NaCl is added to cellulose undergoing pyrolysis, decomposition

of the cellulose into levoglucosan is inhibited [31]. For NaCl-free food waste, the cellulose decomposes to produce levoglucosan during pyrolysis. However, cellulose degradation is inhibited for food waste containing NaCl. Thus, the residual cellulose produced the above peaks. In the pre-wash biochar, the peaks appeared indefinite around 3.78 Å. This can be explained by the strong intensity of the NaCl crystal peak comparatively weakening the cellulose peaks. Therefore, although it was difficult to detect both peaks together in the 20%-NaCl biochar, which had the strongest NaCl peaks, they became discernible after washing, which reduced the NaCl peak intensity.

Table 5. X-ray diffraction analysis peaks for NaCl and food-waste-derived biochar with different NaCl contents.

NaCl	0%	B_5%	A_5%	B_10%	A_10%	B_20%	A_20%
	18.7 (4.74)						
	20.8 (4.27)						
		23.5 (3.78)		23.5 (3.78)		23.5 (3.78)	
27.4 (3.25)	27 (3.30)	27.2 (3.26)	27.2 (3.27)	27.2 (3.27)	27.4 (3.25)	27.2 (3.27)	27.2 (3.27)
	28.4 (3.14)	28.8 (3.10)	28.4 (3.14)	28.8 (3.10)	28.4 (3.14)	28.8 (3.10)	28.4 (3.14)
	30.8 (2.90)						
31.5 (2.84)	31.2 (2.86)	31.6 (2.83)	31.4 (2.85)	31.6 (2.83)	31.7 (2.82)	31.6 (2.83)	
	33 (2.71)	33 (2.71)		33 (2.71)		33 (2.71)	
	34.3 (2.61)						
40.5 (2.22)	41 (2.20)	40.5 (2.22)	41 (2.20)	40.5 (2.22)	41 (2.20)	40.5 (2.22)	40.5 (2.22)
45.5 (1.99)	45 (2.01)	45.5 (1.99)	45 (2.01)	45.5 (1.99)	45.5 (1.99)	45.2 (2.00)	
	50.3 (1.81)	51 (1.79)	50.3 (1.81)		50.3 (1.81)	50.3 (1.81)	
			53.5 (1.71)		53.8 (1.70)		
56.5 (1.63)	55.5 (1.65)	56.5 (1.63)	56 (1.64)	56.4 (1.63)	56.5 (1.63)	56.2 (1.63)	
	61.5 (1.51)	61.5 (1.51)					
65.5 (1.42)	65.2 (1.43)		65.7 (1.42)		66.2 (1.41)		
	66.5 (1.40)	67.5 (1.39)	66.5 (1.40)		66.5 (1.40)		
75.5 (1.26)	74 (1.28)		74.7 (1.27)		75.2 (1.26)		
84 (1.15)	82.5 (1.17)		83.5 (1.16)		84 (1.15)		

Finally, the 0%-NaCl biochar had a peak at 30.8°, which indicates the presence of dolomite ($\text{CaMg}(\text{CO}_3)_2$) [34]. On the other hand, biochar samples with added NaCl had peaks at 20.8° and 33°, which indicates the presence of struvite ($\text{NH}_4\text{MgPO}_4 \cdot 6\text{H}_2\text{O}$) [50], and there is no peak at 30.8°. As

mentioned in Section 3.2.3, when NaCl is present during pyrolysis, phosphorus compound decomposes to the form of PO_4^{3-} not the form of HPO_4^{2-} . These XRD results support those of the FT-IR. A magnesium (Mg) component contained in the food waste became dolomite during pyrolysis. When NaCl is present during pyrolysis, Mg combined with PO_4^{3-} and crystallized.

4. Conclusions

Food waste is difficult to recycle due to the innate NaCl content. It is essential to remove NaCl in order to utilize food waste biochar. The use of NaCl in food waste and desalination process as a template and activation process, respectively, could be a way to improve the value of the biochar. Therefore, this study investigated changes in biochar structure according to varying NaCl solution concentrations added to food waste and desalination. As the NaCl concentration increased from 0% to 20%, cellulose and lignin decomposition inhibited during pyrolysis, ultimately increasing the biochar yield by 2.7% for 20%-NaCl concentration. Furthermore, the added NaCl formed crystals exerting a templating effect, inducing an increase in BET surface area and pore volume in the biochar when it was washed. In comparison to the NaOH-based activation method, the NaCl templating method yielded a minor difference BET surface area, while the pore depth was found to be shallower. Adding 20% NaCl reduced the BET surface area while the mean pore diameter increased, owing to the increased NaCl clusters. The phenomenon in which the NaCl clustering increases as a NaCl concentration increases was shown to have positive effects on NaCl removal through washing. Further, as the NaCl adhered to the KCl scattered among the food waste, the high concentration of NaCl also had positive effects on the KCl removal. Finally, a NaCl induced form of struvite and yielded a valuable biochar that can be used as a soil fertilizer.

Author Contributions: Conceptualization, Y.-E.L. and Y.-S.Y.; Validation, Y.-E.L., J.-H.J., Y.-S.Y.; Formal Analysis, Y.-E.L.; Investigation, Y.-E.L.; Resources, Y.-E.L. and J.-H.J.; Writing—Original Draft Preparation, Y.-E.L.; Writing—Review & Editing, Y.-E.L., J.-H.J., Y.-E.L., and I.-T.K.; Supervision, Y.-S.Y.; Project Administration, I.-T.K.

Acknowledgments: This work was supported by the Major Project of the Korea Institute of Civil Engineering and Building Technology (KICT) [grant number 2018-0063].

Conflicts of Interest: The authors declare no conflict of interest.

References

1. Glaser, B.; Parr, M.; Braun, C.; Kopolo, G. Biochar is carbon negative. *Nat. Geosci.* **2009**, *2*. [[CrossRef](#)]
2. Mathews, J.A. Carbon-negative biofuels. *Energy Policy* **2008**, *36*, 940–945. [[CrossRef](#)]
3. Guizani, C.; Jeguirim, M.; Valin, S.; Limousy, L.; Salvador, S. Biomass chars: The effects of pyrolysis conditions on their morphology, structure, chemical properties and reactivity. *Energies* **2017**, *10*. [[CrossRef](#)]
4. Brassard, P.; Godbout, S.; Raghavan, V.; Palacios, J.H.; Grenier, M.; Zegan, D. The production of engineered biochars in a vertical auger pyrolysis reactor for carbon sequestration. *Energies* **2017**, *10*. [[CrossRef](#)]
5. Ghorbel, L.; Rouissi, T.; Brar, S.K.; López-González, D.; Amarillo Ramirez, A.; Godbout, S. Value-added performance of processed cardboard and farm breeding compost by pyrolysis. *Waste Manag.* **2015**, *38*, 164–173. [[CrossRef](#)] [[PubMed](#)]
6. Ryu, C.; Sharifi, V.N.; Swithenbank, J. Waste pyrolysis and generation of storable char. *Int. J. Energy Res.* **2007**, *31*, 177–191. [[CrossRef](#)]
7. Basu, P. *Biomass Gasification, Pyrolysis and Torrefaction: Practical Design and Theory*, 2nd ed.; Academic Press: Cambridge, MA, USA, 2013.
8. Sohi, S.; Lopez-Capel, E.; Krull, E.; Bol, R. Biochar, climate change and soil: A review to guide future research. *CSIRO Land Water Sci. Rep.* **2009**, *5*, 17–31.
9. Van Zwieten, L.; Kimber, S.; Morris, S.; Chan, K.Y.; Downie, A.; Rust, J.; Joseph, S.; Cowie, A. Effects of biochar from slow pyrolysis of papermill waste on agronomic performance and soil fertility. *Plant Soil* **2010**, *327*, 235–246. [[CrossRef](#)]

10. Kloss, S.; Zehetner, F.; Dellantonio, A.; Hamid, R.; Ottner, F.; Liedtke, V.; Schwanninger, M.; Gerzabek, M.H.; Soja, G. Characterization of slow pyrolysis biochars: Effects of feedstocks and pyrolysis temperature on biochar properties. *J. Environ. Qual.* **2012**, *41*, 990–1000. [[CrossRef](#)] [[PubMed](#)]
11. Ronsse, F.; Van Hecke, S.; Dickinson, D.; Prins, W. Production and characterization of slow pyrolysis biochar: Influence of feedstock type and pyrolysis conditions. *Gcb Bioenergy* **2013**, *5*, 104–115. [[CrossRef](#)]
12. Lin, C.S.K.; Pfaltzgraff, L.A.; Herrero-Davila, L.; Mubofu, E.B.; Solhy, A.; Clark, J.H.; Koutinas, A.A.; Kopsahelis, N.; Stamatelatou, K.; Dickson, F.; et al. Food waste as a valuable resource for the production of chemicals, materials and fuels. Current situation and global perspective. *Energy Environ. Sci.* **2013**, *6*, 426–446. [[CrossRef](#)]
13. Pham, T.P.T.; Kaushik, R.; Parshetti, G.K.; Mahmood, R.; Balasubramanian, R. Food waste-to-energy conversion technologies: Current status and future directions. *Waste Manag.* **2015**, *38*, 399–408. [[CrossRef](#)] [[PubMed](#)]
14. Lee, Y.-E.; Jo, J.-H.; Kim, I.-T.; Yoo, Y.-S. Chemical Characteristics and NaCl Component Behavior of Biochar Derived from the Salty Food Waste by Water Flushing. *Energies* **2017**, *10*. [[CrossRef](#)]
15. Kim, N.C.; Jang, B.M. Sodium chloride decomposting method in food waste compost using triple salt. *J. Korra* **2004**, *12*, 86–94.
16. Fechler, N.; Fellinger, T.-P.; Antonietti, M. “Salt templating”: A simple and sustainable pathway toward highly porous functional carbons from ionic liquids. *Adv. Mater.* **2013**, *25*, 75–79. [[CrossRef](#)] [[PubMed](#)]
17. Liu, X.; Antonietti, M. Molten salt activation for synthesis of porous carbon nanostructures and carbon sheets. *Carbon* **2014**, *69*, 460–466. [[CrossRef](#)]
18. Ministry of Environment (MOE). *A Study on Food Waste Reduction Equipment Guidelines and Quality Standard*; Ministry of Environment: Sejong City, Korea, 2009.
19. Lu, A.-H.; Li, W.C.; Schmidt, W.; Schüth, F. Fabrication of hierarchically structured carbon monoliths via self-binding and salt templating. *Microporous Mesoporous Mater.* **2006**, *95*, 187–192. [[CrossRef](#)]
20. Wu, F.-C.; Tseng, R.-L. High adsorption capacity NaOH-activated carbon for dye removal from aqueous solution. *J. Hazard. Mater.* **2008**, *152*, 1256–1267. [[CrossRef](#)] [[PubMed](#)]
21. Cazetta, A.L.; Vargas, A.M.A.; Nogami, E.M.; Kunita, M.H.; Martins, A.C.; Silva, T.L.; Moraes, J.C.G.; Almeida, V.C.; Guilherme, M.R. NaOH-activated carbon of high surface area produced from coconut shell: Kinetics and equilibrium studies from the methylene blue adsorption. *Chem. Eng. J.* **2011**, *174*, 117–125. [[CrossRef](#)]
22. Vargas, A.M.M.; Garcia, C.A.; Reis, E.M.; Lenzi, E.; Costa, W.F.; Almeida, V.C. NaOH-activated carbon from flamboyant (*Delonix regia*) pods: Optimization of preparation conditions using central composite rotatable design. *Chem. Eng. J.* **2010**, *162*, 43–50. [[CrossRef](#)]
23. Dai, Z.; Meng, J.; Muhammad, N.; Muhammad, L.; Wang, H.; He, Y.; Brookes, P.C.; Xu, J. The potential feasibility for soil improvement, based on the properties of biochars pyrolyzed from different feedstocks. *J. Soils Sedim.* **2013**, *13*, 989–1000. [[CrossRef](#)]
24. Broström, M.; Enestam, S.; Backman, R.; Mäkelä, K. Condensation in the KCl–NaCl system. *Fuel Process. Technol.* **2013**, *105*, 142–148. [[CrossRef](#)]
25. Vandecandelaere, N.; Rey, C.; Drouet, C. Biomimetic apatite-based biomaterials: On the critical impact of synthesis and post-synthesis parameters. *J. Mater. Sci. Mater. Med.* **2012**, *23*, 2593–2606. [[CrossRef](#)] [[PubMed](#)]
26. Bekiaris, G.; Bruun, S.; Peltre, C.; Houot, S.; Jensen, L.S. FTIR–PAS: A powerful tool for characterising the chemical composition and predicting the labile C fraction of various organic waste products. *Waste Manag.* **2015**, *39*, 45–56. [[CrossRef](#)] [[PubMed](#)]
27. Porchelvi, E.; Muthu, S. The spectroscopic (FT-IR, FT-Raman and NMR), NCA, Fukui function analysis first order hyperpolarizability, TGA of 6-chloro-3,4-dihydro-2H-1,2,4-benzothiazine-7-sulphonamide1,1-dioxide by ab initio HF and Density Functional method. *Spectrochim. Acta Part A Mol. Biomol. Spectrosc.* **2014**, *123*, 230–240. [[CrossRef](#)] [[PubMed](#)]
28. Mohanty, P.; Nanda, S.; Pant, K.K.; Naik, S.; Kozinski, J.A.; Dalai, A.K. Evaluation of the physicochemical development of biochars obtained from pyrolysis of wheat straw, timothy grass and pinewood: Effects of heating rate. *J. Anal. Appl. Pyrolysis* **2013**, *104*, 485–493. [[CrossRef](#)]
29. Zhao, S.-X.; Ta, N.; Wang, X.-D. Effect of Temperature on the Structural and Physicochemical Properties of Biochar with Apple Tree Branches as Feedstock Material. *Energies* **2017**, *10*. [[CrossRef](#)]

30. Ahmad, M.; Lee, S.S.; Dou, X.; Mohan, D.; Sung, J.K.; Yang, J.E.; Ok, Y.S. Effects of pyrolysis temperature on soybean stover- and peanut shell-derived biochar properties and TCE adsorption in water. *Bioresour. Technol.* **2012**, *118*, 536–544. [[CrossRef](#)] [[PubMed](#)]
31. Patwardhan, P.R.; Satrio, J.A.; Brown, R.C.; Shanks, R.H. Influence of inorganic salts on the primary pyrolysis products of cellulose. *Bioresour. Technol.* **2010**, *101*, 4646–4655. [[CrossRef](#)] [[PubMed](#)]
32. Nanda, S.; Mohanty, P.; Pant, K.K.; Naik, S.; Kozinski, J.A.; Dalai, A.K. Characterization of North American lignocellulosic biomass and biochars in terms of their candidacy for alternate renewable fuels. *Bioenergy Res.* **2013**, *6*, 663–677. [[CrossRef](#)]
33. Silverstein, R.M.; Webster, F.X.; Kiemle, D.J.; Bryce, D.L. *Spectrometric Identification of Organic Compounds*, 8th ed.; John Wiley & Sons: Hoboken, NJ, USA, 2014.
34. Yuan, J.-H.; Xu, R.-K.; Zhang, H. The forms of alkalis in the biochar produced from crop residues at different temperatures. *Bioresour. Technol.* **2011**, *102*, 3488–3497. [[CrossRef](#)] [[PubMed](#)]
35. Cantrell, K.B.; Hunt, P.G.; Uchimiya, M.; Novak, J.M.; Ro, K.S. Impact of pyrolysis temperature and manure source on physicochemical characteristics of biochar. *Bioresour. Technol.* **2012**, *107*, 419–428. [[CrossRef](#)] [[PubMed](#)]
36. Jin, J.; Li, Y.; Zhang, J.; Wu, S.W.; Cao, Y.; Liang, P.; Zhang, J.; Wong, M.H.; Wang, M.; Shan, S.; et al. Influence of pyrolysis temperature on properties and environmental safety of heavy metals in biochars derived from municipal sewage sludge. *J. Hazard. Mater.* **2016**, *320*, 417–426. [[CrossRef](#)] [[PubMed](#)]
37. Hossain, M.K.; Strezov, V.; Chan, V.S.; Ziolkowski, A.; Nelson, P.F. Influence of pyrolysis temperature on production and nutrient properties of wastewater sludge biochar. *J. Environ. Manag.* **2011**, *92*, 223–228. [[CrossRef](#)] [[PubMed](#)]
38. Lammers, K.; Arbuckle-keil, G.; Dighton, J. FT-IR study of the changes in carbohydrate chemistry of three New Jersey pine barrens leaf litters during simulated control burning. *Soil Biol. Biochem.* **2009**, *41*, 340–347. [[CrossRef](#)]
39. Socrates, G. *Infrared and Raman Characteristic Group Frequencies: Tables and Charts*, 3rd ed.; John Wiley & Sons: Hoboken, NJ, USA, 2004.
40. Zhang, M.; Resende, F.L.P.; Moutsoglou, A.; Raynie, D.E. Pyrolysis of lignin extracted from prairie cordgrass, aspen, and Kraft lignin by Py-GC/MS and TGA/FTIR. *J. Anal. Appl. Pyrolysis* **2012**, *98*, 65–71. [[CrossRef](#)]
41. Kleen, M.; Gellerstedt, G. Influence of inorganic species on the formation of polysaccharide and lignin degradation products in the analytical pyrolysis of pulps. *J. Anal. Appl. Pyrolysis* **1995**, *35*, 15–41. [[CrossRef](#)]
42. Jiang, W.; Saxena, A.; Song, B.; Ward, B.B.; Beveridge, T.J.; Myneni, S.C. Elucidation of functional groups on gram-positive and gram-negative bacterial surfaces using infrared spectroscopy. *Langmuir* **2004**, *20*, 11433–11442. [[CrossRef](#)] [[PubMed](#)]
43. Zhang, B.; Xiong, S.; Xiao, B.; Yu, D.; Jia, X. Mechanism of wet sewage sludge pyrolysis in a tubular furnace. *Int. J. Hydrot. Energy* **2011**, *36*, 355–363. [[CrossRef](#)]
44. Robertson, T.B. Contributions to the theory of the mode of action of inorganic salts upon proteins in solution. *J. Biol. Chem.* **1911**, *9*, 303–326.
45. Sawabe, T.; Akiyoshi, M.; Yoshida, K.; Yano, T. Estimation of neutron-irradiation-induced defect in 3C-SiC from change in XRD peak shift and DFT study. *J. Nucl. Mater.* **2011**, *417*, 430–434. [[CrossRef](#)]
46. Parra, M.R.; Haque, F.Z. Aqueous chemical route synthesis and the effect of calcination temperature on the structural and optical properties of ZnO nanoparticles. *J. Mater. Res. Technol.* **2014**, *3*, 363–369. [[CrossRef](#)]
47. Ewais, E.M.M.; Ahmed, Y.M.Z.; El-Amir, A.A.M.; El-didamony, H. Cement kiln dust/rice husk ash as a low temperature route for wollastonite processing. *Epitoany-J. Silicate Based Composite Mater.* **2014**. [[CrossRef](#)]
48. Ciolacu, D.; Ciolacu, F.; Popa, V.I. Amorphous cellulose—Structure and characterization. *Cell. Chem. Technol.* **2011**, *45*, 13.
49. Wei, L.; Agarwal, U.P.; Hirth, K.C.; Matuana, L.M.; Sabo, R.C.; Stark, N.M. Chemical modification of nanocellulose with canola oil fatty acid methyl ester. *Carbohydr. Polym.* **2017**, *169*, 108–116. [[CrossRef](#)] [[PubMed](#)]
50. Lu, X.; Shih, K.; Li, X.Y.; Liu, G.; Zeng, E.Y.; Wang, F. Accuracy and application of quantitative X-ray diffraction on the precipitation of struvite product. *Water Res.* **2016**, *90*, 9–14. [[CrossRef](#)] [[PubMed](#)]



© 2018 by the authors. Licensee MDPI, Basel, Switzerland. This article is an open access article distributed under the terms and conditions of the Creative Commons Attribution (CC BY) license (<http://creativecommons.org/licenses/by/4.0/>).

Article

Combustion of Flax Shives, Beech Wood, Pure Woody Pseudo-Components and Their Chars: A Thermal and Kinetic Study

Nourelhouda Boukaous ^{1,2}, Lokmane Abdelouahed ^{1,*}, Mustapha Chikhi ²,
Abdeslam-Hassen Meniai ², Chetna Mohabeer ¹ and Taouk Bechara ¹

- ¹ Laboratoire de Sécurité des Procédés Chimiques LSPC-4704, INSA Rouen, UNIROUEN, Normandie Univ., 76000 Rouen, France; boukaous.nourelhouda@insa-rouen.fr (N.B.); chikirsha.mohabeer@insa-rouen.fr (C.M.); bechara.taouk@insa-rouen.fr (T.B.)
- ² Faculté de Génie des Procédés Université de Constantine 3, 25000 Constantine, Algeria; chikhi_mustapha@yahoo.fr (M.C.); meniai@yahoo.fr (A.-H.M.)
- * Correspondence: lokmane.abdelouahed@insa-rouen.fr; Tel.: +33-232-956-655

Received: 30 June 2018; Accepted: 15 August 2018; Published: 17 August 2018

Abstract: Thermogravimetric analysis was employed to investigate the combustion characteristics of flax shives, beech wood, hemicellulose, cellulose, lignin, and their chars. The chars were prepared from raw materials in a fixed-bed reactor at 850 °C. In this study, the thermal behavior based on characteristic temperatures (ignition, maximum, and final temperatures), burnout time and maximum rate was investigated. The kinetic parameters for the combustion of different materials were determined based on the Coats-Redfern approach. The results of our study revealed that the combustion of pure pseudo-components behaved differently from that of biomass. Indeed, principal component analysis showed that the thermal behavior of both biomasses was generally similar to that of pure hemicellulose. However, pure cellulose and lignin showed different behaviors compared to flax shives, beech wood, and hemicellulose. Hemicellulose and cellulose chars had almost the same behaviors, while being different from biomass and lignin chars. Despite the difference between flax shives and beech wood, they showed almost the same thermal characteristics and apparent activation energies. Also, the combustion of the hemicellulose and cellulose chars showed that they have almost the same structure. Their overall thermal and kinetic behavior remained between that of biomass and lignin.

Keywords: biomass; combustion; thermogravimetric analysis; kinetic parameters; thermal characteristics

1. Introduction

Biomass is one of the most environment-friendly renewable sources of energy being used for human needs. Usually, its conversion is considered to be a carbon-free process, because the resulting CO₂ was previously captured by plants. Based on life-cycle assessment comparisons, net carbon emissions from biomass per unit of electricity are below 10% of those from the emissions from fossil fuels [1]. Furthermore, the use of biomass and char as alternative energy carriers in the industry is growing as a result of the depletion of fossil energy. Biomass can be converted into heat and electrical power through several methods, where the easiest one is the direct combustion via a steam turbine dedicated to power production. At present, biomass is already used in several processes for heat and power production [2]. Different criteria have been used in the literature to compare the performance of biomass combustion power generation. Among these criteria, the more important are: The capacity of power production [3], the technology used [4], and the composition of biomass [2].

Also, other classifications can be addressed when comparing pollution generated by the combustion of biomass. Indeed, this last one is becoming more important due to global warming [5].

The contribution of biomass sources in global electricity generation from renewable energy in 2014 was about 7.24% [1]. This contribution can be made directly by the combustion of biomass or one of its derivatives. There are three main pseudo-components that constitute biomass, namely hemicellulose, cellulose, and lignin. Hemicellulose constitutes 16 to 23 wt%, cellulose between 42 and 49 wt%, while lignin represents 21 to 39 wt% of the biomass [6]. These last three can be thermochemically valorized in several ways. Indeed, the pyrolysis of pseudo-components has already been studied in the literature [7], and the interaction between these three polymers during pyrolysis has also been investigated [8]. Moreover, the gasification of these pseudo-components has been examined at different temperatures [9] and using supercritical water conditions [10]. The effect of cellulose and lignin content on the combustion has also been highlighted in the literature [11].

Lignin, which is generally considered as a chemically non-recoverable residue, is usually burned to generate the power and heat required for biomass treatment operations in simultaneous saccharification and co-fermentation processes [12]. According to life-cycle assessments conducted by Daylan and Ciliz [13], the heat generated by the combustion of the residual lignin satisfied and ensured the necessary heat and power needed during the process of ethanol production from lignocellulosic biomass. On the other hand, in the gasification process of biomass, it is the char produced by the process which is burned to provide the heat needed by the pyrolysis and the gasification processes [14]. In the fast internally circulating fluidized bed used for biomass gasification, the residual char from the pyrolysis and gasification processes is burnt in a separate reactor to ensure a major part of the heat required for the pyrolysis and the gasification reactions [15].

Now, the design and the scale-up of combustors require several details concerning the reactivity of the solid fuel to be used [16]. Guizani et al. [17] showed that the pyrolysis temperature of biomass, during the production of char, affected the structure and the reactivity of produced char in a considerable manner. Also, the behavior of biomass cannot be condensed to that of one single pseudo-component because of the chemical and physical alterations caused by the use of acids and bases during the separation of the different pseudo-components [18]. Indeed, the knowledge of the reaction kinetics of the solid fuel is essential to correctly design the reactor for the combustion reaction. Also, the more the solid fuel is burnt at a low temperature and a high conversion rate, the shorter the burnout time is; in other words, the reactivity of the substance is higher [19]. Hence, the most reactive substance is the one which shows the highest rate of consumption at the lowest temperature on one hand, and the lowest activation energy on the other. In literature, several authors evaluated the reactivity of substances from thermogravimetric (TG) curves based on; (i) the ignition temperature [20]; (ii) the maximum rate of mass loss [21]; (iii) the activation energy [22]; or (iv) a combination of different parameters from the TG curves [19]. Indeed, El may et al. [19] estimated the reactivity of different substances as the ratio of the maximum rate of mass loss to maximum temperature. In their case, they did not distinguish between the different stages of the reaction. Haykiri-Açma et al. [23] reported that the most important characteristic temperatures of the combustion reaction were the ignition temperature and the maximum temperature, which corresponded to the maximum consumption rate. Other researchers have compared the TG combustion profiles of different chars obtained from biomass pyrolysis and coal [22] and found that biomass chars, based essentially on the maximum temperature, were more reactive than coal and lignite. According to the latter paper, it seemed that the activation energy had less influence on the reactivity compared to the maximum temperature. In this context, a deeper analysis appears to be necessary to better understand the relationship between the different parameters cited above.

Solid fuel combustion has widely been studied in the literature. However, to the best of our knowledge, the combustion characteristics of cellulose, hemicellulose, lignin, and their chars have not been deeply examined. In addition, the synergistic effect of the pseudo-components during the combustion reaction has not been previously discussed. Consequently, the effect of the heating rates

and the sample structure may affect not only the rate of combustion, but also important characteristics such as ignition and final temperatures.

The aim of this work is to determine various parameters associated with the combustion reaction (kinetic parameters, burnout time, ignition temperature, final temperature, and maximum rate of consumption) using thermogravimetric analysis (TGA). The raw materials considered in this study are beech wood, flax shives, cellulose, hemicellulose, lignin, and their respective chars. Also, in this paper, the relationship between the different determined parameters of the combustion reaction of biomasses and the pure pseudo-components has been discussed in order to better compare the reactivity of the substances with each other. The availability of such data for kinetic and thermal parameters allows an appropriate design of biomass and char combustor.

2. Materials and Methods

2.1. Raw Materials

“ETS Lignex” and “La Coopérative Terre de Lin” companies provided respectively the beech wood and the flax shives used for this study. Beechwood has been chosen in order to compare our results with the literature, while flax shives have been chosen due to their availability in Europe which represents about 85% of the world’s production of scutched flax fibers [24]. The pseudo-components employed were used in their pure form: Microcrystalline cellulose was provided from Merck (Kenilworth, NJ, USA, Ref. 1.02330.0500-500G), hemicellulose was provided from Tokyo Chemical Company Co. Ltd. (Tokyo, Japan, Ref. X0078-100G) and lignin was provided from Sigma-Aldrich (St. Louis, MO, USA, Ref. 471003-100G). All samples were sieved with a diameter of less than 40 micrometers (μm) in order to limit the effects of heat and mass transfer as recommended in [25].

2.2. Char

A fixed-bed reactor was used to prepare the char of the five raw materials by pyrolysis. The pyrolysis was ensured at 850 °C during 2 h under a pure nitrogen flow of 500 $\text{mL}\cdot\text{min}^{-1}$. Afterward, the samples were cooled down under nitrogen to room temperature. The device was already described in a previous work [26]. Experiments were carried out at atmospheric pressure. The proximate and ultimate analyses of the raw material before and after pyrolysis are given in Tables 1 and 2, respectively. The ultimate composition of different raw materials was performed using the CHN elemental analyzer, while the proximate composition was determined based on TG analysis [27]. Low heating value (LHV) of different raw materials were calculated according to Channiwala’s correlation [28].

Table 1. Ultimate and proximate characterization of raw materials.

Component	C (%)	H (%)	O (%)	N (%)	VM * (%)	FC ** (%)	Ash (%)	LHV ($\text{MJ}\cdot\text{kg}^{-1}$)
Flax shives	45.7	5.77	48.12	0.41	75.47	21.77	2.76	17.71
Beech wood	47.38	6.11	46.51	0	80.15	18.92	0.92	18.91
Cellulose	41.74	6.08	52.18	0	96.26	3.74	0	16.34
Hemicellulose	41.47	6.48	52.05	0	80.18	19.57	0.25	16.72
Lignin	57.04	4.76	38.21	0	68.42	24.86	6.72	21.42

* Volatile matter, ** Fixed carbon.

Table 2. Ultimate and proximate characterization of char samples.

Component	C (%)	H (%)	O (%)	N (%)	VM * (%)	FC ** (%)	Ash (%)	LHV ($\text{MJ}\cdot\text{kg}^{-1}$)
Flax shives char	75.87	3.2	19.73	1.21	1.67	81.61	16.72	27.84
Beech wood char	78.24	3.13	18.63	0	1.59	93.83	4.58	28.97
Cellulose char	81.4	3.25	15.35	0	0.39	99.25	0.37	30.64
Hemicellulose char	71.19	3.2	25.61	0	0.74	98.83	0.43	25.96
Lignin char	58.04	2.65	39.3	0	2.75	71.67	25.58	18.78

* Volatile matter, ** Fixed carbon.

2.3. Thermogravimetric Experiments

TGA is one of the most frequently used techniques for solid characterization in an inert or oxidative atmosphere [29,30]. In this work, experiments were performed using a TG SDT Q600-TA instruments analyzer (TA Instruments, New Castle, DE, USA). Pure synthesized air constituting of 21 vol% of oxygen and 79 vol% of nitrogen was used as oxidative gas with a flow rate of 50 mL·min⁻¹. The mass of the sample used in the crucible was 6.5 ± 0.2 mg for all samples. The sample was introduced at room temperature and atmospheric pressure. In this work, experiments were performed under non-isothermal conditions at different heating rates: 10, 20, 30 and 40 °C·min⁻¹. TG experiments were repeated three times for each heating rate to improve the accuracy of the results.

2.4. Kinetic Modelling

Several non-isothermal methods have been reported in the literature to determine the apparent kinetics of the biomass and char combustion reactions from the TG mass loss profiles. The kinetic parameters determined by thermogravimetric measurements are very sensitive to the calculation methods used [19,31]. Therefore, their determination in this study was carried out using the Coats-Redfern method by taking into consideration two different models proposed in the literature [32,33]. Indeed, the Coats-Redfern method is considered the best approach for the determination of kinetic parameters for a combustion reaction [21,34–36]. On the other hand and in contrast to other isoconversional methods, the Coats-Redfern method may integrate some particular models that take into account the effect of boundary and diffusion control [21,37].

The conversion rate, X , was calculated based on the variation of the mass loss of the sample, as follows:

$$X = 1 - \frac{m_t - m_f}{m_i - m_f} \quad (1)$$

where m_i and m_f are the initial and the final masses, respectively.

The reaction rate can be expressed by the following relation:

$$\frac{dX}{dt} = k(T)f(X) \quad (2)$$

where $k(T)$ is the rate constant and is defined as:

$$k(T) = A \cdot \exp\left(-\frac{E_a}{RT}\right) \quad (3)$$

where A is the pre-exponential factor, E_a the apparent activation energy, R the ideal gas constant and $f(X)$ is the kinetic model used for solids conversion.

The final form of the decomposition kinetics of biomass was written as follows:

$$\frac{dX}{dt} = A \cdot \exp\left(-\frac{E_a}{RT}\right)f(X) \quad (4)$$

The rearrangement of the relation (4) gave rise to the Equation (5), as follows:

$$\frac{dX}{f(X)} = \frac{k}{\beta}dT \quad (5)$$

where β is the heating rate and is defined as:

$$\beta = \frac{dT}{dt} \quad (6)$$

The integration of the relation (5) gave the following relation:

$$g(X) = \int_0^X \frac{dX}{f(X)} = \frac{A}{\beta} \int_{T_0}^T \exp\left(-\frac{E_a}{RT}\right) dT \quad (7)$$

where g is the integral function of conversion [21,37]. By using the Coats-Redfern method [38], the relation (7) became:

$$\ln\left|\frac{g(X)}{T^2}\right| = \ln\left[\frac{AR}{\beta E_a}\left(1 - \frac{2RT}{E_a}\right)\right] - \frac{E_a}{RT} \quad (8)$$

The analytic integration of this relation is essentially governed by the form of the function “ g ” and the order of the reaction considered, as already detailed in articles of interest in the literature [21,39].

3. Results and Discussion

3.1. Thermogravimetric and Differential Thermogravimetric (DTG) Characteristic Curves

The combustion of cellulose, hemicellulose, lignin, beech wood, flax shives, and their chars was studied under the same experimental conditions and for different heating rates. Figures 1 and 2 show the evolution of TG and DTG curves for the combustion reaction with temperature. This study was carried out over temperatures ranging from 25 °C to 1000 °C. The mean deviation was calculated based on the reproducibility of the experiments and was found to be between 2.68 and 5.53%. The deviation was more pronounced at high temperatures, probably due to the very low mass in the crucible. Humidity evaporation was observed between ambient temperature and 150 °C, as already mentioned in previous works [19,31].

3.1.1. Raw Materials Combustion

Figure 1 shows the TG and DTG curves of the combustion of flax shives, beech wood, hemicellulose, cellulose, and lignin. As illustrated in this figure, the raw materials were completely consumed at 550 °C, except for lignin, which required a temperature in the vicinity of 850 °C. Based on the curves of Figure 1, it can be seen that the raw materials exhibited more than one stage, unlike char, which showed a unique stage in Figure 2. Despite the difference in the composition of beech wood and flax shives, see Table 1 for details, the two biomasses typically had the same behavior, with only a slightly higher reactivity for beech wood. Indeed, the biomass DTG showed the existence of two peaks—the first peak appeared in the interval from 225 to 375 °C, and the second peak from 375 to 450 °C. This indicated the existence of at least two steps, depending on the combustion mechanism.

The combustion of hemicellulose showed the presence of three peaks, two of them were completely overlapping as seen in Figure 1c. This could be explained by the heterogeneity of hemicellulose, which is majorly constituted of xylose along with a small part of glucuronic acid and other sugars.

As seen in Figure 1d, the combustion of pure cellulose showed only one peak. Indeed, this can be explained by the occurrence of only the combustion of the volatile fraction of cellulose; note the low fixed carbon content (about 3.74%) of cellulose may be the reason the peak of combustion for the latter was not detected.

The lignin combustion showed a different behavior compared to those previously, as shown in Figure 1e. Indeed, the combustion of lignin showed the existence of two independent stages. The first stage was located at low temperature, between 200 and 450 °C, while the second was located at high temperature, between 800 and 900 °C. Also, the second stage of the combustion reaction might be accompanied by the decomposition of calcium carbonates, which happens at high temperature [22,40]. Zhou et al. [41] observed the same behavior for the pyrolysis of lignin. Surprisingly, we did not see this behavior with both biomasses, although some experiments have been carried out up to 1200 °C. Indeed, after 500 °C, the mass loss of the sample was almost negligible. This could probably be explained by the fact that the combustion of char (the second stage in Figure 1e) from pure lignin was different from the behavior of char from biomass. Pure lignin has a complex and branched structure compared to

cellulose and hemicellulose. Also, significant interactions have been reported in the literature between cellulose and lignin during their pyrolysis [8,9], which can modify the global structure of char.

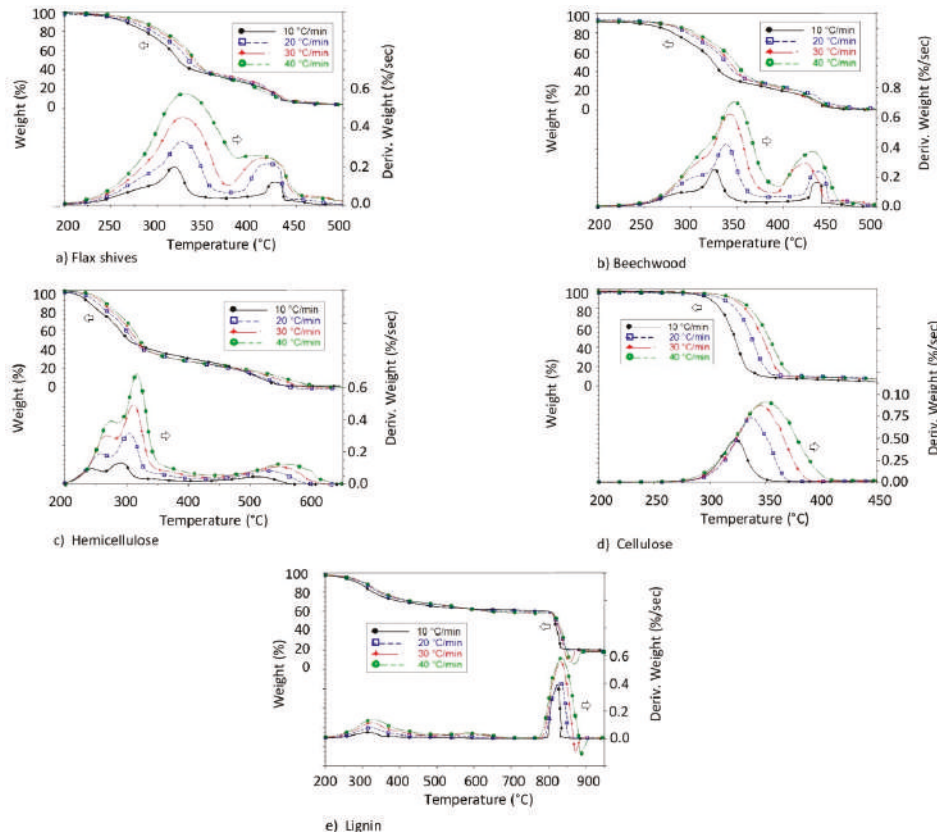


Figure 1. Mass loss and conversion rate of different raw materials combustion.

3.1.2. Char Combustion

DTG curves of the different bio-char samples demonstrated only one single stage, as shown in Figure 2. This was explained by the existence of only one uniform structure in each char used. However, every char (from cellulose, hemicellulose, lignin, and biomasses) showed different behaviors when compared to one another, as shown in Figure 2. Indeed, the chars produced from pure pseudo-components did not have the same properties as the ones produced from biomass. This has already been observed in the literature, where some DTG curves of biomass samples showed one or two stages [22]. Probably, this can be explained by the importance of lignin in the biomass samples.

In some works in the literature, two DTG peaks can be observed during the combustion of char from biomass, more particularly in cases where the pyrolysis temperature of the biomass is less than 600 °C. This can be explained by the combustion of residual unconverted biomass [17].

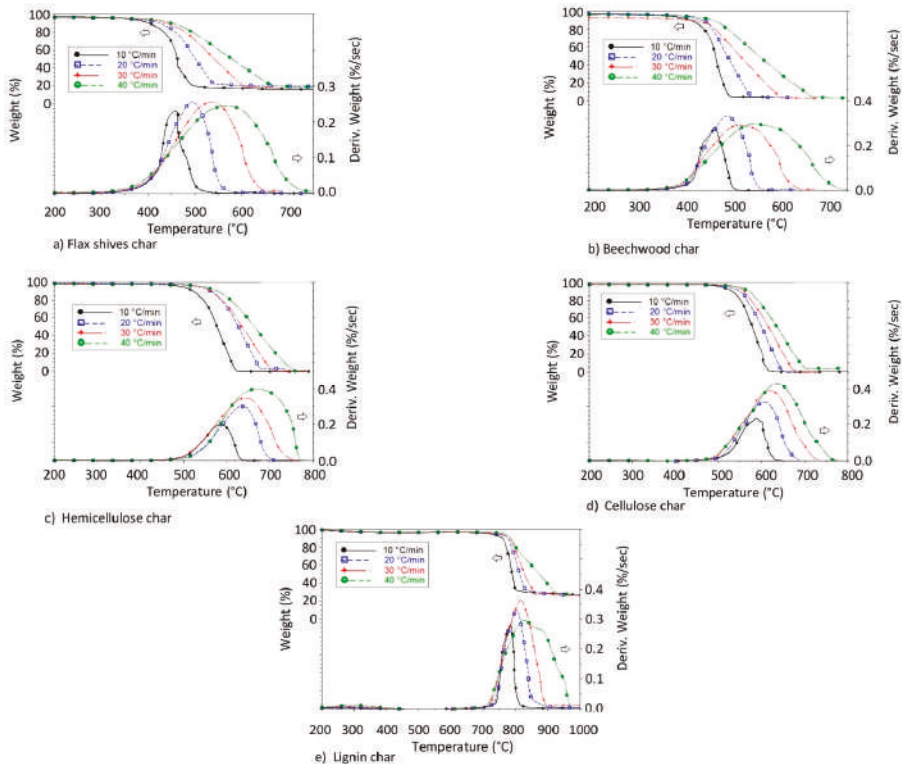


Figure 2. Mass loss and conversion rate of different char samples.

3.2. Thermal Analysis

The DTG curves allowed the determination of various parameters related to the combustion reaction, as shown in Figure 3. These parameters were determined and are discussed in the following sections. The evolution of these parameters with the heating rate obtained from the DTG curves has been summarized in Tables S1 and S2 of the supplementary materials.

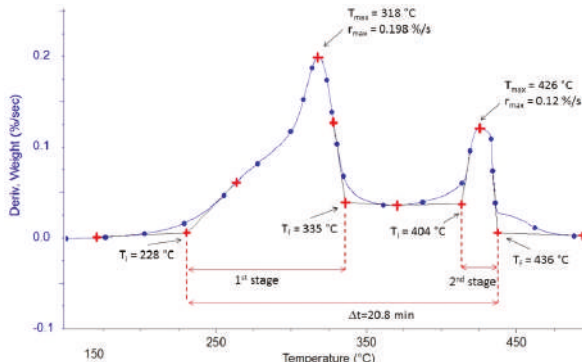


Figure 3. Example of the graphical determination of thermal parameters (for Flax shives with $\beta = 10 \text{ } ^\circ\text{C} \cdot \text{min}^{-1}$).

3.2.1. Ignition and Final Temperatures of Combustion Reaction

The ignition temperature (T_i) is the temperature at which the combustion reaction begins, while the final temperature (T_f) indicates the end of the combustion reaction. These temperatures are essential to ensure the perfect design of the combustor and avoid unburned solid fuel at the outlet of the reactor [22]. It should be noted that T_i is also used to compare the reactivity of several substances [19–23,42–44]. Several methods have been reported and used in the literature to determine T_i and T_f [32,45–48]. In this work, T_i and T_f have been determined according to the work of Grønli et al. [46], which was based on the use of the second derivative of the mass loss curves. Tables 3 and 4 show the evolution of T_i and T_f during the combustion reaction for different raw materials over a heating rate of $10\text{ }^{\circ}\text{C}\cdot\text{min}^{-1}$. Hemicellulose presented the lowest T_i , followed by lignin and biomasses, while cellulose demonstrated the highest T_i . At the end of the first stage, hemicellulose displayed the lowest T_f , while biomasses and cellulose presented almost the same T_f . Furthermore, the T_f of lignin was the highest. In the second stage of combustion, the T_i of the biomasses and hemicellulose remained close to each other. However, the T_i of lignin remained higher.

The T_i of the char from raw materials had approximately the same behavior. These temperatures remained higher compared to the biomasses and the pure pseudo-components. Also, hemicellulose and cellulose chars showed almost the same T_i and T_f . As for lignin combustion, the char from lignin showed the highest T_i and T_f .

Table 3. Characteristics of the combustion stages of raw materials ($\beta = 10\text{ }^{\circ}\text{C}\cdot\text{min}^{-1}$).

Raw Materials	First Stage				Second Stage				Δt (min)
	T_i ($^{\circ}\text{C}$)	T_f ($^{\circ}\text{C}$)	T_{\max} ($^{\circ}\text{C}$)	r_{\max} ($\%\cdot\text{s}^{-1}$)	T_i ($^{\circ}\text{C}$)	T_f ($^{\circ}\text{C}$)	T_{\max} ($^{\circ}\text{C}$)	r_{\max} ($\%\cdot\text{s}^{-1}$)	
Flax shives	228	335	318	0.198	404	436	426	0.12	20.80
Beech wood	245	339	325	0.25	431	444	437	0.164	19.90
Hemicellulose	207	314	291	0.132	448	561	515	0.046	35.40
Cellulose	297	335	323	0.491	-	-	-	-	3.80
Lignin	227	346	314	0.043	806	837	823	0.389	61.00

Table 4. Characteristics of the combustion of char samples ($\beta = 10\text{ }^{\circ}\text{C}\cdot\text{min}^{-1}$).

Chars	T_i ($^{\circ}\text{C}$)	T_f ($^{\circ}\text{C}$)	T_{\max} ($^{\circ}\text{C}$)	r_{\max} ($\%\cdot\text{s}^{-1}$)	Δt (min)
Flax shives char	441	479	458	0.234	3.8
Beech wood char	441	501	468	0.282	6
Hemicellulose char	532	620	587	0.208	8.8
Cellulose char	513	627	587	0.235	11.4
Lignin char	748	801	784	0.279	5.3

3.2.2. Burnout Time

The burnout time (t_R) is defined as the time between the T_i and the T_f . In this work, the t_R has been calculated taking into account the entire reaction interval through the two stages. Overall, t_R of the combustion of beech wood and flax shives was almost the same. Hemicellulose was the first to burn, and it took more time than the biomasses. The lignin t_R was the longest, since the second stage of its combustion needed a higher temperature. The cellulose t_R was not significant, since the second stage was not visible. The t_R of char samples has been shown in Table 4. The same trend as for the t_R of the raw materials was not obtained. Indeed, it seems that the char produced by holocellulose compounds required more time than chars from beech wood, flax shives, and lignin.

3.2.3. Maximum Temperature

The maximum temperature (T_{\max}) is defined as the temperature where the maximum reaction rate (dX/dt) occurs. This temperature is a very important criterion for evaluating the reactivity of substances [19–23,42–44]. Indeed, the lower the T_{\max} , the higher the reactivity of the substance.

According to Table 3, hemicellulose was the most reactive substance. The T_{\max} for flax shives, beech wood, hemicellulose, and cellulose were very similar. As for the char samples, the ones produced from biomass pyrolysis remained the most reactive, while the lignin char proved to be the least reactive, as shown in Table 4. Also, the chars of cellulose and hemicellulose showed almost the same behavior.

3.2.4. Maximum Rate

Maximum rate (r_{\max}) is also usually considered as a criterion to classify the reactivity of substances [19,22]. Indeed, the higher the r_{\max} and the lower the T_{\max} , the more reactive the substance. The maximum reactivity of the different raw materials and char samples are shown in Tables 3 and 4, respectively. In the first stage, the most reactive raw material was cellulose. However, for the second stage, lignin appeared to be the most reactive at high temperatures.

As shown in Figure 1, these parameters, cited above, evolved by increasing the heating rate, more particularly in the first stage of the combustion of raw materials and char. However, the effect of heating rate was more pronounced on r_{\max} than on other parameters.

3.3. Principal Component Analysis

As shown above, the reactivity classification of different substances varied from one criterion to the other. The results were examined using the principal component analysis (PCA), which checks the global behavior of the different raw materials, taking into account the different criteria discussed above. Figure 4 shows the PCA for the first and the second stage of combustion of the raw materials.

PCA is a multivariate technique used in data processing usually presented in a table containing variables and observations. PCA has the goal to detect the existence of similarities or inter-correlation between variables, based on the treatment of observations. PCA is represented by only one orthogonal variable called principal components F1 and F2. In this study, PCA was used to analyze the behavior of raw materials and char based on the different thermal parameters discussed above [49,50].

PCA is a graphical representation of a cloud of points initially drawn in a multidimensional space. The number of dimensions in our case represents the number of axes or variables in this space, and it corresponds to six (T_i , T_{\max} , T_f , β , Δt , and r_{\max}). In order to facilitate the analysis of the existence of any correlation between each of two variables separately, a projection of this cloud in an orthogonal space (F1 and F2) is created, as previously specified. Often, these two axes have no physical meaning, however, they ensure the maximum recovery of information from the projection of the cloud of points. Obviously, a bad projection of a variable on this new space may not be representative, and therefore, the information about this variable is deformed. The conclusions drawn in this case may not have a physical meaning. The closer the segment representing this variable is to the radius of the circle in Figure 4a (segment in red), the better the parameter is represented in this new space. In this study, overall, all parameters were well represented, as shown in Figures 4 and 5.

Figure 4a analyses the existence of a possible linear correlation between the different parameters considered in this study. The correlation coefficient between each two parameters is calculated from the cosine of the angle formed between these two parameters shown by segments in Figure 4a. Tables S3, S4, and S5 detail the values of these correlation coefficients. For example, Figure 4a shows that the cosine of the angle formed by T_i and T_{\max} was about 0.798. Also, T_i and T_{\max} showed a positive correlation given that they were in the same direction (the same remark can be made for T_f and β in Figure 4a). This means that an increase in T_i implies an increase in T_{\max} . A negative correlation can be shown when the correlation coefficient tends to negative values; this means that the two variables show an opposite trend. Δt and T_{\max} in Figure 4a illustrate a negative trend.

The set of four points delimited in Figure 4b for each sample represents the evolution of the different parameters (T_i , T_f , T_{\max} , r_{\max} , and Δt) with the heating rate (10, 20, 30, and 40 $^{\circ}\text{C}\cdot\text{min}^{-1}$) (the evolution of the temperature T_f with the heating rate is shown in Figure 4b, as an example).

According to PCA, some qualitative conclusions can be addressed, as follows:

Regarding the first stage of raw materials combustion:

- A strong positive dependence between T_i , T_{\max} , and r_{\max} .
- A strong positive dependence between β and T_f .
- Opposite evolution between Δt and the rest of the parameters.
- Overall, there is no dependence between T_i , T_{\max} , and r_{\max} .

Regarding the second stage of raw materials combustion:

- A clear opposite trend between Δt and β .
- Δt and β seemed to be unrelated to T_i , T_f , T_{\max} , and r_{\max} during this stage.
- A strong positive dependence between T_i , T_{\max} , and T_f .

Regarding the combustion of chars:

- A strong positive dependence between T_i , T_{\max} , and T_f .
- A strong positive dependence between β and r_{\max} .
- Surprisingly, no characteristic temperature seemed dependent on β .

As shown in Figure 4b, flax shives and beech wood exhibited behavior closest to the hemicellulose (overlapped segments), out of the three pseudo-components. Lignin was less reactive and took more time to be completely consumed. The Figure 5b shows that the chars produced from beech wood and flax shives were more reactive than the chars from pseudo-components. Also, the char from holocellulose was more reactive than that from lignin. This analysis also showed that the cellulose, hemicellulose, and lignin contents can modify the co-combustion of pseudo-component/biomass or pseudo-component/char blend. Indeed, in the case of a cellulose/biomass blend, an increase in T_{\max} and r_{\max} can be expected; while increasing the lignin content can reduce T_{\max} and r_{\max} .

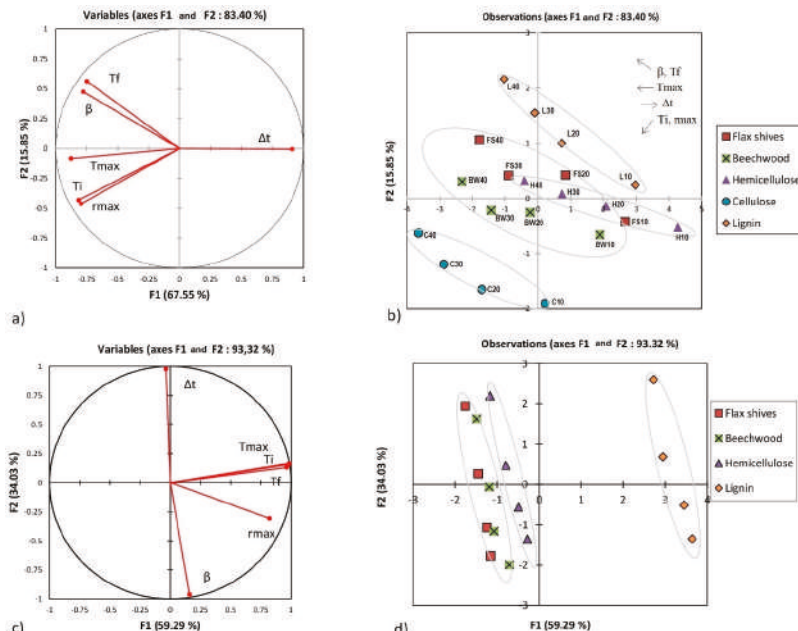


Figure 4. Principal component analysis (PCA) for raw materials: (a,b) represent the first stage combustion; (c,d) represent the second stage combustion.

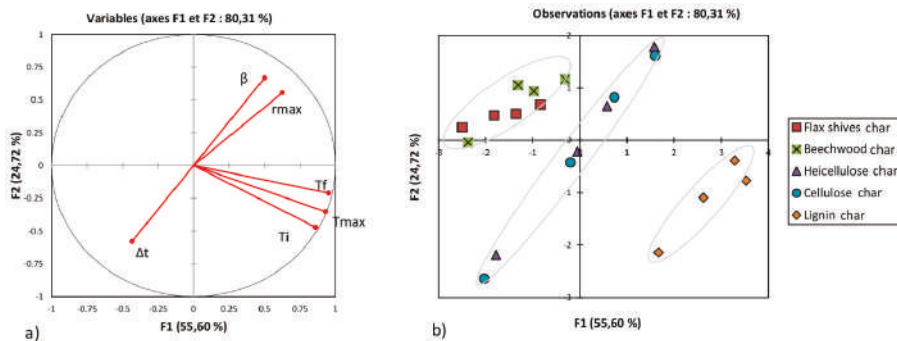


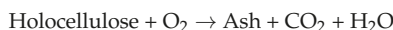
Figure 5. Principal component analysis (PCA) for char samples: (a) Correlation between variables; (b) Effect of heating rate on different variables.

3.4. Mechanism and Kinetic Parameters of Combustion

3.4.1. Mechanism

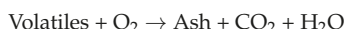
Usually, the mechanism of biomass combustion is composed of two stages, as shown in Figure 1. Some authors reported that the first stage illustrated the combustion of the holocellulose component, while the second stage concerned the combustion of lignin according to mechanism 1 [20,34].

Mechanism 1



Other authors reported that the mechanism of combustion followed the combustion of volatile matter (1st stage) and then fixed carbon (2nd stage), according to mechanism 2 [21,51,52].

Mechanism 2



In light of the results shown above, it seems that both hemicellulose and lignin showed two independent stages. Therefore, the first stage is explained by the combustion of volatile matter derived from the pyrolysis of biomass, while the second stage can be explained by the combustion of residual char produced in the first stage. Cellulose showed only one stage given its low fixed carbon content, as shown in Table 1 (3.75 wt%). Moreover, the second stage of combustion of hemicellulose and lignin corresponded approximately to the same stage of combustion of char produced by hemicellulose and lignin pyrolyzed in the fixed-bed reactor. This observation favored the plausibility of the second mechanism.

In some works in the literature, the reactivity of substances was classified according to the activation energy of their combustion reaction [20]. Therefore, in our case, the activation energy for the combustion reaction was determined for different materials. The combustion of different raw materials was successfully modeled by using two independent reactions (Mechanism 2), with the exception of cellulose (which was modeled using one single reaction, given its low fixed carbon content, as discussed above). The combustion of char samples was modeled assuming one single reaction, according to the DTG curves, see Figure 2.

3.4.2. Kinetic Parameters

The plot of $\ln |\lg(X)/T^2|$ of relation (8) versus $1/T$ gave a straight line with a slope of $-E_a/R$. Relation (8) was applied in the range of temperatures between T_i and T_f of each combustion stage

for different heating rates. The term $2RT/E_a$ can be neglected (compared to 1 in this case) [37]. The E_a was calculated from the slope of relation (8), while A was calculated from the y-intercept. Since this relation was supposed to be independent of the heating rate, the E_a and A were calculated as average values based on the four heating rates.

Several models that take into account the effect of boundary and diffusion control have been tested in order to establish the linearity of relation (8) [21,53,54]. Indeed, flax shives, beech wood, cellulose, lignin, and their char samples followed the first-order kinetics model according to model 1 (relation (9)). The first order is usually considered for combustion reactions [55–58]. The latter model has been the most frequently used in literature and takes into account only the chemical reaction. However, the best fit for hemicellulose combustion was model 2 (relation (10)). In this model, the kinetics of the combustion reaction were fully controlled by the diffusion of oxygen inside the hemicellulose particles. The diffusion limitation has already been observed in the combustion of the pine samples as reported by [52].

Kinetic model function 1:

$$g(X) = (1 - X) \quad (9)$$

Kinetic model function 2:

$$g(X) = \left[1 - (1 - X)^{1/3} \right]^2 \quad (10)$$

The activation energy and the pre-exponential factor for different raw materials are shown in Table 5. A detailed table of kinetic parameters for the raw materials and the char samples has also been provided in Table S6 of the supplementary materials. The deviation of the regression on E_a and A reported in Table 5 has been calculated with respect to the different heating rates. Therefore, the variation in the value of E_a with the different heating rates can be explained by the experimental error on one hand, and, on the other, by the limitations of heat transfer, which tended to increase with high heating rates, as shown in Table S6.

The values of the activation energies shown in Table 5 were globally close to those found in the literature, see Table S7. However, some authors have found much lower values of activation energies for biomass combustion reactions, such as Senneca [59], Sahu et al. [60], and Kumar et al. [61]. For the activation energy of the char combustion, they were globally close to those found in the literature, as shown in Table S8.

Despite the different nature of flax shives and beech wood, their E_a remained similar to each other in the first stage (82.54 ± 2.49 and $99.26 \pm 3.10 \text{ kJ}\cdot\text{mol}^{-1}$, respectively). Also, hemicellulose and cellulose showed E_a in the same range, with a slight elevation for cellulose (172.33 ± 15.14 and $212.21 \pm 8.23 \text{ kJ}\cdot\text{mol}^{-1}$, respectively). However, cellulose and hemicellulose showed high E_a compared to the biomasses. Lignin had the lowest E_a in this stage ($45.97 \pm 0.82 \text{ kJ}\cdot\text{mol}^{-1}$). In the second stage, the E_a of both biomasses and those of the holocellulose components were mostly the same (between 66.08 ± 3.00 and $79.51 \pm 1.90 \text{ kJ}\cdot\text{mol}^{-1}$); unlike lignin, which showed a high E_a in this stage ($348.43 \pm 15.57 \text{ kJ}\cdot\text{mol}^{-1}$) and reacted only at high temperatures.

Table 5. Kinetic parameters of the combustion reaction of different raw materials.

Samples	Raw Materials				Char Samples	
	First Stage		Second Stage		Only One Stage	
	$E_a \text{ (kJ}\cdot\text{mol}^{-1})$	$\log A$	$E_a \text{ (kJ}\cdot\text{mol}^{-1})$	$\log A$	$E_a \text{ (kJ}\cdot\text{mol}^{-1})$	$\log A$
Flax shives	82.54 ± 2.49	9.06 ± 0.51	66.89 ± 2.73	5.26 ± 0.32	134.90 ± 22.32	17.33 ± 0.63
Beech wood	99.26 ± 3.10	11.53 ± 0.32	79.51 ± 1.90	10.17 ± 0.67	151.68 ± 26.3	14.86 ± 6.21
Hemicellulose	172.33 ± 15.14	24.55 ± 2.08	66.08 ± 3.00	1.67 ± 0.08	180.32 ± 15.26	30.19 ± 1.14
Cellulose	212.21 ± 8.23	33.43 ± 2.30	-	-	218.37 ± 7.11	20.54 ± 2.61
Lignin	45.97 ± 0.82	1.36 ± 0.11	348.43 ± 15.57	25.09 ± 7.72	263.91 ± 32.49	20.54 ± 3.92

The flax shives and beech wood char samples showed almost the same range of E_a (134.90 ± 22.32 and 151.68 ± 26.3 $\text{kJ}\cdot\text{mol}^{-1}$, respectively). The same remark for hemicellulose and cellulose can be made with respect to their E_a (180.32 ± 15.26 and 218.37 ± 7.11 $\text{kJ}\cdot\text{mol}^{-1}$, respectively). Lignin char showed the highest E_a (263.91 ± 32.49 $\text{kJ}\cdot\text{mol}^{-1}$) compared to other chars. This observation coincides with the PCA, shown in Figure 5. As reported by several authors, this can be explained by a porous and highly disordered carbon structure of lignin [22,62].

4. Conclusions

In this study, the combustion of flax shives, beech wood, pure pseudo-components, and their chars has been investigated based on TGA. During the combustion reaction, biomass (despite being essentially comprised of cellulose, hemicellulose, and lignin) exhibited a different behavior compared to its pure pseudo-components. This means that the physical interactions between the pure pseudo-components present in biomass cannot be neglected. It also demonstrated that biomass with a higher cellulose content showed faster conversion rates, higher hemicellulose contents in the biomass led to a lower T_i , and higher lignin content implied a higher E_a and a higher T_f . This study also confirmed that the combustion reaction of biomass could be modeled as two independent reactions. Indeed, the first reaction concerned the combustion of the volatile content, while the second corresponded to the combustion of the fixed carbon component. It is therefore important for the design of the combustor to take into account the substance limiting the process.

As this study showed, char produced from flax shives and beech wood had the same behavior both thermally and kinetically. Also, the same remark can be made for char produced from hemicellulose and cellulose. However, the char from lignin behaved differently from those from biomass and the holocellulosic pseudo-components.

Supplementary Materials: The following are available online at <http://www.mdpi.com/1996-1073/11/8/2146/s1>.

Author Contributions: The authors equally contributed to the work reported.

Acknowledgments: This work was supported by the European Union with the European regional development fund (ERDF) and by the Normandie Regional Council.

Conflicts of Interest: The authors declare no conflict of interest.

Nomenclature

A	Pre-exponential factor (s^{-1})
dX/dt	The first derivative of conversion rate with respect to time
DTG	Differential thermogravimetry
E_a	Activation energy ($\text{kJ}\cdot\text{mol}^{-1}$)
m_f	Final mass (kg)
m_i	Initial mass (kg)
m_t	Mass at temperature T (kg)
n	Reaction order (-)
R	Gas constant ($8.314 \text{ J}\cdot\text{K}^{-1}\cdot\text{mol}^{-1}$)
R^2	Correlation coefficient (-)
T	Temperature (K)
T_f	Final temperature (K)
TG	Thermogravimetry
TGA	Thermogravimetry analysis
T_i	Ignition temperature (K)
X	Conversion degree (-)
Greek symbols	
β	Heating rate ($\text{K}\cdot\text{min}^{-1}$)

References

- International Energy Agency. Available online: <http://www.iea.org/> (accessed on 23 March 2017).
- Nunes, L.J.R.; Matias, J.C.O.; Catalão, J.P.S. Biomass in the generation of electricity in Portugal: A review. *Renew. Sustain. Energy Rev.* **2017**, *71*, 373–378. [CrossRef]
- Jones, J.M.; Lea-Langton, A.R.; Ma, L.; Pourkashanian, M.; Williams, A. *Combustion of Solid Biomass: Classification of Fuels. Pollutants Generated by the Combustion of Solid Biomass Fuels*; Springer: London, UK, 2014; pp. 9–24. Available online: https://link.springer.com/chapter/10.1007/978-1-4471-6437-1_2 (accessed on 29 July 2018).
- van den Broek, R.; Faaij, A.; van Wijk, A. Biomass combustion for power generation. *Biomass Bioenergy* **1996**, *11*, 271–281. [CrossRef]
- Jones, J.M.; Lea-Langton, A.R.; Ma, L.; Pourkashanian, M.; Williams, A. *Pollutants Generated by the Combustion of Solid Biomass Fuels*; Springer: London, UK, 2014; Available online: <https://www.springer.com/gb/book/9781447164364> (accessed on 29 July 2018).
- Sannigrahi, P.; Ragauskas, A.J.; Tuskan, G.A. Poplar as a feedstock for biofuels: A review of compositional characteristics. *Biofuels Bioprod. Biorefin.* **2010**, *4*, 209–226. [CrossRef]
- Scheer, A. Thermal Decomposition Mechanisms of Lignin Model Compounds: From Phenol to Vanillin. Physics Graduate Thesis & Dissertations. 2011. Available online: https://scholar.colorado.edu/phys_gradetds/55 (accessed on 15 August 2018).
- Yu, J.; Paterson, N.; Blamey, J.; Millan, M. Cellulose, xylan and lignin interactions during pyrolysis of lignocellulosic biomass. *Fuel* **2017**, *191*, 140–149. [CrossRef]
- Hosoya, T.; Kawamoto, H.; Saka, S. Cellulose–hemicellulose and cellulose–lignin interactions in wood pyrolysis at gasification temperature. *J. Anal. Appl. Pyrolysis* **2007**, *80*, 118–125. [CrossRef]
- Yoshida, T.; Matsumura, Y. Gasification of Cellulose, Xylan, and Lignin Mixtures in Supercritical Water. *Ind. Eng. Chem. Res.* **2001**, *40*, 5469–5474. [CrossRef]
- Gani, A.; Naruse, I. Effect of cellulose and lignin content on pyrolysis and combustion characteristics for several types of biomass. *Renew. Energy* **2007**, *32*, 649–661. [CrossRef]
- González-García, S.; Luo, L.; Moreira, M.T.; Feijoo, G.; Huppé, G. Life cycle assessment of flax shives derived second generation ethanol fueled automobiles in Spain. *Renew. Sustain. Energy Rev.* **2009**, *13*, 1922–1933. [CrossRef]
- Daylan, B.; Ciliz, N. Life cycle assessment and environmental life cycle costing analysis of lignocellulosic bioethanol as an alternative transportation fuel. *Renew. Energy* **2016**, *89*, 578–587. [CrossRef]
- Rajabi Hamedani, S.; Villarini, M.; Colantoni, A.; Moretti, M.; Bocci, E. Life Cycle Performance of Hydrogen Production via Agro-Industrial Residue Gasification—A Small Scale Power Plant Study. *Energies* **2018**, *11*, 675. [CrossRef]
- Gassner, M.; Maréchal, F. Thermodynamic comparison of the FICFB and Viking gasification concepts. *Energy* **2009**, *34*, 1744–1753. [CrossRef]
- Qian, K.; Kumar, A.; Patil, K.; Bellmer, D.; Wang, D.; Yuan, W.; Huhnke, R.L. Effects of Biomass Feedstocks and Gasification Conditions on the Physicochemical Properties of Char. *Energies* **2013**, *6*, 3972–3986. [CrossRef]
- Guizani, C.; Jeguirim, M.; Valin, S.; Limousy, L.; Salvador, S. Biomass Chars: The Effects of Pyrolysis Conditions on Their Morphology, Structure, Chemical Properties and Reactivity. *Energies* **2017**, *10*, 796.
- Di Blasi, C. Modeling chemical and physical processes of wood and biomass pyrolysis. *Prog. Energy Combust. Sci.* **2008**, *34*, 47–90. [CrossRef]
- El may, Y.; Jeguirim, M.; Dorge, S.; Trouvé, G.; Said, R. Study on the thermal behavior of different date palm residues: Characterization and devolatilization kinetics under inert and oxidative atmospheres. *Energy* **2012**, *44*, 702–709. [CrossRef]
- Garcia Torrent, J.; Fernandez Anez, N.; Medic Pejic, L.; Montenegro Mateos, L. Assessment of self-ignition risks of solid biofuels by thermal analysis. *Fuel* **2015**, *143*, 484–491. [CrossRef]
- Gil, M.V.; Casal, D.; Pevida, C.; Pis, J.J.; Rubiera, F. Thermal behaviour and kinetics of coal/biomass blends during co-combustion. *Bioresour. Technol.* **2010**, *101*, 5601–5608. [CrossRef] [PubMed]
- Kastanaki, E.; Vamvuka, D. A comparative reactivity and kinetic study on the combustion of coal–biomass char blends. *Fuel* **2006**, *85*, 1186–1193. [CrossRef]

23. Haykırı-Açma, H. Combustion characteristics of different biomass materials. *Energy Convers. Manag.* **2003**, *44*, 155–162. [[CrossRef](#)]
24. Le Lin et le Chanvre Européen. Available online: <http://www.europeanflax.com/> (accessed on 18 July 2018).
25. Van de Velden, M.; Baeyens, J.; Brems, A.; Janssens, B.; Dewil, R. Fundamentals, kinetics and endothermicity of the biomass pyrolysis reaction. *Renew. Energy* **2010**, *35*, 232–242. [[CrossRef](#)]
26. Mohabeer, C.; Abdelouahed, L.; Marcotte, S.; Taouk, B. Comparative analysis of pyrolytic liquid products of beech wood, flax shives and woody biomass components. *J. Anal. Appl. Pyrolysis* **2017**, *127*, 269–277. [[CrossRef](#)]
27. García, R.; Pizarro, C.; Lavín, A.G.; Bueno, J.L. Biomass proximate analysis using thermogravimetry. *Bioresour. Technol.* **2013**, *139*, 1–4. [[CrossRef](#)] [[PubMed](#)]
28. Channiwala, S.A.; Parikh, P.P. A unified correlation for estimating HHV of solid, liquid and gaseous fuels. *Fuel* **2002**, *81*, 1051–1063. [[CrossRef](#)]
29. Magdziarz, A.; Wilk, M.; Straka, R. Combustion process of torrefied wood biomass. *J. Therm. Anal. Calorim.* **2017**, *127*, 1339–1349. [[CrossRef](#)]
30. Nowak, B.; Karlström, O.; Backman, P.; Brink, A.; Zevenhoven, M.; Voglsam, S.; Winter, F.; Hupa, M. Mass transfer limitation in thermogravimetry of biomass gasification. *J. Therm. Anal. Calorim.* **2012**, *111*, 183–192. [[CrossRef](#)]
31. Abdelouahed, L.; Leveneur, S.; Vernieres-Hassimi, L.; Balland, L.; Taouk, B. Comparative investigation for the determination of kinetic parameters for biomass pyrolysis by thermogravimetric analysis. *J. Therm. Anal. Calorim.* **2017**, *129*, 1201–1213. [[CrossRef](#)]
32. Wang, Z.; Lin, W.; Song, W.; Wu, X. Pyrolysis of the lignocellulose fermentation residue by fixed-bed micro reactor. *Energy* **2012**, *43*, 301–305. [[CrossRef](#)]
33. White, J.E.; Catallo, W.J.; Legendre, B.L. Biomass pyrolysis kinetics: A comparative critical review with relevant agricultural residue case studies. *J. Anal. Appl. Pyrolysis* **2011**, *91*, 1–33. [[CrossRef](#)]
34. Álvarez, A.; Pizarro, C.; García, R.; Bueno, J.L.; Lavín, A.G. Determination of kinetic parameters for biomass combustion. *Bioresour. Technol.* **2016**, *216*, 36–43. [[CrossRef](#)] [[PubMed](#)]
35. Garcia-Maraver, A.; Perez-Jimenez, J.A.; Serrano-Bernardo, F.; Zamorano, M. Determination and comparison of combustion kinetics parameters of agricultural biomass from olive trees. *Renew. Energy* **2015**, *83*, 897–904. [[CrossRef](#)]
36. Yorulmaz, S.Y.; Atimtay, A. Investigation of Combustion Kinetics of Five Waste Wood Samples with Thermogravimetric Analysis. In *Survival and Sustainability*; Springer: Berlin/Heidelberg, Germany, 2010; p. 511. Available online: https://link.springer.com/chapter/10.1007/978-3-540-95991-5_46 (accessed on 5 July 2017).
37. Islam, M.A.; Auta, M.; Kabir, G.; Hameed, B.H. A thermogravimetric analysis of the combustion kinetics of karanja (*Pongamia pinnata*) fruit hulls char. *Bioresour. Technol.* **2016**, *200*, 335–341. [[CrossRef](#)] [[PubMed](#)]
38. Coats, A.W.; Redfern, J.P. Kinetic Parameters from Thermogravimetric Data. *Nature* **1964**, *201*, 68–69. [[CrossRef](#)]
39. Damartzis, T.; Vamvuka, D.; Sfakiotakis, S.; Zabaniotou, A. Thermal degradation studies and kinetic modeling of cardoon (*Cynara cardunculus*) pyrolysis using thermogravimetric analysis (TGA). *Bioresour. Technol.* **2011**, *102*, 6230–6238. [[CrossRef](#)] [[PubMed](#)]
40. Vamvuka, D.; Kastanaki, E.; Lasithiotakis, M. Devolatilization and Combustion Kinetics of Low-Rank Coal Blends from Dynamic Measurements. *Ind. Eng. Chem. Res.* **2003**, *42*, 4732–4740. [[CrossRef](#)]
41. Zhou, H.; Long, Y.; Meng, A.; Chen, S.; Li, Q.; Zhang, Y. A novel method for kinetics analysis of pyrolysis of hemicellulose, cellulose, and lignin in TGA and macro-TGA. *RSC Adv.* **2015**, *5*, 26509–26516. [[CrossRef](#)]
42. Jiang, L.; Yuan, X.; Li, H.; Xiao, Z.; Liang, J.; Wang, H.; Wu, Z.; Chen, X.; Zeng, G. Pyrolysis and combustion kinetics of sludge–camphor pellet thermal decomposition using thermogravimetric analysis. *Energy Convers. Manag.* **2015**, *106*, 282–289. [[CrossRef](#)]
43. Munir, S.; Daood, S.S.; Nimmo, W.; Cunliffe, A.M.; Gibbs, B.M. Thermal analysis and devolatilization kinetics of cotton stalk, sugar cane bagasse and shea meal under nitrogen and air atmospheres. *Bioresour. Technol.* **2009**, *100*, 1413–1418. [[CrossRef](#)] [[PubMed](#)]
44. Sait, H.H.; Hussain, A.; Salema, A.A.; Ani, F.N. Pyrolysis and combustion kinetics of date palm biomass using thermogravimetric analysis. *Bioresour. Technol.* **2012**, *118*, 382–389. [[CrossRef](#)] [[PubMed](#)]

45. Gai, C.; Liu, Z.; Han, G.; Peng, N.; Fan, A. Combustion behavior and kinetics of low-lipid microalgae via thermogravimetric analysis. *Bioresour. Technol.* **2015**, *181*, 148–154. [[CrossRef](#)] [[PubMed](#)]
46. Grønli, M.G.; Varhegyi, G.; Di Blasi, C. Thermogravimetric analysis and devolatilization kinetics of wood. *Ind. Eng. Chem. Res.* **2002**, *41*, 4201–4208. [[CrossRef](#)]
47. Li, Q.; Zhao, C.; Chen, X.; Wu, W.; Li, Y. Comparison of pulverized coal combustion in air and in O₂/CO₂ mixtures by thermo-gravimetric analysis. *J. Anal. Appl. Pyrolysis* **2009**, *85*, 521–528. [[CrossRef](#)]
48. Meng, F.; Yu, J.; Tahmasebi, A.; Han, Y. Pyrolysis and Combustion Behavior of Coal Gangue in O₂/CO₂ and O₂/N₂ Mixtures Using Thermogravimetric Analysis and a Drop Tube Furnace. *Energy Fuels* **2013**, *27*, 2923–2932. [[CrossRef](#)]
49. Principal Component Analysis—Abdi—2010—Wiley Interdisciplinary Reviews: Computational Statistics—Wiley Online Library. Available online: <https://onlinelibrary.wiley.com/doi/abs/10.1002/wics.101> (accessed on 19 July 2018).
50. Duntzman, G.H. *Principal Components Analysis*; SAGE: Newcastle upon Tyne, UK, 1989.
51. Liu, N.A.; Fan, W.; Dobashi, R.; Huang, L. Kinetic modeling of thermal decomposition of natural cellulosic materials in air atmosphere. *J. Anal. Appl. Pyrolysis* **2002**, *63*, 303–325. [[CrossRef](#)]
52. Yorulmaz, S.Y.; Atimtay, A.T. Investigation of combustion kinetics of treated and untreated waste wood samples with thermogravimetric analysis. *Fuel Process. Technol.* **2009**, *90*, 939–946. [[CrossRef](#)]
53. Capart, R.; Khezami, L.; Burnham, A.K. Assessment of various kinetic models for the pyrolysis of a microgranular cellulose. *Thermochim. Acta* **2004**, *417*, 79–89. [[CrossRef](#)]
54. Vyazovkin, S.; Burnham, A.K.; Criado, J.M.; Pérez-Maqueda, L.A.; Popescu, C.; Sbirrazzuoli, N. ICTAC Kinetics Committee recommendations for performing kinetic computations on thermal analysis data. *Thermochim. Acta* **2011**, *520*, 1–19. [[CrossRef](#)]
55. Biagini, E.; Lippi, F.; Petarca, L.; Tognetti, L. Devolatilization rate of biomasses and coal–biomass blends: An experimental investigation. *Fuel* **2002**, *81*, 1041–1050. [[CrossRef](#)]
56. Cai, J.; Wang, Y.; Zhou, L.; Huang, Q. Thermogravimetric analysis and kinetics of coal/plastic blends during co-pyrolysis in nitrogen atmosphere. *Fuel Process. Technol.* **2008**, *89*, 21–27. [[CrossRef](#)]
57. Jayaraman, K.; Gökalp, I. Pyrolysis, combustion and gasification characteristics of miscanthus and sewage sludge. *Energy Convers. Manag.* **2015**, *89*, 83–91. [[CrossRef](#)]
58. Su, W.; Ma, H.; Wang, Q.; Li, J.; Ma, J. Thermal behavior and gaseous emission analysis during co-combustion of ethanol fermentation residue from food waste and coal using TG–FTIR. *J. Anal. Appl. Pyrolysis* **2013**, *99*, 79–84. [[CrossRef](#)]
59. Senneca, O. Kinetics of pyrolysis, combustion and gasification of three biomass fuels. *Fuel Process. Technol.* **2007**, *88*, 87–97. [[CrossRef](#)]
60. Sahu, S.G.; Sarkar, P.; Chakraborty, N.; Adak, A.K. Thermogravimetric assessment of combustion characteristics of blends of a coal with different biomass chars. *Fuel Process. Technol.* **2010**, *91*, 369–378. [[CrossRef](#)]
61. Kumar, A.; Wang, L.; Dzenis, Y.A.; Jones, D.D.; Hanna, M.A. Thermogravimetric characterization of corn stover as gasification and pyrolysis feedstock. *Biomass Bioenergy* **2008**, *32*, 460–467. [[CrossRef](#)]
62. Hurt, R.; Sun, J.-K.; Lunden, M. A Kinetic Model of Carbon Burnout in Pulverized Coal Combustion. *Combust. Flame* **1998**, *113*, 181–197. [[CrossRef](#)]



© 2018 by the authors. Licensee MDPI, Basel, Switzerland. This article is an open access article distributed under the terms and conditions of the Creative Commons Attribution (CC BY) license (<http://creativecommons.org/licenses/by/4.0/>).

Article

The Influence of Char Preparation and Biomass Type on Char Steam Gasification Kinetics

Tilia Dahou ^{1,2,3,*}, Françoise Defoort ¹, Sébastien Thiéry ¹, Maguelone Grateau ¹, Matthieu Campargue ⁴, Simona Bennici ², Mejdi Jeguirim ² and Capucine Dupont ⁵

¹ Université Grenoble Alpes, CEA, LITEN, DTBH, 17 avenue des Martyrs, 38054 Grenoble CEDEX 09, France; francoise.defoort@cea.fr (F.D.); sebastien.thiéry@cea.fr (S.T.); maguelone.grateau@cea.fr (M.G.)

² Institut de Sciences des Matériaux de Mulhouse, UMR 7661 CNRS, 15 rue Jean-Starcky, 68057 Mulhouse CEDEX, France; simona.bennici@uha.fr (S.B.); mejdi.jeguirim@uha.fr (M.J.)

³ Agence de l'Environnement et de la Maîtrise de l'Energie (ADEME), 20 avenue du Grésillé, BP 90406, 49004 Angers CEDEX 01, France

⁴ RAGT Energie, Zone Innoprod, Chemin de la Teulière, 81012 Albi CEDEX 9, France; mcampargue@ragt.fr

⁵ IHE Delft Institute for Water Education, Westvest 7, 2611 AX Delft, The Netherlands; c.dupont@un-ihe.org

* Correspondence: tilia.dahou@cea.fr; Tel.: +33-4-38-78-54-69

Received: 23 July 2018; Accepted: 14 August 2018; Published: 15 August 2018

Abstract: A study was conducted to investigate the parameter that has influence on steam gasification kinetics between the biomass type and char preparation. Thermogravimetric analysis (TGA) was carried out on steam gasification of seven biomass samples as well as chars from three of these samples. Chars were prepared using three different sets of low heating rate (LHR) pyrolysis conditions including temperature and biomass bed geometry. It was shown by a characteristic time analysis that these pyrolysis conditions were not associated with a chemical regime in a large amount of devices. However, it has been shown experimentally that conditions used to prepare the char had a much lower influence on steam gasification kinetics than the biomass type.

Keywords: biomass; steam gasification; kinetics; pyrolysis conditions; thermogravimetric analysis; characteristic time analysis

1. Introduction

Today, there is a consensus about the increasing need of biomass use for energy applications. Given the limited availability of wood, it seems essential to identify and to convert other biomass resources such as agricultural co-products. Among the various techniques for biomass conversion to energy, the gasification process is a promising one [1] such as in the case of hydrogen production [2–4] or liquid fuel synthesis [5–7]. This process includes two main steps that can overlap: biomass pyrolysis leading to char formation and gasification of the char producing syngas, i.e., a gas mixture of mainly CO and H₂. It has been shown that, with steam as a gasifying agent, the char gasification reaction has the slowest reaction under typical operating conditions [8]. Therefore, the design of industrial gasifiers requires the understanding and control of the steam gasification kinetics.

Since char is the starting material for gasification, it is important to identify the main parameter affecting char gasification kinetics.

In literature, two charring parameters are identified as having a potential influence on the steam gasification kinetics including pyrolysis operating conditions and biomass type [9]. The influence of pyrolysis conditions is largely related to the heating rate. Differences are especially noted between slow pyrolysis—low heating rate (LHR), <50 °C·min⁻¹—and fast pyrolysis—high heating rate (HHR), 500 °C·min⁻¹ [10]. The steam gasification rate increases when the heating rate increases, which is linked to char morphology differences. During LHR pyrolysis, the char keeps its natural porosity

while, in HHR pyrolysis, larger cavities are formed [9]. This larger surface area in the case of HHR pyrolysis along with the higher content in oxygen and hydrogen results in more available active sites [11]. The influence of the biomass type is basically related to the inorganic elements content of the biomass [12], which can attain high values for some resources such as agricultural residues [13]. In particular, alkali and alkaline earth metals (AAEMs) have a catalytic effect on gasification [14–17]. In contrast, elements such as silicon or phosphorus have an inhibiting effect [18,19].

To explain the origin of the influence of these two parameters, the first step is to determine the regime of the transformation, i.e., the phenomenon—chemical reaction or transfer—limiting its kinetics. Char preparation in conditions outside the chemical regime could result in variations in the properties of the chars. Differences between the chars obtained could lead to differences between their gasification behaviors. The regime of the transformation can be assessed through an analysis of the characteristic times of the phenomena involved. In literature, such an analysis has already been conducted by several authors. For instance, this can include pyrolysis [20–24], pyrogasification [8], and torrefaction [25] at the particle scale. However, most of these studies were performed for fast pyrolysis (HHR) and not slow pyrolysis (LHR). Moreover, time scale analysis is usually applied to a particle (for micrometric to centimetric scale particles), but more rarely to a bed of fine particles. One example can be found for torrefaction for which Gonzalez Martinez et al. [25] performed such an analysis at particle as well as at bed scale.

The present work combines the analysis of these characteristic times both at a particle scale and at a bed scale and an experimental study through thermogravimetric analysis (TGA). It focuses on slow pyrolysis (LHR) conditions (10 to $24\text{ }^{\circ}\text{C}\cdot\text{min}^{-1}$) and parameters as the amount of biomass treated, i.e., geometry (height and surface) of the crucible and the working temperature ($450\text{ }^{\circ}\text{C}$ or $800\text{ }^{\circ}\text{C}$ in one or two steps). Gasification was carried out on seven biomass samples as well as on chars prepared from three of these samples in four different sets of conditions. It aims to assess the relative influence of the two parameters previously discussed including char preparation conditions and biomass type on steam gasification kinetics.

2. Materials and Methods

2.1. Biomass Samples

Seven biomass samples covering a variety of compositions were selected for this study. The selection mainly includes agricultural residues. Samples were ground below $200\text{ }\mu\text{m}$ in a rotor mill. The ash content and inorganic element composition of the samples was measured, according to solid fuel standards NF EN 14775 [26] and NF EN ISO 16967 [27], respectively. Values obtained for each biomass sample can be found in Table 1. From these values, the three main inorganic elements in mass were identified.

The main inorganic elements contained in all biomasses are Ca and K. The third main element is Si, Mg, or P. Rice husk and wheat straw can be classified as silica-rich. Sunflower seed shells and alfalfa have a high potassium content. The others are rich in calcium.

Table 1. Ash and inorganic element content of the biomass samples (on dry basis).

Biomass Sample	Rice Husk	Wheat Straw [28]	Apple Orchard Residue [28]	Apricot Orchard Residue [28]	Vineyard Residue [28]	Sunflower Seed Shells	Alfalfa
Ash at 550 °C (wt %)	14.1	6.8	3.8	3.7	2.6	3.3	7.8
Si (mg·kg ⁻¹)	60,750	20,757	820	990	1012	258	510
K (mg·kg ⁻¹)	5363	13,063	3771	7254	5045	12,926	25,695
Ca (mg·kg ⁻¹)	1718	5627	9472	10,927	7808	6392	9694
Mg (mg·kg ⁻¹)	538	693	872	1374	1604	2812	1123
P (mg·kg ⁻¹)	630	1373	1325	1161	1011	1323	2997
Na (mg·kg ⁻¹)	270	164	25	41	37	20	289
Al (mg·kg ⁻¹)	166	429	71	104	151	257	83
Fe (mg·kg ⁻¹)	163	299	58	88	113	233	109
Mn (mg·kg ⁻¹)	183	50	11	20	42	12	<11
Main Inorganic Elements	Si K Ca	Si K Ca	Ca K P	Ca K Mg	Ca K Mg	K Ca Mg	K Ca P

2.2. Char Preparation

LHR pyrolysis in 1 L·min⁻¹ N₂ was carried out in three different sets of conditions in order to prepare large amounts of char from the different biomass feedstocks. Two devices were used to carry out the pyrolysis. They are illustrated in Figure 1.

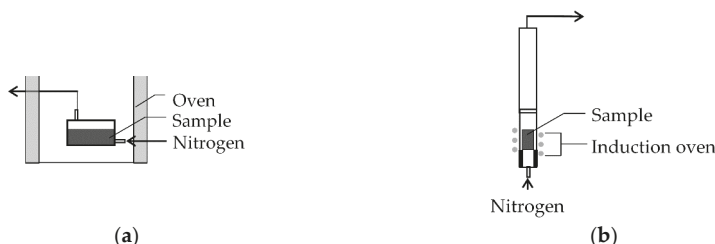


Figure 1. (a) Device M used for pyrolysis; (b) Device P used for pyrolysis.

Device M consists of a sample holder swept by nitrogen and placed in an oven. It can be used for large quantities of sample (30 g to 50 g depending on biomass) but only operates at moderate temperatures (450 °C). Device P consists of a mesh basket sample holder placed in a tube swept by nitrogen and heated by induction. It can reach higher temperatures (800 °C), but a lower amount of sample (approximately 5 g) can be converted at once.

Each set of conditions for char preparation from the biomass samples is described in Table 2. The first set of conditions (char M) is at a low temperature (450 °C) while the two other sets of conditions (char M-P and char P-P) have two temperature steps (450 °C and 800 °C) in the same or different devices.

In addition, char was produced from in-situ pyrolysis of the biomass before gasification in the thermo-balance (see following section), which pyrolysis conditions (char TGA) are listed in Table 2.

Table 2. Pyrolysis conditions for char preparation from the biomass samples.

	Char TGA	Char M	Char M-P	Char P-P
Device for treatment at 450 °C	TGA	Device M	Device M	Device P
Sample holder dimension at 450 °C height × diameter (mm × mm)	2.5 × 7	40 × 70	40 × 70	48 × 32
Heating rate to 450 °C (°C·min ⁻¹)	24	10	10	24
Holding time at 450 °C (min)	60	60	60	60
Cooling between treatment at 450 °C and 800 °C	No	—	Yes	No
Device for treatment at 800 °C	TGA	—	Device P	Device P
Heating rate to 800 °C (°C·min ⁻¹)	24	—	24	24
Holding time at 800 °C (min)	30	—	30	30

TGA: thermogravimetric analysis.

2.3. Steam Gasification Reactivity

Steam gasification reactivities of the four types of char (Table 2) were obtained through thermogravimetric analysis (TGA). Experiments were carried out at an atmospheric pressure using a Setsys thermobalance (SETARAM, Caluire, France) coupled with a Wetsys steam generator. For chars M, M-P, and P-P, which is a mass of 3 mg to 4 mg—i.e., the mass experimentally determined to be independent from heat and mass transfer influence—was placed in a cylindrical crucible of 2.5 mm height and 7 mm diameter. Samples were heated at 24 °C·min⁻¹ until 800 °C under 0.05 L·min⁻¹ N₂ except for char TGA, which starting material was biomass and for which an intermediate step at 450 °C was performed, which is shown in Table 2. In this last case, a mass of 14 mg of biomass was placed in the crucible. Samples were swept by N₂ for 45 min after the final temperature was reached to ensure pyrolysis completion and mass stability. Gas was then switched to a mixture of 20 vol % H₂O in N₂.

Steam gasification reactivities of the biomass samples were also measured. It corresponds to the preparation of char TGA described in the previous section, which is directly followed by steam gasification. The experimental procedure was similar to the one used for chars.

A solid conversion was then defined from mass loss measured as a function of time during TGA by using the following expression.

$$X = \frac{m_i - m(t)}{m_i - m_f}, \quad (1)$$

where m_i , $m(t)$, and m_f are the masses of char before gasification (at the time of steam injection) at the time t and at the end of gasification (remaining ash), respectively.

The gasification rate could then be defined as the variation of conversion versus the equation below.

$$r = X \frac{dX}{dt}. \quad (2)$$

An average reactivity between two values of conversion X_1 and X_2 was also defined below.

$$r_{X_1-X_2} = \frac{\int_{X_1}^{X_2} r(t) dt}{t_{X_2} - t_{X_1}} \frac{1}{1 - X(t)}. \quad (3)$$

2.4. Characteristic Time Calculation

The characteristic time of a phenomenon is the theoretical time needed for a process to occur when it is only controlled by this phenomenon [29]. It depends on the operating conditions. Phenomena to consider can be chemical reactions, heat transfers, mass transport, or other phenomena. From comparing characteristic times, the limiting phenomenon can be identified and the regime of the process can be defined.

In this study, characteristic times were calculated for char preparation through pyrolysis and for steam gasification of the char to represent the chosen experimental procedure as closely as possible in which the two reactions occur one after the other. Analysis of the characteristic times of the pyrolysis step is important since, if other phenomena than the chemical reaction occur, it could result in the production of different chars in the different conditions. Since char is the starting material to gasification, it could mean that these chars would behave differently during gasification. Analysis of the characteristic times of the gasification step is meant to validate the results from steam gasification TGA since reactivities are meaningful only in a chemical regime, i.e., when the chemical reaction is the leading phenomenon.

Phenomena involved in each process are illustrated in Figure 2.

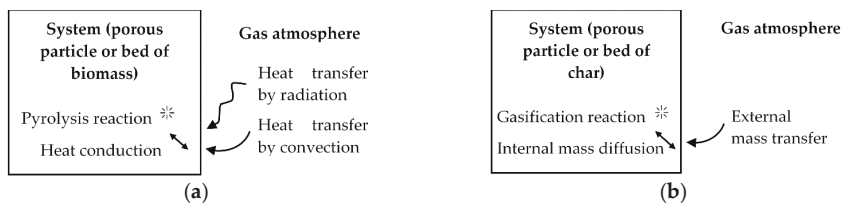


Figure 2. (a) Phenomena involved in pyrolysis; (b) Phenomena involved in gasification.

In the case of pyrolysis, the process is not led under isothermal conditions. Therefore, the characteristic times of the phenomena were compared to the heating time.

Characteristic times of each phenomenon as well as heating time are defined in Tables 3 and 4 for pyrolysis and gasification, respectively.

Table 3. Characteristic time definition for the pyrolysis of biomass.

Phenomenon	Definition of Characteristic Time
Pyrolysis chemical reaction	$t_{pyro} = \frac{1}{k_{pyro}}$
External heat transfer by convection	$t_{conv} = \frac{\rho_{solid} c_p \text{solid} L_c}{h_i}$
External heat transfer by radiation	$t_{rad} = \frac{\rho_{solid} c_p \text{solid} L_c}{\omega_{solid} \sigma (T_{gas} + T_{solid}) (T_{gas}^2 + T_{solid}^2)}$
Internal heat transfer by conduction	$t_{cond} = \frac{\rho_{solid} c_p \text{solid} L_c^2}{\lambda_{solid}}$
Heating	$t_{heating} = \frac{T_{gas} - T_{solid}}{r_{heating}}$

Table 4. Characteristic time definition for the gasification of biomass.

Phenomenon	Definition of Characteristic Time
Gasification chemical reaction	$t_{gasif} = \frac{1}{k_{gasif}}$
External mass transfer	$t_{mass ext} = \frac{\rho_{solid} R T_{gas} L_c}{h_m P_{H_2O} M_{H_2O}}$
Internal mass diffusion	$t_{diff int} = \frac{L_c^2}{D_{eff}}$

Pyrolysis and gasification chemical reactions of kinetic parameters were taken from literature. Pyrolysis kinetic parameters were taken from Di Blasi's review [30]: results were calculated both for the fastest [31] and the slowest [32] laws. For gasification, a law taking into account biomass composition was chosen [18]. Among a fast-reacting biomass, alfalfa, and a slow reacting one, barley straw were chosen for comparison. All kinetic constants and their parameters values are gathered in Table 5.

Table 5. Kinetic constants for pyrolysis and gasification reactions.

Reaction	Kinetic Constant Expression	Biomass	k_0 (s^{-1})	E_a (kJ·mol $^{-1}$)	$\frac{m_K}{m_{Si}}$	a	b
Pyrolysis	$k_{pyro} \exp\left(-\frac{E_a}{RT_{gas}}\right)$	Rice husk	5.8×10^{14}	200	-	-	-
		Sunflower shells	1.0×10^3	78.15	-	-	-
Gasification	$k_{gasif} \exp\left(-\frac{E_a}{RT_{gas}}\right) P_{H_2O}^{0.6} \left(a \frac{m_K}{m_{Si}} + b\right)$	Barley straw	8.8×10^4	167	0.1	0.18	0.59
		Alfalfa	8.8×10^4	167	50	0.18	0.59

Characteristic lengths used in characteristic time calculations are defined in Table 6.

Table 6. Characteristic lengths used for characteristic time calculations with d_p the particle diameter, D_c the bed diameter, and H_c the bed height.

System Considered	Characteristic Length L_c Definition	Device	Characteristic Length L_c Value (m)
Particle scale	$\frac{d_p}{6}$	All devices	3.3×10^{-5}
		TGA	6.3×10^{-4}
Bed scale	$\frac{D_c H_c}{2D_c + 4H_c}$	Device M	1.6×10^{-3}
		Device P	5.3×10^{-3}

Properties of the solids—biomass and char—were estimated from literature data or from our own measurements. They are gathered in Table 7.

Table 7. Physical properties of biomass and char particles and beds.

Property	Biomass Particle	Biomass Bed	Char Particle	Char Bed
Porosity ϵ_{solid} (-)	-	0.5 (estimated)	0.7 [33]	0.5 (estimated)
Tortuosity τ_{solid} (-)	-	-	3 [34]	1.57 [35]
Density ρ_{solid} (kg·m $^{-3}$)	860	430 (measured)	400 (estimated)	200
Specific heat $c_p solid$ (J·kg $^{-1}$ ·K $^{-1}$)	1266 [36]	1266	-	-
Thermal conductivity λ_{solid} (W·m $^{-1}$ ·K $^{-1}$)	0.18 [37]	0.09	-	-
Emissivity ω_{solid} (-)	0.9 [37]	0.9	-	-

Lastly, transfer coefficients were obtained from correlations from literature. They use gas properties from literature [37] and are defined in Table 8.

Table 8. Definition of transfer coefficients.

Transfer Coefficient	Coefficient Definition	Correlation
Heat transfer coefficient h_t (W·m $^{-2}$ ·K $^{-1}$)	$\frac{\lambda_{gas} Nu}{L_c}$	$Nu = 2 + \left(0.4Re^{\frac{1}{2}} + 0.06Re^{\frac{2}{3}}\right)Pr^{0.4}$ [38]
Effective diffusion coefficient D_{eff} (m 2 ·s $^{-1}$)	$\frac{\epsilon_{solid}}{\epsilon_{solid}} D_{H_2O-N_2}$	$D_{H_2O-N_2} = \frac{0.001 T_{gas}^{1.75} \left(\frac{1}{M_{H_2O}} + \frac{1}{M_{N_2}}\right)^{\frac{1}{2}}}{P_{gas} \left(\left(\Sigma v\right)_{H_2O}^{\frac{1}{2}} + \left(\Sigma v\right)_{N_2}^{\frac{1}{2}}\right)^2}$ [39]
Mass transfer coefficient h_m (m·s $^{-1}$)	$\frac{D_{H_2O-N_2} Sh}{L_c}$	$Sh = 2 + \left(0.4Re^{\frac{1}{2}} + 0.06Re^{\frac{2}{3}}\right)Sc^{0.4}$ [38]

Gas properties have a satisfactory accuracy while biomass and char properties as well as heat and mass transfer coefficients and kinetic parameters are estimated or calculated from empirical equations. Therefore, this low accuracy on the values used for calculations must be taken into account when analyzing the results obtained for characteristic times.

3. Results and Discussion

The experimental method used to demonstrate the influence of char preparation and biomass type involves various experimental devices at different scales. Therefore, it is necessary to look at the time scales of the phenomena involved in the process to determine its regime, i.e., chemical regime or regime led by heat or mass transfer. The analysis was conducted separately on pyrolysis and on gasification since these two steps were experimentally separated.

3.1. Characteristic Time Analysis

3.1.1. Analysis of Characteristic Times of the Pyrolysis Step

Characteristic times of the pyrolysis step are represented in Figure 3 for particle scale and for bed scale in the conditions of TGA, device M, and device P for a particle size below 200 μm . Results are shown as a function of temperature between 200 °C and 450 °C, i.e., in the range of temperature corresponding to biomass degradation, according to the literature [40].

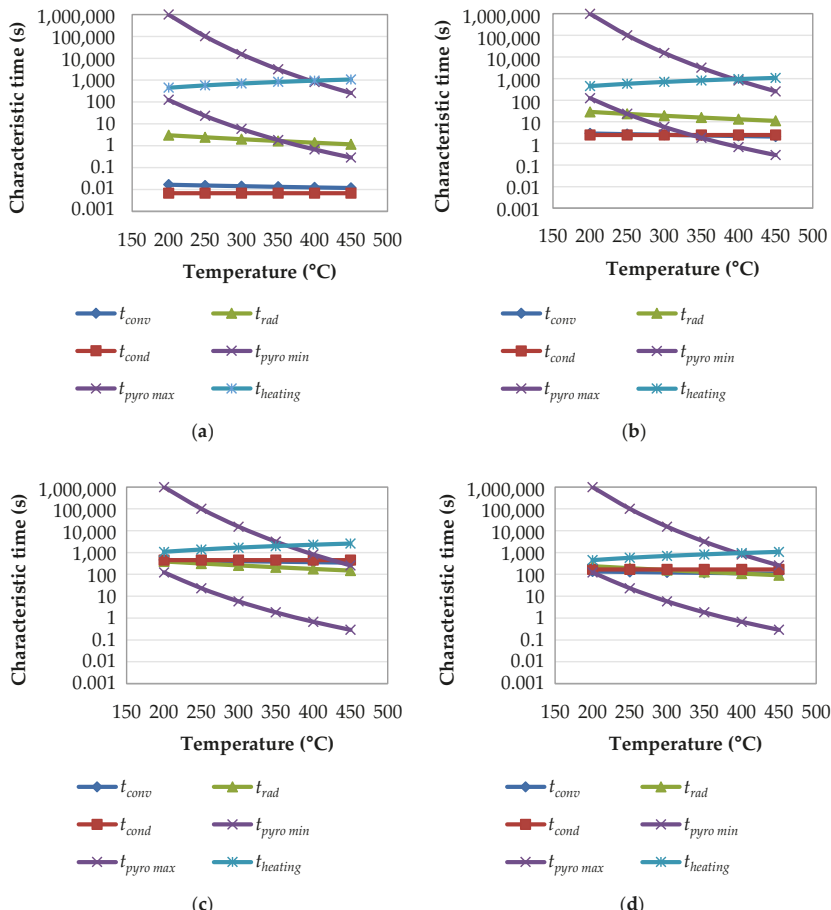


Figure 3. Characteristic times of the pyrolysis step as a function of temperature for: (a) particle scale in TGA conditions; (b) bed scale in TGA conditions; (c) bed scale in device M conditions; and (d) bed scale in device P condition. TGA: thermogravimetric analysis.

Calculations at particle scale were carried out for each of the three device conditions but results showed very negligible differences that were not noticeable through graphical representation. Therefore, only results obtained from TGA conditions are presented in this paper.

In all four cases, heating time and pyrolysis reaction times are the same except for heating time in device M conditions, but its variation is negligible. Only the three heat transfer characteristic times vary since they depend on the geometry of the system. Clearly, these characteristic times increase when the scale of the system—particle and beds of different sizes—increases.

When comparing heat transfers to the pyrolysis chemical reaction, it can be seen that their characteristic times are of the same order magnitude at least in part of the temperature range. This indicates that these phenomena occur simultaneously and none can be neglected.

Moreover, since pyrolysis was experimentally carried out in a dynamic mode, these times need to be compared with the heating time. For the phenomena to have enough time to occur, heating time should be higher than the phenomena characteristic times. In this study, heating times chosen for preparing the chars are of the same order of magnitude as the characteristic times of the phenomena involved.

In conclusion, characteristic time analysis shows that the pyrolysis step does not occur in a chemical regime. All phenomena occur simultaneously—none of them is negligible—and heating is too fast for the phenomena to occur.

Not being in a chemical regime during pyrolysis could result in chars that have different properties. Having different starting materials for gasification could, therefore, induce different kinetic behaviors. This is why it is important to check experimentally that chars produced under various conditions give the same gasification kinetics.

3.1.2. Analysis of Characteristic Times of the Gasification Step

Characteristic times of the gasification step are represented in Figure 4 for particle scale and bed scale under TGA conditions. Results are shown as a function of temperature between 500 °C and 1000 °C with the experimental study carried out at 800 °C in our study.

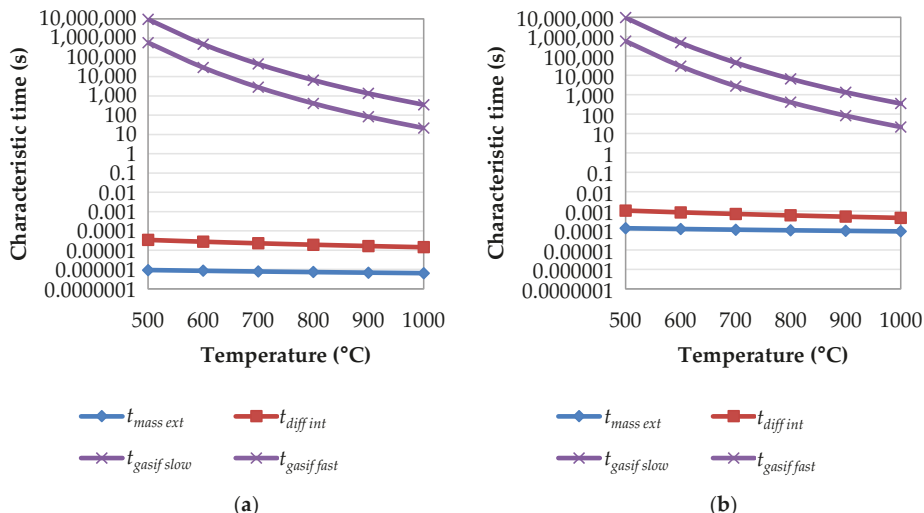


Figure 4. Characteristic times of the gasification step as a function of temperature for TGA conditions at: (a) particle scale and (b) bed scale.

At both scales, gasification chemical reactions with characteristic times remain the same. Mass transfer times slightly increase when the scale increases. However, at both scales and for both gasification kinetic laws, the gasification chemical reaction times are significantly higher—five to eight orders of magnitude—than mass transfer times. Therefore, according to time scales analysis, the gasification chemical reaction is the limiting phenomenon and mass transfers are negligible in comparison. The process occurs in the chemical regime.

This result is important since it means that kinetics obtained through TGA in these conditions should be intrinsic. According to this analysis, they exclusively represent the gasification chemical reaction without any bias from mass transfers.

However, Di Blasi's review [9] states that, even in TGA, typical operating condition mass transfers can have a non-negligible effect on char gasification. To verify this result experimentally for the conditions of the work presented in this study, gasification was carried out on different masses of the same char sample ranging from the full crucible (14 mg) to 3 mg. Only gasification of 4 mg or below showed the same kinetics. Higher masses of samples reacted more slowly, which indicated mass transfer limitations. These observations were close to previous results obtained on the same apparatus under similar conditions [12]. It shows the limits of characteristic time analysis, which relies on parameters known with limited accuracy.

3.2. Influence of Biomass Type

The influence of the biomass type on gasification kinetics was investigated through TGA of the biomass samples, i.e., preparation of char TGA and gasification of this char. Results from the mass loss as a function of time in these experiments are presented in Figure 5. Replicates are not shown in this paper but were carried out to ensure repeatability of the process, which was validated—variability can be seen in Figure 6 through error bars.

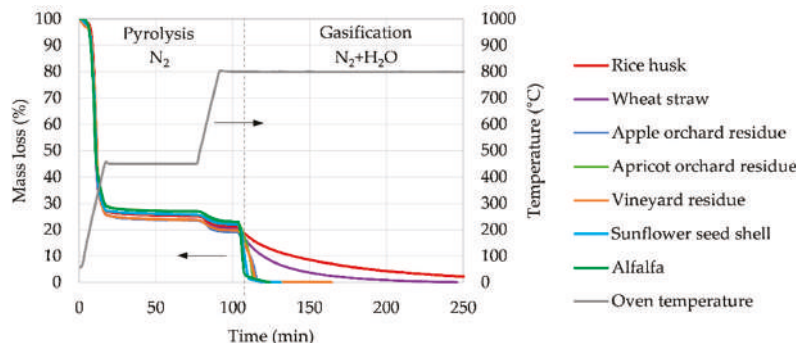


Figure 5. TGA of biomass samples presented as a mass loss and as a function of time. Pyrolysis: $0.05 \text{ L} \cdot \text{min}^{-1} \text{ N}_2$, $24^\circ\text{C}/\text{minutes}$, $1 \text{ h hold at } 450^\circ\text{C}$, $15\text{-min hold at } 800^\circ\text{C}$. Gasification: $0.05 \text{ L} \cdot \text{min}^{-1}$ mixture $80 \text{ vol \% N}_2/20 \text{ vol \% H}_2\text{O}$, 800°C .

It can be noted that mass loss profiles obtained during the pyrolysis of biomass samples are very similar.

The highest mass loss is observed for temperatures below 450°C with approximately 75% of the mass volatilized. Subsequently, around 5% of the mass is lost between 450°C and 800°C . These yields align with results from literature [41]. They can be compared with char yields obtained after pyrolysis in other devices used for char preparation, which are gathered in Figure 6.

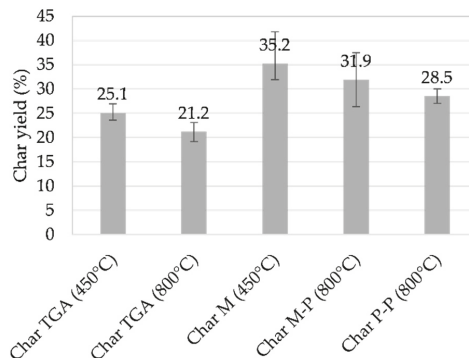


Figure 6. Char yield obtained in each char preparation condition (see Table 2).

There is a visible difference between values obtained at the thermo-balance scale and values obtained on devices M and P. This observation might be due to heat transfer limitations that are higher in the devices M and P, which are seen with characteristic times and can result in a lower solid conversion, i.e., a higher char yield. However, large scale values are close to what is expected for slow pyrolysis at pilot or industrial scale—35% char, 30% condensable products, and 35% non-condensable products [40,42].

The focus is made on the gasification step in Figure 7 and presented as a solid conversion and as a function of time.

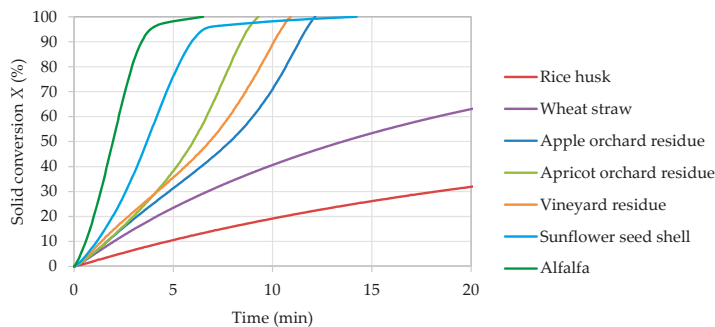


Figure 7. Solid conversion of biomass samples as a function of time during the gasification step (char TGA, $0.05 \text{ L} \cdot \text{min}^{-1}$ mixture 80 vol % N_2 /20 vol % H_2O , 800°C). Including data from Dupont et al. [28].

Three families of behavior can be identified, which is identified in literature [18]:

- Family 1 and its conversion rate is the highest and is constant and then increases such as in apple orchard residue, apricot orchard residue, and vineyard residue.
- Family 2 and its conversion rate is the slowest and is continuously decreasing such as in a rice husk and wheat straw.
- Family 3 and its conversion rate is intermediate and is constant and then decreases such as in sunflower seed shells and in alfalfa.

In addition, average reactivities of these biomass samples can be compared. Values of average reactivities between 1% and 80% conversion rates are gathered in Figure 8.

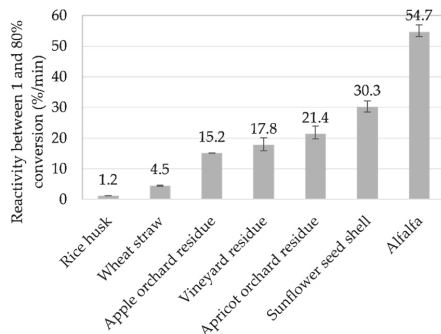


Figure 8. Gasification average reactivity between 1% and 80% conversion of biomass samples (char TGA, 0.05 L·min⁻¹ mixture 80 vol % N₂/20 vol % H₂O, 800 °C).

Substantial variation between biomasses is noted due to a factor of almost 50 between average reactivities of rice husk—slowest sample to be gasified at 1.2%·min⁻¹—and alfalfa—fastest sample to be gasified at 54.7%·min⁻¹.

These results could be related to inorganic composition of biomass samples. Silica-rich samples tended to have lower reaction rates than silica-poor samples. Among the latter, the reaction rate tends to increase with increasing content of potassium, which is in accordance with literature [18,43]. Other physicochemical characterizations such as a surface area measurement or H and O quantification have not been performed in the present study and may bring a better understanding of the results.

3.3. Influence of Char Preparation

To investigate the influence of char preparation, steam gasification kinetics of chars prepared in different conditions were compared. To carry out this comparison, samples with extreme behaviors were selected from the study of biomass samples. Sunflower seed shells and alfalfa were chosen for their high reactivity, high potassium content, and low silicon content. The rice husk was chosen for its low reactivity, low potassium content, and high silicon content.

TGA of the gasification step was conducted on this chars selection. Results expressed in the form of solid conversion as a function of time are presented in Figure 9. Reactivities between 1% and 80% were derived from these results and are given in Figure 10.

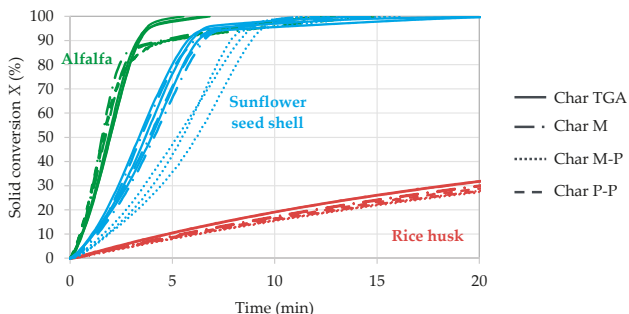


Figure 9. Solid conversion of chars as a function of time during gasification (0.05 L·min⁻¹ mixture 80 vol % N₂/20 vol % H₂O, 800 °C).

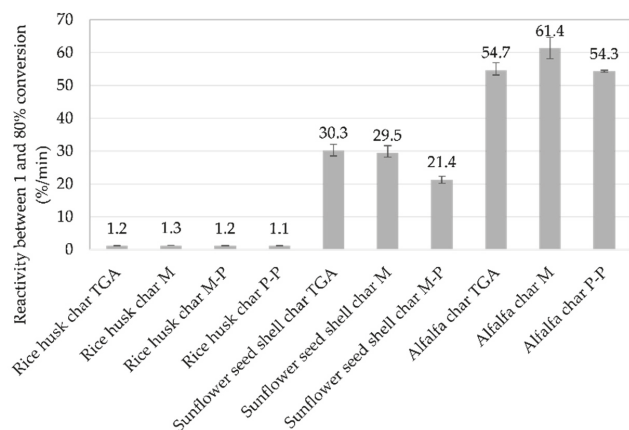


Figure 10. Gasification average reactivity between 1% and 80% conversion of biomass and char samples (see Table 2).

For each biomass, chars prepared in different conditions—in particular LHR pyrolysis conditions and not in a chemical regime—have the same reactivity during gasification. One exception for char M-P comes from the sunflower seed shells. No explanation was found regarding this result but it may be found by characterizing the chars. However, variations are negligible compared to differences that are observed between fast-reacting and slow-reacting biomass types. There is a factor of 1.2 in average between reactivities of the various char samples from each biomass, which is very low when compared to the factor of almost 50 calculated between reactivities of rice husk and alfalfa.

4. Conclusions

Thermogravimetric analysis (TGA) of biomass samples and of chars prepared from these biomasses in different LHR pyrolysis conditions outside the chemical regime showed that the biomass type has a significantly higher influence on steam gasification kinetics than char preparation conditions. In the range of the seven studied biomass samples, a factor of almost 50 was measured between average reactivities of the two samples with extreme behavior (rice husk with 1.2-min^{-1} and alfalfa with 54.7-min^{-1}). In comparison, chars prepared in conditions outside the chemical regime from various amounts of biomass depending on the crucible geometry (height and surface) and several working temperatures ($450\text{ }^{\circ}\text{C}$ or $800\text{ }^{\circ}\text{C}$ in one or two steps) showed a much lower difference with an average factor of 1.2 for a given biomass type.

The influence of biomass type could be assumed to be related to inorganic content of the biomass as opposed to its molecular constituents—lignin, hemicellulose, cellulose. This assumption is supported by literature data. However, further investigations are in progress and consist of physicochemical characterization of chars from different biomass samples. It will confirm if inorganic composition is the main influential parameter or if it should rather be explained by structural or textural properties of the char.

Author Contributions: Conceptualization, F.D., M.C., S.B., M.J. and C.D. Investigation, T.D., S.T. and M.G. Formal Analysis, T.D. Resources, M.C. Writing-Original Draft Preparation, T.D. Writing-Review & Editing, F.D., M.J. and C.D. Supervision, F.D., M.J. and C.D.

Funding: This research was funded by the Agence de l’Environnement et de la Maîtrise de l’Energie.

Conflicts of Interest: The authors declare no conflict of interest.

Nomenclature

$c_p \text{solid}$	(J·kg ⁻¹ ·K ⁻¹)	Specific heat of the solid phase (bed or particle)
d_p	(m)	Particle diameter
D_c	(m)	Diameter of the cylindrical bed
D_{eff}	(m ² ·s ⁻¹)	Effective diffusion coefficient
D_{H2O-N2}	(m ² ·s ⁻¹)	Diffusion coefficient of the mixture N ₂ -H ₂ O
h_m	(m·s ⁻¹)	External mass transfer coefficient
h_t	(W·m ⁻² ·K ⁻¹)	Heat transfer coefficient
H_c	(m)	Height of the cylindrical bed
k_{gasif}	(s ⁻¹)	Kinetic constant of the gasification reaction
k_{pyro}	(s ⁻¹)	Kinetic constant of the pyrolysis reaction
M_{H2O}	(kg·mol ⁻¹)	Molecular weight of water
M_{N2}	(kg·mol ⁻¹)	Molecular weight of nitrogen
Nu	(−)	Nusselt number
P_{H2O}	(Pa)	Partial pressure of steam
P_{gas}	(Pa)	Pressure of the gas
Pr	(−)	Prandtl number
r	(s ⁻¹)	Gasification rate
$r_{heating}$	(K·s ⁻¹)	Heating rate
R	(J·mol ⁻¹ ·K ⁻¹)	Universal gas constant
Re	(−)	Reynolds number
Sc	(−)	Schmidt number
Sh	(−)	Sherwood number
t_{cond}	(s)	Internal heat conduction time
t_{conv}	(s)	External heat convection time
$t_{diff\ int}$	(s)	Characteristic time of internal mass diffusion
t_{gasif}	(s)	Characteristic time of the gasification chemical reaction
$t_{heating}$	(s)	Heating time
$t_{mass\ ext}$	(s)	Characteristic time of external mass transfer
t_{pyro}	(s)	Characteristic time of the pyrolysis chemical reaction
t_{rad}	(s)	External radiation time
T_{gas}	(K)	Gas temperature
T_{solid}	(K)	Solid (bed or particle) temperature
X	(−)	Solid conversion
ε_{solid}	(−)	Porosity of the solid phase (bed or particle)
λ_{gas}	(W·m ⁻¹ ·K ⁻¹)	Thermal conductivity of the gas phase
λ_{solid}	(W·m ⁻¹ ·K ⁻¹)	Thermal conductivity of the solid phase (bed or particle)
ρ_{solid}	(kg·m ⁻³)	Density of the solid phase (bed or particle)
σ	(W·m ⁻² ·K ⁻⁴)	Boltzmann constant
$(\Sigma v)_{H2O}$	(m ³ ·mol ⁻¹)	Diffusion volume of H ₂ O
$(\Sigma v)_{N2}$	(m ³ ·mol ⁻¹)	Diffusion volume of N ₂
τ_{solid}	(−)	Tortuosity of the solid phase (bed or particle)
ω_{solid}	(−)	Emissivity of the biomass

References

1. Kumar, A.; Jones, D.D.; Hanna, M.A. Thermochemical Biomass Gasification: A Review of the Current Status of the Technology. *Energies* **2009**, *2*, 556–581. [[CrossRef](#)]
2. Bartocci, P.; Zampilli, M.; Bidini, G.; Fantozzi, F. Hydrogen-rich gas production through steam gasification of charcoal pellet. *Appl. Therm. Eng.* **2018**, *132*, 817–823. [[CrossRef](#)]
3. Luo, S.; Xiao, B.; Guo, X.; Hu, Z.; Liu, S.; He, M. Hydrogen-rich gas from catalytic steam gasification of biomass in a fixed bed reactor: Influence of particle size on gasification performance. *Int. J. Hydrog. Energy* **2009**, *34*, 1260–1264. [[CrossRef](#)]

4. Yan, F.; Luo, S.; Hu, Z.; Xiao, B.; Cheng, G. Hydrogen-rich gas production by steam gasification of char from biomass fast pyrolysis in a fixed-bed reactor: Influence of temperature and steam on hydrogen yield and syngas composition. *Bioresour. Technol.* **2010**, *101*, 5633–5637. [[CrossRef](#)] [[PubMed](#)]
5. Rafati, M.; Wang, L.; Dayton, D.C.; Schimmel, K.; Kabadi, V.; Shahbazi, A. Techno-economic analysis of production of Fischer-Tropsch liquids via biomass gasification: The effects of Fischer-Tropsch catalysts and natural gas co-feeding. *Energy Convers. Manag.* **2017**, *133*, 153–166. [[CrossRef](#)]
6. Snehesh, A.S.; Mukunda, H.S.; Mahapatra, S.; Dasappa, S. Fischer-Tropsch route for the conversion of biomass to liquid fuels—Technical and economic analysis. *Energy* **2017**, *130*, 182–191. [[CrossRef](#)]
7. Chiodini, A.; Bua, L.; Carnelli, L.; Zwart, R.; Vreugdenhil, B.; Vociante, M. Enhancements in Biomass-to-Liquid processes: Gasification aiming at high hydrogen/carbon monoxide ratios for direct Fischer-Tropsch synthesis applications. *Biomass Bioenergy* **2017**, *106*, 104–114. [[CrossRef](#)]
8. Dupont, C.; Boissonnet, G.; Seiler, J.-M.; Gauthier, P.; Schweich, D. Study about the kinetic processes of biomass steam gasification. *Fuel* **2007**, *86*, 32–40. [[CrossRef](#)]
9. Di Blasi, C. Combustion and gasification rates of lignocellulosic chars. *Prog. Energy Combust. Sci.* **2009**, *35*, 121–140. [[CrossRef](#)]
10. Ballerini, D.; Alazard-Toux, N. *Les Biocarburants*; Editions Technip: Paris, France, 2006; ISBN 978-2-7108-0969-2.
11. Guerrero, M.; Ruiz, M.P.; Millera, Á.; Alzueta, M.U.; Bilbao, R. Oxidation Kinetics of Eucalyptus Char Produced at Low and High Heating Rates. *Energy Fuels* **2008**, *22*, 2084–2090. [[CrossRef](#)]
12. Dupont, C.; Nocquet, T.; Da Costa, J.A.; Verne-Tournon, C. Kinetic modelling of steam gasification of various woody biomass chars: Influence of inorganic elements. *Bioresour. Technol.* **2011**, *102*, 9743–9748. [[CrossRef](#)] [[PubMed](#)]
13. Vassilev, S.V.; Baxter, D.; Andersen, L.K.; Vassileva, C.G. An overview of the chemical composition of biomass. *Fuel* **2010**, *89*, 913–933. [[CrossRef](#)]
14. Feng, D.; Zhao, Y.; Zhang, Y.; Xu, H.; Zhang, L.; Sun, S. Catalytic mechanism of ion-exchanging alkali and alkaline earth metallic species on biochar reactivity during CO₂/H₂O gasification. *Fuel* **2018**, *212*, 523–532. [[CrossRef](#)]
15. Jiang, L.; Hu, S.; Wang, Y.; Su, S.; Sun, L.; Xu, B.; He, L.; Xiang, J. Catalytic effects of inherent alkali and alkaline earth metallic species on steam gasification of biomass. *Int. J. Hydrg. Energy* **2015**, *40*, 15460–15469. [[CrossRef](#)]
16. Kajita, M.; Kimura, T.; Norinaga, K.; Li, C.Z.; Hayashi, J.I. Catalytic and noncatalytic mechanisms in steam gasification of char from the pyrolysis of biomass. *Energy Fuels* **2009**, *24*, 108–116. [[CrossRef](#)]
17. Lahijani, P.; Zainal, Z.A.; Mohamed, A.R.; Mohammadi, M. CO₂ gasification reactivity of biomass char: Catalytic influence of alkali, alkaline earth and transition metal salts. *Bioresour. Technol.* **2013**, *144*, 288–295. [[CrossRef](#)] [[PubMed](#)]
18. Dupont, C.; Jacob, S.; Marrakchy, K.O.; Hognon, C.; Grateau, M.; Labalette, F.; Da Silva Perez, D. How inorganic elements of biomass influence char steam gasification kinetics. *Energy* **2016**, *109*, 430–435. [[CrossRef](#)]
19. Kannan, M.P.; Richards, G.N. Gasification of biomass chars in carbon dioxide: dependence of gasification rate on the indigenous metal content. *Fuel* **1990**, *69*, 747–753. [[CrossRef](#)]
20. Cuervo, N.; Dufaud, O.; Torrado, D.; Bardin-Monnier, N.; Perrin, L.; Laurent, A. Experimental study and modeling of the pyrolysis of organic dusts: application to dust explosions. *Chem. Eng. Trans.* **2013**, *931*–936. [[CrossRef](#)]
21. Dufour, A.; Ouattassi, B.; Bounaceur, R.; Zoullalian, A. Modelling intra-particle phenomena of biomass pyrolysis. *Chem. Eng. Res. Des.* **2011**, *89*, 2136–2146. [[CrossRef](#)]
22. Gómez-Barea, A.; Leckner, B. Modeling of biomass gasification in fluidized bed. *Prog. Energy Combust. Sci.* **2010**, *36*, 444–509. [[CrossRef](#)]
23. Palumbo, A.W.; Weimer, A.W. Heat transfer-limited flash pyrolysis of woody biomass: Overall reaction rate and time analysis using an integral model with experimental support. *J. Anal. Appl. Pyrolysis* **2015**, *113*, 474–482. [[CrossRef](#)]
24. Septien, S.; Valin, S.; Dupont, C.; Peyrot, M.; Salvador, S. Effect of particle size and temperature on woody biomass fast pyrolysis at high temperature (1000–1400 °C). *Fuel* **2012**, *97*, 202–210. [[CrossRef](#)]

25. Martinez, M.G.; Dupont, C.; Thiery, S.; Meyer, X.M.; Gourdon, C. Characteristic time analysis of biomass torrefaction phenomena—Application to thermogravimetric analysis device. *Chem. Eng. Trans.* **2016**, *50*, 61–66. [[CrossRef](#)]
26. European Standards. Solid Biofuels—Determination of Ash Content (EN 14775). Available online: https://www.google.com.tw/url?sa=t&rct=j&q=&esrc=s&source=web&cd=1&ved=2ahUKEwjPrM-E1t_cAhVWfd4KHUe6BNIQFjAAegQIABAC&url=https%3A%2F%2Fwww.researchgate.net%2Fprofile%2FAlain_Celzard%2Fpost%2FWhich_ASTM_standard_should_I_refer_to_in_order_to_determine_the_moisture_and_volatiles_content_in_biomass%2Fattachment%2F59d62117c49f478072e9848e%2FAS%253A271759398375424%25401441803897376%2Fdownload%2Fsolid%2Bbiofuels%2B-%2BDetermination%2Bof%2Bash%2Bcontent.pdf&usg=AOvVaw0FjluSmH5RWZsNzKmNjEL_ (accessed on 11 June 2018).
27. International Organization for Standardization. Solid Biofuels—Determination of Major Elements—Al, Ca, Fe, Mg, P, K, Si, Na and Ti (ISO 16967: 2015). Available online: <https://www.iso.org/standard/58065.html> (accessed on 11 June 2018).
28. Dupont, C.; Karakashov, B.; Dahou, T.; Martinez, M.G.; Saavedra, C.; Da Silva Perez, D.; Karakasova, L. Quality of agricultural waste from orchards and vineyards as feedstock for thermal processes with focus on torrefaction and gasification. *Biomass Bioenergy* **2018**, submitted.
29. Villieraux, J.; Antoine, B. Pyrolyse éclair de solides divisés dans un réacteur continu: 1. Un nouveau modèle de volatilisation thermique de particules solides. *Rev. Générale Therm.* **1980**, *227*, 851–860.
30. Di Blasi, C. Modeling chemical and physical processes of wood and biomass pyrolysis. *Prog. Energy Combust. Sci.* **2008**, *34*, 47–90. [[CrossRef](#)]
31. Nunn, T.R.; Howard, J.B.; Longwell, J.P.; Peters, W.A. Product compositions and kinetics in the rapid pyrolysis of sweet gum hardwood. *Ind. Eng. Chem. Process Des. Dev.* **1985**, *24*, 3. [[CrossRef](#)]
32. Samolada, M.C.; Vasalos, I.A. A kinetic approach to the flash pyrolysis of biomass in a fluidized bed reactor. *Fuel* **1991**, *70*, 883–889. [[CrossRef](#)]
33. Brewer, C.E.; Chuang, V.J.; Masiello, C.A.; Gonnermann, H.; Gao, X.; Dugan, B.; Driver, L.E.; Panzacchi, P.; Zygourakis, K.; Davies, C.A. New approaches to measuring biochar density and porosity. *Biomass Bioenergy* **2014**, *66*, 176–185. [[CrossRef](#)]
34. Johnsson, J.E.; Jensen, A. Effective diffusion coefficients in coal chars. *Proc. Combust. Inst.* **2000**, *28*, 2353–2359. [[CrossRef](#)]
35. Dalloz-Dubrujeaud, B.; Faure, R.; Tadrist, L.; Giraud, G. Perte de pression et vitesse minimum de fluidisation dans un lit de particules 2D. *Comptes Rendus l’Académie Sci.-Ser. IIB-Mech. Phys. Astron.* **2000**, *328*, 231–236. [[CrossRef](#)]
36. Dupont, C.; Chiriac, R.; Gauthier, G.; Toche, F. Heat capacity measurements of various biomass types and pyrolysis residues. *Fuel* **2014**, *115*, 644–651. [[CrossRef](#)]
37. Perry, R.H.; Green, D.W. *Perry’s Chemical Engineers’ Handbook*; McGraw-Hill: London, UK, 1998; ISBN 978-0-07-115982-1.
38. Whitaker, S. Forced convection heat transfer correlations for flow in pipes, past flat plates, single cylinders, single spheres, and for flow in packed beds and tube bundles. *AICHE J.* **1972**, *18*, 361–371. [[CrossRef](#)]
39. Fuller, E.N.; Schettler, P.D.; Giddings, J.C. New method for prediction of binary gas-phase diffusion coefficients. *Ind. Eng. Chem.* **1966**, *58*, 18–27. [[CrossRef](#)]
40. Kan, T.; Strezov, V.; Evans, T.J. Lignocellulosic biomass pyrolysis: A review of product properties and effects of pyrolysis parameters. *Renew. Sustain. Energy Rev.* **2016**, *57*, 1126–1140. [[CrossRef](#)]
41. Anca-Couce, A. Reaction mechanisms and multi-scale modelling of lignocellulosic biomass pyrolysis. *Prog. Energy Combust. Sci.* **2016**, *53*, 41–79. [[CrossRef](#)]
42. Deglise, X.; Donnot, A. Bois énergie—Propriétés et voies de valorisation. *Tech. Ing. Énerg. Renouvelables* **2017**. Available online: <https://www.techniques-ingieur.fr/base-documentaire/energies-th4/energies-renouvelables-42594210/bois-energie-be8535/> (accessed on 11 June 2018).
43. Zhang, Y.; Ashizawa, M.; Kajitani, S.; Miura, K. Proposal of a semi-empirical kinetic model to reconcile with gasification reactivity profiles of biomass chars. *Fuel* **2008**, *87*, 475–481. [[CrossRef](#)]



© 2018 by the authors. Licensee MDPI, Basel, Switzerland. This article is an open access article distributed under the terms and conditions of the Creative Commons Attribution (CC BY) license (<http://creativecommons.org/licenses/by/4.0/>).

Article

Possible Interactions and Interferences of Copper, Chromium, and Arsenic during the Gasification of Contaminated Waste Wood [†]

Shurooq Badri Al-Badri ^{1,2}, Ying Jiang ¹ and Stuart Thomas Wagland ^{1,*}

¹ School of Water, Energy, and Environment, Cranfield University, Cranfield MK43 0AL, UK; s.b.albadri@cranfield.ac.uk (S.B.A.-B.); y.jiang@cranfield.ac.uk (Y.J.)

² Department of Chemistry, College of Science, University of Baghdad, Baghdad 10071, Iraq

* Correspondence: s.t.wagland@cranfield.ac.uk; Tel.: +44(0)-1234-750-111

† This paper is an extended version of our paper published in the 9th International Renewable Energy Congress (IREC), Hammamet, Tunisia, 20–22 March 2018.

Received: 3 July 2018; Accepted: 25 July 2018; Published: 28 July 2018

Abstract: A considerable proportion (about 64%) of biomass energy is produced from woody biomass (wood and its wastes). However, waste wood (WW) is very often contaminated with metal(loid) elements at concentrations leading to toxicity emissions and damages to facilities during thermal conversion. Therefore, procedures for preventing and/or alleviating the negative impacts of these elements require further development, particularly by providing informative and supportive information regarding the phase transformations of the metal(loid)s during thermal conversion processes. Although it is well known that phase transformation depends on different factors such as elements' vaporization characteristics, operational conditions, and process configuration; however, the influences of reaction atmosphere composition in terms of interactions and interferences are rarely addressed. In response, since Cu, Cr, and As (CCA-elements) are the most regulated elements in woody biomass, this paper aims to explore the possible interactions and interferences among CCA-elements themselves and with Ca, Na, S, Cl, Fe, and Ni from reaction atmosphere composition perspectives during the gasification of contaminated WW. To do so, thermodynamic equilibrium calculations were performed for Boudouard reaction (BR) and partial combustion reaction (PCR) with temperature ranges of 0–1300 °C and 0–1800 °C, respectively, and both reactions were simulated under pressure conditions of 1, 20, and 40 atm. Refinement of the occurred interactions and interferences reveals that Ni-As interactions generate dominant species As_2Ni_5 and $\text{As}_8\text{Ni}_{11}$, which increase the solid–gaseous transformation temperature of As. Moreover, the interactions between Ca and Cr predominantly form C_3Cr_7 ; whereas the absence of Ca leads to $\text{Cr}_2\text{Na}_2\text{O}_4$ causing instability in the Cr phase transformation.

Keywords: waste wood; interactions; interferences; partial combustion reaction in gasification; Boudouard reaction in gasification; MTDATA

1. Introduction

Waste wood (WW) is the term used for wood material that has previously been used for various purposes and is now being treated as a waste material; in the context of this study the waste wood is being utilized for energy production [1]. It comprises a wide variety of wood materials primarily from industrial and commercial activities and from construction and demolition operations [2,3]. Since it is collected from diverse sources, WW may contain both physical and chemical contaminants [1,4]. Physical contaminates can simply be separated by sorting or using mechanical techniques. However, the majority of chemical contaminates are usually linked to the metal(loid) elements contained in wood

that has been treated with preservatives, paintings, coatings, and other related activities, and, of course, mechanical separation is not applicable.

Essentially, gasification process involves the conversion of solid carbonaceous fuels into combustible gases composed of a mixture of N_2 , H_2O , CH_4 , H_2 , CO_2 , CO , and very small quantities of low molecular weight hydrocarbons and contaminants including ash, tar, and carbon particles [5,6]. In general, biomass gasification consists of four processing steps: drying, pyrolysis of dried biomass particles (de-volatilization), partial oxidation of pyrolysis gases and/or char, and char gasification (reduction) [7], as depicted in Figure 1 [8]. Technically, gasification is an exothermic partial oxidation of biomass operating at high temperatures between 800 and 1300 °C with the presence of gasifying mediums such as carbon dioxide, steam, and air (or a mixture of air and steam) [7,9–11]. Further, the compositions and properties of the gasification products vary according to the operational conditions, gasifier type, and biomass materials.

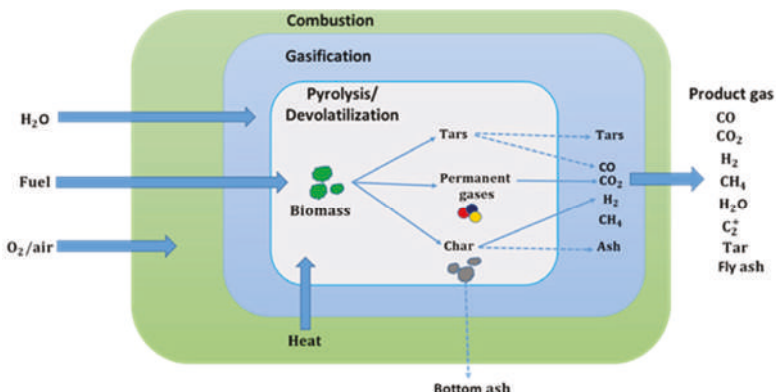


Figure 1. Schematic of the processes in a typical gasifier.

Currently, because of its efficiency and flexibility [12], gasification is vastly employed for generating renewable energy and waste disposal. However, when conducting gasification, metal(loid)s in biomass can cause severe human health and environmental problems as well as significant technical damages when they present at high concentrations. Hence, to avoid and/or limit the risks of metal(loid) elements, the transformation behaviours of these elements across the different phases require further investigating.

A range of studies [13–17] have focused on the distribution of the metal(loid)s between gaseous and solid phases during gasification. These studies report that the partitioning of metal(loid) elements can be directly influenced by a combination of several factors such as feedstock characteristics, operational conditions, and process agents. In fact, phase transformation temperatures of metal(loid)s cannot be accurately determined using traditional analytical tools/instruments because the generated species cannot be easily identified, and hence measured. As such, the mass distribution of metal(loid) elements during gasification is a quite complex problem. Fortunately, thermodynamic equilibrium modelling based on Gibbs energy minimization has effectively been used for yielding the best predictions of the behaviours of metal(loid) elements, and in turn allowing for precise evaluation of the speciation during the thermochemical processes [18–25].

Jiang et al. [18] studied the solid–gaseous transition of Zn, Pb, Ni, Mn, Mg, Fe, Cu, Cr, Co, Cd, As, and Al in five biomass samples during typical gasification scenarios. This study reports that the most volatilized elements are As, Cd, Pb, and Zn, whereas Cu, Co, Ni, and Mn are moderately volatilized, and the phase transformation temperatures of Mg, Fe, Cr, and Al are $> 1200^{\circ}\text{C}$. Froment et al. [19] assessed the volatilization and condensation of certain elements in woody biomass during gasification with temperatures ranging from 500 to 1500°C , and pressure conditions from 1 to 10 bar. The calculation results showed that Zn, Pb, Se, Sb, S, N, Hg, F, Cd, and Cl completely volatilized as either elemental or species, whereas, Ca, Si, Al, P, Cu, Mn, Ti, Fe, Cr, Mg, and Ba remained as oxides in the condensed phase, except copper which condensed as Cu_3As . Kramb et al. [20] modelled the behavior of As during the gasification of CCA-treated wood, and reported that about 99.6% of As can be captured. Thompson and Argent [21] categorized the trace elements in a PRENLFO gasifier into “virtually immobile (Cr, Ba, Ni, V), somewhat mobile (Mo, Be, Cu), mobile (Sb, B) and almost totally mobilized (As, Cd, Pb, Sn, Zn)”. Kilgallon et al. [22] investigated the impacts of both pressure conditions and chlorine/sulphur on element phase transitions. Reed et al. [23] reported the speciation prediction of Cd, As, B, Co, Be, Pb, Cu, Sb, V, Sn, and Zn in fuel gas from a gasifier. They explicitly partitioned these elements into three groups: condensed phase (Cu, Be, V, Zn and Co; at $T_{50} \gg 900\text{ K}$), gas phase (As without Ni, B without Ca, Sb, and Sn), and condensed phase (As with Ni, B with Ca, Cd, and Pb; at $T_{50} < 900\text{ K}$). Liu et al. [24] also reported the speciation of Ni, As, Pb, Cd, Se, and Sb during underground coal gasification with specific agent injection and pressure. A study by Bradshaw et al. [25] showed that the elements Hg, As, Pb, Sb, Cd, Sn, Se, and Te, and alkali metals remained in fuel gas, and the species of Pb, Sb, and Cd can pass through the path of fuel gas forming surface deposits.

Although the modelling of phase transformation yields beneficial information (e.g., elemental vaporization and condensation, optimized operational conditions) about the distribution of metal(loid) elements, factors including the interactions and interferences among these elements cannot be ignored. In particular, metal(loid)s can interact and/or interfere, leading to the generation of new species, which may induce remarkable influence on the volatilization of metal(loid)s. At present, to the best of the authors' knowledge, there has been no single study towards the assessment of occurred interferences between metal(loid)s during thermochemical processes. In fact, only a study by K. Svoboda [26] investigated the instantaneous interferences of both HF and HCl on H_2S sorption. Also, two studies evaluated the effect of interactions on elemental behaviour during coal combustion. Contreras et al. [27] evaluated the interactions between Cd, As, Sb, and Hg, and pointed out that some species can be dominant under specific conditions. For example, As-Cd interaction forms $\text{Cd}_3(\text{AsO}_4)_2$, which reduces the concentration of gaseous oxides. Yan et al. [28] showed that interactions among Se, Hg, and As lead to the generation of HgSe(g) and AsSe(g) as dominant species under reduced conditions.

In this paper, thermodynamic equilibrium calculations were carried out to explore the possible interactions and interferences between Cu, Cr, and As (CCA-elements) themselves and with Ca, Na, S, Cl, Fe, and Ni in contaminated WW during two reactions of gasification: Boudouard reaction (BR) and partial combustion reaction (PCR). The calculations were performed using MTDATA software (Version 5.10, NPL, London, UK) to predict the phase transformation temperatures and speciation of the considered metal(loid)s. Moreover, contaminated WW samples with complete composition data were selected from the ECN PHYLLIS2 database [29] for the modelling.

2. Thermodynamic Equilibrium Modelling

Thermodynamic equilibrium modellings for Boudouard reaction (BR) and partial combustion reaction (PCR) were carried out using the multiphase module of the MTDA software coupled with the Scientific Group Thermodata Europe (SGTE) database. With each modelling, the calculations were conducted to study the effects of the occurred interactions and interferences on the fate of the

CCA-elements as consequence of different contents of CCA-elements and of Ca, Na, S, Cl, Fe, and Ni in WW samples.

For model simulations, a primary search of the SGTE database was carried out to reveal the relevant species of CCA-elements. A complete list of the adopted species are given in Table 1. The best fit probability distributions of the composition data of the selected WW samples (#2712, #679, #1779, #1364, #871, #1448, #3498, #2901, #2900) [29] are estimated through the @Risk analysis simulation package (Version 6.1, Palisade Corp., Ithaca, NY, USA), and the estimation results are exhibited in Table 2. As an illustrative example, the statistical analysis of the moisture content is demonstrated in Figure 2. The elements to be introduced to the MTDATA were grouped into major elements (Ar, C, N, O, and H) and minor elements (As, Cr, Cu, Co, Cl, Ca, Ni, S, Na, and Fe). Note that the mass ranges of the minor elements, Table 3, were assumed inconsistent with the information provided by the ECN PHYLLIS2 database [29] concerning the contaminated woody biomass.

Table 1. The selected Cu, Cr, and As (CCA-elements) species.

Species	As	Cr	Cu
Gaseous		ClCr, CrHO, CrHO ₂ CrHO ₃ , CrH ₂ O ₂ , CrH ₂ O ₃ , Cl ₄ Cr, Cl ₅ Cr, Cl ₆ Cr, ClCrO,	
	As ₄ O ₁₀ , AsS, As ₄ S ₄ AsH ₂ ,	CrH ₂ O ₄ , CrH ₃ O ₃ , Cl ₄ CrO,	Cl ₅ Cu ₅ , Cu, Cl ₃ Cu ₃ , Cl ₄ Cu ₂ ,
	AsH ₃ , As ₄ O ₈ , As, As ₂ , AsN,	Cr, Cr ₂ , CrH, CrH ₃ O ₄ ,	CuO, CuS, ClCu, Cu ₂ S,
	AsO, AsO ₂ , AsCl ₃ , AsH,	CrH ₄ O ₄ , Cl ₂ Cr, Cl ₃ Cr, CrO ₂ ,	Cu ₂ , CuH, CuHO, Cl ₂ Cu,
	As ₄ O ₆ , As ₄ O ₇ , As ₃ , As ₄ O ₉ .	CrO ₃ , Cr ₂ O, ClCrO ₂ ,	Cl ₂ Cu ₂ , Cl ₄ Cu ₄ .
		Cl ₂ CrO, Cl ₂ CrO ₂ , Cl ₃ CrO,	
		Cr ₂ O ₄ , CrH ₄ O ₅ , CrN, CrO,	
		Cr ₂ O ₂ , Cr ₂ O ₃ , CrS.	
Liquid	AsCl ₃ , As ₄ S ₄ .	-	-
Solid			CuH ₆ O ₇ S, CuH ₁₀ O ₉ S, CuO,
	As, As ₂ Cu ₃ O ₈ , As ₂ Fe ₃ O,	AsCrO ₄ , Cl ₃ Cr, CoCr ₂ O ₄ ,	Cu ₂ O, CuO ₄ S, Cu ₂ O ₄ S,
	As ₂ S ₂ , AsNa ₃ , AsCu ₃ ,	Cr, Cr ₂ O ₁₂ S ₃ , CrS, CaCrO ₃ ,	Cu ₂ O ₅ S, CuS, Cu ₂ S, AsCu ₃ ,
	As ₂ Ca ₃ O ₈ , As ₂ Co ₃ O ₈ ,	CaCr ₂ O ₄ , Cl ₂ Cr, Cr ₂ O ₃ ,	AsCu ₃ O ₄ , As ₂ Cu ₃ O ₈ , CCuN,
	AsNa ₃ O ₄ , AsNi, As ₂ Ni ₅ ,	Cr ₅ O ₁₂ , Cr ₅ O ₂₁ , CrNa ₂ O ₄ ,	CCuO ₃ , CaCu, Ca ₂ CuO ₃ ,
	As ₈ Ni ₁₁ , AsCrO ₄ , As ₂ Cr ₃ O ₈ ,	Cr ₂ Na ₂ O ₄ , As ₂ Cr ₃ O ₈ ,	ClCu, Cl ₂ Cu, Cu, CuFeO ₂ ,
	AsS, AsCu ₃ O ₄ , As ₂ Ni ₃ O ₈ ,	C ₂ Cr ₃ , C ₃ Cr ₇ , C ₆ Cr ₂₃ ,	CuFe ₂ O ₄ , Cu ₂ Fe ₂ O ₄ ,
	As ₂ O ₅ , As ₂ S ₃ , AsFeO ₄ .	C ₆ CrO ₆ , Cr ₂ FeO ₄ , CrN,	CuFeS ₂ , Cu ₅ FeS ₄ , CaCu ₅ ,
		Cr ₂ N, Cr ₂ NiO ₄ , CrO ₂ , CrO ₃ .	Ca ₂ Cu, CaCu ₂ O ₃ ,
			CuH ₂ O ₂ , CuH ₂ O ₅ S.

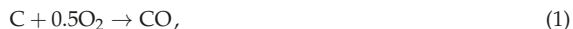
Table 2. Statistical analysis results of the composition data.

Composition	Min	Mean	Max	5%	95%
Moisture content (Ar) (%)	4.68	14.86	33	3.82	27.31
Ash content (Ar) (%)	0.79	12.09	70.41	0.843	48.54
Carbon (C) (Dry) (%)	43.31	46.55	49.8	42.84	50.24
Hydrogen (H) (Dry) (%)	5.26	5.69	5.93	5.26	5.95
Nitrogen (N) (Dry) (%)	0.19	1.06	1.93	0.069	2.04
Oxygen (O) (Dry) (%)	37.13	40.57	55.79	37.3	47.34
Sulphur (S) (Dry) (%)	0.03	0.09	0.18	0.02489	0.176
Chlorine (Cl) (Dry) (mg/kg)	113	556.49	1000	48.19	1077.8
Copper (Cu) (Dry) (mg/kg)	4.8	63.64	385	5.04	286.8
Nickel (Ni) (Dry) (mg/kg)	2.8	15.69	46	2.19	43.99
Arsenic (As) (Dry) (mg/kg)	1.3	5.5	13	1.35	35.45
Cobalt (Co) (Dry) (mg/kg)	0.8	4.88	25	84%	21.92
Chromium (Cr) (Dry) (mg/kg)	21	30.2	37	21.73	36.87
Sodium (Na) (Dry) (mg/kg)	210	703.92	1613	162.0	1645.5
Calcium (Ca) (Dry) (mg/kg)	2200	4061.41	6537	2247.0	8959.29
Iron (Fe) (Dry) (mg/kg)	340.3	655.96	1082	348.16	2037.09

Table 3. Mass ranges of minor elements.

Element	Concentration (mole/h)	Element	Concentration (mole/h)	Element	Concentration (mole/h)
As	0, 0.7, 1.4, 5	Ca	0, 100, 250, 500, 1000	Ni	0, 5, 10, 20
Cu	0, 4, 6, 8	Cl	0, 10, 50, 100	Na	0, 100, 200, 500
Cr	0, 5, 10, 21	Fe	0, 50, 100, 500	S	0, 0.05, 0.1, 0.2

Moreover, the operational conditions and process agents for each reaction are presented in Table 4, in which the required oxygen for PCR and the required carbon dioxide for BR are determined using Equation (1) [30] and Equation (2) [7], respectively, as follows:

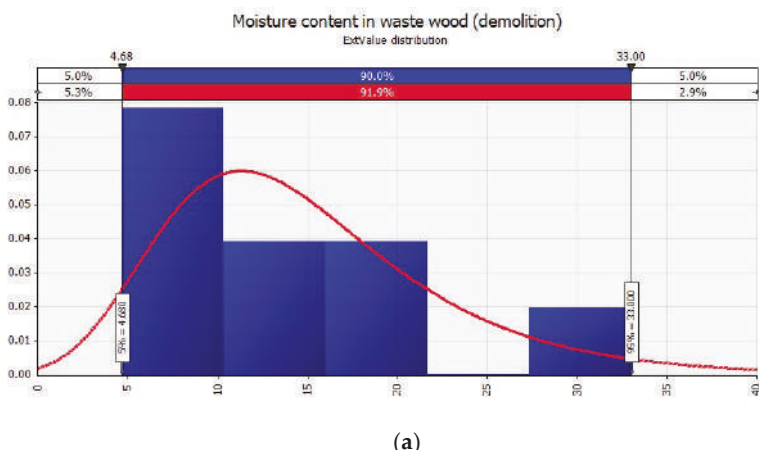


Note that the air composition (under standard dry at atmospheric pressure) consists of 1.28% Ar, 23.2% O₂, 0.046% CO₂, and 75.47% N₂. Biomass feed rates for both reactions were calculated by means of the higher heating value (HHV_d) from Equation (3) [30].

$$\text{HHV}_d = 0.3491\text{C} + 1.1783\text{H} + 0.1005\text{S} - 0.015\text{N} - 0.1034\text{O} - 0.0211\text{Ash}. \quad (3)$$

Table 4. Operational parameters and gasification agents for partial combustion reaction (PCR) and Boudouard reaction (BR).

Parameter	PCR	BR
Temperature range (°C)	0–1800	0–1300
Pressure (atm)	1	1
Equivalence ratio (kg/h)	0.2	0
Biomass rate (m ³ /h)	3.59	3.59
Air rate (m ³ /h)	0.72	-
Steam rate	1.44	-
Steam/Air	2:1	-
CO ₂	-	1.19
CO ₂ /Biomass	-	1:3

**Figure 2. Cont.**

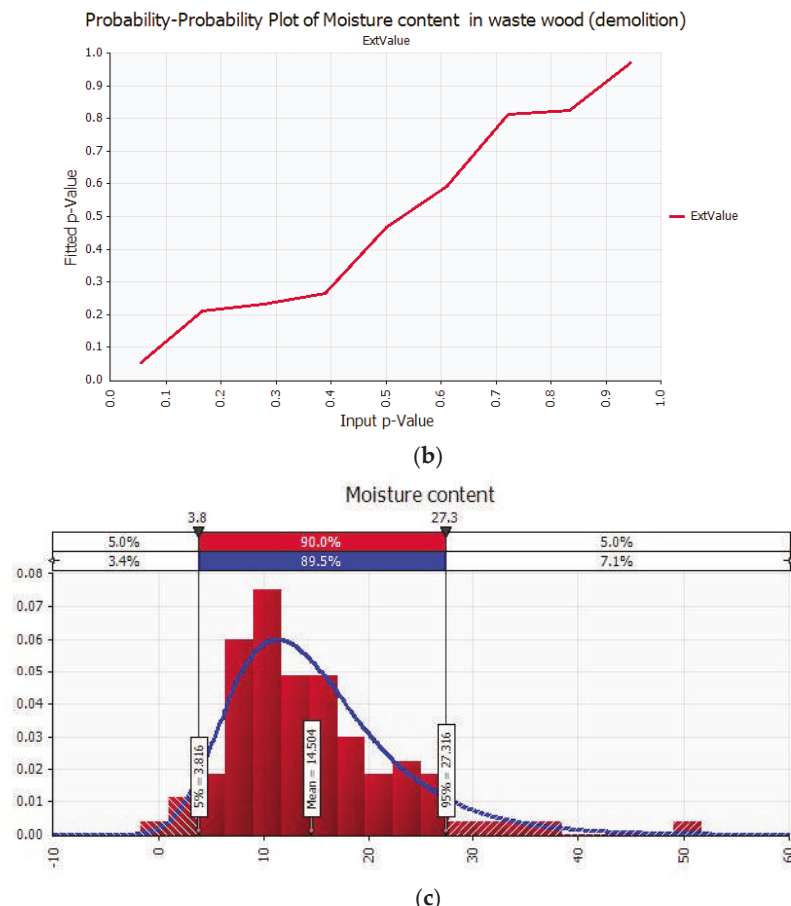


Figure 2. (a) Probability distribution of moisture content; (b) p -value; and (c) interval confidence of probability distribution.

3. Results and Discussion

3.1. Under Partial Combustion Reaction (PCR)

3.1.1. Equilibrium Composition of CCA-Elements

Initially, the modelling of PCR was based on composition data in Table 2 (the mean values) and process parameters of PCR in Table 4 in order to predict the equilibrium partitioning of the CCA-elements. The simulation results show that, at temperatures ≤ 1350 °C, about 100% of Cu remained in solid phase as a dominant species of CaCu resulting from Ca-Cu interaction (Figure 3). When the temperature increases from 1350 to 1800 °C, new gaseous species CuH (0.47–4.49%), Cu₂ (0.02–0.43%), and CuCl (5.5×10^{-3} – 5.544×10^{-1} %) are formed due to Cu-Cl and Cu-H interactions. At temperatures between 1450 and 1600 °C, Cu is proportionally distributed as elemental between gaseous phase (4.29–94.52%) and solid phase (88.84–33.57%).

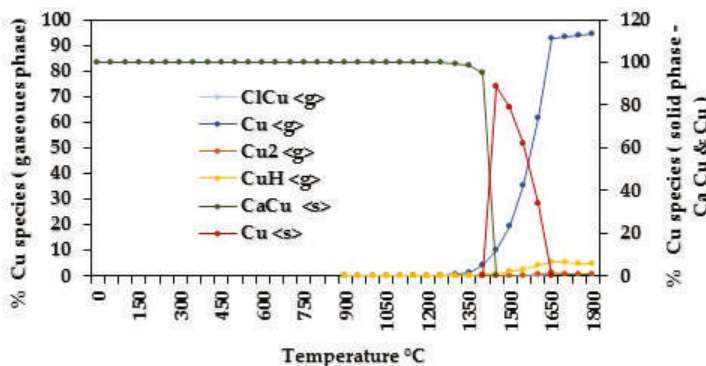


Figure 3. Speciation of copper.

The predicated distribution of Cr is shown in Figure 4. Obviously, at temperatures ≤ 1550 °C, Cr remained in solid phase as C_3Cr_7 (100%), and this was mainly due to C-Cr interaction. Additionally, at temperatures between 1550 and 1800 °C, the mass percentage of C_3Cr_7 decreased from 100% to 67.34%, while at the same time it was released as elemental Cr (3.16–32.48%) and as a new set of gaseous species generated by Cr-Cl, Cr-H, Cr-N, and Cr-O interactions; the total mass percentage of these gaseous species was less than 0.2%.

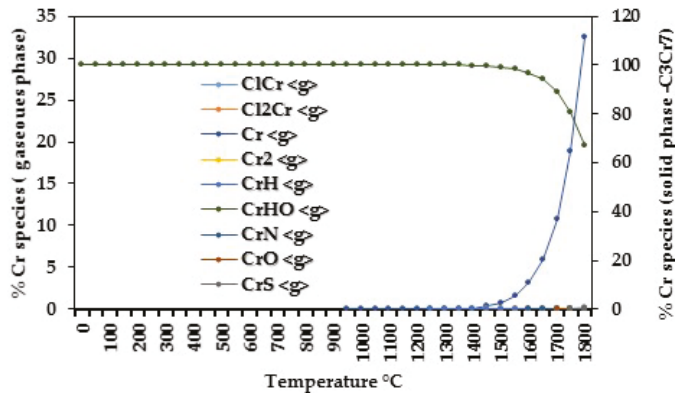


Figure 4. Speciation of chromium.

Figure 5 shows the equilibrium distribution of As. It is clear that at temperatures ≤ 1400 °C, As is predicated as stable solid species AsNa_3 (100%) and As_2Ni_5 (99.99–99.15%) as consequence of As-Na interaction and As-Ni interaction, respectively. As the temperature increases from 1400 to 1800 °C, the mass percentage of As decreases rapidly in solid phase, and it reforms as new gaseous species predominately by interactions. Among them, the dominant ones are As_2 (1.90–46.00%), AsH (0.24–7.13%), and As (5–46.55%). Indeed, AsH is generated by As-H interaction.

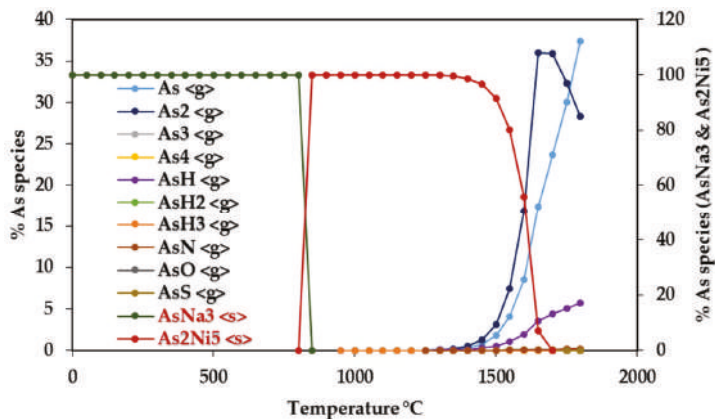


Figure 5. Speciation of arsenic.

To highlight the influence of increased pressure conditions on phase transition temperatures of CCA-elements, the reaction pressure was set to 20 atm and to 40 atm. Not surprisingly, Cr remained completely in condensed phase under both pressures, as shown in Figure 6a. Whereas, under 20 atm, the phase transformation temperatures of Cu and As increased by 300 and 250 °C, respectively, compared to those under 1 atm. Also, under 40 atm, the phase transformation temperatures of Cu and As, respectively, increased by 350 and 300 °C compared to those predicated under 1 atm, as depicted in Figure 6b,c.

3.1.2. Influence of Elemental Contents

Since the elemental content is one of the most important factors that directly affects species formation, different element content in WW samples were simulated to identify the possible interactions and interferences in terms of speciation during PCR, such that the element concentration were introduced to the model as presented in Table 3. Note here that the interactions and interferences that lead to appreciable effects on elemental phase transformation temperature and species formation were ranked as significant.

Influences on CCA-elements

In this case, the concentrations of each CCA-elements were individually changed. The simulation results show that the CCA-elements contents exhibit almost no influence on their phase transformation temperatures, but only concentration shifts are observed as shown in Figure 7a–c. Nevertheless, an exception is that when As concentration is relatively high (5 mole/h), its solid–gaseous transformation temperature decreased by 400 °C because the Ni contained becomes less than the limit to interact with As, and hence captures 100% of the As. Additionally, As₂Ni₅ (solid) and AsN (gaseous) are the dominant species of As.

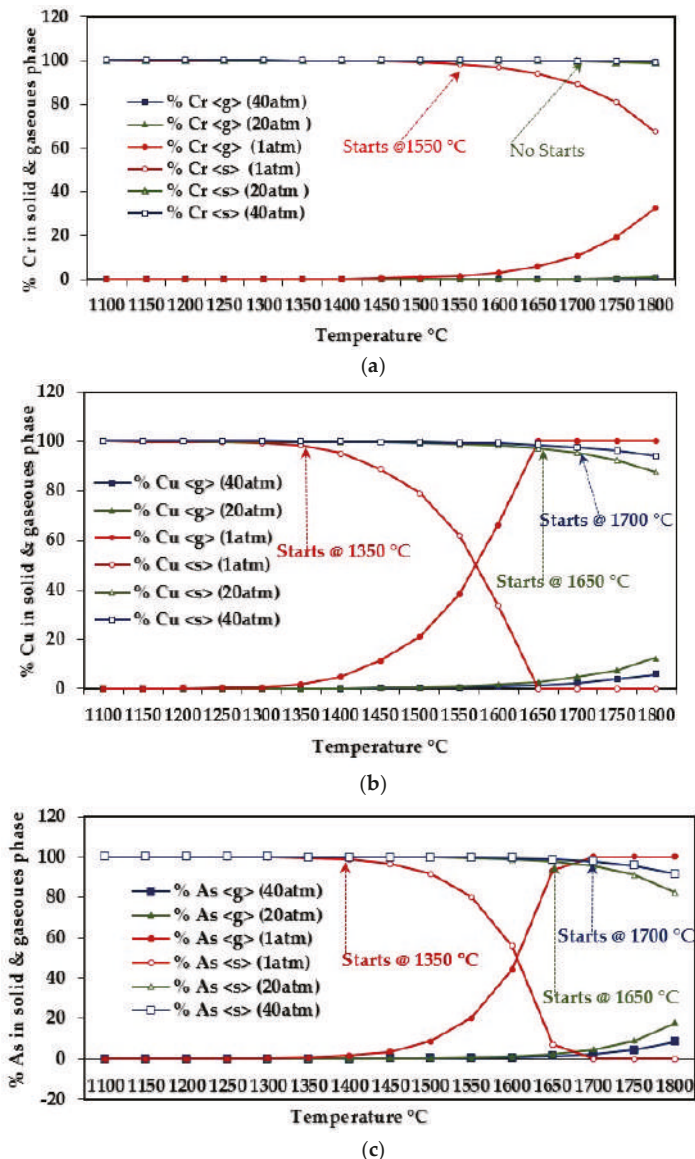


Figure 6. Cu, Cr, and As (CCA-elements) solid/gaseous transitions under 1, 20, and 40 atm: (a) chromium; (b) copper; (c) arsenic.

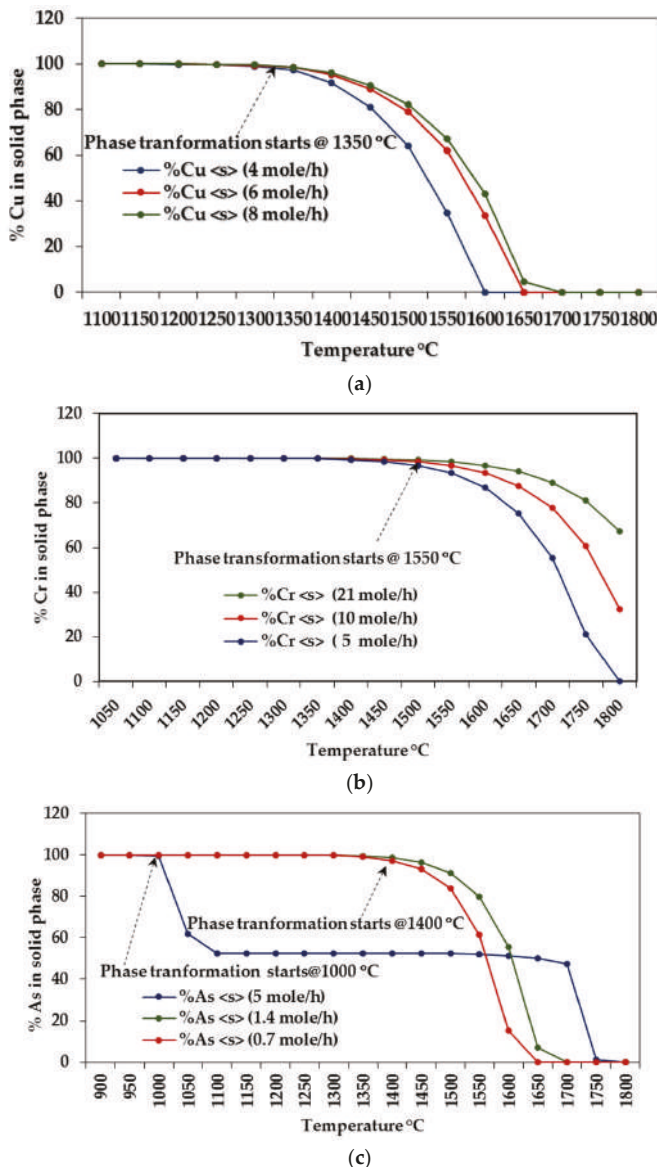


Figure 7. Resulting phase transformations of CCA-elements by changing the concentrations of each element individually: (a) copper; (b) chromium; (c) arsenic.

Influences of Ca, Na, S, Cl, Fe, and Ni on CCA-element

An illustration of the occurred interactions and interferences between CCA-elements and individual presence/absence of each of the elements Ca, Na, S, Cl, Fe and Ni are given in Figure 8. Note that, in all the simulations, the CCA-elements concentrations were kept fixed (as listed in Table 2) while the concentrations of other minor elements were considered as in Table 3.

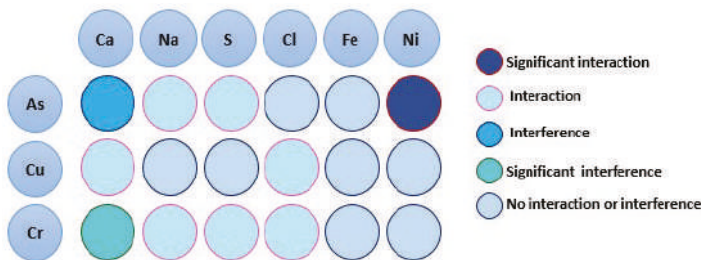


Figure 8. Interactions and interferences between the CCA-elements and each of Ca, Na, S, Cl, Fe, and Ni.

1. Copper

As presented in Figure 8, Cu interacts with Ca and Cl; however, all Cl-Cu interactions release only a single gaseous species—ClCu. The solid and gaseous species formed by Ca-Cu interactions are listed in Table 5. The analysis shows that the dominant species in solid phase are CaCu, CaCu and CaCu₅, and CaCu when Ca is present, respectively at concentrations of 250, 500, and 1000 mole/h. On the other hand, the presence of Ca at low concentrations would not be sufficient to interact with Cu; alternatively, it interacts with O and Cr, forming CaCr₂O₄ and CaO, respectively. Further, it is noted that the volatilization of Cu is not affected by the various concentrations of Ca, which is similar to Cl-Cu interactions.

Table 5. Calcium-copper interactions during PCR.

Ca Concentration (mole/h)	Species	Temperature Range (°C)
100	Cu <s>	0–800
	Cu <s>, Cu <g>, CuH <g>	850–950
	Cu <s>, ClCu <g>, Cu <g>, CuH <g>	1000–1800
250	CaCu <s>	0–800
	Cu <g>, CuH <g>, CaCu <s>	850–1150
	ClCu <g>, Cu <g>, Cu ₂ <g>, CuH <g>, CaCu <s>	1350–1800
500	CaCu <s>, CaCu ₅ <s>	0–800
	Cu, Cu <g>, CuH <g>	850–950
	Cu <g>, CuH <g>, CaCu <s>	1000–1150
	ClCu <g>, Cu <g>, Cu ₂ <g>, CuH <g>, CaCu <s>	1250–1800
1000	CaCu <s>	0–800
	Cu <g>, CuH <g>, CaCu <s>	850–950
	Cu <g>, CuH <g>, CaCu <s>	1000–1150
	ClCu <g>, Cu <g>, Cu ₂ <g>, CuH <g>, CaCu <s>	1250–1800

2. Chromium

The analysis reveals that Ca plays an important role in Cr distribution across the solid and gaseous phases (Figure 9 and Table 6). That is, Na and Cr interact only when the concentration of Ca is ≤ 100 mole/h, leading to the formation of instable solid specie Cr₂Na₂O₄ between 1100 and 1550 °C. CaCr₂O₄ (solid) is the most likely to be generated by Ca-Cr interactions when Ca is present at 100 mole/h, thereby about 100% of Cr remains in solid phase at temperatures ≤ 1550 °C. As the Ca content increases (> 100 mole/h), Ca-Cr interferences and C-Cr interactions take place simultaneously, forming C₂Cr₃ and C₃Cr₇ in solid phase at temperatures up to 1550 °C. A most apparent observation in this case is the concentration shift in gaseous phase of Cr.

Other interactions, specifically, S-Cr and Cl-Cr interactions, exhibit no influence on Cr volatilization and solely yield gaseous species CrS, ClCr and Cl₂Cr, respectively.

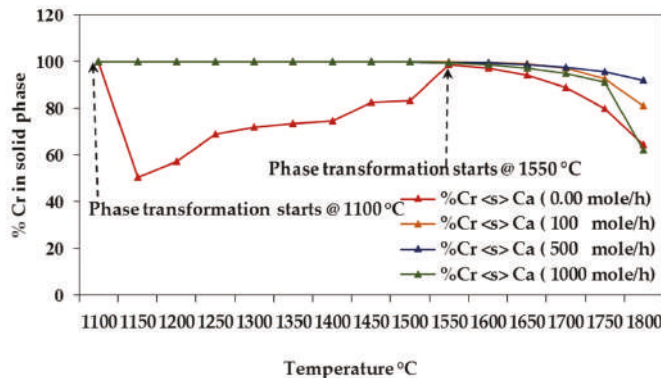


Figure 9. Effects of Ca on Cr phase formation.

Table 6. Chromium-calcium interactions.

Ca Concentration (mole/h)	Species	Temperature Range (°C)
0	Cr ₂ Na ₂ O ₄ <s>	0–300
	C ₂ Cr ₃ <s>, Cr ₂ Na ₂ O ₄ <s>	350–400
	Cr ₂ Na ₂ O ₄ <s>	450–600
	Cr <g>, C ₂ Cr ₃ <s>, Cr ₂ Na ₂ O ₄ <s>	650–1200
	ClCr <g>, Cl ₂ Cr <g>, Cr <g>, CrHO <g>, CrS <g>, C ₂ Cr ₃ <s>, Cr <s>, C ₃ Cr ₇ <s>, C ₆ Cr ₂₃ <s>	1250–1800
100	C ₂ Cr ₃ <s>, CaCr ₂ O ₄ <s>, CrN <s>, Cr ₂ Na ₂ O ₄ <s>	0–300
	C ₂ Cr ₃ <s>, Cr ₂ Na ₂ O ₄ <s>	350–400
	C ₂ Cr ₃ <s>, CaCr ₂ O ₄ <s>	450–600
	ClCr <g>, Cr <g>, C ₂ Cr ₃ <s>, CaCr ₂ O ₄ <s>	650–1200
	ClCr <g>, Cl ₂ Cr <g>, Cr <g>, C ₂ Cr ₃ <s>	1250–1800
250–500	C ₂ Cr ₃ <s>	0–300
	C ₂ Cr ₃ <s>, C ₃ Cr ₇ <s>	350–600
	C ₃ Cr ₇ <s>	650–1200
	C ₂ Cr ₃ <s>, ClCr <g>, Cl ₂ Cr <g>, Cr <g>, CrH <g>, C ₃ Cr ₇ <s>, CrO <g>, CrS <g>, CrN <g>	1250–1800
10000	C ₃ Cr ₇ <s>	0–600
	Cr <g>, C ₃ Cr ₇ <s>	650–1200
	ClCr <g>, Cl ₂ Cr <g>, Cr <g>, CrH <g>, CrO <g>, CrS <g>, CrN <g>, C ₃ Cr ₇ <s>	1250–1800

3. Arsenic

When Ni content is present at various concentrations, all Ni-As interactions generate solid species As₂Ni₅, by which the phase transformation temperature of As (Figure 10) increases to about 450 °C. In contrast, the absence of Ni leads to the formation of As₂ (gaseous) and AsNa₃ (solid) as dominant species, as shown in Figure 11. Similarly, Na-As interactions yield AsNa₃. While the absence of Na shows no influence on the As phase formation; it enhances Ni to capture As, generating As₂Ni₅ (100–99.15%) up to 1400 °C, as illustrated in Figure 12. Also, S tends to interact with As, yielding, at very low mass percentage, gaseous species AsS between 1750 and 1800 °C.

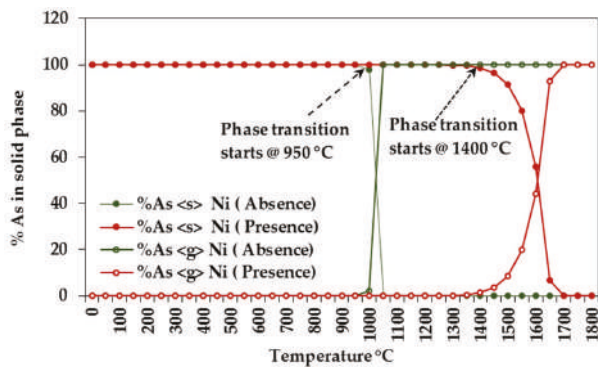


Figure 10. Arsenic distribution according to the presence/absence of Ni.

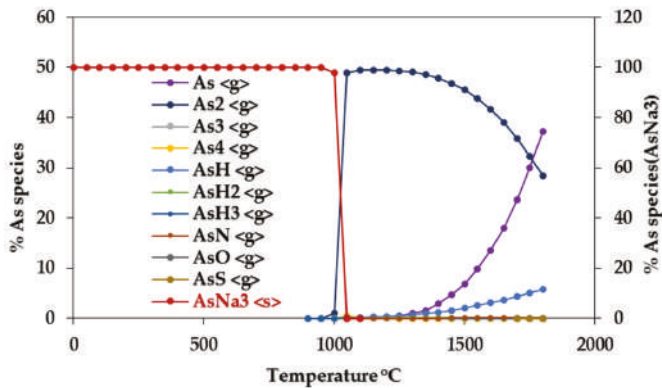


Figure 11. Arsenic speciation in the absence of Ni.

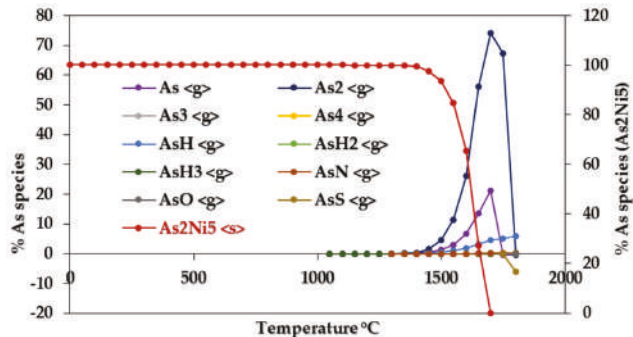


Figure 12. Arsenic speciation in the absence of Na.

Assessing CCA-elements Reactivity

All the minor elements were introduced to the model at the same concentration (0.25 mole/h) to assess the reactivity of the CCA-elements. In this case, the resulted speciation of CCA-elements are demonstrated in Figure 13a–c.

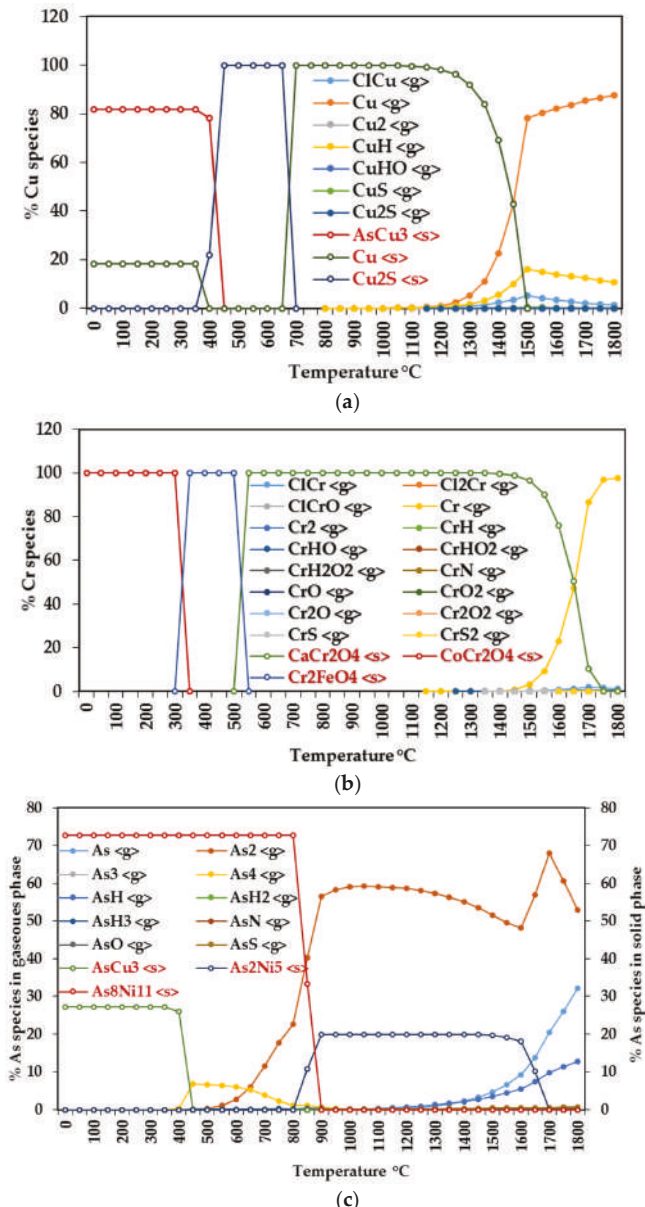


Figure 13. Speciation of CCA-elements when all minor elements are present at the same concentrations: (a) copper; (b) chromium; (c) arsenic.

As can be seen in Figure 13a, the behavior of Cu between 0 and 700 °C indicates that Cu interacts favorably with As and S, forming the solid species AsCu_3 (81.89–78.24%) and Cu_2S (100%), respectively. At temperatures above 700 °C, Cu is redistributed as elemental and a set of gaseous species, and its phase transformation temperature becomes 1200 °C, which is less than about 11% of that obtained with equilibrium composition (Figure 3). The predictive calculations, as shown in

Figure 13b, originate the Cr solid species CoCr_2O_4 (100% between 0–300 °C), Cr_2FeO_4 (100% between 350–500 °C), and CaCr_2O_4 (100% between 550–1450 °C) to the Co-O-Cr, Fe-O-Cr, and Ca-O-Cr interactions, respectively. Figure 13c shows As species formation. Intuitively, AsCu_3 (27.27% between 0–400 °C) and $\text{As}_8\text{Ni}_{11}$ (72.73% between 0–800 °C) are the most probable solid species from Cu-As and Ni-As interactions, respectively.

In this view, the distribution profiles of CCA-elements during gasification offer important trend towards their emissions control. More specifically, the presence of Ni and S enhances As and Cu capture in ash, respectively. Also, Cu and As interactions cause both of them to remain in solid phase, and the elements Ca, Co, and Fe are favored to Cr retention.

3.2. Under Boudouard Reaction (BR)

The modelling of BR was carried out using the composition data and BR process parameters, respectively, as reported in Tables 2 and 4. The simulation scenarios were considered similar to those for the case of PCR. On the whole, the obtained results were similar to those observed with the PCR model, except that at equilibrium partitioning, about 99.99% of the CCA-elements remained in solid phase at temperatures less than 1300 °C; also no gaseous species were formed under pressure conditions of 20 and 40 atm. Table 7 demonstrates the phase and species formation of CCA-elements at equilibrium composition under 1 atm.

Table 7. Phase transformations and speciation of the CCA-elements.

Elements	Solid Phase	Temperature (°C)	Gaseous Phase	Temperature (°C)
Cr	C_3Cr_7	0–1300	Cr	1000–1300
			CrCl	1250–1300
			CrH	1300
Cu	CaCu	0–1300	Cu, CuH	900–1300
			Cu_2, ClCu	1150–1300
As	AsNa_3 As_2Ni_5	0–800 850–1300	$\text{As}, \text{As}_2, \text{AsH}, \text{AsH}_2$	1150–1300
			AsH_3	1150–1300

4. Conclusion

This paper introduces two predictive models for PCR and BR to understand the behavior of CCA-elements in terms of interactions and interferences during the gasification of contaminated WW. The refinement of the predicated results from PCR modelling indicates that most of the occurred Ni-As interactions led to about 100% of As remaining in solid phase at temperatures less than 1400 °C. It also indicates that Ca-Cr interferences form solid specie C_3Cr_7 , but the absence of Ca causes instability in Cr distribution at temperatures from 1100 to 1550 °C. Whereas Co-O-Cr, Fe-O-Cr, and Ca-O-Cr interactions reduced the Cr volatilization as consequence of the generated solid species CoCr_2O_4 , Cr_2FeO_4 , and CaCr_2O_4 , respectively. Most importantly, in both PCR and BR, the presence of Na and or Ni played a vital role for As remaining in solid phase at temperatures ≤ 800 °C. Eventually, these modellings are valuable for mitigating the negative impacts of toxicity emissions associated with CCA-elements; particularly, by systematically blending different types of contaminated WW prior to gasification.

Author Contributions: All authors contributed to this work. S.B.A.: Writing—Original Draft Preparation; S.T.W. and Y.J.: Supervision and Guidance.

Acknowledgments: The authors would like to thank Cranfield University for the facilities provided to carry out this work.

Conflicts of Interest: The authors declare no conflict of interest.

References

- Edo, M.; Björn, E.; Persson, P.E.; Jansson, S. Assessment of chemical and material contamination in waste wood fuels-A case study ranging over nine years. *Waste Manag.* **2016**, *49*, 311–319. [[CrossRef](#)] [[PubMed](#)]
- Brown, M.; Kearley, V. Role of wood waste as source of biomass fuel in the UK. *Energy Mater.* **2009**, *4*, 162–165. [[CrossRef](#)]
- Department for Environment, Food and Rural Affairs. *Wood Waste: A Short Review of Recent Research*; Department for Environment, Food and Rural Affairs: London, UK, 2012.
- Vassilev, S.V.; Baxter, D.; Andersen, L.K.; Vassileva, C.G. An overview of the chemical composition of biomass. *Fuel* **2010**, *89*, 913–933. [[CrossRef](#)]
- Kamińska-Pietrzak, N.; Smoliński, A. Selected Environmental Aspects of Gasification and Co-Gasification of Various Types of Waste. *J. Sustain. Min.* **2013**, *12*, 6–13. [[CrossRef](#)]
- Couto, N.; Rouboa, A.; Silva, V.; Monteiro, E.; Bouziane, K. Influence of the biomass gasification processes on the final composition of syngas. *Energy Procedia* **2013**, *36*, 596–606. [[CrossRef](#)]
- Pandey, A.; Bhaskar, T.; Stöcker, M.; Sukumaran, R. *Recent Advances in ThermoChemical Conversion of Biomass*; Elsevier: New York, NY, USA, 2015.
- Gomez-Barea, A.; Leckner, B. Modeling of biomass gasification in fluidized bed. *Prog. Energy Combust. Sci.* **2010**, *36*, 444–509. [[CrossRef](#)]
- James, R.; Arthur, M.; Yuan, W.; Boyette, M.D. The effect of biomass physical properties on top-lit updraft gasification of woodchips. *Energies* **2016**, *9*, 283. [[CrossRef](#)]
- González-Vázquez, M.P.; García, R.; Pevida, C.; Rubiera, F. Optimization of a bubbling fluidized bed plant for low-temperature gasification of biomass. *Energies* **2017**, *10*, 306. [[CrossRef](#)]
- Tanger, P.; Field, J.L.; Jahn, C.E.; DeFoort, M.W.; Leach, J.E. Biomass for thermochemical conversion: targets and challenges. *Front. Plant Sci.* **2013**, *4*, 218. [[CrossRef](#)] [[PubMed](#)]
- Tripathi, M.; Sahu, J.N.; Ganesan, P. Effect of process parameters on production of biochar from biomass waste through pyrolysis: A review. *Renew. Sustain. Energy Rev.* **2016**, *55*, 467–481. [[CrossRef](#)]
- Vervaeke, P.; Tack, F.M.G.; Navez, F.; Martin, J.; Verloo, M.G.; Lust, N. Fate of heavy metals during fixed bed downdraft gasification of willow wood harvested from contaminated sites. *Biomass Bioenergy* **2006**, *30*, 58–65. [[CrossRef](#)]
- Šyc, M.; Pohořelý, M.; Jeremiáš, M.; Vosecký, M.; Kameníková, P.; Skoblia, S.; Svoboda, K.; Punčochář, M. Behavior of heavy metals in steam fluidized bed gasification of contaminated biomass. *Energy Fuels* **2011**, *25*, 2284–2291. [[CrossRef](#)]
- Tafur-Marinós, J.A.; Ginepro, M.; Pastero, L.; Torazzo, A.; Paschetta, E.; Fabbri, D.; Zelano, V. Comparison of inorganic constituents in bottom and fly residues from pelletised wood pyro-gasification. *Fuel* **2014**, *119*, 157–162. [[CrossRef](#)]
- Zhou, X.; Liu, W.; Zhang, P.; Wu, W. Study on Heavy Metals Conversion Characteristics During Refused Derived Fuel Gasification Process. *Procedia Environ. Sci.* **2016**, *31*, 514–519. [[CrossRef](#)]
- Wu, M.H.; Lin, C.L.; Zeng, W.Y. Effect of waste incineration and gasification processes on heavy metal distribution. *Fuel Process. Technol.* **2014**, *125*, 67–72. [[CrossRef](#)]
- Jiang, Y.; Ameh, A.; Lei, M.; Duan, L.; Longhurst, P. Solid–gaseous phase transformation of elemental contaminants during the gasification of biomass. *Sci. Total Environ.* **2016**, *563–564*, 724–730. [[CrossRef](#)] [[PubMed](#)]
- Froment, K.; Defoort, F.; Bertrand, C.; Seiler, J.M.; Berjonneau, J.; Poirier, J. Thermodynamic equilibrium calculations of the volatilization and condensation of inorganics during wood gasification. *Fuel* **2013**, *107*, 269–281. [[CrossRef](#)]
- Kramb, J.; Konttinen, J.; Backman, R.; Salo, K.; Roberts, M. Elimination of arsenic-containing emissions from gasification of chromated copper arsenate wood. *Fuel* **2016**, *181*, 319–324. [[CrossRef](#)]
- Thompson, D.; Argent, B.B. Prediction of the distribution of trace elements between the product streams of the Prenflo gasifier and comparison with reported data. *Fuel* **2002**, *81*, 555–570. [[CrossRef](#)]
- Kilgallon, P.J.; Simms, N.J.; Oakey, J.E. Fate of trace contaminants from biomass fuels in gasification systems. *Mater. Adv. Power Eng.* **2002**, *21*, 903–912.
- Reed, G.P.; Dugwell, D.R.; Kandiyoti, R. Control of trace elements in a gasifier hot gas filter: A comparison with predictions from a thermodynamic equilibrium model. *Energy Fuels* **2001**, *15*, 1480–1487. [[CrossRef](#)]

24. Liu, S.; Wang, Y.; Yu, L.; Oakey, J. Thermodynamic equilibrium study of trace element transformation during underground coal gasification. *Fuel Process. Technol.* **2006**, *87*, 209–215. [[CrossRef](#)]
25. Bradshaw, A.; Simms, N.J.; Nicholls, J.R. Passage of trace metal contaminants through hot gas paths of gas turbines burning biomass and waste-fuels. *Fuel* **2008**, *87*, 3529–3536. [[CrossRef](#)]
26. Svoboda, K.; Leitner, J.; Havlicka, J.; Hartman, M.; Pohofelý, M.; Brynda, J.; Šyc, M.; Chyou, Y.P.; Chen, P.C. Thermodynamic aspects of gasification derived syngas desulfurization, removal of hydrogen halides and regeneration of spent sorbents based on La₂O₃/La₂O₂CO₃ and cerium oxides. *Fuel* **2017**, *197*, 277–289. [[CrossRef](#)]
27. Contreras, M.L.; Arostegui, J.M.; Armesto, L. Arsenic interactions during co-combustion processes based on thermodynamic equilibrium calculations. *Fuel* **2009**, *88*, 539–546. [[CrossRef](#)]
28. Yan, R.; Gauthier, D.; Flamant, G. Possible interactions between As, Se, and Hg during coal combustion. *Combust. Flame* **2000**, *120*, 49–60. [[CrossRef](#)]
29. Energy Research Centre of the Netherlands. Available online: <https://www.ecn.nl/phyllis2/> (accessed on 20 March 2017).
30. Prabir, B. *Biomass Gasification, Pyrolysis, and Torrefaction Practical Design and Theory*, 2nd ed; Academic Press: Cambridge, MA, USA, 30 July 2013.



© 2018 by the authors. Licensee MDPI, Basel, Switzerland. This article is an open access article distributed under the terms and conditions of the Creative Commons Attribution (CC BY) license (<http://creativecommons.org/licenses/by/4.0/>).

Article

Investigation of the Olive Mill Solid Wastes Pellets Combustion in a Counter-Current Fixed Bed Reactor

Mohamed Ali Mami ¹, Hartmut Mätzing ², Hans-Joachim Gehrmann ², Dieter Stapf ²,
Rainer Bolduan ³ and Marzouk Lajili ^{1,*}

¹ Ionized and Reactive Media Studies Research Unit (EMIR), Preparatory Institute of Engineering Studies of Monastir (IPEIM), University of Monastir, 15 Avenue Ibn El Jazar Monastir 5019, Tunisia;
Mohamedali.Mami@ipeim.rnu.tn

² Institute for Technical Chemistry (ITC), Karlsruhe Institute of Technology (KIT), Hermann-von-Helmholtz-Platz 1, 76344 Eggenstein-Leopoldshafen, Germany;

hartmut.maetzing@kit.edu (H.M.); hans-joachim.gehrmann@kit.edu (H.-J.G.); dieter.stapf@kit.edu (D.S.)

³ European Institute for Energy Research (EIFER), Karlsruhe Institute of Technology (KIT), Emmy-Noether-Str. 11, 76131 Karlsruhe, Germany; Rainer.Bolduan@eifer.uni-karlsruhe.de

* Corresponding: marzouk.lajili@ipeim.rnu.tn; Tel.: +216-73500277 or +216-97369126

Received: 28 June 2018; Accepted: 23 July 2018; Published: 28 July 2018

Abstract: Combustion tests and gaseous emissions of olive mill solid wastes pellets (olive pomace (OP), and olive pits (OP_i)) were carried out in an updraft counter-current fixed bed reactor. Along the combustion chamber axis and under a constant primary air flow rate, the bed temperatures and the mass loss rate were measured as functions of time. Moreover, the gas mixture components such as O₂, organic carbon (C_{org}), CO, CO₂, H₂O, H₂, SO₂, and NO_x (NO + NO₂) were analyzed and measured. The reaction front positions were determined as well as the ignition rate and the reaction front velocity. We have found that the exhaust gases are emitted in acceptable concentrations compared to the combustion of standard wood pellets reported in the literature (EN 303-5). It is shown that the bed temperature increased from the ambient value to a maximum value ranging from 750 to 1000 °C as previously reported in the literature. The results demonstrate the promise of using olive mill solid waste pellets as an alternative biofuel for heat and/or electricity production.

Keywords: olive mill solid wastes (OMSWs); fixed bed combustor; pellets; combustion parameters; gaseous emissions

1. Introduction

Agro-industrial by-products are viable alternatives to fossil fuels to reduce greenhouse gases emissions such as CO₂ and NO_x [1–3]. Among these by-products, olive mill solid wastes (OMSWs) are generated in large quantities in the leading producers in the olive oil industry, including Spain, Italy, Greece, and Tunisia. However, these by-products can present serious environmental problems affecting soil, air, and water when stockpiled and left untreated. However, these lignocellulosic biomasses can be considered as a promising source of renewable energy [4,5]. Indeed, these residues can be separated as olive pomace (OP) and olive pits (OP_i). Olive pits (OP_i) are a major bio-fuel in Spain [6], which is used in combustion processes to produce heat [7] owing to its low moisture content, high heating value, uniform size, and relatively high bulk density [8]. Using this material as a biofuel can be considered as an economically viable alternative to fossil fuels [9]. Despite this potential, only a few studies have been dedicated to characterizing this biofuel for the purpose of energy conversion [5]. Nevertheless, the value of the utilization of olive pomace as a biofuel is widely recognized [10,11]. Moreover, both OP and OP_i can be processed into cylindrical pellets (up to 40 mm length, at standard diameter from 6 to 10 mm, typically 6 mm). This process increases the energy density of these pellets [12,13].

Although the pelletization is a very complicated technique, with the potential for technical problems to arise, we concluded that when using the olive mill solid wastes with moisture content in the vicinity of 15%, and at the optimal conditions of frequency and temperature as we mention below, no problems will be encountered. The reason for this is that the lignocellulosic biomass contains its own binder (abrasive matter). However, it should be mentioned that in the case of this study, pelletization was successful without any additive binder and with the appropriate individual die. The samples of about 1 mm in size needed neither milling nor moisture adjustment and could directly be pelletized after homogenization.

The combustion behavior of pellets, either mixed with other residues or only derived from the OMSWs, has been studied in small powered pellets boilers (<50 kW). These investigations have shown that olive solid residue pellets are ecologically beneficial and are an environmentally friendly energy source for producing heat and/or electricity [14–16]. Nevertheless, the combustion of such biofuels in fixed/fluidized beds is rarely reported in the literature. Moreover, these high calorific pellets have not been commonly used in large-scale combustion systems. Indeed, except for the high quality woody pellets like DIN-plus which is commercialized in European markets, pellets like those considered in our work have not yet been investigated which may be because of the additional cost of transport and pelletization. For this reason, countries like Spain and Italy are still using raw olive mill by-products which have been dried and exhausted without pelletization. However, the pelletization has proven to be very suitable for heat production (domestic use for household boilers and stoves) [14,15]. Due to the higher ash volume ($\approx 5\%$) of olive residues in comparison with woody biomass for DIN plus (<1%) filtering/ash management/burner suitability, as well as standardized industrial pellet requirement, must be considered for large-scale application. Further, their combustion produces more emissions than high quality woody pellets.

González et al. [14] have studied the combustion of different pellets made from olive stones (OP_i), tomato residues, and cardoon, respectively, in a mural boiler used for domestic heating (11.6 kW). The results were compared with forest wood pellets which are recommended as standard fuels. The authors showed that when using OP_i pellets, characterized by lower percentages of sulfur and nitrogen contents, they obtained a significant decrease in NO_x and SO_2 emissions. These biofuels represented the most favorable and attractive fuels from an environmental point of view by comparison to the tomato, cardoon, and forest wood pellets.

In the same context, Miranda et al. [17] conducted combustion tests on OMSWs (OP_i and OP) in their raw state (not pelletized). They used a prototype furnace to analyze the main combustion emissions: CO , CO_2 , NO_x , N_2O , SO_2 , and O_2 . The tests resulted in a good combustion efficiency with relatively low emissions.

Several groups are currently focusing on the modeling of the combustion of pellets in reactors such as pilot fixed bed/fluidized bed, before expanding these studies to large scales (industrial plants) [18]. The choice of the fixed bed reactor for our study is based on its relative simplicity, which will be easier to eventually model. At the same time, our study allows the determination of the independent characteristic numbers needed to scale our results to an industrial scale [19–21].

To the best of our knowledge, the combustion of olive solid residues, such as OP and OP_i , in a counter-current fixed bed reactor has not been reported in the literature. In this study, the combustion pellets tests were carried out in the 40 kW fixed bed reactor “KLEAA” at Karlsruhe Institute of Technology (KIT) (Germany) [22,23]. To determine the combustion characteristics of these samples, the axial temperature evolution was measured. This permits the determination of the reaction front positions in terms of time during the combustion process. In addition, the mass loss is continuously measured during the test. Further, gaseous emission such as CO , CO_2 , H_2 , H_2O , O_2 , and organic carbon (C_{org}) were analyzed and measured as well as other pollutants: SO_2 and NO_x ($NO + NO_2$). Consequently, some scale independent characteristic numbers such as the reaction front velocity u_{RF} , the ignition rate (IR), the mass conversion rate (MCR) and the specific heat release rate (HR) were derived. These specific numbers can serve to quantify and to assess the combustion quality.

All obtained results are compared to those of similar studies in literature and to standard wood pellets (EN-303-5).

2. Materials and Methods

2.1. Samples Preparation

Olive pomace (OP) and olive pits (OP_i) used in this study were obtained from the Zouila Oil Press Company located in the Sahel region of Tunisia (Mahdia-Tunisia). About 6 kg of pellets were prepared from the biofuels at EIFER (European Institute for Energy Research, Karlsruhe, Germany): 100% OP with a die compaction rate of 1:5 (conical pressing) and 100% OP_i with a compaction rate of 1:4 at 24 mm press channel length for both. The pellet press used is a Kahl lab scale flat matrix press 14–175 (with a maximum olive pellet production in the range 15–20 kg/h). The specific optimum rotation frequency was determined to be 85 Hz, and the optimum temperature for stable pellets in literature was 75 °C. The produced pellets were in compliance with the German and European standards (EN 303-5, EN 17225-6). After pelletization and air-cooling, the pellets were stored for minimum 24 h under room conditions to equalize any moisture differences as shown in Table 1.

Table 1. Operating pelletization condition.

Pelletizer Performance	100% Olive Pomace (OP)	100% Olive Pits (OP _i)
Pelletizing temperature (°C)	60	51
Biomass moisture (% w.b.)	14.7 ± 0.5	15.3 ± 0.3
Pellet moisture (% w.b.)	12.4 ± 0.4	13.7 ± 0.2

(% w.b. is the percentage on wet basis).

Table 1 indicates that the moisture content decreases after pelletization. This decrease is due to the evaporation associated with the rising temperature during the pelletization process. Finally, the obtained products were moisture-balanced cylindrical pellets of 6 mm diameter and 20–30 mm in length. As it is notable, the two OMSWs were pelletized under two different temperatures 60 and 51 °C for OP and OP_i, respectively. Indeed, because of its oil content and lubricity, pelletizing of olive pomace caused higher resistance (see compaction rate), and the higher friction, subsequently, raised the temperature to evaporate more water than during olive pits pelletizing. Hence, final moisture contents should be different because pelletization started with different initial moistures under different temperatures and calculations were done on wet basis. It can be observed that the difference between final moisture content on wet basis does not exceed 1.3%. Thereby, even though the moisture directly affects the low heating value (LHV), the difference between the two fuel types will be small.

2.2. Samples Characterizations

2.2.1. Raw Samples Characterizations

Ultimate and proximate analysis of the raw samples as olive pomace (OP), olive pits (OP_i) and sawdust (S) are summarized in Table 2.

Tables 2 and 3 show the ultimate and proximate analyses and the energy characteristics of the used raw materials. These characteristics are compared with those found in the literature for different agro-industrial wastes. All analyses were carried out at the Chemical and Microbiological Institute UEG GmbH (Germany). Ultimate, proximate and energy contents were realized according to the standards analytical methods for solid fuels. High heating value (HHV) is measured using a calorimetric bomb, and the LHV is then calculated using:

$$LHV = HHV - L_v \left(\frac{9\% H + \% M}{100} \right) \quad (1)$$

where, LHV is the low heating value, HHV is the high heating value, % H is the hydrogen content and % M is the moisture content.

The energy density (ED) is obtained when multiplying the bulk density ρ_{BD} by the LHV :

$$ED = \rho_{BD} \times LHV \quad (2)$$

where, ED is the energy density and ρ_{BD} is the bulk density.

Table 2. Raw materials characteristics.

Samples	Equivalent Formula d.b.a.f. ^a	Ultimate Analysis (% d.b.)			Proximate Analysis (% d.b.)			
		% C	% H	% O	% N	% S	% ash	% FC
Olive pomace (OP)	CH _{1.54} O _{0.56} N _{0.024}	52.2 ± 0.8	6.70 ± 0.3	39.6 ± 0.6	1.50 ± 0.1	0.08 ± 0.01	5.10 ± 0.10	18.90 * ± 0.3
Olive pits (OP _i)	CH _{1.97} O _{0.92} N _{0.018}	41.4 ± 0.4	5.20 ± 0.2	52.5 ± 0.9	0.91 ± 0.1	<0.2	0.80 ± 0.1	15.20 * ± 0.2
Sawdust (S)	CH _{1.49} O _{0.6} N _{0.035}	51.5 ± 0.5	6.40 ± 0.3	41.9 ± 0.5	0.20 ± 0.1	<0.1	0.5 ± 0.1	24.50 * ± 0.10
Spruce wood [24,25]	CH _{1.41} O _{0.59} N _{0.0033}	51.9	6.10	40.9	0.30	0.30	1.70	18.10
Wood [26,27]	CH _{1.46} O _{0.6} N _{0.016}	51.6	6.3 ^b	41.5	0.10	0.10 ^b	1.0	17.0
Palm Kernels [3,27]	CH _{1.52} O _{0.58} N _{0.038}	51.0	6.50	39.5	2.30	0.27	5.20	17.50
OP (Turkish) [28]	CH _{1.36} O _{0.53} N _{0.021}	51.3	5.85	36.9	1.27	0.08	4.51	17.90
OP (Italy) [29]	CH _{1.57} O _{0.91} N _{0.034}	44.2	5.80	48.2	1.80	-	5.40	29.60
OP _i (Spain) [17]	CH _{1.71} O _{0.57} N _{0.0009}	52.2	7.48	40.0	0.06	<0.1	0.56	18.50
OP _i (Spain) [30]	CH _{1.6} O _{0.82} N _{0.0019}	44.8	6.0	49.1	0.10	0.01	1.40	13.80
								74.40

% d.b. is the percentage on dry basis; * Calculated by difference: % O = 100 – (% H + % C + % N), % FC = 100 – (%

ash + % VM), ^a dry basis ash free, ^b Average value, ^c Not determined.

Table 3. Energy contents in the raw materials.

Samples	LHV (MJ/kg)	ρ_{BD} (kg/m ³)	ED (GJ/m ³)
Olive pomace (OP)	17.90 ± 0.40	539 ± 10	9.60 ± 0.50
Olive pits (OP _i)	17.29 ± 0.20	764 ± 12	13.20 ± 0.36
Sawdust (S)	16.30 ± 0.10	103 ± 3	1.60 ± 0.06
Spruce wood [24,25]	18.10	105	1.90
Palm Kernels [26,27]	17.00	500	8.50
OC (Turkish) [31]	19.60	591	11.58
OC (Jordan) [32]	23.056	558	12.86
OP _i (Spain) [8]	14.70 **	651.90 **	9.85
Oke (Greece) [33]	19.36	573	11.09
Rice Husks [34]	14.90	200	2.820

OC: Olive cake, Oke: Olive kernels, ** As received.

Furthermore, Table 2 shows high Nitrogen contents for OP and OP_i in comparison with the sawdust (0.2%) and wood (0.1%). This fact will explain why nitrogen oxide emissions were relatively high.

As can be seen from Table 2, the ash content in the two samples (OP and OP_i) is high (3% and 4.7%) compared with 0.5% value for sawdust. For the two samples, the Energy density is higher than many biomass types in Table 3. Hence, the pelletization process is a compulsory process to increase the energy density of pellets and to make their transport and storage easier, ensuring a high hardness and long durability [35,36].

2.2.2. Pellets Samples Characterizations

Two pellets samples types were prepared: 100% olive pomace (OP) and 100% olive pits (OP_i). It needs to be clarified that the number of pellets used depends on the nature of characterization test we realize. For example, in the case of measuring the average length, diameter, and unit density (mass of the pellet divided by its volume) at least a 100 pellets are required to decrease the error according to the central limit theorem ($\varepsilon \sim \frac{1}{\sqrt{N}}$), where ε is the error and N is the number of samples. For the bulk density determination, the volume of the container (100 cm³ in our case) ensured a large number of pellets was achieved. For the moisture content determination, the volume of the stove allowed a maximum of 10 crucibles containing one 1 pellet each to be used. The same process was undertaken when determining the ash content with a muffle furnace. However, for measuring the HHV via a calorimetric bomb, we used about 1 g of pellet and we repeated the test 5 times to attain the average

value (this test is delicate and costly). In addition, during the pyrolysis tests to determine the volatile matter in a thermogravimetric balance, tests were repeated 3 times because this test type is time and cost intensive. Nevertheless, it was found that relative uncertainties were smaller than 5% of the mean value.

The main chemical characteristics of the produced pellets based on ultimate and proximate analysis are summarized in Table 4. These analyses are compared to the standard wood pellets and to other pellets presented in the literature. We observe that our prepared pellets show typical compositions when compared to other biomasses available in the literature [16,17,37].

The ash content was determined using a muffle furnace for which the temperature was fixed at 815 °C. The resulting values were lower than those fixed by the European normalization (<5%). In addition, the nitrogen content was 1.26% for OP and 0.61% for OP_i, respectively. These values were relatively higher than 0.11% obtained for wood pellets. The sulphur content was <0.1% for both samples. Therefore, SO_x emissions are expected to be insignificant.

Table 4. Pellets characteristics.

Samples	Equivalent Formula d.b.a.f.	Ultimate Analysis (% d.b.)					Proximate Analysis (% d.b.)		
		% C	% H	% O	% N	% S	% ash	% FC	% VM
100% OP	CH _{1.3} O _{0.57} N _{0.021}	49.50 ± 0.50	5.4 ± 0.5	43.70 * ± 1.80	1.3 ± 0.6	<0.10	2.90 ± 0.10	17.70 * ± 0.10	79.40 ± 0.20
100% OP _i	CH _{1.65} O _{0.74} N _{0.011}	46.50 ± 0.80	6.3 ± 0.1	46.60 * ± 0.90	0.5 ± 0.1	<0.10	1.90 ± 0.10	15.70 * ± 0.20	82.40 ± 1.00
wood pellets	CH _{1.4} O _{0.63} N _{0.002}	46.30 ± 0.20	5.4 ± 0.2	48.19 * ± 1.00	0.11	<0.10	0.30 ± 0.02	24.30 ± 0.90	75.40 ± 0.70
OP (Spain) [16]	CH _{1.52} O _{0.49} N _{0.032}	54.75	6.17	37.00	1.98	<0.10	5.55	17.28	77.17
OP (Spain) [17]	CH _{1.65} O _{0.47} N _{0.007}	58.20	6.00	35.40	0.40	0	2.50	17.69	79.81

* Calculated by difference.

In Table 5 the LHV values range between 17.45 and 20.36 MJ/kg. The energy density values of our samples were reasonably good (14.42 GJ/m³ for OP_i and 15.59 GJ/m³ for OP). However, the effect of pelletization was much more notable with OP than with OP_i. This is because of the difference in the bulk density between the two raw materials attributable to the better compressibility of the pomace (along with higher pressing energy needs) compared to the pits. On the other hand, the durability (Du), which is determined as a function of the percentage of fine particles leaving the pellets after appropriate mechanical tests, showed acceptable percentages with high regression factor (R² = 0.985) [38]. Indeed, after pelletization the pellets can be stored for longer before its use. During this period fine particles can leave the pellets so that the mass and, thereby, the energy of the fuel decreases. By using a centrifugation system based in a gyratory motor under standard normalizations (ISO 17831-1), the mechanical durability can be determined by weighing the mass before starting the experiment and subsequently. Thereafter, a percentage of material which is remaining in the fuel can be calculated: This is the so-called durability. The durability provides a reasonable assessment in regard to the transport and storage of a given solid biofuel [39]. Values of durability for both prepared samples (OP and OP_i) were in the same range of standard wood pellets. In addition, obtained durability (88–89%) for the peanut hull pellets agreed with our results [38].

Table 5. Energy contents in the pellets samples.

Samples	LHV (MJ/kg)	ρ_{BD} (kg/m ³)	ED (GJ/m ³)	Du (% w.b.)
OP pellets	19.02 ± 0.40	820 ± 15	15.59 ± 0.62	88 ± 2
OP _i pellets	18.38 ± 0.10	785 ± 10	14.42 ± 0.25	85 ± 2
wood pellets	17.45 ± 0.30	660 ± 8	11.51 ± 0.33	89 ± 2
OP (Spain) [16]	20.36	780	15.80	-
OP (Tunisia) [37]	19.23	920	17.69	-

3. Combustion Test

The experimental studies were carried out in a batch fixed bed reactor (KLEAA) characterized by a nominal power of 40 kW. This device is located at the Institute for Technical Chemistry (ITC) at the Karlsruhe Institute of Technology (KIT) in Germany.

The counter-current fixed bed reactor KLEAA has three main components: The combustion chamber composed by a fixed bed and a heated furnace, the post (or secondary) combustion chamber, and the flue gas cleaning system, which is equipped with a heat exchanger, a bag filter, and a carbon absorber.

The facility is suited to perform limited tests of solid fuel samples (about 3 kg for each test). The fuel bed has a total volume of 10 L. The furnace, and the secondary combustion chamber can be heated electrically up to a temperature of 1100 °C. The major components of the installation are represented schematically in Figure 1. A more detailed description of the facility is available elsewhere [21–23].

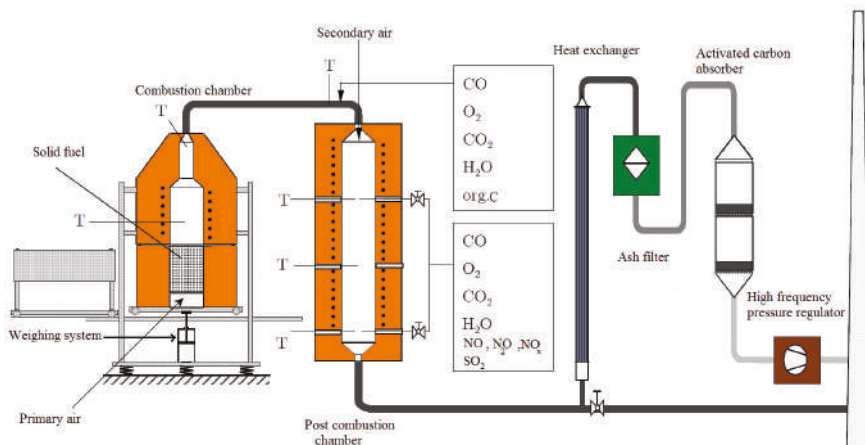


Figure 1. Sketch of the counter-current fixed bed reactor (KLEAA) facility at ITC, Karlsruhe, Germany.

The fixed bed has a height, h , of 250 mm and a diameter, d , of 230 mm. It is equipped with thirteen K-type thermocouples which are arranged in 20 mm intervals along the chamber's axis to measure the central bed temperature as it is shown in Figure 2.

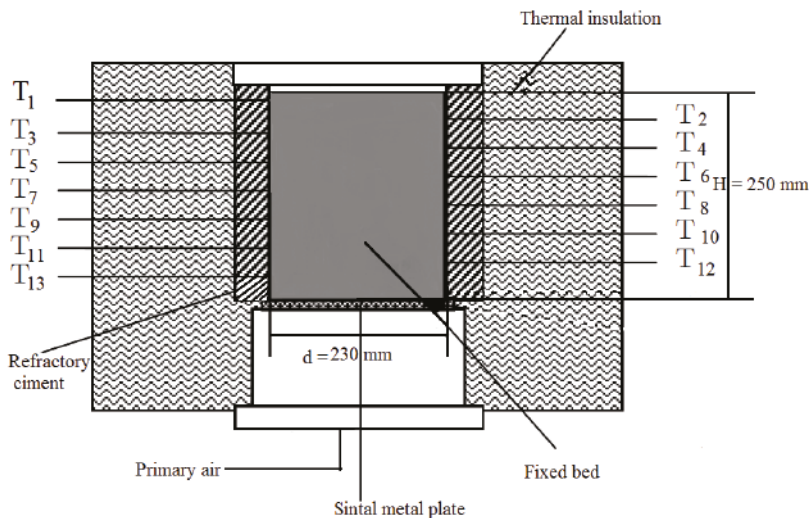


Figure 2. The fixed bed reactor and the thermocouples disposition.

Two experimental tests were performed with the biofuel pellets:

- 3.5 kg of 100% olive pomace (OP).
- 3.75 kg of 100% olive pits (OP_i).

The pellet samples were introduced into the combustion chamber. Then, the pellet samples were moved to the hot furnace, so that the fixed bed will be heated by radiation from the hot furnace wall (900°C). The primary air was supplied at the bottom of the fixed bed via a sintered metal plate. The flow rate of the primary air was fixed at $10 \text{ Nm}^3/\text{h}$. The temperatures of the primary and the secondary air ($25 \text{ Nm}^3/\text{h}$) were about 25°C . Gaseous emissions were analyzed based on physical phenomena. Respectively CO, CO₂, and H₂O were analyzed by infrared techniques, C_{org} by flame ionization detector, O₂ by a paramagnetic system, and H₂ by heat conductivity. Trace gases, such as NO, NO_x, N₂O, and SO₂ were followed and also measured at the outlet of the post-combustion chamber. Thus, CO₂, CO, H₂O, and SO₂ were measured at the outlet of the post-combustion chamber. A heat exchanger has served for the heating of the water recovery system. After the combustion, the fly ash was emitted and collected in a special box under the grate via an ash filter. A pressure regulator ensured a pressure drop across the plant of about 50 Pa.

As stated earlier, there are limited studies on the types of biofuels in this study. Therefore, our results are compared to the results of some previous experiments conducted with conventional wood pellets under almost similar conditions [21–23,40,41].

4. Results and Discussion

4.1. Temperature Evolution in the Fuel Bed

Figure 3 shows the evolution of the bed temperature as a function of time at various bed heights from the bottom during the combustion process of olive pomace (OP), olive pits (OP_i), and the standard wood pellets. The thermocouple-based temperature measurements were collected at time intervals of 5 s.

Starting from the bed top to the bottom, the temperature profiles of the pellets samples show three distinct stages: (1) the ignition delay time, (2) the main combustion phase, and (3) the final char combustion.

During the ignition delay time, the bed surface is heated slowly. Hence, it dries and ignites by the radiation heat coming from the hot furnace wall. Then the ignition front propagates from the top of the bed downwards opposite to the gas flow [42]. The ignition delay time was measured by thermocouples T₂ and/or T₃ (blue and pink). It was determined to be equal to 3.5 min, 3.2 min, and 5.1 min, respectively (Figures 3 and 4).

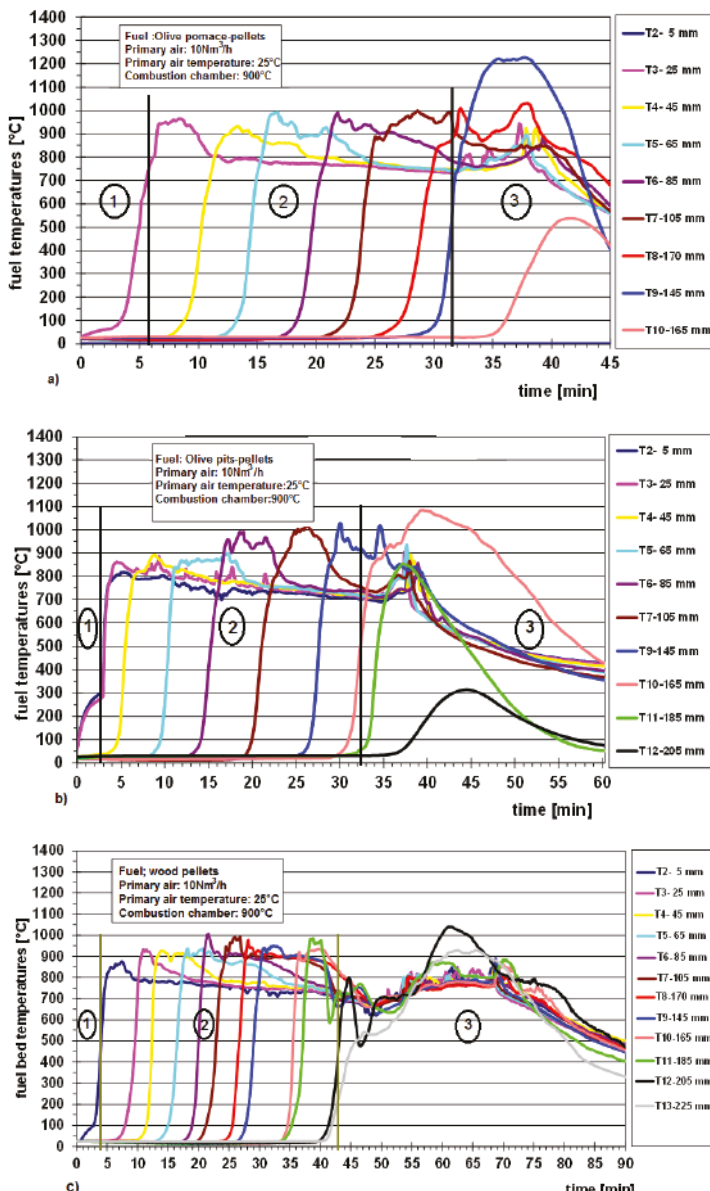


Figure 3. Thermocouples' readings during the passage of the flame front. (a) 100% olive pomace (OP); (b) 100% olive pits; (c) standard biofuel wood pellets.

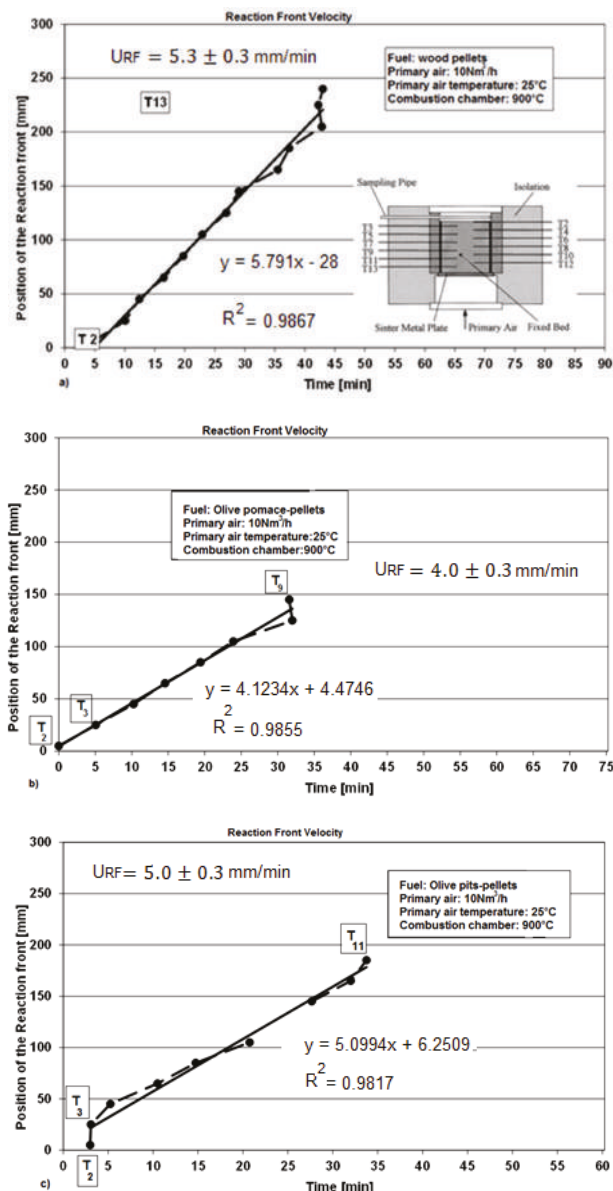


Figure 4. Reaction front positions derived from experimental pellets tests: (a) standard wood pellets; (b) 100% olive pomace (OP); (c) 100% olive pits (OP_i). Experimental conditions: Primary air 10 Nm³/h; primary air temperature 25 °C and combustion chamber temperature 900 °C.

Thereafter, the main combustion phase starts when the flame front reaches and passes the thermocouples successively, and the temperature increases rapidly from ambient to almost 1000 °C. We observed that the temperatures rise from the initial values (25–30 °C) to reach about 880 °C for wood pellets, 800–875 °C for OP_i, and approximately 975 °C for OP. The observed overshoots of temperature can be explained by the highly exothermic combustion of a small amount of carbon

(coke). The arrival time and the position of the reaction front are derived from the inflection point of the temperature curves. After the passage of the reaction front, the thermocouples recorded the temperature of the hot combustion gas.

For the time interval between 30 min and 45 min (Figures 3 and 4), the reaction front reaches the bottom of the bed, and the fuel bed temperature rises again due to the heat generated by the residual char oxidation with air (T_9 , T_{10} , T_{12} , and T_{13}). In this stage, some of the thermocouples may have lower temperatures than others. This resulted in a faster convective cooling [43]. A second difference appears in the maximum value of the temperature, especially during the residual carbon combustion. The OP generated a higher flame front temperature reaching 1200 °C by comparison with 1090 °C and 1050 °C for the OP_i and the wood pellets, respectively. The high temperature observed in the case of olive pomace pellets can be attributed to its high heating value (22.03 MJ/kg on a dry basis). Indeed, this characteristic is strongly related to the carbon content in this sample type (49.5%) [37,44], by comparison with the 46.5% carbon content and 19.4 MJ/kg (HHV on a dry basis) for OP_i [14], and also to the 46.3% carbon content and 18.5 MJ/kg (on a dry basis) for the wood pellets [45].

During the main combustion phase characterized by the combustion of the pyrolysis gases, no effect on heat release is observed. Thus, the temperatures profiles are quite similar for the different biofuel pellets. However, during the burning of char, the heat release (HR) appears quite different due to different amounts of residual carbon (Table 6). Consequently, the maximum of temperature differs significantly for each sample.

4.2. Mass Loss History in the Fuel Bed and Reaction Front Velocity

Further analysis of experimental results leads to the determination of some combustion parameters, such as:

The reaction front velocity:

$$u_{RF} = \frac{dh}{dt} \quad (3)$$

where u_{RF} is the reaction front velocity, h is the bed height, and dt is the time increment.

The mass conversion rate:

$$MCR = \frac{\dot{m}}{A(1 - Y_{ash})} \quad (4)$$

where MCR is the mass conversion rate, \dot{m} is the mass loss rate, A is the fuel bed cross section, and Y_{ash} is the ash mass fraction.

The ignition rate:

$$IR = u_{RF} \times \rho_{BD} \quad (5)$$

IR is the ignition rate, and other variables are defined in the above equations.

The specific heat release rate:

$$HR = MCR \times HHV \quad (6)$$

where HR is the heat release, and the two other variables are defined in the above equations.

These characteristic numbers are useful to predict and understand quantitatively the combustion process in the fixed bed. Moreover, these parameters are independent and good indicators of the combustion behavior in large industrial facilities. They are determined in similar ways as described in the literature [22,23,46–48].

4.2.1. Reaction Front Velocity

The position of the reaction front is obtained based on the inflection point in the temperature profiles shown above. In Figure 4a–c, the reaction front position is plotted as a function of the elapsed time, and almost linear curves are obtained. This result indicates a steady and uniform propagation of the flame front. For both samples (OP and OP_i), the reaction front velocities were equal to 3.50 mm/min and 4.00 mm/min respectively (Figure 4b,c); whereas, in the case of wood pellets the

reaction front velocity is almost 4.40 mm/min (Figure 4a). The regression factor (R^2) exceeds 0.90 for all reported regressions.

4.2.2. Mass Loss History

The mass conversion rate (*MCR*) is defined as the mass loss per unit area and per unit time. It is obtained directly from the measured mass of the fixed bed, and thereafter, corrected by considering the ash content of the fuel.

The ignition rate (*IR*) defines the quantity of fuel ignited per unit area and per unit time due to the reaction front. This ignition rate is a crucial parameter used to estimate the grate position, where the reaction front reaches its limit at the bottom of the bed, indicating the end of the fuel combustion. Moreover, the heat release rate (*HR*) is determined by multiplying the *HHV* value and the mass conversion rate (Equation (6)).

However, the specific heat release in the main combustion zone (*HR I*) is calculated using *MCR I* and the *HHV* of the fuel. In the char residual oxidation phase, this value (*HR II*) is obtained from values of *MCR II* and *HHV*, respectively of the residual coke. It should be noted that the *HHV* of residual coke is calculated according to [49,50]:

$$HHV_{coke} = 19.6 Y_{coke} + 14.119 \quad (7)$$

where Y_{coke} is the mass fraction of carbon in the coke, which is approximately 0.85 for lignocellulosic biomass coke [51,52]. HHV_{coke} then is approximately 30.80 MJ/kg.

Figure 5 shows the mass loss of OP, OP_i , and the standard wood pellets as a function of time. During the ignition interval from 0 to 3 min, the mass decreases slightly. This zone corresponds to the moisture evaporation and to the start of devolatilization. Thereafter, in the main combustion phase, the mass decreases steadily and almost linearly. In this important zone, it is possible to determine the two combustion parameters described above: The mass conversion rate (*MCR I*) and the specific heat release *HR I*. Finally, in the char oxidation zone, the decrease of the mass slows down again. *MCR II* (Figure 5) and *HR II* (Table 6) confirm this observation. The *HR* parameter should be below 1 MW/m² in the bottom of the bed [23].

The decrease of the heat release rate (*HR II*) in the third zone can be explained by the small oxidation rate of carbon. Moreover, the ignition rates (*IR*) for OP and OP_i are 0.05 (kg/m²)/s and 0.06 (kg/m²)/s, respectively. These values are of the same order of magnitude of the standard wood pellets (0.05 (kg/m²)/s).

Table 6. Specification Heat Release in the fuel bed.

Heat Release	100% OP	100% OP_i	Wood Pellets
<i>HR I</i> (MW/m ²)	0.96 ± 0.06	0.98 ± 0.08	1.01 ± 0.06
<i>HR II</i> (MW/m ²)	0.12 ± 0.01	0.12 ± 0.02	0.070 ± 0.005

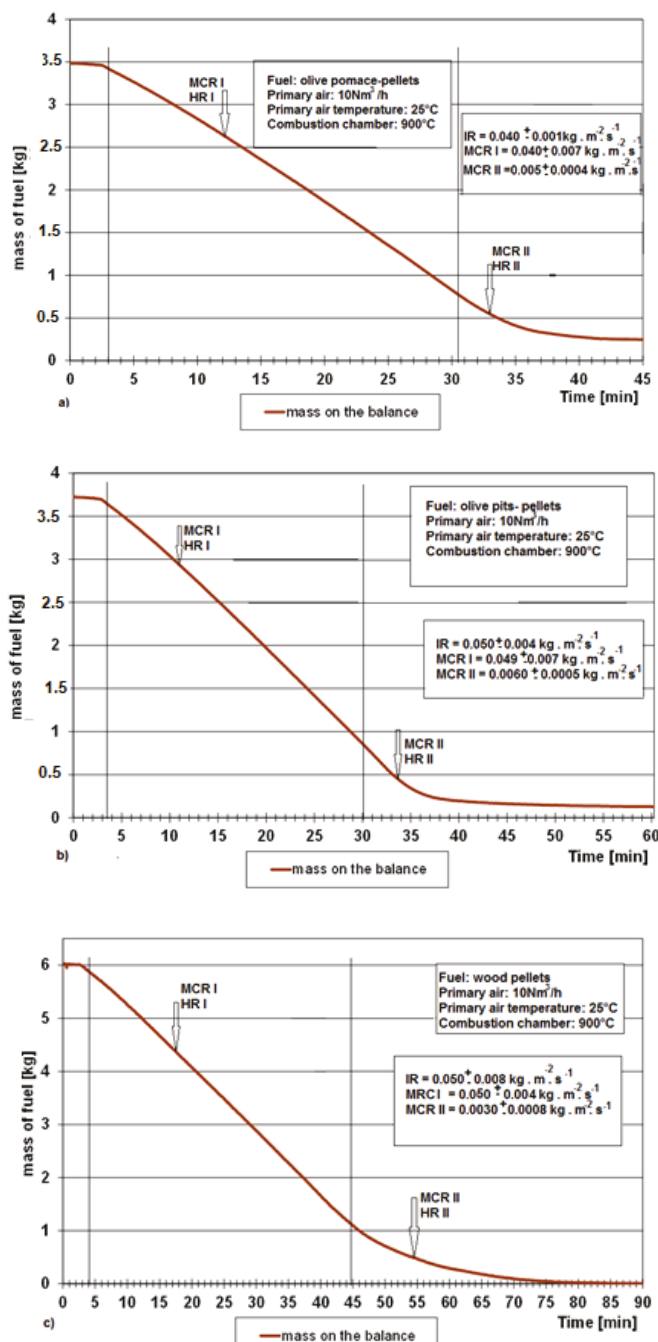


Figure 5. Mass loss curves in the fuel bed: (a) 100% OP; (b) 100% OP_i; (c) standard wood pellets. Experimental conditions: Primary air 10 Nm³/h; primary air temperature 25 °C, and combustion chamber temperature 900 °C.

4.3. Gaseous Emissions

4.3.1. Gaseous Emissions Analysis above the Bed

Figure 6 shows the temporal evolution of the gas concentrations measured directly above the fixed bed (freeboard zone) versus the time during the combustion tests of the different samples. The considered gaseous emissions are respectively; O_2 , CO_2 , H_2O (steam), H_2 , and C_{org} (organic carbon). All components are expressed in % vol. wet basis. Moreover, the local constant of air (λ) is plotted on the right axis.

At the beginning of all experimental tests, only the O_2 concentration in the flue gases is detected in the freeboard due to the primary air supply, and then it decays quickly from the ambient level of 21% to zero percent. In contrast, the H_2O mass flow increases due to the fuel bed drying process. After 4 to 5 min, the fuel ignites. Consequently, the concentrations of CO and CO_2 increases rapidly, while, H_2 , C_{org} , and H_2O are released. Hence, the concentration of O_2 is significantly decreased. In addition, we observe that the gaseous emissions remain at a roughly constant level during the combustion process. This period is called: The main combustion zone or the quasi-stationary combustion zone [23]. During the time interval [37 min, 56 min], the reaction front reaches the bottom of the bed. Consequently, we observe a rise in the O_2 concentration again, while the concentrations of H_2 and C_{org} are decreased to their minimum levels. During this period, the char residue burning is enhanced exhibiting a little increase of CO_2 . In contrast, CO rises also steeply with the decrease in CO_2 and stabilizes between 20% and 28%. This observation can be attributed to the gasification process for which the residual char is exposed, especially in the presence of CO_2 in the medium [21] according to the following reaction:



In this zone, the OP pellets are characterized by a high emission of CO which rises to 23% by comparison to 20.2% for the OP_i . But, this concentration remains quietly smaller than the 24.5% for the wood pellets. However, during the combustion process, these values remain still higher than those of CO_2 emissions. This growth may be attributed to the gasification process of the residual char in the presence of the water/steam (H_2O) according to the following reaction:



Indeed, this reaction yields an increase in CO and H_2 at the same time [21,53]. Moreover, Figure 6a shows that OP results in the highest percentage of CO_2 ($\approx 13\%$) compared to the 11% for OP_i . This result can be attributed to the high percentage of carbon content (about 49.5%) against only 46.5% of the OP_i . After a combustion time within the interval from 43 to 70 min, all gaseous emissions tend to zero, indicating the end of fuel conversion process.

Therefore, the comparison of the different samples shows that the wood pellets (Figure 6c) have the most stable emissions compared to OP and OP_i . Such behavior may be attributed first, to the lower moisture content (about 6.5%) compared with other samples, and second, to the chemical complexity of OMSWs samples when compared with wood pellets. Indeed, the chemical composition of the olive mill solid wastes is more complex with polyphenols, pectin, and fatty acids. In addition, this difference of behavior between woody pellets and OMSWs pellets can be attributed to the fact that the used reactor was designed to be fed by woody biomass rather than by olive mill by-products. Hence, modifications concerning primary air and secondary air positions and flow rates should be undertaken to increase the reactor efficiency when using OMSWs pellets.

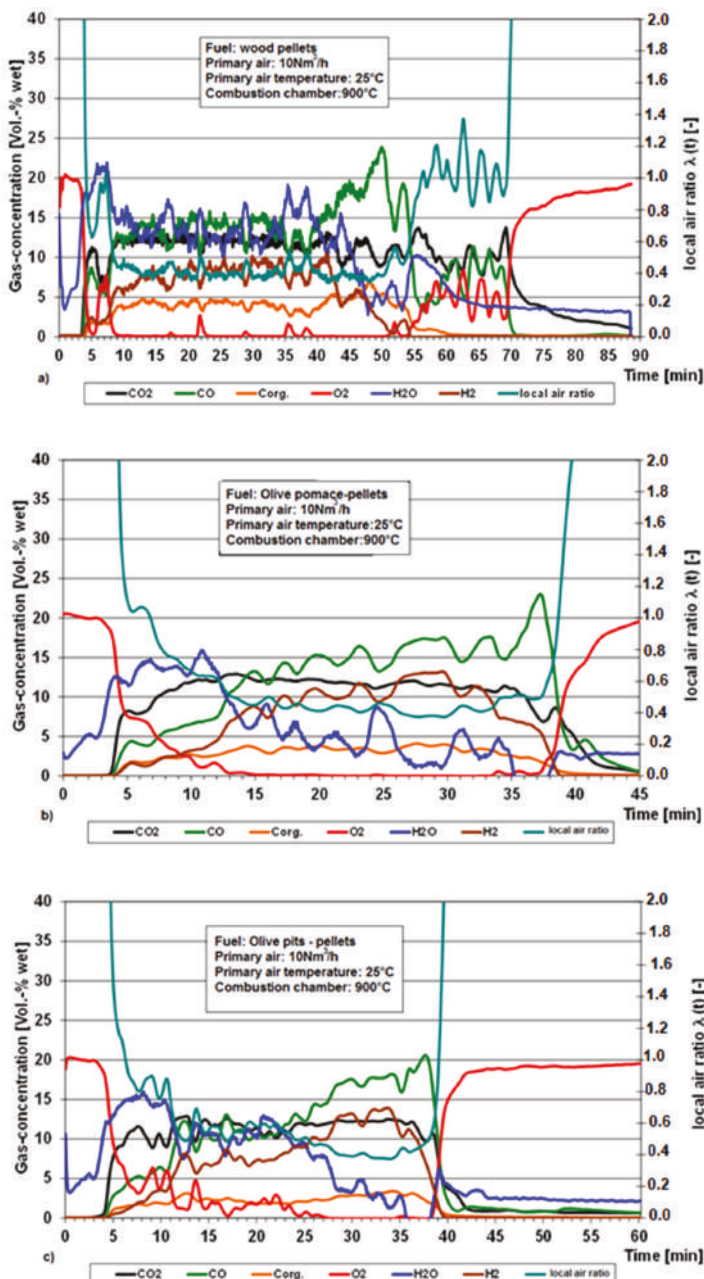


Figure 6. Concentrations of gaseous emissions analysis above the fixed bed (in the freeboard): (a) 100% standard wood pellets, (b) OP and (c) 100% OP_i. Experimental conditions: Primary air 10 Nm³/h; primary air temperature 25 °C and combustion chamber temperature 900 °C.

4.3.2. Gaseous Emissions Analysis in the Post-Combustion Chamber

Figure 7 shows the temporal distribution of the traces of gas concentrations versus time in the flame front, especially, at the outlet of the post-combustion chamber. More specifically, we focus in this section on NO_x (nitrogen oxides), N_2O (nitrous oxide), and SO_2 (sulphur dioxide), expressed in mg/Nm^3 , dry at normal temperature (25°C) and pressure. Meanwhile, O_2 , CO_2 , and CO concentrations are also considered.

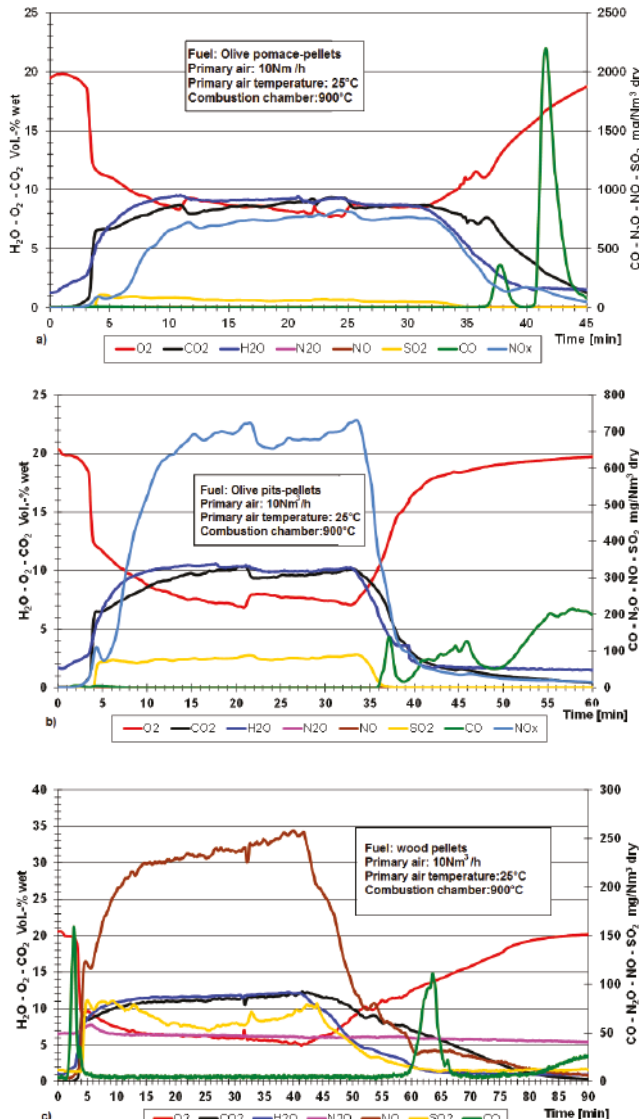


Figure 7. Traces of gases measured at the outlet of the post-combustion chamber (a) 100% OP; (b) 100% OP_i and (c) wood pellets.

When examining Figure 7, we observe that the emissions of NO_x at the secondary combustion chamber are relatively high when compared to the SO₂ emission. This increase may be attributed to the fuel-N combustion occurring in the post-combustion especially in the presence of a high flow of injected secondary air. Hence, a notable increase of the temperature in the medium results in NO formation (or thermal NO), and the corresponding mechanism is the so-called Zel'dovich mechanism. This mechanism consists of molecules dissociation at high temperature so that each molecule of oxygen and nitrogen in lean flame condition (Equivalence ratio less than 1.0) is dissociated into two atoms. Hence, the pair of reactions was first proposed by Y.B. Zel'dovich [54]:



Furthermore, the reduction of CO is consistent with the increase of the excess air in the secondary combustion chamber [55]. In contrast, Garijo et al. [56] and Staiger et al. [57] indicate that an increase in the CO concentration or another carbonaceous compound can inhibit the formation of NO_x. This is mainly due to a reduction of the temperature by heat absorption in the medium. On the other hand, the emissions of NO_x (Figure 7a) of the OP showed the highest value with about 895 mg/Nm³ compared to 720 mg/Nm³ (Figure 7b) of the OP_i and to almost 255 mg/Nm³ (Figure 7c) of the wood pellets. In fact, this result is expected because the nitrogen content in olive pomace (1.26%) is higher than that of wood pellets (0.11%) and also than that of olive pits (0.61%) [58,59]. Moreover, this NO_x concentration growth can also be justified by the abundance of O₂ supplied to the post-combustion chamber [28]. In contrast, the emissions of SO₂ during the combustion tests of the pellets samples (OP and OP_i) exhibit only small traces of this compared to standards biofuels (ex. wood pellets). This may be attributed to the low sulphur contents (≤ 0.1) for the different samples.

4.3.3. Conversion Unit of Gaseous Emissions

The gaseous emissions that we obtained were corrected and converted at 10% and 13% O₂ according to the following formula:

$$X_{\text{O}_2,\text{ref}} = X_{\text{O}_2,\text{meas}} \frac{21 - [\text{O}_2]_{\text{ref}}}{21 - [\text{O}_2]_{\text{meas}}} \quad (12)$$

The purpose of this conversion is to allow comparison between our results and those found by authors working under same conditions (10% O₂ and 13% O₂) and for which gaseous concentrations were expressed either in ppm or in mg/Nm³ as it is summarized in Table 7.

where X is the gas concentration, the subscript “O₂, ref” refers to the fixed oxygen concentration under which we want calculate X, and the subscript “O₂, meas” is related to the measured X value under the fixed oxygen value during the experiment.

We notice that gaseous emissions obtained in our study, with a fixed bed of 40 kW, are in the same range as other lignocellulosic materials. However, the concentrations of nitrogen oxides (NO₂ + NO) obtained at the post-combustion chamber were equal to 142 ppm and 116 ppm, at 10% O₂ for OP and OP_i, respectively. These values are of the same magnitude than 113 ppm NO_x obtained for the standard wood pellets. However, these values are higher than value obtained with the DIN plus (54 ppm at 10% O₂) [60]. In fact, the concentrations of NO_x were comparatively smaller (<30 ppm at 13% O₂), during the combustion of commercial pine pellets in a domestic pellets boiler (22 kW) [61]. Moreover, these values are close to those found in the literature for various pellets such as exhausted olive mill solid wastes (EOMSW) (115 ppm at 10% O₂), and olive pruning pellets (340 ppm at 10% O₂) [62]. Furthermore, the values of SO₂ varied between 14 and 22 ppm at 10% O₂ and between 10 and 16 ppm at 13% O₂ according to the obtained results. Nevertheless, these values remain lower than 36 ppm at 10% O₂ obtained for Sunflower shells [63]. Mohon et al. [64] showed that the combustion

of grass pellet and three different types of wood pellets, when tested in a prototype pellet furnace (7–32 kW), emit between 0 and 7 ppm of SO₂ at 10% O₂.

Table 7. Emissions values corrected at respectively; (a) 10% O₂ and (b) 13% O₂.

Samples	O ₂ %	CO ₂ %	CO ¹ %	H ₂ O%	H ₂ %	CO ² (ppm)	NO _x (ppm)	SO ₂ (ppm)
100 OP	11	6.84	11.58	8	7.63	(a) 1446 (b) 1054	(a) 142 (b) 104	(a) 22 (b) 16
100 OP _i	10.37	5.85	10.64	8	7.72	(a) 133 (b) 97	(a) 116 (b) 84	(a) 17 (b) 12
Wood pellets	9.94	7	12.62	11.57	5.26	(a) 46 (b) 34	(a) 13 for N ₂ O; 100 for NO (b) 11 for N ₂ O; 73 for NO	(a) 14 (b) 10
Spent coffee ground (SCG) [65]	4	5	-	-	-	(a) 2456 (b) 1785	(a) 245 for NO; 39 for N ₂ O (b) 178 for NO; 28 for N ₂ O	-
Wood DIN plus [60]	12	6	-	-	-	(b) 153	(b) 19	-
EOMSW [36]	12	8	-	-	-	(a) 795 (b) 578	(a) 115 (b) 85	-
Sawdust (S) [36]	12	6	-	-	-	(a) 277 (b) 202	(a) 36 (b) 26	-
Sunflower shells [61]	13	-	-	-	-	(a) 252	(a) 55	(a) 36
French Wood pellets [61]	15	6	-	-	-	(a) 277	(a) 36	(a) 7
Pine pellets [62]	13.22	4.5	-	-	-	(b) 470	(b) 50	-

OMSW: olive mill solid waste, EOMSW: exhaust olive mill solid waste; ¹ At the primary combustion chamber;

² At the post-combustion chamber.

5. Conclusions

In this paper, olive pomace OP and olive pits OP_i have been investigated as renewable and environmentally friendly energy sources. More precisely, we focused on the combustion of the pelletized biofuels in a 40 kW counter-current fixed bed reactor. The temperature inside the bed and the mass loss were measured. Three distinct phases for the progress of the combustion process were observed: The ignition delay time, the main combustion phase, and the char oxidation phase. Moreover, some crucial combustion parameters were evaluated: The reaction front velocity, the ignition rate, the heat release rate, and the mass conversion rate.

We have found that the results are quite similar to results of the standard wood pellets which are used currently in European markets. Moreover, we have observed that the gaseous emissions are produced in acceptable concentrations compared to Germany and European standards. Hence, these results motivate future investigations to reuse the olive mill solid wastes for producing alternative biofuels which can be used for heat and/or electricity production, either in domestic or in industrial plants.

Author Contributions: Funding acquisition, H.-J.G. and M.L.; Investigation, H.M. and M.L.; Methodology, H.M., D.S. and M.L.; Project administration, H.-J.G.; Resources, R.B.; Supervision, H.M. and M.L.; Writing—original draft, M.A.M. and M.L.; Writing—review and editing, H.M., H.-J.G., D.S. and R.B.

Funding: This research received no external funding.

Acknowledgments: Mohamed Ali Mami would like to thank the Doctoral School of Monastir University for the Financial Support of this project. In addition, the author is grateful to Zouila Company (Mahdia-Tunisia) for providing him the raw biomass. In addition, the author expresses deep thanks to A. Gerig and other technical team members of KIT for their assistance during the experimental tests. Marzouk Lajili would like to address special thanks to Professor T. Echekki (N.C.U.) for his precious comments and for his help with English.

Conflicts of Interest: The authors declare no conflict of interest.

Nomenclature

<i>A</i>	Fuel bed cross-section (m^2)
<i>HHV</i>	Higher heating value ($\text{MJ}\cdot\text{kg}^{-1}$)
<i>HR</i>	Heat release rate ($\text{MW}\cdot\text{m}^{-2}$)
<i>IR</i>	Ignition rate ($\text{kg}\cdot\text{m}^{-2}\cdot\text{s}^{-1}$)
<i>MCR</i>	Mass conversion rate ($\text{kg}\cdot\text{m}^{-2}\cdot\text{s}^{-1}$)
<i>h</i>	Bed height (mm)
<i>ṁ</i>	Mass loss rate ($\text{kg}\cdot\text{s}^{-1}$)
<i>u</i>	Velocity ($\text{mm}\cdot\text{min}^{-1}$)
<i>y</i>	Mass fraction (-)
<i>ρ</i>	Density ($\text{kg}\cdot\text{m}^{-3}$)
<i>L</i>	Latent heat ($\text{kJ}\cdot\text{kg}^{-1}$)

Subscripts and Superscripts

<i>ash</i>	ash
<i>RF</i>	Reaction front
<i>C_{coke}</i>	Carbon in coke
<i>BD</i>	Bulk density
<i>v</i>	vaporization

References

- Demirbas, A. Combustion characteristics of different biomass fuels. *Prog. Energy Combust. Sci.* **2004**, *30*, 219–230. [[CrossRef](#)]
- Heschel, W.; Rweyemamu, L.; Scheibner, T.; Meyer, B. Abatement of emission in small-scale combustors through utilization of blended pellet fuels. *Fuel Process. Technol.* **1999**, *61*, 223–242. [[CrossRef](#)]
- Saidur, R.; Abdelaziz, E.A.; Demirbas, A.; Hossain, M.S.; Mekhilef, S. A review on biomass as a fuel for boilers. *Renew. Sustain. Energy Rev.* **2011**, *15*, 2262–2289. [[CrossRef](#)]
- Christoforou, E.; Fokaides, P.A. A review of olive mill solid wastes to energy utilisation techniques. *Waste Manag.* **2016**, *49*, 346–363. [[CrossRef](#)] [[PubMed](#)]
- Rodríguez, G.; Lama, A.; Rodríguez, R.; Jiménez, A.; Guillén, R.; Fernández-Bolaños, J. Olive stone an attractive source of bioactive and valuable compounds. *Bioresour. Technol.* **2008**, *99*, 5261–5269. [[CrossRef](#)] [[PubMed](#)]
- Lopez, F.J.; Pinzi, S.; Ruiz, J.J.; Lopez, A.; Dorado, M.P. Economic viability of the use of olive tree pruning as fuel for heating systems in public institutions in South Spain. *Fuel* **2010**, *89*, 1386–1391. [[CrossRef](#)]
- Moya López, A.J.; Mateo Quero, S. Aprovechamiento de los residuos del olivar. Available online: https://www.researchgate.net/publication/259228577_Aprovechamiento_de_los_residuos_del.olivar (accessed on 20 June 2018).
- Mata-Sánchez, J.; Pérez-Jiménez, J.A.; Díaz-Villanueva, M.J.; Serrano, A.; Núñez-Sánchez, N.; López-Giménez, F.J. Development of Olive stones quality system based on biofuel energetic parameters study. *Renew. Energy* **2014**, *66*, 251–256. [[CrossRef](#)]
- Pattara, C.; Cappelletti, G.M.; Cichelli, A. Recovery and use of olive stones: commodity, environmental and economic assessment. *Renew. Sustain. Energy Rev.* **2010**, *14*, 1484–1489. [[CrossRef](#)]
- Alkhamis, T.M.; Kablan, M.M. Olive cake as an energy source and catalyst for oil shale production of energy and its impact on the environmental. *Energy Convers. Manag.* **1999**, *40*, 1863–1870. [[CrossRef](#)]
- Ramachandran, S.; Singh, S.K.; Larroche, C.; Soccol, C.R.; Pandey, A. Oil cakes and their biotechnological applications—A reviews. *Bioresour. Technol.* **2007**, *98*, 2000–2009. [[CrossRef](#)] [[PubMed](#)]
- Brlek, T.; Pezo, L.; Voća, N.; Krička, T.; Vukmirović, Đ.; Čolović, R.; Bodroža-Solarov, M. Chemometric approach for assessing the quality of olive cake pellets. *Fuel Process. Technol.* **2013**, *116*, 250–256. [[CrossRef](#)]
- Christoforou, E.; Kyllili, A.; Fokaides, P.A. Technical and economical evaluation of olive mills solid waste pellets. *Renew. Energy* **2016**, *96*, 33–41. [[CrossRef](#)]
- González, J.F.; González-García, C.M.; Ramiro, A.; González, J.; Sabio, E.; Gañán, J.; Rodríguez, M.A. Combustion optimisation of biomass residue pellets for domestic heating with a mural boiler. *Biomass Bioenergy* **2004**, *27*, 145–154. [[CrossRef](#)]

15. Lajili, M.; Jeguirim, M.; Kraiem, N.; Limousy, L. Performance of a household boiler fed with agropellets blended from olive mill solid waste and pine sawdust. *Fuel* **2015**, *153*, 431–436. [[CrossRef](#)]
16. Miranda, T.; Arranz, J.I.; Montero, I.; Román, S.; Rojas, C.V.; Nogales, S. Characterization and combustion of olive pomace and forest residue pellets. *Fuel Process. Technol.* **2012**, *103*, 91–96. [[CrossRef](#)]
17. Miranda, M.T.; Cabanillas, A.; Rojas, S.; Montero, I.; Ruiz, A. Combined combustion of various phases of olive wastes in a conventional combustor. *Fuel* **2007**, *86*, 367–372. [[CrossRef](#)]
18. Khodaei, H.; Al-Abdeli, Y.M.; Guzzomi, F.; Yeoh, G.H. An overview of processes and considerations in the modelling of fixed-bed biomass combustion. *Energy* **2015**, *88*, 946–972. [[CrossRef](#)]
19. Yang, Y.B.; Sharifi, V.N.; Swithenbank, J. Effect of air flow rate and fuel moisture on the burning behaviours of biomass and simulated municipal solid wastes in packed beds. *Fuel* **2004**, *83*, 1553–1562. [[CrossRef](#)]
20. Porteiro, J.; Patiño, D.; Collazo, J.; Granada, E.; Moran, J.; Miguez, J.L. Experimental analysis of the ignition front propagation of several biomass fuels in a fixed-bed combustor. *Fuel* **2010**, *89*, 26–35. [[CrossRef](#)]
21. Ménard, Y. Modélisation de l’incinération sur Grille D’ordures Ménagères et Approche Thermodynamique du Comportement des Métaux Lourds. Ph.D. Thesis, National Polytechnic Institute of Lorraine, Nancy, France, July 2008.
22. Mätzing, H.; Germann, H.-J.; Kolb, T.; Seifert, H. Experimental and numerical investigation of wood particle combustion in fixed bed reactors. *Environ. Eng. Sci.* **2012**, *29*, 907–914. [[CrossRef](#)]
23. Baris, D.; Gehrmann, H.-J.; Mätzing, H.; Stafp, D.; Seifert, H.; McGowan, T. Characterization of the combustion behavior of “DMC fuel™”. In Proceedings of the 34th International Conference on Thermal Treatment Technologies and Hazardous Waste Combustors, Houston, TX, USA, 20–22 October 2015.
24. Demirbas, A. Potential applications of renewable energy sources, biomass combustion problems in boiler power systems and combustion related environmental issues. *Prog. Energy Combust. Sci.* **2005**, *31*, 171–192. [[CrossRef](#)]
25. Demirbas, A. Calculation of higher heating values of biomass fuels. *Fuel* **1997**, *76*, 431–434. [[CrossRef](#)]
26. McKendry, P. Energy production from biomass (part 1): Overview of biomass. *Bioresour. Technol.* **2002**, *83*, 37–46. [[CrossRef](#)]
27. Vassilev, S.V.; Baxter, D.; Andersen, L.K.; Vassileva, C.G. An overview of the chemical composition of biomass. *Fuel* **2010**, *89*, 913–933. [[CrossRef](#)]
28. Varol, M.; Atimay, A.T. Combustion of olive cake and coal in a bubbling fluidized bed with secondary air injection. *Fuel* **2007**, *86*, 1430–1438. [[CrossRef](#)]
29. Borello, D.; De Caprariis, B.; DeFilippis, P.; Di Carlo, A.; Marchegiani, A.; Marco Pantaleo, A.; Shah, N.; Venturini, P. Thermo-economic Assessment of a olive pomace Gasifier for Cogeneration Applications. *Energy Procedia* **2015**, *75*, 252–258. [[CrossRef](#)]
30. González, J.F.; Román, S.; Encinar, J.M.; Martínez, G. Pyrolysis of various biomass residues and char utilization for the production of activated carbons. *J. Anal. Appl. Pyrolysis* **2009**, *85*, 134–141. [[CrossRef](#)]
31. Atimay, A.T. Combustion of agro-waste with coal in fluidized bed. *Clean Technol. Environ. Policy* **2010**, *12*, 43–52. [[CrossRef](#)]
32. Abu-Qudais, M. Fluidized bed combustion for energy production from olive cake. *Energy* **1996**, *21*, 173–178. [[CrossRef](#)]
33. Skoulou, V.; Koufodimos, G.; Samaras, Z.; Zabaniotou, A. Low temperature gasification of olive kernels in a 5-kW fluidized bed reactor for H₂-rich producer gas. *Int. J. Hydrogen Energy* **2008**, *33*, 6515–6524. [[CrossRef](#)]
34. Chiang, K.-Y.; Chien, K.-L.; Lu, C.-H. Characterization and comparison of biomass produced from various sources: suggestions for selection of pretreatment technologies in biomass-to-energy. *Appl. Energy* **2012**, *100*, 164–171. [[CrossRef](#)]
35. Nunes, L.J.R.; Matias, J.C.O.; Catalão, J.P.S. Mixed biomass pellets for thermal energy production: a review of combustion models. *Appl. Energy* **2014**, *127*, 135–140. [[CrossRef](#)]
36. Karkania, V.; Fanara, E.; Zabaniotou, A. Review of sustainable biomass pellets production—A study for agricultural residues pellets’ market in greece. *Renew. Sustain. Energy Rev.* **2012**, *16*, 1426–1436. [[CrossRef](#)]
37. Lajili, M.; Limousy, L.; Jeguirim, M. Physico-chemical properties and thermal degradation characteristics of agropellets from olive mill by-products/sawdust blends. *Fuel Process. Technol.* **2014**, *126*, 215–221. [[CrossRef](#)]
38. Fasina, O.O. Physical properties of peanut hull pellets. *Bioresour. Technol.* **2008**, *99*, 1259–1266. [[CrossRef](#)] [[PubMed](#)]

39. Lehtikangas, P. Quality properties of pelletised sawdust, logging residues and bark. *Biomass Bioenergy* **2001**, *20*, 351–360. [[CrossRef](#)]
40. Markovic, M.; Bramer, E.A.; Brem, G. Experimental investigation of wood combustion in a fixed bed with hot air. *Waste Manag.* **2014**, *34*, 49–62. [[CrossRef](#)] [[PubMed](#)]
41. Kolb, T.; Bleckwehl, S.; Gehrmann, H.-J.; Seifert, H. Characterisation of combustion behaviour of refuse derived fuel. *J. Energy Inst.* **2008**, *81*, 1–6. [[CrossRef](#)]
42. Thunman, H.; Leckner, B. Co-current and counter-current fixed bed Combustion of biofuel: A comparison. *Fuel* **2003**, *82*, 275–283. [[CrossRef](#)]
43. Porteiro, J.; Patiño, D.; Miguez, J.L.; Granada, E.; Moran, J.; Collazo, J. Study of the reaction front thickness in a counter-current fixed-bed combustor of a pelletised biomass. *Combust. Flame* **2012**, *159*, 1296–1302. [[CrossRef](#)]
44. Meranda, T.; Montero, I.; José Sepúlveda, F.; Arranz, J.I.; Rojas, C.V.; Nogales, S. A review of pellets from different sources. *Materials* **2015**, *8*, 1413–1427. [[CrossRef](#)] [[PubMed](#)]
45. Magelli, F.; Boucher, K.; Bi, H.T.; Melin, S.; Bonoli, A. An environmental impact assessment of exported wood pellets from canada to europe. *Biomass Bioenergy* **2009**, *33*, 434–441. [[CrossRef](#)]
46. Ryu, C.; Phan, A.N.; Yang, Y.; Sharifi, V.N.; Swithenbank, J. Ignition and burning rates of segregated waste combustion in packed beds. *Waste Manag.* **2007**, *27*, 802–810. [[CrossRef](#)] [[PubMed](#)]
47. Gehrmann, H.-J.; Kolb, T.; Seifert, H.; Mark, F.E.; Frankenhaeuser, M.; Schanssema, A.; Wittstock, K.; Kolb, J.J. Synergies between biomass and solid recovered fuel in energy conversion processes. *Environ. Eng. Sci.* **2010**, *27*, 557–567. [[CrossRef](#)]
48. Shin, D.; Choi, S. The combustion of simulated waste in a fixed bed. *Combust. Flame* **2000**, *180*, 121–167. [[CrossRef](#)]
49. Ahmaruzzaman, M. Proximate analyses and predicting hhv of chars obtained from cocracking of petroleum vacuum residue with coal, plastics and biomass. *Bioresour. Technol.* **2008**, *99*, 5043–5050. [[CrossRef](#)] [[PubMed](#)]
50. Vargas-Moreno, J.M.; Callejón-Ferre, A.J.; Pérez-Alonso, J.; Velázquez-Martí, B. A review of the mathematical models for predicting the heating value of biomass materials. *Renew. Sustain. Energy Rev.* **2012**, *16*, 3065–3083. [[CrossRef](#)]
51. Kawakami, M.; Karato, T.; Takenaka, T.; Yokoyama, S. Structure analysis of coke, wood charcoal and bamboocharcoal by Raman spectroscopy and the irreaction rate with CO₂. *ISIJ Int.* **2005**, *45*, 1027–1034. [[CrossRef](#)]
52. Mueller, A.; Haustein, H.D.; Stoesser, P.; Kreitzberg, T.; Kneer, R.; Kolb, T. Gasification kinetics of biomass- and fossil-based fuels: Comparison study using fluidized bed and thermogravimetric analysis. *Energy Fuels* **2015**, *29*, 6717–6723. [[CrossRef](#)]
53. Imen, G.; Mejdi, J.; Uta, S.; Lionel, L.; Simona, B.; Eckhard, D.; Christof, A.; Roman, L.; Frank, S.; Abedlmottaleb, O. The Potential of Activated Carbone Made From Agro-Industrial Residues in NO_x Immessions. *Energies* **2017**, *10*, 1508. [[CrossRef](#)]
54. Anetor, L.; Odetunde, C.; Osakue, E.E. Computational Analysis of Extended Zel'dovich Mechanism. *Arab. J. Sci. Eng.* **2014**, *39*, 8287–8305. [[CrossRef](#)]
55. Atimtay, A.T.; Varol, M. Investigations of co-combustion of coal and olive cake in a bubbling fluidized bed with secondary air injection. *Fuel* **2009**, *88*, 1000–1008. [[CrossRef](#)]
56. Garijo, E.G.; Jensen, A.D.; Glarborg, P. Kinetic Study of NO Reduction over Biomass Char under Dynamic Conditions. *Energy Fuels* **2003**, *17*, 1429–1436. [[CrossRef](#)]
57. Staiger, B.; Unterberger, S.; Berger, R.; Hein, K.R.G. Development of an air staging technology to reduce NO_x emissions in grate-fired boilers. *Energy* **2005**, *30*, 1429–1438. [[CrossRef](#)]
58. Nussbaumer, T. Combustion and co-combustion of biomass: Fundamentals, Technologies and Primary measures for Emission Reduction. *Energy Fuels* **2003**, *15*, 10–21. [[CrossRef](#)]
59. Stubenberger, G.; Scharler, R.; Zahirovic, S.; Obernberger, I. Experimental investigation of nitrogen species release from different solid biomass fuels as basis for release models. *Fuel* **2008**, *87*, 793–806. [[CrossRef](#)]
60. Kraiem, N.; Lajili, M.; Limousy, L.; Said, R.; Jeguirim, M. Energy recovery from Tunisian agri-food wastes: Evaluation of combustion performance and emissions characteristics of green pellets prepared from tomato residues and grape marc. *Energy* **2016**, *107*, 409–418. [[CrossRef](#)]

61. Fernandes, U.; Costa, M. Particle emissions from a domestic pellets-fired boiler. In Proceedings of the 4th International Congress on Energy and Environment Engineering and Management, Mérida, Spain, 26–27 May 2011.
62. Garcia-Maraver, A.; Zamorano, M.; Fernandes, U.; Rabaçal, M.; Costa, M. Relationship between fuel quality and gaseous and particulate matter emission in a domestic pellet-fired boiler. *Fuel* **2014**, *119*, 141–152. [[CrossRef](#)]
63. Cardozo, E.; Erlich, C.; Alejo, L.; Fransson, T.H. Combustion of agriculture residues: An experimental study for small-scale applications. *Fuel* **2014**, *115*, 778–787. [[CrossRef](#)]
64. Roy, M.M.; Dutta, A.; Corscadden, K. An experimental study of combustion and emissions of biomass pellets in a prototype pellet furnace. *Appl. Energy* **2013**, *108*, 298–307. [[CrossRef](#)]
65. Limousy, L.; Jeguirim, M.; Dutournié, P.; Kraiem, N.; Lajili, M.; Said, R. Gaseous products and particulate matter emissions of biomass residual boiler fired with spent coffee ground pellets. *Fuel* **2013**, *107*, 323–329. [[CrossRef](#)]



© 2018 by the authors. Licensee MDPI, Basel, Switzerland. This article is an open access article distributed under the terms and conditions of the Creative Commons Attribution (CC BY) license (<http://creativecommons.org/licenses/by/4.0/>).

Article

Preparation and Evaluation of a Coconut Shell-Based Activated Carbon for CO₂/CH₄ Separation

Amna Abdeljaoued ^{1,2,*}, Nausika Querejeta ³, Inés Durán ³, Noelia Álvarez-Gutiérrez ³, Covadonga Pevida ³ and Mohamed Hachemi Chahbani ^{1,4}

¹ LR11ES54-Laboratory of "Chemical Processes and Industrials Systems", University of Gabes, Gabès 6029, Tunisia; chahbani.med_hachemi@yahoo.com

² National School of Engineers of Gabes (ENIG), University of Gabes, Omar Ibn Elkhattab Street, Zrig, Gabès 6029, Tunisia

³ Instituto Nacional del Carbón, INCAR-CSIC, c/Francisco Pintado Fe 26, 33011 Oviedo, Spain; n.querejeta@incar.csic.es (N.Q.); i.duran@incar.csic.es (I.D.); noeag0591@gmail.com (N.Á.-G.); cpevida@incar.csic.es (C.P.)

⁴ Higher Institute of Applied Sciences and Technology of Gabes, University of Gabes, Omar Ibn Elkhattab Street, Zrig, Gabes 6029, Tunisia

* Correspondence: amna.abdeljawad.2009@gmail.com

Received: 7 June 2018; Accepted: 29 June 2018; Published: 3 July 2018

Abstract: Biomass is a widely distributed and renewable source of carbon. The main objective of this work is to produce an activated carbon from coconut shells with suitable characteristics to separate CO₂ from biogas. The textural characterization of the adsorbent has been determined. Pure component adsorption isotherms of CO₂ and CH₄ at 30, 50 and 70 °C have been measured. The results reveal that the activated carbon had high CO₂ adsorption capacity. Equilibrium of adsorption of CO₂ and CH₄ adsorption on the produced activated carbon reached 8.36 mmol/g and 4.63 mmol/g, respectively, at 30 °C and 10 bars. Moreover, the performance of the produced activated carbon, as a potential adsorbent for CO₂ capture from a CO₂/CH₄ gas mixture, has been evaluated under dynamic conditions in a dedicated fixed-bed setup. The CO₂ and CH₄ adsorption capacities of the produced activated carbon are estimated to be 1.86 and 0.52 mol/kg, respectively, at 30 °C and 1 bar.

Keywords: biogas purification; coconut shells; biomass valorization; textural characterization; adsorption isotherms; breakthrough curves

1. Introduction

Biogas is a biofuel that is naturally produced by the decomposition of various types of organic matter. Upgrading of biogas has gained important attention due to the steady growth in global energy demand, coupled with the depletion of fossil fuel resources, their unaffordable prices, and the environmental damage they cause [1–3].

Methane and carbon dioxide are the main components of biogas. The energy value of biogas is much lower than natural gas due to the presence of carbon dioxide. Thus, to increase its heating value, the carbon dioxide content must be reduced. From the economic side, the CO₂ removal is the most important step in biogas upgrading.

Capture and storage of CO₂ has gained an important place in efforts to reduce greenhouse gas emissions [4,5].

Key economic and environmental factors promote the development of energy-efficient CO₂ separation technologies [6].

Among the various processes proposed to remove CO₂ from biogas, namely adsorption, absorption, membrane and cryogenic separation, pressure swing adsorption (PSA) processes are often used [7–13].

The selection of the adsorbent is a key factor for the efficient operation of a PSA unit. The properties of the adsorbents are one of the most important aspects of unit performance for a determined cycle configuration [14]. Many solid adsorbents have been investigated for the separation of CO₂ from gas effluents, such as zeolites, calcium oxides, activated carbons, hydrotalcites, metal–organic framework (MOF) materials and supported amines [15–20]. Over the past few decades, the use of biomass to prepare carbon-based materials to reduce greenhouse gas emissions has attracted special attention [21–26].

In general, activated carbons can be synthesized from a wide range of biomass materials given that they present low levels of inorganic compounds (ash content) and high carbon content. Many carbon-based materials such as peat, wood, lignite, coal and nut shells are being used in the production of commercial activated carbons. The (CNS) is characterized with high lignin, high carbon content and low ash content; these properties make the material suitable for the production of microporous activated carbons [27,28].

Two conventional methods for biomass activation have been reported: physical and chemical activation procedure [29,30].

Chemical activation is considered an ineffective environmental procedure as it uses solvents to dissolve reagents, extract and wash products, separate mixtures, clean reaction apparatus and disperse products for practical applications. On the contrary, physical activation is ecological in relation to chemical activation. In the present work, a physical activation method using a single step was selected.

The activated carbon produced can be found in pellet, powder or granular form [31–33]. The main purpose of this work is to produce an activated carbon from dry CNS utilizing a physical activation procedure and to evaluate the textural characteristics and the performance of the produced adsorbent for CO₂ separation from biogas effluents.

2. Material and Methods

2.1. Precursor Material

CNS was selected as carbon-based material for the production of the activated carbon. The carbon material was ground and sieved and particles between 1 and 3 mm were selected. The UNE 32-004-84 standard was adopted to conduct the proximate analysis using a thermogravimetric analyser TAG24 Ultimate analyses were carried out in a LECO VTF-900 and in a LECO CHNS-932, respectively.

The non-isothermal mass-loss profile of the precursor material in carbon dioxide atmosphere was determined using a thermogravimetric analyzer Setaram TGA92 (France) in order to elucidate optimal activation time and temperature.

The raw CNS was introduced in a platinum crucible (70 µL) and was dried for one hour at 100 °C in nitrogen flow; then a carbon dioxide (activating agent) flow (50 mL/min) was used to heat up the sample up to 1000 °C using a heating rate of 15 °C/min and kept at this final temperature during 30 min.

2.2. Activated Carbon Production

Once the activation conditions were selected, the production of the activated carbon was initiated. A vertical tubular kiln was used for that purpose. The raw CNS was introduced in a quartz jacketed reactor and then placed in the vertical tubular kiln. The experimental set-up has been described elsewhere [34].

After a drying step, the reactor was cleaned with N₂ flow for 30 min at ambient temperature and a CO₂ gas flow rate of 100 mL/min was used to heat up the system up to 900 °C at a heating rate of 10 °C/min. A thermocouple was placed in the reactor to control the temperature variation. The sample

was kept at this temperature in carbon dioxide atmosphere for 73 min. Then the gas was shifted to nitrogen and the sample was cooled down to ambient temperature.

The adsorption capacity of CO₂ of the synthetized activated carbon was tested in a TGA 92 thermogravimetric analyzer from Setaram following the procedure described elsewhere [35].

The produced activated carbon particles between 1 and 2 mm were selected for this study. A Micromeritics ASAP 2010 was used for the characterization of the adsorbent by N₂ physical adsorption at −196 °C. A Micromeritics TriStar 3000 volumetric apparatus was used to assess the CO₂ adsorption at 0 °C.

Before gas adsorption experiments, the sample was purged overnight at 100 °C under vacuum. The N₂ adsorbed quantity, at a relative pressure of 0.99, was used to calculate the total pore volume (V_p). The Brunauer–Emmett–Teller (BET) equation was used to estimate the apparent surface area using the N₂ adsorption isotherms at −196 °C [36]. The helium density was determined using an Accupyc 1330 equipment at 35 °C. The micropore volume (W_0) was calculated using Dubinin–Radushkevich (DR) and Dubinin–Astakhov (DA) equations [37]. The average micropore width was estimated by means of the Stoeckli–Ballerini relation [38]. A Micromeritics Autopore IV 9500 mercury porosimeter was used to calculate the apparent density at 0.1 MPa.

2.3. Adsorption Isotherms

To evaluate the performance of the prepared adsorbent for biogas upgrading, adsorption isotherms of pure CO₂ and CH₄ experiments were conducted using a high-pressure magnetic suspension balance, Rubotherm-VTI.

Three temperatures (30, 50 and 70 °C) and pressure up to 10 bars were selected for the study. Before the adsorption experiment, the sample (approximately 1 g) was placed in the measuring cell, which was dried at 100 °C for 120 min under vacuum. The temperature was then decreased to the desired temperature, and pressurized with pure CO₂ or CH₄ gas. When equilibrium was achieved, the weight variation of the sample, the pressure and temperature were collected. Experiments with helium were performed to account for the buoyancy correction. CO₂ and CH₄ absolute quantity adsorbed at pressures up to 10 bars were calculated based on the procedure mentioned in a precedent work [39].

2.4. Breakthrough Measurements

To study the performance of the synthesized activated carbon for CO₂/CH₄ separation under dynamic conditions, breakthrough measurements of an equimolar gas mixture were performed in a lab-scale fixed-column packed with 5.914 g of adsorbent material. The experimental set-up is described in detail elsewhere [40].

The amount of gas flow at the exit of the fixed bed was measured using a mini CORIFLOW meter from Bronkhorst. The concentration of the outlet gas was assessed using a dual-channel micro-gas chromatograph, Varian CP-4900, fitted with a thermal conductivity detector (TCD).

The column was filled with the CNS adsorbent to evaluate the CO₂/CH₄ adsorption under dynamic conditions. An equimolar biogas CO₂/CH₄ gas mixture was fed (30 mL/min STP) to the column and the performance of the sample was evaluated under isothermal conditions (30 °C) at 1 bar. The adsorbed gases were completely desorbed by flowing 50 mL/min STP of He and increasing the column temperature to 180 °C at 1 bar.

Adsorption–desorption cycles were carried out to explore the reproducibility of the system, where adsorption was maintained until saturation was achieved and desorption was carried out until the adsorbent bed was totally regenerated. For the adsorption step, the concentrations of CO₂ and CH₄ in the bed effluent gas were incessantly controlled as a time-depending function (breakthrough curve), and for dynamic equilibrium, the capacity of adsorption of adsorbent was determined when the concentration of CO₂ is equal to that of the feed.

Breakthrough time, t_b , defined as the time required for the detection of CO₂ at the exit of the column, and the adsorption capacity of CO₂ at equilibrium, were calculated as the average of the values obtained from the six successive cycles [34].

3. Results and Discussion

3.1. Precursor Material

The data obtained from the proximate and ultimate analyses of CNS are summarized in Table 1. Proximate analysis shows that CNS are characterized by low ash content (0.42 wt.%), which is a desirable feature for activated carbon production. Ultimate analysis shows that the raw material possesses a high carbon content (i.e., 51.6 wt.%) and low hydrogen and oxygen contents. In addition, the absence of sulfur in the raw material eliminates the possibility of sulfur dioxide emission during the production process. These data make CNS a promising material to be utilized as an activated carbon precursor.

Table 1. Proximate and ultimate analyses of the raw (CNS).

Sample	Proximate Analysis (wt.%)		Ultimate Analysis (wt.%, daf)				
	Moisture	Ash (db)	C	H	N	S	O
CNS	12.55	0.42	51.6	5.6	0.1	0	42.7

db: dry basis; daf: dry ash free basis.

Weight loss of the CNS during heat treatment under carbon dioxide is presented in Figure 1. This figure indicates that the greater weight losses for (CCS) mainly occur between 27 and 627 °C. The first mass loss at 100 °C corresponds to humidity and other guest molecules adsorbed on the material. Waste agricultural biomass commonly consists of cellulose, hemi-cellulose and lignin. The second and third peaks in the derivative of the thermogravimetric (TG) curve (DTG curve) represent the fragmentation of hemi-cellulose and that of cellulose, respectively.

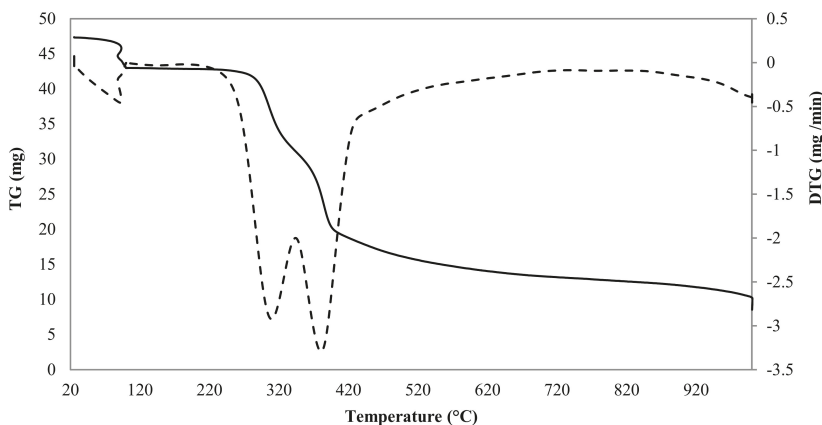


Figure 1. Mass loss and rate of mass loss profiles for CNS. The solid line corresponds to the thermogravimetric (TG) curve and the dashed line represents the derivative of the curve (DTG).

According to the experimental results of the weight-loss profile, the activation temperature was set at 900 °C and three activation times were selected, 35, 73 and 115 min, which correspond to the following yields, as estimated from Equation (1): 21.51, 16.92, and 10.47%, respectively.

$$\text{Yield (\%)} = \left(\frac{\text{mass of the sample after activation (g)}}{\text{initial mass of dried sample (g)}} \right) \times 100 \quad (1)$$

3.2. (CNS)Activated Carbon Characterization and Evaluation

3.2.1. Textural Characterization

Figures 2 and 3 represent the N₂ and CO₂ adsorption isotherms at −196 and 0 °C, respectively, on the activated carbon produced from CNS.

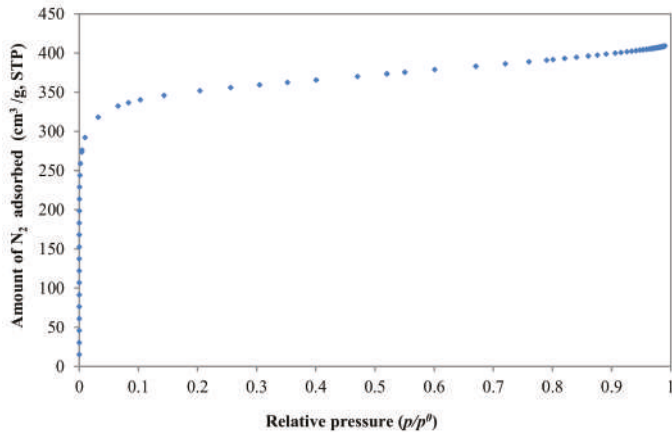


Figure 2. Adsorption isotherm of N₂ at −196 °C for the synthesized adsorbent.

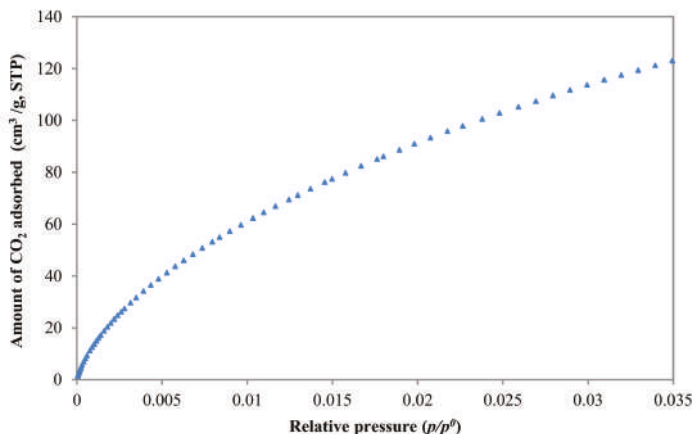


Figure 3. Adsorption isotherms of CO₂ at 0 °C for the synthesized adsorbent.

According to the International Union of Pure and Applied Chemistry (IUPAC) classification, the N₂ adsorption isotherm is of type I; this indicates that the produced activated carbon is strictly

microporous. As can be noted from Figure 2, the nitrogen uptake is high at low relative pressure ($p/p^0 < 0.1$) and can be explained by micropores filling. As expected, the use of CO₂ as activating agent in a single step physical activation method mainly develops microporosity in biomass activated carbons [41].

CO₂ adsorption in Figure 3 assesses the narrower microporosity (<1 nm). A wide narrow micropore size distribution characterizes the shape of the CO₂ isotherm.

As can be noted from Table 2, the BET surface area estimated, 1378 m²/g is considerably high and it is on the range of a commercial biomass-based carbon (500–1500 m²/g). Micropores (W_0) represent more than 85% of the whole volume of pores (V_p). It is also observed that average narrow micropore size, L_0 as estimated from CO₂ adsorption, is close to the average micropore size, L_0 as estimated from N₂ adsorption.

Table 2. Main textural characteristics of the produced CNS-activated carbon.

Adsorbate	V_p (cm ³ /g)	S_{BET} (m ² /g)	Dubinin				
			n	S_{mic} (m ² /g)	L_0 (nm)	E_0 (kJ/mol)	W_0 (cm ³ /g)
N ₂	0.63	1378	2	1043	1.04	21.76	0.54
CO ₂	-	-	1.77	1126	0.84	24.22	0.47

3.2.2. Adsorption Isotherms

The experimental adsorption isotherm data collected at 30, 50 and 70 °C were fit to three different models to account for the equilibrium of adsorption, namely Sips, Toth and Dual-Site Langmuir (D-S), (Equations (2)–(8)).

The first isotherm model used for the representation of the experimental data is the Sips model whose equation is given as follow [42]:

$$q = \frac{q_s(bP)^{\frac{1}{n}}}{1 + (bP)^{\frac{1}{n}}} \quad (2)$$

where q (mol/g) refers to the gas adsorbed quantity and q_s (mol/g) the adsorbed quantity at equilibrium, P (Pa) the adsorption pressure and b the affinity constant. The parameter n indicates the heterogeneity of the system. Generally, n value is greater than unity; thus, the higher the value of n , the more heterogeneous the system that is obtained.

q_s (mol/g) was considered temperature independent whereas n and b (Pa⁻¹) were considered temperature dependent as shown in Equations (3) and (4) [42].

$$b = b_0 \exp \left[\frac{Q}{RT_0} \left(\frac{T_0}{T} - 1 \right) \right] \quad (3)$$

$$\frac{1}{n} = \frac{1}{n_0} + \alpha \left(1 - \frac{T_0}{T} \right) \quad (4)$$

In the equations above, b_0 , n_0 and α are the constants related to the temperature-dependent correlations; R (J/(mol.k)) is the ideal gas constant and T (K) is the temperature. Q is the isosteric heat of adsorption at a fractional loading of 0.5 and T_0 (K) is the reference temperature (30 °C).

The Toth model is used as the second isotherm model for fitting the experimental results which is represented by Equation (5) [42]:

$$q^* = q_s^* \frac{b^* P}{\left[1 + (b^* P)^t \right]^{\frac{1}{t}}} \quad (5)$$

where q^* (mol/g) is the adsorbed quantity, q_s^* (mol/g) is adsorbed quantity at equilibrium and P (Pa) is the adsorption pressure. b^* (Pa⁻¹) and t are characteristic of the adsorbate–adsorbent couple. Thus,

as n in the Sips relation, t characterizes the heterogeneity of the system. However, t is generally less than unity.

As in the Sips relation, the dependence of the equilibrium parameters with temperature in the Toth equation must also be taken into account [42].

$$t = t_0 + \alpha^* \left(1 - \frac{T}{T_0} \right) \quad (6)$$

In Equation (6), t_0 and α^* are the constants related to the temperature dependency of t . The variation of b^* (Pa^{-1}) with temperature is analogue to the dependence of b (Pa^{-1}) in the Sips equation, but in this case, Q accounts for the isosteric heat of adsorption at a nil fractional loading.

Finally, the third isotherm model selected for the prediction of the experimental results is the Dual-Site Langmuir model (D-S) (Equation (7)). This model accounts for the heterogeneity of adsorption of a pure component on the adsorbent which is composed of two homogeneous but different energy sites [43–45]. All assumptions of the Langmuir model are applicable to each site, with an absence of interactions between the two.

$$q = \frac{q_{s1}b_1P}{1+b_1P} + \frac{q_{s2}b_2P}{1+b_2P} \quad (7)$$

where q_{s1} (mol/g) and q_{s2} (mol/g) are respectively the equilibrium adsorbed quantity at sites 1 and 2, so the addition of those quantities define the total capacity of saturation ($q_s = q_{s1} + q_{s2}$) (mol/kg); b_1 (Pa^{-1}) and b_2 (Pa^{-1}) represent free energy parameters for sites 1 and 2 respectively, or affinity, which depend on temperature as shown in Equation (8), where the subscript j refers to free energy sites (1 or 2), $b_{0,j}$ are the pre-exponential factors or entropies of adsorption, and E_j (J/mol) are their energies of adsorption [42].

$$b_j = b_{0,j} \exp\left(\frac{E_j}{RT}\right) j = 1, 2 \quad (8)$$

The comparison between experimental and fitted data of adsorption of pure CO_2 and CH_4 on the CNS-activated carbon is shown in Figures 4 and 5. The experimental pure CO_2 and CH_4 adsorption isotherms of the CNS adsorbent at 30, 50 and 70 °C are represented by symbols. Sips, Toth and Dual-Site Langmuir (D-S) model fitting are represented by dashed lines with symbols.

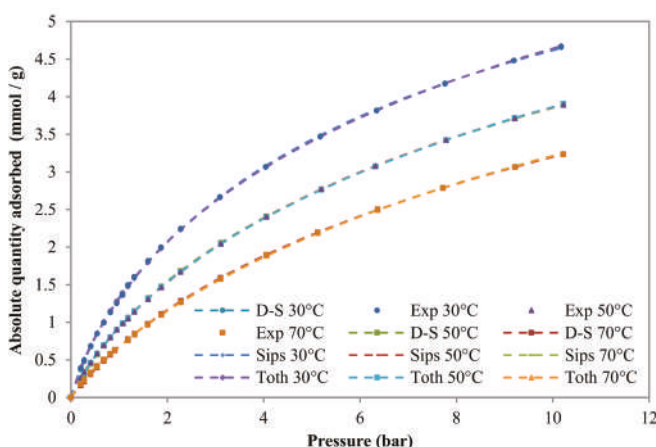


Figure 4. CH_4 isotherm at different temperatures (dashed line with symbols for Sips, Dual-Site Langmuir and Toth models predictions and symbols for experimental data).

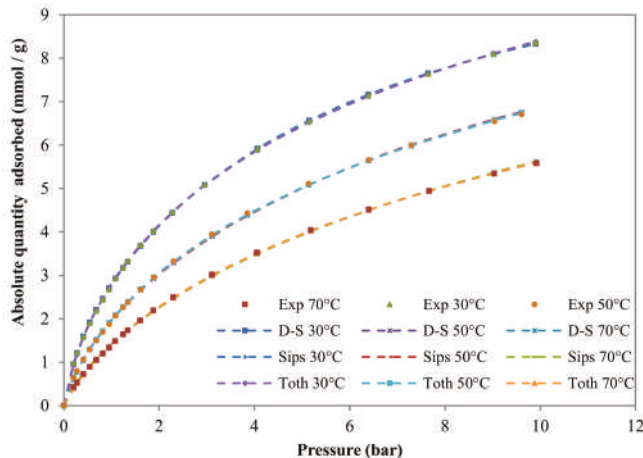


Figure 5. CO₂ isotherm at different temperatures (dashed line with symbols for Sips, Dual-Site Langmuir and Toth models fitting and symbols for experimental results).

Capacity of adsorption is an important factor to estimate the gas separation aptitude of an adsorbent. As can be noted, the CO₂ uptake capacities of CO₂ and CH₄ increased by increasing the pressure but decreased when the temperature increased. This is the expected behaviour for a physical adsorption-based process. The activated carbon produced presents a high CO₂ adsorption capacity compared to that of CH₄ over the studied pressure and temperature range.

The Excel tool Solver was used to fit the experimental results to the different models, and the different values of the parameters were calculated by minimizing the minimum residual sum of squares (SSR) i.e., by reducing the gap between the model predictions and empirical amounts adsorbed at the evaluated temperatures for a specific adsorbate–adsorbent system. Equation 9 shows the objective function used in Solver.

$$\text{SSR (\%)} = \sum_{T_1}^{T_3} \frac{\sum_{i=1}^N (q_{\text{exp},i} - q_{\text{mod},i})^2}{N} \times 100 \quad (9)$$

where $q_{\text{exp},i}$ (mol/g) and $q_{\text{mod},i}$ (mol/g) are the empirical and prediction models of the amounts adsorbed, respectively, and N is the number of experimental points.

Figures 4 and 5 show the results for the three models. The optimal fitting parameters and the values of the minimum residual sum of squares (SSR) are reported in Table 3.

As can be noted in Table 3, the maximum adsorption capacities predicted by the three models for CO₂ are always much higher than those for CH₄. Such a difference in adsorption capacity is advantageous for separation via adsorption. The Toth's predictions of the adsorbed amounts at saturation are higher than those estimated by Sips and Dual-Site Langmuir, respectively. This difference can be justified by the fact that experimental data only correspond to fractional loadings of up to about 0.5 [46].

It is clearly observed that values of b^* , b_1 , b_2 and b are reduced with temperature increase. This supposes that, at high temperature, the attraction of molecules to the surface is weaker.

The n constant in the Sips model and the t constant in the Toth model reflect the degree of heterogeneity of the system. As can be noted in Table 3, the heterogeneity of the system remains practically unchanged with the temperature increase.

Table 3. Sips, Dual-Site Langmuir, and Toth-fitting parameters models to CO₂ and CH₄ pure component adsorption isotherms for the CNS-activated carbon.

Model	Component	T (°C)	q_{s1} , q_{s2} , q_s and q_s^* (mol/kg)	b_1 , b_2 , b and b^* (kPa)	n (Sips) t(Toth)	ff ff*	SSR (%)
Dual-site	CH ₄	30		0.0137 0.0012	-	-	
		50	1.00	6.63	0.0078 0.0008	-	-
		70		0.0049 0.0006	-	-	0.04
	CO ₂	30		0.0235 0.0017	-	-	
		50	1.86	10.50	0.0133 0.0010	-	-
		70		0.0078 0.0006	-	-	0.20
	Sips	30		0.0013	1.21		
		50	8.32	0.0008	1.20	0.25	0.03
		70		0.0006	1.18		
Toth	CH ₄	30		0.0016	1.30		
		50	14.25	0.0009	1.31	0.22	0.12
		70		0.0006	1.29		
	CO ₂	30		0.0022	0.54		
		50	11.64	0.0013	0.56	0.21	0.03
		70		0.0008	0.57		

3.2.3. Breakthrough Curves

In Figure 6, it can also be noted that the CNS adsorbent bed presents a stable performance in consecutive cycling under fixed-bed operations.

Figure 7 shows an example of six-consecutive adsorption and desorption experiments for an equimolar CO₂/CH₄ gas mixture fed to the adsorption fixed-bed at 1 bar. It was used as carrier gas during the preconditioning and regeneration steps. It is observed that during the initial period preceding the saturation of the bed, both components in the feed gas, CO₂ and CH₄, are completely adsorbed on the CNS activated carbon bed. Then, as expected according to the data from the adsorption isotherms (see Figures 4 and 5), CH₄ breaks through first.

The CH₄ breakthrough curve presents a so-called roll-up (see Figure 7). This is because the CH₄ adsorbed is displaced by CO₂ adsorption. This phenomenon has been previously reported for a similar separation in [47]. The strong adsorption of CO₂ over CH₄ can be justified by the fact that the molecules have different adsorption strength.

From Figure 7, it has to be noted that consecutive breakthrough curves overlap showing that the adsorbent was totally regenerated in each cycle and maintained a stable adsorption performance over the six successive sorption cycles. Based on the timing noted in the concentration fronts of CH₄ and CO₂, the CO₂/CH₄ gas separation is technically possible on the CNS-based activated carbon. The required time for the CO₂ front to reach the column outlet is approximately 18 min, whereas CH₄ need a much shorter time to breaks the column (6 min).

The adsorption capacities of CO₂ and CH₄ of the produced activated carbon are estimated to be 1.86 and 0.52 mol/kg, respectively, at 30 °C and 1 bar.

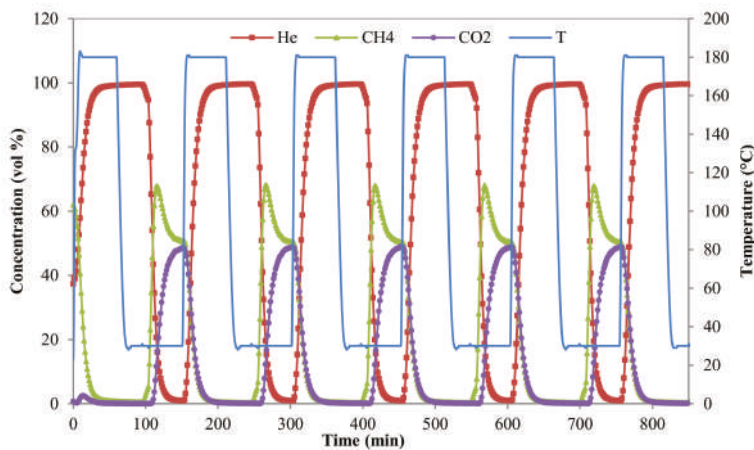


Figure 6. Breakthrough experiments composed of six successive sorption cycles for an equimolar CO_2/CH_4 gas mixture at 1 bar. (Solid lines with symbols represent the concentration profiles of CH_4 , CO_2 and He. The blue solid line represents the temperature).

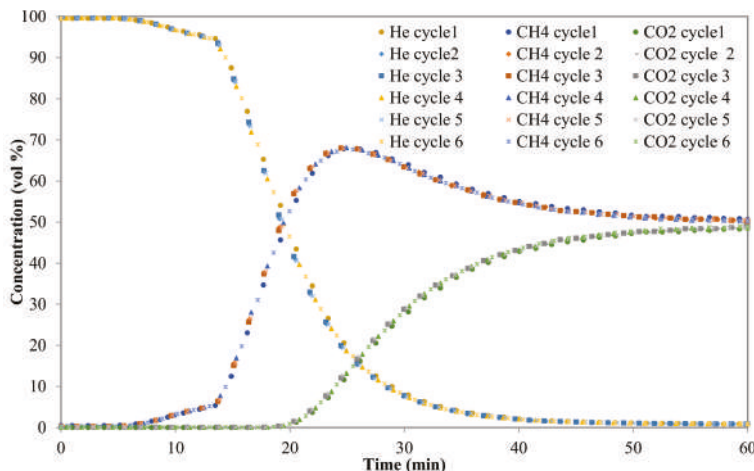


Figure 7. Breakthrough curves for a 50/50 vol % CO_2/CH_4 binary gas mixture at 1 bar. (Symbols represent CO_2 and CH_4 concentrations for different cycles).

For the design of the PSA, it is essential to determine precisely the breakthrough time of CO_2 at the adsorption pressure chosen. This could be done experimentally or using a simulation tool with a model already validated. CH_4 , separated from CO_2 , has to be collected from the bed exit during the period preceding the breakthrough of CO_2 . Just before CO_2 breaks through, the collection of CH_4 should be stopped and the bed undergoes the next step according to the retained PSA cycle design (equalization, depressurization, regeneration, etc.).

3.2.4. Adsorption Selectivity

Aiming to assess the efficiency of the produced activated carbon for CO₂/CH₄ separation, the adsorption selectivity (S_{CO_2/CH_4}) was calculated using Equation (10) [48]

$$S_{CO_2/CH_4} = \frac{x_{CO_2} y_{CH_4}}{x_{CH_4} y_{CO_2}} \quad (10)$$

where x refers to the molar fraction in the adsorbed phase and y refers to the molar fraction in the gas.

The selectivity of CO₂ over CH₄ for the CNS at 1 bar and 30 °C was approximately 3.6. It was found that the value of selectivity was comparable to that of carbon-based adsorbents [49].

Many works reported that (MOF) possess high CO₂ selectivity and high CO₂ working capacities compared to zeolites and carbon-based adsorbents [50–52]. In general, the separation of CO₂ / CH₄ can be affected by many parameters such as temperature and pressure.

4. Conclusions

In this work an activated carbon from dry CNS using one-pot activation procedure was produced. The results of this study showed that the activated carbon presented good development and high BET surface area. The characterization of the CNS-based activated carbon indicated that the adsorbent is basically microporous with a BET surface of 1378 m²/g. CNS can be utilized as a suitable precursor to prepare a microporous activated carbon for CO₂ adsorption from biogas streams.

Pure component CO₂ and CH₄ adsorption isotherms were carried out at three different temperatures. As expected, CO₂ is the strongest adsorbate. Afterwards, breakthrough tests consisting of six successive sorption cycles were run in a lab-scale fixed-column. The CNS based activated carbon maintains its activity during the experiments which reflect a perfect cyclability and regenerability under the evaluated conditions.

Based on the timing observed in the concentration fronts of CH₄ and CO₂, the gas separation of CO₂/CH₄ is technically feasible using the CNS-based activated carbon. For instance, the CO₂ and CH₄ adsorption fronts reach the outlet of the column after approximately 18 min and 6 min, respectively.

The adsorption capacities of CO₂ and CH₄ of the produced activated carbon are estimated to be 1.86 and 0.52 mol/kg, respectively, at 30 °C and 1 bar.

The collected preliminary data report that the synthesized CNS-adsorbent shows suitable characteristics for the CO₂/CH₄ separation.

Author Contributions: A.A. conducted the experimental work with the assistance of N.Q. in the sample preparation and characterization and I.D. and N.Á.-G. in the fixed-bed experiments and data processing. C.P. and M.H.C. supervised the work. All authors contributed to the writing and/or revision of the paper.

Funding: This research was funded by The Tunisian Ministry of Higher Education and Scientific Research.

Conflicts of Interest: The authors declare no conflicts of interest.

References

1. Zheng, B.; Xu, J. Carbon Capture and Storage Development Trends from a Techno-Paradigm Perspective. *Energies* **2014**, *7*, 5221–5250. [[CrossRef](#)]
2. Rodrigues, C.F.A.; Dinis, M.A.P.; Lemos de Sousa, M.J. Review of European energy policies regarding the recent “carbon capture, utilization and storage” technologies scenario and the role of coal seams. *Environ. Earth Sci.* **2015**, *74*, 2553. [[CrossRef](#)]
3. Yoro, K.O.; Sekoai, P.T. The Potential of CO₂ Capture and Storage Technology in South Africa’s Coal-Fired Thermal Power Plants. *Environments* **2016**, *3*, 24. [[CrossRef](#)]
4. Lackner, K.S.; Park, A.H.A.; Miller, B.G. Eliminating CO₂ emissions from coal-fired power plants. In *Generating Electricity in a Carbon-Constrained World*; Academic Press: Cambridge, MA, USA, 2010; pp. 127–173.

5. Pires, J.C.M.; Martins, F.G.; Alvim-Ferraz, M.C.M.; Simões, M. Recent developments on carbon capture and storage: An overview. *Chem. Eng. Res. Des.* **2011**, *89*, 1446–1460. [[CrossRef](#)]
6. Zhou, K.; Chaemchuen, S.; Verpoort, F. Alternative materials in technologies for Biogas upgrading via CO₂ capture. *Renew. Sustain. Energy Rev.* **2017**, *79*, 1414–1441. [[CrossRef](#)]
7. Sarkar, S.C.; Bose, A. Role of activated carbon pellets in carbon dioxide removal. *Energy Convers. Manag.* **1997**, *38*, S105–S110. [[CrossRef](#)]
8. Horikawa, M.S.; Rossi, F.; Gimenes, M.L.; Costa, C.M.M.; Da Silva, M.G.C. Chemical absorption of H₂S for biogas purification. *Braz. J. Chem. Eng.* **2004**, *21*, 415–422. [[CrossRef](#)]
9. Yeo, Z.Y.; Chew, T.L.; Zhu, P.W.; Mohamed, A.R.; Chai, S.P. Conventional processes and membrane technology for carbon dioxide removal from natural gas: A review. *J. Natl. Gas Chem.* **2012**, *21*, 282–298. [[CrossRef](#)]
10. Tuinier, M.J.; van Sint Annaland, M. Biogas Purification Using Cryogenic Packed-Bed Technology. *Ind. Eng. Chem. Res.* **2012**, *51*, 5552–5558. [[CrossRef](#)]
11. Shigaki, N.; Mogi, Y.; Haraoka, T.; Sumi, I. Reduction of Electric Power Consumption in CO₂-PSA with Zeolite 13X Adsorbent. *Energies* **2018**, *11*, 900. [[CrossRef](#)]
12. Xu, G.; Liang, F.; Yang, Y.; Hu, Y.; Zhang, K.; Liu, W. An Improved CO₂ Separation and Purification System Based on Cryogenic Separation and Distillation Theory. *Energies* **2014**, *7*, 3484–3502. [[CrossRef](#)]
13. Abdeljaoued, A.; Relvas, F.; Mendes, A.; Chahbani, M.H. Simulation and experimental results of a PSA process for production of hydrogen used in fuel cells. *J. Environ. Chem. Eng.* **2018**, *6*, 338–355. [[CrossRef](#)]
14. Maring, B.J.; Webley, P.A. A new simplified pressure/vacuum swing adsorption model for rapid adsorbent screening for CO₂ capture applications. *Int. J. Greenh. Gas Control* **2013**, *15*, 16–31. [[CrossRef](#)]
15. Ghouma, I.; Jeguirim, M.; Sager, U.; Limousy, L.; Bennici, S.; Däuber, E.; Asbach, C.; Ligotski, R.; Schmidt, F.; Ouederni, A. The Potential of Activated Carbon Made of Agro-Industrial Residues in NO_x Immissions Abatement. *Energies* **2017**, *10*, 1508. [[CrossRef](#)]
16. Ferella, F.; Puca, A.; Taglieri, G.; Rossi, L.; Gallucci, K. Separation of carbon dioxide for biogas upgrading to biomethane. *J. Clean. Prod.* **2017**, *164*, 1205–1218. [[CrossRef](#)]
17. Siriwardane, R.V.; Shen, M.-S.; Fisher, E.P.; Poston, J.A. Adsorption of CO₂ on Molecular Sieves and Activated Carbon. *Energy Fuels* **2001**, *15*, 279–284. [[CrossRef](#)]
18. Li, G.; Xiao, P.; Webley, P.; Zhang, J.; Singh, R.; Marshall, M. Capture of CO₂ from high humidity flue gas by vacuum swing adsorption with zeolite-13X. *Adsorption* **2008**, *14*, 415–422. [[CrossRef](#)]
19. Millward, A.R.; Yaghi, O.M. Metal-Organic Frameworks with Exceptionally High Capacity for Storage of Carbon Dioxide at Room Temperature. *J. Am. Chem. Soc.* **2005**, *127*, 17998–17999. [[CrossRef](#)] [[PubMed](#)]
20. Furukawa, H.; Ko, N.; Go, Y.B.; Aratani, N.; Choi, S.B.; Choi, E.; Yazaydin, A.O.; Snurr, R.Q.; O'Keeffe, M.; Kim, J.; et al. Ultrahigh Porosity in Metal-Organic Frameworks. *Science* **2010**, *329*, 424–428. [[CrossRef](#)] [[PubMed](#)]
21. Choi, S.; Dreser, J.H.; Jones, C.W. Adsorbent materials for carbon dioxide capture from large anthropogenic point sources. *ChemSusChem* **2009**, *2*, 796–854. [[CrossRef](#)] [[PubMed](#)]
22. Wei, H.; Deng, S.; Hu, B.; Chen, Z.; Wang, B.; Huang, J.; Yu, G. Granular Bamboo-Derived Activated Carbon for High CO₂ Adsorption: The Dominant Role of Narrow Micropores. *ChemSusChem* **2012**, *5*, 2354–2360. [[CrossRef](#)] [[PubMed](#)]
23. Samanta, A.; Zhao, A.; Shimizu, G.K.H.; Sarkar, P.; Gupta, R. Post-Combustion CO₂ Capture Using Solid Sorbents: A Review. *Ind. Eng. Chem. Res.* **2012**, *51*, 1438–1463. [[CrossRef](#)]
24. Jeguirim, M.; Limousy, L. Biomass Chars: Elaboration, Characterization and Applications. *Energies* **2017**, *10*, 2040. [[CrossRef](#)]
25. Álvarez-Gutiérrez, N.; Gil, M.V.; Martínez, M.; Rubiera, F.; Pevida, C. Phenol-Formaldehyde Resin-Based Carbons for CO₂ Separation at sub-atmospheric pressures. *Energies* **2016**, *9*, 189. [[CrossRef](#)]
26. Guizani, C.; Jeguirim, M.; Valin, S.; Limousy, L.; Salvador, S. Biomass Chars: The Effects of Pyrolysis Conditions on Their Morphology, Structure, Chemical Properties and Reactivity. *Energies* **2017**, *10*, 796. [[CrossRef](#)]
27. Heschel, W.; Klose, E. On the suitability of agricultural by-products for the manufacture of granular activated carbon. *Fuel* **1995**, 1786–1791. [[CrossRef](#)]
28. Kirubakaran, C.J.; Krishnaiah, K.; Seshadri, S.K. Experimental Study of the Production of Activated Carbon from Coconut Shells in a Fluidized Bed Reactor. *Ind. Eng. Chem. Res.* **1991**, *30*, 2411–2416. [[CrossRef](#)]

29. Prauchner, M.J.; Rodríguez-Reinoso, F. Chemical versus physical activation of coconut shell: A comparative study. *Microporous Mesoporous Mater.* **2012**, *152*, 163–171. [[CrossRef](#)]
30. Juárez-Galán, J.M.; Silvestre-Albero, A.; Silvestre-Albero, J.; Rodríguez-Reinoso, F. Synthesis of activated carbon with highly developed “mesoporosity”. *Microporous Mesoporous Mater.* **2009**, *117*, 519–521. [[CrossRef](#)]
31. Bartocci, P.; Bidini, G.; Saputo, P.; Fantozzi, F. Biochar pellet carbon footprint. *Chem. Eng. Trans.* **2016**, *50*, 217–222. [[CrossRef](#)]
32. Orrego-Romero, A.F.; Arbeláez-Pérez, O.F.; Bustamante-Londoño, F.; Villa-Holguín, A.L. Pelletization of catalysts supported on activated carbon. A Case Study: Clean synthesis of dimethyl carbonate from methanol and CO₂. *Revista Facultad de Ingeniería Universidad de Antioquia* **2016**, 38–47. [[CrossRef](#)]
33. Chen, T.; Gu, W.; Li, G.; Wang, Q.; Liang, P.; Zhang, X.; Huang, X. Significant enhancement in catalytic ozonation efficacy: From granular to super-fine powdered activated carbon. *Front. Environ. Sci. Eng.* **2018**, *12*, 6. [[CrossRef](#)]
34. Gil, M.V.; Álvarez-Gutiérrez, N.; Martínez, M.; Rubiera, F.; Pevida, C.; Morán, A. Carbon adsorbents for CO₂ capture from bio-hydrogen and biogas streams: Breakthrough adsorption study. *Chem. Eng. J.* **2015**, *269*, 148–158. [[CrossRef](#)]
35. Plaza, M.G.; González, A.S.; Pis, J.J.; Rubiera, F.; Pevida, C. Production of microporous biochars by single-step oxidation: Effect of activation conditions on CO₂ capture. *Appl. Energy* **2014**, *114*, 551–562. [[CrossRef](#)]
36. Brunauer, S.; Emmett, P.H.; Teller, E. Adsorption of gases in multimolecular layers. *J. Am. Chem. Soc.* **1938**, *60*, 309–319. [[CrossRef](#)]
37. Dubinin, M.M. Porous structure and adsorption properties of active carbons. In *Chemistry and Physics of Carbon*; Walker, P.L., Ed.; Marcel Dekker Inc.: New York, NY, USA, 1966; pp. 51–119.
38. Stoeckli, F.; Ballerini, L. Evolution of microporosity during activation of carbon. *Fuel* **1991**, *70*, 557–559. [[CrossRef](#)]
39. García, S.; Pis, J.J.; Rubiera, F.; Pevida, C. Predicting mixed-gas adsorption equilibria on activated carbon for precombustion CO₂ capture. *Langmuir* **2013**, *29*, 6042–6052. [[CrossRef](#)] [[PubMed](#)]
40. García, S.; Gil, M.V.; Martín, C.F.; Pis, J.J.; Rubiera, F.; Pevida, C. Breakthrough adsorption study of a commercial activated carbon for pre-combustion CO₂ capture. *Chem. Eng. J.* **2011**, *171*, 549–556. [[CrossRef](#)]
41. Rodríguez-Reinoso, F.; Molina-Sabio, M.; González, M.T. The use of steam and CO₂ as activating agents in the preparation of activated carbons. *Carbon* **1995**, *33*, 15–23. [[CrossRef](#)]
42. Do, D.D. *Adsorption Analysis: Equilibria and Kinetics*; Imperial College Press: London, UK, 1998.
43. Langmuir, I. The adsorption of gases on plane surfaces of glass, mica and platinum. *J. Am. Chem. Soc.* **1918**, *40*, 1361–1403. [[CrossRef](#)]
44. Ritter, J.A.; Bhadra, S.J.; Ebner, A.D. On the use of the dual process Langmuir model for correlating unary equilibria and predicting mixed-gas adsorption equilibria. *Langmuir* **2011**, *27*, 4700–4712. [[CrossRef](#)] [[PubMed](#)]
45. Bhadra, S.J.; Ebner, A.D.; Ritter, J.A. On the use of the dual process Langmuir model for predicting unary and binary isosteric heats of adsorption. *Langmuir* **2012**, *28*, 6935–6941. [[CrossRef](#)] [[PubMed](#)]
46. Esteves, I.A.; Lopes, M.S.; Nunes, P.M.; Mota, J.P. Adsorption of natural gas and biogas components on activated carbon. *Sep. Purif. Technol.* **2008**, *62*, 281–296. [[CrossRef](#)]
47. Álvarez-Gutiérrez, N.; García, S.; Gil, M.V.; Rubiera, F.; Pevida, C. Dynamic performance of biomass-based carbons for CO₂/CH₄ separation. Approximation to a pressure swing adsorption process for biogas upgrading. *Energy Fuels* **2016**, *30*, 5005–5015. [[CrossRef](#)]
48. Ruthven, D.M.; Farooq, S.; Knaebel, K.S. *Pressure Swing Adsorption*; VCH Publishers: New York, NY, USA, 1994.
49. Álvarez-Gutiérrez, N.; Gil, M.V.; Rubiera, F.; Pevida, C. Adsorption performance indicators for the CO₂/CH₄ separation: Application to biomass-based activated carbons. *Fuel Proc. Technol.* **2016**, *142*, 361–369. [[CrossRef](#)]
50. Ben-Mansour, R.; Habib, M.; Bamidele, O.; Basha, M.; Qasem, N.; Peedikakkal, A.; Laoui, T.; Ali, M. Carbon Capture by Physical Adsorption: Materials, Experimental Investigations and Numerical Modeling and Simulations—A Review. *Appl. Energy* **2016**, *161*, 225–255. [[CrossRef](#)]

51. Xu, X.; Zhao, X.; Sun, L.; Liu, X. Adsorption separation of carbon dioxide, methane, and nitrogen on H β and Na-exchanged β -zeolite. *J. Natl. Gas Chem.* **2008**, *17*, 391–396. [[CrossRef](#)]
52. Altintas, C.; Avci, G.; Daglar, H.; Azar, A.N.V.; Velioglu, S.; Erucar, I.; Keskin, S. A database for CO₂ Separation Performances of MOFs based on Computational Materials Screening. *ACS Appl. Mater. Interfaces* **2018**. [[CrossRef](#)] [[PubMed](#)]



© 2018 by the authors. Licensee MDPI, Basel, Switzerland. This article is an open access article distributed under the terms and conditions of the Creative Commons Attribution (CC BY) license (<http://creativecommons.org/licenses/by/4.0/>).

Article

Value-Added Performance and Thermal Decomposition Characteristics of Dumped Food Waste Compost by Pyrolysis

Ye-Eun Lee ^{1,2}, Jun-Ho Jo ¹, I-Tae Kim ¹ and Yeong-Seok Yoo ^{1,2,*}

¹ Division of Environment and Plant Engineering, Korea Institute of Civil Engineering and Building Technology, 283, Goyang-daero, Ilsanseo-gu, Goyang-si 10223, Gyeonggi-do, Korea; yeeunlee@kict.re.kr (Y.-E.L.); junkr@kict.re.kr (J.-H.J.); itkim@kict.re.kr (I.-T.K.)

² Department of Construction environment Engineering, University of Science and Technology, 217, Gajeong-ro, Yuseong-gu, Daejeon KS015, Korea

* Correspondence: ysyoo@kict.re.kr; Tel.: +82-31-910-0298; Fax: +82-31-910-0288

Received: 6 March 2018; Accepted: 20 April 2018; Published: 25 April 2018

Abstract: Food waste compost has a high Na content, which interferes with plant growth when used as a soil enhancer and therefore makes it difficult to use. And, compared to the amount of compost produced every day, the amount of consumption required in farms is smaller, and the rest is buried underground, which releases greenhouse gases and pollutes underground water. This research compared and analyzed thermal degradation behavior, calorific value, and gas spectrometry during the pyrolysis between food waste compost and sawdust to suggest producing food waste compost biochar by pyrolysis as a new alternative solution to utilize the massive amount of food waste compost. Biochar from pyrolysis of food waste compost had a high carbon content of 51% at 300 °C, and the carbon content decreased as the pyrolysis temperature increased. According to the thermogravimetric analysis (TGA) and derivative thermo-gravimetric (DTG) analysis results, compost showed the largest weight reduction from 240 °C to 365 °C. The weight reduction temperature ranges for compost and sawdust were quite similar. This occurred because food waste of the compost was degraded, but sawdust of compost remained nearly during the composting process. A gas chromatography and mass spectrometry (GC-MS) analysis found that the gases were fragments of fatty acids, protein, and hemi-cellulose. These results could also have been caused by degradation of microorganisms involved in the composting process, sawdust, and small fragments of food waste. In the calorific value of biochar, the highest value (24.33 kJ/g) was obtained 300 °C. At a low pyrolysis temperature, carbon fixation occurred easily since the food waste in compost was degraded by microorganism, and the volatilization of sawdust, which plays an important role in determining the calorific value, was also small. That is why the highest calorific value was shown at 300 °C, not 400 °C or 500 °C. Hence, it seems that food waste compost can be used as a promising alternative fuel at a low pyrolysis temperature, as other lignocellulosic refuse-derived fuels (RDF).

Keywords: food waste compost; sawdust; pyrolysis; biochar; thermogravimetric analysis (TGA); calorific value

1. Introduction

Even though food waste, which has a high content of organic matter, contains much potential energy, it is not used frequently. It takes compost produced from the composting process, which is mainly applied for food waste treatment and recycling, a lot of time to fully mature, and it is difficult to produce compost with consistent quality. In addition, when the compost has high Na content, it interferes with plant growth, which makes it difficult to use [1,2]. The salt content in food waste in Korea is high because of its unique food culture, and it is difficult to use food waste as compost [3]. As of 2015, 33.9% of the

13,546.9 tons/day of the food waste generated in Korea is treated via composting, and only 6.49% is recycled for farms [4]. This amount accounts for just 2.1% of the total food waste, and it shows that the recycling rate is very low. Furthermore, compared to the amount of compost produced every day, the amount of consumption required in farms is smaller, and the rest is not consumed and has to be used as landfill, which releases greenhouse gases, pollutes underground water [5], and causes other environmental problems. Accordingly, a new solution is needed to utilize the excess food waste compost that is not used for its original production purposes and requires treatment.

Pyrolysis is a process that breakdown of large complex molecules into several smaller molecules [6]. Gases, such as carbon dioxide and carbon monoxide, liquids such as bio-oil, or solid chars such as charcoal are generated during this process [6]. Pyrolysis reduces the large volume of biomass which is difficult to recycle and converts it into the material which has an economic value, such as bio-oil and biochar [7]. In fact, many studies have been conducted on the recycling of organic waste using pyrolysis. Iman and Capareda [8] analyzed the characteristics of synthetic gases and biochar produced by pyrolysis on dry grass, at temperatures ranging from 400 °C to 600 °C and demonstrated that biofuel can be produced through pyrolysis. Jahiru reviewed the previous studies that used pyrolysis and produced biofuels, but most were limited to botanical waste such as rice, straw, nut shells, and sugarcane [9].

There have also been studies that used compost as biomass. Agustin [10] performed a study using the gases generated from the composting process, including a study on compost degradation to produce hydrogen gases, but it did not utilize the compost itself. Ghorbel et al. [5] performed pyrolysis on farm breeding compost and cardboard, compared them, and revealed that the value of compost as a biofuel was not good enough, as cardboard had a much higher calorific value than compost. Ryu et al. [11] performed a study that combined mushroom compost with coal tailings and recycled it as a pellet-type fuel, but compost was only used to play a supporting role for coal tailings. In addition, the main source of compost used in these studies was vegetable waste, and no study performed pyrolysis of food waste compost to produce solid fuels. This is because there was a lack of awareness about the necessity of re-treating the waste that had been previously treated, or they were not convinced of the possibility of converting it into valuable matter. A new study is required to explore the scope of fuels other than those researched previously.

Lee et al. [12] researched the possibility of turning food waste containing grain, vegetables, or meat into a fuel. Pyrolysis at temperatures ranging from 200 °C to 400 °C produced a product with calorific value ranging from 23.7 to 29.7 kJ/g, whose energy content did not lag behind Ghorbel [5] calorific value from cardboard pyrolysis of 22.8 to 26.8 kJ/g, Phan et al. [13] calorific value from waste wood char pyrolysis of 27.1 to 31.4 kJ/g, and Ryu et al. [14] calorific value from pine wood pyrolysis of 31.7 to 32.5 kJ/g. In other words, it is possible to recycle food waste compost into a solid fuel, unlike compost containing vegetable matter only.

Hence, after performing pyrolysis of food waste compost, this study aims to compare and analyze the calorific values and thermal degradation of biochar produced at pyrolysis temperatures in the range 300–500 °C. Gas chromatography and mass spectrometry (GC-MS) of gases generated from food waste and sawdust contained in compost will also be used to examine the value of biochar as an energy-storing fuel.

2. Materials and Methods

2.1. Materials

Food waste compost was collected from the Un-Jeong Environment Management Center, Paju-si, Gyeonggi-do, Korea. To remove large foreign matter, this study used food waste compost sieved through a 1.18 mm sieve.

The Un-Jeong Environment Management Center receives 20 tons of food waste from the region each day and washes it with water to remove salt. 10 tons of solid matter is obtained from the dehydrating process and is converted into compost in an aerobic composting tank. 1.1 tons of sawdust is added each day as a bulking agent. The aerobic composting tank goes through two stages. The 1st stage involves 14 days

of accelerated degradation, and the 2nd stage involves 20 days of maturation. The process produces 3 tons of compost every day.

2.2. Experimental Method

The experiment was carried out in four steps, including sample homogenization, pyrolysis, washing, and dehydration. Food waste compost was placed in a pyrolysis furnace at 300 °C, 400 °C, and 500 °C for 2 h. Nitrogen gas was added at 5 L/min to prevent oxidation. The 200 g of food waste compost sample was put in an open container with a width, length, and height of 5 cm, 20 cm, and 4.5 cm, and was then placed into the pyrolysis furnace. Figure 1 shows the reactor design.

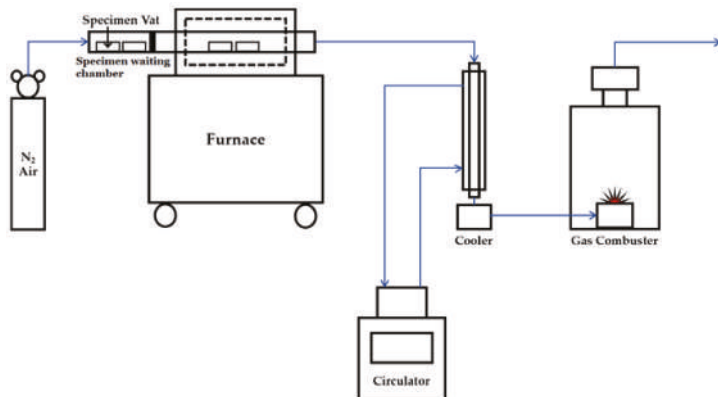


Figure 1. The pyrolysis reactor design diagram.

After the sample completed pyrolysis, it was cooled down to room temperature. Some portion of the sample was washed in distilled water at a 1:10 ratio for 30 min to remove any remaining salt, which is characteristic of Korean food waste. Biochar in the washed sample was separated using a 47 mm glass microfiber filters (Whatman, Maidstone, UK), and was dried again at 100 °C. Samples from each pyrolysis temperature were analyzed for chemical composition, thermal degradation behavior, calorific value, and gases released during pyrolysis. Whole experiment proceeded three times, and analysis results represent average values. This process allowed the food waste compost pyrolysis characteristics to be examined as a potential solid fuel. Sawdust was added to the food waste composting process as a bulking agent. Sawdust is not degraded well by microorganisms and is likely to remain in the compost. This study also compared sawdust with a compost samples when analyzing the characteristics of compost and pyrolysis biochar.

2.3. Analysis Method

To obtain the elemental composition of food waste compost and biochar after pyrolysis, this study used the CHNS analyser (2400 Series II CHNS, Perkin Elmer, Boston, MA, USA). The raw compost and sawdust were analyzed only once as it is considered homogeneous as it was made using a specimen in the form of fully blended and sieved powder. All the biochar samples obtained from the three times of experiments were analyzed, and average values are stated. This study measured the Cl content using the combustion ion chromatography (AQF-2100H, Mitsubishi Chemical Analytech, Chigasaki, Japan) to determine the salt content in food waste compost, as well as the amount of salt removed from the biochar. An atomic absorption photometer (AAnalyst400, PerkinElmer, Boston, MA, USA) was used to measure the Na content.

To measure the energy amount of the biochar, this study measured the calorific value using a calorimeter (6400Automatic Isoperibol Calorimeter, Parr, Moline, IL, USA). The thermal degradation behavior was

investigated with a thermogravimetric analyser (TGA), and the heating rate was set at 10 °C/min and 20 °C/min in different experiments. The balance purge and sample purge was nitrogen gas 40 mL/min, 20 mL/min each. GC injection temperature is 320 °C, and 520 °C. Gases generated during pyrolysis were analyzed using thermogravimetric analysis (TGA)—gas chromatography (GC)—mass spectrometry (MS), and based on TGA results, this study analyzed released gases during the highest weight loss period.

3. Results and Discussion

3.1. Characterization of Raw Material and Biochar

The chemical composition of the sawdust, food waste compost, and food waste is shown in Table 1. This study referenced other papers for data on food waste. Jo et al. [15] used mixed food produced according to the average composition of Korean food waste. Similar to this study, Zhang, Ruihong, et al. [16] were provided with food waste from a waste management company in Northern California. Kwon and Lee et al. [17] were provided with food waste from a university cafeteria in Seoul.

Table 1. Physical-chemical characterization of food waste compost and sawdust.

Sample	C	H	N	Moisture	Dry Basis			Reference
					Ash	Volatile	Fixed Carbon	
Food waste compost	29.7	4.3	2.9	21.6 ± 4.4	9.8	78.3	11.9	
Sawdust	24.4	2.9	-	28.6 ± 3.1	0.6	83.3	16.14	This study
Mixed food	47.5	12.2	2.9	85.7 ± 2.9	3.8 ± 0.1	79.0 ± 2.7	17.25	Jo et al. [15]
Food waste	46.8	-	3.2	-	-	85.3 ± 0.7	4.54	Zhang, Ruihong, et al. [16]
Cafeteria food waste	-	-	-	80.0 ± 2.3	1.3 ± 0.3	93.6 ± 1.9	-	Kwon and Lee et al. [17]

Carbon and volatile content in food waste compost were found to be lower than that of food waste in other studies because organic matter contained in food waste was degraded and volatilized by microorganisms through the composting process [18]. While the carbon content in food waste was greatly decreased, its nitrogen content did not change very much because nitrogen is a nutrient necessary for the growth of microorganisms and is absorbed into microorganisms to form their cells, while some nitrogen is degraded and volatilized into ammonia.

The carbon content in food waste compost decreased by about 40% compared with food waste down to 29.7%, which is twice as high as the 14.8% content in farm breeding compost from Ghorbel study [5]. Unlike Ghorbel's finding that farm breeding compost has little value as a fuel, food waste compost is more promising as a source of energy.

Food waste compost showed higher carbon and ash content than sawdust, but a lower moisture content. Notably, the amount of ash produced from sawdust was small, whereas, the ash content in food waste compost was more than 50 times higher. It was also higher than the content of food waste. The high ash content in food waste compost is due to the composting process, where the remaining inorganic matter that was not degraded after the organic matter is degraded and volatilized are concentrated. Table 2 shows the C, H, N, and S content in biochar produced after pyrolysis of food waste compost and the salt content analysis results:

Table 2. Element and salt content analysis of biochar at various pyrolysis temperatures.

(wt %)	C	H	N	S	Cl	Na
Compost	29.73	4.27	2.90	-	0.66	0.77
300 ¹	51.04 ± 0.11	5.53 ± 0.09	4.55 ± 0.09	-	0.18 ± 0.03	0.64 ± 0.02
300 ²	51.83 ± 0.16	5.39 ± 0.10	4.68 ± 0.22	-	1.13 ± 0.14	1.57 ± 0.12
400 ¹	48.67 ± 0.46	4.28 ± 0.09	3.74 ± 0.05	-	0.30 ± 0.03	1.11 ± 0.08
400 ²	47.58 ± 0.45	3.75 ± 0.74	3.25 ± 0.88	-	1.73 ± 0.03	1.91 ± 0.05
500 ¹	51.72 ± 1.31	2.24 ± 0.21	3.39 ± 0.31	-	1.03 ± 0.24	1.52 ± 0.01
500 ²	48.42 ± 0.55	1.94 ± 0.07	3.61 ± 0.39	-	2.52 ± 0.02	2.64 ± 0.00

¹ Washed biochar. ² Unwashed biochar.

According to the salt content of compost before pyrolysis, around 1.4% of the salt content remained, despite the fact it was washed to remove salt from the food waste before the composting process. It shows that washing raw food waste cannot completely remove salt content, even though some salt on the surface can be washed away, and additional treatment is required. In addition, salt remaining after washing is one of the primary factors that decreases its value as compost.

The Cl and Na content of biochar after pyrolysis of food waste compost increased as the pyrolysis temperature increased, which demonstrated that salt was not volatilized but concentrated during pyrolysis, while the organic matter was reduced in weight and volatile substances were released as gases. Na and Cl did not exist independently. Instead, they existed as solid NaCl. Therefore, salt was not volatilized during pyrolysis [19]. After washing, the Cl and Na content decreased rapidly, demonstrating that they were removed through washing after carbonization. The Na content after washing was relatively higher than the Cl content because some Na ions from washing water were absorbed due to biochar's cation exchange capacity (CEC) [17]. When the Cl content is high in combustion fuel, it can cause corrosion and boiler slagging, and it is regulated as it can produce hazardous substances such as hydrochloric acid (HCl) and polychlorinated dibenzodioxins (PCDD). The British-adopted European Standard (BS EN 15359: 2011) [20] for solid recovery fuel defines Grade 1 fuel as having a Cl content less than 0.2%, Grade 2 as less than 0.6%, and Grade 3 as less than 0.8%. The Cl content in biochar washed after pyrolysis at 300 °C to 400 °C was 0.18% and 0.3%, which put them into Grade 1 and Grade 2, respectively.

Another characteristic found in the table is the carbon content in biochar more than doubled compared to raw food waste compost. That content level is similar to or higher than that of food waste, which means that its possibility as a fuel is further increased. Its carbon, nitrogen, and hydrogen content all tended to decrease as the pyrolysis temperature increased because volatile substances were released as gases, and degradation and weight reduction occurred during pyrolysis.

Differences were also observed before and after washing. There were few differences at 300 °C, and differences increased as pyrolysis temperature increased. It seems that each element content per unit weight increased relatively as concentrated NaCl was removed during washing.

3.2. Thermogravimetric Analysis

To examine the thermal degradation behavior of food waste compost, sawdust and compost were analyzed with a TGA.

Figure 2a,b show TGA and DTG results for sawdust. The weight is reduced as moisture is evaporated at temperatures below 100 °C. If this range is excluded, there are two decomposition ranges: one from 275 °C to 360 °C, and another from 500 °C to 550 °C. Weight reduction in the range of 275 °C to 360 °C seems to be the result of hemi-cellulose decomposition [5,21] and lignin decomposition, which takes place gradually over temperatures ranging from 160 °C to 900 °C [22]. According to the thermal degradation behavior of pine sawdust in Ningbo Gao [23], hemi-cellulose decomposition took place at temperatures ranging from 225 °C to 375 °C, similar to the results found in this study. In the range of 500 °C to 550 °C, like the findings of Ulloa et al. [24], TGA-DTG results from coal and in radiated pine sawdust blend, weight reduction could be explained by the transition into aliphatic or aromatic compounds due to char decomposition and lignin volatilization.

According to the food waste kinetic study by Jo et al. [15], the key differential thermogravimetric (DTG) peaks in food waste were reached from 325 °C (10 °C/min) to 366 °C (20 °C/min) due to carbohydrate decomposition, and from 336 °C to 376 °C and from 399 °C to 446 °C due to protein and fat decomposition, and from 330 °C to 360 °C and from 200 °C to 500 °C due to cellulose and lignin decomposition. According to the DTG peaks in Figure 3 for food waste compost, there were two decomposition ranges of 250 °C to 370 °C and 500 °C to 560 °C, which were different from the results presented by Jo et al. The 250 °C to 370 °C temperature range was similar to the hemi-cellulose decomposition range (240 °C to 365 °C) described by Vamvukaa [21] and Ghorbel [5], whereas the 500 °C to 560 °C range was similar to the saturated fatty acid degradation range (480 °C to 550 °C) stated by Souza et al. [25] and the polypeptide decomposition range (500 °C or higher) described by Bihari-Varga et al. [26].

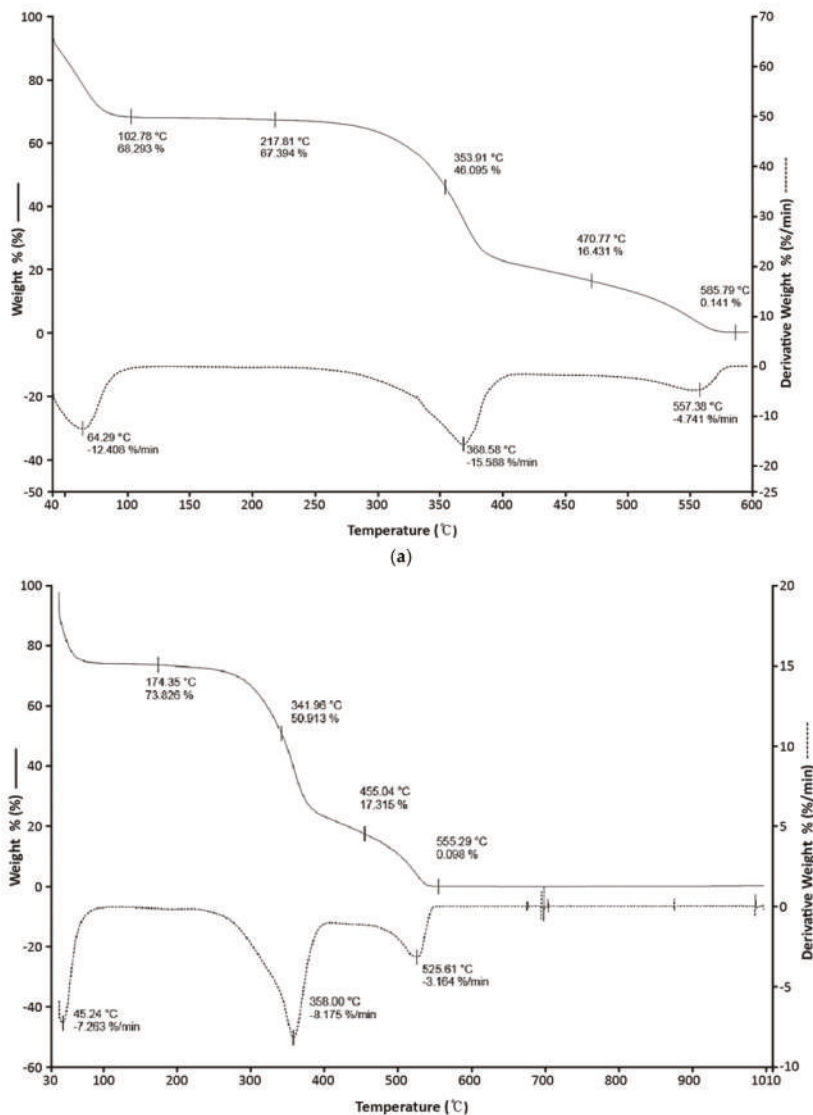


Figure 2. (a) Sawdust at 600 °C, 20 °C/min; (b) Sawdust 1000 °C, 10 °C/min.

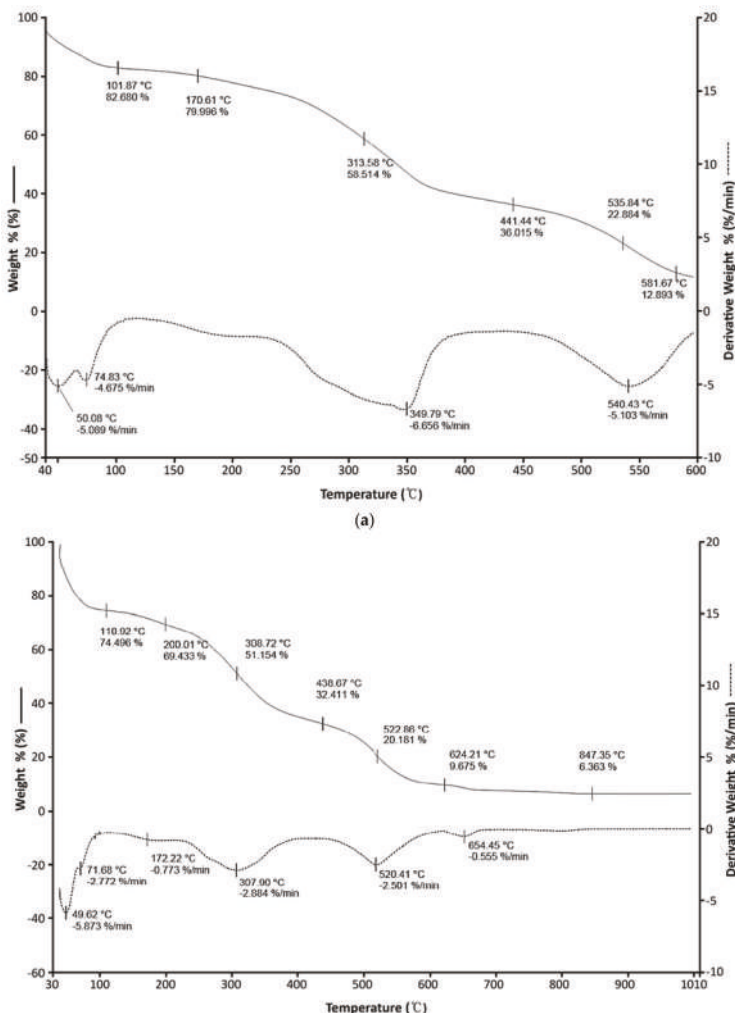


Figure 3. (a) Compost at 600 °C, 20 °C/min; (b) Compost at 1000 °C, 10 °C/min.

As mentioned earlier, these differences could be interpreted as a phenomenon that occurred as compost was degraded by microorganisms beforehand, even though the raw material properties were similar. Carbohydrates, proteins, and fat in food waste are digested by microorganisms during the composting process and are degraded into glucose, polypeptide, and fatty acids, or most of them convert into carbon dioxide or ammonia. In the end, small fractions of food waste remain in the final compost [18].

When the thermal degradation tendencies of sawdust and compost were compared, their decomposition took place in nearly the same temperature ranges. This happens when most of the food in food waste compost is degraded, and sawdust, which is not degraded, accounts for most of the compost. Their hemi-cellulose decomposition ranges of 275 °C to 360 °C and 250 °C and 370 °C were nearly identical. When their second decomposition ranges were compared, it was found that compost tended to be degraded more than sawdust. According to James [18], fat in food waste composting was degraded more slowly than protein or carbohydrate, and after 412 h

of composting, protein fractions were very low while fat fractions remained high. Hence, one can see that decomposition in compost is greater than sawdust because the decomposition of fatty acids, a byproduct of fat decomposition, and the decomposition of char, which also occurred in sawdust, took place simultaneously in the second decomposition range in food waste compost.

3.3. Mass Spectrometry Analysis

To analyze the gases released during the pyrolysis of sawdust and compost, this study performed a TGA-GC-MS analysis within the largest decomposition temperature range. Figure 4 show GC-MS peak results for gases released from the TGA process of compost and sawdust, and each peak is described in Tables 3 and 4. Since Si-C compounds found in sawdust and compost TGA-GC-MS results around 12~36 (min) in Figure 4 are influenced by moisture which is one of the emitted gases (H_2O , CH_4 , CO_2 , etc.) during the decomposition process into several smaller molecules [27], it was excluded from the interpretation. The Si-C compounds are not produced by the degradation of food waste compost. But the detection was inevitable since it is a GC column substance measured by the moisture generated by the food waste compost's decomposition affects the GC column.

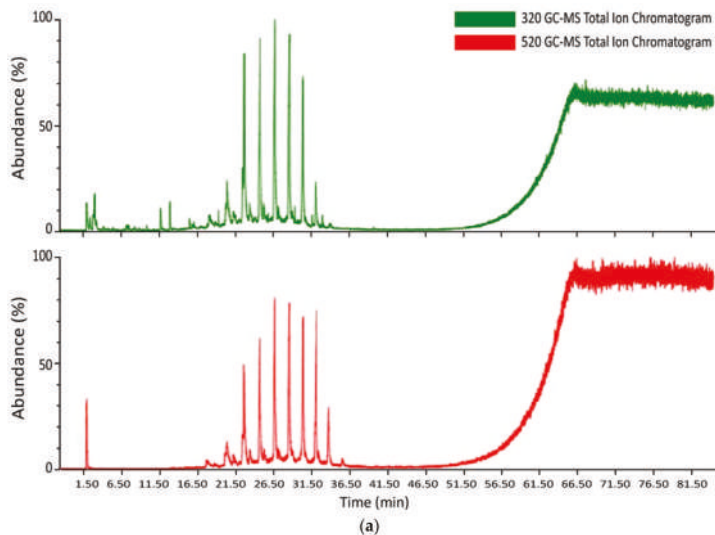


Figure 4. *Cont.*

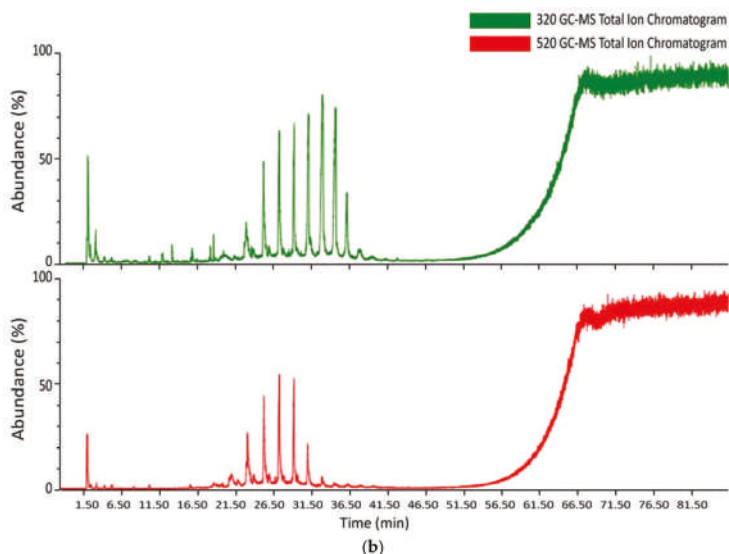


Figure 4. (a) Sawdust TGA-GC-MS results; (b) Compost TGA-GC-MS results.

Table 3. TGA-GC-MS analysis results for sawdust.

Temperature	Time (min)	MW	Compound Name	Formula
320 °C	1.973	130	thiocyanic acid, methylene ester	C ₃ H ₂ N ₂ S ₂
	2.279	122	Butanoic acid, 4-chloro	C ₄ H ₇ O ₂ Cl
	6.617	96	furfural	C ₅ H ₈ O ₂
	7.21	98	furanmethanol	C ₅ H ₈ O ₂
	8.503	84	2(5H)-furanone	C ₄ H ₆ O ₂

Table 4. TGA-GC-MS analysis results for compost.

Temperature	Time (min)	MW	Compound Name	Formula
320 °C	1.962	285	fumaric Acid 2-dimethylaminoethyl-heptyl ester (N-contain)	C ₁₅ H ₂₂ O ₄ N
	2.296	88	Thiophene, Tetrahydro	C ₄ H ₈ S
	6.634	96	1H-pyrazole, 3,4-dimethyl(C)	C ₅ H ₈ N ₂
	7.213	88	methylene cyclo propane carboxylic acid	C ₅ H ₈ O ₂
	8.497	84	2(5H)-furanone(C,P)	C ₄ H ₆ O ₂
	9.694	106	Benzaldehyde	C ₇ H ₆ O
	9.892	157	Glycine, N-Cyclopropylcarbonyl-methyl ester	C ₇ H ₁₁ O ₃ N
520 °C	2.356	202	1,3-propanediol, 2-methyl-dipropanoate(Fatty acids, aliphatic compounds)	C ₁₀ H ₁₈ O ₄
	2.866	78	Benzene	C ₆ H ₆
	3.334	258	oxalic acid butyl 2-Ethylhexyl ester(Fatty acids, aliphatic compounds)	C ₁₄ H ₂₆ O ₄
	5.764	214	pentanoic acid 2-Ethylhexyl ester	C ₁₃ H ₂₆ O ₂
	8.384	214	propanoic acid, 2,2-Dimethyl-2-Ethylhexyl ester	C ₁₃ H ₂₆ O ₂

Based on the TGA results, the TGA-GC-MS analysis was conducted at the biggest weight reduction range around 320 °C and around 520 °C. Sawdust analysis result in Table 3 shows most of the substances are emitted is furan groups. Furan organics were produced by hemi-cellulose decomposition [23,27]. Compared with TGA-GC-MS analysis result and sawdust TGA result at a 320 °C, detecting of furan groups at 320 °C is reasonable because a large weight loss at 320 °C is caused by the decomposition of hemi-cellulose. On the other hand, sawdust GC-MS results at 520 °C show that only Si-C compounds are detected. As in the TGA results, most weight loss is done at around 320 °C, so the amount of emission gases at around 520 °C appears to be small. Si-C compounds detected in this section indicates that the substances slight decomposition occurs, and moisture from

the light gas (H_2O , CH_4 , CO_2 , etc.) produced during the decomposition process seems to have affected the GC-MS results.

Food waste compost analysis result at 320 °C shows that furan groups are detected as in sawdust. This indicates that the sawdust contained in the compost is broken down and discharged. Fatty acids, which are generated from thermo-chemolysis of fat during the composting process, are detected in the form of methyl esters in pyrolysis gases, and include propanoic acids and 2,2-dimethyl-2-ethylhexyl esters. In addition, C12–C19 polymeric carbon compounds are also found as products of fatty acid degradation [28]. In particular, while C12–C19 carbon compounds could have simply come from fat fractions in food waste, they also could have originated from degradation by microorganisms. As compost includes many microorganisms in the final product, both of those possibilities are considered.

Smidt, Ena, et al. [29] detected m/z 202, 258 compounds as the decomposition products of fatty acids, or aliphatic compounds. Oxalic acid butyl 2-ethylhexyl esters, 1,3-propanediol, and 2-methyl-dipropanoate were detected in the TGA-GC-MS results. This confirmed that the second decomposition of food waste compost yielded fatty acids and aliphatic compounds, as mentioned in the TGA-DTG results. Nitrogen compounds, which are released by protein decomposition, were detected in the form of glycine and fumaric acid 2-dimethylaminoethyl-heptyl esters. Proteins in food waste, however, were not present with a high content in compost, and it seems that proteins were absorbed as elements essential for bacteria and microorganisms. In other words, they had been discharged by microorganism decomposition. In addition, low molecular weight compounds, such as benzene and benzaldehyde, are produced by microorganism pyrolysis [30], but they are also generated by lignin and hemi-cellulose decomposition. Therefore, it is difficult to track their exact origin.

3.4. Biochar Production

Table 5 shows biochar mass yield results. They were calculated by dividing the weight of the residue after pyrolysis by that of the input at each temperature.

Table 5. Food waste compost biochar yield.

Temperature (°C)	Before Pyrolysis (g)	After Pyrolysis (g)	Yield (%)
300	200.52 ± 0.38	88.52 ± 2.07	44.14 ± 0.95
400	200.32 ± 0.16	60.57 ± 0.04	30.24 ± 0.05
500	200.31 ± 0.12	45.09 ± 3.20	22.51 ± 1.61

As the pyrolysis temperature increased, the yield decreased by 14% from 300 °C to 400 °C, which was higher than the 8% decrease observed between 400 °C to 500 °C. The weight reduction was greatest from 300 °C to 400 °C as demonstrated in TGA results in Section 3.2.

Figure 5 compares the calorific values of food waste compost biochar, pre-pyrolysis raw material compost, and the food waste calorific values of Lee et al. [12] and Jo et al. [15]. Food waste compost showed 17.85 kJ/g, a lower calorific value than raw food waste 19.46 kJ/g, because the organic matter in food waste was degraded. As a result, the substances that increase the calorific value (e.g., carbon) was relatively lower. After pyrolysis, food waste compost has increased in the calorific value compared with raw food waste compost as the pyrolysis temperature changes from 300 °C to 500 °C. Considering a large amount of organic matter was degraded by microorganisms, the calorific value did not show a large decrease; sawdust played a supporting role. In fact, Chen and Leung [31] showed that sawdust had a calorific value of 18.064 kJ/g.

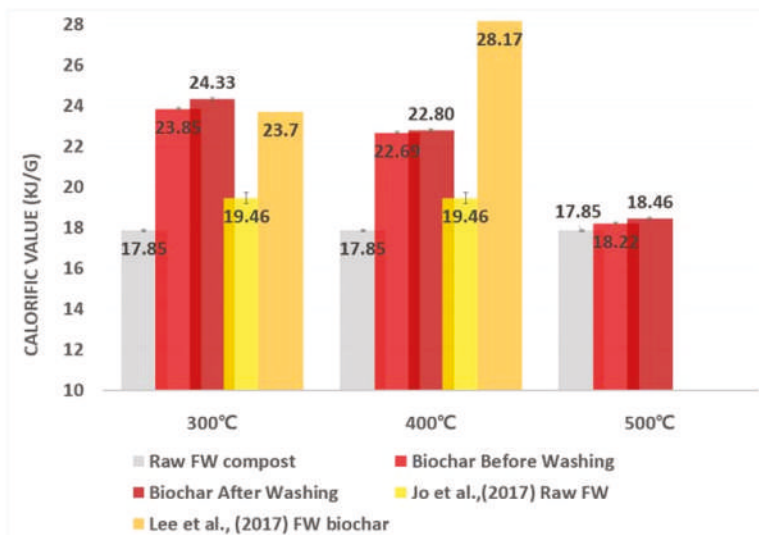
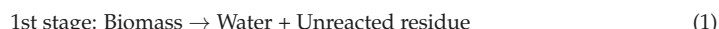


Figure 5. Calorific values of food waste compost biochar and raw material.

The calorific value of biochar, which was produced after pyrolysis of food waste compost, tended to decrease from 24.33 kJ/g to 18.46 kJ/g as the pyrolysis temperature increased. This tendency was also found in Ghorbel's study [5], in which the calorific value fell from 25.3 kJ/g to 22.8 kJ/g when the pyrolysis temperature increased from 250 °C to 350 °C and pyrolysis was performed for 2 h. By contrast, Lee et al. [12], who performed pyrolysis of food waste, found that the calorific value increased from 23.7 kJ/g to 28.17 kJ/g when the pyrolysis temperature rose from 200 °C to 400 °C. This occurs because Lee et al. [12] used food waste as a raw material, while this study used food waste compost. When raw food waste is used for pyrolysis, the carbon content increases as volatile substances and containing moistures are removed by supplied energy, and key components are carbonized [32]. Demirbas [33] interpreted the char generation process from biomass through pyrolysis with the following scheme:



In other words, while the raw food waste requires much energy for the 1st, 2nd, and 3rd stages, food waste compost has a lower moisture content and has already been degraded fracture by microorganisms. Therefore, the reaction at the 1st and 2nd stage can take place with lower energy. At 300 °C, Char 1 is produced and increases the calorific value. Since the compost has low volatile matter and water content, 300 °C is enough to conduct 1st and 2nd stage. But when the pyrolysis temperature increases, volatilization occurs in Char 1 and decreases the carbon content, the yield, and the calorific value.

In addition, in food waste compost, sawdust plays an important role in producing a calorific value. This is in contrast to raw food waste. As described in the TGA results, hemi-cellulose, a major component in sawdust, is degraded rapidly from 300 °C to 400 °C, and lignin and other components continue to be degraded at 400 °C or higher. Therefore, food waste compost shows a lower calorific value when the pyrolysis temperature increases from 300 °C to 500 °C.

Consequently, food waste compost already degraded by microorganisms has carbon fixation at a low pyrolysis temperature and produces a high calorific value. Sawdust, which plays an important role in producing the calorific value, shows little volatilization, and it shows a higher calorific value than food waste at 300 °C pyrolysis temperature.

4. Conclusions

This study intended to examine the value of biochar produced from pyrolysis of food waste compost as an energy storing fuel. Food waste compost had a lower carbon and higher ash content than food waste because the organic matter was degraded. This decreased the carbon content during the composting process, while the ash content increased relatively. Biochar from pyrolysis of food waste compost had a high carbon content of 51% at 300 °C, and the carbon content decreased as the pyrolysis temperature increased. According to the TGA-DTG analysis results, compost showed the largest weight reduction from 240 °C to 365 °C. The weight reduction temperature ranges for compost and sawdust were quite similar. This occurred because organic matter in food waste was degraded, and sawdust, which showed relatively lower degradation, remained during the composting process. A GC-MS analysis on gases released in these ranges found that the gases were fragments of fatty acids, protein, carbohydrate, and hemi-cellulose. These results could also have been caused by degradation of microorganisms and sawdust involved in the composting process or small fragments of food waste. This study measured the calorific value of biochar and found that biochar showed the highest calorific value of 24.33 kJ/g at 300 °C in proportion to the carbon content. At a low pyrolysis temperature, carbon fixation occurred easily since the food waste in compost was degraded by microorganisms, and the volatilization of sawdust, which plays an important role in determining the calorific value, was also small. That is why it showed a higher calorific value than food waste at 300 °C. Hence, it seems that food waste compost can be used as a promising alternative fuel compared with other refuse-derived fuels (RDF) since food waste compost is able to convert into a fuel that shows similar calorific values to other fuels with a smaller energy supply.

Author Contributions: J.-H.J. and Y.-S.Y. designed the experiment devices; Y.-S.Y., I.-T.K., and Y.-E.L. contributed to the analysis of experimental results; Y.-E.L. performed the experiments, analyzed the data, and wrote the paper.

Funding: This research was funded by the major project (2018-0063) of the Korea Institute of Civil engineering and building Technology (KICT).

Acknowledgments: This study was supported by the major project (2018-0063) of the Korea Institute of Civil engineering and building Technology (KICT).

Conflicts of Interest: The authors declare no conflict of interest.

References

- Lee, S.E.; Ahn, H.J.; Youn, S.K.; Kim, S.M.; Jung, K.W. Application effect of food waste compost abundant in NaCl on the growth and cationic balance of rice plant in paddy soil. *Kor. J. Soil Sci. Fertil.* **2000**, *33*, 100–108.
- Zhao, S.-X.; Ta, N.; Wang, X.-D. Effect of Temperature on the Structural and Physicochemical Properties of Biochar with Apple Tree Branches as Feedstock Material. *Energies* **2017**, *10*, 1293.
- Lee, J.J.; Park, R.D.; Kim, Y.W.; Shim, J.H.; Chae, D.H.; Rim, Y.S.; Sohn, B.K.; Kim, T.H.; Kim, K.Y. Effect of food waste compost on microbial population, soil enzyme activity and lettuce growth. *Bioresour. Technol.* **2004**, *93*, 21–28. [[CrossRef](#)] [[PubMed](#)]
- Ministry of Environment. *2015 Food Waste Treatment Facility Installation and Operation Status (Nationwide)*; Ministry of Environment: Sejong City, Korea, 2015.
- Ghorbel, L.; Rouissi, T.; Brar, S.K.; López-González, D.; Ramirez, A.A.; Godbout, S. Value-added performance of processed cardboard and farm breeding compost by pyrolysis. *Waste Manag.* **2015**, *38*, 164–173. [[CrossRef](#)] [[PubMed](#)]
- Williams, P.T. *Waste Treatment and Disposal*; John Wiley & Sons: New York, NY, USA, 2005.
- Brassard, P.; Godbout, S.; Raghavan, V.; Palacios, J.H.; Grenier, M.; Zegan, D. The Production of Engineered Biochars in a Vertical Auger Pyrolysis Reactor for Carbon Sequestration. *Energies* **2017**, *10*, 288. [[CrossRef](#)]

8. Imam, T.; Capareda, S. Characterization of bio-oil, syn-gas and bio-char from switchgrass pyrolysis at various temperatures. *J. Anal. Appl. Pyrolysis* **2012**, *93*, 170–177. [[CrossRef](#)]
9. Jahirul, M.I.; Rasul, M.G.; Chowdhury, A.A.; Ashwath, N. Biofuels production through biomass pyrolysis—A technological review. *Energies* **2012**, *5*, 4952–5001. [[CrossRef](#)]
10. Barneto, A.G.; Carmona, J.A.; Conesa Ferrer, J.A.; Diaz Blanco, M.G. Kinetic study on the thermal degradation of a biomass and its compost: Composting effect on hydrogen production. *Fuel* **2010**, *89*, 462–473. [[CrossRef](#)]
11. Ryu, C.; Finney, K.; Sharifi, V.N.; Swithenbank, J. Pelletised fuel production from coal tailings and spent mushroom compost—Part I: Identification of pelletisation parameters. *Fuel Process. Technol.* **2008**, *89*, 269–275. [[CrossRef](#)]
12. Lee, Y.-E.; Jo, J.-H.; Kim, S.-M.; Yoo, Y.-S. Recycling Possibility of the Salty Food Waste by Pyrolysis and Water Scrubbing. *Energies* **2017**, *10*, 210. [[CrossRef](#)]
13. Phan, A.N.; Ryu, C.; Sharifi, V.N.; Swithenbank, J. Characterisation of slow pyrolysis products from segregated wastes for energy production. *J. Anal. Appl. Pyrolysis* **2008**, *81*, 65–71. [[CrossRef](#)]
14. Ryu, C.; Sharifi, V.N.; Swithenbank, J. Waste pyrolysis and generation of storable char. *Int. J. Energy Res.* **2007**, *31*, 177–191. [[CrossRef](#)]
15. Jo, J.-H.; Kim, S.-S.; Shim, J.-W.; Lee, Y.-E.; Yoo, Y.-S. Pyrolysis Characteristics and Kinetics of Food Wastes. *Energies* **2017**, *10*, 1191. [[CrossRef](#)]
16. Zhang, R.; El-Mashad, H.M.; Hartman, K.; Wang, F.; Liu, G.; Choate, C.; Gamble, P. Characterization of food waste as feedstock for anaerobic digestion. *Bioresour. Technol.* **2007**, *98*, 929–935. [[CrossRef](#)] [[PubMed](#)]
17. Kwon, S.-H.; Lee, D.-H. Evaluation of Korean food waste composting with fed-batch operations I: Using water extractable total organic carbon contents (TOCw). *Process Biochem.* **2004**, *39*, 1183–1194. [[CrossRef](#)]
18. Chang, I.J.; Hsu, T. Effects of compositions on food waste composting. *Bioresour. Technol.* **2008**, *99*, 8068–8074. [[CrossRef](#)] [[PubMed](#)]
19. Lee, Y.-E.; Jo, J.-H.; Kim, I.-T.; Yoo, Y.-S. Chemical Characteristics and NaCl Component Behavior of Biochar Derived from the Salty Food Waste by Water Flushing. *Energies* **2017**, *10*, 1555. [[CrossRef](#)]
20. EN, BS. 15359: 2011 Solid Recovered Fuels. Specifications and Classes; BSI: London, UK, 2011; p. 30.
21. Vamvuka, D.; Kakaras, E.; Kastanaki, E.; Grammelis, P. Pyrolysis characteristics and kinetics of biomass residuals mixtures with lignite ☆. *Fuel* **2003**, *82*, 1949–1960. [[CrossRef](#)]
22. Yang, H.; Yan, R.; Chen, H.; Lee, D.H.; Zheng, C. Characteristics of hemicellulose, cellulose and lignin pyrolysis. *Fuel* **2007**, *86*, 1781–1788. [[CrossRef](#)]
23. Gao, N.; Li, A.; Quan, C.; Du, L.; Duan, Y. TG-FTIR and Py-GC/MS analysis on pyrolysis and combustion of pine sawdust. *J. Anal. Appl. Pyrolysis* **2013**, *100*, 26–32. [[CrossRef](#)]
24. Ulloa, C.A.; Gordon, A.L.; García, X.A. Thermogravimetric study of interactions in the pyrolysis of blends of coal with radiata pine sawdust. *Fuel Process. Technol.* **2009**, *90*, 583–590. [[CrossRef](#)]
25. De Souza, A.G.; Santos, J.C.O.; Conceição, M.M.; Silva1, M.C.D.; Prasad, S. A thermoanalytic and kinetic study of sunflower oil. *Braz. J. Chem. Eng.* **2004**, *21*, 265–273. [[CrossRef](#)]
26. Bihari-Varga, M.; Sepulchre, C.; Moczár, E. Thermoanalytical studies on protein-polysaccharide complexes of connective tissues. *J. Therm. Anal. Calorim.* **1975**, *7*, 675–683. [[CrossRef](#)]
27. Gu, X.; Ma, X.; Li, L.; Liu, C.; Cheng, K.; Li, Z. Pyrolysis of poplar wood sawdust by TG-FTIR and Py-GC/MS. *J. Anal. Appl. Pyrolysis* **2013**, *102*, 16–23. [[CrossRef](#)]
28. Som, M.-P.; Lemée, L.; Amblès, A. Stability and maturity of a green waste and biowaste compost assessed on the basis of a molecular study using spectroscopy, thermal analysis, thermodesorption and thermochemolysis. *Bioresour. Technol.* **2009**, *100*, 4404–4416. [[CrossRef](#)] [[PubMed](#)]
29. Smidt, E.; Eckhardt, K.U.; Lechner, P.; Schulten, H.R.; Leinweber, P. Characterization of different decomposition stages of biowaste using FT-IR spectroscopy and pyrolysis-field ionization mass spectrometry. *Biodegradation* **2005**, *16*, 67–79. [[CrossRef](#)] [[PubMed](#)]
30. Simmonds, P.G. Whole microorganisms studied by pyrolysis-gas chromatography-mass spectrometry: Significance for extraterrestrial life detection experiments. *Appl. Microbiol.* **1970**, *20*, 567–572. [[PubMed](#)]
31. Chen, G.; Leung, D.Y.C. Experimental investigation of biomass waste, (rice straw, cotton stalk, and pine sawdust), pyrolysis characteristics. *Energy Sources* **2003**, *25*, 331–337. [[CrossRef](#)]

32. Kim, K.-S.; Choi, E.-A.; Ryu, J.-S.; Lee, Y.P.; Park, J.-Y.; Choi, S.-H.; Park, S.-J. A study on pyrolysis characterization and heating value of semi-carbonized wood chip. *Appl. Chem. Eng.* **2012**, *23*, 440–444.
33. Demirbas, A. Effects of temperature and particle size on bio-char yield from pyrolysis of agricultural residues. *J. Anal. Appl. Pyrolysis* **2004**, *72*, 243–248. [[CrossRef](#)]



© 2018 by the authors. Licensee MDPI, Basel, Switzerland. This article is an open access article distributed under the terms and conditions of the Creative Commons Attribution (CC BY) license (<http://creativecommons.org/licenses/by/4.0/>).

Article

Advanced One-Dimensional Entrained-Flow Gasifier Model Considering Melting Phenomenon of Ash

Jinsu Kim ¹, Hyunmin Oh ², Seokyung Lee ¹ and Young-Seek Yoon ^{2,*}

¹ Department of Chemical Engineering, Pohang University of Science and Technology (POSTECH), Pohang 37673, Korea; jinsukim1102@postech.ac.kr (J.K.); lsylove0626@postech.ac.kr (S.L.)

² Graduate Institute of Ferrous Technology, Pohang University of Science and Technology (POSTECH), Pohang 37673, Korea; min0808@postech.ac.kr

* Correspondence: ysyoon@postech.ac.kr; Tel.: +82-54-279-0149; Fax: +82-54-279-0138

Received: 3 March 2018; Accepted: 17 April 2018; Published: 21 April 2018

Abstract: A one-dimensional model is developed to represent the ash-melting phenomenon, which was not considered in the previous one-dimensional (1-D) entrained-flow gasifier model. We include sensible heat of slag and the fusion heat of ash in the heat balance equation. To consider the melting of ash, we propose an algorithm that calculates the energy balance for three scenarios based on temperature. We also use the composition and the thermal properties of anorthite mineral to express ash. gPROMS for differential equations is used to solve this algorithm in a simulation; the results include coal conversion, gas composition, and temperature profile. Based on the Texaco pilot plant gasifier, we validate our model. Our results show good agreement with previous experimental data. We conclude that the sensible heat of slag and the fusion heat of ash must be included in the entrained flow gasifier model.

Keywords: Texaco pilot plant; reactor modelling; ash fusion temperature (AFT); melting phenomenon

1. Introduction

Generally, an entrained flow gasifier (EFG) uses finely pulverized coal with steam and oxygen co-current to make syngas. This design forms a uniform internal temperature, and has a residence time of only a few seconds [1]. The coal conversion reaches approximately 100%, because the gasifiers use pulverized coal at high temperature. An EFG is not affected by the rank of the coal [2]. Currently many commercial EFGs are operated by enterprises such as (General Electric) GE, Shell, Siemens, CB&I, MHI and ThyssenKrupp [3]. These types of gasifiers are operated at a temperature higher than the AFT. The ash, which is a coal residue, is discharged in the form of molten slag. The slag that is discharged to the bottom has a considerable amount of sensible heat. The design of the gasifier should consider this heat, because it affects the internal maximum temperature.

Existing EFG models [4–6] focus on calculating the composition of the gas. To improve the model, representations of the reaction mechanism of coal have been improved. Previous models have proposed various reaction kinetic models, such as random pore model [7], shrinking core model [8,9], and shrinking sphere model [10]. In addition, equilibrium models have been suggested calculating the reaction between gases [11–14]. Most of the studies [7–13,15] have focused on developing reaction models and adjusting parameters. The energy balance is not considered sufficiently to find the optimal gasifier design. They have developed heat balance with two variables: (i) input and output heat flow; and, (ii) reaction heat.

The Texaco pilot plant is a typical EFG. Several studies (Table 1) [4–6,16,17] have attempted to model it based on experimental data [18] acquired from the Electric Power Research Institute (EPRI). Wen et al. (1979) proposed a model that uses three reaction zones: (i) pyrolysis and volatile combustion zone; (ii) combustion and gasification zone; and, (iii) only gasification zone; the model applies a

Stokes' law approximation instead of momentum balance [16]. Govind and Shah (1984) used the same kinetics as those of Wen et al., but neglected the momentum balance [17]. Vamvuka et al. (1995) used thermogravimetric analysis data to develop the kinetics based on bituminous coal, but does not consider the momentum balance [4,5]. Hwang et al. (2015) expressed two reaction zones without considering the 'pyrolysis and volatile combustion' zone; this model applies the Stokes' law approximation, and adjust parameters, such as outer wall temperature and the reaction rate constant [6].

Table 1. Texaco pilot plant entrained flow gasifier (EFG) model based on the Electric Power Research Institute (EPRI) data.

Researcher	Kinetics	Momentum	Energy Balance
Wen et al.	3 reaction zones	Stokes' law approximation	Thermal
Govind and Shah	3 reaction zones	Not considered	Thermal
Vamvuka et al.	Parameter based on thermogravimetric analysis	Not considered	Thermal
Hwang et al.	2 reaction zones	Stokes' law approximation	Thermal

All of these models of the EFG have limitations. For energy balance, they all consider only input and output heat flow, and reaction enthalpy; they neglect energy that is absorbed by the melting of ash, and therefore do not accurately represent the inside of the gasifier in the real world. As a result, the calculated temperature is too high. For this purpose, previous papers introduce an additional term that represents heat loss to the outer wall. This calculation of heat loss requires assumptions about variables such as wall temperature, overall heat transfer coefficient, and thermal conductivity. These assumptions decrease the accuracy of the models.

The objective of this study is to improve the existing one-dimensional EFG model by including the ash-melting phenomenon instead of approximating it as heat loss at the outer wall. We propose a model to increase the accuracy of the temperature profile. The resulting model can predict the composition change of the product gas. We apply a shrinking sphere model to consider the combustion reaction, and then suggest reaction kinetics to calculate the amount of ash. We also design a new algorithm to consider the melting phenomenon of ash to improve the accuracy of the predicted temperature profile. We discuss the energy balance equation in three cases, according to the temperature: (i) temperature is lower than AFT; (ii) temperature in the first cell is higher than AFT; and, (iii) temperature in the second cell is higher than AFT. Finally, we compare the simulation results with the experimental results.

2. EFG Model

2.1. Basic Assumptions

To build the model, we assumed that:

- The inside of the gasifier is cylindrical; this assumption is suitable for modeling the Texaco EFG [17].
- Coal and gas mass flow rates are constant.
- Temperature and gas concentration are uniform in the radial direction.
- Each cell is perfectly mixed.
- The reactor consists of equally divided cells (Figure 1). The reaction rate depends on each cell's conditions.
- Spherical coal particles react from the outer surface while moving through the cell from front to end. As the reaction of the coal progresses, the size of the particles decreases.
- All of the coal grains in the same cell are uniform.

- Ash changes to slag after temperature exceed an AFT.
- Ashes are inert.

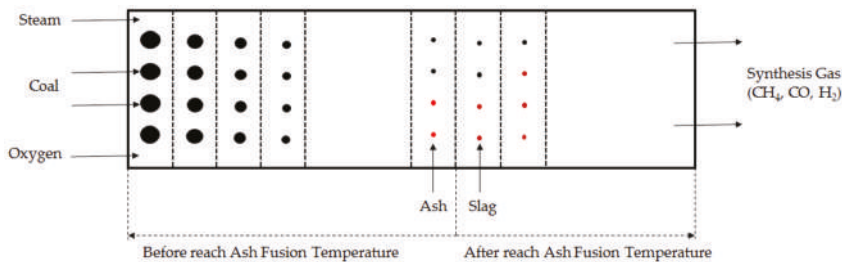


Figure 1. Gasifier internal scheme that considers melting of ash. Red dot: ash; brown dot: slag.

2.2. Reaction Kinetics

The reaction type can be divided into a heterogeneous reaction and a homogeneous reaction. The heterogeneous reaction indicates that the coal particles react with the gas. Coal reacts with oxygen, carbon dioxide, steam, and hydrogen (Table 2). The water gas shift reaction (WGS) and CO oxidation were considered as major reactions. The WGS reaction proceeds rapidly at a high temperature, and was therefore considered to be at equilibrium. CO oxidation was regarded as irreversible; as a consequence, gasification and combustion reaction could be expressed without dividing the reaction zone. Therefore, we solved reaction kinetics based on the single reaction zone; i.e., the six reaction schemes that are presented below were considered equally from the first cell to the last cells. The EFG does not produce much methane [19], so the methane–steam reforming reaction was not considered in this model.

Table 2. Homogeneous and heterogeneous reaction list used in this study.

Reaction Type	Reaction	Description
Heterogeneous	$R_1 : C_a H_b O_c N_d S_e A_f + \left(\frac{a}{\phi} + \frac{b}{4} - \frac{c}{2} - \frac{e}{2} \right) O_2 \rightarrow \left(\frac{2}{\phi} - 1 \right) aCO_2 + 2 \left(1 - \frac{1}{\phi} \right) aCO + \left(\frac{b}{2} - e \right) H_2O + eH_2S + \frac{d}{2} N_2 + fA$	Coal \rightarrow O ₂
	$R_2 : C_a H_b O_c N_d S_e A_f + aCO_2 \rightarrow 2aCO + cH_2O + \left(\frac{b}{2} - c - e \right) H_2 + eH_2S + \frac{d}{2} N_2 + fA$	Coal \leftrightarrow CO ₂
	$R_3 : C_a H_b O_c N_d S_e A_f + (a - c)H_2O \rightarrow aCO + \left(a + \frac{b}{2} - c - e \right) H_2 + eH_2S + \frac{d}{2} N_2 + fA$	Coal \leftrightarrow H ₂ O
	$R_4 : C_a H_b O_c N_d S_e A_f + \left(2a - \frac{b}{2} + c - e \right) H_2 \rightarrow aCH_4 + cH_2O + eH_2S + \frac{d}{2} N_2 + fA$	Coal \leftrightarrow H ₂
Homogeneous	$R_5 : CO + H_2O \leftrightarrow CO_2 + H_2$	WGS
	$R_6 : CO + \frac{1}{2} O_2 \rightarrow CO_2$	CO oxidation

* ϕ is a function of absolute temperature T , and adjusts the ratio of complete and incomplete combustion.

$$\phi = \frac{2w+2}{w+2}, w = 2500 \cdot \exp\left(-\frac{6249}{T}\right). [4].$$

To incorporate the coal components in reaction kinetics, the ultimate analysis was applied. The reaction kinetics (Table 3) of coal used in this study was based on Hwang et al.'s work. One difference is that we have attempted to quantify ash. We introduce subscript f , which means that the ash component contained in 1 g of coal, and is the result of the proximate analysis. The subscripts a through e represent elements contained in 1g of coal. For heterogeneous reactions, the reaction rate of coal was proportional to both the surface area of the coal particles and the partial pressure of each gas. In homogeneous reactions, all of the gases were assumed to be ideal.

Table 3. Reaction kinetics and parameters that were used in this study.

action Type	Reaction Rate (g/s)	k (g/(m ² ·atm·s))	Reference
Heterogeneous	$k_1\pi d_c^2 P_{O_2}$	$6180 \cdot e^{(-\frac{10,233.9}{T})}$	[5,6]
	$k_2\pi d_c^2 P_{CO_2}$	$198, 100 \cdot e^{(-\frac{10,233.9}{T})}$	
	$k_3\pi d_c^2 P_{H_2O}$	$198, 100 \cdot e^{(-\frac{10,233.9}{T})}$	
	$k_4\pi d_c^2 P_{H_2}$	$385 \cdot e^{(-\frac{17,451.7}{T})}$	
Equilibrium	Equilibrium Constant	Reference	
Homogeneous	$K = \frac{P_{CO_2} P_{H_2}}{P_{CO} P_{H_2O}}$	$-2.4198 + 0.003855 \cdot T + \frac{2180.6}{T}$	[20]
	Reaction Rate (mole/s)	k (m ³ /(mole·s))	Reference
	$k_6 C_{CO} C_{CO_2}$	$3.09 \cdot e^{(-\frac{11,199}{T})}$	[21]

3. Solving Procedure

3.1. Mass Balance

For mass balance, only production and consumption due to the reaction were calculated. The kinetics of the coal reaction was based on one coal grain. The number of coal particles per unit volume came from the following Equation (1):

$$N_v = \frac{W_{c,0}}{m_c v_c A} \quad (1)$$

The four coal reactions caused the coal conversion when the coal particles passed through the unit cell. Δz is unit cell length. The change of coal mass was calculated as

$$\Delta W_c = -N_v \cdot A \sum_{i=1}^4 R_i \cdot \Delta z \quad (2)$$

Mass balance of the ash could be expressed in the same way as that of coal. The only difference is that the stoichiometric coefficients f are added. The stoichiometric coefficients that correspond to ashes were all equal to f (Equation (3)). For slag, the mass balance was not considered separately. When the temperature was higher than AFT, ash was regarded as slag.

$$\Delta W_a = -N_v \cdot A \sum_{i=1}^4 R_i \cdot f \cdot \Delta z \quad (3)$$

For gas mass balance, R_5 and R_6 were also included. R_6 is irreversible, so it was applied in the same manner as the heterogeneous reactions. α means the degree of deviation from equilibrium. To calculate α , we used Equation (4)

$$K = \frac{(F_{CO_2} - \alpha) \cdot (F_{H_2} - \alpha)}{(F_{CO} + \alpha) \cdot (F_{H_2O} + \alpha)} \quad (4)$$

After converting this to an explicit form, we took a small root of the quadratic equation. The reason was that large roots make the mole flow negative.

Equation (5) is the mass balance of gases where ξ_i is a stoichiometric coefficient for each component. Heterogeneous and homogeneous reactions were considered in different forms. The terms

on the right side of the equation mean in order: (i) initial value; (ii) heterogeneous reactions; (iii) CO oxidation; and, (iv) each cell reaches equilibrium.

$$F_i = F_{i,0} - \left(N_v \cdot A \cdot \Delta z \cdot \sum_{j=1}^4 \xi_{i,j} \cdot \frac{R_j}{MW_i} \right) + (R_5 \cdot \xi_{i,5}) \pm \alpha \quad (5)$$

3.2. Energy Balance

Heat flow of input and output and reaction enthalpy were considered equally in all cells. In some existing models [5,6,16,17], oxygen, steam, and coal temperature were set differently. When the temperatures of coal and gas are separately calculated, the temperature difference between them is generally ~10 K [22]. In this study, we simplified the problem by assuming that the gas temperature was the same as the coal temperature.

Coal residue is ash or slag depending on temperature condition (Figure 1). To consider ash melting, energy balance was calculated by dividing it into three cases. At temperature <AFT, Equation (6) was applied. It did not incorporate the fusion heat of ash.

$$\Delta \left\{ \left(W_c \cdot c_{p,c} + W_a \cdot c_{p,a} + W_s \cdot c_{p,s} + \sum_i F_i \cdot c_{p,i} \right) T \right\} = -N_v \cdot A \cdot \sum_{j=1}^6 R_j \cdot \Delta H_j - H_{loss} \quad (6)$$

Cells with temperature >AFT were considered using Equations (7) and (8). Equation (7) was applied only to the first cell, which has temperature >AFT. This equation calculates all of the latent heat of the accumulated ashes.

$$\Delta \left\{ \left(W_c \cdot c_{p,c} + W_a \cdot c_{p,a} \cdot W_s \cdot c_{p,s} + \sum_i F_i \cdot c_{p,i} \right) T \right\} = -N_v \cdot A \cdot \sum_{j=1}^6 R_j \cdot \Delta H_j + W_a \cdot \Delta H_{ash} - H_{loss} \quad (7)$$

Equation (8) was applied to the remaining cells. It considers the heat of fusion of ash that occurs as it passes through each cell.

$$\Delta \left\{ \left(W_c \cdot c_{p,c} + W_a \cdot c_{p,a} \cdot W_s \cdot c_{p,s} + \sum_i F_i \cdot c_{p,i} \right) T \right\} = -N_v \cdot A \cdot \sum_{j=1}^6 R_j \cdot \Delta H_j + \Delta W_a \cdot \Delta H_{ash} - H_{loss} \quad (8)$$

Calculation of the heat loss must consider radiation, convection, and conduction. In addition, the thermal conductivity varies depending on the material of the refractory. If these cannot be reasonably estimated, the overall heat transfer coefficient will produce large errors. In a previous study, the heat transfer coefficient was indirectly estimated instead of calculating the heat loss [6,16,17]; the authors claimed that 30% of the reaction heat was lost to the outer wall, and that the corresponding calorific value is about 7–10% of the heating value of coal. However, heat losses typically considered in an EFG range from 1 to 4% [23,24]. This value is dependent on the gasifier scale. When compared with industrial gasifiers, pilot-scale gasifiers have higher heat losses. Therefore, we assumed a heat loss of 4%.

3.3. Solving Algorithm

The length of the gasifier was divided into 1650 cells (500 parts/m). Each cell was a system. Mass and energy balance were calculated sequentially. The computational algorithm was terminated when it reached the end of the reactor, and we obtain a sufficiently smooth curve in the simulation result. The information calculated in each cell was as follows:

- Information about coal: coal conversion, coal mass flow rate.
- Molar flow rate of product gas.
- Temperature profile.

The proposed algorithm (Figure 2) was designed to apply the energy balance of three cases according to temperature. gPROMS simulation software (Process Systems Enterprise Ltd., London, UK) was used to perform the algorithm. The DASolver was applied; it could be used to solve differential equations in the steady state. Both the relative tolerance and absolute tolerance were fixed as 1.0×10^{-5} .

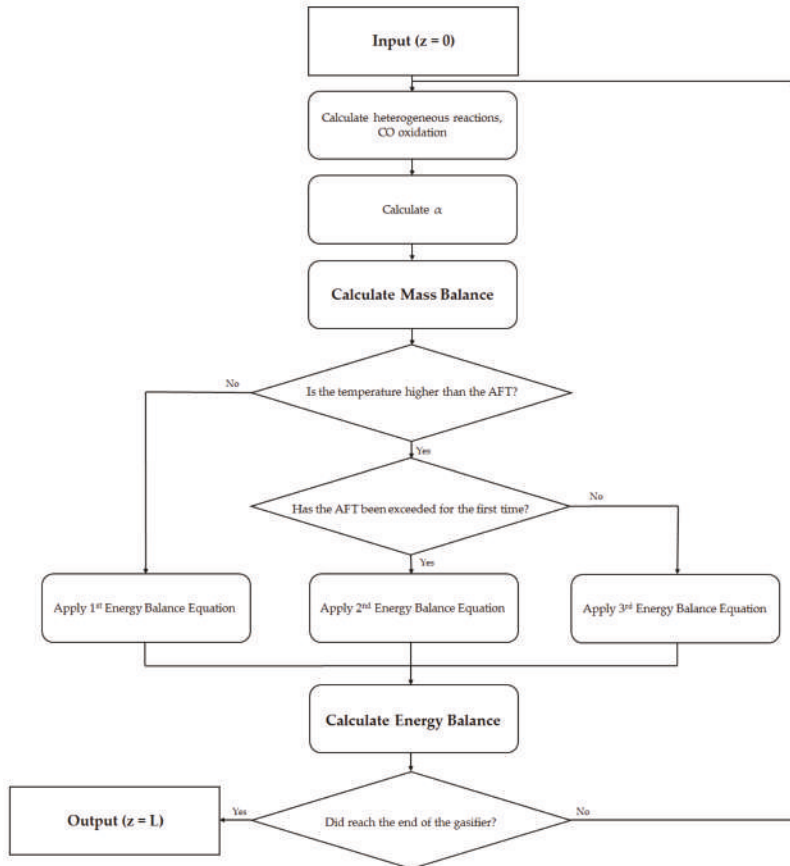


Figure 2. Algorithm that includes the melting of ash.

4. Required Information for Simulation

4.1. Operating Variables and Reactor Size

Required inputs, including operating variables and particle sizes (Table 4), were those of the existing pilot gasifier. These results were compared with those of previous studies. The experimental conditions were presented in the work of Govind and Shah, which is the same as for their simulation conditions. Experimental information on the outer wall temperature of the gasifier was not provided. The existing model assumed that the temperature of the outer wall started at 2100 K, and then decreased linearly [16,17]. We indirectly estimated the amount of heat loss from the coal heating value, instead of assigning an initial outer wall temperature.

Table 4. Comparison of operating variables and gasifier size between this and previous studies.

Operating Variables	This Work	Wen	Govind
Coal feed rate (g/s)	50	75	77
Steam to coal ratio (-)	0.24	0.24	0.241
Oxygen to coal ratio (-)	0.86	0.86	0.86
Feed coal temperature (K)	900	900	505
Feed gas temperature (K)	900	900	697(H ₂ O), 298(O ₂)
Gasifier pressure (MPa)	2.0	2.0	2.4
Gasifier wall temperature (K)	Not considered	2100–600(Z/L)	2100–600(Z/L)
Gasifier Size	This Work	Wen	Govind
Gasifier length (cm)	330	330	330
Inner diameter (cm)	152	152	152

4.2. Coal Properties

This study considered Illinois no. 6 coal, which is the same type using previous modeling studies. The results (Table 5) of coal elemental analysis were acquired from the EPRI [18]. Density and specific heat capacity of the coal were the same as in previous work [16,17]. We considered a smaller particle size (41 μm) of coal than did previous work, for two reasons. First, 41 μm is closer to the size of the particles that were used in the EFG in real industry; particularly, when entering a dry feed, the particle size is < 100 μm [25]. Second, the reaction of coal is directly related to particle size and kinetic parameters, so particle size is an important factor in kinetics. Therefore, the kinetic parameter and particle size must be taken from the same reference. We used the same kinetics parameters and the coal particle size as Hwang's model [6].

Table 5. Element analysis (wt %), coal properties, and feed conditions that were used in this study.

Element	Measurement
C	74.05
H	6.25
O	1.32
N	0.71
S	1.77
Ash	15.33
Coal Properties	Assumed
Density (g/cm ³)	1.80
Specific heat capacity (cal/(g·K))	0.45
Feed Conditions	Set
Feed particle size (μm)	41
Velocity (cm/s)	50

4.3. Ash and Slag Properties

The EPRI provided only the coal analysis data; it does not provide information about ash. One way to remedy this lack of information is to assume the ash component. However, the physical properties differ depending on the ash component. Calculate of thermal properties that consider its components is a difficult task. In some documents [26,27], a formula for predicting thermal properties according to the temperature have been proposed. However, they were out of the range of gasifier operating temperature.

In this study, different approaches were used. Coal ashes are composed of minerals (Figure 3). About 70–90% of the constituents are CaO, Al₂O₃, and SiO₂. They also include such as Fe₂O₃ and MgO [28,29]. In this work, we adopt the thermal properties of gehlenite (Figure 3) to represent ash.

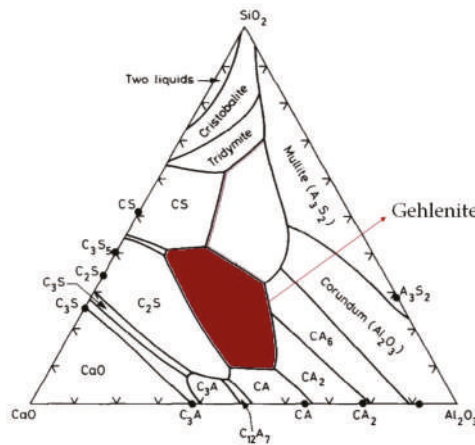


Figure 3. Ternary phase diagram of Al₂O₃-CaO-SiO₂. Brown: gehlenite.

The properties (Table 6) of ash and slag used in this study were obtained from the literature because the ash was considered to be a well-known mineral, and its thermal properties were set accordingly.

Table 6. Thermal properties of ash and slag used in this study.

Thermal Properties	Value	Reference
Fusion heat of ash (J/g)	627.6	[30]
Ash fusion temperature (K)	1863	[30]
Specific heat capacity of ash (J/(g·K))	$-0.976 + \ln T + \frac{279}{T} - \frac{1.094 \cdot 10^5}{T^2} + \frac{1.169 \cdot 10^7}{T^3}$	[31]
Specific heat capacity of slag (J/(g·K))	1.15	[32]

5. Results and Discussion

5.1. Model Validation

To validate the model, several main variables were selected: final coal conversion rate; major product gas composition at exit; and, the hydrogen-to-carbon monoxide ratio (H₂/CO). The results (Table 7) of this simulation are presented together with the results of the previous researchers and experimental data. We did not arbitrarily adjust the kinetic parameters that were used in this study. We applied the same reactor size and operating conditions of the existing pilot gasifier. For this reason, results of this work were similar to results of previous studies. In addition, we considered the melting phenomenon of ash that was not considered in the existing one-dimensional (1-D) model and reduced the estimated heat loss in the previous model. As a result, the modeling results are improved.

Table 7. Simulation results and comparison of previous models with experimental data (Dry based).

Major Variables	This Work	Wen [16]	Govind [17]	Experiment [17]
Conversion (%)	98.8	98.9	98.1	98.6
H ₂ (mole %)	38.6	39.8	40.0	39.1
CO (mole %)	57.7	56.6	55.5	57.6
H ₂ /CO ratio	0.668	0.703	0.721	0.679
CO ₂ (mole %)	2.56	2.92	3.95	2.95

5.2. Simulation Results

5.2.1. Coal Conversion

Most of the reaction proceeded rapidly at the front of the gasifier (Figure 4). Only 10% of coal was reacted at around 0.15 m of the gasifier, but 80% had reacted at 0.24 m. This increase occurred because the combustion reactions were accelerated. The reaction rate of coal decreased as the size of coal particles decreased. Especially after oxygen was completely consumed, the reaction rates were very slow. This trend is characteristic of typical EFGs; it is consistent with the results in past research [5,6,16]. The final coal conversion was 98.8%.

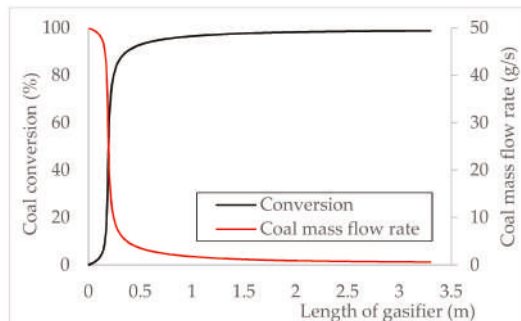


Figure 4. The profile of the coal conversion and coal mass flow rate.

5.2.2. Gas Composition

The mole fractions of the major gases changed over the reactor length (Figure 5). Oxygen was abruptly consumed near 0.25 m; this change is the result of rapid combustion. Syngas was generated in an oxygen-free environment. Steam was slightly generated in the front of the gasifier; afterwards, the proportion of steam was controlled by WGS equilibrium. After all of the oxygen was consumed, the gas composition did not change significantly. CH₄, H₂S, and N₂ were < 1% of the product; they are not represented in Figure 5. Trends in the graph agreed with trends that were reported in previous research [5,6,16]. The exit gas consists mainly (mole fraction 98.9%) of carbon dioxide, hydrogen, steam, and carbon monoxide. All of these compositions are determined by WGS equilibrium, which is a function of temperature and is closely related to the outlet temperature of the gasifier. The attempt to calculate the temperature is the first step in predicting the composition of the gas, and this study is significant in that respect.

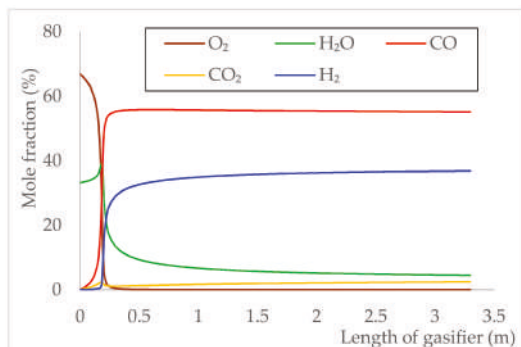


Figure 5. The profile of the major product gas mole fraction.

5.2.3. Temperature and Heat Flow

Simulations were used to calculate two temperature profiles (Figure 6). The heat balance of the first case (Figure 6, blue line) considered the sensible heat of the slag and the latent heat of the ash. The second case (Figure 6, red line) neglected these phenomena; both were set to 0. Below AFT, the temperatures of the two cases were the same, but the peak and outlet temperatures differed between the two cases. The same results were obtained in the temperature range below AFT; they are acceptable because the melting of ash had not yet been considered. The maximum temperature was calculated as 2112 K when sensible heat of the slag and the latent heat of the ash were considered, but 2155 K when they were neglected. The exit temperatures were 1464 K when the sensible heat of the slag and the latent heat of the ash were considered, and 1521 K when they were neglected; the difference between the two outlet temperatures was 57 K. The difference can be explained, as follows. The heat capacity of ash and slag is not taken into account in the system, and the corresponding energy was transferred to the gas, so the calculated temperature increased. Previous models have released heat to outside. EFGs generally use thick refractories. The assumption that a significant amount of heat escapes to the outside must be modified: these two temperature profiles show that the ash melting phenomenon must be considered when the internal temperature of the gasifier is calculated. This is a reasonable conclusion, given the fact that the internal peak temperature of the gasifier is higher than the AFT.

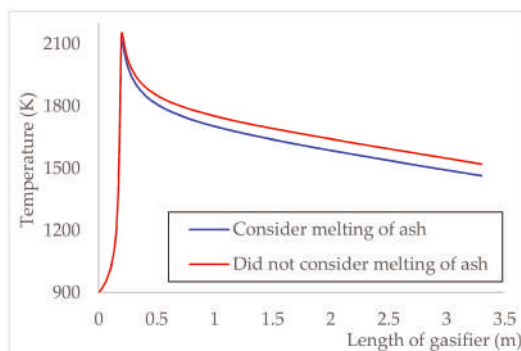


Figure 6. Differences in temperature profile depending on whether melting of ash is considered or not.

In this study, ash accounted for 15% of the mass of the coal and 7% of the total mass. The effect of sensible heat of slag is evident when the heat flows are divided into the solid and gas (Figure 7). Solids include coal, ash, and slag. After most of the reaction has proceeded, the solids are mainly in slag form. Especially at the exit condition, >99% of the solid was slag, which accounted for 5.0% of the total heat. In the coal that was used in this study, the ash was not negligible. As a result, our new attempt was meaningful. This phenomenon must be considered, especially for coal that has high ash content.

5.3. Consideration of Ash Melting Effect

The melting of ash has a similar effect on energy balance, as does heat loss from the outer wall. Because the ash melts and absorbs energy, the temperature of the system is lowered. In contrast, the loss to the outer wall lowers the temperature because heat escapes from of the system. These are different phenomena that occurred inside the gasifier, and were considered independently.

We quantitatively calculated the melting effect. This approach used the same method that was used to consider the heat loss. Based on the coal heating value, the latent heat of the ash and the

sensible heat of the slag were calculated. The melting effect at the outlet was ~1%. This is not negligible given that heat loss is assumed to be 4% in this study. We calculated the melting effect at the exit as

$$\frac{\text{Slag Sensible Heat} + \text{Ash Fusion Heat}}{\text{Coal Heating Value(HHV)}} = \frac{W_{s,L} \cdot c_{P,s,L} \cdot T_L + W_{a,L} \cdot X_L \cdot \Delta H_{ash}}{W_{c,0} \cdot \text{HHV of Illinois No.6}} \quad (9)$$

In this way, we corrected the overestimate of heat loss that occurred in previous studies. In addition, we could explain some of the uncertainty of heat loss.

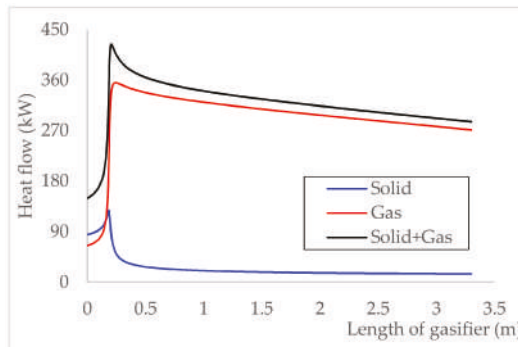


Figure 7. Heat flow of solid and gas.

5.4. Applicability of High Ash Content Coal and Limitations

Coal containing a large amount of ash can be applied in the same manner. If information about the ash component is available, then it can be used to calculate the slag properties and incorporate thermal properties in the heat balance. When the ash content is high, modeling errors can be reduced by considering the fusion heat of ash and the sensible heat of the slag.

However, the reaction kinetic parameters that are cited in this study represent only coal combustion and gasification, so the model is only applicable to the entrained coal gasifier. In addition, lab-scale or pilot-scale data of other coal that has high ash content should be used to further assess applicability of this model.

6. Conclusions

This study suggests that a heat-balance model of an EFG must consider the effects of melting of ash. We attempted modeling based on kinetic models similar to those of previous researchers. Our proposed 1-D model is the only one that includes ash in the heat-balance and temperature-calculation algorithm. Gas production and coal conversion trends were similar to those of existing ones, and the results at the exit were mostly consistent with the experiments.

This result is meaningful in that it reflects actual phenomena occurring inside the EFG. Ash melts in any slagging-type gasifier. We can expect to calculate the internal temperature more accurately based on this study. These results can be used to guide the choice of design elements of EFG, such as material and thickness of the refractory wall.

One limitation of this model is that information on the ash component was not available. We used minerals to express ash components. This demerit must be eliminated. For further research, advanced modelling should use thermal properties based on ash analysis data. This model can be extended to account for radial direction temperature distribution.

Acknowledgments: This work was financially supported by the Pohang Iron & Steel Company Limited in South Korea (No. 2017Y005).

Author Contributions: Jinsu Kim programmed the gasifier model and wrote draft paper. Hyunmin Oh checked the coding results, analyzed the simulation results, and corrected minor errors. Seokyung Lee did the validation work and wrote the figure. Young-Seek Yoon proposed idea, supervised research based on literature review and finished the paper.

Conflicts of Interest: The authors declare no conflict of interest.

Nomenclature

A	cross section area of gasifier (m^2)
C	molar concentration (mole/m^3)
c_p	specific heat capacity ($\text{J}/\text{g}\cdot\text{K}$ for solid, $\text{J}/\text{mole}\cdot\text{K}$ for gas)
d_c	coal particle size (m)
F	molar flow rate of gas (mole/s)
H	enthalpy (J)
H_{loss}	heat loss to outer wall (J/s)
HHV	high heating value of coal (J/g)
K	equilibrium constant of water gas shift reaction (-)
k_i	rate constant of i th reaction
L	reactor length (m)
m_c	mass of one coal particle (g/#)
MW	molecular weight (g/gmole)
N_v	number of particles contained in coal (#/ m^3)
P_i	partial pressure of gas i (atm)
R_j	reaction rate of j (g/s for heterogeneous reaction, mole/s for homogeneous reaction)
T	temperature (K)
v_c	coal velocity (m/s)
W_a	ash mass flow rate (g/s)
W_c	coal mass flow rate (g/s)
W_s	slag mass flow rate (g/s)
w	phi control function according to temperature (-)
X	Coal conversion (-)
Z	the coordinates of the axis of the gasifier in the previous model (m)
z	the coordinates of the axis of the gasifier in this model (m)

Greek Characters

α	degree of deviation from equilibrium (mole/s)
ϕ	the stoichiometric coefficient to adjust the complete, incomplete combustion
ξ	stoichiometric coefficient

Subscripts

a	the weight of C contained in 1 g of coal
b	the weight of H contained in 1 g of coal
c	the weight of O contained in 1 g of coal
d	the weight of N contained in 1 g of coal
e	the weight of S contained in 1 g of coal
f	the weight of ash contained in 1 g of coal
i	gas species
j	reaction
L	value at the reactor exit
0	value at the reactor inlet

References

- Phillips, J. Different types of gasifiers and their integration with gas turbines. In *The Gas Turbine Handbook*; 2006; Volume 1. Available online: <https://www.netl.doe.gov/File%20Library/Research/Coal/energy%20systems/turbines/handbook/1-2-1.pdf> (accessed on 2 January 2018).
- Guo, X.; Dai, Z.; Gong, X.; Chen, X.; Liu, H.; Wang, F.; Yu, Z. Performance of an entrained-flow gasification technology of pulverized coal in pilot-scale plant. *Fuel Process. Technol.* **2007**, *88*, 451–459. [[CrossRef](#)]
- Wang, T.; Stiegel, G.J. *Integrated Gasification Combined Cycle (IGCC) Technologies*; Woodhead Publishing: Cambridge, UK, 2016; ISBN 978-0-08-100185-1.
- Vamvuka, D.; Woodburn, E.T.; Senior, P.R. Modelling of an entrained flow coal gasifier. 2. Effect of operating conditions on reactor performance. *Fuel* **1995**, *74*, 1461–1465. [[CrossRef](#)]
- Vamvuka, D.; Woodburn, E.T.; Senior, P.R. Modelling of an entrained flow coal gasifier. 1. Development of the model and general predictions. *Fuel* **1995**, *74*, 1452–1460. [[CrossRef](#)]
- Hwang, M.; Song, E.; Song, J. One-Dimensional Modeling of an Entrained Coal Gasification Process Using Kinetic Parameters. *Energies* **2016**, *9*, 99. [[CrossRef](#)]
- Bhatia, S.K.; Perlmutter, D.D. A random pore model for fluid-solid reactions: II. Diffusion and transport effects. *AIChE J.* **1981**, *27*, 247–254. [[CrossRef](#)]
- Ishida, M.; Wen, C.Y. Comparison of kinetic and diffusional models for solid-gas reactions. *AIChE J.* **1968**, *14*, 311–317. [[CrossRef](#)]
- Sadhukhan, A.K.; Gupta, P.; Saha, R.K. Modelling of combustion characteristics of high ash coal char particles at high pressure: Shrinking reactive core model. *Fuel* **2010**, *89*, 162–169. [[CrossRef](#)]
- Gupta, P.; Sadhukhan, A.K.; Saha, R.K. Analysis of the combustion reaction of carbon and lignite char with ignition and extinction phenomena: Shrinking sphere model. *Int. J. Chem. Kinet.* **2007**, *39*, 307–319. [[CrossRef](#)]
- Kong, X.; Zhong, W.; Du, W.; Qian, F. Three Stage Equilibrium Model for Coal Gasification in Entrained Flow Gasifiers Based on Aspen Plus. *Chin. J. Chem. Eng.* **2013**, *21*, 79–84. [[CrossRef](#)]
- Biagini, E.; Bardi, A.; Pannochia, G.; Tognotti, L. Development of an Entrained Flow Gasifier Model for Process Optimization Study. *Ind. Eng. Chem. Res.* **2009**, *48*, 9028–9033. [[CrossRef](#)]
- Chen, C.; Horio, M.; Kojima, T. Numerical simulation of entrained flow coal gasifiers. Part I: Modeling of coal gasification in an entrained flow gasifier. *Chem. Eng. Sci.* **2000**, *55*, 3861–3874. [[CrossRef](#)]
- Eri, Q.; Wu, W.; Zhao, X. Numerical Investigation of the Air-Steam Biomass Gasification Process Based on Thermodynamic Equilibrium Model. *Energies* **2017**, *10*, 2163. [[CrossRef](#)]
- Liu, X.; Wei, J.; Huo, W.; Yu, G. Gasification under CO₂–Steam Mixture: Kinetic Model Study Based on Shared Active Sites. *Energies* **2017**, *10*, 1890. [[CrossRef](#)]
- Wen, C.Y.; Chaung, T.Z. Entrainment Coal Gasification Modeling. *Ind. Eng. Chem. Process Des. Dev.* **1979**, *18*, 684–695. [[CrossRef](#)]
- Govind, R.; Shah, J. Modeling and simulation of an entrained flow coal gasifier. *AIChE J.* **1984**, *30*, 79–92. [[CrossRef](#)]
- Robin, A.M. *Hydrogen Production from Coal Liquefaction Residues*; Final Report; Montebello Research Lab, Texaco, Inc.: Montebello, CA, USA, 1976.
- Basu, P. *Biomass Gasification and Pyrolysis: Practical Design and Theory*; Academic Press: New York, NY, USA, 2010; ISBN 978-0-08-096162-0.
- Callaghan, C.A. Kinetics and Catalysis of the Water-Gas-Shift Reaction: A Microkinetic and Graph Theoretic Approach. Ph.D Dissertation, Worcester Polytechnic Institute, Worcester, MA, USA, 2006.
- Deng, Z.; Xiao, R.; Jin, B.; Huang, H.; Shen, L.; Song, Q.; Li, Q. Computational Fluid Dynamics Modeling of Coal Gasification in a Pressurized Spout-Fluid Bed. *Energy Fuels* **2008**, *22*, 1560–1569. [[CrossRef](#)]
- Breault, R.W. Gasification Processes Old and New: A Basic Review of the Major Technologies. *Energies* **2010**, *3*, 216–240. [[CrossRef](#)]
- Gazzani, M.; Manzolini, G.; Macchi, E.; Ghoniem, A.F. Reduced order modeling of the Shell–Prenflo entrained flow gasifier. *Fuel* **2013**, *104*, 822–837. [[CrossRef](#)]
- Tremel, A.; Becherer, D.; Fendt, S.; Gaderer, M.; Spliethoff, H. Performance of entrained flow and fluidised bed biomass gasifiers on different scales. *Energy Convers. Manag.* **2013**, *69*, 95–106. [[CrossRef](#)]

25. Krishnamoorthy, V.; Pisupati, S.V. A Critical Review of Mineral Matter Related Issues during Gasification of Coal in Fixed, Fluidized, and Entrained Flow Gasifiers. *Energies* **2015**, *8*, 10430–10463. [[CrossRef](#)]
26. Richardson, M.J. The specific heats of coals, cokes and their ashes. *Fuel* **1993**, *72*, 1047–1053. [[CrossRef](#)]
27. Rezaei, H.R.; Gupta, R.P.; Bryant, G.W.; Hart, J.T.; Liu, G.S.; Bailey, C.W.; Wall, T.F.; Miyamae, S.; Makino, K.; Endo, Y. Thermal conductivity of coal ash and slags and models used. *Fuel* **2000**, *79*, 1697–1710. [[CrossRef](#)]
28. Mills, K.C.; Rhine, J.M. The measurement and estimation of the physical properties of slags formed during coal gasification: 1. Properties relevant to fluid flow. *Fuel* **1989**, *68*, 193–200. [[CrossRef](#)]
29. Blissett, R.S.; Rowson, N.A. A review of the multi-component utilisation of coal fly ash. *Fuel* **2012**, *97*, 1–23. [[CrossRef](#)]
30. Žigo, O.; Adamkovičová, K.; Kosa, L.; Nerád, I.; Proks, I. Determination of the heat of fusion of $2\text{CaOAl}_2\text{O}_5\text{SiO}_2$ (gehlenite). *Chem. Pap.* **1987**, *41*, 171–181.
31. Richet, P.; Fiquet, G. High-Temperature Heat Capacity and Premelting of Minerals in the System $\text{MgO-CaO-Al}_2\text{O}_3-\text{SiO}_2$. *J. Geophys. Res.* **1991**, *96*, 445–456. [[CrossRef](#)]
32. Berman, R.G.; Brown, T.H. Heat capacity of minerals in the system $\text{Na}_2\text{O-K}_2\text{O-CaO-MgO-FeO-Fe}_2\text{O}_3-\text{Al}_2\text{O}_3\text{SiO}_2-\text{TiO}_2-\text{H}_2\text{O-CO}_2$: Representation, estimation, and high temperature extrapolation. *Contrib. Mineral. Petrol.* **1985**, *89*, 168–183. [[CrossRef](#)]



© 2018 by the authors. Licensee MDPI, Basel, Switzerland. This article is an open access article distributed under the terms and conditions of the Creative Commons Attribution (CC BY) license (<http://creativecommons.org/licenses/by/4.0/>).

Article

Pyrolysis of Grape Marc from Tunisian Wine Industry: Feedstock Characterization, Thermal Degradation and Kinetic Analysis

Besma Khiari ¹ and Mejdi Jeguirim ^{2,*}

¹ Laboratoire des Sciences et Technologies de l'Environnement, University of Carthage, BP 50 Borj Cedria Technopark, 2050 Hammam-Lif, Tunisia; besmakhiali@yahoo.com

² Institut de Sciences des Matériaux de Mulhouse, UMR 7661 CNRS, 15 rue Jean Starcky, 68057 Mulhouse, France

* Correspondence: mejdi.jeguirim@uha.fr; Tel.: +33-389-608-661

Received: 7 March 2018; Accepted: 22 March 2018; Published: 23 March 2018

Abstract: Despite the huge amounts of grape marc generated in Tunisia from the wine industry, very few efforts have been exerted to manage this harmful waste. Therefore, thermal processes may contribute to an environmental friendly management and also help winemakers to create new economic profitable circuits in an increasingly competitive context. Among the various thermochemical conversion process, pyrolysis is suitable for the recovery of food processing residues, due to their high minerals content and ability to create high added values of the derived products (biochar, bio-oil and syngas). In this context, the aim of this work is to optimize the pyrolysis process in order to benefit from the grape marc potential for achieving highest product yields. Therefore, physico-chemical and energy characteristics of grape marc issued from a Tunisian wine cooperative were determined according to international standards. Thermogravimetric analyzes were also performed to predict the grape marc behavior during degradation under an inert atmosphere. The profile of the mass loss rate shows two decomposition peaks corresponding to the cellulose and lignin decomposition. These peaks are shifted to lower temperatures comparing to several lignocellulosic biomass feedstocks due to high content of minerals that may play a catalytic role in the thermal degradation process. The biochar yield was about 40%, which was never met in literature for agricultural biomass in slow pyrolysis. Such behavior may be attributed to high lignin content in grape marc. Activation energies were calculated using integral Flynn-Wall-Ozawa and Kissinger-Akahira-Sunose methods and differential Friedman method. The obtained values were 226.8, 224.2 and 229.5 kJ/mol, respectively. Such kinetics data are crucial in the design of the pyrolyzer for Tunisian grape marc recovery.

Keywords: grape marc; kinetic models; characterization; pyrolysis

1. Introduction

Grape is one of the most important fruit crops in the world with over 74 million tons produced annually [1]. Pressing grapes give juice, which is mostly for fermentation, and marc, which is also called pomace (solid product) [2], containing skins, seeds and stalks [3]. Although the pressing grape method depends strongly on the type of wine (white or red), Toscano et al. [3] described a general process giving the following proportions of grape products: 73% of juice and 27% of grape marc. The grape marc is distributed as follows: 19.5% of skins, 4.5% of seeds and 3% of stalks [3]. Grape marc may be processed further in distilleries in order to extract alcohol and the generated waste is called the exhausted grape marc residues. Wine cave (fresh grape marc) and alcohol distilleries (exhausted grape marc) produce large amounts of wastes, which are estimated at 7 million tons worldwide per year [4].

Grape marc characteristics depend strongly on the climatic conditions [5]. In general, grape marc is a wet (60% of moisture content) and heterogeneous waste [2]. Fresh grape marc are considered as a non-contaminated material with harmful characteristics, such as low pH and high organic matter (90%), including phytotoxic and antibacterial phenolic substances [6]. The most common methods to recover these residues include production of alcohol, tartar, pharmaceuticals, cosmetics [6], feedstuff [7], yeast [8], extraction of phenolic compounds [9], production of oil [10] or energy [11], decontamination of effluents containing metals, such as copper and nickel [12], composting [13] and direct use as an organic fertilizer [14]. According to the European Council Regulation EC1493/1999 involving the common organization of wine market, fresh grape marc (except stalks) must be transferred to alcohol distilleries [6]. In Spain, several studies showed that exhausted grape marcs have a high content of lignin and tannin and are not easily digested. Therefore, they are not appropriate as nutritional supplements for animals. Besides, their high C/N ratio limits their potential as soil fertilizers [14]. In this way, Italian laws (2010) require wine producers to send their wastes to distilleries [3]. Thus, some recovery methods are no longer permitted. In the same context, composting was also declared to not be economically viable in France and is gradually disappearing. Therefore, 60% of distilleries in France are using grape marc as combustible [4]. In fact, grape marc has interesting physical and thermal properties and energy contents [2,15]. However, a particular attention should be paid to the ash accumulation and pollutants emissions factors during grape marc combustion.

Similar to other Mediterranean countries, Tunisia is committed to finding a solution for environmental and economical disposal of their wastes and to participate further to reduce the global greenhouse effect. The wine industry in Tunisia generates annually about 25,000 tons of grape marc issued from internationally-known varieties, such as Grenache, Syrah, Cinsaut, Muscat of Alexandria, and from 54 aboriginal varieties, such as Razzegui, Tebourbi, Asli, Bazzoul Khaddem, Sakalsi, Garrat, Hamri, Chetoui and Chaouch. The grape plantations and the wine extraction processes are spread almost all over the country, although they are mainly located in the North East [16]. The discharge of the generated grape marc is usually centralized and seasonal in a short period of the year (August–October) [16]. Furthermore, only 10% from the generated grape marc are used as nutritional ferment. A small part is used for compost production or dried and used as fertilizer [5]. The rest is either dumped or used as a traditional combustible in an uncontrolled manner, leading to the release of hazardous pollutants.

Currently, there is no sustainable strategy for the grape marc recovery in Tunisia. Recently, Kraiem et al. [17,18] showed that despite suitable lower heating, high mineral contents and low bulk densities limit their direct use as biofuels in a combustion appliance for the residential heating sector. Authors had then resort to the densification and the blend of grape marc with woody biomass, which has low ash content [17,18]. However, combustion tests showed the high particular matter emissions, which limit the recovery of grape marc in domestic heating [17,18]. Therefore, the pyrolysis process could be a promising issue for the grape marc valorization since their mineral contents may be blocked in the residual char. This pyrolysis process could be interesting for wine, juice or jam-making industries [19,20]. However, as far as we know, a similar survey was never conducted in Tunisia, despite big potential gains. In fact, storage, handling and transport costs may be reduced with nearby, decentralized pretreatment establishments. Moreover, the pyrolytic gases can provide the power required for the endothermic pyrolysis process, ensuring self-sufficient operating system. In addition, the bio-oil and the biochar obtained from the pyrolysis process could be recuperated by winemakers for biofuels or soil amendments applications.

Consequently, the aim of this experimental work is to contribute to the understanding of the Tunisian grape marc behavior within an industrial processed pyrolysis. In particular, characteristics, including proximate and ultimate analyses, are determined. Thermogravimetric analyzes are also performed to predict the behavior of this waste during thermal degradation under different inert types of atmosphere. The obtained data are used for determining kinetic parameters that are subsequently used for determining the optimum pyrolysis process parameters.

2. Materials and Methods

Grape marc used in this study was collected from a wine cooperative located in the north of Tunisia (Bou Argoub, Nabeul). The sample was fresh with 60% (wb) of moisture, which was reduced to 10%. The sample was characterized through moisture content (EN 14774-1), ash content (EN 14775) and Low Heating Value, LHV (EN 14918) determination. Volatile matters and fixed carbon were determined using the Thermogravimetric analysis method [21]. Furthermore, elemental analysis was performed using a CHNOS analyzer (ThermoFisher Scientific, Villebon, France).

Thermogravimetric analyses (TGA) were carried out using a Mettler-Toledo TGA/DSC3+ (Mettler-Toledo, Columbus, OH, USA) thermobalance apparatus and repeated at least three times, with good reproducibility. The experiments were performed under nitrogen with flows of $12 \text{ NL} \cdot \text{h}^{-1}$ according to different linear heating programs (5, 10, 20 and 30 $^{\circ}\text{C}/\text{min}$) in the range of 20–950 $^{\circ}\text{C}$.

3. Kinetic Approach

Many works have focused on the data analysis method for extracting reliable kinetic data from TGA experiments. There are three types of kinetic methods used for the analysis of biomass pyrolysis kinetics: differential, isoconversional, model-fitting and pseudo-components kinetics methods [22–25].

The fundamental rate equation used in all kinetic studies is generally described as:

$$\frac{dX}{dt} = k(T)f(X), \quad (1)$$

where k is the rate constant and $f(X)$ is the reaction model that describes the reaction mechanism. The conversion rate X is given by Equation (2):

$$X = \frac{W_0 - W_t}{W_0 - W_f}, \quad (2)$$

where W_t , W_0 , and W_f are time t , initial and final weights of the sample, respectively.

The Arrhenius equation (Equation (3)) expresses the rate constant k :

$$k = A \exp\left(\frac{-Ea}{RT}\right), \quad (3)$$

where Ea is the activation energy (kJ/mol), R is the universal gas constant (8.314 J/K mol), A is the pre-exponential factor (s^{-1}) and T is the absolute temperature (K).

Energy activation is defined as the minimum energy requirement that must be overcome before molecules can get close enough to react and form products. Accordingly, the reactions with a high Ea need a high temperature or a long reaction time.

By combining Equations (1) and (3), we obtain:

$$\frac{dX}{dt} = A \exp\left(\frac{-Ea}{RT}\right) f(X). \quad (4)$$

If the temperature is varied by a constant designed by β , which is the heating rate ($\beta = \frac{dT}{dt}$), the introducing of β in the Equation (4) gives:

$$\frac{dX}{dT} = \frac{A}{\beta} \exp\left(\frac{-Ea}{RT}\right) f(X). \quad (5)$$

By taking the logarithms of both sides of Equation (5), the first proposed differential Friedman method (Equation (6)) is obtained [26]:

$$\ln \frac{dX}{dt} = \ln \left(\beta \frac{dX}{dT} \right) = \ln[Af(X)] - \frac{Ea}{RT}. \quad (6)$$

If we rearrange Equation (6), we can obtain:

$$L \frac{dX}{f(X)} = \frac{A}{\beta} \exp \left(\frac{-Ea}{RT} \right) dT. \quad (7)$$

After integrating Equation (7), it can be obtained:

$$g(X) = \int_0^X \frac{dX}{f(X)} = \frac{A}{\beta} \int_0^T \exp \left(\frac{-Ea}{RT} \right) dT \quad (8)$$

By taking logarithms and using the Doyle approximation, Equation (8) can be rewritten as Equation (9). This equation is known as the Flynn-Wall-Ozawa method (FWO) [27]:

$$\ln \beta = \ln \frac{AEa}{g(X)R} - 2.315 - \left(\frac{1.0516Ea}{RT} \right). \quad (9)$$

By using the derivation of Equation (3), and applying the logarithmic scale with the temperature data for each conversion rate (X) at different heating rates ($\beta_j = \frac{dT}{dt}$), the Kissinger method (KAS) calculates activation energy by plotting Equation (9) [28]:

$$\ln \frac{\beta}{T^2} = \ln \frac{AR}{Eag(X)} - \frac{Ea}{RT}. \quad (10)$$

The kinetic methods used in this study are Friedman, Flynn-Wall-Ozawa (FWO) and Kissinger-Akahira-Sunose (KAS) and their principles are listed in Table 1.

Table 1. Isoconversional Kinetic methods used in evaluating activation energy in this study.

Method	Expression	Plots	Reference
Friedman	$\ln \frac{dX}{dt} = \ln \left(\beta \frac{dX}{dT} \right) = \ln[Af(X)] - \frac{Ea}{RT}$	$\ln \left(\beta \frac{dX}{dT} \right)$ vs. $\frac{1}{T}$	[26]
FWO	$\ln \beta = \ln \frac{AEa}{g(X)R} - 2.315 - \left(\frac{1.0516Ea}{RT} \right)$	$\ln \beta$ vs. $\frac{1}{T}$	[27]
KAS	$\ln \frac{\beta}{T^2} = \ln \frac{AR}{Eag(X)} - \frac{Ea}{RT}$	$\ln \frac{\beta}{T^2}$ vs. $\frac{1}{T}$	[28]

4. Results and Discussions

4.1. Grape Marc Characterization

Table 2 shows the proximate and ultimate analyses of the Tunisian grape marc. Moisture is reduced to 10%, since it was very high after the wine extraction process (60 wt %). Furthermore, the direct use of the grape marc has a negative effect on the thermochemical process efficiency and temperature [29].

Table 2. Proximate and ultimate analyses of grape marc.

	This Study	Miranda et al. [15]	Gonzalez-Vazquez et al. [30]	Makela et al. [31]
Proximate Analysis	%			
Moisture ^{wb}	10	7.49	-	1.4
Fixed Carbon ^{db}	31.1	24.73	19.7	-
Volatile matter ^{db}	55.6	67.80	67.6	-
Ash ^{db}	13.3	7.47	12.7	8.23
LHV ^{db} (MJ·kg ⁻¹)	18.02	19.54	18.7	19.6
Elemental Analysis ^{db}	%			
C	42.2	42.97	45.5	48.7
H	3.5	9.28	5.1	5.57
O	37.7	-	34.7	35.9
N	3.0	2.05	1.8	1.66
S	0.3	0.17	0.17	-

^{wb} Wet basis, ^{db} dry basis.

The ash content is 13.3%, which is higher than wood chips, at the same level as the grape marc was found by other authors, although this was lower than wheat straw [3]. The fixed carbon (31.1%) is higher than the value obtained by Miranda et al. (25%) for grape marc and higher than several biomass resources, such as olive husk (19%) and pine sawdust (17%). However, as expected, the volatile matter (55.6%) is lower than the grape marc of Miranda et al. (67.8%), olive husk (76%) and pine sawdust (69%) [15,32–34]. The high ash and fixed carbon contents confirm that slow pyrolysis is the suitable thermochemical conversion process for the grape marc recovery. In particular, the char yield (fixed carbon fix and ash contents) was about 44.4%, which was never met in literature for agricultural biomass under slow pyrolysis conditions. This feature distinguishes Tunisian grape marc from European ones and even from Chinese and American pomace. Many factors can explain these differences, such as local wine making practices and Tunisian grapevine specificity. The pyrolytic char derived from the Tunisian grape marc may have several applications, including soil amendment, adsorbents, biocoal, etc.

Elemental analysis also shows some differences with values met in literature, although this is consistent with the wide range of biomass composition that would undergo efficient pyrolysis. Carbon, hydrogen and oxygen are lower than the mean reported values, while N and S are quite high. This repartition is close to the composition of grape skins, although it is quite different from that of its seeds or stalks [32–34]. If nitrogen remains in char, this would be a supplementary argument in favor of pyrolysis against combustion, as biochar can be used as nutrients for soils.

4.2. Thermal Degradation of Grape Marc under Inert Atmosphere

The thermal degradation of biomass feedstocks was well described in the literature, which serves the main purpose of ensuring that from an energy standpoint, the pyrolysis process is self-sufficient [24–28,33,35]. Many factors affect the kinetic parameters based on the processing of TGA data, including processing conditions; heat and mass transfer limitations; physical and chemical heterogeneity of the sample; and systematic errors.

Figure 1 shows the mass loss (X) and the derivative (DTG) of mass loss (dX/dt) curves obtained during the pyrolysis of Tunisian grape marc. Thermogravimetric analysis could evaluate the thermal behavior of fuels under an inert atmosphere. The results are helpful in the fundamental understanding of biomass fuels when developing biomass utilization for the pyrolysis plant.

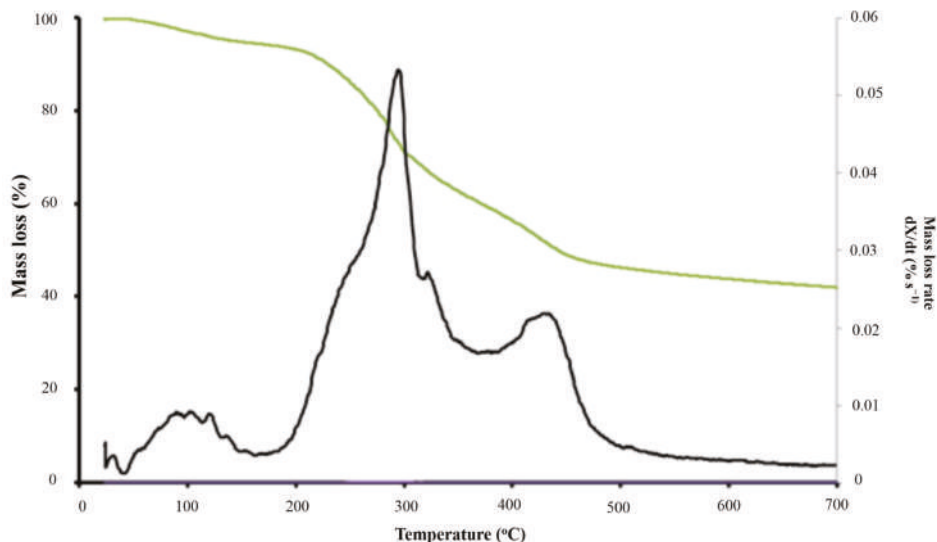


Figure 1. TG and DTG curves of Grape Marc under an inert atmosphere at 5 °C/min.

The shape of Derivative Thermo-Gravimetric (DTG) curve includes three regions in ascending order of temperature variation, corresponding to three degradation steps. The first region occurred between 23 and 166 °C, which corresponds to the biomass drying by moisture loss and the departure of light volatiles. The second region corresponds to the devolatilization step, which occurs between 166 °C and 500 °C. This step was called in the literature as the active pyrolysis includes two zones. The first one occurs between 166 and 362 °C, which corresponds to the decomposition of cellulose and hemicellulose. A clear peak at 288 °C is attributed to the decomposition of cellulose with an overall maximum rate of 0.055 %·s⁻¹. A second zone occurs between 362 °C and 500 °C, which corresponds to the lignin degradation. After the devolatilization step, a third step of passive pyrolysis is observed. This step characterized by a low and a continuous mass loss rate corresponds to the end of lignin degradation as well as char formation and rearrangement.

Several phenomena occur within grape marc pyrolysis and to varying extents: cracking, reforming, dehydration, condensation, polymerization and even oxidation and gasification reactions, which take place after the release of the oxygen and the vapors present in the product.

The obtained TG data, T (temperature), X (mass loss), T_{peak} (peak temperature), dX/dt (mass loss rate) and R_M (mean reactivity) are shown in Table 3. One may remind that reactivity is calculated as follows:

$$R_M = 100 \sum \left(\frac{R_{peak}}{T_{peak}} \right). \quad (11)$$

The comparison of the obtained values with those found in literature for various lignocellulosic biomass feedstocks shows several differences. First, the peak temperature obtained at 288 °C is lower than the reported peak temperatures for cellulose decomposition, which is between 310 and 320 °C. Furthermore, this is lower than the peak temperature of 332 °C for pure cellulose [36] and for various lignocellulosic biomass in the literature [22,35,37]. However, this peak was at 261 °C for palm kernel shells for example [38]. The high content of minerals initially present in the Tunisian grape marc [20,21] is thought to be responsible for the shift to lower levels of temperatures as they may play a catalyzing role in the process. The impact of these minerals, especially Na, K and Mg, were evidenced in previous investigations [39].

Table 3. TG under inert atmosphere (5 °C/min).

Pyrolysis Zone	T (°C)	166–750
	X (%)	94.5–41.3
Zone 1	T (°C)	166–362
	X (%)	94.5–61.2
	T _{peak 1} (°C)	288
	R ₁ (%·s ⁻¹)	0.032
Active Pyrolysis	T (°C)	362–500
	X (%)	64.81–46.4
	T _{peak 2} (°C)	423
	R ₂ (%·s ⁻¹)	0.021
$R_M \times 10^3$ (%·s ⁻¹ ·°C ⁻¹)		0.14
Passive Pyrolysis	T (°C)	500–750
	X (%)	46.4–41.3

Hemicellulose decomposition is identified through the shoulder between 238 and 257 °C, which is in the interval of 195–306 °C. Such behavior is well-known in the literature and the hemicellulose decomposition step appears usually as a more or less pronounced shoulder instead of a well-defined peak [38]. Similar to cellulose decomposition, during the grape marc thermal degradation, hemicellulose decomposition occurs at a lower temperature due to the catalytic effect of alkali and alkali-earth metals [39].

The lignin degradation step also shows a clear difference compared to the usual shape of the DTG curve of lignocellulosic biomasses. In particular, the DTG curve of the Tunisian grape marc shows a specific region occurring between 362 and 500 °C, with a peak at 425 °C that yields an overall rate around 0.021 %·s⁻¹. This peak is attributed to the high contents of lignin. Otherwise, the zone corresponding to the cracking of the polymeric structure of C–C or C–O–C bonds in lignin would result in only a flat tailing section. Generally, the thermal degradation of lignocellulosic biomass is not characterized by a sharp peak for lignin decomposition.

The reactivity value (0.14×10^{-3} %·s⁻¹·°C⁻¹) is in the same magnitude as those of various biomasses, such as the coffee husk around 0.19×10^{-3} %·s⁻¹·°C⁻¹ [38] or palm residues (0.23×10^{-3} %·s⁻¹·°C⁻¹) [40] for the same heating rate.

The char yield of 39.68% is expected in view of the proximate analysis, although this is higher than any agricultural waste. The char resulting from the first stages also probably contributed to the secondary reactions, which mainly occurred by catalyzing cracking and polymerization reactions that promoted recombination reactions among the volatile species to yield more condensed char structures [39].

In order to extract the kinetic parameters of the thermal degradation of Tunisian grape marc under pyrolysis conditions, the impact of different heating rates was investigated. Figure 2 showed that increasing the heating rate leads to a shift in the peak temperature towards higher values together with higher mass loss rates. Indeed, when heating rate is increased from 5 to 30 °C/min, the maximum peak temperature moves from 288 to 322 °C. The explanation is that the material reaches the cracking temperature in a shorter time when higher heating rates are considered. Due to the heat and mass transfer limitations inside the particle, these higher heating rates are a consequence of inner temperature gradients. In fact, increasing the reactor temperature ramp does not allow good temperature stabilization within the grape marc, which causes a delay in the volatile matter departure. The same behavior has been reported in the literature for numerous biomasses [40–42].

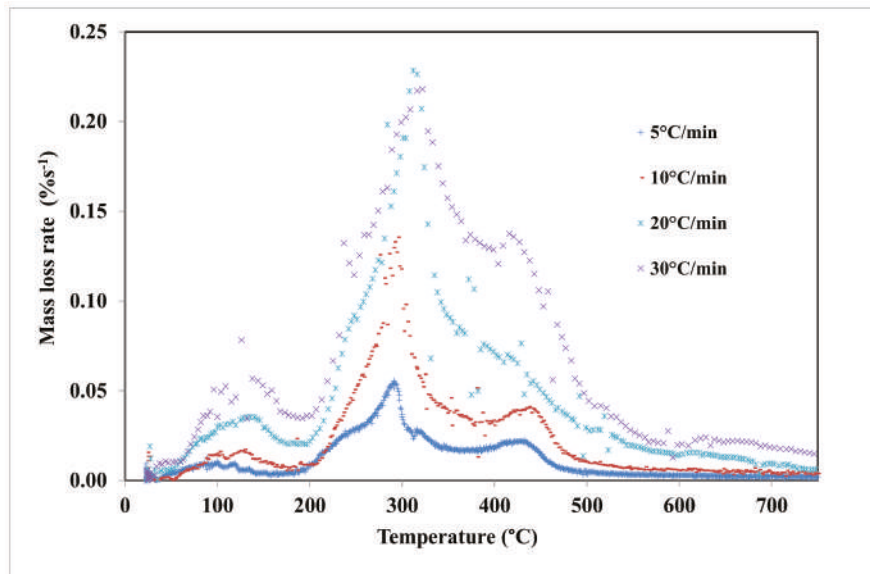


Figure 2. Mass loss rate for different heating rates.

4.3. Kinetic Study

The linear plots of KAS, FWO and Friedman are shown in Figure 3. As the initial mass loss is attributed to the moisture loss, the first conversion rate selected to determine the kinetic parameters is 0.2, while the final point is taken at 0.65. Above this value, no good determination coefficients were obtained, which may be attributed to the complexity of the char production and rearrangement.

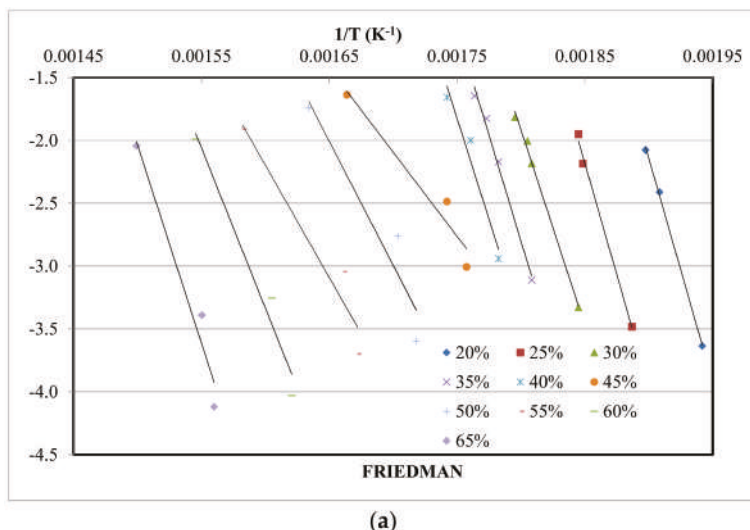


Figure 3. Cont.

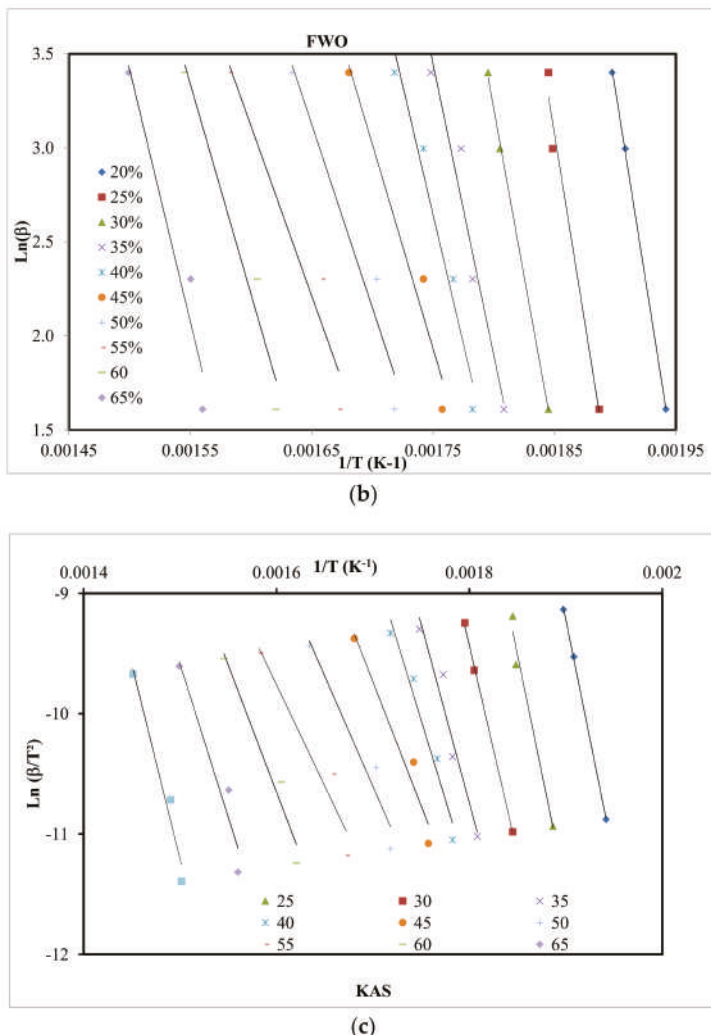


Figure 3. Plots for kinetic models. (a) Friedman; (b) FWO; (c) KAS.

The calculated corresponding values are presented for each conversion ratio in Table 4. The mean activation energy values for GM with the use of the KAS, FWO and Friedman methods were 224.2, 226.8 and 229.5 kJ/mol, respectively. Table 4 depicts that the activation energy decreases when the conversion increases. It is assumed that a good biomass thermal degradation meets low activation energy values. In the initial stages and for KAS, FWO and Friedman methods, the E_a values were high (333.3, 323.3 and 295.9 kJ/mol, respectively, at $X = 0.2$). However, these values gradually decrease as the conversion rate X goes up until it reaches 55%, before increasing again (an exception point around 45% is probably due to an experimental error). This phenomenon was not reported in other works, where E_a was decreasing continuously, for several cellulosic biomasses [43,44]. This is explained by the quick and first scission of the weakly bonded amorphous cellulose and hemicelluloses. Once all-crystalline cellulose has decomposed, lignin accounted for a further decrease in activation energy [44].

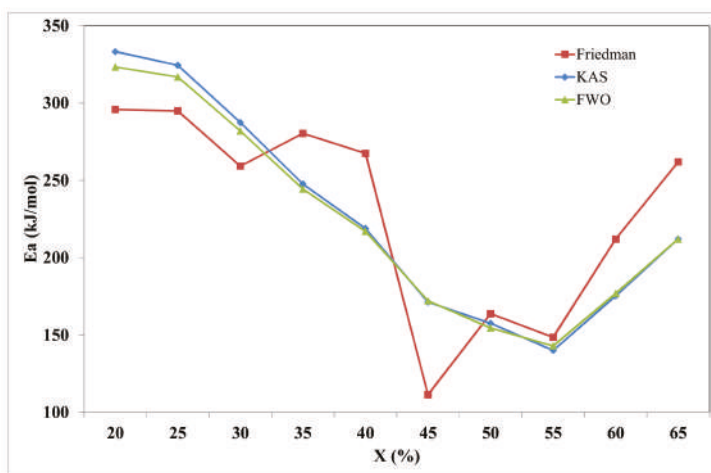
Table 4. Calculated Energy activation with R^2 values from Friedman, FWO and KAS models (E, kJ/mol).

X	Friedman		FWO		KAS	
	Ea	R ²	Ea	R ²	Ea	R ²
0.20	295.9	0.999	323.3	0.999	333.3	0.999
0.25	295.0	0.995	316.9	0.979	324.4	0.978
0.30	259.2	0.995	282.0	0.999	287.4	0.999
0.35	280.5	0.991	244.4	0.947	247.7	0.943
0.40	267.5	0.955	217.0	0.964	218.8	0.961
0.45	111.4	0.947	172.1	0.959	171.3	0.954
0.50	163.8	0.911	154.5	0.948	157.6	0.941
0.55	148.5	0.936	142.9	0.939	140.0	0.930
0.60	212.3	0.965	176.9	0.962	175.3	0.958
0.65	262.2	0.959	212.1	0.941	212.1	0.935
Mean	229.5		226.8		224.2	

In our case and according to previous studies [2–5,14,31,41], lignin content in grape marc is much higher than cellulose. Consequently, the whole pyrolysis is thought to be mainly controlled by the lignin and its intermediate products.

In another hand, it is noticed that the activation energy for grape marc is greater than the values obtained for the pyrolysis of lignin [45,46] and other biomass [32,47–50]. These activation energies are high even when compared to other grape marc that originated from Italy. Fiori et al. found values between 171 and 178 kJ/mol for heating rates between 3 and 30 °C/min [51].

The isoconversional methods were applied to four different experimental data sets (5, 10, 20 and 30 °C/min). The results are presented in Figure 4. KAS and FWO are very close. The calculated Ea at the different conversion levels can be attributed to a different macro-component decomposition. At low conversion levels (0.2–0.3), the activation energies between 250 and 340 kJ/mol can be regarded as being related to hemicelluloses degradation. The lower Ea in the range of 140–240 kJ/mol are obtained for the conversion levels of 0.25 and 0.50, which can be attributed to cellulose cracking. The activation energy increases to 212 kJ/mol for KAS and OFW models and to 262 for the Friedman model at higher conversion levels, for which lignin is thought to be responsible. At higher temperatures, activation energies decrease, which may be explained by an overlapping of cellulose and lignin continuing degradation as well as by char rearrangement through secondary and more complex reactions, which was found in literature [52–55].

**Figure 4.** Activated Energies for Friedman, FWO and KAS method for conversion from 20 to 65%.

5. Conclusions

In these times, where the circular economy is at the service of the economic actors, the slow pyrolysis of grape marc can be an advantage in the wine industry and distilleries on more than one level, especially in the Tunisian context. Furthermore, as better environmental management of grape marc is increasingly necessary, this study is required to achieve a better understanding of the economics of grape marc pyrolysis for bio-fuel production and for resolving issues related to the capabilities of this technology in practical applications. Indeed, the pyrolysis process applied to these residues provides a high biochar yield of around 40%, which was never reached by any other agricultural waste. This fact is explained by the inhibition of hemicellulose and cellulose decomposition on one hand and by high lignin content on the other hand. With the same aim to improve some characteristics of grape marc by increasing its bulk density and reducing its ash content, densification and blending with woody biomass can help to solve the problem. The biochar is interesting as it may be used as nutritional ferment for soils or may undergo direct and efficient gasification. Minerals, which were an obstacle in combustion operations, become a major asset in pyrolysis. Furthermore, their presence played a catalytic role and shifted the cracking temperatures to lower values, thus reducing the operation cost.

To optimize this and to achieve high energy recovery from grape marc, kinetics data were calculated and helped in the design of pyrolysis reactors for grape marc. Integral and differential methods used in the frame of this work showed very close and reliable kinetic parameters.

Author Contributions: All authors contributed equally to the work done.

Conflicts of Interest: The authors declare no conflict of interest.

Nomenclature

A	pre-exponential factor (s^{-1})
Ea	activation energy (kJ/mol)
k	rate constant (s^{-1})
R	universal gas constant (J/K mol)
R_M	mean reactivity (%·s ⁻¹ ·°C ⁻¹)
t	time (s)
T	absolute temperature (K)
T_{peak}	peak temperature (K)
W_0	initial weight of the sample (mg)
W_f	final weight of the sample (mg)
W_t	time t weight of the sample (mg)
X	mass loss (%)
β	heating rate (K/s)

References

- Moncayo, J.R.; Aurand, J.M. *Table and Dried Grapes*; Food and Agriculture Organisation (FAO): Rome, Italy, 2016; ISBN 978-92-5-109708-3.
- Celma, A.R.; Rojas, S.; Lopez-Rodriguez, F. Waste-to-energy possibilities for industrial olive and grape by-products in Extremadura. *Biomass Bioenergy* **2007**, *31*, 522–534. [[CrossRef](#)]
- Toscano, G.; Riva, G.; Duca, D.; Pedretti, E.F.; Corinaldesi, F.; Rossini, G. Analysis of the characteristics of the residues of the wine production chain finalized to their industrial and energy recovery. *Biomass Bioenergy* **2013**, *55*, 260–267. [[CrossRef](#)]
- Dwyer, K.; Hosseiniyan, F.; Rod, M. The Market Potential of Grape Waste Alternatives. *J. Food Res.* **2014**, *3*, 91–106. [[CrossRef](#)]
- Souza, E.C.; Uchoa-Thomaz, A.M.A.; Carioca, J.O.B.; Lima, A.; Martin, C.G.; Alexandrino, C.D.; Ferreira, P.A.T.; Rodrigues, A.L.M.; Rodrigues, S.P.; Silva, J.N.; et al. Chemical composition and bioactive compounds of grape pomace (*Vitis vinifera*, L.), Benitaka variety, grown in the semiarid region of Northeast Brazil. *Food Sci. Technol., Campinas* **2014**, *34*, 135–142. [[CrossRef](#)]

6. Bustamante, M.A.; Moral, R.; Paredes, C.; Perez-Espinosa, A.; Moreno-Caselles, J.; Pérez-Murcia, M.D. Agrochemical characterisation of the solid by-products and residues from the winery and distillery industry. *Waste Manag.* **2008**, *28*, 372–380. [[CrossRef](#)] [[PubMed](#)]
7. Vaccarino, C.; Tripodo, M.M.; Lo Curto, R.B.; Cimino, G. The effects of NaOH treatments of grape-marc, vinasse, and wheat-straw mixtures on their degradability in vitro. *Bioresour. Technol.* **1993**, *44*, 197–202. [[CrossRef](#)]
8. Lo Curto, R.B.; Tripodo, M.M. Yeast production from virgin grape marc. *Bioresour. Technol.* **2001**, *78*, 5–9. [[CrossRef](#)]
9. Louli, V.; Ragoussis, N.; Magoulas, K. Recovery of phenolic antioxidants from wine industry by-products. *Bioresour. Technol.* **2004**, *92*, 201–208. [[CrossRef](#)] [[PubMed](#)]
10. Xu, C.; Zhang, Y.; Wang, J.; Lu, J. Extraction, distribution and characterisation of phenolic compounds and oil in grapeseeds. *Food Chem.* **2010**, *122*, 688–694. [[CrossRef](#)]
11. Kabir, M.J.; Chowdhury, A.A.; Rasul, M.G. Pyrolysis of Municipal Green Waste: A Modelling, Simulation and Experimental Analysis. *Energies* **2015**, *8*, 7522–7541. [[CrossRef](#)]
12. Villaescusa, I.; Fiol, N.; Martinez, M.; Miralles, N.; Poch, J.; Serarols, J. Removal of copper and nickel ions from aqueous solutions by grape stalks wastes. *Water Res.* **2004**, *38*, 992–1002. [[CrossRef](#)] [[PubMed](#)]
13. Bertran, E.; Sort, X.; Soliva, M.; Trillas, I. Composting winery waste: Sludges and grape stalks. *Bioresour. Technol.* **2004**, *95*, 203–208. [[CrossRef](#)] [[PubMed](#)]
14. Bustamante, M.A.; Pérez-Murcia, M.D.; Paredes, C.; Moral, R.; Pérez-Espinosa, A.; Moreno-Caselles, J. Short-term carbon and nitrogen mineralisation in soil amended with winery and distillery organic wastes. *Biores. Technol.* **2007**, *98*, 3269–3277. [[CrossRef](#)] [[PubMed](#)]
15. Miranda, M.T.; Arranz, J.I.; Román, S.; Rojas, S.; Montero, I.; López, M. Characterization of grape pomace and pyrenean oak pellets. *Fuel Process Technol.* **2011**, *92*, 278–283. [[CrossRef](#)]
16. Agence Nationale de Gestion des Déchets—ANGED. *Strategic Options for the Promotion of Value of Organic Waste VDO Tunisia*; Agence Nationale de Gestion des Déchets: Tunis, Tunisie, 2009.
17. Kraiem, N.; Lajili, M.; Limousy, L.; Said, R.; Jeguirim, M. Energy recovery from Tunisian agri-food wastes: Evaluation of combustion performance and emissions characteristics of green pellets prepared from tomato residues and grape marc. *Energy* **2016**, *107*, 409–418. [[CrossRef](#)]
18. Jeguirim, M.; Kraiem, N.; Lajili, M.; Guizani, C.; Zorras, A.; Leva, Y.; Michelin, L.; Josien, L.; Limousy, L. The relationship between mineral contents, particle matter and bottom ash distribution during pellet combustion: Molar balance and chemometric analysis. *Environ. Sci. Pollut. Res. Int.* **2017**, *24*, 9927–9939. [[CrossRef](#)] [[PubMed](#)]
19. Brassard, P.; Godbout, S.; Raghavan, V.; Palacios, J.H.; Grenier, M.; Zegan, D. The Production of Engineered Biochars in a Vertical Auger Pyrolysis Reactor for Carbon Sequestration. *Energies* **2017**, *10*, 288. [[CrossRef](#)]
20. Yang, X.; Wang, H.; Strong, P.J.; Xu, S.; Liu, S.; Lu, K.; Sheng, K.; Guo, J.; Che, L.; He, L.; et al. Thermal Properties of Biochars Derived from Waste Biomass Generated by Agricultural and Forestry Sectors. *Energies* **2017**, *10*, 469. [[CrossRef](#)]
21. Jeguirim, M.; Elmay, Y.; Limousy, L.; Lajili, M.; Said, R. Devolatilization behavior and pyrolysis kinetics of potential Tunisian biomass fuels. *Environ. Prog. Sustain. Energy* **2014**, *33*, 1452–1458. [[CrossRef](#)]
22. Mishra, R.K.; Mohanty, K. Pyrolysis kinetics and thermal behavior of waste sawdust biomass using thermogravimetric analysis. *Biores. Tech.* **2018**, *25*, 63–74. [[CrossRef](#)] [[PubMed](#)]
23. White, J.E.; Catallo, W.J.; Legendre, B.L. Biomass pyrolysis kinetics: A comparative critical review with relevant agricultural residue case studies. *J. Anal. Appl. Pyrol.* **2011**, *9*, 11–33. [[CrossRef](#)]
24. Cepeliogullar, O.; Haykiri Acma, H.; Yaman, S. Kinetic modelling of RDF pyrolysis: Model-fitting and model-free approaches. *Waste Manag.* **2016**, *48*, 275–284. [[CrossRef](#)] [[PubMed](#)]
25. Bartocci, P.; Anca Couce, A.; Slopiecka, K.; Nefkens, S.; Evic, N.; Retschitzegger, S.; Barbanera, M.; Buratti, C.; Cotana, F.; Bidini, G.; et al. Pyrolysis of pellets made with biomass and glycerol: Kinetic analysis and evolved gas analysis. *Biomass Bioenergy* **2017**, *97*, 11–19. [[CrossRef](#)]
26. Friedman, H.L. Kinetics of thermal degradation of char-forming plastics from thermogravimetry. Application to a phenolic plastic. *J. Polym. Sci. Polym. Symp.* **1964**, *6*, 183–195. [[CrossRef](#)]
27. Flynn, J.H.; Wall, L.A. General treatment of thermogravimetry of polymers. *J. Res. NBS A Phys. Chem.* **1966**, *70*, 487–523. [[CrossRef](#)]

28. Kissinger, H.E. Variation of peak temperature with heating rate in differential thermal analysis. *J. Res. Natl. Bur. Stand.* **1956**, *57*, 217–221. [[CrossRef](#)]
29. Guizani, C.; Jeguirim, M.; Valin, S.; Limousy, L.; Salvador, S. Biomass Chars: The Effects of Pyrolysis Conditions on Their Morphology, Structure, Chemical Properties and Reactivity. *Energies* **2017**, *10*, 796. [[CrossRef](#)]
30. González-Vázquez, M.P.; Garcia, R.; Pevida, C. Optimization of a Bubbling Fluidized Bed Plant for Low-Temperature Gasification of Biomass. *Energies* **2017**, *10*, 306. [[CrossRef](#)]
31. Makela, M.; Kwong, C.W.; Bostrom, M.; Yoshikawa, K. Hydrothermal treatment of grape marc for solid fuel applications. *Energy Convers. Manag.* **2017**, *145*, 371–377. [[CrossRef](#)]
32. Arvelakis, S.; Koukios, E.G. Physicochemical upgrading of agroresidues as feedstocks for energy production via thermochemical conversion methods. *Biomass Bioenergy* **2002**, *22*, 331–348. [[CrossRef](#)]
33. Limousy, L.; Jeguirim, M.; Dutournié, P.; Kraiem, N.; Lajili, M.; Said, R. Gaseous products and particulate matter emissions of biomass residential boiler fired with spent coffee grounds pellets. *Fuel* **2013**, *107*, 323–329. [[CrossRef](#)]
34. Gamzenur, O.; Ayse Eren, P. Kinetics and evolved gas analysis for pyrolysis of food processing wastes using TGA/MS/FT-IR. *Waste Manag.* **2017**. [[CrossRef](#)]
35. ElSayed, S.A.; Khairy, M. Effect of heating rate on the chemical kinetics of different biomass pyrolysis materials. *Biofuels* **2015**, *6*, 157–170. [[CrossRef](#)]
36. Orfao, J.J.M.; Antunes, F.J.A.; Figueiredo, J.L. Pyrolysis kinetics of lignocellulosic materials of three independent reactions model. *Fuel* **1999**, *78*, 349–358. [[CrossRef](#)]
37. ElSayed, S.A.; Mostafa, M.E. Kinetic Parameters Determination of Biomass Pyrolysis Fuels Using TGA and DTA Techniques. *Waste Biomass Valoriz.* **2015**, *6*, 401–415. [[CrossRef](#)]
38. Jeguirim, M.; Bikai, J.; Elmay, Y.; Limousy, L.; Njeugna, E. Thermal characterization and pyrolysis kinetics of tropical biomass feedstocks for energy recovery. *Energy Sustain. Dev.* **2014**, *23*, 188–193. [[CrossRef](#)]
39. Haddad, K.; Jeguirim, M.; Jellali, S.; Guizani, C.; Delmotte, L.; Benniccia, S.; Limousy, L. Combined NMR structural characterization and thermogravimetric analyses for the assessment of the AAEM effect during lignocellulosic biomass pyrolysis. *Energy* **2017**, *134*, 10–23. [[CrossRef](#)]
40. El may, Y.; Jeguirim, M.; Dorge, S.; Trouvé, G.; Said, R. Study on the thermal behavior of different date palm residues: Characterization and devolatilization kinetics under inert and oxidative atmospheres. *Energy* **2012**, *44*, 702–709. [[CrossRef](#)]
41. Yuan, H.; Xing, S.; Huhtaoli, L.T.; Chen, Y. Influences of copper on the pyrolysis process of demineralized wood dust through thermogravimetric and PyeGC / MS analysis. *J. Anal. Appl. Pyrolysis* **2015**, *112*, 325–332. [[CrossRef](#)]
42. Jeguirim, M.; Dorge, S.; Trouvé, G. Thermogravimetric analysis and emission characteristics of two energy crops in air atmosphere: Arundo donax and Miscanthus giganteus. *Bioresour. Technol.* **2010**, *101*, 788–793. [[CrossRef](#)] [[PubMed](#)]
43. Skreiber, A.; Skreiber, O.; Sandquist, J.; Sorum, L. TGA and macro-TGA characterisation of biomass fuels and fuel mixtures. *Fuel* **2011**, *90*, 2182–2197. [[CrossRef](#)]
44. Chouchene, A.; Jeguirim, M.; Khiari, B.; Zagrouba, F.; Trouvé, G. Thermal degradation of olive solid waste: Influence of particle size and oxygen concentration. *Resour. Conserv. Recycl.* **2010**, *54*, 271–277. [[CrossRef](#)]
45. Rhén, C.; Ohman, M.; Gref, R.; Wasterlund, I. Effect of raw material composition in woody biomass pellets on combustion characteristics. *Biomass Bioenergy* **2007**, *1*, 66–72. [[CrossRef](#)]
46. Chouchene, A.; Jeguirim, M.; Trouvé, G.; Favre-Reguillon, A.; Le Buzit, G. Combined process for the treatment of olive oil mill wastewater: Absorption on sawdust and combustion of the impregnated sawdust. *Bioresour. Technol.* **2010**, *101*, 6962–6971. [[CrossRef](#)] [[PubMed](#)]
47. Jahirul, M.I.; Rasul, M.G.; Chowdhury, A.A.; Ashwath, N. Biofuels Production through Biomass Pyrolysis—A Technological Review. *Energies* **2012**, *5*, 4952–5001. [[CrossRef](#)]
48. Ghouma, I.; Jeguirim, M.; Guizani, C.; Ouederni, A.; Limousy, L. Pyrolysis of Olive Pomace: Degradation Kinetics, Gaseous Analysis and Char Characterization. *Waste Biom. Valoriz.* **2017**, *8*, 1689–1697. [[CrossRef](#)]
49. Jun-Ho, J.; Seung-Soo, K.; Ye-Eun, L.; Yeong-Seok, Y. Pyrolysis Characteristics and Kinetics of Food Wastes. *Energies* **2017**, *10*, 1191. [[CrossRef](#)]
50. McKendry, P. Energy production from biomass (part 1): Overview of biomass. *Bioresour. Technol.* **2002**, *83*, 37–46. [[CrossRef](#)]

51. Ghetti, P.; Ricca, L.; Angelini, L. Thermal analysis of biomass and corresponding pyrolysis products. *Fuel* **1996**, *75*, 565–573. [[CrossRef](#)]
52. Fiori, L.; Valbusa, M.; Lorenzi, D.; Fambri, L. Modeling of the devolatilization kinetics during pyrolysis of grape residues. *Biores. Tech.* **2012**, *103*, 389–397. [[CrossRef](#)] [[PubMed](#)]
53. Marculescu, C.; Ciuta, S. Wine industry waste thermal processing for derived fuel properties improvement. *Renew. Energy* **2013**, *57*, 645–652. [[CrossRef](#)]
54. Di Blasi, C. Modeling chemical and physical processes of wood and biomass pyrolysis. *Prog. Energy Combust. Sci.* **2008**, *34*, 47–90. [[CrossRef](#)]
55. Wang, P.; Bret, H.; Howard, B.H. Impact of Thermal Pretreatment Temperatures on Woody Biomass Chemical Composition, Physical Properties and Microstructure. *Energies* **2018**, *11*, 25. [[CrossRef](#)]



© 2018 by the authors. Licensee MDPI, Basel, Switzerland. This article is an open access article distributed under the terms and conditions of the Creative Commons Attribution (CC BY) license (<http://creativecommons.org/licenses/by/4.0/>).

Article

Release Mechanism of Fuel-N into NO_x and N₂O Precursors during Pyrolysis of Rice Straw

Xiaorui Liu, Zhongyang Luo *, Chunjiang Yu, Bitao Jin and Hanchao Tu

State Key Laboratory of Clean Energy Utilization, Zhejiang University, Hangzhou 310027, China;
liuxiaorui214@zju.edu.cn (X.L.); chunjiang@zju.edu.cn (C.Y.); 21627061@zju.edu.cn (B.J.);
21527068@zju.edu.cn (H.T.)

* Correspondence: zyluo@zju.edu.cn; Tel.: +86-571-8795-2440

Received: 25 January 2018; Accepted: 24 February 2018; Published: 28 February 2018

Abstract: Rice straw, which is a typical agricultural residue in China, was pyrolyzed in a horizontal tube reactor connected with a Fourier transform infrared (FTIR) analyzer at temperatures ranging from 500 to 900 °C to research the release mechanism of fuel-N into NO_x and N₂O precursors. The concentrations of gaseous nitrogen components were monitored online. NH₃, HCN, HNCO, as well as NO were identified components. A high dependency between the gaseous products and temperature was found. NH₃ and HNCO preferred to be formed at lower temperatures and HCN tended to form at higher temperatures. It is worth noting that NO was also an important product. X-ray photoelectron spectroscopy (XPS) was performed to analyze the nitrogen species in rice straw. The result showed that amino-N (N-A) was the main form of nitrogen which accounted for 88.85%. Pyrrolic-N (N-5) was also identified and occupied the rest. Then nitrogen modeling compounds, glycine and pyrrole, were appropriately selected based on the results of XPS to well understand the nitrogen release mechanism during pyrolysis of rice straw. The formation routes of all the nitrogen gaseous components were confirmed. NH₃, HNCO and NO were originated from the decomposition of amino-N. While both amino-N and pyrrolic-N produced HCN. NO was not detected during the pyrolysis of pyrrole and a little NO was found during the pyrolysis of glycine. Hence, it can be deduced that the large amount of NO formed during the pyrolysis of rice straw was due to the direct oxidization reaction of –NH and –OH, the latter is abundant in the raw material. In order to provide evidence for this deduction, cellulose was added to increase the amount of –OH and co-pyrolysis of cellulose and glycine was conducted. The effect of –OH on the formation of NO was confirmed. Then, the release mechanism of fuel-N into NO_x and N₂O precursors during rice straw pyrolysis was concluded based on the experimental results.

Keywords: nitrogen; biomass; amino acid; pyrrole; NO_x; pyrolysis

1. Introduction

Biomass is considered as one of the most promising alternative energy because of its renewability and carbon-neutrality [1–8]. About 300 million tons of straw wastes, as well as the same amount of forestry wastes, are generated in China [9]. Direct combustion power generation is the major technology for large scale utilization of biomass [10]. Rice straw, which is abundant in southern China, dominates the amount of straw wastes, and is widely used as a fuel for biomass power plants. NO_x and N₂O, which can lead to environmental pollution [11], are the main gaseous pollutants during biomass combustion although the nitrogen content in most biomass is lower than that of coal. It is well known that pyrolysis is the first step of combustion, during which, part of the nitrogen in biomass is converted into NO_x and N₂O precursors (that is, NH₃, HCN, HNCO, et al.). These precursors will produce NO_x and N₂O via subsequent combustion. It was reported that about 80% of the nitrogen in biomass is released into gaseous precursors during pyrolysis at temperatures above 850–900 K [12].

It means that most of NO_x and N₂O originate from the combustion of volatile-N. Hence, it is necessary to understand the release mechanism of nitrogen during pyrolysis well, so that the emission of NO_x can be reduced by appropriate in-furnace low-nitrogen combustion measures.

Researches have been conducted to investigate the nitrogen release during biomass pyrolysis. It was reported that the gaseous components generally contain NH₃, HCN, HNCO, and NO [13–15]. Two approaches, chemical method and thermogravimetry infrared spectrum (TG-FTIR) method, were frequently used to research the conversion of fuel-N into gaseous nitrogen components.

Chemical method was carried out by many researches [13,14,16–22]. In those studies, NH₃ and HCN were absorbed by acid and alkaline solutions to form NH₄⁺ and CN[−], respectively. The total yields of NH₃ and HCN could be confirmed based on the ion concentrations of NH₄⁺ and CN[−] in the solutions. However, the yield of NH₃ was actually the sum of NH₃ and HNCO. HNCO, the precursor of N₂O [23], could not be investigated due to the reaction HNCO + H₂O → NH₃ + CO₂ [10,15–17]. The yield of NO was also not measured. Additionally, only the yields of NH₃ and HCN could be measured by chemical method, rather than the dynamic variation of concentrations for the precursors.

The nitrogen release was also studied by TG-FTIR [15,24–27], during which, the temperature of the sample was heated from ambient temperature to a higher temperature at a certain heating rate. However, the temperature of the sample was instantly heated up in an industrial combustor. For this reason, the results obtained from those researches could not accurately represent the nitrogen conversion in industrial combustors.

Rice straw is a typical agricultural residue and contains a higher nitrogen content, therefore, it was employed to investigate the release of fuel-N into NO_x and N₂O precursors during pyrolysis. The conversion of fuel-N into gaseous components during rice straw pyrolysis was researched in a few previous studies [17,28]. Yuan et al. [14] investigated the fuel-N conversion characteristic during rapid pyrolysis of rice straw at temperatures ranging from 600 to 1200 °C using a high frequency furnace. The yields of NH₃ and HCN were measured by chemical method. The results showed that HCN was the main nitrogen product while little NH₃ was found. Ren et al. [28] researched the formation of NO_x precursors during rice straw pyrolysis using TG-FTIR. They found that HCN and HNCO were the main nitrogen products. However, the results obtained from previous studies were based on TG-FTIR or chemical method, the shortcomings of which were discussed above.

A review of literatures shows that researches on nitrogen release during the pyrolysis of rice straw are rare and the release mechanism is still not well understood. Therefore, pyrolysis experiments of rice straw were conducted in a horizontal tube furnace in this study, and the concentrations of NH₃, HCN, HNCO, and NO were accurately and dynamically monitored by a FTIR gas analyzer (Gasmet DX4000, Gasmet Technologies Inc., Helsinki, Finland) during the whole reaction process at temperatures ranging from 500 to 900 °C. Compared with previous studies, in which chemical method was employed, the concentrations of gaseous nitrogen products were on-line monitored, not only the yields. HNCO was also measured in current work. Besides, different from TG, the temperature of the sample could be heated up to the set value instantly so that the pyrolysis process could be more similar to that of an industrial combustor.

It was reported that the nitrogen conversion mechanism of biomass could be explained by nitrogen modeling compounds to some extent [23,29–33], while X-ray photoelectron spectroscopy (XPS) was reliable to investigate the nitrogen occurrence form in biomass [12,34–36]. Therefore, in order to further understand the fuel-N release mechanism during pyrolysis, XPS was performed to analyze the occurrence form in rice straw, and the appropriate nitrogen modeling compounds were selected according to the XPS result.

2. Materials and Methods

2.1. Materials

Rice straw, a widely available biomass raw material in China, was employed. The samples were first dried for 2 h at 105 °C and then pulverized. The particle size was between 0.15 and

0.25 mm. Proximate analysis of the sample was performed using an Automatic Industrial Analyzer (5E-MAG6700, Kaiyuan Instruments Co., Changsha, China). Ultimate analysis was conducted with an elemental analyzer (LECO-CHNS932, LECO Co., St. Joseph, MI, USA). The results are shown in Table 1.

Table 1. Proximate (ar, wt. %) and ultimate analysis (ad, wt. %) of rice straw.

Proximate Analysis				Ultimate Analysis				
M ^a	A ^a	V ^a	FC ^a	C	H	N	S	O
1.51	11.31	69.09	18.09	42.66	5.68	0.64	0.44	39.10

^a M, A, V, FC represent moisture, ash, volatile and fixed carbon, respectively.

The occurrence form of nitrogen in rice straw was characterized using XPS (Escalab 250Xi, Thermo Fisher Scientific, Waltham, MA, USA), equipped with Al K α radiation source. The constant analyzer energy (CAE) mode with 30 eV pass energy was used for survey spectra and 20 eV was used for high resolution spectra. To calibrate the binding energy, the C1s peak was set to 284.8 eV and the Shirley background was subtracted from the spectra. The N1s peaks were fitted using Gaussian (80%)–Lorentzian (20%) and established with XPSpeak. According to the result of XPS, as shown in Figure 1, the main peak at 399.9 eV was assigned to amino-A and the other peak at 400.5 eV was assigned to pyrrolic-N. Thus, the nitrogen in rice straw was composed of 11.15% pyrrolic-N (N-5) and 88.85% amino-N (N-A). Therefore, Pyrrole and glycine, commercial reagents with high purity of 98% or more, were chosen as the modeling compounds for mechanism research. Cellulose, with a purity of 99%, was also purchased as an additive to research the effect of –OH on NO formation. All of the modeling compounds were purchased from Sigma-Aldrich (St. Louis, MO, USA).

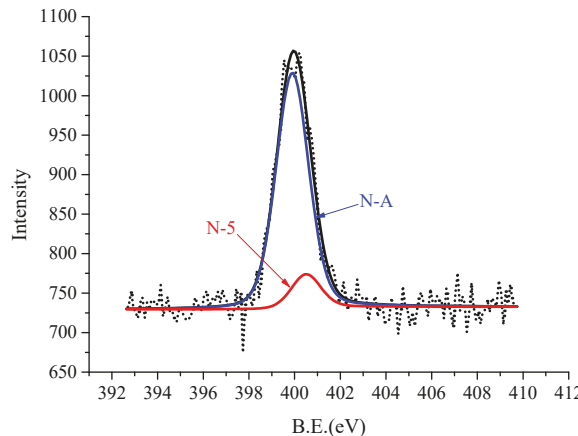


Figure 1. Nitrogen species in rice straw.

2.2. Experimental Methods

Experiments were conducted in a horizontal tube furnace reactor system, as shown in Figure 2. The furnace was 800 mm long and the inner diameter was 60 mm. The quartz tube was 1000 mm long and the inner diameter was 36 mm. The temperature of the reaction zone was controlled by a thermocouple connected to a temperature controller. The monitoring point of the thermocouple was set inside the quartz tube where the solid materials were placed to ensure an accurate temperature control. During experiments, 20 mg samples (rice straw or modeling compounds) were employed and were placed in a quartz boat (with length of 100 mm, width of 25 mm, and thickness of 1 mm). The reactor was heated by an electric furnace up to the given temperature ranging from 500 to 900 °C and maintained for 15 min. Then, the quartz boat that contained the sample was quickly pushed into the reaction zone. The carrier gas was argon (Ar) with a high purity of 99.999%. The gas flow rate was controlled at 4 L/min by mass flow meters. The volatiles released during pyrolysis were removed out from the reactor immediately by the carrier gas to keep a short residence time (less than 1.5 s) and to avoid the secondary reactions. Gasmet DX4000 (Gasmet DX 4000, Gasmet Technologies Inc., Helsinki, Finland), a kind of Fourier transform infrared gas analyzer, was employed to measure the concentrations of nitrogen containing components (NH₃, HCN, HNCO, and NO) on line. A sampling line was connected between the reactor and the gas analyzer, the temperature of which was maintained at 180 °C to avoid secondary pyrolysis and components condensing. The measurement time interval of the analyzer was set to be 3 s. Each test was repeated for three times to make sure that the relative standard deviations were less than 5%.

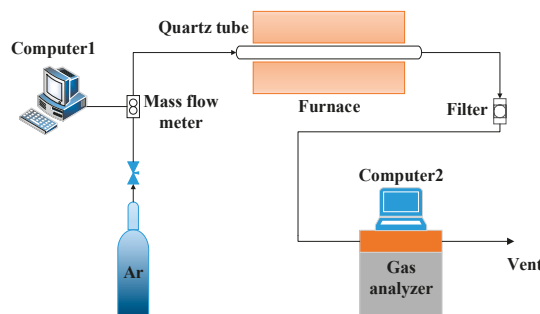


Figure 2. Schematic diagram of the horizontal tube furnace reactor system.

The convert ratios of fuel-N to gaseous nitrogen containing products (NH₃, HCN, HNCO, and NO) were calculated by Equation (1):

$$R_{\text{gas-N}} = \frac{\int c dt \times Q}{22.4 \times 10^6 \times 60} \times \frac{M_N}{m \times N_{pc}} \times 100\% \quad (1)$$

where $R_{\text{gas-N}}$ is the convert ratio of fuel-N to gaseous nitrogen components (%), c is the concentration of gaseous species (mg/Nm³), t is the measuring time (s), Q is the flow rate of flue gas (L/min), M_N is the molar mass of nitrogen (g/mol), and m is the weight of initial rice straw sample (g).

3. Results and Discussion

3.1. Nitrogen Release during Pyrolysis of Rice Straw

NH₃, HCN, HNCO, and NO were all found during the pyrolysis experiments of rice straw. Their concentrations were measured by a FTIR gas analyzer and recorded online. Figure 3 shows the release behavior of these gaseous products at temperatures ranging from 500 to 900 °C.

As shown in Figure 3, the peaks of the concentration curves of all the species appeared earlier as the temperature increased. This means that the chemical bond was broken more easily and that the reaction was more drastic at higher temperatures. NH_3 was detected at lower temperatures. Its concentration decreased with increasing temperature and totally disappeared at temperatures higher than 700°C . HNCO also decreased with rising temperature, and was disappeared at 800°C . On the contrary, HCN was first detected at 600°C and the concentration increased with an increasing temperature. It should be noted that NO was also a very important product, the concentration of which firstly increased with temperature and reached its maximum at 800°C and then decreased.

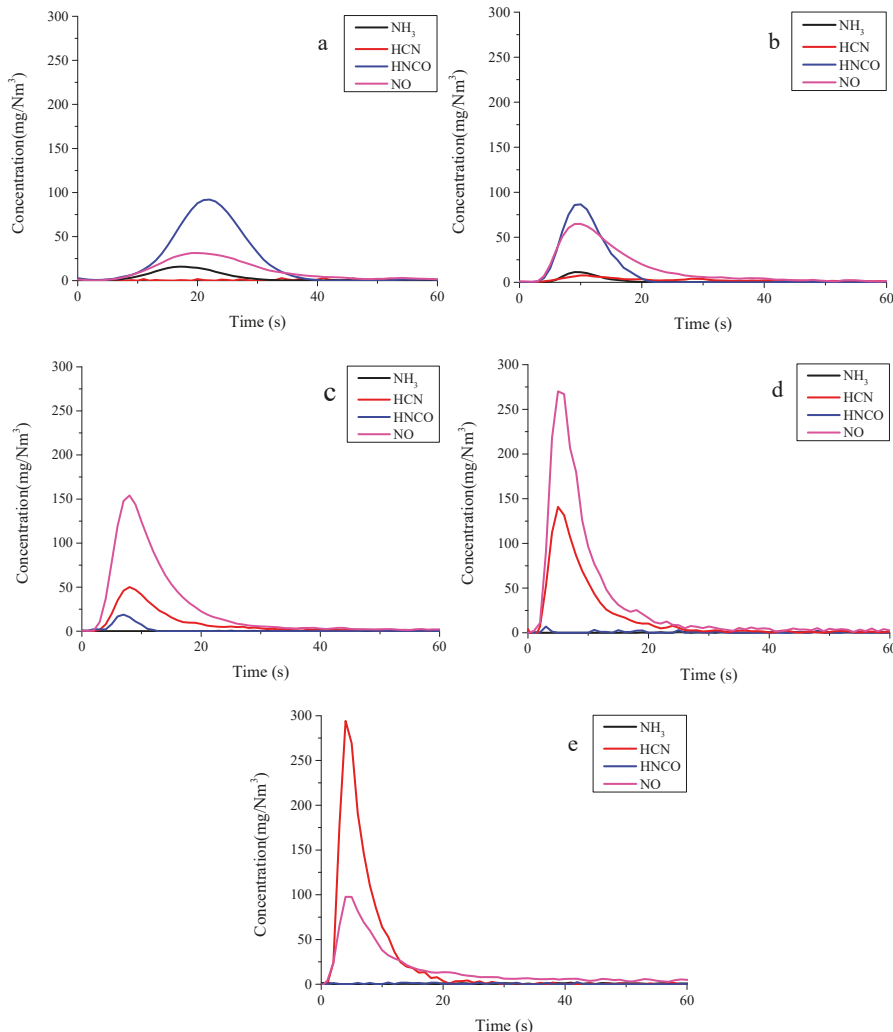


Figure 3. Release behaviors of nitrogen gaseous products during rice straw pyrolysis. (a) 500°C , (b) 600°C , (c) 700°C , (d) 800°C , (e) 900°C .

The convert ratios of fuel-N to gaseous products are shown in Figure 4. The convert ratios of fuel-N to NH_3 and HNCO decreased, while that of HCN increased with the increasing temperature.

Previous researchers also reported that HCN is preferentially formed at a higher temperature or at a higher heating rate, and that NH₃ is formed at a lower temperature or a lower heating rate [4,17,23,24]. Nitrogen release during rice straw pyrolysis was also studied by other researchers [17,28]. They also reported that HCN was the main product and little NH₃ was found. These results are in accordance with the result of the current study. The convert ratio of fuel-N to NO, a very important product, firstly increased and reached its maximum yield at 800 °C, and then decreased.

It is well known that the nitrogen species in biomass is mostly composed of amino acids [2,10,23,28]. The primary decomposition step of amino acid during pyrolysis contains decarboxylation, dehydration and deamination [32,33,37]. In present experiments, NH₃ was produced at temperatures lower than 700 °C, while at higher temperatures, NH₃ thoroughly disappeared. It was reported that amino acid could be converted into heterocyclic nitrogen compounds during thermal treatment [2], which would then lead to the decrease of amino acid. Due to this, the convert ratio of fuel-N to NH₃ decreased with the increase of temperature.

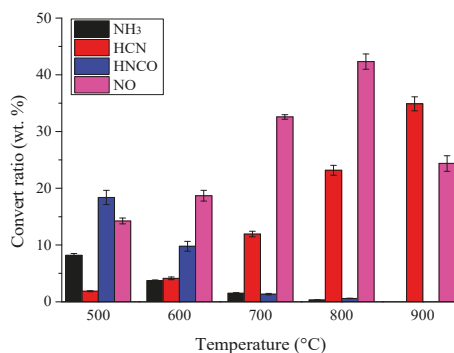


Figure 4. Convert ratios of fuel-N to gaseous products during pyrolysis of rice straw.

Cyclic amide, which was produced by dehydration, could be decomposed into HNCO and HCN further [15,23,32]. The convert ratio of fuel-N to HNCO decreased with the increase of temperature, while the reverse of HCN was observed. This corresponded with a previous study [38]. Therefore, the decomposition of cyclic amide has a high selectivity [15,23]. At lower temperatures, the convert ratio of fuel-N to HNCO was larger than that of HCN, while HCN was the main product at the higher temperatures. Hansson [38] pointed out that the activation energy for the formation of HNCO was lower than that of HCN during the decomposition of all cyclic amides. Besides, HNCO could be decomposed into HCN at high temperatures via the following reaction [24,32]:



which also led to the decrease of HNCO.

The peaks of NO concentration curves appeared simultaneously with that of other products at the same temperature, even a little earlier at lower temperatures. Hence, NO was definitely attributed to the direct oxidization reaction of N-sites with -OH, which is abundant in rice straw. The convert ratio of fuel-N to NO firstly increased with the increase of temperature and decreased at 900 °C. It was probably caused by the reduction reaction of NO and CO, which was catalyzed by inorganic impurities and even the chars at high temperatures [12,39]. CO was largely generated during pyrolysis and the reduction reaction easily occurred at higher temperatures. The concentration of CO was also tested by the gas analyzer in the experiments, as shown in Figure 5, which was powerful evidence for this explanation.

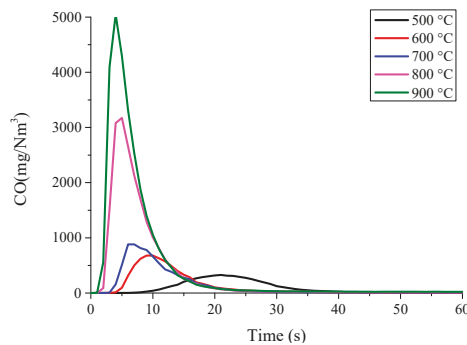


Figure 5. Variation of CO concentration with temperature.

3.2. Nitrogen Release during Pyrolysis of Nitrogen Modeling Compounds

Nitrogen in rice straw consisted of N-5 and N-A, as shown in Figure 1. It was reported that glycine is one of the major amino acids in agricultural straw [40]. Therefore, glycine and pyrrole were employed as modeling compounds to provide evidence for the release mechanism of fuel-N into gaseous components proposed above.

3.2.1. Pyrolysis of Glycine

Figure 6 shows the nitrogen release behavior during glycine pyrolysis at different temperatures. The concentrations of gaseous nitrogen containing products were much higher than that of rice straw. This was attributed to the high purity of glycine as well as its higher nitrogen content of 18.7%. The peaks of the concentration curves also appeared much earlier with the increasing temperature. The concentrations of HCN and NH₃ increased with the rising temperature, while the concentrations of other products firstly increased, and reached their maximum at 800 °C, then decreased.

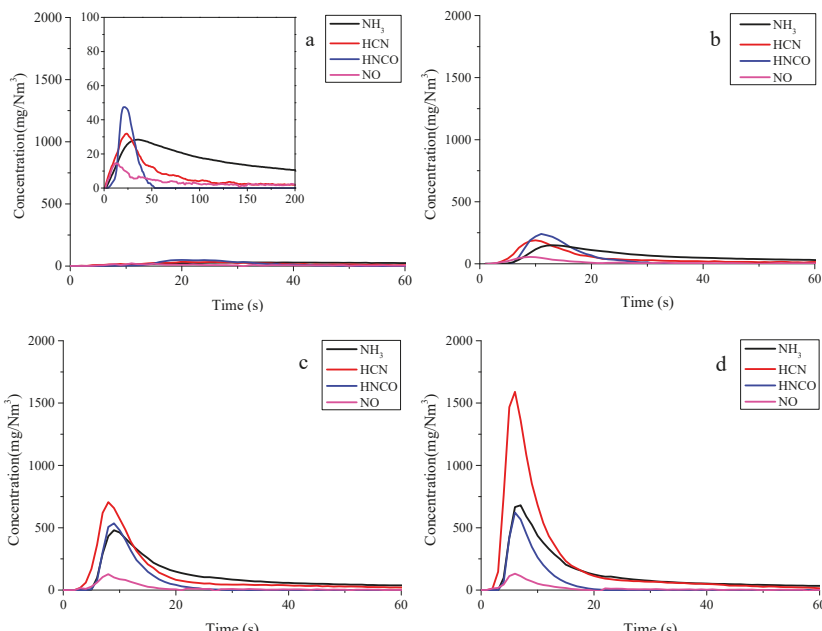


Figure 6. Cont.

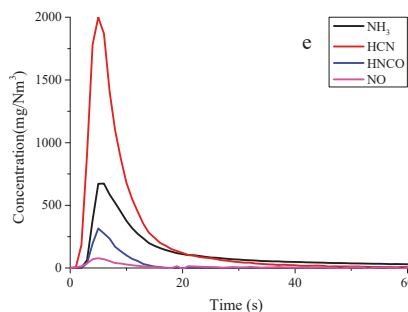


Figure 6. Release behavior of nitrogen gaseous products during glycine pyrolysis. (a) 500 °C, (b) 600 °C, (c) 700 °C, (d) 800 °C, (e) 900 °C.

The convert ratios of fuel-N into gaseous nitrogen containing products are shown in Figure 7. Different from the pyrolysis of rice straw, the convert ratios of fuel-N to NH₃ and HNCO firstly increased, and reached their maximum at 800 °C, then decreased. In particular, the proportion of NO was much smaller than that of rice straw.

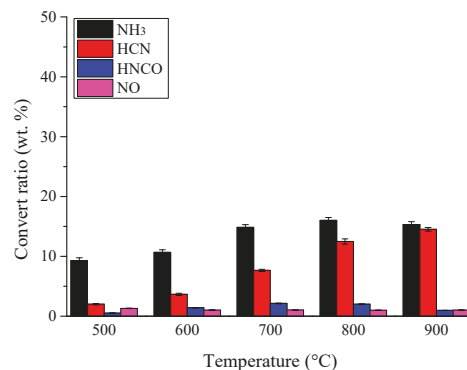
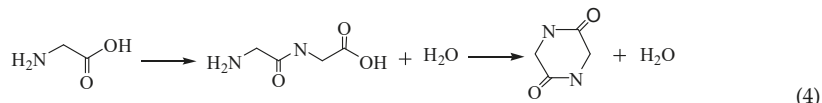
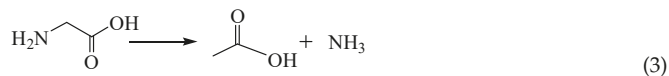
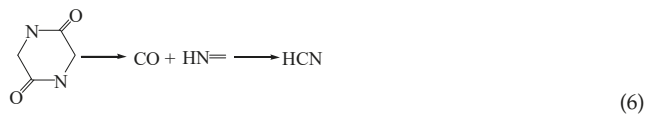


Figure 7. Convert ratios of fuel-N to gaseous nitrogen containing products during pyrolysis of glycine.

It was reported that during the pyrolysis of glycine, the main primary decomposition reactions are deamination and dehydration [33]. NH₃ and HNCO were formed via Equations (3) and (4). Additionally, the decomposition reaction of primary amines, as well as the bimolecular reactions between imine and amine, could also produce NH₃ [41].



HNCO was produced by the decomposition of cyclic amino, which was formed by the dehydration reaction, as shown in Equation (5). Meanwhile, the cracking of cyclic amino also produced HCN (see Equation (6)). HNCO could be further decomposed into HCN and CO at higher temperatures, and then the reduction of HNCO could be explained.



The peaks of NO concentration curves appeared a little earlier than that of other products at the same temperature. Hence, it is undoubted that NO was formed by the direct oxidization reaction of $-\text{NH}$ with $-\text{OH}$. The less convert ratio of NO might be caused by the lack of $-\text{OH}$ in glycine when compared to that rice straw.

3.2.2. Pyrolysis of Pyrrole

HCN was found to be the only product and was detected at temperatures higher than $700\text{ }^{\circ}\text{C}$ during the pyrolysis of pyrrole, as shown in Figure 8. The concentration of HCN at higher temperatures was much higher than that of rice straw. It was caused by the high purity of pyrrole and the high nitrogen content of 20.90%.

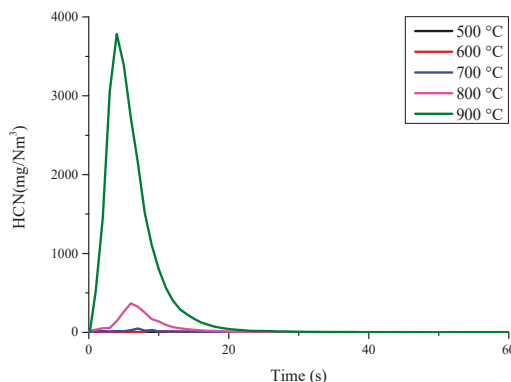
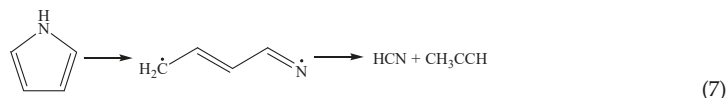


Figure 8. Variation of HCN concentration with temperature during pyrrole pyrolysis.

As it was reported in previous researches in regard to pyrrole pyrolysis [41–43], C–N was broken to generate an intermediate that decomposed into HCN and $\dot{\text{CH}}_2\text{—CH=CH}$ subsequently, as shown in Equation (7). The formation of HCN tended to occur at temperatures higher than $700\text{ }^{\circ}\text{C}$ [17,44]. This highly corresponded with the current study.



3.2.3. Effect of $-\text{OH}$ on the Formation of NO

NO was a major product during rice straw pyrolysis, however, it was not detected during the pyrolysis of pyrrole and little was formed during the pyrolysis of glycine. Therefore, it can be deduced that the large amount of NO formed during pyrolysis of rice straw was due the direct oxidization reaction of $-\text{NH}$ and $-\text{OH}$, which is abundant in rice straw.

Cellulose is the major component in lignocellulosic biomass, which accounts for 32–47% [45,46]. The percentage of cellulose in rice straw is 35% [46]. In order to prove the deduction of NO formation, cellulose was mixed into glycine to increase the amount of –OH and co-pyrolysis of glycine and cellulose was conducted. The mass ratio of cellulose to glycine was 1:4. The convert ratios of fuel-N to NO are shown in Figure 9. It is obvious that the convert ratio of NO increased with the addition of –OH. Furthermore, the ratio of –OH to amino acid in rice straw is much higher than in the mixed samples. Therefore, the larger amount of NO that is produced during pyrolysis of rice straw than model amino acid could be explained.

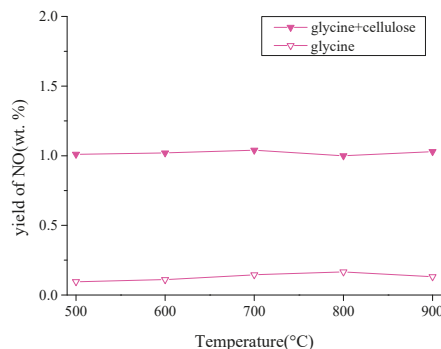


Figure 9. Convert ratios of fuel-N to NO during pyrolysis of glycine and co-pyrolysis of glycine and cellulose.

3.3. Mechanism of Nitrogen Release during Rice Straw Pyrolysis

As discussed above, NH₃ and HNCO were derived from the pyrolysis of amino acid. HCN was produced by pyrolysis of both amino acid and pyrrole. NO was an important product during rice straw pyrolysis, while a small amount of NO was found during amino acid pyrolysis, and it was not detected during pyrrole pyrolysis. Therefore, the formation of NO was attributed to the oxidization reaction of –NH and –OH, which is abundant in rice straw. This was proved by the co-pyrolysis of glycine and cellulose.

The nitrogen in rice straw was more complex than the model compounds of glycine and pyrrole. The transformation of nitrogen was reported to be affected by mineral matters [28,29,47] and the three major components of raw material, that is, cellulose, hemicellulose, and lignin [10,30,40] during pyrolysis of biomass. However, the research on modeling compounds could explain the nitrogen release route during pyrolysis due to the definite nitrogen occurrence forms in rice straw analyzed by XPS. Thus, the release mechanism of fuel-N into NO_x and N₂O precursors during rice straw pyrolysis was concluded in Figure 10.

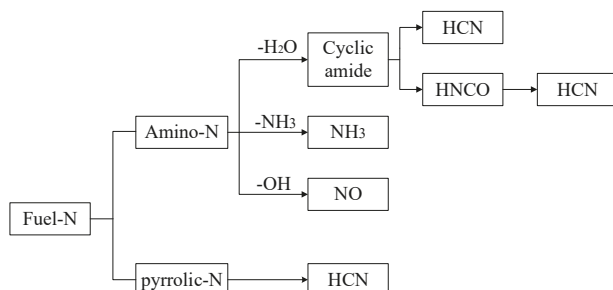


Figure 10. Release mechanism of fuel-N during rice straw pyrolysis.

4. Conclusions

Pyrolysis of rice straw was conducted to research the release mechanism of fuel-N into NO_x and N₂O precursors. The concentration variations of gaseous nitrogen components, i.e., NH₃, HCN, HNCO, and NO were dynamically monitored. The formation of gaseous nitrogen components was found to be highly dependent on temperature. NH₃ and HNCO preferred to be formed at lower temperatures and HCN tended to form at higher temperatures. It is worth noting that NO was also an important product.

The nitrogen occurrence form in rice straw was analyzed by XPS. Amino-N and pyrrolic-N were identified. Therefore, glycine, as well as pyrrole, were chosen as the nitrogen modeling compounds based on the results of XPS to understand the release mechanism of nitrogen during rice straw pyrolysis well. The formation routes of all nitrogen gaseous components were confirmed. NH₃, HNCO, and NO originated from the decomposition of amino acid. HCN was formed by the decomposition of both amino acid and pyrrole. NO was not detected during pyrolysis of pyrrole, and a little NO was found during amino acid pyrolysis. Therefore, a considerable proportion of NO formed during the pyrolysis of rice straw was due to the direct oxidization reaction of –NH and –OH in the raw material. To provide evidence for this proposal, cellulose was selected as an additive to increase the amount of –OH and co-pyrolysis of glycine and cellulose was conducted. Then, the release mechanism of fuel-N into NO_x and N₂O precursors during rice straw pyrolysis was proposed based on the experimental results. In future research, various biomass materials with different nitrogen occurrence forms would be employed to investigate the effect of fuel type on nitrogen release.

Acknowledgments: This work is supported by the National Natural Science Foundation of China (NO. 51336008).

Author Contributions: Zhongyang Luo and Chunjiang Yu conceived and designed the experiments; Xiaorui Liu performed the experiments; Xiaorui Liu analyzed the data; Hanchao Tu and Bitao Jin contributed reagents/materials/analysis tools; Xiaorui Liu wrote the paper.

Conflicts of Interest: The authors declare no conflict of interest.

References

- Tripathi, M.; Sahu, J.N.; Ganesan, P. Effect of process parameters on production of biochar from biomass waste through pyrolysis. *Renew. Sustain. Energy Rev.* **2016**, *55*, 467–481. [[CrossRef](#)]
- Chen, H.; Si, Y.; Chen, Y.; Yang, H.; Chen, D.; Chen, W. NO_x precursors from biomass pyrolysis: Distribution of amino acids in biomass and Tar-N during devolatilization using model compounds. *Fuel* **2017**, *187*, 367–375. [[CrossRef](#)]
- Shan, F.; Lin, Q.; Zhou, K.; Wu, Y.; Fu, W.; Zhang, P.; Song, L.; Shao, C.; Yi, B. An experimental study of ignition and combustion of single biomass pellets in air and oxy-fuel. *Fuel* **2017**, *188*, 277–284. [[CrossRef](#)]
- Wang, S.; Hu, Y.; Wang, Q.; Xu, S.; Lin, X.; Ji, H.; Zhang, Z. TG-FTIR-MS analysis of the pyrolysis of blended seaweed and rice husk. *J. Therm. Anal. Calorim.* **2016**, *126*, 1689–1702. [[CrossRef](#)]
- Houshfar, E.; Løvås, T.; Skreiberg, Ø. Experimental Investigation on NO_x Reduction by Primary Measures in Biomass Combustion: Straw, Peat, Sewage Sludge, Forest Residues and Wood Pellets. *Energies* **2012**, *5*, 270–290. [[CrossRef](#)]
- Molina-Moreno, V.; Leyva-Díaz, J.; Sánchez-Molina, J. Pellet as a Technological Nutrient within the Circular Economy Model: Comparative Analysis of Combustion Efficiency and CO and NO_x Emissions for Pellets from Olive and Almond Trees. *Energies* **2016**, *9*, 777. [[CrossRef](#)]
- Yang, X.; Wang, H.; Strong, P.J.; Xu, S.; Liu, S.; Lu, K.; Sheng, K.; Guo, J.; Che, L.; He, L.; et al. Thermal Properties of Biochars Derived from Waste Biomass Generated by Agricultural and Forestry Sectors. *Energies* **2017**, *10*, 469. [[CrossRef](#)]
- Gao, P.; Xue, L.; Lu, Q.; Dong, C. Effects of Alkali and Alkaline Earth Metals on N-Containing Species Release during Rice Straw Pyrolysis. *Energies* **2015**, *8*, 13021–13032. [[CrossRef](#)]
- Ren, X.; Sun, R.; Meng, X.; Vorobiev, N.; Schiemann, M.; Levendis, Y.A. Carbon, sulfur and nitrogen oxide emissions from combustion of pulverized raw and torrefied biomass. *Fuel* **2017**, *188*, 310–323. [[CrossRef](#)]

10. Ren, Q.; Zhao, C. Evolution of fuel-N in gas phase during biomass pyrolysis. *Renew. Sustain. Energy Rev.* **2015**, *50*, 408–418. [[CrossRef](#)]
11. Ghouma, I.; Jeguirim, M.; Sager, U.; Limousy, L.; Bennici, S.; Däuber, E.; Asbach, C.; Ligotski, R.; Schmidt, F.; Ouederni, A. The Potential of Activated Carbon Made of Agro-Industrial Residues in NO_x Immissions Abatement. *Energies* **2017**, *10*, 1508. [[CrossRef](#)]
12. Glarborg, P.; Jensen, A.D.; Johnsson, J.E. Fuel nitrogen conversion in solid fuel fired systems. *Prog. Energy Combust. Sci.* **2003**, *29*, 89–113. [[CrossRef](#)]
13. Chen, H.; Wang, Y.; Xu, G.; Yoshikawa, K. Fuel-N Evolution during the Pyrolysis of Industrial Biomass Wastes with High Nitrogen Content. *Energies* **2012**, *5*, 5418–5438. [[CrossRef](#)]
14. Yuan, S.; Zhou, Z.J.; Li, J.; Chen, X.L.; Wang, F.C. HCN and NH₃ (NO_x precursors) released under rapid pyrolysis of biomass/coal blends. *J. Anal. Appl. Pyrolysis* **2011**, *92*, 463–469. [[CrossRef](#)]
15. Ren, Q.; Zhao, C.; Wu, X.; Liang, C.; Chen, X.; Shen, J.; Wang, Z. Formation of NO_x precursors during wheat straw pyrolysis and gasification with O₂ and CO₂. *Fuel* **2010**, *89*, 1064–1069. [[CrossRef](#)]
16. Yuan, S.; Chen, X.L.; Li, W.F.; Liu, H.F.; Wang, F.C. Nitrogen conversion under rapid pyrolysis of two types of aquatic biomass and corresponding blends with coal. *Bioresour. Technol.* **2011**, *102*, 10124–10130. [[CrossRef](#)] [[PubMed](#)]
17. Yuan, S.; Zhou, Z.J.; Li, J.; Chen, X.L.; Wang, F.C. HCN and NH₃ Released from Biomass and Soybean Cake under Rapid Pyrolysis. *Energy Fuels* **2010**, *24*, 6166–6171. [[CrossRef](#)]
18. Tian, F.J.; Yu, J.; Mckenzie, L.J.; Hayashi, J.I.; Li, C.Z. Conversion of Fuel-N into HCN and NH₃ during the Pyrolysis and Gasification in Steam: A Comparative Study of Coal and Biomass. *Energy Fuels* **2007**, *21*, 517–521. [[CrossRef](#)]
19. Tian, F.J.; Yu, J.L.; Mckenzie, L.J.; Hayashi, J.I.; Chiba, T.; Li, C.Z. Formation of NO precursors during the pyrolysis of coal and biomass. Part VII. Pyrolysis and gasification of cane trash with steam. *Fuel* **2005**, *84*, 371–376. [[CrossRef](#)]
20. Chang, L.; Xie, Z.; Xie, K.C.; Pratt, K.C.; Hayashi, J.I.; Chiba, T.; Li, C.Z. Formation of NO_x precursors during the pyrolysis of coal and biomass. Part VI. Effects of gas atmosphere on the formation of NH₃ and HCN. *Fuel* **2003**, *82*, 1159–1166. [[CrossRef](#)]
21. Tan, L.L.; Li, C. Formation of NO_x and SO_x precursors during the pyrolysis of coal and biomass. Part I. Effects of reactor configuration on the determined yields of HCN and NH₃ during pyrolysis. *Fuel* **2000**, *79*, 1883–1889. [[CrossRef](#)]
22. Zhan, H.; Yin, X.; Huang, Y.; Yuan, H.; Xie, J.; Wu, C.; Shen, Z.; Cao, J. Comparisons of Formation Characteristics of NO_x Precursors during Pyrolysis of Lignocellulosic Industrial Biomass Wastes. *Energy Fuels* **2017**, *31*, 9557–9567. [[CrossRef](#)]
23. Hansson, K.M.; Samuelsson, J.; Tullin, C.; Åmand, L.E. Formation of HNCO, HCN, and NH₃ from the pyrolysis of bark and nitrogen-containing model compounds. *Combust. Flame* **2004**, *137*, 265–277. [[CrossRef](#)]
24. Zhu, X.; Yang, S.; Wang, L.; Liu, Y.; Qian, F.; Yao, W.; Zhang, S.; Chen, J. Tracking the conversion of nitrogen during pyrolysis of antibiotic mycelial fermentation residues using XPS and TG-FTIR-MS technology. *Environ. Pollut.* **2016**, *211*, 20–27. [[CrossRef](#)] [[PubMed](#)]
25. Wang, X.; Si, J.; Tan, H.; Ma, L.; Pourkashanian, M.; Xu, T. Nitrogen, Sulfur, and Chlorine Transformations during the Pyrolysis of Straw. *Energy Fuels* **2010**, *24*, 5215–5221. [[CrossRef](#)]
26. De Jong, W.; Di Nola, G.; Venneker, B.C.; Spliethoff, H.; Wójtowicz, M.A. TG-FTIR pyrolysis of coal and secondary biomass fuels: Determination of pyrolysis kinetic parameters for main species and NO_x precursors. *Fuel* **2007**, *86*, 2367–2376. [[CrossRef](#)]
27. Becidan, M.; Skreiber, Ø.; Hustad, J.E. NO_x and N₂O Precursors (NH₃ and HCN) in Pyrolysis of Biomass Residues. *Energy Fuels* **2007**, *21*, 1173–1180. [[CrossRef](#)]
28. Ren, Q.; Zhao, C. Effect of mineral matter on the formation of NO_x precursors during biomass pyrolysis. *J. Anal. Appl. Pyrolysis* **2009**, *85*, 447–453. [[CrossRef](#)]
29. Ren, Q.; Zhao, C. NO_x and N₂O Precursors from Biomass Pyrolysis: Role of Cellulose, Hemicellulose and Lignin. *Environ. Sci. Technol.* **2013**, *47*, 8955–8961. [[CrossRef](#)] [[PubMed](#)]
30. Ren, Q.; Zhao, C. NO_x and N₂O precursors (NH₃ and HCN) from biomass pyrolysis: Interaction between amino acid and mineral matter. *Appl. Energy* **2013**, *112*, 170–174. [[CrossRef](#)]
31. Ren, Q.; Zhao, C. NO_x and N₂O Precursors from Biomass Pyrolysis: Nitrogen Transformation from Amino Acid. *Environ. Sci. Technol.* **2012**, *46*, 4236–4240. [[CrossRef](#)] [[PubMed](#)]

32. Jie, L.; Yuwen, L.; Jingyan, S.; Zhiyong, W.; Ling, H.; Xi, Y.; Cunxin, W. The investigation of thermal decomposition pathways of phenylalanine and tyrosine by TG–FTIR. *Thermochim. Acta* **2008**, *467*, 20–29. [[CrossRef](#)]
33. Li, J.; Wang, Z.; Yang, X.; Hu, L.; Liu, Y.; Wang, C. Evaluate the pyrolysis pathway of glycine and glycylglycine by TG–FTIR. *J. Anal. Appl. Pyrolysis* **2007**, *80*, 247–253. [[CrossRef](#)]
34. Titantah, J.T.; Lamoen, D. Carbon and nitrogen 1s energy levels in amorphous carbon nitride systems: XPS interpretation using first-principles. *Diam. Relat. Mater.* **2007**, *16*, 581–588. [[CrossRef](#)]
35. Schmiers, H.; Friebel, J.; Streubel, P.; Hesse, R.; Köpsel, R. Change of chemical bonding of nitrogen of polymeric N-heterocyclic compounds during pyrolysis. *Carbon* **1999**, *37*, 1965–1978. [[CrossRef](#)]
36. Jansen, R.J.J.; van Bekkum, H. XPS of nitrogen-containing functional groups on activated carbon. *Carbon* **1995**, *33*, 1021–1027. [[CrossRef](#)]
37. Deng, L.; Jin, X.; Zhang, Y.; Che, D. Release of nitrogen oxides during combustion of model coals. *Fuel* **2016**, *175*, 217–224. [[CrossRef](#)]
38. Hansson, K.; Samuelsson, J.; Åmand, L.; Tullin, C. The temperature's influence on the selectivity between HNCO and HCN from pyrolysis of 2,5-diketopiperazine and 2-pyridone. *Fuel* **2003**, *82*, 2163–2172. [[CrossRef](#)]
39. Johnsson, J.E. Formation and reduction of nitrogen oxides in fluidized-bed combustion. *Fuel* **1994**, *73*, 1398–1415. [[CrossRef](#)]
40. Ren, Q.; Zhao, C.; Chen, X.; Duan, L.; Li, Y.; Ma, C. NO_x and N₂O precursors (NH₃ and HCN) from biomass pyrolysis: Co-pyrolysis of amino acids and cellulose, hemicellulose and lignin. *Proc. Combust. Inst.* **2011**, *33*, 1715–1722. [[CrossRef](#)]
41. Lifshitz, A.; Tamburu, C.; Suslensky, A. Isomerization and Decomposition of Pyrrole at Elevated Temperatures: Studies with a Single-Pulse Shock Tube. *J. Chem. Phys.* **1989**, *93*, 5802–5808. [[CrossRef](#)]
42. Zhai, L.; Zhou, X.; Liu, R. A Theoretical Study of Pyrolysis Mechanisms of Pyrrole. *J. Phys. Chem. A* **1999**, *103*, 3917–3922. [[CrossRef](#)]
43. Mackie, J.C.; Colket, M.B.; Nelson, P.F.; Esler, M. Shock Tube Pyrolysis of Pyrrole and Kinetic Modeling. *Int. J. Chem. Kinet.* **1991**, *23*, 733–760. [[CrossRef](#)]
44. Li, C.; Tan, L.L. Formation of NO_x and SO_x precursors during the pyrolysis of coal and biomass. Part III. Further discussion on the formation of HCN and NH₃ during pyrolysis. *Fuel* **2000**, *79*, 1899–1906. [[CrossRef](#)]
45. Binod, P.; Sindhu, R.; Singhania, R.R.; Vikram, S.; Devi, L.; Nagalakshmi, S.; Kurien, N.; Sukumaran, R.K.; Pandey, A. Bioethanol production from rice straw: An overview. *Bioresour. Technol.* **2010**, *101*, 4767–4774. [[CrossRef](#)] [[PubMed](#)]
46. Saha, B.C. Hemicellulose bioconversion. *J. Ind. Microbiol. Biotechnol.* **2003**, *30*, 279–291. [[CrossRef](#)] [[PubMed](#)]
47. Wei, L.; Wen, L.; Liu, M.; Yang, T. Interaction Characteristics of Mineral Matter and Nitrogen during Sewage Sludge Pyrolysis. *Energy Fuels* **2016**, *30*, 10505–10510. [[CrossRef](#)]



© 2018 by the authors. Licensee MDPI, Basel, Switzerland. This article is an open access article distributed under the terms and conditions of the Creative Commons Attribution (CC BY) license (<http://creativecommons.org/licenses/by/4.0/>).

Article

Towards Biochar and Hydrochar Engineering—Influence of Process Conditions on Surface Physical and Chemical Properties, Thermal Stability, Nutrient Availability, Toxicity and Wettability

Alba Dieguez-Alonso ^{1,*}, Axel Funke ², Andrés Anca-Couce ³, Alessandro Girolamo Rombolà ⁴, Gerardo Ojeda ⁵, Jörg Bachmann ⁶ and Frank Behrendt ¹

- ¹ Institute of Energy Engineering, Technische Universität Berlin, Chair for Energy Process Engineering and Conversion Technologies for Renewable Energies, Fasanenstr. 89, 10623 Berlin, Germany; frank.behrendt@tu-berlin.de
- ² Institute of Catalysis Research and Technology (IKFT), Karlsruhe Institute of Technology, Hermann-von-Helmholtz-Platz 1, 76344 Eggenstein-Leopoldshafen, Germany; axel.funke@kit.edu
- ³ Institute of Thermal Engineering, Graz University of Technology, Inffeldgasse 25b, 8010 Graz, Austria; anca-couce@tugraz.at
- ⁴ Department of Chemistry “Giacomo Ciamician”, C.I.R.I. Energia Ambiente and C.I.R.S.A., Università di Bologna, Ravenna Campus, Via S. Alberto 163, 48123 Ravenna, Italy; alessandro.rombola@unibo.it
- ⁵ Ecological and Forestry Applications Research Centre (CREAF), 08193 Cerdanyola del Vallès, Spain; g.ojeda@creaf.uab.cat
- ⁶ Institute of Soil Science, Leibniz University of Hannover, Herrenhaeuser Str. 2, 30419 Hannover, Germany; bachmann@ifbk.uni-hannover.de

* Correspondence: alba.dieguezalonso@tu-berlin.de; Tel.: +49-(30)-314-24381

Received: 31 December 2017; Accepted: 11 February 2018; Published: 27 February 2018

Abstract: The impact of conversion process parameters in pyrolysis (maximum temperature, inert gas flow rate) and hydrothermal carbonization (maximum temperature, residence time and post-washing) on biochar and hydrochar properties is investigated. Pine wood (PW) and corn digestate (CD), with low and high inorganic species content respectively, are used as feedstock. CD biochars show lower H/C ratios, thermal recalcitrance and total specific surface area than PW biochars, but higher mesoporosity. CD and PW biochars present higher naphthalene and phenanthrene contents, respectively, which may indicate different reaction pathways. High temperatures ($>500\text{ }^{\circ}\text{C}$) lead to lower PAH (polycyclic aromatic hydrocarbons) content ($<12\text{ mg/kg}$) and higher specific surface area. With increasing process severity the biochars carbon content is also enhanced, as well as the thermal stability. High inert gas flow rates increase the microporosity and wettability of biochars. In hydrochars the high inorganic content favor decarboxylation over dehydration reactions. Hydrochars show mainly mesoporosity, with a higher pore volume but generally lower specific surface area than biochars. Biochars present negligible availability of NO_3^- and NH_4^+ , irrespective of the nitrogen content of the feedstock. For hydrochars, a potential increase in availability of NO_3^- , NH_4^+ , PO_4^{3-} , and K^+ with respect to the feedstock is possible. The results from this work can be applied to “engineer” appropriate biochars with respect to soil demands and certification requirements.

Keywords: pyrolysis; hydrothermal carbonization; biochar engineering; porosity; nutrients; polycyclic aromatic hydrocarbon (PAH)

1. Introduction

The definitions of biochar provided by the European Biochar Certificate (EBC) [1] and the IBI (International Biochar Initiative) Biochar Standards [2] address biochar properties requirements for its application, as well as methodological standards to assess them, but they do not describe in detail the production process and its influence on biochar properties. As an example, the EBC considers mainly pyrolysis as the process to produce biochar, including gasification as part of the pyrolysis technology spectrum. However, the IBI Biochar Standards consider all forms of thermochemical conversion with limited presence of oxygen as appropriate technologies to produce biochar. Therefore, hydrothermal carbonization (HTC) could be included as well. In recent years, a lot of research has been done in the field of biochar to understand the impact of process conditions on biochar properties, as well as biochar dynamics once applied to soil and, consequently, its potential positive and/or negative impacts on crops, environment and soil. However, as Abiven et al. [3] pointed out, it is necessary to develop tailor-made biochar systems according to individual applications, taking into account soil type, climate and social environments, instead of considering biochar as an universal soil enhancer. Besides, biochar can have other applications, such as its use for soil and water remediation through the adsorption and immobilization of organic and inorganic contaminants [4–7]. Within its agronomic use, and according to a review by Mohan et al. [8], biochar can potentially increase nutrient availability (direct and indirect pathways), water retention, soil organic matter, microbial activity and crop yields. This may contribute to a reduction in nutrient leaching, fertilizer demand or emissions [9–11].

- Direct biochar contribution to nutrient availability relies on the macro- and /or micronutrients that biochar contains and their availability [5,9,10]. This is strongly dependent on the composition of the initial feedstock [10] and on the pyrolysis conditions. High retention of alkali species and P is reported for pyrolysis temperatures below 600–700 °C and low heating rates [12–15], with increase in total, soluble and exchangeable base cations with increasing process severity [13]. However, Uchimiya et al. [16] showed that NaOH-EDTA extractable P increased at 300–350 °C pyrolysis temperature and decreased at higher temperatures for plant and manure biochars. Hossain et al. [17] showed that total N content and N availability decreased with increasing pyrolysis temperature in wastewater sludge biochars.
- Indirect contribution to nutrient availability relies on the capacity of biochars to retain applied nutrients, potentially reducing leaching and increasing fertilizer-use efficiency, on their liming effect or on their impact on other soil properties, such as the potential increase in water-holding capacity, among others, as reviewed by Chan and Xu in [10]. Biochars nutrient retention capacity is associated to their surface charge and surface physical properties as stated by Chan and Xu in [10].
- Biochar surface charge will impact the biochar capacity to adsorb positively or negatively charged nutrients. The cation exchange capacity (CEC) is a measure of the biochar capacity to retain positively charged species, mainly through electrostatic interactions [7,18]. Budai et al. [19] reported that CEC is influenced by different factors, with no clear dominance. These may include: the presence of negatively charged oxygen-containing functional groups on the biochar surface, such as carboxylate (from carboxylic acid) and hydroxyl functional groups [13,18–20], which are reported to decrease with increasing conversion temperature [13,18,19,21,22]; the pH of the solution [18]; the content and composition of the inorganic fraction [23,24]. Values for biochars CEC and its dependence on process conditions and feedstock vary significantly in literature [18,19,24]. Biochars anion exchange capacity (AEC) is scarcely reported in literature [20], with studies even showing negligible AEC [18]. Little is known about the origin of AEC on the surface of biochar [20]. However, due to the relevance of this topic, especially towards the reduction in negatively charged nutrients leaching, such as phosphates and nitrates, plenty of recent research activity focuses on the modification of biochar surfaces to enhance their capacity or adsorb such species.

- Biochar specific surface area and pore volume increase with pyrolysis temperature [19,21,25] up to approximately 600–700 °C, when further ordering of the biochar structure may lead to a decrease in surface area [19,25]. Mainly micropores contribute to the specific surface area in biochars [21]. Other process parameters, such as biomass composition, specially inorganic species content, heating rate and pressure can have also a significant impact on porosity development [26,27]. Surface area and pore network may impact biochar adsorption capacity due to the influence on accessibility [18] and availability of adsorption sites.
- With respect to water retention, this depends on both the physical and chemical surface properties of biochar. The nature of surface functional groups impacts the hydrophobic/hydrophilic behavior of biochars [20]. As reported by Schimmelpfenning et al. [21], polar functional groups on the biochar surface may increase the uptake of water due to electrostatic interactions and hydrogen bonds. Their reduction can lead to higher hydrophobic character [28]. Hagemann et al. [29] reported that biochar-water interactions enhancement, leading to higher nutrient retention, can be achieved with higher mesoporosity, redox-active sites and hydrophilicity on the surface of biochars.
- Biochars pH is of high relevance for its application in soil, since it determines not only its potential liming effect, but it also has an influence on other properties, such as CEC, water holding capacity or adsorption capacity for different nutrients or heavy metals [18,30].

Consequently, in order to achieve the capacity of “engineering biochar”, not only further knowledge of the mechanisms behind biochar interactions in soil (including quantification and durability of the impact and variability in response) [9,31] is required, but also a deeper mechanistic understanding of the influence of conversion process and feedstock on biochar properties and its function in soil. This is a complex issue due to the highly relevant influence of (1) feedstock, (2) type of process, and (3) process parameters on biochar characteristics, as briefly introduced.

For pyrolysis, temperature and feedstock properties are the main process parameters under consideration when investigating the influence of conversion process on biochar properties. However, other process variables such as inert gas flow rate, heating rate, particle size, atmosphere and pressure can dramatically change biochar properties as well [26,32,33]. Furthermore, with HTC the chemical pathways involved differ significantly from those of pyrolysis. The different nature of these chemical reactions open up the potential to design carbon materials with a variety of interesting functionalities [34].

Comparison of chars produced from pyrolysis (termed biochars in the following) and chars produced from HTC (termed hydrochars in the following) has been previously done in literature, as summarized in Table 1. Huff et al. [35] reported higher O/C ratios for hydrochars than for biochars, as well as a significantly higher CEC, which, however, did not correlate well with the capacity of these chars to adsorb organic compounds (methylene blue). Budai et al. [19] showed that volatile matter and H/C and O/C ratios can be good parameters to determine the carbonization degree, irrespective of conversion process and feedstock, but poor predictors for agronomic properties (SSA and CEC). Liu et al. [28] reported that HTC creates oxygen-containing functional groups on the hydrochar surface with respect to the feedstock, while pyrolysis reduces their presence. Both biochar and hydrochar develop a rough surface and pore structure and are able to remove metal species from wastewater, such as copper, although different adsorption mechanisms can be responsible [28]. Based on a wide comparison of biochars, produced through different methods, and hydrochars, quality indicators for biochar production were suggested, such as H/C ratios below 0.6, O/C ratios below 0.4 and black carbon content higher than 15% (based on C), to ensure stability in soil [21]. Moreover, BET SSA higher than $100 \text{ m}^2 \text{ g}^{-1}$ and PAHs content according to the precautionary values defined by the German federal soil protection ordinance (“Bundesbodenschutzverordnung”) should be achieved [21]. Regarding chemical structure, it was shown that while biochar is mostly aromatic, with small traces of alkyl carbons, hydrochars contain mostly alkyl moieties [36]. This was further confirmed in [37], where it was also reported that hydrochars have higher nutrient retention capacity than biochars. At the same time, both were within the EBC [1] recommended limits for PAHs content [37]. It was concluded

that conversion conditions strongly affect the char properties and that, while biochar standards are described in the EBC [1], hydrochars need their own directive [37]. In [36], it was also shown that the aromatic cluster size of biochar is larger than the one of hydrochar. Furthermore, acid prewashing and water and acetone washing can change the chemical structure of hydrochars [36]. Genotoxic and phytotoxic risk assessment showed hydrochars to be phytotoxic, inhibiting germination, although this effect could be eliminated with biological post-treatment [38]. Moreover, hydrochar is less suitable for long-term C sequestration in comparison to biochar, due to a lower stability, but it can deliver essential nutrients, having therefore potential for soil amelioration [39].

The objective of the present work is to contribute to the comparison between biochars and hydrochars by investigating the influence of conversion process conditions and feedstock on relevant properties. For this purpose, biochars and hydrochars were produced from two biomass feedstocks with varying mineral content (pine wood and corn digestate). Biochar was produced by pyrolysis in a fixed bed reactor at two maximum conversion temperatures (400 and 600 °C) and two inert gas flow rates (20 and 40 NL min⁻¹ of N₂). Hydrochars were produced by HTC in a batch autoclave at two conversion temperatures (200 and 240 °C), two residence times (10 and 360 min) and with and without water washing after production (3 and 6 times). Together with primary characterization properties, such as proximate and elemental analyses, other characteristics, which can contribute to the understanding of biochar and hydrochar behavior once applied to soil, are analyzed: pH, acidic surface functional groups, pore size distribution with N₂ and CO₂ adsorption, nutrient availability, thermal stability, PAHs content and wettability.

Comparing the objectives of the present work and the previously reviewed literature, this study introduces a more detailed analysis on (1) the influence of conversion process parameters and (2) the characterization of products properties. With respect to process conditions, temperature, time and water washing have been chosen for HTC because very little data is available in the above mentioned publications regarding their combined influence on hydrochars. Moreover, the influence of inert gas flow rate in pyrolysis, and therefore the retention time of volatiles in the bed, is a novelty in this comparative study. This work represents a fundamental characterization of char produced under different and relevant process conditions and, therefore, issues regarding the energetic costs associated with inert gas flow rates, process temperatures or residence times cannot be evaluated based on these laboratory scale results. Furthermore, beyond the investigated product properties in the reviewed literature, a deep analysis is performed for the first time on the porous structure of both biochars and hydrochars combining N₂ and CO₂ adsorption, as well as research and comparison on nutrient availability and wettability. Finally, the results are analyzed from a conversion process perspective, in order to achieve an advance in the state-of-the-art of the “engineering biochar” concept.

Table 1. Summary of literature studies comparing biochars and hydrochars. CEC: cation exchange capacity, FTIR: Fourier-transform infrared spectroscopy, SSA: specific surface area, SEM: scanning electron microscopy, EDs: energy-dispersive X-ray spectroscopy, CT: CarbonTerra (Augsburg, Germany), BC: Black-Carbon (Barrit, Denmark), AGT: Advanced Gasification Technology (Atosio, Italy).

Authors	Process Conditions	Feedstock	Methods
Budai et al. [19]	Biochars from slow pyrolysis (235–800 °C), flash carbonization char (600 °C) and hydrochars (230 °C for 6 h)	Corn cob and miscanthus	Proximate and elemental (CHNO) analyses, pH, CEC, SSA with N ₂ adsorption
Schimmeleffmennig and Glaser [21]	Biochars from slow pyrolysis (Pyreg unit) (550 °C), hydrochars (200 °C), rotary kiln biochars (350–550, 750 °C), gasification biochars (800 °C), traditional kiln biochars (350 °C), other biochars (350, 500, 650, 800 °C)	Wood, animal meal, sugar cane/beet, wheat, bamboo, maize, rice hulls, peanut shells, sewage sludge, walnut shells, girasol, coconut shells, lop bark/needles	Elemental (CHNO) analysis, black carbon content, SSA with N ₂ adsorption, PAHs content
Liu et al. [28]	Biochars from slow pyrolysis (700 °C), hydrochars (300 °C for 20 min)	Pine wood	Proximate and elemental (CHNO) analyses, Boehm titration, pH, FTIR spectroscopy, surface morphology with SEM, SSA and micro-, meso- and macropores volume with N ₂ adsorption, copper removal capacity (adsorption) from wastewater
Huff et al. [35]	Biochars from slow pyrolysis (300, 400 and 500 °C) and hydrochars (300 °C for 30 min)	Pine wood, peanut shell and bamboo	Proximate and elemental (CHN) analyses, methylene blue adsorption, CEC, FTIR spectroscopy
Cao et al. [36]	Biochars from slow pyrolysis (620 °C) and hydrochars (with acid prewashing and water and acetone washing) (250 °C for 20 h)	Swine-manure	Major chemical structural components with Quantitative ¹³ C Direct Polarization/Magic-Angle Spinning (DP/MAS) NMR, ¹³ C Cross-Polarization/Total Suppression of Sidebands (CP/TOS) and ¹³ C CP/TOSS Plus Dipolar Dephasing, ¹³ C Chemical-Shift-Anisotropy (CSA) Filter. Connectivities of different functional groups in hydrochars with ¹ H- ¹³ C Two-Dimensional Heteronuclear Correlation (2D HETCOR) NMR. Aromatic cluster sizes with ¹ H- ¹³ C Long-Range Recoupled H-C Dipolar Dephasing Experiments
Wiedner et al. [37]	Biochars (pyrolysis-Pyreg up to 850 °C, pyrolysis/gasification-BC up to 760 °C, gasification-AGT up to 1200 °C, gasification-CT up to 550 °C) and hydrochars (1st stage at 230 °C for at least 15 min and 2nd stage at 180 °C for at least 75 min; 170 °C for 90 min)	Wheat straw-AGT, wood chips-AGT, poplar-AGT, sorgnum-AGT, olive residues-AGT, wood chips-CT, wood chips-BC, draft-Pyreg, miscanthus-Pyreg, Maize silage, leftover food, biogas digestate, grass, greenery and sewage sludge for hydrochars	pH, EC, ash content, elemental composition (CHNO), ¹³ C NMR, SEM-EDS, black carbon content, PAHs content, polychlorinated dibenzodioxines (PCDDs) and polychlorinated dibenzofurans (PCDFs) content
Busch et al. [38]	Biochars (gasification-AGT up to 1200 °C and pyrolysis at 400–600 °C) and hydrochars (230 °C for 1 h and 180 °C for at least 4 h; 170 °C)	Olive residues-AGT, poplar wood chips-AGT, wheat straw-AGT, miscanthus-pyrolysis. Maize silage, food leftovers, biogas digestate grass and sewage elutte for hydrochars	Tradescantia genotoxicity assay, plant germination and growth tests and impact on soil pH
Busch and Glasser [39]	Biochar (pyrolysis-Pyreg), hydrochar (230 °C for 1 h and 180 °C for at least 4 h), co-composted biochar (1:1 w/w) and hydrochar (1:3 w/w) with raw biomass residues from vegetable waste from horticulture and landscaping, kept for 4 weeks in temperature range 55–75 °C	Conifer wood bark residues for biochar and maize silage for hydrochar	Stability of co-composted hydrochar and biochar under field conditions in a temperate soil. TOC, total N content, pH, EC and black carbon analysis of biochars, hydrochars, compost and co-composted biochars and hydrochars before and after application in soil

2. Materials and Methods

Two different raw materials, pine wood chips (PW) and corn digestate (CD), were used for the production of biochar (pyrolysis) and hydrochar (HTC). PW was provided by Robeta Holz OHG (Milmersdorf, Germany) while CD was obtained from an anaerobic digester in Dorf Mecklenburg (Germany). The substrate used for mesophilic (39°C) anaerobic digestion was 70% corn silage and 30% cow manure. The digestate was dried and stored on site. Due to storing conditions, the dry digestate contained a significant amount of calcium carbonate. The properties of both raw materials are shown in Table 2.

Table 2. Raw material, conversion process, experimental conditions and solid yields for biochar and hydrochar production. Ash content and elemental composition of pine wood chips (PW) and corn digestate (CD). Determination of ash content was done according to the DIN norm 51719. Elemental analysis was performed using a Vario EL elemental analyzer. Oxygen content was obtained by difference. The values are given in % mass, dry basis (%), db). * Maximum conversion temperature measured in the reference position, according to the description provided in the Section 1 of Supplementary Material.

Material	Ash (%), db)	C (%), db)	H (%), db)	O (%), db)	N (%), db)	
CD	19.6 ± 0.1	40.7 ± 0.7	5.5 ± 0.1	31.7 ± 0.8	2.4 ± 0.5	
PW	0.2 ± 0.0	49.4 ± 0.4	6.7 ± 0.1	43.7 ± 0.4	0.1 ± 0.0	
Sample	Raw material	Process	HTT * ($^{\circ}\text{C}$)	Flow (NL min $^{-1}$)	Char yield (%), db)	
PW400-20	Pine wood	Pyrolysis	400	20	30.01 ± 0.18	
PW400-40	Pine wood	Pyrolysis	400	40	25.83 ± 2.12	
PW600-20	Pine wood	Pyrolysis	600	20	24.94	
PW600-40	Pine wood	Pyrolysis	600	40	22.82 ± 0.49	
CD400-20	Corn digest.	Pyrolysis	400	20	50.89 ± 0.36	
CD400-40	Corn digest.	Pyrolysis	400	40	52.00 ± 0.21	
CD600-20	Corn digest.	Pyrolysis	600	20	49.76 ± 0.40	
CD600-40	Corn digest.	Pyrolysis	600	40	48.54 ± 1.08	
Sample	Raw material	Process	HTT ($^{\circ}\text{C}$)	Time (min)	Wash. times	Char yield (%), db)
PW200-10	Pine wood	HTC	200	10	-	82.30 ± 0.35
PW200-360	Pine wood	HTC	200	360	-	75.68 ± 0.01
PW240-10	Pine wood	HTC	240	10	-	76.26 ± 0.07
PW240-360	Pine wood	HTC	240	360	-	59.09 ± 0.19
CD200-10-0	Corn digest.	HTC	200	10	0	83.49
CD200-10-6	Corn digest.	HTC	200	10	6	73.49
CD200-360-0	Corn digest.	HTC	200	360	0	74.38
CD200-360-6	Corn digest.	HTC	200	360	6	70.29
CD220-185-3	Corn digest.	HTC	220	185	3	64.57 ± 2.02
CD240-10-0	Corn digest.	HTC	240	10	0	70.82
CD240-10-6	Corn digest.	HTC	240	10	6	66.85
CD240-360-0	Corn digest.	HTC	240	360	0	62.06

CD and PW biochars were produced at the Technische Universität Berlin (Berlin, Germany), in a technical-scale fixed-bed reactor, with capacity for several kg of biomass. The setup used in these experiments has been presented elsewhere [40]. In these experiments, the influence of maximum pyrolysis temperature (400 and 600°C) and residence time of the volatiles in contact with the solid bed (with inert gas flow rates of 20 and 40 NL min^{-1}) was investigated. Experiments were conducted in duplicates.

The hydrothermal carbonization experiments were carried out at the Leibniz Institute for Agricultural Engineering and Bioeconomy (Potsdam, Germany). Distilled water was added to the dry digestate in each experiment to achieve the desired solid content of 20% by mass. The experiments were conducted in a 1 L autoclave (Series 4520, stainless steel T 316, Parr Instruments, Moline, IL, USA) equipped with a temperature controller. The influence of maximum conversion temperature (200, 220 and 240 °C), time at this temperature (10, 185 and 360 min) and washing effect (0, 3 and 6 times with distilled water) on hydrochar properties was investigated.

Further details on biochar and hydrochar production conditions are given in Table 2 and in the Supplementary Material.

Analytical Methods

Biochars ash content determination was done following the DIN norm 51719. Hydrochars ash content was characterized according to the method described in Chapter 8.4 from the VDLUFA Methodenbuch Band III [41]. Validation of both methods for both raw materials showed that the results according to the DIN norm are within the standard deviation of the results from the VDLUFA method. For elemental analysis (CHNS), a Vario EL elemental analyzer (Elementar Analysensysteme GmbH, Lagenselbold, Germany) was used for hydrochars and biochars. Inorganic elemental analysis for hydrochars was performed in an ICP-OES (iCap 6300 Duo, from Thermo Scientific, Schwerte, Germany). Prior to the analysis, milled samples were digested according to the method exposed in Chapter 10.8 of the VDLUFA Methodenbuch Band III [41], using a microwave (ultraClave-IV high pressure microwave, from MWS Vertriebs GmbH, Leutkirch, Germany) with nitric acid 65% (260 °C, 140 bar, 2 h) and stored at room temperature. Biochar inorganic elemental characterization was also performed with an ICP-OES (Varian 720-ES, now Agilent Technologies, Inc., Santa Clara, CA, USA) after digestion in a microwave (Multiwave 3000, from Anton Paar, Graz, Austria) with nitric acid 65% (Rotipuran ® p.a., ISO, max 0.005 ppm Hg, Carl Roth GmbH + Co. Kg, Karlsruhe, Germany) and hydrogen peroxide 30% (Rotipuran ® p.a., ISO, stabilisiert, Carl Roth GmbH + Co. Kg, Karlsruhe, Germany).

The pH of biochars and hydrochars was measured in deionized water solution. The determination of oxygen-containing functional groups on the char surface was done applying the Boehm titration method [42]. The experimental procedure is based on the description by Goertzen et al. [43], including the sample pretreatment proposed by Tsechansky and Gruber [44]. Further details on this characterization method are given in the Section 2 of Supplementary Material.

The pore structure, including specific surface area, pore volume and pore size distribution, was characterized with gas adsorption, combining the measurement of N₂ and CO₂ adsorption isotherms at 77 K and 273 K respectively. The pretreatment of the samples, prior to adsorption measurements, included milling and degassing in vacuum at 150 °C during 6 h, with the objective of cleaning the surfaces from other adsorbed species and reducing transport limitations (milling). For both degassing and adsorption/desorption measurements the gas sorption system Nova 2200, provided by Quantachrome Instruments (Boynton Beach, FL, USA), was used. Several methods were applied to the isotherms in order to derive pore surface areas and volumes, all of them included in the NovaWin software (Version 11.04, also from Quantachrome Instruments). The methods applied to the N₂ adsorption/desorption isotherms included: the BET method [45] to measure the total specific surface area; the BJH method [46] to characterize the specific surface area and volume of pores bigger than ≈3 nm; and the density functional theory (DFT) [47] method, in particular, the quenched solid density functional theory (QSDFT) method, considering slit/cylindrical pores (Quantachrome Instruments). With the QSDFT method, the specific surface area and volume of micropores and mesopores up to ≈34 nm were characterized. The total pore volume was determined from the volume of N₂ adsorbed at a relative pressure P/P₀ ≈ 1, assuming that at this point the pores are filled with liquid N₂. For CO₂ adsorption, the non local density functional theory (NLDFT) method (Quantachrome Instruments) was applied to determine the specific surface area and volume due to micropores up to ≈1.5 nm.

Biochar thermal stability was analyzed by thermogravimetric analysis (TGA 1, STARe system, from Mettler Toledo, Columbus, OH, USA) with a heating rate of $5\text{ }^{\circ}\text{C min}^{-1}$, in synthetic air (20.5% O_2 , 200 mL min^{-1} air flow) and up to a temperature of $600\text{ }^{\circ}\text{C}$. Initial mass below 5 mg was used to guarantee kinetic regime and avoid self-heating due to the exothermicity of the oxidation reactions. Conversion rate of biochar oxidation is defined here as the change of conversion (α) over time ($\frac{d\alpha}{dt}$). Conversion (α) is defined as $1 - (m_0 - m)/(m_0 - m_f)$, where m is the biochar mass at each time step, m_0 is the initial biochar mass and m_f is the mass of the combustion product at $600\text{ }^{\circ}\text{C}$, i.e., ash.

Plant available ammonium (NH_4^+) and nitrate (NO_3^-) were determined according to the DIN 19746:2005-06 (extraction of the samples with 0.0125 mol L^{-1} of CaCl_2 in distilled water). Plant available phosphate (PO_4^{3-}) and potassium (K^+) were determined according to VDLUFA Methodenbuch Band I [48], Chapter 6.2.1.1 (extraction with a solution of 0.02 mol L^{-1} of calcium lactate and 0.02 mol L^{-1} hydrochloric acid in distilled water). The analysis of the extracts was conducted by IC-CD (ICS 1000, from DIONEX). Anions were analyzed with an IonPac AS9-HC $4 \times 250\text{ mm}$ column from DIONEX (chromatographic conditions: $9\text{ mmol Na}_2\text{CO}_3$, 1.2 mL min^{-1} , 160 bar) and cations with an IonPac CS 16 $5 \times 250\text{ mm}$ column from DIONEX (chromatographic conditions: $30\text{ mmol methanesulfonic acid (MSA)}$, 1.0 mL min^{-1} , 80 bar , $40\text{ }^{\circ}\text{C}$).

The method applied for characterization of the 16 USEPA (United States Environmental Protection Agency) PAHs has been developed by Fabbri et al. [49], with the difference that in the present study a standard solution of deuterated 16 PAHs (PAH-Mix 9 deuterated, 10 mg L^{-1} , Dr. Ehrenstorfer, Augsburg, Germany) was used, instead of 3 deuterated PAHs as in [49]. Briefly, the biochar samples, spiked with 0.1 mL of a 5 mg L^{-1} solution of the above deuterated 16 PAHs solution, were Soxhlet extracted with an acetone (CHROMASOLV, for HPLC, $\geq 99.9\%$, Sigma-Aldrich, St. Louis, MO, USA)/cyclohexane (ACS reagent, $\geq 99.5\%$, Sigma-Aldrich, St. Louis, MO, USA) ($1:1, v/v$) solvent mixture for 36 h and then the PAHs were analyzed in an Agilent HP 6850 gas chromatograph (GC) coupled to an Agilent HP 5975 quadrupole mass spectrometer (MS) (Agilent Technologies, Inc., Santa Clara, CA, USA); GC-MS conditions were those detailed in [49].

Biochar wettability measurements were performed according to the method described by Ojeda et al. [50]. Briefly, a glass tube 6 cm high with 0.9 cm of internal diameter was filled with the different biochar samples up to a height of 3 cm . Then the tube was attached to a high precision scale (DCAT, dynamic contact angle measuring instrument, DataPhysics®, Germany). Below the tube, a glass filled with distilled water or n-hexane (AnalR NORMAPUR –for synthesis– $\geq 95\%$) was placed and carefully risen until touching the bottom part of the tube. Distilled water/n-hexane capillary absorption was measured by registering the weight increase in the biochar column during 200 s .

3. Results and Discussion

3.1. Primary Characterization: Yields, Elemental and Proximate Analysis

In Table 2 biochars and hydrochars yields are presented. Hydrochars show significantly higher char yields than biochars, consistent with the lower conversion temperatures and the higher pressures. For biochars, the lower the conversion temperature the higher the char yield. CD biochars also present higher yields than PW biochars, due to the significantly higher inorganic species content, which remain in the solid product after pyrolysis. Besides, a higher N_2 flow rate during pyrolysis generally reduces the char yield, due to a reduction in the residence time of the volatiles in the bed, minimizing secondary reactions and formation of secondary char [12]. In the case of hydrochars, the solid yields for both raw materials are similar. Besides, both conversion temperature and retention time at the conversion temperature play an important role. Noteworthy to mention in the case of hydrochars is the impact of washing. With the same conversion temperature and retention time, washing the hydrochar after production can reduce up to 10% the solid yield. This indicates that a significant part of the solid is actually condensed volatiles and water soluble inorganic species.

In Figure 1 (left), the Van Krevelen diagram, i.e., the representation of H/C molar ratio versus O/C molar ratio is presented for biochars and hydrochars. This diagram is often used to illustrate the degree of maturity and aromaticity of chars [51]. Results in Figure 1 show that hydrochar and biochar chemical composition depends on the conversion conditions, but also on the initial feedstock composition, having potentially a significant impact on final char chemical properties. This is illustrated with the results of CD biochars/hydrochars versus those for PW biochars/hydrochars. For the same O/C molar ratio, the H/C molar ratio of CD biochars is lower than for PW biochars. Looking at the relation of these molar ratios with the volatiles content (% mass, dry ash free), it is observed that while biochar O/C molar ratio follows a linear trend with respect to the volatiles content, the behavior of H/C ratio seems only linear for PW biochars, while very scattered for CD biochars.

As it has been introduced in Section 2, corn digestate contains calcium carbonates, mainly due to storing conditions. The inorganic C content of CD biochars, due to carbonates, is approximately 4–5%, as determined by Rombolà et al. [52]. The presence of these carbonates could explain, to some extent, the higher volatiles content of CD biochars in comparison with PW biochars, since at the conversion temperatures used in this study (400 and 600 °C) carbonates are stable and therefore remain in the biochar. However, this could not explain the lower content in hydrogen for CD biochars. Besides, the elemental composition of CD presented in Table 2 is similar to the one reported by Mumme et al. [53] for maize silage digestate. This suggests different reaction pathways for low and high inorganic matter content biochars, with a potential enhancement of aromatization for high inorganic matter content biochars. Li et al. [54] also reported lower H/C ratios for biochar produced from pyrolysis of rice husk, blended with CaCO₃ prior pyrolysis, than for unmodified biochars, which they correlated with an increase in the carbon aromaticity degree. The potential formation of oxides or other metal composites on the biochar surface, associated to the high content of inorganic matter, could also play a role [55].

With respect to hydrochars, CD hydrochars present in general higher H/C ratios and lower O/C ratios than PW hydrochars, in some cases even lower than CD biochars. This indicates different reaction mechanisms for both materials. The higher H/C ratios of CD hydrochars suggests that decarboxylation reactions are favored over dehydration reactions [53]. In the case of PW hydrochars, dehydration reactions seem to be more significant in comparison to CD hydrochars, while the influence of decarboxylation reactions is lower, except for the highest conversion temperature and highest retention time (240 °C – 360 min), where both are relevant. This is further supported by the composition of the producer gas (collected during the HTC experiments in gas bags and analyzed with a SSM6000 analyzer from Pronova, Germany), with a concentration of CO₂ increasing from around 50% vol. to approximately 80% vol. for the highest conversion degree. It is also important to point out that retention time at the conversion temperature is as significant as the conversion temperature itself. With respect to CD hydrochars, CO₂ increases from approximately 58% vol. from the mildest conditions to around 75% for the most severe conditions. In this case, a significant emission of CH₄ (2.5% vol.) was also registered. Alkaline conditions during HTC enhance the formation of carboxylic acids, reducing therefore the O/C ratio of the hydrochar [56]. In the present study, although the pH of both solid and liquid products are acid, they are higher for CD hydrochars than for PW hydrochars, as shown in Section 3.2. Similar composition for digestate hydrochars has been also shown by Mumme et al. [53], who highlighted that this could be due to the decarboxylation reactions. Liu et al. [28], who compared a hydrochar produced at 300 °C with a biochar produced at 700 °C using pine wood, reported similar H/C and O/C ratios for their biochar as for the PW biochars produced at 600 °C in the present study. The values for the hydrochar were slightly higher in comparison to PW hydrochars produced at 240 °C during 360 min in the present study. Besides, for similar hydrochar H/C ratio, the hydrochar O/C ratio is lower in the present study than in [28]. This could be related to the high amount of ash reported by Liu et al. [28].

According to the guidelines given by the European Biochar Certificate (EBC) [1] and the International Biochar Initiative (IBI) Standards [2] on H/C and O/C ratios, the biochars presented in this Section could be considered as certified biochars. With respect to hydrochars, it is shown that it is also possible to produce hydrochars able to fulfill those requirements, with a conversion temperature of at least 240 °C and a retention time of 360 min, but only with starting HTC conditions enhancing both dehydration and decarboxylation reactions (as it is the case for PW), not only decarboxylation reactions (as in the case of CD).

Inorganic elemental characterization is shown in Table 4 and in the Supplementary Material (Table S1). It is observed that the elemental inorganic composition of CD hydrochars and biochars is much higher than the one for PW hydrochars and biochars, in good agreement with their high ash content.

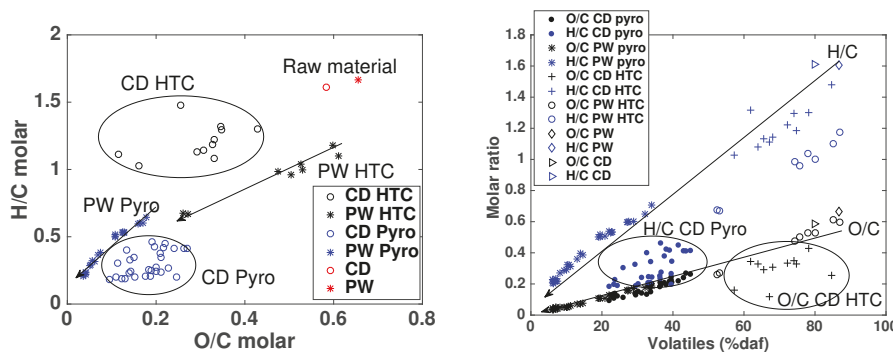


Figure 1. Left: Van Krevelen diagram, i.e., H/C molar ratio versus O/C molar ratio of PW and CD biochars and hydrochars. Right: H/C and O/C molar ratios versus volatiles content (% mass, daf) for PW and CD biochars and hydrochars.

3.2. pH and Surface Functional Groups

It has been reported in literature that pH may be dependent on both, the surface chemistry and the ash content [22,23,57,58]. These both influences are further confirmed in the present study. In Figure 2a,b the variation of pH with ash content is presented. Biochars with higher ash content show also higher pH. However, the strongest correlations for biochars are not between pH and the ash content, but between pH and H/C and O/C molar ratios. Specially remarkable is the correlation between pH of CD biochars and H/C molar ratio ($r = -0.95$, shown in Figure 2c, being r the Pearson correlation coefficient), when considering that the latter shows such scattered behavior in Figure 1. It must be also taken into account that CD contains calcium carbonate due to storing conditions, which has a high liming effect. However, the correlation between CD biochars ash content and pH is significantly worse than between pH and H/C. With respect to PW biochars, pH presents also stronger relations with H/C and O/C molar ratios ($r = -0.91$ and $r = -0.89$ respectively, shown in Figure 2d,f) than with ash content, being this correlation similar in both cases.

Therefore, with respect to biochars pH, it can be concluded that despite the fact that ash content has an influence on the pH value, a better correlation exists between the pH value and H/C and O/C ratios. In the case of CD biochars, the relation between pH and H/C ratio is strongly linear.

For hydrochars the behavior is slightly different. Figure 2a shows that pH of CD hydrochars has a stronger correlation with ash content ($r = 0.88$) than with H/C (Figure 2c) or O/C ratios (Figure 2e). Despite the fact that the slope of the linear fitting for pH-ash in Figure 2a for CD hydrochars is lower than those for pH-H/C for CD and PW biochars in Figure 2c,d respectively, the correlation is still much better for pH-ash than for pH-H/C or pH-O/C. This indicates that the pH in CD hydrochars is

mainly correlated to ash content, although with a weaker dependency than PW and CD biochars pH with H/C ratio. PW hydrochars show similar relations with H/C and O/C molar ratios.

In Figure 3, information about the acidic functional groups present on the chars surface is given, in particular, for carboxylic, phenolic and lactonic groups. In Figure 3a the total acidic functional groups (carboxylic, lactonic and phenolic) and the carboxylic functional groups with respect to the organic fraction of the chars ($\text{mmol g}_{\text{org}}^{-1}$, db) are plotted versus the O/C molar ratio for PW600-20, PW400-20, PW400-40, PW400-40, CD600-20, CD400-20, PW240-10. For biochars, independently of the inorganic matter content, a good correlation ($r = 0.80$) is observed between total acidic groups and O/C ratio. Hydrochar PW240-10 presents a high O/C molar ratio which does not correlate well with the total acidic functional groups, according to the biochars behavior. This may indicate that still a significant amount of oxygen is embedded in the hydrochar skeleton, which is in good agreement with the structure of hydrochar formed mainly by alkyl moieties reported by Cao et al. [36]. In Figure 3b the total acidic groups and the carboxylic groups (with respect to the organic fraction of the chars) are plotted versus H/C molar ratio. No good correlations are observed. However, in Figure 3c a quite strong linear correlation ($r = 0.84$) is present between the total surface acidic groups with respect to the total char mass (mmol g^{-1} , db) and the H/C molar ratio, independently of the inorganic matter content and the conversion process. Figure 3d shows the comparison of these groups with pH. A relation between the increase in pH and the decrease in total acidity of the biochar surface is observed.

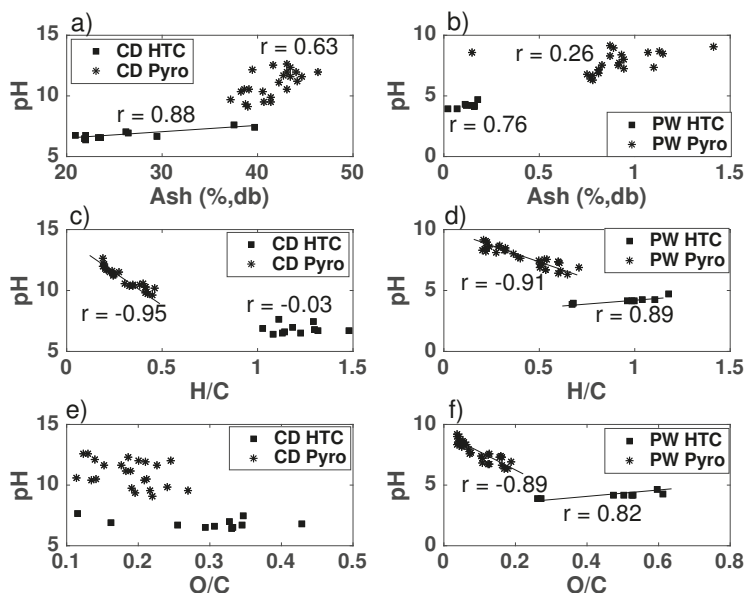


Figure 2. pH versus ash (% mass, db) in (a,b), H/C molar ratio in (c,d) and O/C molar ratio in (e,f) for CD (left) and PW (right) biochars and hydrochars. The strength of the correlations is indicated with the Pearson correlation coefficient (r).

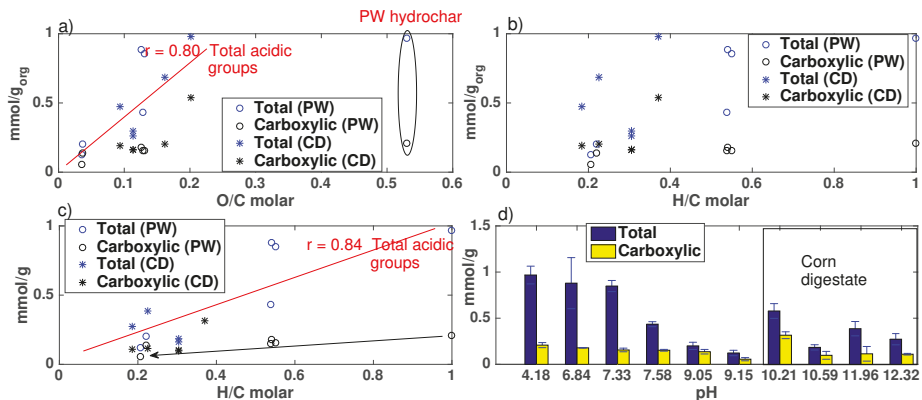


Figure 3. Surface oxygen-containing functional groups of the biochars determined with the Boehm titration method. (a,b) show the amount of functional groups with respect to the mass of the chars organic fraction versus the O/C and H/C molar ratios; (c) shows the amount of functional groups with respect to the total chars mass versus the H/C molar ratio; (d) shows the amount of functional groups versus the pH.

3.3. Porosity Characterization

In Figure 4, the evolution of the total specific surface area (BET method using N₂ adsorption) is plotted versus the biochars/hydrochar volatiles content (% mass, daf). In general, the lower the volatiles content, the higher the specific surface area (SSA). However, for CD biochars different BET SSA behaviors are observed for similar volatiles content. The highest SSA values correspond to biochar produced at 600 °C with a N₂ sweeping flow rate of 40 NL min⁻¹. In Figure 4b the SSA evolution is plotted versus the H/C molar ratio. The decrease of H/C molar ratio is indicative of the formation of structures containing unsaturated carbon such as aromatic rings [59], and therefore, represents the increase in aromaticity with charring degree, as reported in [25]. It is possible to observe that the behavior of CD biochars differs significantly from the one of PW biochars. Taking into account that CD biochars have around 40% ash content, the SSA would be higher as function of the organic fraction, but it would be still lower than for PW biochars. This may be a consequence of two possible phenomena: (a) porosity development is different for materials with high inorganic content and (b) potential filling or access blocking of micropores by the inorganic species [60,61], which could explain the lower SSA value despite the lower H/C molar ratio in CD biochars.

In order to further characterize the porous structure, in Figure 5 the pore size distribution according to pore surface area (left) and pore volume (right) is presented, characterized with the methods introduced in Section “Analytical Methods”. SSA and volume from CO₂ adsorption are also shown in Figure 5. With CO₂ adsorption, micropores up to 1.5 nm in pore width are characterized. Despite this, the SSA area measured with CO₂ adsorption is higher than the total SSA (up to 100–200 nm in pore width, depending on the sample porous structure) measured with N₂ adsorption. This indicates that the samples have a microporous structure which cannot be completely characterized by N₂ adsorption, mostly due to diffusion limitations, consequence of the low temperature measurements in N₂ adsorption.

The CO₂ SSA is around 25% higher than the N₂ SSA for PW biochars produced at 600 °C, with inert gas flow rates of 20 and 40 NL min⁻¹. However, the CO₂ SSA for CD biochars produced in the same conditions is 90% and 80% higher respectively. This indicates that the diffusion limitations are stronger in CD biochars, in good agreement with the previous explanation for the low specific surface of high inorganic content biochar. That is to say, the inorganic species may provoke partial blocking or constriction of the porous structure, limiting the access of N₂ to micropores but not of CO₂.

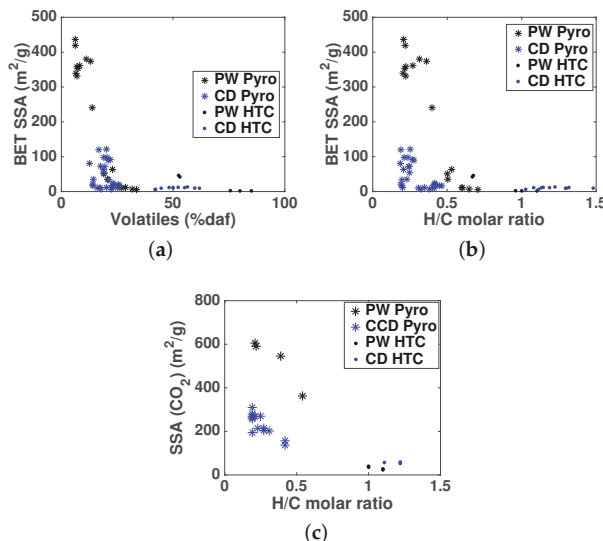


Figure 4. (a): Total specific surface area (SSA) determined with the BET method (N_2 adsorption) versus the volatiles content (% mass, daf) for PW and CD biochars and hydrochars; (b): SSA determined with the BET method (N_2 adsorption) versus H/C molar ratio for PW and CD biochars and hydrochars; (c): SSA determined with CO_2 adsorption applying the NLDFT method versus H/C molar ratio for PW and CD biochars and hydrochars.

With respect to the pore volume, higher N_2 pore volume than CO_2 pore volume is measured for PW biochars produced at 600 °C. This is due to the smaller size of pores characterized by CO_2 adsorption. Noteworthy to mention is the fact that higher N_2 sweeping flow during the pyrolysis process leads to higher SSA and pore volume in the biochar. For PW biochars the effect is clearer when looking at the pore volume distribution. This is also stronger for biochars produced at 400 °C than for biochars produced at 600 °C. For CD biochars the difference for biochars produced at 600 °C is already very significant, as introduced in Figure 4. This shows that higher flow rates lead to a more open porous structure, due potentially to a combination of higher removal of volatiles (more significant for biochars produced at 400 °C) and inorganic species (present in CD biochars), together with lower extent of intraparticle heterogeneous secondary reactions, leading to the formation of secondary char.

Interestingly, while the major contribution to pores in PW biochars comes from micropores (observed in the CO_2 adsorption results), in CD biochars the contribution of mesopores is also significant. Therefore, inorganics in CD biochars would not only reduce the presence of micropores through potential blocking, but could also enhance the development of mesopores.

Comparing the porous structure of hydrochars with the one of biochars, the former follows quite a different behavior. According to Figure 4, hydrochars present low SSA, in good agreement with the high volatiles content and high H/C molar ratio. This suggests low charring and aromatization degree in comparison with biochars. However, in Figure 5, results for hydrochars pore size distribution, according to volume (bottom right), show that the volume of these samples is in many cases higher than the one of biochars. Contribution of micropore volume to the total pore volume of hydrochars is low. Therefore, it can be concluded that porosity (pore volume) in hydrochars is mainly due to meso- and macropores. Comparing PW hydrochars and CD hydrochars produced at 240 °C, with a retention time at maximum conversion temperature of 360 min, it is possible to see that PW hydrochars present significantly higher SSA and volume. This could be attributed to the high inorganic matter content

of CD hydrochars. However, PW hydrochars produced at 240 °C during 10 min or at 200 °C during 360 and/or 10 min show lower SSA and volume than CD hydrochars produced at 240 °C and 200 °C during 360 min. Comparing the behavior of CD hydrochars produced at 240 °C and 200 °C during 360 min, the SSA and pore volume of the latter are higher despite the lower conversion temperatures. This is due to the washing of the hydrochar produced at 200 °C during 360 min. This washing removes inorganics and volatiles partially blocking the pores, which leads to an underestimation of the porous structure with N₂ adsorption, as previously introduced for biochars. However, CO₂ adsorption results show similar values of microporosity for both cases, indicating that this pore blocking does not affect CO₂ adsorption.

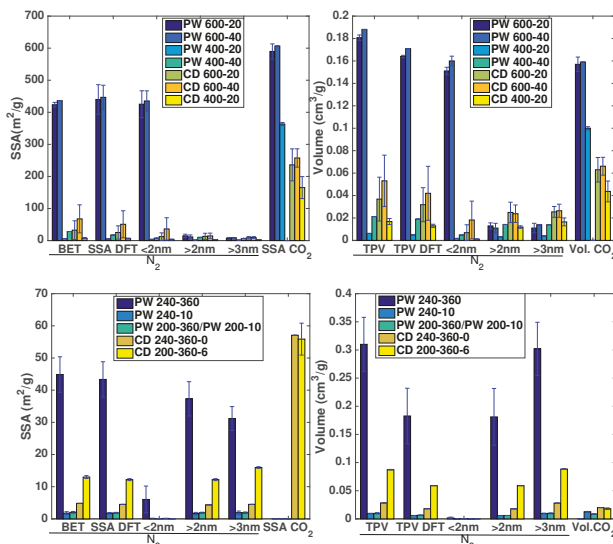


Figure 5. Pore size distribution (PSD) of PW and CD biochars (top) and hydrochars (bottom). **Top left:** SSA distribution with pore size for biochars according to the BET method (for total specific surface area), quenched solid density functional theory (QSDFT, for total specific surface area, surface area due to pores $< 2 \text{ nm}$ and pores $2 \text{ nm} < \text{pore size} < 34 \text{ nm}$) method, and BJH method (surface area due to pores $> 3 \text{ nm}$). Total specific surface area for pores $< 1.5 \text{ nm}$ determined with CO₂ adsorption. **Top right:** Volume distribution with pore size for biochars. **Bottom left:** SSA distribution with pore size for hydrochars according to the aforementioned methods. **Bottom right:** Volume distribution with pore size for hydrochars. CO₂ adsorption was not measured for samples PW400-40 and PW240-360.

3.4. Thermal Stability

Oxidation behavior of biochar in the presence of synthetic air has been performed in a thermogravimetric analyzer (TGA) to assess biochar stability to oxidation [62,63].

In Figure 6, the conversion rate under oxidation conditions is plotted versus the temperature for hydrochars (top) and biochars (bottom). The higher the temperature correspondent to the peak of the conversion rate, the lower the reactivity, and therefore, the higher the stability to oxidation.

For most hydrochars, except the ones produced under the highest severity (240 °C, 360 min retention time), a first peak in the conversion rate is observed at temperatures slightly above 300 °C, consistent with further oxidative pyrolysis of the sample [64]. The second peak at higher temperatures is related to char oxidation. For PW hydrochars, these oxidation peaks take place at significantly higher temperatures than for CD hydrochars. At the same time, water washing of the hydrochars after production seems to also affect their oxidation behavior. Those not being washed experience an

earlier second oxidation peak. For biochars, the higher the conversion temperature, the higher the temperature correspondent to the maximum of the oxidation peak. For hydrochars, residence time at the maximum conversion temperature and post-washing, as previously introduced, also play a significant role.

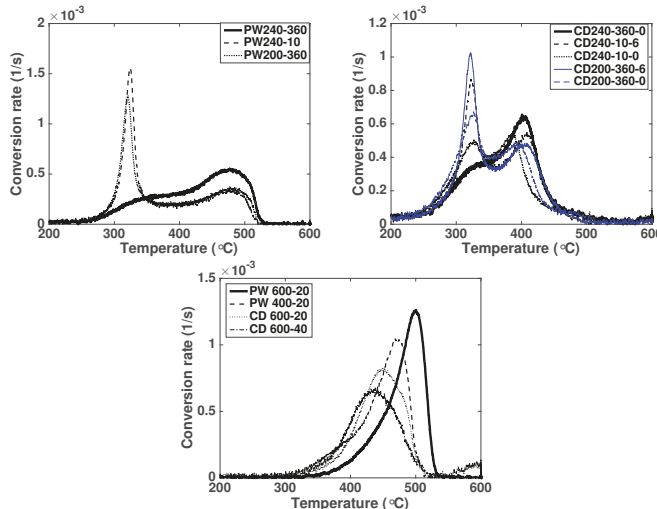


Figure 6. Conversion rate of char oxidation for PW hydrochars (**top left**), CD hydrochars (**top right**), PW and CD biochars (**bottom**).

The initial feedstock seems to have a stronger influence on the thermal stability (based on the shape and peak position of the char oxidation curve) than the conversion process conditions. It is known from literature [12] that char reactivity (in oxidation and gasification conditions) depends on the char structure at molecular level, the inorganic matter in the carbon skeleton, specially alkali and alkaline earth metals (AAEM), and the concentration and type of functional groups in the carbon skeleton. Consequently, the high inorganic content of CD biochars, including AAEM, could act as catalyst in biochar oxidation. This is also consistent with the washing of hydrochars, since with washing, inorganic species can be removed from the hydrochar surface. Harvey et al. [65] showed a similar behaviour with biochars (produced in [66]) from loblolly pine and cord grass, i.e., lower $R_{50,biochar}$ for biochars with high inorganic content (up to 30% ash content for cord grass). However, regardless of the inorganic content, they attributed the differences in biochar thermal stability to the extent of carbonization/aromatization. Therefore, samples with similar H/C and O/C ratios can have different recalcitrance depending on the rearrangement of these atoms in the biochar structure [65].

Correlation between the thermal stability and the biogeochemical stability of soil organic matter has been proposed by Plante et al. [67]. Harvey et al. [65] reported also a strong negative exponential-type relationship between biochar degradability (based on the amount of carbon mineralized after 1 year of incubation [68]) and the thermal recalcitrance $R_{50,biochar}$, defined according to Equation (1). $T_{50,biochar}$ is the temperature correspondent to 50% conversion of biochar (i.e., 50% of the total mass loss due to oxidation/volatilization) and $T_{50,graphite}$ is analog for graphite. In Table 3, the $R_{50,biochar}$ values for several biochars and hydrochars are shown, considering $T_{50,graphite} = 844$ °C [62]. If a $T_{50,graphite} = 886$ °C is used, as measured by Harvey et al. [65], slightly lower $R_{50,biochar}$ values are registered (values between parentheses in Table 3).

$$R_{50,biochar} = \frac{T_{50,biochar}}{T_{50,graphite}} \quad (1)$$

Table 3. $R_{50,biochar}$, C (% mass, daf), H/C and O/C molar ratios for biochar and hydrochar samples. The $R_{50,biochar}$ values are calculated considering a $T_{50,graphite} = 844$ °C [62]. The $R_{50,biochar}$ values between parentheses correspond to a $T_{50,graphite} = 886$ °C [65].

	$R_{50,biochar}$	C (% mass, daf)	H/C (molar)	O/C (molar)
PW200-360	0.43 (0.41)	56.94	0.96	0.50
PW240-10	0.41(0.39)	55.77	1.00	0.53
PW240-360	0.51 (0.48)	70.33	0.67	0.27
CD200-360-0	0.41 (0.39)	62.93	1.19	0.33
CD200-360-6	0.41 (0.39)	62.86	1.22	0.33
CD240-10-0	0.43 (0.41)	61.69	1.29	0.35
CD240-10-6	0.42 (0.40)	61.77	1.32	0.35
CD240-360-0	0.45 (0.43)	76.35	1.11	0.12
PW400-20	0.53 (0.50)	82.10	0.54	0.13
PW600-20	0.57 (0.54)	93.49	0.22	0.04
CD600-20	0.52 (0.50)	84.62	0.18	0.09
CD600-40	0.52 (0.50)	81.99	0.19	0.13

According to a biochar classification proposed by Harvey et al. [65], all analyzed biochars are Class B biochars ($0.50 \leq R_{50,biochar} < 0.70$), with intermediate C sequestration potential, while the rest are Class C biochars ($R_{50,biochar} < 0.50$), which indicate that those chars have carbon sequestration potential comparable to uncharred biomass. The PW240-360 hydrochar could belong to both classes, depending on the considered $T_{50,graphite}$.

3.5. Nutrients

The total content of macronutrients, such as Ca, Mg, N, P and K, is presented in Table 4 for PW and CD biochars and hydrochars. These values are compared with the available nutrient content in the form of NH_4^+ , NO_3^- , PO_4^{3-} and K^+ .

Due to methodical issues, the values of hydrochars nutrient availability, determined from the solid fraction, cannot be directly compared with those for biochars. A significant fraction of the investigated species is solved in the liquid phase during HTC, which might still be present upon drying of the hydrochar. This fact leads to measured nutrient availability in the hydrochar that is not a representative hydrochar characteristic [69]. Instead, the behavior of the nutrients under consideration is investigated via measurements of the liquid phase for the case of hydrochars. Therefore, for hydrochars, the content of Ca, Mg, K and P in the solid and in the liquid phase are presented.

It is observed that the main factor affecting nutrient content in the final product is the feedstock, since both present very different composition, with higher inorganic species and N content in CD. It is obvious that PW has negligible potential for direct nutrient value from this point of view. Such direct nutrient value is high for CD due to high amount of available N, P, and K (see Table 4). In the case of CD it becomes important to investigate how the total nutrient content and their availability changes with the conversion process. PW results are also presented as comparison.

The ratio C/N can be used as a possible indicator for nitrogen mineralization or immobilization, taking $\text{C}/\text{N} < 20$ as predictor for nitrogen mineralization and $\text{C}/\text{N} > 30$ as indicator of initial net nitrogen immobilization [37,70]. For PW biochars the molar C/N ratio is very high, with values above 500, which could potentially lead to a high degree of N immobilization once applied to soil, as previously explained. This is due to the low content of nitrogen in the initial feedstock, which would

still decrease during the conversion process due to nitrogen volatilization, leaving negligible amount of available N-species in the biochar [17]. In the case of CD, the initial nitrogen content in feedstock is significantly higher, leading to C/N ratios between 20 and 30, which would indicate possibility of mineralization or higher availability for plants once applied to soil [37]. However, the amount of available N-species for CD biochars is negligible, similar to PW biochars. It must be taken into account that the C/N ratios for hydrochars are indicative, due to the aforementioned methodical issues.

With respect to P and K, PW biochars present higher nutrient availability (PO_4^{3-} and K^+) in comparison to the raw feedstock. This may be explained by accumulation of these elements due to release of volatile organic matter during pyrolysis for the case of K^+ availability, which also shows a highly significant ($p < 0.001$) dependency on pyrolysis temperature. PO_4^{3-} availability does not seem to be dependent on temperature but rather on N_2 gas flow at 600 °C ($p < 0.05$). In contrast to PW, CD biochars PO_4^{3-} availability is reduced in comparison to the feedstock. Also, there is the same significant ($p < 0.05$) dependency on N_2 gas flow at 600 °C pyrolysis temperature. The observed reduction in K^+ availability for the case of CD is not significant due to the high uncertainty associated with the results (which stems from the high heterogeneity of the feedstock).

A reduction in the availability of PO_4^{3-} has been reported elsewhere, but different to the observed results in this study, a dependency on pyrolysis temperature has been reported [16,17]. Instead, in this study an increase in N_2 flow leads to a significant increase in PO_4^{3-} availability at high pyrolysis temperature. This hints to the hypothesis that P is somehow included in carbonaceous solids formed upon recondensation of primary pyrolysis vapors because it has been shown that biochar extractable P is primarily orthophosphate at pyrolysis temperatures > 350 °C [16]. More detailed studies are required to understand this phenomenon. Finally it has to be concluded that pyrolysis leads to a significant loss of plant available nutrient species, specifically NH_4^+ , NO_3^- , and PO_4^{3-} , which has to be considered when nutrient rich feedstock is being used.

In contrast to the observations from pyrolysis experiments, HTC of PW does lead to a significant increase of N, P, and K availability (as defined by the analytical method applied here). Twice to ten times the amount of nutrients are recovered in the process water of HTC as compared to the leachate after extracting with CaCl_2 or double lactate (see Table 4, note that at least four times as much process water is present after HTC as dry solid input). These leached nutrients are lost to the hydrochar, but can be potentially re-used together with the process water. Different to pyrolysis, nitrogen compounds are not lost during the conversion process [69,71]. HTC of nutrient rich CD leads to different observations: the same amount of available nutrients of the feedstock are recovered in the process water for the case of NH_4^+ and K^+ , but there is a significant reduction of NO_3^- and PO_4^{3-} . This is likely due to the precipitation of salts, leading to a recovery of these nutrients with the solids [72]. Indeed, the observed high amount of extractable PO_4^{3-} on the hydrochar (data not shown) cannot be explained by solved PO_4^{3-} in the hydrochar's moisture content, i.e., that a significant amount of solid PO_4^{3-} precipitates during the reaction. It is also noted that the P contained in the liquid phase is almost exclusively detected as PO_4^{3-} whereas only a fraction of the hydrochar's P is extractable by the applied methods (10–30%). The recovery of nutrients in the process water allows for a decoupling of fertilizing and soil amendment with the potential to flexibly combine these two in a designed hydrochar product. There is only little influence of the applied HTC process conditions on these findings. For the case of PW, more severe carbonization leads to a significant but small reduction of NH_4^+ and PO_4^{3-} in the liquid phase ($p < 0.05$). This might be due to an increase in adsorption capacity of the produced hydrochar or increased precipitation of these species. For the case of CD, this decrease with reaction severity is only observed for NO_3^- and PO_4^{3-} ($p < 0.05$). These results are in contrast to observations from other HTC experiments, which reported an increase of NH_4^+ in the liquid phase with reaction temperature or no significant change at all [69,72]. These contradicting results can be possibly explained with the varying nutrient concentrations used in the different experiments.

Table 4. Total content of N, Mg, Ca, P and K, as well as available N, P and K (mean \pm standard deviation). The inorganic species content is given for the solid phase (sol) in biochars and for the solid (sol) and liquid phase (liq) in hydrochars.^a determined by biochar extraction, ^b measured in the liquid phase of the hydrothermal carbonization experiments. n.d.: not detected. * The ratio C/N is molar ratio.

	C/N _{sol} [*]	N _{sol} (dB)	Mg _{sol} (dB)	Ca _{sol} (dB)	P _{sol} (dB)	K _{sol} (dB)	Mg _{liq}	Ca _{liq}	P _{liq}	NH ₄ ⁺	NO ₃ ⁻	PO ₄ ³⁻	K ⁺
	—	%	mg/kg	mg/kg	mg/kg	mg/kg	mg/kg ^a	mg/kg ^a	mg/kg ^a	mg/kg ^a	mg/kg ^a	mg/kg ^a	mg/kg ^a
PW	912.7	0.1	178.1 \pm 38.7	894.5 \pm 305.7	322.1 \pm 81.6	960.0 \pm 360	—	—	—	1200 \pm 110	1800 \pm 130	1800 \pm 160	6100 \pm 350
CD	20.1	2.4	—	—	—	—	—	—	—	n.d.	0.9	27 \pm 9	300 \pm 30
PW400-20	550.9 \pm 57.9	0.2 \pm 0.0	—	13,900 \pm 440	960.0 \pm 360	—	—	—	—	n.d.	n.d.	37 \pm 2	370 \pm 60
PW400-40	729.2 \pm 54.2	0.1 \pm 0.0	—	—	—	—	—	—	—	0.9 \pm 0.2	n.d.	16 \pm 2	900 \pm 40
PW600-20	634.1 \pm 106.8	0.2 \pm 0.0	—	—	—	—	—	—	—	0.4 \pm 0.1	0.6	43 \pm 6	750 \pm 40
PW600-40	694.3 \pm 91.3	0.2 \pm 0.0	—	—	—	—	—	—	—	—	—	—	—
CD400-20	226 \pm 3.5	2.4 \pm 0.4	20,568.0 \pm 2233.3	139,051.2 \pm 23,155.2	26,458.0 \pm 2163.8	11,882.6 \pm 1303.1	—	—	—	1.2 \pm 0.5	r.d.	1360 \pm 110	4610 \pm 1680
CD400-40	223 \pm 0.2	2.3 \pm 0.1	22,608.3 \pm 3140.2	154,160.6 \pm 25,380.1	30,319.7 \pm 3287.0	13,184.2 \pm 1594.7	—	—	—	2.6	r.d.	1650	7460
CD600-20	294 \pm 1.5	1.8 \pm 0.1	21,796.2 \pm 1781.4	135,010.5 \pm 15,038.8	27,975.3 \pm 2270.6	12,410.9 \pm 1441.5	—	—	—	1.4 \pm 0.4	11	960 \pm 130	7890 \pm 1580
CD600-40	296 \pm 1.4	1.7 \pm 0.1	22,150.4 \pm 2930.0	156,042.0 \pm 13,715.9	29,015.1 \pm 3091.5	12,601.1 \pm 1442.5	—	—	—	1.3 \pm 0.1	r.d.	1510 \pm 50	8210 \pm 1410
[1]	—	—	mg/kg	mg/kg	mg/kg	mg/kg	mg/kg	mg/kg	mg/kg	mg/kg ^b	mg/kg ^b	mg/kg ^b	mg/kg ^b
PW200-10	522.8 \pm 80.7	0.1 \pm 0.0	95.8 \pm 9.8	733.1 \pm 54.3	61.5 \pm 4.2	213.1 \pm 19.5	60.0 \pm 8.8	126.7 \pm 38.3	31.7 \pm 9.4	5.1 \pm 0.2	5.3 \pm 0.5	24.2 \pm 7.5	124 \pm 20
PW200-300	841.7 \pm 68.6	0.1 \pm 0.0	99.3 \pm 14.8	446.6 \pm 14.1	787.5 \pm 31.3	255.4 \pm 9.6	48.2 \pm 8.7	145.1 \pm 10.7	16.0 \pm 1.1	11.1 \pm 0.1	11.4 \pm 1.1	112 \pm 2	—
PW240-10	616.1 \pm 248.0	0.1 \pm 0.1	72.0 \pm 0.1	500.1 \pm 4.0	489 \pm 3.0	183.4 \pm 9.3	42.8 \pm 1.4	135.6 \pm 1.2	22.3 \pm 0.1	2.1 \pm 0.2	5.9 \pm 0.0	174 \pm 6	115 \pm 3
PW240-350	1802.3 \pm 1351.3	0.1 \pm 0.1	—	184.4 \pm 4.6	624.8 \pm 16.7	71.2 \pm 1.3	40.9 \pm 1.0	148.3 \pm 1.2	10.4 \pm 1.1	1.2 \pm 0.3	5.0 \pm 0.3	3.5 \pm 0.6	121 \pm 6
CD200-10/0/6	288 \pm 2.1	1.9 \pm 0.1	9565.4	44,518.8 \pm 5335.0	15,735.0 \pm 1087.1	5339.6 \pm 2479.4	3.5	1027.5 \pm 298.6	341.2 \pm 131.4	230 \pm 30	19.2 \pm 4.2	190 \pm 48	1490 \pm 20
CD200-360/0/6	27.3 \pm 1.8	2.0 \pm 0.1	11,292.0	54,222.0 \pm 9737.7	18,429.3 \pm 602.5	4226.9 \pm 2928.9	189.0 \pm 263.3	2356.9 \pm 4389.9	63.9 \pm 19.1	260 \pm 65	16.0 \pm 4.1	60 \pm 31	2180 \pm 160
CD220-185-3	25.6 \pm 0.5	2.2 \pm 0.0	12,970.2	53,535.0 \pm 194.2	19,555.3 \pm 671.9	2141.8 \pm 492.8	3.1	1985.0 \pm 990.0	180.8 \pm 60	10.8 \pm 2.3	51 \pm 8	1890 \pm 360	—
CD240-10/0/6	27.3 \pm 1.9	1.8 \pm 0.1	10,752.2 \pm 1330.7	101,259.3 \pm 50,630.1	15,962.0 \pm 335.4	3158.0 \pm 476.1	473.5 \pm 61.1	2301.6 \pm 530.4	112.9 \pm 84.6	360 \pm 81	81.1 \pm 1.9	100 \pm 80	1870 \pm 240
CD240-360-0	22.5	2.5	—	110,882.0	—	20,862.4	4656.2	—	2172.0	50.5	140	1.6	32

3.6. PAH

The PAHs content in the biochar is dependent on the process conditions, mainly maximum temperature reached in the process, feedstock and mass transport limitations due to potential enhancement of heterogeneous secondary reactions. For example, as reported in [73], the emission of PAHs (detected in the vapor phase) for pine wood chips starts when the temperatures inside the solid bed range between 300–350 °C, being at those temperatures 2- and 3-ring aromatic compounds the main species. This is in good agreement with the results shown in Figure 7, where it is already observable that in the temperature range from 350–400 °C the highest amount of PAHs is present in the PW biochar, being phenanthrene the most significant species, as shown in Figure 7 (bottom left and right). However, as the temperature increases, the presence of PAHs decreases significantly. At those temperatures almost no more volatiles, which can further react within the solid matrix, are being produced and the temperatures are also high enough for a good part of the PAHs still present in the solid matrix to be removed. Inert gas flow rate may have also a significant impact on the formation of PAHs, since higher flow rates lead to lower volatiles concentration and retention time in the gas phase. Hence, the potential intraparticle heterogeneous secondary reactions may be reduced, main mechanism for PAHs formation at conversion temperatures lower than 500 °C [40,64,73]. This is further confirmed by results recently shown by Buss et al. [74].

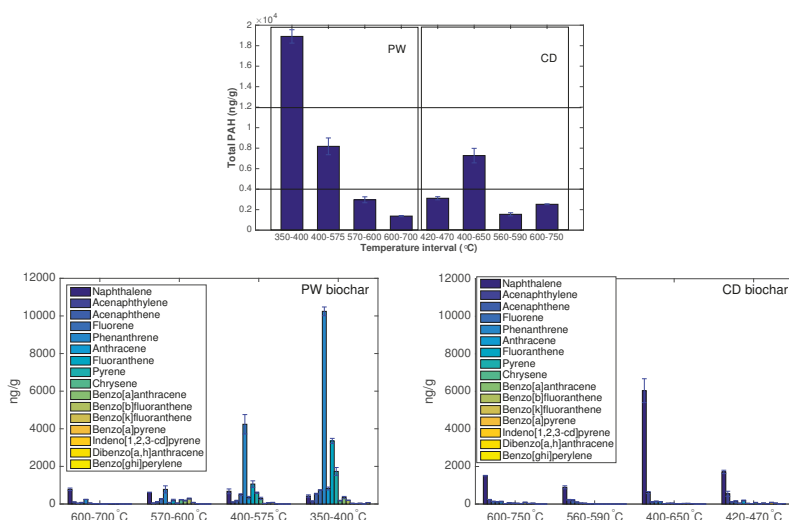


Figure 7. Top: Total content in PAHs (16 EPA PAHs) for PW and CD biochars. Horizontal lines correspond to the limits of PAHs content for basic (12 mg/kg) and premium (4 mg/kg) class biochars (EBC). Bottom: Content of PAHs species for PW and CD biochars.

For CD, however, the trend is not the same, since the highest contents in PAHs are shifted to higher temperatures, suggesting that the pathways behind their formation are different from the ones of PW biochar. This is further supported by their composition. In Figure 7, bottom left and right, it is shown that PAHs present in CD biochar are mainly naphthalene and acenaphthylene, while for PW biochars phenanthrene and fluoranthene are the main species at low temperatures. At high temperatures, naphthalene is the main species.

It must be taken also into account that the ash content in the CD biochar is very high, with values around 40% in mass, dry basis. Since the PAHs are produced in the organic phase, to compare the total PAHs in the same basis for CD and PW biochars (% mass, dry ash free basis), the PAHs content in the

case of CD should be multiplied by an approximate factor of 1.7. This leads to higher PAHs content, as function of the organic fraction, in CD than PW, except PW biochars produced at around 400 °C.

Regarding the application of biochar to soil, while in almost all cases a basic grade biochar is obtained, it can be concluded that for a high quality biochar temperatures close to 600 °C must be reached.

According to Schimmelpfennig and Glaser [21], hydrochars have very low total PAH content and low naphthalene/phenanthrene ratios, similar to PW biochars produced at low temperatures. Therefore, PAHs content in hydrochars should not be a major issue with respect to their application and they have not been measured in this study.

3.7. Wettability

In Figure 8, the water absorption behavior of several biochars is shown. On the top, those for PW biochars and, on the bottom, the behavior for CD biochars. CD biochars show increasing capacity in water absorption with higher conversion severity, probably due to an increase in porosity and reduction in surface functional groups. PW biochars present two completely different behaviors. While chars produced at the highest severity (600 °C, 40 NL min⁻¹) show similar patterns to those from CD biochars (although with slightly lower capacity to absorb water), those produced at lower temperatures do not show almost capacity to absorb water, reaching an asymptotic behavior after the first seconds.

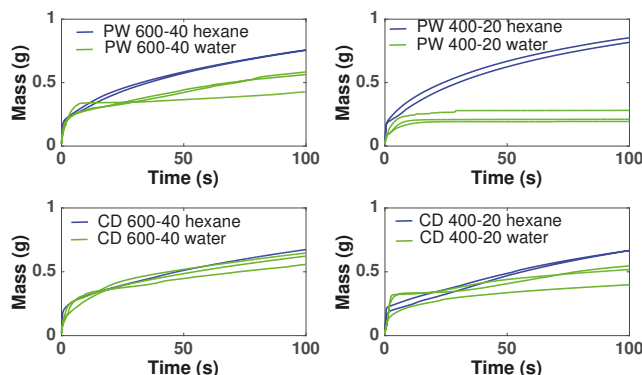


Figure 8. Water and hexane absorption curves of PW600-40, PW400-20, CD600-40, CD400-20.

When water is substituted by hexane, CD biochars still show similar absorption capacity in comparison to water, however the capacity of absorbing hexane by pine wood biochars is much higher than the one for water. If both absorption curves are compared, the contact angle can be determined, as explained in [50]. The contact angles obtained are shown in the Supplementary Material (Table S2). PW biochars present contact angles close to 90°, except PW600-40, while CD biochars present slightly lower contact angles. Although the theoretical definition of hydrophobicity is contact angle >90°, the fact that the values reported here are so close to 90° is an indication of high potential hydrophobicity [50]. From these results it can be concluded that biochars present mostly hydrophobic behavior, although this could be reduced with higher inert flow gas rates during the pyrolysis process, suggesting that a potential source of hydrophobicity is the condensation of volatiles on the char surface. It has been also shown in literature [50] that after one year in soil, biochars loose part of their hydrophobicity.

4. Conclusions

The influence of process conditions and feedstock on several biochars and hydrochars properties has been studied in a comprehensive way and analyzed from mechanistic perspectives. This work

aims at contributing to biochar engineering, i.e., the capacity of designing and producing biochars able to perform a specific function for given soil, crop and climate requirements and constraints. Based on the current results, the following conclusions can be derived:

- Regarding primary characterization, biochars O/C molar ratio is linearly correlated to volatiles content, independently of the pyrolysis conditions and feedstock. However, H/C molar ratios of CD biochars are generally lower than those of PW biochars, which may be attributed to the higher inorganic matter content of CD, leading to different pyrolysis reaction pathways and enhancing aromatization. PW hydrochars H/C molar ratio and CD hydrochars O/C molar ratio are also outliers with respect to the linear behavior. This shows that elemental and proximate analysis are not enough to determine the chemical properties of biochars [19], due to the influence of feedstock properties on reaction pathways.
- The pH depends on both conversion process parameters and feedstock, having in general higher pH biochars and hydrochars produced from CD, with much higher inorganic content, including carbonates. In both PW and CD biochars pH correlates strongly with H/C molar ratio. PW biochars and PW hydrochars present also correlation with the O/C ratio. Only CD hydrochars show good correlation ($r = 0.88$) with the ash content. This shows that the H/C molar ratio may be a better indicator of surface chemistry than O/C ratios or volatiles content, which is also supported by measurements of the total acidic functional groups.
- The porous structure varies greatly among biochars. PW biochars produced at 600 °C present mainly microporosity with N₂-SSAs around 400 m² g⁻¹. In CD biochars this microporosity is lower (<100 m² g⁻¹). The significantly lower microporosity for all CD biochars is attributed to the high inorganic content, which could potentially block the micropores and enhance mesoporosity. PW and CD biochars produced at 400 °C present also micropores (as shown by CO₂ adsorption), but much less developed than at higher temperatures, i.e., microporosity must be still developed through volatiles release, to open the pores, and further solid aromatization. Furthermore, a higher N₂ sweeping flow during pyrolysis enhances microporosity (more than double for CD biochars at 600 °C). This indicates that micropores blocking is related to volatiles, which may further react to form secondary char or condense in the pores to a greater extent for lower flow rates, when the concentration and retention time of volatiles is higher. Hydrochars, on the contrary, present mainly mesoporosity, independently of the raw material and the process severity, having higher pore volume but generally lower SSA than biochars. Washing of hydrochars further increases the SSA and pore volume due to removal of condensed species.
- Regarding nutrients, NO₃⁻ and NH₄⁺ availability is negligible after pyrolysis, irrespective of feedstock nitrogen content. The absolute availability of PO₄³⁻ is reduced compared to the feedstock. For PW biochars the relative availability increases with the pyrolysis conversion. Higher inert gas flow rate leads also to higher PO₄³⁻ availability. For hydrochars, HTC can potentially lead to an increase in availability of NO₃⁻, NH₄⁺, PO₄³⁻, and K⁺; however, these species are primarily solved in the process water. One exception is PO₄³⁻ which appears to form precipitates at higher concentration, i.e., for feedstocks with high direct nutrient potential. Similar to pyrolysis, there is the tendency that the availability of the investigated species is decreased at higher HTC temperatures.
- Biochars have a higher stability to oxidation than hydrochars. Besides the influence of process conditions, PW biochars show higher thermal stability than CD biochars. The same holds true for hydrochars. This may be related to the catalytic effect of AAEM during oxidation reactions.
- PAHs are already produced in biochars at temperatures as low as 340 °C. The maximum quantity is detected for temperatures around 400 °C, exceeding in the case of PW the maximum level for certification. At higher temperatures the PAHs content is reduced again due to vaporization of these species from the solid matrix, achieving a premium quality for temperatures above 550 °C. The composition of these species is highly dependent on the feedstock: naphthalene is the main

species in CD biochars, while phenanthrene and fluoranthene are the main species in PW biochars at low temperatures.

- Both PW and CD biochars present mostly a hydrophobic behavior, although it can be reduced with higher conversion temperatures and higher inert gas flow rates during pyrolysis, which reduces the extent of secondary reactions and recondensation of volatiles.

Based on the previous conclusions, the following general recommendations for biochar and hydrochar production can be derived. Pyrolysis temperatures above 550 °C guarantee low H/C and O/C ratios, PAHs content below the limit according to quality criteria (EBC), independently of the initial feedstock, higher SSAs and lower hydrophobicity. N₂ flow during pyrolysis can also contribute to further microporosity development and hydrophobicity reduction. High inorganic content in the feedstock potentially reduces SSA and hydrophobicity, but increases mesoporosity and pH. With respect to hydrochars, the EBC requirement regarding elemental composition can only be fulfilled for high temperature and residence times PW hydrochars. Hydrochars have a lower SSA than biochars, but a higher mesoporosity, total pore volume and nutrient availability. Washing of hydrochars after production further increases their surface area and pore volume. The results from this work can be applied to “engineer” appropriate biochars with respect to soil demands and certification requirements, as well as to improve biochar certification, and they are summarized in Figure 9.

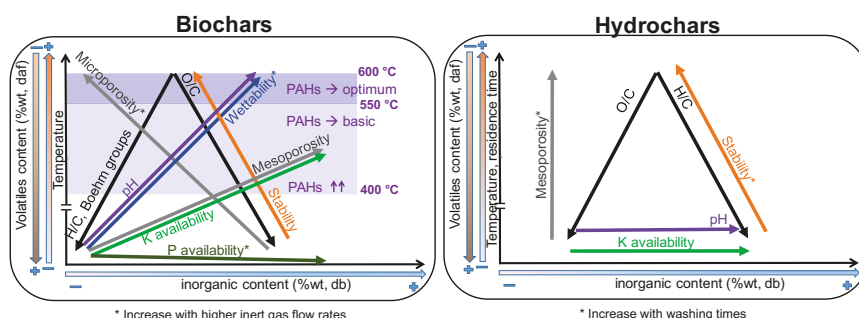


Figure 9. Conclusions. The direction of the arrows indicates increasing values for all properties.

Supplementary Materials: The following are available online at www.mdpi.com/1996-1073/11/3/496/s1.

Acknowledgments: The authors thank Susanne Hoffmann, Hernán Almuina Villar, Alba Domínguez Yebra, Alberto García Rueda and Christina Eichenauer (Technische Universität Berlin) for their support with the analytic characterization of biochars and hydrochars. The authors also thank the Leibniz Institute for Agricultural Engineering and Bioeconomy (Potsdam, Germany) for preparation of hydrochar samples. The authors acknowledge support by the German Research Foundation and the Open Access Publication Funds of Technische Universität Berlin.

Author Contributions: Alba Dieguez-Alonso, Axel Funke and Andrés Anca-Couce conceived and designed the experiments; Alba Dieguez-Alonso and Axel Funke performed the pyrolysis and hydrothermal carbonization experiments respectively; Alba Dieguez-Alonso, Axel Funke, Alessandro Girolamo Rombolà, Gerardo Ojeda and Jörg Bachmann analyzed the different biochar and hydrochar properties, with the further support from those mentioned in the acknowledgements; Alba Dieguez-Alonso, Andrés Anca-Couce, Axel Funke, Alessandro Girolamo Rombolà, Gerardo Ojeda and Jörg Bachmann and Frank Behrendt analyzed the data. Alba Dieguez-Alonso wrote the paper with important contributions from Andrés Anca-Couce and Axel Funke; the rest of the co-authors reviewed the manuscript and contributed to it when necessary according to their data analysis and interpretation. Frank Behrendt supervised the work.

Conflicts of Interest: The authors declare no conflict of interest.

Abbreviations

The following abbreviations are used in this manuscript:

CD	Corn digestate
PW	Pine wood
HTC	Hydrothermal carbonization
PSD	Pore size distribution
PAH	Polycyclic aromatic hydrocarbon
USEPA	United States Environmental Protection Agency

References

- European Biochar Certificate (EBC). *European Biochar Certificate—Guidelines for Sustainable Production of Biochar*; Version 6.2E; European Biochar Foundation (EBC): Arbaz, Switzerland, 2012. Available online: <http://www.europeanbiochar.org/en/download> (accessed on 4 February 2016).
- Standardized Product Definition and Product Testing Guidelines for Biochar That Is Used in Soil. International Biochar Initiative. Version 2.1. 2015. Available online: <http://www.biochar-international.org/characterizationstandard> (accessed on 19 October 2016).
- Abiven, S.; Schmidt, M.; Lehmann, J. Biochar by design. *Nat. Geosci.* **2014**, *7*, 326–327.
- Lee, M.E.; Park, J.H.; Chung, J.W. Adsorption of Pb(II) and Cu(II) by Ginkgo-Leaf-Derived Biochar Produced under Various Carbonization Temperatures and Times. *Int. J. Environ. Res. Public Health* **2017**, *14*, 1528.
- Frišták, V.; Pipíška, M.; Soja, G. Pyrolysis treatment of sewage sludge: A promising way to produce phosphorus fertilizer. *J. Clean. Prod.* **2018**, *172*, 1772–1778.
- Frišták, V.; Pipíška, M.; Lesný, J.; Soja, G.; Friesl-Hanl, W.; Packová, A. Utilization of biochar sorbents for Cd²⁺, Zn²⁺, and Cu²⁺ ions separation from aqueous solutions: Comparative study. *Environ. Monit. Assess.* **2014**, *187*, 4093, doi:10.1007/s10661-014-4093-y.
- Inyang, M.I.; Gao, B.; Yao, Y.; Xue, Y.; Zimmerman, A.; Mosa, A.; Pullammanappallil, P.; Ok, Y.S.; Cao, X. A review of biochar as a low-cost adsorbent for aqueous heavy metal removal. *Crit. Rev. Environ. Sci. Technol.* **2016**, *46*, 406–433.
- Mohan, D.; Sarswat, A.; Ok, Y.S.; Charles, U.P., Jr. Organic and inorganic contaminants removal from water with biochar, a renewable, low cost and sustainable adsorbent—A critical review. *Bioresour. Technol.* **2014**, *160*, 191–202.
- Sohi, S.P.; Krull, E.; Lopez-Capel, E.; Bol, R. Chapter 2—A Review of Biochar and Its Use and Function in Soil. In *Advances in Agronomy*; Sparks, D.L., Ed.; Academic Press: Cambridge, MA, USA, 2010; Volume 105, pp. 47–82.
- Chan, K.Y.; Xu, Z. Nutrient Properties and Their Enhancement. In *Biochar for Environmental Management. Science and Technology*; Earthscan: Abingdon, UK, 2009; Chapter 5, pp. 67–84, ISBN 978-1-84407-658-1.
- Thies, J.E.; Rillig, M.C. Characteristics of Biochar: Biological Properties. In *Biochar for Environmental Management. Science and Technology*; Earthscan: Abingdon, UK, 2009; Chapter 6, pp. 85–105.
- Anca-Couce, A.; Dieguez-Alonso, A.; Zobel, N.; Berger, A.; Kienzl, N.; Behrendt, F. Influence of Heterogeneous Secondary Reactions during Slow Pyrolysis on Char Oxidation Reactivity of Woody Biomass. *Energy Fuels* **2017**, *31*, 2335–2344.
- Yuan, J.H.; Xu, R.K.; Zhang, H. The forms of alkalis in the biochar produced from crop residues at different temperatures. *Bioresour. Technol.* **2011**, *102*, 3488–3497.
- Angst, T.E.; Sohi, S.P. Establishing release dynamics for plant nutrients from biochar. *GCB Bioenergy* **2013**, *5*, 221–226.
- Zambon, I.; Colosimo, F.; Monarca, D.; Cecchini, M.; Gallucci, F.; Proto, R.A.; Lord, R.; Colantoni, A. An Innovative Agro-Forestry Supply Chain for Residual Biomass: Physicochemical Characterisation of Biochar from Olive and Hazelnut Pellets. *Energies* **2016**, *9*, 526.
- Uchimiya, M.; Hiradate, S.; Antal, M.J. Dissolved Phosphorus Speciation of Flash Carbonization, Slow Pyrolysis, and Fast Pyrolysis Biochars. *ACS Sustain. Chem. Eng.* **2015**, *3*, 1642–1649.
- Hossain, M.K.; Strezov, V.; Chan, K.Y.; Ziolkowski, A.; Nelson, P.F. Influence of pyrolysis temperature on production and nutrient properties of wastewater sludge biochar. *J. Environ. Manag.* **2011**, *92*, 223–228.

18. Mukherjee, A.; Zimmerman, A.; Harris, W. Surface chemistry variations among a series of laboratory-produced biochars. *Geoderma* **2011**, *163*, 247–255.
19. Budai, A.; Wang, L.; Gronli, M.; Strand, L.T.; Antal, M.J.; Abiven, S.; Dieguez-Alonso, A.; Anca-Couce, A.; Rasse, D.P. Surface Properties and Chemical Composition of Corncob and Miscanthus Biochars: Effects of Production Temperature and Method. *J. Agric. Food Chem.* **2014**, *62*, 3791–3799.
20. Lawrinenco, M.; Laird, D.A. Anion exchange capacity of biochar. *Green Chem.* **2015**, *17*, 4628–4636.
21. Schimmelpfennig, S.; Glaser, B. One step forward toward characterization: Some important material properties to distinguish biochars. *J. Environ. Qual.* **2011**, *42*, 1001–1013.
22. Zhao, S.X.; Ta, N.; Wang, X.D. Effect of Temperature on the Structural and Physicochemical Properties of Biochar with Apple Tree Branches as Feedstock Material. *Energies* **2017**, *10*, 1293.
23. Carrier, M.; Hardie, A.G.; Uras, A.; Görgens, J.; Knoetze, J.H. Production of char from vacuum pyrolysis of South-African sugar cane bagasse and its characterization as activated carbon and biochar. *J. Anal. Appl. Pyrolysis* **2012**, *96*, 24–32.
24. Gaskin, J.W.; Steiner, C.; Harris, K.; Das, K.C.; Bibens, B. Effect of low-temperature pyrolysis conditions on biochar for agricultural use. *Trans. ASABE* **2008**, *51*, 2061–2069.
25. Keiluweit, M.; Nico, P.S.; Johnson, M.G.; Kleber, M. Dynamic Molecular Structure of Plant Biomass-Derived Black Carbon (Biochar). *Environ. Sci. Technol.* **2010**, *44*, 1247–1253.
26. Cetin, E.; Moghtaderi, B.; Gupta, R.; Wall, T. Influence of pyrolysis conditions on the structure and gasification reactivity of biomass chars. *Fuel* **2004**, *83*, 2139–2150.
27. Downie, A.; Crosky, A.; Munroe, P. Physical Properties of Biochar. In *Biochar for Environmental Management. Science and Technology*; Earthscan: Abingdon, UK, 2009; Chapter 2, pp. 13–32, ISBN 978-1-84407-658-1.
28. Liu, Z.; Zhang, F.S.; Wu, J. Characterization and application of chars produced from pinewood pyrolysis and hydrothermal treatment. *Fuel* **2010**, *89*, 510–514.
29. Hagemann, N.; Joseph, S.; Schmidt, H.P.; Kammann, C.I.; Harter, J.; Borch, T.; Young, R.B.; Varga, K.; Taherymoosavi, S.; Elliott, K.W.; et al. Organic coating on biochar explains its nutrient retention and stimulation of soil fertility. *Nat. Commun.* **2017**, *8*, 1089, doi:10.1038/s41467-017-01123-0.
30. Van Zwieten, L.; Kimber, S.; Morris, S.; Chan, K.Y.; Downie, A.; Rust, J.; Joseph, S.; Cowie, A. Effects of biochar from slow pyrolysis of papermill waste on agronomic performance and soil fertility. *Plant Soil* **2010**, *327*, 235–246.
31. McCormack, S.A.; Ostle, N.; Bardgett, R.D.; Hopkins, D.W.; Vanbergen, A.J. Biochar in bioenergy cropping systems: Impacts on soil faunal communities and linked ecosystem processes. *GCB Bioenergy* **2013**, *5*, 81–95.
32. Antal, M.J.; Grønli, M. The Art, Science, and Technology of Charcoal Production. *Ind. Eng. Chem. Res.* **2003**, *42*, 1619–1640.
33. Brassard, P.; Godbout, S.; Raghavan, V.; Palacios, H.J.; Grenier, M.; Zegan, D. The Production of Engineered Biochars in a Vertical Auger Pyrolysis Reactor for Carbon Sequestration. *Energies* **2017**, *10*, 288.
34. Titirici, M.M.; White, R.J.; Falco, C.; Sevilla, M. Black perspectives for a green future: Hydrothermal carbons for environment protection and energy storage. *Energy Environ. Sci.* **2012**, *5*, 6796–6822.
35. Huff, M.D.; Kumar, S.; Lee, J.W. Comparative analysis of pinewood, peanut shell, and bamboo biomass derived biochars produced via hydrothermal conversion and pyrolysis. *J. Environ. Manag.* **2014**, *146*, 303–308.
36. Cao, X.; Ro, K.S.; Chappell, M.; Li, Y.; Mao, J. Chemical Structures of Swine-Manure Chars Produced under Different Carbonization Conditions Investigated by Advanced Solid-State ¹³C Nuclear Magnetic Resonance (NMR) Spectroscopy. *Energy Fuels* **2011**, *25*, 388–397.
37. Wiedner, K.; Naisse, C.; Rumpel, C.; Pozzi, A.; Wieczorek, P.; Glaser, B. Chemical modification of biomass residues during hydrothermal carbonization—What makes the difference, temperature or feedstock? *Org. Geochem.* **2013**, *54*, 91–100.
38. Busch, D.; Stark, A.; Kammann, C.I.; Glaser, B. Genotoxic and phytotoxic risk assessment of fresh and treated hydrochar from hydrothermal carbonization compared to biochar from pyrolysis. *Ecotoxicol. Environ. Saf.* **2013**, *97*, 59–66.
39. Busch, D.; Glaser, B. Stability of co-composted hydrochar and biochar under field conditions in a temperate soil. *Soil Use Manag.* **2015**, *31*, 251–258.
40. Dieguez-Alonso, A.; Anca-Couce, A.; Zobel, N. On-line tar characterization from pyrolysis of wood particles in a technical-scale fixed-bed reactor by applying Laser-Induced Fluorescence (LIF). *J. Anal. Appl. Pyrolysis* **2013**, *102*, 33–46.

41. Naumann, C.; Bassler, R.; Seibold, R.; Barth, C. *Methodenbuch. Band III, Die Chemische Untersuchung von Futtermitteln*; VDLUFA-Verlag: Darmstadt, Germany, 1997.
42. Boehm, H.P.; Diehl, E.; Heck, W.; Sappok, R. Surface Oxides of Carbon. *Angew. Chem. Int. Ed.* **1964**, *3*, 669–677.
43. Goertzen, S.L.; Theriault, K.D.; Oickle, A.M.; Tarasuk, A.C.; Andreas, H.A. Standardization of the Boehm titration. Part I. CO₂ expulsion and endpoint determination. *Carbon* **2010**, *48*, 1252–1261.
44. Tsechansky, L.; Gruber, E.R. Methodological limitations to determining acidic groups at biochar surfaces via the Boehm titration. *Carbon* **2014**, *66*, 730–733.
45. Brunauer, S.; Emmett, P.H.; Teller, E. Adsorption of Gases in Multimolecular Layers. *J. Am. Chem. Soc.* **1938**, *60*, 309–319.
46. Barrett, E.P.; Joyner, L.G.; Halenda, P.P. The Determination of Pore Volume and Area Distributions in Porous Substances. I. Computations from Nitrogen Isotherms. *J. Am. Chem. Soc.* **1951**, *73*, 373–380.
47. Seaton, N.; Walton, J.; Quirk, N. A new analysis method for the determination of the pore-size distribution of porous carbons from nitrogen adsorption measurements. *Carbon* **1989**, *27*, 853–861.
48. Hoffmann, G. *Methodenbuch. Band I, Die Untersuchung von Böden*; VDLUFA-Verlag: Darmstadt, Germany, 1991.
49. Fabbri, D.; Rombola, A.G.; Torri, C.; Spokas, K.A. Determination of polycyclic aromatic hydrocarbons in biochar and biochar amended soil. *J. Anal. Appl. Pyrolysis* **2013**, *103*, 60–67.
50. Ojeda, G.; Mattana, S.; Avila, A.; Alcaniz, J.M.; Volkmann, M.; Bachmann, J. Are soil-water functions affected by biochar application? *Geoderma* **2015**, *249–250*, 1–11.
51. Krull, E.S.; Baldock, J.A.; Skjemstad, J.O.; Smernik, R.J. Characteristics of Biochar: Organo-Chemical Properties. In *Biochar for Environmental Management. Science and Technology*; Earthscan: Abingdon, UK, 2009; Chapter 4, pp. 53–65, ISBN 978-1-84407-658-1.
52. Rombolà, A.G.; Fabbri, D.; Meredith, W.; Snape, C.E.; Dieguez-Alonso, A. Molecular characterization of the thermally labile fraction of biochar by hydropyrolysis and pyrolysis-GC/MS. *J. Anal. Appl. Pyrolysis* **2016**, *121*, 230–239.
53. Mumme, J.; Eckervogt, L.; Pielert, J.; Diakité, M.; Rupp, F.; Kern, J. Hydrothermal carbonization of anaerobically digested maize silage. *Bioresour. Technol.* **2011**, *102*, 9255–9260.
54. Li, F.; Cao, X.; Zhao, L.; Wang, J.; Ding, Z. Effects of Mineral Additives on Biochar Formation: Carbon Retention, Stability, and Properties. *Environ. Sci. Technol.* **2014**, *48*, 11211–11217.
55. Liu, W.J.; Jiang, H.; Yu, H.Q. Development of Biochar-Based Functional Materials: Toward a Sustainable Platform Carbon Material. *Chem. Rev.* **2015**, *115*, 12251–12285.
56. Yin, S.; Mehrotra, A.K.; Tan, Z. Alkaline hydrothermal conversion of cellulose to bio-oil: Influence of alkalinity on reaction pathway change. *Bioresour. Technol.* **2011**, *102*, 6605–6610.
57. Pulido-Novicio, L.; Hata, T.; Kurimoto, Y.; Doi, S.; Ishihara, S.; Imamura, Y. Adsorption capacities and related characteristics of wood charcoals carbonized using a one-step or two-step process. *J. Wood Sci.* **2001**, *47*, 48–57.
58. Nguyen, B.T.; Lehmann, J. Black carbon decomposition under varying water regimes. *Org. Geochem.* **2009**, *40*, 846–853.
59. Baldock, J.A.; Smernik, R.J. Chemical composition and bioavailability of thermally altered *Pinus resinosa* (Red pine) wood. *Org. Geochem.* **2002**, *33*, 1093–1109.
60. Lee, J.W.; Kidder, M.; Evans, B.R.; Paik, S.; Buchanan, A.C., III; Garten, C.T.; Brown, R.C. Characterization of Biochars Produced from Cornstovers for Soil Amendment. *Environ. Sci. Technol.* **2010**, *44*, 7970–7974.
61. Ronsse, F.; van Hecke, S.; Dickinson, D.; Prins, W. Production and characterization of slow pyrolysis biochar: Influence of feedstock type and pyrolysis conditions. *GCB Bioenergy* **2013**, *5*, 104–115.
62. Yang, F.; Zhao, L.; Gao, B.; Xu, X.; Cao, X. The Interfacial Behavior between Biochar and Soil Minerals and Its Effect on Biochar Stability. *Environ. Sci. Technol.* **2016**, *50*, 2264–2271.
63. Guizani, C.; Jeguirim, M.; Valin, S.; Limousy, L.; Salvador, S. Biomass Chars: The Effects of Pyrolysis Conditions on Their Morphology, Structure, Chemical Properties and Reactivity. *Energies* **2017**, *10*, 796.
64. Anca-Couce, A. Reaction mechanisms and multi-scale modelling of lignocellulosic biomass pyrolysis. *Prog. Energy Combust. Sci.* **2016**, *53*, 41–79.
65. Harvey, O.R.; Kuo, L.J.; Zimmerman, A.R.; Lououcharn, P.; Amonette, J.E.; Herbert, B.E. An Index-Based Approach to Assessing Recalcitrance and Soil Carbon Sequestration Potential of Engineered Black Carbons (Biochars). *Environ. Sci. Technol.* **2012**, *46*, 1415–1421.

66. Kuo, L.J.; Herbert, B.E.; Loucheurn, P. Can levoglucosan be used to characterize and quantify char/charcoal black carbon in environmental media? *Org. Geochem.* **2008**, *39*, 1466–1478.
67. Plante, A.F.; Fernández, J.M.; Haddix, M.L.; Steinweg, J.M.; Conant, R.T. Biological, chemical and thermal indices of soil organic matter stability in four grassland soils. *Soil Biol. Biochem.* **2011**, *43*, 1051–1058.
68. Zimmerman, A.R. Abiotic and Microbial Oxidation of Laboratory-Produced Black Carbon (Biochar). *Environ. Sci. Technol.* **2010**, *44*, 1295–1301.
69. Funke, A. Fate of Plant Available Nutrients during Hydrothermal Carbonization of Digestate. *Chem. Ing. Tech.* **2015**, *87*, 1713–1719.
70. Singh, B.; Singh, B.P.; Cowie, A.L. Characterisation and evaluation of biochars for their application as a soil amendment. *Aust. J. Soil Res.* **2010**, *48*, 516–525.
71. Funke, A.; Mumme, J.; Koon, M.; Diakité, M. Cascaded production of biogas and hydrochar from wheat straw: Energetic potential and recovery of carbon and plant nutrients. *Biomass Bioenergy* **2013**, *58*, 229–237.
72. Kruse, A.; Koch, F.; Stelzl, K.; Wüst, D.; Zeller, M. Fate of Nitrogen during Hydrothermal Carbonization. *Energy Fuels* **2016**, *30*, 8037–8042.
73. Dieguez-Alonso, A.; Anca-Couce, A.; Zobel, N.; Behrendt, F. Understanding the primary and secondary slow pyrolysis mechanisms of holocellulose, lignin and wood with laser-induced fluorescence. *Fuel* **2015**, *153*, 102–109.
74. Buss, W.; Graham, M.C.; MacKinnon, G.; Masek, O. Strategies for producing biochars with minimum {PAH} contamination. *J. Anal. Appl. Pyrolysis* **2016**, *119*, 24–30.



© 2018 by the authors. Licensee MDPI, Basel, Switzerland. This article is an open access article distributed under the terms and conditions of the Creative Commons Attribution (CC BY) license (<http://creativecommons.org/licenses/by/4.0/>).

Article

Estimation of Effective Diffusion Coefficient of O₂ in Ash Layer in Underground Coal Gasification by Thermogravimetric Apparatus

Xi Lin, Qingya Liu and Zhenyu Liu *

Beijing Advanced Innovation Center for Soft Matter Science and Engineering, and State Key Laboratory of Chemical Resource Engineering, Beijing University of Chemical Technology, Beijing 100029, China; buctlinxi@outlook.com (X.L.); qyliu@mail.buct.edu.cn (Q.L.)

* Correspondence: liuzy@mail.buct.edu.cn; Tel.: +86-(0)10-6442-1073

Received: 28 January 2018; Accepted: 14 February 2018; Published: 22 February 2018

Abstract: Underground coal gasification (UCG) proceeds generally in the presence of an ash layer on coal (or char) surface. The ash layer increases the mass transfer resistance of O₂ to the gasification surface, which may become the limiting step of whole process. This paper studies O₂ diffusion in ash layer formed on cylindrical char samples using a specially designed one-dimension setup in a thermogravimetric apparatus (TGA). The effective internal diffusion coefficient (D_e) is found to increase with an increase in ash layer thickness, due to an increase in median pore diameter. Methods are established to correlate D_e with operating conditions and to estimate the role of internal diffusion resistance in overall mass transfer resistance.

Keywords: underground coal gasification; ash layer; effective diffusion coefficient; internal diffusion resistance

1. Introduction

Underground coal gasification (UCG) has been viewed as a potential technology because it requires no mining and transportation of coal and leaves the gasification residue underground. In UCG, gasification agents, such as O₂ and H₂O, are injected into predrilled cavity in which the reaction of O₂ with coal yields a high temperature, in a range of 1173–1473 K [1], to allow the reactions of H₂O and CO₂ with coal to occur to produce CO and H₂. The CO and H₂ can be used as feedstock for many chemical industries and fuels for various purposes [2]. This process has been tested for more than one hundred years, such as in the former Soviet Union, and has been studied extensively in recent decades in many countries including Poland, China, Australia and Ukraine [3]. These studies, ranged from field scale to laboratory scale, have advanced this technology significantly. However, there is still no commercial application of this technology to date due mainly to difficulties in steady state operation for a sufficient long period of time. Therefore, laboratory studies in all aspects of the process were emphasized by many researchers. For instance, Urych studied UGC in a TGA/DSC system and evaluated pyrolysis of coal, a step prior to gasification, in a temperature range of 298–1173 K [4]. Prabu et al. studied UCG through combustion of wood block and coal in laboratory to simulate the cavity formation [5]. The impact of reactant gas composition and injection rate on UCG product distribution are also studied by laboratory research [6,7].

It has been found in past studies that the main gasification reaction in UCG is the reaction of coal pyrolysis char with the gasification agents, which is also the limiting step in overall UCG process [8]. In this gasification reaction, minerals in char, which usually accounts 10–20 wt. % of coal, up to 50 wt. % in some coals [9], form an ash layer on the char surface due to exhaustion of carbon by

gasification. This ash layer increases the internal resistance of gas and makes the mass transfer of gasification agents the rate controlling step [10,11].

Experimental and numerical modeling studies have been carried out to study mass transfer in the ash layer in UCG. Some experimental studies [12,13] observed formation of cracks and fractures in coal during gasification, which shatters coal char and ash layer and reduces the mass transfer resistance of gasification agents in ash layer. However, this shattering effect was found by a percolation model [14] to be insufficient to diminish the mass transfer limitation of the gasification agents because the new char surface formed would be quickly covered by an ash layer. The laboratory [15] and field test [16] studies of UCG showed that the ash layers in the order of centimeter on the char surface, as well as in char cracks, constitute the major scenes of internal diffusion.

Conventional modeling studies on UCG [17–19] also studied mass transfer of gasification agents from the bulk gas flow to the surface of solid, which depends largely on temperature distribution and turbulence extent of gasification agents. It should be noted that, however, this mass transfer resistance, from the bulk gas flow to the surface of solid, varies little with the flow rate of gasification agents in the channel of UCG because they are perpendicular to each other [20] (pp. 1835–1836). Huang et al. [21] showed the vertical velocity to the surface is mainly affected by the permeability and fracture of solid, rather than the air flow rate in the axle direction.

Since it is hard to reduce diffusion resistance in ash layer in UCG by manipulating the operating conditions only a few studies addressed the diffusion behavior of gasification agents in ash layer, and most of them assumed a constant diffusion coefficient in the ash layer. However, many coal gasification and combustion studies, other than those of UCG, showed obvious changes in ash structure during the course of gasification, so do the mass transfer coefficients. For instance, Barea et al. [22] suggested the effective diffusion coefficients of CO₂ depends on temperature and porosity of char, and obvious mass transfer resistance was found in char bed as thin as several millimeters in a TGA study. Yan [23] studied combustion of 10 coals and showed that the diffusion coefficient is proportional to effective porosity in ash layers. Liu [24] studied the anisotropy of the ash layer of oil shale, showed that the diffusion coefficients increased with increasing ash layer thickness, but the reaction turns to internal diffusion control under an ash layer of several millimeters.

Due to the importance of mass transfer in ash layer in UCG and little information can be found in the literature on the subject, this work studies the mass transfer behavior of O₂ with increasing thickness of ash layer at various temperatures and O₂ concentrations using a specially designed one-dimensional gasification setup in a TGA.

2. Materials and Methods

2.1. Theoretical Section

In principle, as shown in Figure 1, the mass transfer of O₂ during the gasification of char with an ash layer includes the following steps: (a) diffusion of O₂ with a concentration of C_f in the bulk gas to the external surface of the ash layer, (b) diffusion of O₂ with a concentration of C_{S1} at the surface of ash layer to the char interface, and (c) reaction of O₂ with a concentration of C_{S2} at the char interface with char following the first order reaction [25] respecting to O₂ to produce CO then to CO₂ as shown in our previous study [26]. Under the quasi-steady state, the flux of O₂ (N_{O₂}) from the bulk gas to the external surface of ash layer is equal to the flux of O₂ diffusing through the ash layer, as well as to the reaction of O₂ at the char interface. These steps can be expressed by Equation (1), where K_c is the mass transfer coefficient of convection, L is the thickness of ash layer, D_e is the effective diffusivity in the ash layer, K is the rate constant of C-O₂ reaction, while C_f, C_{S1} and C_{S2} are O₂ concentration in the gas bulk, at the external surface of ash layer, and at the char surface, respectively:

$$N_{O_2} = K_c(C_f - C_{S1}) = \frac{D_e}{L}(C_{S1} - C_{S2}) = KC_{S2} \quad (1)$$

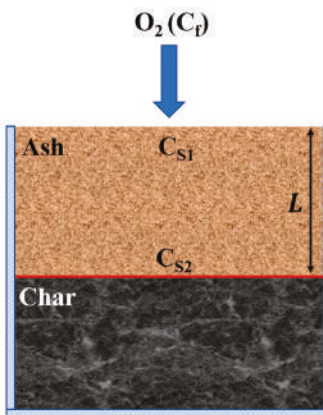


Figure 1. Schematic representation of a char sample with one-dimensional ash layer formation.

N_{O_2} can also be expressed by Equation (2) in terms of mass transfer resistance of these steps or by Equation (3) in terms of carbon consumption rate at the char surface. In these equations M_C is molecular mass of carbon (char), dn_c/dt is carbon consumption rate in mole/min, dm/dt is carbon consumption rate in g/min, and DTG is mass loss rate of sample in g/min measured by TGA. Based on these equations D_e can be expressed by Equation (4).

$$N_{O_2} = \frac{C_f}{\frac{1}{K_c} + \frac{L}{D_e} + \frac{1}{K}} \quad (2)$$

$$N_{O_2} = -\frac{dn_c}{dt} = -\left(\frac{1}{M_C} \frac{dm}{dt}\right) = -\frac{DTG}{M_C} \quad (3)$$

$$D_e = \frac{L}{-\frac{M_C C_f}{DTG} - \left(\frac{1}{K_c} + \frac{1}{K}\right)} \quad (4)$$

Since the ash layer thickness L at a given gasification time is not easy to be determined accurately by the sample's appearance it is estimated from the amount of carbon gasified by Equation (5) based on the following assumptions: (a) The cylindrical char samples consist of C and ash only, and they are distributed uniformly; (b) The ash remained in the gasification maintains the same cylindrical shape as the char sample; and (c) There is no C in the ash layer. In Equation (5), L_f is the final ash layer thickness in an experiment, Δm and Δm_f are the mass losses at the given time and the end of the experiment, respectively.

$$L = \frac{\Delta m}{\Delta m_f} \times L_f \quad (5)$$

The rate constant of C-O₂ reaction (K) can be expressed by Equation (6), where A , E_a , R and T are the pre-exponential factor, the apparent activation energy, the gas constant, and temperature, respectively.

$$K = AT^n e^{-E_a/RT} \quad (6)$$

The convective mass-transfer coefficient (K_c) can be estimated by the Sherwood number (Sh) that is the ratio of convective mass transfer and diffusion mass transfer as shown in Equation (7), where L' is the feature size of char sample, D_{O_2} is the molecular diffusivity of oxygen in the bulk gas.

$$Sh = \frac{K_c L'}{D_{O_2}} \quad (7)$$

When the fluid flows through a single particle as in this paper, the Sherwood number can be approximated by Equation (8) according to Bews et al. [27], where Re is the Reynolds number, Sc is the Schmidt number, d is the inner diameter of TGA tube, u is the flow velocity, v is the kinematic viscosity of gas flow.

$$Sh = 2.0 + 0.69Sc^{1/3}Re^{1/2} = 2.0 + 0.69\left(\frac{v}{D_{O_2}}\right)^{1/3}\left(\frac{ud}{v}\right)^{1/2} \quad (8)$$

The combination of Equations (7) and (8) yields Equation (9) for K_c .

$$K_c = \frac{D_{O_2}}{L'}(2.0 + 0.69\left(\frac{v}{D_{O_2}}\right)^{1/3}\left(\frac{ud}{v}\right)^{1/2}) \quad (9)$$

2.2. Experimental Section

A Chinese low volatile bituminous coal, Luxian coal, is used in the study. After pyrolysis at 1173 K in N_2 for 3 h, a char with 37 wt. % ash was obtained. The char was crushed and sieved to 60–100 mesh size and then pressed to cylindrical form of 10 mm in diameter and 9 mm in length. The porosity of cylindrical char sample is 0.37, similar to that of the char prior to crushing, 0.35. The purpose of crushing and pelletizing the char is to minimize the macroscopic anisotropy of char structure [24]. In addition, the diameter range of crashed char powder, 0.15–0.25 mm, is much larger than the mean free path of O_2 and the size of the large pores (around 0.0001 mm).

The cylindrical char sample is enclosed in a size-compatible cylindrical TGA crucible with an inner diameter of 10 mm and a depth of 9 mm as shown in Figure 2. Since only the top of char sample is in contact with the gasification reagent, the gasification proceeds along the axial direction with a constant gasification area and the ash layer remained in the gasification maintains the cylindrical shape as the char, similar to that described by the shrinking-core model [28]. After been heated to a gasification temperature in Ar at a rate of 20 K/min, the char sample was exposed to a flow of 10% O_2 in balance Ar at a rate of 100 mL/min, which replaced 99% Ar in the TGA in 5 min. After a given gasification time, the gas flow was switched to Ar and the char sample was cool down to room temperature. Re at 1273 K is about 5, the same magnitude as that reported on the coal surface in an underground study [21].



Figure 2. The appearance of char sample before and after gasification at 1273 K for 99 min.

3. Results and Discussion

Figure 3 shows the cross-section view of samples gasified at 1273 K for about 19 and 99 min with mass losses of 90 and 338 mg, respectively. Clearly the gasification front moves along the axial direction of the cylindrical char as expected by the one-dimensional shrinking-core model and the ash remained adheres to the char surface to form a layer of similar thickness. The ash shrinks slightly as evidenced in the radial direction and small amounts of char at the lateral surface closing to the reacting front

gasify due to diffusion of O₂ into the gap between the crucible wall and the sample. Based on the ash layer of 4.0 mm thick in the axis at a mass loss of 338 mg an ash layer of 1.07 mm thick is determined by Equation (5) for a mass loss of 90 mg, which is very close to the observed ash layer thickness of 1.02 mm, indicating sufficient accuracy of Equation (5) in estimating the ash layer thickness.



Figure 3. The cross-section view of a sample gasified at 1273 K to different mass losses.

Figure 4 shows the TG and DTG curves of char gasification at 1273 K which yield the samples in Figure 3. The maximum gasification rate (DTG) appears at the beginning, about 5.42 mg/min, due to the absence of an ash layer. As the gasification proceeds, the DTG decreases continuously to about 2.47 mg/min at 99 min, indicating an increase in diffusion resistance of O₂ with an increase in ash layer thickness. This behavior, however, may also include changes in the effective diffusion coefficient D_e .

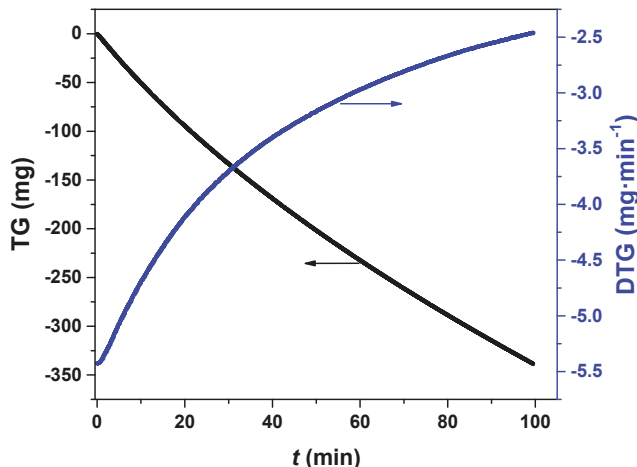


Figure 4. TG and DTG curves during gasification at 1273 K.

3.1. Estimation of Effective Diffusion Coefficient

Since the gasification temperature in Figures 3 and 4 is higher than 1173 K, the boundary of oxidation zone in the “three zones theory” [29], higher than which the resistance of C-O₂ reaction is negligible compared with that of interparticle diffusion [30], Equation (4) can be simplified to Equation (10).

$$D_e = \frac{L}{-\frac{M_C C_f}{DTG} - \frac{1}{K_c}} \quad (10)$$

Figure 5 shows D_e determined by Equation (10). As expected D_e increases with an increase in temperature, $1.51 \times 10^{-4} \text{ m}^2/\text{s}$ at 1173 K while $2.82 \times 10^{-4} \text{ m}^2/\text{s}$ at 1373 K both at the mass loss of 250 mg, corresponding to an ash layer thickness of 3 mm. The range of D_e is the same as that determined in our previous study [26] in coal gasification (around $1 \times 10^{-4} \text{ m}^2/\text{s}$) and that reported by Chen et al. [31] for combustion of coal particles of 16 mm in diameter with 53% ash ($1.5 \times 10^{-4} \text{ m}^2/\text{s}$ at 1145 K). Figure 5 also shows that D_e increases with increasing time, indicating increasing pore size or fractures in the ash layer over time. This behavior is similar to that reported by Sotirchos [32], who studied combustion of a char with 25% ash and showed increasing macropore volume over time for ash layers of millimeter thick, and increasing D_e over time in a range around $1 \times 10^{-4} \text{ m}^2/\text{s}$ at 1173 K. Clearly, the compressed cylindrical char sample prepared in this work can be used to study D_e of char particles.

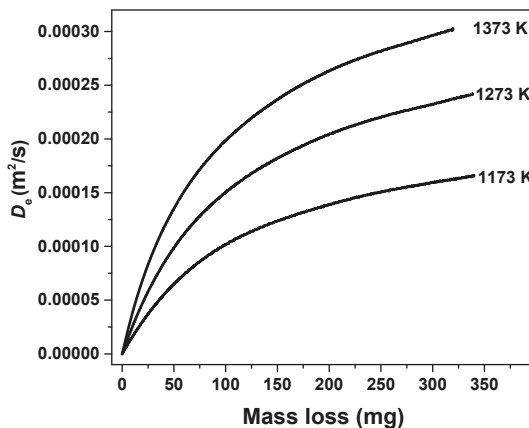


Figure 5. Diffusion coefficient at different temperatures in gasification.

It is noted that in addition to porosity, pore size distribution in the ash layer may also influence mass transfer rate of O_2 . To explore this effect ash layers formed on cylindrical char samples during gasification at 1273 K for different time, as shown in Figure 6, were sampled at every 2 mm thick and subjected to mercury intrusion porosimetry analysis. The ash samples listed in Table 1 are these formed initially, 0–2 mm in Figure 6a (Sample 1); 0–2 mm in Figure 6b (Sample 2) that exposed to 1273 K longer than that of Sample 1; 2–4 mm in Figure 6b (Sample 3); and that exposed to 1273 K for a time much longer than other samples (Sample 4) in addition. The t in the table is the residence time the ash sample exposed to 1273 K. It seems that the porosity of these samples is similar, around 0.7, but the median pore diameter of these samples increases with an increase in gasification time, from about 1400 nm in 20–30 min to 1700 nm in 175 min. Since these median pore diameters are less than 5 times the mean free path of O_2 at 1273 K (about 381 nm), in which the collision between gas molecule and the pore wall cannot be ignored, so the increasing D_e in gasification in Figure 5 can be attributed to increasing pore diameter in the ash layers during the gasification.

Table 1. Median pore diameter of ash samples from gasification at 1273 K for different time.

Parameter	Sample 1	Sample 3	Sample 2	Sample 4
t (min)	20	30	65	175
Porosity	0.68	0.69	0.70	0.70
diameter (nm)	1397	1401	1601	1710

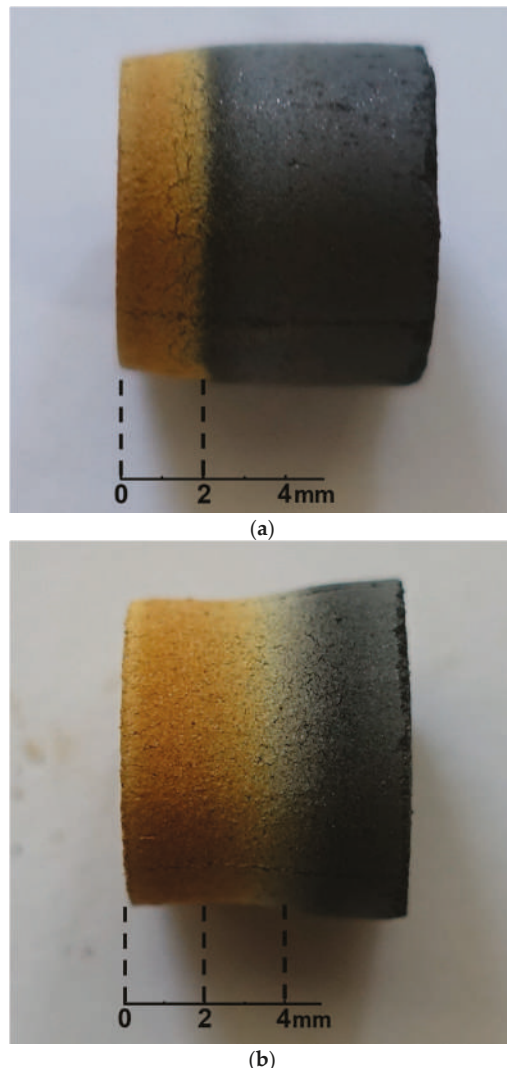
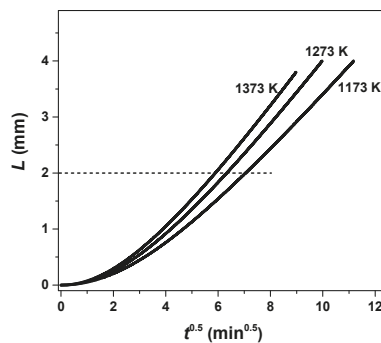


Figure 6. Samples subjected to gasification at 1273 K for different time: (a) with an ash layer of 2 mm; (b) with an ash layer of 4 mm.

3.2. Internal Diffusion Resistance

For a one-dimensional gas-solid reaction, the traditional shrinking-core model suggests a linear relationship between reaction time (t) and square of ash thickness (L) if internal diffusion is the rate limiting step and effective diffusivity D_e is constant [33]. The plot in Figure 7 shows that the $L-t^{0.5}$ relation of this work is close to a linear relation at ash layer thickness of greater than 2 mm. This however does not necessarily indicate that the gasification is under internal diffusion control because the D_e in the ash layer varies with ash layer thickness as indicated in Figure 5.

Figure 7. Relation between $t^{0.5}$ and thickness of ash layer L .

To understand the role of O₂ diffusion in ash layer the internal diffusion resistance (L/D_e) at the ash layer thickness of 1, 2 and 3 mm is compared with the reaction resistance at the char surface ($1/K$) and the convection resistance in the bulk gas ($1/K_c$) in Table 2. The $1/K$ and $1/K_c$ are determined by Equations (6) and (9) based on the experimental data of this work and those in the literature [34]. It can be seen that the reaction resistance ($1/K$) is much smaller than the diffusion resistances of $1/K_c$ and L/D_e under the conditions used, indicating that the overall gasification rate is always under mass transfer control. The L/D_e increases with an increase in ash layer thickness although D_e also increases with an increase in ash layer thickness as shown in Figure 5, suggesting that the diffusion resistance of O₂ in the ash layer is more affected by L than by D_e .

Table 2. Resistance of reaction and mass transfer in gas film and ash layer (s/m).

Resistance	1173 K	1273 K	1373 K
$1/K$	0.3	0.07	0.02
$1/K_c$	6.4	5.6	5.0
L/D_e ($L = 1$ mm)	10.8	7.3	5.5
L/D_e ($L = 2$ mm)	15.4	10.5	8.1
L/D_e ($L = 3$ mm)	19.8	13.5	10.6

The contribution of L/D_e to overall mass transfer resistance (η) can be determined with sufficient accuracy by Equation (11), ignoring the contribution of $1/K$, and shown in Figure 8. Clearly, η increases nonlinearly with an increase in ash layer thickness while decreases almost linearly with an increase in temperature, and the O₂ diffusion in ash layer plays a dominant role especially when the ash layer thickness is greater than 1 mm. For instance, at 1273 K, $1/K_c$ is 5.6 s/m while η is around 70% at an ash thickness of 3 mm, corresponding to a mass loss about 250 mg. This η indicates that the diffusion resistance in ash layer is more than twice as much as the external diffusion resistance. This increase in diffusion resistance in the ash layer leads to a decrease in O₂ diffusion rate and a decrease in overall gasification rate, by about 50% from the initial value as indicated in Figure 4. This behavior is similar to that reported by Perkins et al. [35] in which a 20% reduction in gasification rate was observed at an ash layer of 1 mm thick in a meter-scale UCG simulation study.

$$\eta = \frac{L/D_e}{\frac{L}{D_e} + \frac{1}{K_c}} \times 100\% \quad (11)$$

The temperature effect on η in Figure 8 shows that the diffusion resistance in ash layer is more important at a lower temperature than that at a higher temperature. For instance, at an ash layer thickness of 3 mm, the η is about 75.5% at 1173 K but 70.7% and 68.0% at 1273 and 1373 K, respectively.

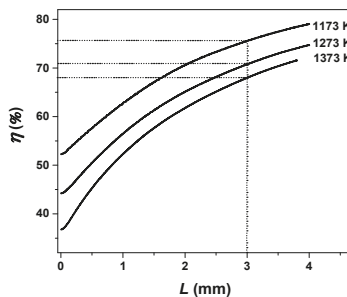


Figure 8. The contribution of L/D_e to overall mass transfer resistance (η) at different ash layer thickness.

3.3. The Influence of Gas Concentration

In UCG, O₂ concentration decreases from the injection well to the production well due to its consumption in gasification. A higher O₂ concentration leads to a higher gasification rate and perhaps also to a change in D_e due to local melting of ash caused by the heat of reaction between O₂ and CO in the ash layer as indicated in our earlier study [26]. It can be seen in Figure 9 that at 1273 K the gasification rate increases with an increase in O₂ concentration, the time needed for gasifying 300 mg char is 115 min under 7.5% O₂ but 72 min under 12% O₂. It can also be seen in Figure 10 that D_e determined by Equation (10) varies little with O₂ concentration at the temperatures used, indicating little ash melting under these conditions, agreeing with our earlier study that the apparent ash melting of this particular coal is at 1573 K [26]. The data in Figure 10 suggest that O₂ concentration plays a minor role while temperature and ash layer thickness play major roles in D_e in Equation (10).

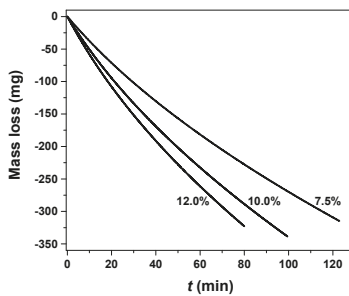


Figure 9. Gasification at 1273 K under different O₂ concentrations.

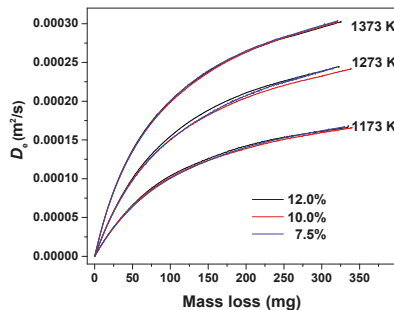


Figure 10. Effective diffusion coefficient in ash layer under different temperatures and O₂ concentrations.

3.4. Effective Diffusion Coefficient with Temperature and Ash Layer Thickness

Since it is not easy to obtain flow parameters in UCG and therefore to estimate $1/K_c$, and the $1/K_c$ is smaller than L/D_e when ash layer is thick, Equation (10) can be simplified to Equation (12) by omitting $1/K_c$ with accuracy θ defined by Equation (13). It can be seen in Figure 11 that θ increases with an increase in ash layer thickness and is higher than 50% when ash layer thickness is higher than 1 mm, especially at low temperatures. For instance, at 1273 K, θ is 44% initially but becomes 76% at an ash layer thickness of 4 mm. Clearly in a continuous operation of UCG with a much thicker ash layer the O_2 diffusion resistance in ash layer is the dominant resistance.

$$D'_e = -\frac{L \times DTG}{M_C C_f} \quad (12)$$

$$\theta = \frac{D'_e}{D_e} \times 100\% = \frac{DTG}{DTG + \frac{M_C C_f}{K_c}} \times 100\% \quad (13)$$

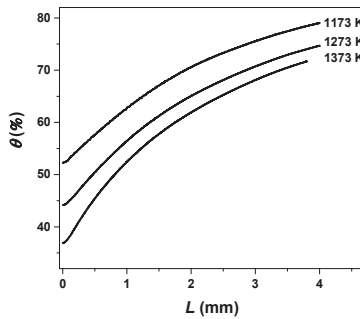


Figure 11. Accuracy of diffusion coefficient (θ) under omitting external diffusion resistance.

Since L/D_e dominants the overall mass transfer resistance in UCG it is useful to establish a relation between D_e in the ash layer and the D_{O_2} in the bulk gas. At a reaction temperature this relation however involves correlations in two regions separated by the pore size that is 10 times the mean free path of O_2 , 10λ , i.e., free diffusion in pores (and fractures) of larger than 10λ in size with the coefficient approximately D_{O_2} and restrictive diffusion in pores of smaller than 10λ in size with a coefficient D_1 , which is smaller than D_{O_2} . Previous study [36] suggested that D_1 is proportional to the porosity as shown in Equation (14), where ε_1 is porosity of the pores with diameters less than 10λ and τ is tortuosity of pores generally within 2 to 6 [37].

$$D_1 = \frac{\varepsilon_1}{\tau} \times D_{O_2} \quad (14)$$

$$D_e = (0.7 - \varepsilon_1)D_{O_2} + \varepsilon_1 D_1 \quad (15)$$

$$D_e = D_{O_2}(0.7 - \varepsilon_1 + \frac{\varepsilon_1^2}{\tau}) \quad (16)$$

As shown in Table 1 the total porosity of ash layer is approximately 0.7, hence the fraction of pores with diameter larger than 10λ is $0.7 - \varepsilon_1$ which is also the porosity of any cross section in the ash layer [38]. The effective diffusion coefficient D_e therefore can be expressed by Equation (15), and the relation between D_e and D_{O_2} can be expressed as Equation (16).

If the pores in the ash layer coalesce in continuous high temperature UCG operation ε_1 can be described by Equation (17) according to the format of relationship between porosity and time in porous ceramics at high temperature [39] (p. 380), where t is time while B and c are parameters obtained by

fitting experimental data. Then Equation (16) can be rewritten as Equation (18) and then Equation (19) because time t is proportionate linearly with the square of ash layer thickness as discussed earlier.

$$\varepsilon_1 = Be^{-ct} \quad (17)$$

$$D_e = D_{O_2} \left(0.7 - Be^{-ct} + \frac{B^2}{\tau} \times (e^{-ct})^2 \right) \quad (18)$$

$$D_e = D_{O_2} \left(0.7 - Be^{-cdL^2} + \frac{B^2}{\tau} (e^{-cdL^2})^2 \right) \quad (19)$$

Since the higher-order term in Equation (20), $\frac{B^2}{\tau} (e^{-cdL^2})^2$, is relatively small at a higher ash layer thickness and can be omitted, and D_{O_2} is proportional to $T^{1.75}$ according to the formula proposed by Fuller Schettler Giddings [38] Equation (19) can be rewritten as Equation (20) with F as the product of c and d .

$$D_e = 1.78 \times 10^{-5} \left(\frac{T}{273} \right)^{1.75} (0.7 - Be^{-FL^2}) \quad (20)$$

Table 3 shows the parameters B and F determined by fitting Equation (20) with the data at 1173, 1273 and 1373 K using the least squares method. It can be found that B changes little with a change in temperature indicating that B is determined by the physical properties of ash layer, while F varies relatively strongly with temperature.

Table 3. Parameters of Equation (20).

Parameter	1173 K	1273 K	1373 K
B	0.530	0.548	0.556
F	114,914	210,240	279,638

Figure 12 shows D_e determined by Equation (20) and that observed in the experiments (dots) under different temperatures and ash layer thickness. Clearly the D_e determined from Equation (20) fits the experimental data well with small residual sum of square, approximately $7.1 \times 10^{-11} \text{ m}^4/\text{s}^2$ at 1273 K and ash layer thickness of 2.5–3.5 mm, for example.

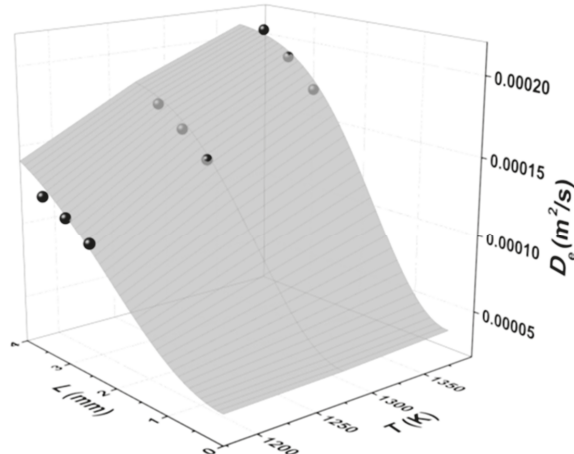


Figure 12. Diffusion coefficient in ash layer under different temperature and ash layer thickness.

Figure 13 shows η , the proportion of internal diffusion resistance in overall mass transfer resistance defined earlier by Equation (11), under different temperatures and ash layer thickness. The contours of η of 70, 75 and 80% show that the internal diffusion resistance plays a major role in overall mass transfer resistance, more than 75% when the ash layer is thicker than 2.5 mm at 1250–1300 K, for example.

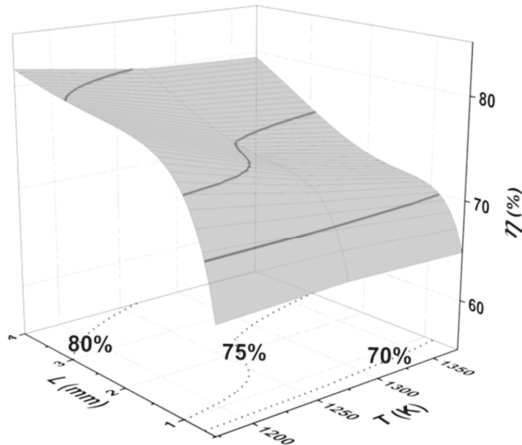


Figure 13. The contribution of L/D_e to overall mass transfer resistance (η) under different temperatures and ash layer thickness.

The increase in η with increasing ash layer thickness would reduce the O_2 flux through ash layer leading to reduced gasification rate and low char conversion, as well as a shift of gasification zone toward the downstream in a UCG operation. This agrees with that reported in the field test [40], where 30% char was not converted even though spalling of coal and ash were observed.

4. Conclusions

This paper studies mass transfer of oxygen in ash layer of UCG using cylindrical char samples in a TGA. It is found that an ash layer is formed and remained on the surface of char, which reduces the rate of carbon conversion significantly in gasification. The effective internal diffusion coefficient of O_2 (D_e) is estimated based on the ash layer thickness observed and estimated from carbon conversion. The mean pore diameter of ash layer increases with an increase in ash layer thickness, so does the D_e . The mass transfer resistance of O_2 in the ash layer (L/D_e) also increases with an increase in ash layer thickness, which is the dominant resistance when the ash layer is a few millimeters thick.

Acknowledgments: The work is financially supported by the National Key Research and Development Program of China (2016YFB0600300).

Author Contributions: Zhenyu Liu and Qingya Liu designed research; Xi Lin performed the experiment; Xi Lin and Qingya Liu analyzed the data; Xi Lin and Zhenyu Liu wrote the paper.

Conflicts of Interest: The authors declare no conflict of interest.

References

1. Najafi, M.; Jalali, S.M.E.; KhaloKakaie, R. Thermal-mechanical-numerical analysis of stress distribution in the vicinity of underground coal gasification (UCG) panels. *Int. J. Coal Geol.* **2014**, *134–135*, 1–16. [[CrossRef](#)]
2. Otto, C.; Kempka, T. Prediction of steam jacket dynamics and water balances in underground coal gasification. *Energies* **2017**, *10*, 739. [[CrossRef](#)]
3. Shafirovich, E.; Varma, A. Underground coal gasification: a brief review of current status. *Ind. Eng. Chem. Res.* **2009**, *48*, 7865–7875. [[CrossRef](#)]

4. Urych, B. Determination of kinetic parameters of coal pyrolysis to simulate the process of underground coal gasification (UCG). *J. Sustain. Min.* **2014**, *13*, 3–9. [[CrossRef](#)]
5. Prabu, V.; Jayanti, S. Simulation of cavity formation in underground coal gasification using bore hole combustion experiments. *Energy* **2011**, *36*, 5854–5864. [[CrossRef](#)]
6. Konstantinou, E.; Marsh, R. Experimental study on the impact of reactant gas pressure in the conversion of coal char to combustible gas products in the context of underground coal gasification. *Fuel* **2015**, *159*, 508–518. [[CrossRef](#)]
7. Hamanaka, A.; Su, F.; Itakura, K.; Takahashi, K.; Kodama, J.; Deguchi, G. Effect of injection flow rate on product gas quality in underground coal gasification (UCG) based on laboratory scale experiment: development of Co-Axial UCG system. *Energies* **2017**, *10*, 238. [[CrossRef](#)]
8. Ollero, P.; Serrera, A.; Arjona, R.; Alcantarilla, S. Diffusional effects in TGA gasification experiments for kinetic determination. *Fuel* **2002**, *81*, 1989–2000. [[CrossRef](#)]
9. Sadhukhan, A.K.; Gupta, P.; Saha, R.K. Modelling of combustion characteristics of high ash coal char particles at high pressure: shrinking reactive core model. *Fuel* **2010**, *89*, 162–169. [[CrossRef](#)]
10. Park, K.Y.; Edgar, T.F. Modeling of early cavity growth for underground coal gasification. *Ind. Eng. Chem. Res.* **1987**, *26*, 237–246. [[CrossRef](#)]
11. Perkins, G.; Sahajwalla, V. Modelling of heat and mass transport phenomena and chemical reaction in underground coal gasification. *Chem. Eng. Res. Des.* **2007**, *85*, 329–343. [[CrossRef](#)]
12. Su, F.; Nakanowataru, T.; Itakura, K.; Ohga, K.; Deguchi, G. Evaluation of structural changes in the coal specimen heating process and UCG model experiments for developing efficient UCG Systems. *Energies* **2013**, *6*, 2386–2406. [[CrossRef](#)]
13. Prabu, V.; Jayanti, S. Heat-affected zone analysis of high ash coals during ex-situ experimental simulation of underground coal gasification. *Fuel* **2014**, *123*, 167–174. [[CrossRef](#)]
14. Wang, Z.; Liang, J.; Shi, L.; Xi, J.; Li, S.; Cui, Y. Expansion of three reaction zones during underground coal gasification with free and percolation channels. *Fuel* **2017**, *190*, 435–443. [[CrossRef](#)]
15. Daggupati, S.; Mandapati, R.N.; Mahajani, S.M.; Ganesh, A.; Mathur, D.K.; Sharma, R.K.; Aghalayam, P. Laboratory studies on combustion cavity growth in lignite coal blocks in the context of underground coal gasification. *Energy* **2010**, *35*, 2374–2386. [[CrossRef](#)]
16. Cena, R.J.; Britten, J.A.; Thorsness, C.B. Excavation of the partial CRIP underground coal gasification test site. In Proceedings of the 13th Annual Underground Coal Gasification Symposium, Laramie, WY, USA, 24–30 August 1987.
17. Yang, L.H. Three-Dimensional non-linear numerical analysis on the oxygen concentration field in underground coal gasification. *Fuel Process. Technol.* **2004**, *85*, 1605–1622. [[CrossRef](#)]
18. Eftekhari, A.A.; Wolf, K.H.; Rogut, J.; Bruining, H. Mathematical modeling of alternating injection of oxygen and steam in underground coal gasification. *Int. J. Coal Geol.* **2015**, *150*, 154–165. [[CrossRef](#)]
19. Kuyper, R.A.; Meer, T.H.V.D.; Hoogendoorn, C.J. Turbulent natural convection flow due to combined buoyancy forces during underground coal gasification of thin seams. *Chem. Eng. Sci.* **1994**, *49*, 851–861. [[CrossRef](#)]
20. Elliott, M.A. *Chemistry of Coal Utilization*; John Wiley and Sons: New York, NY, USA, 1981; pp. 1835–1836.
21. Huang, J.; Bruining, J.; Wolf, K.-H.A.A. Modeling of gas flow and temperature fields in underground coal fires. *Fire Saf. J.* **2001**, *36*, 477–489. [[CrossRef](#)]
22. Barea, A.G.; Ollero, P.; Arjona, R. Reaction-diffusion model of TGA gasification experiments for estimating diffusional effects. *Fuel* **2005**, *84*, 1695–1704. [[CrossRef](#)]
23. Yan, J.; Ni, M.; Zhao, H.; Cen, K. Gas diffusion through the ash layer of coal particle during the combustion process. *Int. J. Thermophys.* **1994**, *15*, 341–344. [[CrossRef](#)]
24. Liu, J.G.; Yan, J.W.; Han, X.X.; Jiang, X.M. Study on the anisotropy of mass transfer for oxygen in the ash layer of shale char particles. *Energy Fuels* **2010**, *24*, 3488–3497. [[CrossRef](#)]
25. Hwang, M.; Song, E.; Song, J. One-dimensional modeling of an entrained coal gasification process using kinetic parameters. *Energies* **2016**, *9*, 99. [[CrossRef](#)]
26. Lin, X.; Liu, Q.; Liu, Z.; Guo, X.; Wang, R.; Shi, L. The role of ash layer in syngas combustion in underground coal gasification. *Fuel Process. Technol.* **2016**, *143*, 169–175. [[CrossRef](#)]
27. Bews, I.M.; Hayhurst, A.N.; Richardson, S.M.; Taylor, S.G. The order, Arrhenius parameters, and mechanism of the reaction between gaseous oxygen and solid carbon. *Combust. Flame* **2001**, *124*, 231–245. [[CrossRef](#)]

28. Khan, M.M.; Mmbaga, J.P.; Shirazi, A.S.; Trivedi, J.; Liu, Q.; Gupta, R. Modelling underground coal gasification—A review. *Energies* **2015**, *8*, 12603–12668. [[CrossRef](#)]
29. Yang, L.H.; Zhang, X.; Liu, S.Q.; Yu, L.; Zhang, W.L. Field test of large-scale hydrogen manufacturing from underground coal gasification (UCG). *Int. J. Hydrogen Energy* **2008**, *33*, 1275–1285. [[CrossRef](#)]
30. Su, J.L.; Perlmuter, D.D. Effect of Pore Structure on Char Oxidation Kinetics. *AIChE J.* **1985**, *31*, 973–981. [[CrossRef](#)]
31. Chen, C.; Kojima, T. Single char particle combustion at moderate temperature: effects of ash. *Fuel Process. Technol.* **1996**, *47*, 215–232. [[CrossRef](#)]
32. Sofirchos, S.V.; Amundson, N.R. Dynamic behavior of a porous char particle burning in an oxygen-containing environment. *AIChE J.* **1984**, *30*, 537–549. [[CrossRef](#)]
33. Wen, C.Y. Non-Catalytic Heterogeneous Solid-Fluid Reaction Models. *Ind. Eng. Chem.* **1968**, *60*, 34–54. [[CrossRef](#)]
34. Perkins, G. Mathematical Modelling of Underground Coal Gasification. Ph.D. Thesis, The University of New South Wales, Sydney, Australia, 2005.
35. Perkins, G.; Sahajwalla, V. A numerical study of the effects of operating conditions and coal properties on cavity growth in underground coal gasification. *Energy Fuels* **2006**, *20*, 596–608. [[CrossRef](#)]
36. Sadhukhan, A.K.; Gupta, P.; Saha, R.K. Analysis of the dynamics of coal char combustion with ignition and extinction phenomena: shrinking core model. *Int. J. Chem. Kinet.* **2008**, *40*, 569–582. [[CrossRef](#)]
37. Kelebopile, L.; Sun, R.; Wang, H.; Zhang, X.; Wu, S.H. Pore development and combustion behavior of gasified semi-char in a drop tube furnace. *Fuel Process. Technol.* **2013**, *111*, 42–54. [[CrossRef](#)]
38. Parlange, J.Y. Reviewed Work: Dynamics of Fluids in Porous Media by J. BEAR. *Am. Sci.* **1973**, *6*, 758–759.
39. Kingery, W.D. *Introduction to Ceramics*, 1st ed.; Wiley: New York, NY, USA, 1960; p. 380, ISBN 0471478601.
40. Hill, R.W.; Hill, C.B. *Summary Report on Large Block Experiments in Underground Coal Gasification, Tono Basin, Washington: Volume 1. Experimental Description and Data Analysis*; Report No. UCRL-53305; Lawrence Livermore National Laboratory, University of California: Berkeley, CA, USA, 9 July 1982.



© 2018 by the authors. Licensee MDPI, Basel, Switzerland. This article is an open access article distributed under the terms and conditions of the Creative Commons Attribution (CC BY) license (<http://creativecommons.org/licenses/by/4.0/>).

Article

Steam Gasification of Sawdust Biochar Influenced by Chemical Speciation of Alkali and Alkaline Earth Metallic Species

Dongdong Feng, Yijun Zhao *, Yu Zhang, Shaozeng Sun and Jianmin Gao

School of Energy Science and Engineering, Harbin Institute of Technology, Harbin 150001, China; 08031175@163.com (D.F.); 14B902024@hit.edu.cn (Y.Z.); sunsz@hit.edu.cn (S.S.); yagjm@hit.edu.cn (J.G.)

* Correspondence: zhaoyijun@hit.edu.cn; Tel.: +86-451-8641-3231; Fax: +86-451-8641-2528

Received: 8 December 2017; Accepted: 8 January 2018; Published: 15 January 2018

Abstract: The effect of chemical speciation ($H_2O/NH_4Ac/HCl$ -soluble and insoluble) of alkali and alkaline earth metallic species on the steam gasification of sawdust biochar was investigated in a lab-scale, fixed-bed reactor, with the method of chemical fractionation analysis. The changes in biochar structures and the evolution of biochar reactivity are discussed, with a focus on the contributions of the chemical speciation of alkali and alkaline earth metallic species (AAEMs) on the steam gasification of biochar. The results indicate that $H_2O/NH_4Ac/HCl$ -soluble AAEMs have a significant effect on biochar gasification rates. The release of K occurs mainly in the form of inorganic salts and hydrated ions, while that of Ca occurs mainly as organic ones. The sp^3 -rich or sp^2-sp^3 structures and different chemical-speciation AAEMs function together as the preferred active sites during steam gasification. H_2O/HCl -soluble AAEMs could promote the transformation of biochar surface functional groups, from ether/alkene C-O-C to carboxylate COO^- in biochar, while they may both be improved by NH_4Ac -soluble AAEMs. H_2O -soluble AAEMs play a crucial catalytic role in biochar reactivity. The effect of NH_4Ac -soluble AAEMs is mainly concentrated in the high-conversion stage (biochar conversion >30%), while that of HCl -soluble AAEMs is reflected in the whole activity-testing stage.

Keywords: biochar; steam; gasification; chemical speciation; AAEMs

1. Introduction

Compared to fossil fuels, biomass—which is a carbon neutral renewable energy, since the CO_2 from its utilization can be captured via photosynthesis—exhibits great prospects for limiting global gas pollution (NO_x , SO_2 and greenhouse gases) and the energy crisis [1]. Biomass gasification is considered a promising technology with relatively lower temperatures, low energy consumption and a high ability of CO_2 capture, attracting a lot of attention all over the world [2]. Usually, gasification can be divided into two steps, namely biomass devolatilization (first stage, relatively fast) and biochar gasification (second stage, relatively slow). According to previous studies [3–7], the gasification of pyrolysis biochar is the rate-limiting step for the overall gasification reaction, which is usually the focus of research on biomass gasification reactions. Besides, among the various gasifying agents (air, oxygen, CO_2 and steam) for biomass/biochar gasification [8,9], steam is preferred for increasing the heating value of syngas and producing a gaseous fuel with relatively higher H_2 for application in the fuel cells and hydrogen engines [10]. Thus, the steam gasification of pyrolysis biochar is urged to be investigated, especially for catalytic steam gasification [11], where the most important heterogeneous gasification reactions are the water gas reaction ($C + H_2O \rightarrow CO + H_2$), the Boudouard reaction ($C + CO_2 \rightarrow 2CO$) and the heterogeneous methanation ($C + 2H_2 \leftrightarrow CH_4$) [12].

In the current investigation, many researchers [13–18] found that alkali and alkaline earth metallic species (AAEMs) dispersed in biomass and/or biochar as different chemical speciations, play significant catalytic roles in biochar gasification reactivity, and that AAEMs volatilized as a gaseous phase would also take part in homogeneous reforming reactions [19]. The concentration and dispersion of AAEMs, according to the results obtained by Wu et al. [20], is a significant factor affecting the catalytic activity of AAEMs during biomass gasification, which varies constantly due to the carbon consumption and the release/migration of AAEMs [21,22]. Moreover, for various gasifying agents, the AAEMs show different catalytic abilities when chars react with various gasifying agents such as H_2O and CO_2 , because their catalysis mechanisms during biochar gasification may be different [19,23–25]. In addition, for the comparison of AAEM catalytic activities, Zhang et al. [26] studied the gasification reactivity of several biochar samples catalyzed by metals and reported that the gasification reactivity was enhanced with the alkali metals followed by alkaline earth metals. Furthermore, for the catalytic role of AAEMs on the microcosmic chemical bonds during gasification, the oxidation-reduction cycle [27–31] was postulated, in which O atoms/ions dissociated from the gasifying agents could transferred to the carbon active sites through catalytically-active AAEMs, where the breakage of C-C bonds would occur to realize the liberation of the C(O) structure.

In addition, as our previous study mentioned [32], the AAEMs in biomass/biochar usually exist in a variety of chemical speciations, such as inorganic salts/ion states, organic forms linked to biochar and/or crystal forms. Jordan et al. [33] investigated the speciation and distribution of AAEMs in raw biomass and major ash-forming elements during gasification to evaluate the volatilization of these elements into the syngas, although they did not mention the state of AAEMs in biochar and their effects on the gasification reactivity of biochar. Besides, the catalytic effects of AAEMs with different chemical speciations on biochar reactivity are obviously different [34]. Thus, it is easy to deduce that their influence on the characteristics of biochar gasification would be significant, although relevant studies are rarely reported. In order to characterize the chemical speciation of AAEMs in biomass/biochar, a sequential selective extraction procedure known as chemical fractionation analysis (CFA) was introduced and standardized [35,36]. This method was first developed by Benson and Holm [37] for coals and had been modified by Zevenhoven-Onderwater et al. [38] and Petterson et al. [39] for biomass fuels. Moreover, besides their direct catalytic effects on biochar gasification, the AAEMs could have a dynamic impact on the biochar structures, including the carbon skeleton, side chains and functional groups [21,22,40]. It has been confirmed that the changes in biochar structure catalyzed by AAEMs are an important aspect influencing biochar reactivity during gasification [41]. However, there are few reports on the effect of AAEMs with different speciations on the biochar structure during gasification, which would in turn affect the biochar gasification reactivity. Biochar gasification can be significantly altered via the catalytic alteration of the above reaction pathways by different speciations of AAEMs. Thus a good understanding of the effect of the chemical speciation of AAEMs during biochar steam gasification would lay a solid foundation for developing a gasification technology for biomass.

The objectives are to understand the steam gasification behavior of pyrolysis biochar with different speciations of AAEMs, the key inherent chemical speciation of AAEMs affecting biochar reactivity, and the most probable catalytic route of AAEMs on biochar structure and reactivity during steam gasification, all of which are essential to gasification process design and development.

2. Experimental

2.1. Origin Biochar Preparation

Manchurian walnut sawdust, obtained from Harbin, Heilongjiang Province, China, was used in the experiments. The sawdust samples were dried overnight at 105 °C, pulverized and sieved to obtain a fraction with particle sizes between 0.15 and 0.25 mm. The proximate and ultimate analyses for the sawdust samples are listed in Table 1.

Table 1. Proximate and ultimate analysis of the origin sawdust sample. (Note: diff. = by difference, ad. = air dry basis.)

Samples	Proximate Analysis				Ultimate Analysis				
	M _{ad.} (wt%)	A _{ad.} (wt%)	V _{ad.} (wt%)	FC _{ad.} (wt%)	C _{ad.} (wt%)	H _{ad.} (wt%)	O _{ad.(diff.)} (wt%)	N _{ad.} (wt%)	S _{t,ad.} (wt%)
Sawdust	9.49	0.96	77.13	12.42	43.72	5.31	40.39	0.12	0.01

As shown in Figure 1, the origin pyrolysis biochar samples were obtained in the entrained-flow reactor at 800 °C with nitrogen gas of 5.70 L/min. The details of the pyrolysis experimental system can be seen in our previous investigation [32]. The origin pyrolysis biochar was used for the following treatment and steam gasification.

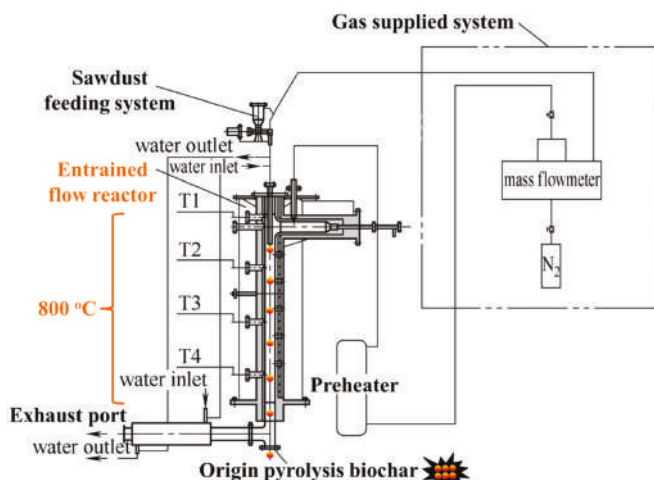


Figure 1. Schematic diagram of the entrained-flow reactor.

2.2. Sample Preparation

In order to investigate the effects of the solid-phase chemical speciation of AAEMs on the steam gasification of sawdust biochar, the CFA process was carried out. There are four kinds of chemical speciation of AAEMs in biochar [42]: One is a separate form of AAEM ions, which is soluble in water, also soluble in a solution of ammonium acetate (NH_4Ac) and hydrochloric acid (HCl); The second is organic matter, which is in the form of carboxylate and/or coordination connected with the oxygen functional groups on the biochar surface, and is insoluble in water, but soluble in a solution of NH_4Ac and HCl; The third is attached to the clay surface in an amorphous form, which is insoluble in water and NH_4Ac solution, but soluble in hydrochloric acid; The fourth is in the aluminosilicate form, which is insoluble in water, NH_4Ac and HCl. In the CFA process, as shown in Figure 2, the pyrolysis biochar is leached step-wise in increasingly aggressive solvents: deionized water, 1.0 mol/L ammonium acetate solution, and 1.0 mol/L hydrochloric acid solution with a mass ratio (1:30) of solid to liquid, in order to classify the AAEMs with respect to solubility.

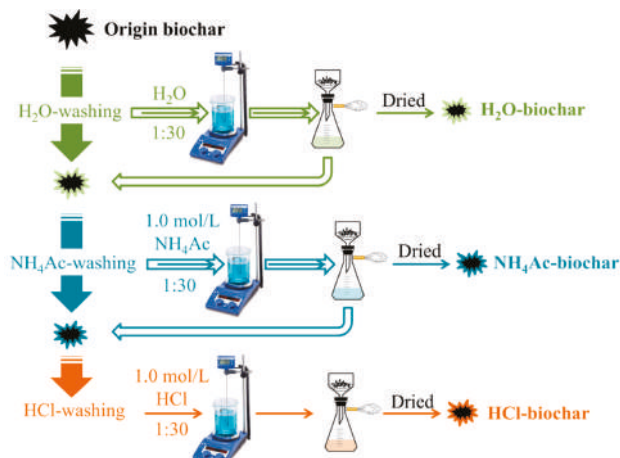


Figure 2. Schematic of the chemical fractionation analysis of biochar.

2.3. Steam Gasification of Biochar

As shown in Figure 3, the steam gasification of sawdust biochar was carried out. A total of 0.5 g of biochar from the CFA, namely the origin-biochar/H₂O-biochar/NH₄Ac-biochar/HCl-biochar samples, were pre-loaded into the top fixed-bed stage of the reactor. After being purged for 5 min by argon (Ar), the system was heated up to 800 °C with argon gas of 1.53 L/min at a heating rate of 20 °C/min. As the temperature stabilized at 800 °C, the atmosphere was switched to 15 vol% steam for the gasification reaction, which was achieved by feeding deionized water of 0.214 L/min through a high-performance liquid chromatography (HPLC) pump into the heated zone of reactor where the water was evaporated into steam directly. The steam gasification reaction of biochar at 800 °C lasted for 10 min. After that, reactions were terminated by switching the atmosphere to argon and removing the reactor from the furnace. Argon was passed through the reactor until the reactor had completely cooled to room temperature to avoid oxidation. The steam gasification biochar was collected and stored at 4 °C for further analysis.

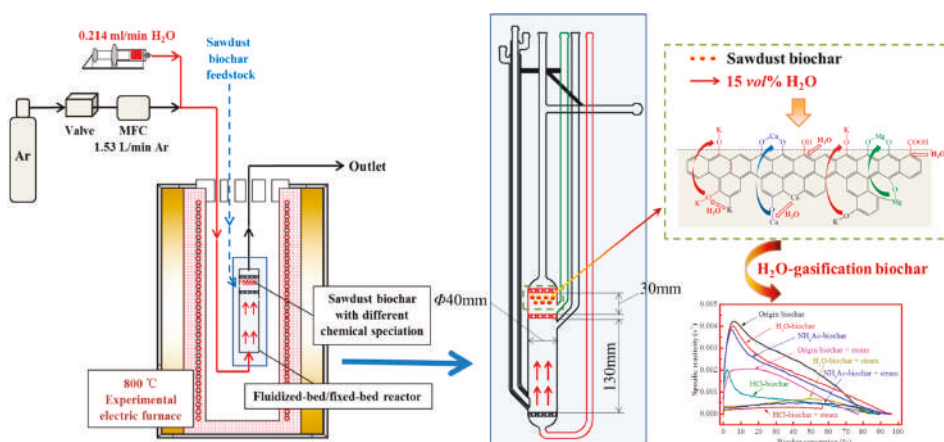


Figure 3. A schematic diagram of the steam gasification experimental process.

2.4. Analysis of Biochar

2.4.1. Gasification Rate

The gasification rate of biochar was measured three times by weighing the biochar-containing reactor before and after the reactions. Each experiment was repeated at least three times, and the test results are well-reproducible.

2.4.2. AAEM Analysis

The chemical speciation of AAEMs in biochar was quantified by inductively-coupled plasma-atomic emission spectroscopy (ICP-AES). The biochar sample (0.1 g) was digested in a 1:3:8 (*v/v/v*) mixture of 40% HF, 30% H₂O₂, and 65% HNO₃ at 200 °C for 60 min.

The percentage of AAEMs released during the steam gasification of biochar can be obtained by Equation (1) as follows:

$$X_{\text{Release}} \% = \left[1 - X_{\text{Steam gasification biochar}} \times \frac{(1 - \text{Gasification rate})}{X_{\text{Pyrolysis biochar}}} \right] \times 100\% \quad (1)$$

where X is the AAEM species (Na, K, Mg and Ca); X_{Release} is the percentage of AAEM release during the steam gasification of biochar; X_{Pyrolysis biochar} is the X in origin/H₂O-/NH₄Ac-/HCl-pyrolysis biochar; and X_{Steam gasification biochar} is the X in origin/H₂O-/NH₄Ac-/HCl-steam gasification biochar.

2.4.3. Raman Analysis

The aromatic structure analysis of biochar was carried out in a Raman spectrometer (inVia, Renishaw, New Mills, UK), with an excitation laser at 633 nm. The sample was mixed and ground with spectroscopic-grade Potassium bromide (KBr) in the ratio of 0.25 wt% biochar. The Raman spectra at 800~1800 cm⁻¹ were recorded.

2.4.4. FTIR Analysis

The surface functional groups of the biochar were analyzed by Fourier Transform infrared spectroscopy (Nicolet 5700, FTIR, Thermo Fisher Scientific, Waltham, MA, USA). Biochar was mixed and ground with spectroscopic-grade KBr in a ratio of 1:200. All FTIR spectra were obtained at a resolution of 4 cm⁻¹ in the range of 400~4000 cm⁻¹.

2.4.5. Biochar Reactivity Analysis

The specific reactivity of the biochar was determined in air at 370 °C with a thermogravimetric analyzer (TGA: Mettler Toledo, Switzerland). Nearly 4 mg of biochar sample was placed in a Pt crucible and heated in Ar in the TGA to 105 °C to remove moisture from the sample. The stabilized weight of the biochar at 105 °C was taken as the weight of dry biochar. The temperature was then increased to 370 °C at 50 °C/min. After 2 min, the atmosphere was switched into air starting the biochar reactivity test. Once the mass was stable, the sample was heated at 50 °C/min to 600 °C, where it was held for another 30 min to ensure complete combustion. The calculation of biochar-specific reactivity from the differential thermal gravity (DTG) data (dW/dt) can be seen in our previous study [22].

3. Results and Discussion

3.1. Steam Gasification Rate

As shown in Figure 4, it can be seen that the steam gasification rate of pyrolysis biochar after the fraction of H₂O, NH₄Ac and HCl decreased sequentially, from 79.00% of origin biochar to 66.54% of HCl-biochar. Our previous investigation [43] indicated that during the chemical fractionation analysis, the changes in oxygen-containing functional groups and aromatic ring structures could be ignored.

It can be speculated that the difference in the gasification rate is mainly caused by the different chemical speciation of the AAEM species. The difference in gasification rate was used to describe the effect of different-speciation AAEMs on the steam gasification reaction of biochar, as shown in Figure 4. The decrease of 5.81% in the steam gasification rate from origin biochar to H₂O-biochar sample is entirely due to the removal of H₂O-soluble AAEMs, and this part mainly deals with K⁺ and Na⁺ ion salts in biochar [32]. After that, the decline of the biochar steam gasification rate is gradually reduced, to 4.20% and 2.45% due to the removal of the NH₄Ac-soluble and HCl-soluble AAEMs, respectively. Finally, the HCl-biochar sample, with only some insoluble aluminosilicate AAEMs, still retains a relative high gasification rate (as 66.54%), mainly due to the relatively active carbon structures and the insoluble AAEMs to maintain the basic reactions between carbon and steam.

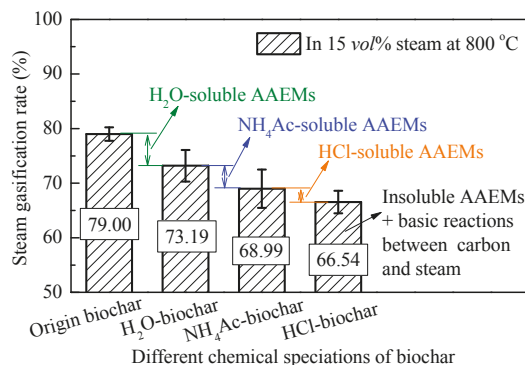


Figure 4. Steam gasification rate of biochar from chemical analysis fractionation.

3.2. AAEM Analysis of Steam-Gasified Biochar

Figure 5 shows the AAEM content of the origin pyrolysis biochar and their chemical speciation. In the original pyrolysis biochar at 800 °C, the AAEMs exhibited a rich distribution of K (0.70 wt%) and Ca (2.08 wt%), and less Na (0.05 wt%) and Mg (0.17%). Besides, the main existing form of K in pyrolysis biochar is a water-soluble form, while that of Ca is a NH₄Ac-soluble and insoluble form. As Mitsuoka et al. [44] suggested, the most significant catalysts for biochar gasification in woody biomass are calcium (Ca) and potassium (K), namely the two main kinds of AAEM.

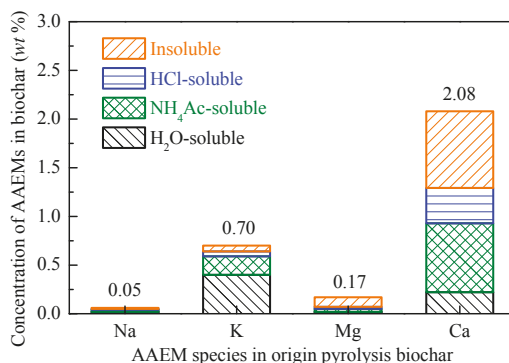


Figure 5. Concentration of AAEMs in origin pyrolysis biochar.

As mentioned above, the role of AAEMs is not only in the solid-phase heterogeneous transformation of biochar, their migration and precipitation characteristics also play a significant role in homogeneous steam reform. It is often agreed that the volatilization of AAEMs occurs during gasification [45,46]. According to Marschner et al. [47], the behavior of Na and K were different from that of Mg and Ca, at least partly due to the different chemical status of K/Na and Mg/Ca in the biomass/biochar. It is also related to the different occurrence of K/Na and Mg/Ca. For the H₂O-soluble AAEMs, the specific precipitation amount of AAEMs cannot be calculated directly by the difference in this paper. However, the total amount of AAEMs in the fractional speciation can be calculated to characterize the precipitation of AAEMs in the absence of H₂O-soluble ones. This effectively avoids the influence of AAEM transformation with different chemical speciations during steam gasification [33].

The release of K and Ca during the steam gasification of biochar can be seen in Figure 6. K_{Release} and Ca_{Release} did not change significantly after H₂O washing, and it can be seen that the H₂O-washing removal amount and the amount of volatilization during the gasification of K and Ca were very close, indicating that the precipitation rate of H₂O-soluble K and Ca was close to 100%. After the fraction of NH₄Ac and HCl solution, the K_{Release} was significantly reduced and Ca_{Release} was still relatively high, indicating that during gasification the release of K occurs mainly in the form of inorganic salts and hydrated ions, while volatilization of the organic compounds is the main release mechanism for Ca.

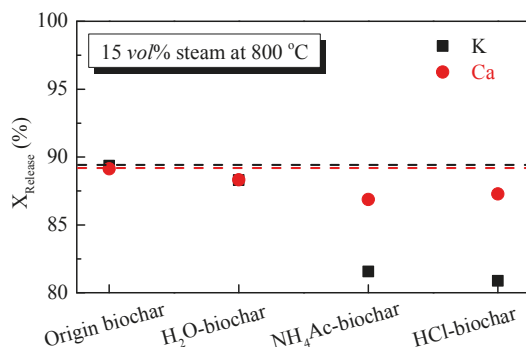


Figure 6. Release of K and Ca species during the steam gasification of biochar.

3.3. Raman Analysis of Steam-Gasified Biochar

As shown in Figure 7, the total Raman area between 800 and 1800 cm⁻¹ of the pyrolysis biochar samples from the CFA process changed little, with a total intensity of 1.62~1.72 × 10⁶. The total Raman peak areas could reflect electron-rich structures such as O/N-containing functional groups in biochar [48–51]. During the steam gasification of biochar, it can be seen that the total Raman areas of gasified biochar decreased from 3.58 × 10⁶ to 2.23 × 10⁶ with the fractionation of H₂O, NH₄Ac and HCl in turn. According to Guo et al. [41], both the thermal decomposition of biochar, and biochar gasification reactions leading to the loss of oxygen and hydrogen from biochar, could result in changes to biochar structures during gasification with a decrease of total Raman intensity. Also, another possible factor may be the preferential consumption of smaller rings due to their gasification and/or conversion to larger ones. Briefly, during steam gasification, the decrease in Raman intensity with the CFA process reflected the limited increase in O-containing functional groups and, more importantly, the condensation/growth of aromatic ring systems. For the HCl-biochar, with few active AAEMs (in the absence of catalysts), the O-containing functional groups formed in the biochar during steam gasification were closely associated with the aromatic structure and thus tended to loosen the aromatic structure. The non-catalyzed gasification was slow and took place on some specific (especially sp³-rich or sp²-sp³ mixture) sites distributed throughout the biochar [52]. While the gasification of biochar

took place everywhere but slowly in the HCl-biochar in order to consume the small ring systems selectively, the reaction in the AAEM-containing biochar was more focused on/around the AAEM sites and took place much more rapidly [53]. As shown in Figure 7, comparing the results of steam-gasified origin biochar and H₂O-biochar samples, there is a significant decrease of 0.65×10^6 , showing that the increase of surface O-containing functional groups during gasification was limited after the fraction of H₂O, mainly due to the H₂O-soluble AAEMs, namely the K and Na species. For the total Raman area between gasified H₂O-biochar and NH₄Ac-biochar, the decrease was only 0.22×10^6 , showing that the effects of NH₄Ac-soluble AAEMs were limited. Although the AAEM content is relatively large, their low ability of migration led to a limited catalytic role. After that, the effect of HCl-soluble AAEMs, namely the organic Ca species, led to another obvious decrease of 0.48×10^6 in the total Raman area, showing its significant catalytic role on the formation of surface O-containing functional groups.

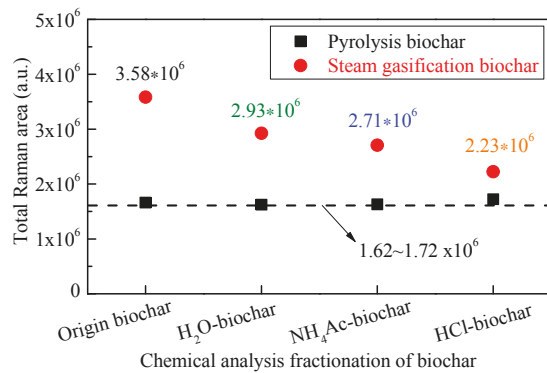


Figure 7. Total Raman area of biochar during steam gasification.

As shown in Figure 8, the Raman spectrum of the gasified biochar was divided into 10 small peaks, representing the typical structures of biochar. Other detailed information on this part can be seen in our previous studies [19,32], where the $I_{(Dr+VI+Vr)}/I_D$ represents the ratio of the smaller aromatic rings in the biochar to the larger aromatic ring structures, and I_S/I_{Total} refers to the content of sp³-rich structures as alkyl–aryl C–C structures and methyl carbon dangling to an aromatic ring, including some surface O-containing structures in biochar, with little long chain aliphatics and hydroaromatic structures.

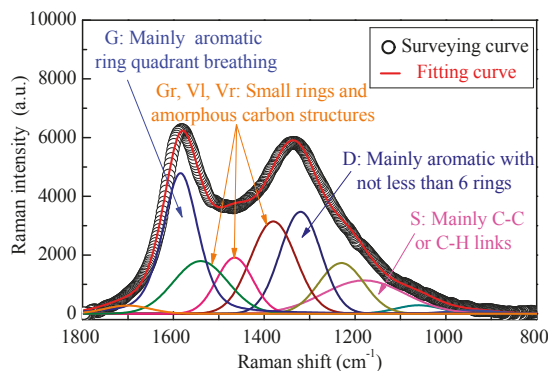


Figure 8. Curve fitting of the Raman spectrum of biochar.

As shown in Table 2, the influence of chemical fraction analysis on biochar aromatic ring structures could be ignored, while both NH₄Ac and HCl can change the cross-linking structures of biochar [43]. During steam gasification, according to Chen et al. [54], the sites on either the zigzag face or the armchair face of large aromatic layers of biochar are believed to be active for gasification reactions and they are affected by AAEMs. In addition, according to Li et al. [52], the smaller aromatic ring systems were preferentially consumed during gasification. During the steam gasification of biochar, with the presence of H₂O-soluble AAEMs, the $I_{(Dr+Vl+Vr)}/I_D$ decreased significantly from 1.84 to 0.64, indicating the transformation of the smaller aromatic ring systems into larger ones to a great extent. The conversion of biochar during steam gasification is believed to be due to the rapid penetration of H radicals from the biochar surface deep into the biochar matrix [55]. Also the AAEMs, as the active sites for the gasification reaction, could promote the process of this transformation to a large extent, especially for the alkali metal species (K and Na). With the fraction of NH₄Ac and HCl solutions, the decrease of $I_{(Dr+Vl+Vr)}/I_D$ became more and more weak, showing the smaller catalytic effect of NH₄Ac/HCl-soluble AAEMs on the aromatic ring structures in biochar. As shown in Table 2, due to the steam gasification of HCl-biochar, the I_S/I_{Total} decreased from 0.18 to 0.10. These data indicate that the sp³-rich or sp²-sp³ mixed structures represented by the S band are the preferential sites of reaction with steam with few active AAEMs catalysts, with only insoluble ones left. The results are consistent with the opinion of Li et al. [52] for coal char. In addition, the effect of the NH₄Ac/HCl-soluble AAEMs is limited as the active site during gasification, and consequently the corresponding I_S/I_{Total} decreases, since the sp³-rich or sp²-sp³ structures are consumed. However, few changes in the relative intensity of S band were observed for the corresponding biochars from the origin biochar during gasification (from 0.38 to 0.37). This indicated that with the H₂O-soluble AAEMs, the S band structures were no longer the preferred sites for reactions with steam. The AAEM catalytic species appeared to be preferentially accommodated on carbons of an aromatic nature.

Table 2. Ratios of band peak areas in pyrolysis and steam gasification biochar from Chemical fractionation analysis (CFA.).

Conditions	Band Ratio	Origin Biochar	H ₂ O-Biochar	NH ₄ Ac-Biochar	HCl-Biochar
Pyrolysis	$I_{(Vl+Dr+Vr)}/I_D$	1.84	1.97	2.06	2.19
	I_S/I_{Total}	0.38	0.34	0.22	0.18
Gasification	$I_{(Vl+Dr+Vr)}/I_D$	0.64	1.51	1.91	2.02
	I_S/I_{Total}	0.37	0.28	0.17	0.10

3.4. FTIR Analysis of Steam-Gasified Biochar

The CFA process has less destructive effects on the surface carbon–oxygen functional groups of pyrolysis biochar, which was already present in our previous study [43]. With the result of the total Raman area related with the surface functional groups, the additional O-containing functional groups were not present in the pyrolysis biochar before steam gasification. To gain evidence for the formation of additional O-containing functional groups during gasification, the FTIR spectra of the biochar samples were recorded, as shown in Figure 9. According to Černý et al. [56], the FTIR spectra of 4000~400 cm⁻¹ are divided into 3600~3000 cm⁻¹, 3000~2800 cm⁻¹, 1800~1000 cm⁻¹ and 900~700 cm⁻¹, which represent the surface hydroxyl group, aliphatic hydrocarbons, oxygen-containing functional groups, and aromatic hydrocarbons, respectively. As shown in Figure 9, for the steam-gasified biochar with different chemical fractions, the main difference appears in the oxygen-containing functional groups. In order to describe in detail the changes in the various oxygen-containing functional groups, the FTIR curve was fitted into the aromatic C=C structure at 1480 cm⁻¹, the carboxylate COO⁻ structure at 1400 cm⁻¹ and the aromatic ether/alkene C-O-C at 1243 and 1080 cm⁻¹ [57,58].

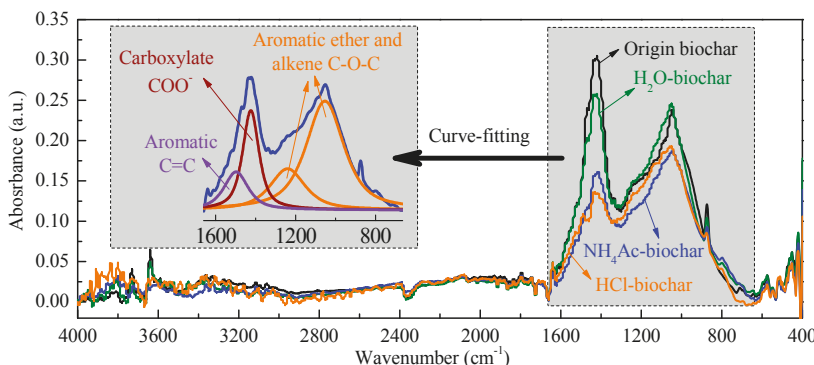


Figure 9. FTIR analysis of steam-gasified biochar with different chemical fractions.

The result of the curve-fitting FTIR analysis on O-containing functional groups can be seen in Table 3.

Table 3. FTIR analysis of O-containing functional groups on steam-gasified biochar surface.

Steam-Gasified Biochar	Surface Main Functional Groups		
	Aromatic C=C	Carboxylate COO ⁻	Aromatic Ether/Alkene C-O-C
Gasified origin biochar	10.63	26.46	62.90
Gasified H ₂ O-biochar	9.94	21.82	68.23
Gasified NH ₄ Ac-biochar	10.27	14.10	75.62
Gasified HCl-biochar	11.39	9.98	78.62

The FTIR curve between the two successive steps can be used to indirectly reflect the specific catalytic effect of different AAEMs on the formation of oxygen-containing functional groups during steam gasification. Walker and co-workers [59] have also pointed out in a review that a significant amount of O complex builds up on the surface of active sites, which is referred to the AAEMs. The content of aromatic C=C on the steam gasified biochar from different CFA processes fluctuated in the range of 9.94~11.39%, with little change. In addition, the main changes existed between the carboxylate COO⁻ and aromatic ether/alkene C-O-C. In the absence of active AAEMs, the HCl-biochar exhibits the lowest surface functional group content, which is consistent with the Raman analysis results. The HCl-soluble AAEMs (mainly for the organic Ca compounds mentioned above), are mainly used to promote the formation of carboxylate COO⁻ (from 9.98% to 14.10%), and to limit the increase of aromatic ether/alkene C-O-C (from 78.62% to 75.62%), which can be considered to be the transformation from ether/alkene C-O-C to carboxylate COO⁻ catalyzed by HCl-soluble AAEMs. However, for the NH₄Ac-soluble AAEMs, as shown in Figure 9, the relative contents of carboxylate COO⁻ and aromatic ether/alkene C-O-C were both significantly improved, indicating that the AAEMs played a positive role in promoting the formation of surface oxygen-containing functional groups. Compared to the FTIR results for the origin biochar and the H₂O-biochar after gasification, the catalytic effect of the H₂O-soluble AAEMs in biochar was investigated. A similar result can be seen in that during the steam gasification, the H₂O-soluble AAEMs promote the increase of the total amount of oxygen-containing functional groups, and the catalytic effect on the increase of carboxylate COO⁻ is the most significant.

3.5. Biochar Reactivity in Air

The specific reactivity of biochar in combustion as a function of biochar conversion can be seen in Figure 10. As usual, the biochar reactivity is mainly controlled by two factors: the biochar structure [60]

and AAEM species in biochar [3]. The chemical fractionation process has little effect on the pyrolysis biochar structure [43], thus the AAEMs in the biochar are considered to be the main controlling factor affecting the pyrolysis biochar activity in this experiment. Given the high quantities of AAEMs and their possible catalytic activities, the catalytic activity of AAEMs may be the most likely factor causing the difference in reactivity, because reactions under a steam atmosphere make a difference in the concentration and dispersion of AAEMs in the resulting chars [40]. During steam gasification, the AAEMs only increase the concentration of the active complexes on carbon rather than changing the reaction pathway [61–65]. Figure 10 shows the typical specific reactivity of the pyrolysis biochar samples from the CFA process. After the chemical fractionation, the content of AAEMs decreased gradually, resulting in a decrease of the total reaction activity of the pyrolysis biochar. The specific reactivity showed broad maxima at about 5.8%, 5.2%, 5.0% and 2.0% char conversions for the pyrolysis origin biochar, H₂O-biochar, NH₄Ac-biochar and HCl-biochar, respectively. The maximum reactivity tended to shift towards lower conversion levels with the CFA steps. The main reason for the initial increase in the biochar reactivity (Figure 10) at small biochar conversion levels was the accumulation of AAEMs on the biochar surface with the removal of carbonaceous matter. During the air gasification of biochar, the high mobility of AAEMs allows them to migrate onto the biochar surface to form catalytically-active species such as –O-AAEM and/or AAEM clusters [66]. At high biochar conversion levels, where the biochar structure is more inert and highly condensed, the catalytic activity of AAEMs is reduced compared to its activity at low biochar conversion levels. In other words, at the beginning, the increase of AAEMs on the biochar surface are the main factor influencing the biochar reactivity. At a later stage, changes in the biochar structure become significant. The preferential removal of smaller aromatic ring systems and the persistence of crosslinking structures mean that the large aromatic ring systems are increasingly concentrated with little flexibility [52].

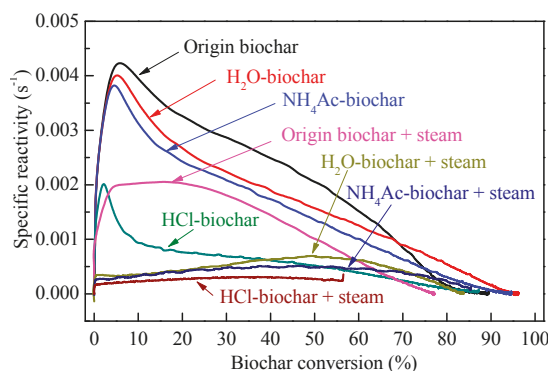


Figure 10. Specific reactivity of biochar samples as a function of biochar conversion.

For the steam-gasified biochar samples, the catalytic activity of AAEMs is a result of the interaction between AAEMs and biochar/carbon structures. As in the initial stage of the biochar reactivity test, unlike the pyrolytic one, there were significant differences in the biochar structure (i.e., O-containing functional groups and aromatic structures) by CFA in the steam gasification process. Furthermore, the AAEM-containing species in the biochar during the steam gasification improved the O-containing functional groups that would be consumed quickly during the reactivity measurement, contributing to the increase in reactivity [67], while the AAEMs would decrease the relative content of small aromatic ring structures in the biochar during steam gasification leading to the decrease in reactivity. Thus, the final decision of the steam-gasified biochar depends on the synergetic effects of the biochar structure and AAEMs [22]. According to Li et al. [68], the AAEMs would not be volatilized during the oxidation of biochar with air in the TGA at 370 °C during the measurement of biochar reactivity. However, during

gasification, it can be seen from Section 3.4 that the AAEMs could be significantly precipitated, especially for the H₂O-soluble AAEMs (nearly 100% volatilization). As shown in Figure 10, there is a significant decrease of biochar reactivity between the “origin biochar + steam” and the other three samples. For the biochar gasification in 15 vol% steam at 800 °C, the water-soluble AAEMs play a crucial role in the catalytic activity of gasification biochar. Despite its nearly complete volatilization, the water-soluble AAEMs have a significant effect on the biochar structure, which is a key factor in determining the highest reactivity of the biochar. The difference between “H₂O-biochar + steam” and “NH₄Ac-biochar + steam” is mainly concentrated in the higher carbon conversion stage (biochar conversion >30%), which is mainly due to the biochar structure determining the reaction [66]. The effect of HCl-soluble AAEMs on the biochar reactivity functions from start to finish. For “HCl-biochar + steam”, the reactivity is the lowest, mainly due to the least amount of catalytically active elements (AAEMs) and the less active structure formation in the biochar.

4. Conclusions

- (1) The AAEMs in different chemical speciations, such as the H₂O/NH₄Ac/HCl-soluble ones, have significant effects on the steam gasification rate of sawdust biochar. During steam gasification, the release of K occurs mainly in the form of inorganic salts and hydrated ions, while the release of Ca is mainly for the organic ones.
- (2) During steam gasification, the limited increase of O-containing functional groups and, more importantly, the condensation/growth of aromatic ring systems existed for the AAEMs with different chemical speciations. Without the active AAEMs (such as HCl-biochar), the sp³-rich or sp²-sp³ structures are the preferred sites for steam gasification. With NH₄Ac/HCl-soluble AAEMs, the preferred sites with sp³-rich or sp²-sp³ structures are gradually shared by AAEMs, until the presence of H₂O-soluble AAEMs completely replaces them as the gasification sites.
- (3) H₂O/HCl-soluble AAEMs promote the transformation from ether/alkene C-O-C to carboxylate COO⁻ while promoting the increase of total surface oxygen functional groups. The relative contents of carboxylate COO⁻ and aromatic ether/alkene C-O-C were significantly improved by the NH₄Ac-soluble AAEMs.
- (4) The H₂O-soluble AAEMs play a crucial role in the catalytic activity of gasification biochar and is a key factor in determining its highest reactivity. The effect of NH₄Ac-soluble AAEMs on gasification biochar activity is mainly concentrated in the high carbon conversion stage (biochar conversion >30%), and the effect of HCl-soluble AAEMs is reflected in the whole activity-testing stage.

Acknowledgments: The Collaborative Innovation Center of Clean Coal Power Plant with Poly-Generation, the national key R&D program of China (2016YFE0102500) and the National Natural Science Foundation innovation research group Heat Transfer and Flow Control (51421063) are gratefully acknowledged.

Author Contributions: D.F., Y.Z. and S.S. conceived and designed the experiments; D.F. and Y.Z. performed the experiments; D.F., J.G. and Y.Z. analyzed the data; J.G. and Y.Z. contributed reagents/materials/analysis tools; D.F. wrote the paper.

Conflicts of Interest: The authors declare no conflict of interest.

Nomenclature

AAEMs	Alkali and alkaline earth metallic species
X	AAEMs (Na, K, Mg and Ca)
X _{Release}	X(AAEMs) release during gasification
X _{Pyrolysis biochar}	X(AAEMs) in pyrolysis biochar
X _{Steam gasification biochar}	X(AAEMs) in steam gasification biochar
CFA	Chemical fractionation analysis
NH ₄ Ac	Ammonium acetate
H ₂ O-soluble	Soluble in water
NH ₄ Ac-soluble	Soluble in NH ₄ Ac solution

HCl-soluble	Soluble in HCl solution
Insoluble	Insoluble in water/NH ₄ Ac/HCl
H ₂ O	Deionized water
HCl	Hydrochloric acid
Origin-biochar	Origin pyrolysis biochar
H ₂ O-biochar	H ₂ O-washed biochar
NH ₄ Ac-biochar	NH ₄ Ac-washed biochar
HCl-biochar	HCl-washed biochar

References

1. Damartzis, T.; Zabaniotou, A. Thermochemical conversion of biomass to second generation biofuels through integrated process design—A review. *Renew. Sustain. Energy Rev.* **2011**, *15*, 366–378. [[CrossRef](#)]
2. Parthasarathy, P.; Narayanan, K.S. Hydrogen production from steam gasification of biomass: Influence of process parameters on hydrogen yield—A review. *Renew. Energy* **2014**, *66*, 570–579. [[CrossRef](#)]
3. Li, C.-Z. Importance of volatile-char interactions during the pyrolysis and gasification of low-rank fuels—A review. *Fuel* **2013**, *112*, 609–623. [[CrossRef](#)]
4. Nowicki, L.; Markowski, M. Gasification of pyrolysis chars from sewage sludge. *Fuel* **2015**, *143*, 476–483. [[CrossRef](#)]
5. Qi, X.; Guo, X.; Xue, L.; Zheng, C. Effect of iron on Shenfu coal char structure and its influence on gasification reactivity. *J. Anal. Appl. Pyrolysis* **2014**, *110*, 401–407. [[CrossRef](#)]
6. Duman, G.; Uddin, M.A.; Yanik, J. The effect of char properties on gasification reactivity. *Fuel Proc. Technol.* **2014**, *118*, 75–81. [[CrossRef](#)]
7. Liu, L.; Cao, Y.; Liu, Q. Kinetics studies and structure characteristics of coal char under pressurized CO₂ gasification conditions. *Fuel* **2015**, *146*, 103–110. [[CrossRef](#)]
8. Shen, Y.; Zhao, P.; Shao, Q.; Ma, D.; Takahashi, F.; Yoshikawa, K. In-situ catalytic conversion of tar using rice husk char-supported nickel-iron catalysts for biomass pyrolysis/gasification. *Appl. Catal. B Environ.* **2014**, *152–153*, 140–151. [[CrossRef](#)]
9. Kirtania, K.; Joshua, J.; Kassim, M.A.; Bhattacharya, S. Comparison of CO₂ and steam gasification reactivity of algal and woody biomass chars. *Fuel Proc. Technol.* **2014**, *117*, 44–52. [[CrossRef](#)]
10. Luo, S.; Xiao, B.; Hu, Z.; Liu, S.; Guo, X.; He, M. Hydrogen-rich gas from catalytic steam gasification of biomass in a fixed bed reactor: Influence of temperature and steam on gasification performance. *Int. J. Hydrogen Energy* **2009**, *34*, 2191–2194. [[CrossRef](#)]
11. Li, C.-Z. Special issue—Gasification: A route to clean energy. *Proc. Saf. Environ. Prot.* **2006**, *84*, 407–408. [[CrossRef](#)]
12. Nanou, P.; Gutiérrez Murillo, H.E.; van Swaaij, W.P.M.; van Rossum, G.; Kersten, S.R.A. Intrinsic reactivity of biomass-derived char under steam gasification conditions—potential of wood ash as catalyst. *Chem. Eng. J.* **2013**, *217*, 289–299. [[CrossRef](#)]
13. Kajita, M.; Kimura, T.; Norinaga, K.; Li, C.-Z.; Hayashi, J.-I. Catalytic and noncatalytic mechanisms in steam gasification of char from the pyrolysis of biomass. *Energy Fuels* **2009**, *24*, 108–116. [[CrossRef](#)]
14. Eom, I.-Y.; Kim, J.-Y.; Kim, T.-S.; Lee, S.-M.; Choi, D.; Choi, I.-G.; Choi, J.W. Effect of essential inorganic metals on primary thermal degradation of lignocellulosic biomass. *Bioresour. Technol.* **2012**, *104*, 687–694. [[CrossRef](#)] [[PubMed](#)]
15. Lahijani, P.; Zainal, Z.A.; Mohamed, A.R.; Mohammadi, M. CO₂ gasification reactivity of biomass char: Catalytic influence of alkali, alkaline earth and transition metal salts. *Bioresour. Technol.* **2013**, *144*, 288–295. [[CrossRef](#)] [[PubMed](#)]
16. Yu, M.M.; Masnadi, M.S.; Grace, J.R.; Bi, X.T.; Lim, C.J.; Li, Y. Co-gasification of biosolids with biomass: Thermogravimetric analysis and pilot scale study in a bubbling fluidized bed reactor. *Bioresour. Technol.* **2015**, *175*, 51–58. [[CrossRef](#)] [[PubMed](#)]
17. Zolin, A.; Jensen, A.; Jensen, P.A.; Frandsen, F.; Dam-Johansen, K. The influence of inorganic materials on the thermal deactivation of fuel chars. *Energy Fuels* **2001**, *15*, 1110–1122. [[CrossRef](#)]

18. Long, J.; Song, H.; Jun, X.; Sheng, S.; Lun-shi, S.; Kai, X.; Yao, Y. Release characteristics of alkali and alkaline earth metallic species during biomass pyrolysis and steam gasification process. *Bioresour. Technol.* **2012**, *116*, 278–284. [[CrossRef](#)] [[PubMed](#)]
19. Feng, D.; Zhao, Y.; Zhang, Y.; Sun, S. Effects of H₂O and CO₂ on the homogeneous conversion and heterogeneous reforming of biomass tar over biochar. *Int. J. Hydrogen Energy* **2017**, *42*, 13070–13084. [[CrossRef](#)]
20. Wu, H.; Quyn, D.M.; Li, C.-Z. Volatilisation and catalytic effects of alkali and alkaline earth metallic species during the pyrolysis and gasification of Victorian brown coal. Part III. The importance of the interactions between volatiles and char at high temperature. *Fuel* **2002**, *81*, 1033–1039. [[CrossRef](#)]
21. Feng, D.; Zhao, Y.; Zhang, Y.; Zhang, Z.; Sun, S. Roles and fates of K and Ca species on biochar structure during in-situ tar H₂O reforming over nascent biochar. *Int. J. Hydrogen Energy* **2017**, *42*, 21686–21696. [[CrossRef](#)]
22. Feng, D.; Zhao, Y.; Zhang, Y.; Zhang, Z.; Zhang, L.; Gao, J.; Sun, S. Synergetic effects of biochar structure and AAEM species on reactivity of H₂O-activated biochar from cyclone air gasification. *Int. J. Hydrogen Energy* **2017**, *42*, 16045–16053. [[CrossRef](#)]
23. Walker, P.L.; Matsumoto, S.; Hanzawa, T.; Muira, T.; Ismail, I.M. Catalysis of gasification of coal-derived cokes and chars. *Fuel* **1983**, *62*, 140–149. [[CrossRef](#)]
24. De Lecea, C.S.-M.; Almela-Alarcón, M.; Linares-Solano, A. Calcium-catalysed carbon gasification in CO₂ and steam. *Fuel* **1990**, *69*, 21–27. [[CrossRef](#)]
25. Feng, D.; Zhao, Y.; Zhang, Y.; Sun, S.; Meng, S.; Guo, Y.; Huang, Y. Effects of K and Ca on reforming of model tar compounds with pyrolysis biochar under H₂O or CO₂. *Chem. Eng. J.* **2016**, *306*, 422–432. [[CrossRef](#)]
26. Zhang, Y.; Ashizawa, M.; Kajitani, S.; Miura, K. Proposal of a semi-empirical kinetic model to reconcile with gasification reactivity profiles of biomass chars. *Fuel* **2008**, *87*, 475–481. [[CrossRef](#)]
27. Holstein, W.; Boudart, M. Uncatalyzed and platinum-catalyzed gasification of carbon by water and carbon dioxide. *J. Catal.* **1982**, *75*, 337–353. [[CrossRef](#)]
28. Radovic, L.R.; Walker, P.L.; Jenkins, R.G. Importance of catalyst dispersion in the gasification of lignite chars. *J. Catal.* **1983**, *82*, 382–394. [[CrossRef](#)]
29. Mouljin, J.A.; Cerpontain, M.; Kapteijn, F. Mechanism of the potassium catalysed gasification of carbon in CO₂. *Fuel* **1984**, *63*, 1043–1047. [[CrossRef](#)]
30. Mims, C.; Pabst, J. Alkali-catalyzed carbon gasification kinetics: Unification of H₂O, D₂O, and CO₂ reactivities. *J. Catal.* **1987**, *107*, 209–220. [[CrossRef](#)]
31. Chang, J.-S.; Lauderback, L.L.; Falconer, J.L. Aes and sims analysis of potassium/graphite surfaces. *Carbon* **1991**, *29*, 645–652. [[CrossRef](#)]
32. Zhao, Y.; Feng, D.; Zhang, Y.; Huang, Y.; Sun, S. Effect of pyrolysis temperature on char structure and chemical speciation of alkali and alkaline earth metallic species in biochar. *Fuel Proc. Technol.* **2016**, *141*, 54–60. [[CrossRef](#)]
33. Andrea Jordan, C.; Akay, G. Speciation and distribution of alkali, alkali earth metals and major ash forming elements during gasification of fuel cane bagasse. *Fuel* **2012**, *91*, 253–263. [[CrossRef](#)]
34. Feng, D.; Zhao, Y.; Zhang, Y.; Sun, S. Effect of speciation of AAEM species on reactivity of biochar. *J. Harbin Inst. Technol.* **2017**, *49*, 69–73.
35. Nutalapati, D.; Gupta, R.; Moghtaderi, B.; Wall, T. Assessing slagging and fouling during biomass combustion: A thermodynamic approach allowing for alkali/ash reactions. *Fuel Proc. Technol.* **2007**, *88*, 1044–1052. [[CrossRef](#)]
36. Miller, S.F.; Miller, B.G. The occurrence of inorganic elements in various biofuels and its effect on ash chemistry and behavior and use in combustion products. *Fuel Proc. Technol.* **2007**, *88*, 1155–1164. [[CrossRef](#)]
37. Benson, S.A.; Holm, P.L. Comparison of inorganic constituents in three low-rank coals. *Ind. Eng. Chem. Prod. Res. Dev.* **1985**, *24*, 145–149. [[CrossRef](#)]
38. Zevenhoven-Onderwater, M.; Backman, R.; Skrifvars, B.-J.; Hupa, M. The ash chemistry in fluidised bed gasification of biomass fuels. Part I: Predicting the chemistry of melting ashes and ash-bed material interaction. *Fuel* **2001**, *80*, 1489–1502. [[CrossRef](#)]
39. Pettersson, A.; Åmand, L.-E.; Steenari, B.-M. Chemical fractionation for the characterisation of fly ashes from co-combustion of biofuels using different methods for alkali reduction. *Fuel* **2009**, *88*, 1758–1772. [[CrossRef](#)]

40. Bai, Y.; Zhu, S.; Luo, K.; Gao, M.; Yan, L.; Li, F. Coal char gasification in H₂O/CO₂: Release of alkali and alkaline earth metallic species and their effects on reactivity. *Appl. Therm. Eng.* **2017**, *112*, 156–163. [[CrossRef](#)]
41. Guo, X.; Tay, H.L.; Zhang, S.; Li, C.-Z. Changes in char structure during the gasification of a Victorian brown coal in steam and oxygen at 800 °C. *Energy Fuels* **2008**, *22*, 4034–4038. [[CrossRef](#)]
42. Weng, Q.C.; Wang, C.A.; Che, D.F.; Fu, Z.W. Alkali metal occurrence mode and its influence on combustion characteristics in zhundong coals. *J. Combust. Technol.* **2014**, *20*, 216–221.
43. Feng, D.; Zhang, Y.; Liu, P.; Guo, Y.; Huang, Y.; Sun, S. Effects of chemical fractionation analysis on physical and chemical structures of biomass char. *CIESC J.* **2015**, *66*, 4634–4642.
44. Mitsuoka, K.; Hayashi, S.; Amano, H.; Kayahara, K.; Sasaoaka, E.; Uddin, M.A. Gasification of woody biomass char with CO₂: The catalytic effects of K and Ca species on char gasification reactivity. *Fuel Proc. Technol.* **2011**, *92*, 26–31. [[CrossRef](#)]
45. Manzoori, A.R.; Agarwal, P.K. The fate of organically bound inorganic elements and sodium chloride during fluidized bed combustion of high sodium, high sulphur low rank coals. *Fuel* **1992**, *71*, 513–522. [[CrossRef](#)]
46. Srinivasachar, S.; Helble, J.; Ham, D.; Domazetis, G. A kinetic description of vapor phase alkali transformations in combustion systems. *Prog. Energy Combust. Sci.* **1990**, *16*, 303–309. [[CrossRef](#)]
47. Marschner, H. *Marschner's Mineral Nutrition of Higher Plants*; Academic Press: Cambridge, MA, USA, 2011.
48. Nordgreen, T.; Liliedahl, T.; Sjöström, K. Metallic iron as a tar breakdown catalyst related to atmospheric, fluidised bed gasification of biomass. *Fuel* **2006**, *85*, 689–694. [[CrossRef](#)]
49. Zhang, S.; Min, Z.; Tay, H.-L.; Asadullah, M.; Li, C.-Z. Effects of volatile-char interactions on the evolution of char structure during the gasification of Victorian brown coal in steam. *Fuel* **2011**, *90*, 1529–1535. [[CrossRef](#)]
50. Tay, H.-L.; Kajitani, S.; Zhang, S.; Li, C.-Z. Effects of gasifying agent on the evolution of char structure during the gasification of Victorian brown coal. *Fuel* **2013**, *103*, 22–28. [[CrossRef](#)]
51. Leites, L.A.; Bukalov, S.S. Raman intensity and conjugation with participation of ordinary σ-bonds. *J. Raman Spectrosc.* **2001**, *32*, 413–424. [[CrossRef](#)]
52. Li, X.; Hayashi, J.; Li, C. Volatilisation and catalytic effects of alkali and alkaline earth metallic species during the pyrolysis and gasification of Victorian brown coal. Part VII. Raman spectroscopic study on the changes in char structure during the catalytic gasification in air. *Fuel* **2006**, *85*, 1509–1517. [[CrossRef](#)]
53. Li, X.; Li, C. Volatilisation and catalytic effects of alkali and alkaline earth metallic species during the pyrolysis and gasification of Victorian brown coal. Part VIII. Catalysis and changes in char structure during gasification in steam. *Fuel* **2006**, *85*, 1518–1525. [[CrossRef](#)]
54. Chen, S.; Yang, R. The Active Surface Species in Alkali-Catalyzed Carbon Gasification: Phenolate (C-O-M) Groups vs Clusters (Particles). *J. Catal.* **1993**, *141*, 102–113. [[CrossRef](#)]
55. Li, C.-Z. Some recent advances in the understanding of the pyrolysis and gasification behaviour of Victorian brown coal. *Fuel* **2007**, *86*, 1664–1683. [[CrossRef](#)]
56. Černý, J. Structural dependence of CH bond absorptivities and consequences for FT-i.r. analysis of coals. *Fuel* **1996**, *75*, 1301–1306. [[CrossRef](#)]
57. Lua, A.C.; Yang, T. Effects of vacuum pyrolysis conditions on the characteristics of activated carbons derived from pistachio-nut shells. *J. Colloid Interface Sci.* **2004**, *276*, 364–372. [[CrossRef](#)] [[PubMed](#)]
58. Lin-Vien, D.; Colthup, N.B.; Fateley, W.G.; Grasselli, J.G. *The Handbook of Infrared and Raman Characteristic Frequencies of Organic Molecules*; Elsevier: Amsterdam, The Netherlands, 1991.
59. Walker, P.; Taylor, R.; Ranish, J. An update on the carbon-oxygen reaction. *Carbon* **1991**, *29*, 411–421. [[CrossRef](#)]
60. Liu, X.; Xu, M.; Yao, H.; Gu, Y.; Si, J.; Xiong, C. Comparison of char structural characteristics and reactivity during conventional air and oxy-fuel combustion. In *Cleaner Combustion and Sustainable World*; Springer: Berlin, Germany, 2013; pp. 989–998.
61. Kelemen, S.; Freund, H. Model CO₂ gasification reactions on uncatalyzed and potassium catalyzed glassy carbon surfaces. *J. Catal.* **1986**, *102*, 80–91. [[CrossRef](#)]
62. Freund, H. Gasification of carbon by CO₂: A transient kinetics experiment. *Fuel* **1986**, *65*, 63–66. [[CrossRef](#)]
63. Pereira, P.; Csencsits, R.; Somorjai, G.A.; Heinemann, H. Steam gasification of graphite and chars at temperatures <1000 K over potassium-calcium-oxide catalysts. *J. Catal.* **1990**, *123*, 463–476.
64. Kapteijn, F.; Peer, O.; Moulijn, J.A. Kinetics of the alkali carbonate catalysed gasification of carbon: 1. CO₂ gasification. *Fuel* **1986**, *65*, 1371–1376. [[CrossRef](#)]
65. Freund, H. Kinetics of carbon gasification by CO₂. *Fuel* **1985**, *64*, 657–660. [[CrossRef](#)]

66. Quyn, D.M.; Wu, H.; Hayashi, J.-I.; Li, C.-Z. Volatilisation and catalytic effects of alkali and alkaline earth metallic species during the pyrolysis and gasification of Victorian brown coal. Part IV. Catalytic effects of NaCl and ion-exchangeable Na in coal on char reactivity. *Fuel* **2003**, *82*, 587–593. [[CrossRef](#)]
67. Yu, J.; Tian, F.-J.; Chow, M.C.; McKenzie, L.J.; Li, C.-Z. Effect of iron on the gasification of Victorian brown coal with steam: Enhancement of hydrogen production. *Fuel* **2006**, *85*, 127–133. [[CrossRef](#)]
68. Li, C.-Z.; Sathe, C.; Kershaw, J.; Pang, Y. Fates and roles of alkali and alkaline earth metals during the pyrolysis of a Victorian brown coal. *Fuel* **2000**, *79*, 427–438. [[CrossRef](#)]



© 2018 by the authors. Licensee MDPI, Basel, Switzerland. This article is an open access article distributed under the terms and conditions of the Creative Commons Attribution (CC BY) license (<http://creativecommons.org/licenses/by/4.0/>).

Article

Efficient Low Temperature Hydrothermal Carbonization of Chinese Reed for Biochar with High Energy Density

Chang Liu ^{1,2}, Xin Huang ¹ and Lingzhao Kong ^{2,*}

¹ School of Environmental and Chemical Engineering, Shanghai University, Shanghai 200444, China; liuchang@sari.ac.cn (C.L.); huangxin2008@shu.edu.cn (X.H.)

² Shanghai Advanced Research Institute, CAS. No. 100 Haike Road, Shanghai 201210, China

* Correspondence: konglz@sari.ac.cn; Tel.: +86-21-2060-8002

Received: 15 November 2017; Accepted: 6 December 2017; Published: 11 December 2017

Abstract: Hydrothermal carbonization (HTC), as an environmental friendly process, presents wide potential applicability for converting biomass to biochar with high energy density. Reed, a major energy crop, was converted by a HTC process in a batch reactor at 200–280 °C for 0.5 to 4 h. Biochar mass yield changed from 66.7% to 19.2% and high heating value (HHV) from 20.0 kJ/g to 28.3 kJ/g, respectively, by increasing the carbonization temperature from 200 °C to 280 °C and decreasing the residence time from 2 h to 1 h. The Fourier Transform infrared spectroscopy (FTIR), X-ray Diffraction (XRD), and Scanning Electron Microscope (SEM) results indicated the lignocellulosic crosslink structure of reed is broken and biochar having a high energy density is obtained with the increase of temperature. The microcrystal features of reed are destroyed and biochar contained mainly lignin fractions. The HTC of biocrude is carried out at 200–280 °C for 2.0 h and the results showed that the obtained biochar has uniform particles filled with carbon microspheres.

Keywords: hydrothermal carbonization (HTC); Chinese reed; biocrude; biochar; high heating value (HHV)

1. Introduction

Recently, abundant research efforts have been focused on the use of renewable biomass for producing energy, chemicals and materials. During the whole process for biomass growth and utilization, the carbon balance has been realized, so the concentration of CO₂ in the atmosphere theoretically remains constant during this cycle [1]. Most of the biomass is inefficiently used for the heating purposes in the absence of other reliable and cheaper sources of energy. The biomass has been exploited in ways involving pyrolysis, gasification, fermentation and hydrothermal processes to obtain the useful clean energy, materials and biochemicals. H₂ [2], ethanol [3], lactic acid [4], biochemicals [5], and biochar [6–8] can be obtained in different reaction processes. Recently, the acceleration of carbonization in a hydrothermal medium by a factor of 10⁶–10⁹ under rather mild conditions, down to a scale of hours, makes it a useful pathway for biochar production. The research attention has largely focused on the conversion of biomass to biochar which has higher heating value (over 28.0 kJ/g) and better carbonaceous materials performance [9].

Hydrothermal carbonization (HTC) is a thermochemical process to produce biochar from raw biomass or carbohydrates under mild temperatures (180–350 °C) and self-generated pressures in subcritical water. Compared to the typical carbonization routes such as pyrolysis (500 to 800 °C), HTC is able to explore fresh feedstock without any drying treatment [10,11]. During the HTC process, subcritical water serves as green solvent, reagent and catalyst that facilitate the hydrolysis and cleavage of lignocellulosic biomass [12,13]. Hydrolysis, dehydration, decarboxylation, condensation

polymerization and aromatization take place during the HTC process [14]. In the past decades, HTC has been explored to reveal the mechanisms of natural coalification in the coal-forming process, but attention was seldom paid to the production of solid residues. The biochar obtained by the HTC process from fresh biomass even bio-waste, can be used as a solid fuel, adsorbent and soil amendment with wide applicability. Some research has indicated a series of novel carbon materials with specific properties could be prepared through the HTC process under mild conditions using carbohydrates as starting materials [15,16].

A HTC process was used for the conversion of eucalyptus bark (EB) into biochar in the range of 220–300 °C after 2–10 h. The results showed that the biochar yield decreased slightly from 46.4% at 220 °C to 40.0% at 300 °C and high heating value (HHV) increased from 20.2 to 29.2 kJ/g [17]. The optimum conditions for maximum yield production of biochar through HTC of palm shell were also discussed. Using 180 °C, 0.5 h, and 1.60 wt.%, optimized biochar was obtained and the temperature was proven to have a greater influence on the efficiency of biochar production [18]. Liu carried out HTC of glucose, sucrose, and starch at temperatures ranging from 170 to 240 °C. The results indicated that biochar is made up of uniform spherical micrometer-sized particles that have a 0.4–6 mm diameter, which can be modulated by modifying the preparation conditions [19]. Sevilla et al. provided a method for producing carbonaceous materials by means of the HTC of cellulose at 220–250 °C. The formation of this material essentially follows the path of a dehydration process, similar to the HTC of saccharides such as glucose, sucrose or starch [20,21].

In the present work, our interest was the production of biochar with higher energy density and carbonaceous materials from biocrude, so the HTC process was explored to convert reed into biochar and biocrude in a batch reactor under mild conditions. The effect of reaction time, temperature and pressure in the range of 0.5–4 h, 200–280 °C and 2.4–27.2 MPa, respectively, were studied. The HTC of biocrude was carried out in a batch reactor at 200 °C for 2 h. Through Fourier Transform infrared spectroscopy (FTIR), X-ray Diffraction (XRD), and Scanning Electron Microscope (SEM) analysis of the biochar produced from reed, the transformation process, structure performance and energy value of biochar were discussed. Based on the yields and SEM analysis, the possible pathways for HTC of biocrude into carbon microspheres were provided.

2. Results

The characteristics of the reed raw material are presented in Table 1. Details of yield, HHV and energy yield of biochar prepared under various conditions using the setup illustrated in Figure 1 are shown in Table 2. In general, biochar yield (wt.%) decreased with temperature whereas HHV increased. The results are discussed in the following sections. The effects of residence time and pressure on the carbonization of reed for biochar production at 200 °C and 230 °C are discussed. The time and pressure ranged from 2.0 to 4.0 h and 17.6 and 27.2 MPa, respectively. The reed and biochar were characterized by FTIR (wave number: 4000–400 cm⁻¹) and a typical spectrum was shown in Figure 2. Typically bands in FTIR spectrum for reed and biochar were listed in Table 3. As the hydrolysis product of reed in the HTC process, biocrude contains various sugars and organic acids. The glucose, lactic acid, acetic acid, HMF (5-hydroxymethylfurfural) and furan in biocrude obtained from 200 °C to 280 °C are listed in the Table 4.

Table 1. The main properties of the reed.

Properties	Mass
Moisture (wt.%)	2.6
Lignin (wt.%)	23.5
Cellulose (wt.%)	39.5
Hemicellulose (wt.%)	26.7
Carbon (wt.%)	44.6
HHV (kJ/g)	17.1

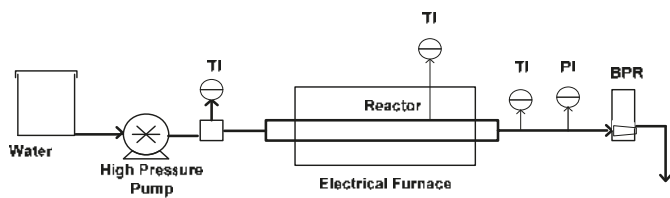


Figure 1. Setup for hydrothermal carbonization (HTC) of reed biomass to produce biochar.

Table 2. Experiment summary and results.

Run	Temp. (°C)	Time (h)	P (MPa)	Yield (wt.%)	HHV (kJ/g)	Energy Yield (%)
1	200	2.0	17.2	59.8	21.5	75.2
2	200	2.0	27.6	66.7	20.9	81.5
3	200	4.0	17.2	63.2	21.5	79.5
4	200	4.0	27.6	60.6	21.8	77.2
5	230	2.0	17.2	48.9	26.9	76.9
6	230	4.0	27.6	45.6	24.3	64.8
7	230	2.0	17.2	52.8	25.7	79.4
8	230	4.0	27.6	49.1	25.4	72.9
9	200	4.0	2.4	66.4	20.3	78.9
10	230	4.0	4.1	37.8	23.5	51.9
11	260	4.0	6.5	28.4	25.9	43.0
12	280	4.0	8.3	19.0	28.1	31.2
13	280	0.5	7.2	20.7	24.7	29.9
14	280	1.0	7.2	19.2	28.3	31.8

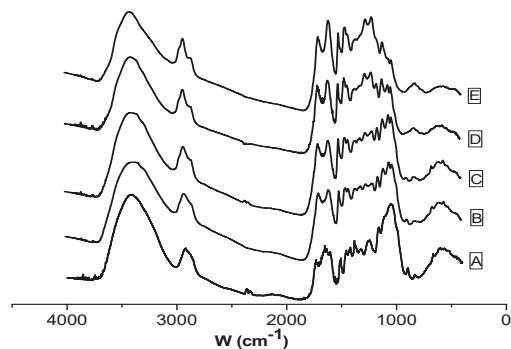


Figure 2. Transform infrared spectroscopy (FTIR) results of reed and biochar, processing time 4.0 h (A—Reed, B—200 °C, C—230 °C, D—260 °C, E—280 °C).

Table 3. FRIR spectrum of the reed and biochar.

Position of the Bands (cm^{-1})	Functional Group
3401	O—H stretching vibration
2920	CH, CH_2 stretching vibration
1700	Carbonyl C=O stretching vibration
1600	C=C stretching vibration
1513	Benzene ring stretching vibration
1424	CH_2 shearing, CH_2 bending vibration
1383	CH bending vibration
1267	C—O—C stretching vibration in alkyl aromatic
1160	C—O—C asymmetry stretching vibration
1060	C—O stretching vibration

Table 4. The main organic compounds in biocrude.

Composition	200 °C	230 °C	260 °C	280 °C
Glucose (g/L)	2.7	1.2	0.4	0.3
Lactic acid (g/L)	3.2	3.5	3.6	2.7
Acetic acid (g/L)	-	0.6	1.1	0.9
HMF (g/L)	-	-	-	0.7
Furan (g/L)	-	-	-	1.9

3. Discussion

3.1. Performance of HTC for Biochar

At 200 °C, the higher yield and HHV for biochar were obtained at 2.0 h, 27.6 MPa and 4.0 h, 27.6 MPa, respectively, and the values were determined as 66.7% and 21.8 kJ/g. A higher temperature favored the conversion of raw materials to higher energy density fuel and HHV, as indicated by the values provided at 230 °C which were 26.9 kJ/g at 2 h and 17.2 MPa. Compared to the yield of biochar at 200 °C, it showed a descending trend at the same conditions for 230 °C. Higher yield and HHV can be obtained at 200 °C and 230 °C, respectively. The desired pressure was achieved by pumping water into the reactor. The increased pressure of the reaction system keeps the water in its aqueous phase and influences the density properties of water [10]. At comparatively low temperature (200–230 °C), the amorphous components of reed were mainly hydrolyzed and the liquid product mainly contained oligomers and monomers produced by the hydrolysis of the sugar components in reed. The HHV of the product biochar remained low because of low deoxygenation rate in this temperature range.

Temperature plays a key role in the conversion of reed to biochar. Further experiments were performed at 200 °C to 280 °C for 4.0 h and the results are shown in the Table 2. Fifty mL of water was added into the reactor and the mass ratio of biomass and water was changed from 1:6.5 (shown in the Table 2) to 1:25. The pressure was autogenously adjusted and it increased above the vapor pressure of water because of the formation of gaseous products during the HTC process. The influence of temperature is obviously, though biochar yield decreased at 280 °C, the HHV of the product was increased considerably with temperature.

The highest yield of 60.6% for biochar was obtained at 200 °C. At the same time, the higher temperature is propitious to obtain higher energy density fuel and this value reached 28.1 kJ/g at 280 °C. The yield and HHV obtained at 230 °C are 37.8% and 23.5 kJ/g, which lower than the results under the set pressure. The results showed that high pressure provides a higher yield and HHV for the conversion of reed to biochar despite it being lower from the influence of temperature. Based on the results of yield and HHV at different temperatures, the energy conversion efficiency, which was defined as the ratio of contained energy in raw reed and obtained biochar, were 52.4%, 43.0%, and 31.2% at 230, 260, and 280 °C, respectively. The results indicated that energy conversion efficiency displays a decreasing tendency with the increase of temperature. To obtain a higher energy conversion efficiency and biochar with higher energy density, a higher temperature should be used and the reaction conditions should be changed to improve the HHV of biochar.

Table 2 displays the obtained biochar yield and HHV at 280 °C from 0.5 to 4.0 h. The yield of biochar shows a descending curve, but the values of HHV increase slightly from 0.5 h to 4.0 h. The HHV obtained from 0.5 h at 280 °C is higher than that of 4 h at 230 °C, but the yield (20.7%) is lower than with the former conditions (37.8%). Reed provides less biochar yield in the case of 1.0 h at 280 °C than 4.0 h at 260 °C, but the HHV for biochar were high as 28.4 and 25.9 kJ/g. Similar biochar yield and HHV results were obtained at 1.0 h and 4.0 h under 280 °C. Future work will focus on getting the optimal conditions for conversion of reed to biochar with higher yield and energy density.

3.2. Characterization of Reed and Biochar

The FTIR spectrum of biochar was partly similar to that of reed and the typical peaks of lignin were maintained in biochar. These results indicated that the biochar had a high degree of polymerization oligomers with lingo-like molecular structures. The reed was not liquefied completely for the appearance of absorption peaks at 1060 and 1160 cm^{-1} at 200 °C and 230 °C. From Figure 2, it can be seen that the absorbance peaks in the raw, 200 °C and 230 °C materials are similar and hemicellulose and cellulose were present in the biochar obtained at lower temperature [22]. As for 260 °C and 280 °C, the FTIR displays peak changes for the biochar obtained at higher temperature which is different from reed and lower temperature product. The results showed that the two kinds of biochar have a different functional groups than reed. In the higher temperature process, the hemicellulose and cellulose were converted and a polymerization process was realized. From the spectral difference of FTIR spectra of these biochar obtained at higher temperature and reed, the absorbance peak appeared in the range of 1600–650 cm^{-1} . It was shown that the aromatic rings started to recombine at this temperature. The possible presence of alkenes was indicated by the absorbance peaks between 1680 and 1580 cm^{-1} . The ether linkages around 1200 cm^{-1} and 1000 cm^{-1} between the cellulose skeleton units were hydrolyzed with the hydrothermal treatment from 260 °C to 280 °C under subcritical conditions [23–25]. As for the skeleton structure of reed, the lignin remained in the biochar when the temperature increased from 200 °C to 280 °C. The results were confirmed by the lignin peaks at 1265, 1424 and 1513 cm^{-1} in the FTIR. At the same time, peaks of polymeric product were also shown in the FTIR spectra at 1600 and 1700 cm^{-1} . These results proved that the biochar was composed by the conserved lignin and polymeric products produced in the HTC process [22].

We conducted SEM observations of reed and biochar after the HTC process. The SEM images for biochar and reed are shown in Figure 3. These results suggested that biochar has a different macromolecular structure from reed and their average particle sizes grew smaller at the temperature reached 260 °C. The results show that the lignocellulosic structure of reed was destroyed as the hemicellulose and cellulose were hydrolyzed in the HTC process. Small globular particles which come from the polymer particles of reed decomposition can be seen precipitated over thin fibers. The cross-linked structure which was made up by the lignin and cellulose in reed was broken in the HTC process as the cellulose was hydrolyzed into aqueous phase [26,27]. Compared with lignin, the microcrystal structure of cellulose is relatively easily damaged under higher temperature conditions and the results were demonstrated in the FTIR analysis. As shown in the Figure 3B, the lignin can resist the higher temperature disruption and form the main skeleton structure for biochar obtained in higher temperature.

The XRD patterns for biochar (obtained 280 °C, 4.0 h) and reed were compared and are shown in Figure 4. The distinct sharp crystalline cellulosic peak ($2\theta = 22.7^\circ$) which comes from the crystal structure of cellulose was displayed in the reed, but the peak was absent in the biochar, which confirms that it contained mainly less crystalline or amorphous components. As the cellulose in the reed was decomposed, the transformation from microcrystal features to a non-crystalline structure were realized in the HTC process. A carbon-rich product with an amorphous structure and lignin as the major component was retained in the biochar. The results are consistent with the FTIR and SEM analyses. Through the analysis of FTIR, SEM and XRD for the reed and obtained biochar, the change for structure, morphology and composition from reed to biochar were displayed to help understand the HTC process for biochar production. Through fragmentations and deoxygenation, reed conversion into biochar is realized. The main components of the biochar obtained at higher temperature are lignin and cellulose was hydrolyzed into biocrude. The elemental analysis of the biochar obtained at 280 °C indicated that the elemental carbon is over 70%. The results confirm that O/C ratio decrease with temperature from 0.90 for reed to 0.32 for biochar obtained at 280 °C. The decrease in O/C ratio may be attributed to the deoxygenation, caused mainly by the dehydration of reed.

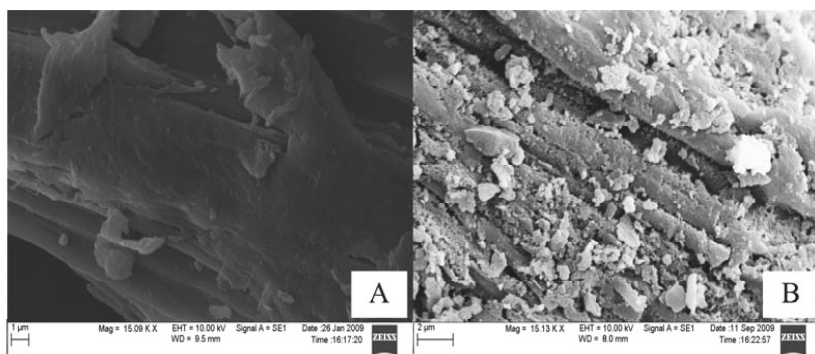


Figure 3. Scanning Electron Microscope (SEM) results for reed (A) and biochar (B) obtained at 260 °C, 4.0 h.

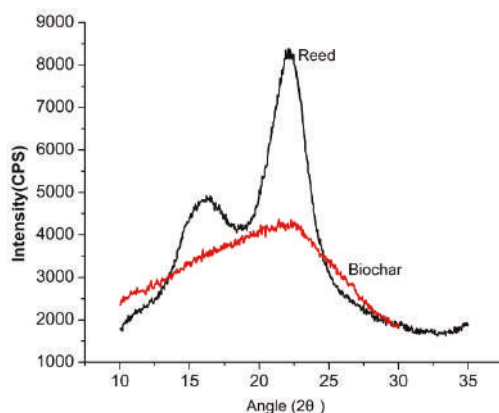


Figure 4. X-ray Diffraction (XRD) results for reed and biochar obtained at 280 °C, 4.0 h.

3.3. HTC of Biocrude for Biochar

From Table 4 we know that glucose serves as the main contributor in the biocrude which is obtained at low temperature. The main hydrolysis products of reed include glucose, acetic acid, lactic acid, HMF and furan. The oligomers and glucose constitute the majority of the organic compounds in the liquefaction of reed at low temperatures such as 200 °C. Organic acids and aromatic compounds are formed by different pathways, especially in the high temperature interval. As the temperature increases from 200 °C to 280 °C, the amount of glucose decreases whereas that of organic acids displays an upward trend. For the hydrolysis product of hemicellulose and cellulose, lower temperature is favorable for the production of glucose and higher temperature is beneficial for producing organic acids. We carried out experiments on the HTC of biocrude at 200 °C for 2.0 h. The biocrude was obtained in the HTC of reed in a temperature range from 200 °C to 280 °C. The conversion efficiency of carbon from biocrude to biochar is shown in Figure 5. The conversion efficiency of carbon was 35.5% when the biocrude was obtained at 200 °C. As for the biocrude obtained at 280 °C and 4.0 h, the value decreased to 4.4%. The conversion efficiency of carbon for biocrude obtained from 230 °C and 260 °C were 26.2% and 6.5%, respectively. The experimental results indicated that biocrude produced at lower temperature is favorable for the conversion of organic carbon to biochar. Sugar plays an important role in the HTC process for biochar production which was similar to that use the glucose as a raw material. Through polycondensation and molecular rearrangements

of sugar, the conversion of biocrude to biochar was realized in the HTC process [28]. The SEM image for HTC conversion biocrude obtained at 200 °C to biochar is shown in Figure 6.

As shown in the Figure 6, the biochar obtained in the HTC of biocrude has uniform features. Interestingly, the majority of the 2 µm particles are composed of the biochar and biocrude transformed into carbon microspheres during the hydrothermal carbonization process. A comparison of biochar produced from reed and biocrude indicated that different formation pathways lead to various biochar properties. The biochar obtained the HTC of reed can be used as a higher energy density fuel for its higher carbon content. Because of the homogenization characteristics, the biochar resulting from the HTC of biocrude can provide a new method for producing carbonaceous materials.

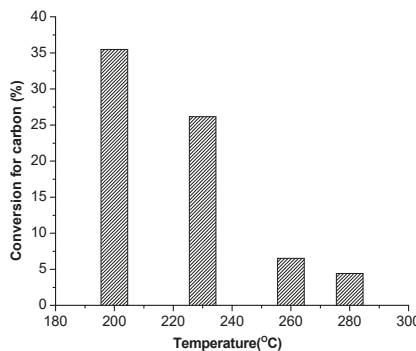


Figure 5. The conversion efficiency of carbon from biocrude obtained at different temperature (experiments on the HTC of biocrude at 200 °C, 2.0 h).

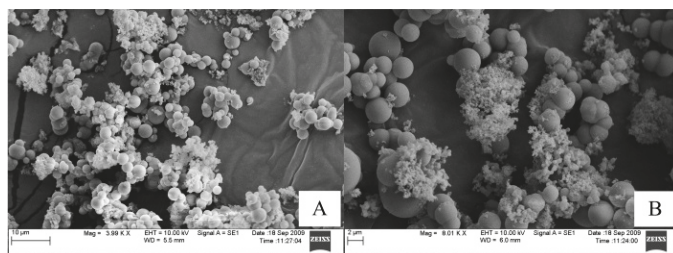


Figure 6. SEM image of biochar (HTC of biocrude obtained at 200 °C), 200 °C, 2.0 h. (A: scale: 10 µm; B: scale: 2 µm.)

4. Materials and Methods

4.1. Material

Reed (2–5 mm long pieces, powdered) was used as raw material for the HTC experiments. The physical and chemical properties of the reed are listed in Table 1. Biocrude obtained from liquefaction of reed also was used for producing biochar.

4.2. Apparatus and Procedure

HTC of reed was carried out in a batch reactor with an internal volume of 65.0 cm³ (Figure 1). The experiments were carried out at 200–280 °C for 0.5–4.0 h. The HTC process was as follows: the desired amount of reed (10.0 g) and water (45 cm³) was put into the reactor, which was then sealed. The reactor was heated up to a desired temperature for HTC of reed. After the set time, the reactor

was rapidly cooled to room temperature using air flow. The reaction time was defined as the time at the reaction temperature excluding preheating and cooling time. To study the effect of pressure on HTC process, reactor pressure was controlled by pumping water into the reactor until the set value was reached. After HTC of Chinese reed, the biochar and biocrude were separated with a 0.22 μm filtration membrane. The biocrude was used as starting material for preparing carbon materials. As for the biochar produced from the biocrude, the experiments on the HTC of biocrude were carried out at 200 °C for 2.0 h in the batch reactor. The reactor was filled with liquid phase (biocrude) which was obtained from the different HTC processes and the biochar was collected through a 0.22 μm filtration membrane after the reaction. The biochar obtained from biomass and biocrude was washed using deionized water and oven dried for 24 h at 105 °C.

4.3. Characterization

Surface morphology of the sample was recorded using an environmental scanning electron microscope (SEM, EVO 50, Zeiss, Jena, Germany). XRD patterns of the reed and biochar were obtained on a Miniflex powder X-ray diffractometer (Rigaku, Tokyo, Japan) with a Cu K α radiation source in a 2 θ range from 10° to 35° with a scanning rate of 1°/min. Infrared spectra (4000–400 cm^{-1}) were analyzed by a IR100 infra-red spectroscopy (FTIR) instrument (Nicolet, Waltham, MA, USA) which was equipped with a TGS/PE detector and a silicon beam splitter with 1 cm^{-1} resolution. The higher heating value (HHV) of reed and biochar was determined by an IKA-C200 calorimeter (IKA Works, Wilmington, NC, USA). The collected liquid solution was filtered through a 0.22 μm pore-size filter prior to analysis. The main products in the resultant solution were identified based on standard compounds and their structures were further confirmed by HPLC (LC-20AD system, Shimadzu, Tokyo, Japan) equipped with an Aminex HPX-87H Ion Exclusion Column, 300 mm × 7.8 mm) with a differential refraction detector (RID-10A). The column was held at 65°C. H_2SO_4 (0.01 mol/L) was used as the mobile phase at a flow rate of 1.0 mL/min. The peak identification was accomplished by comparison of sample peak retention times with those of standard solutions of pure compounds. The total organic carbon (TOC) in aqueous phase was measured with a TOC analyzer (Shimadzu TOC 5000 A).

5. Conclusions

Reed was converted into biochar in a temperature range of 200–280 °C for 0.5–4.0 h in a batch reactor. Compared with the residence time and pressure, the temperature plays a key role in the conversion of reed to biochar. Higher temperature is favorable for the production of a higher energy density fuel but is negative for the mass of biochar. The yield of biochar decreased when the temperature increased from 200 °C to 280 °C. The FTIR and SEM results suggested that the complete breakdown of the lignocellulosic crosslinked structure of reed is realized at higher temperature and biochar contained mainly lignin fractions. The XRD image of untreated reed and biochar indicated that the microcrystal features are converted into a non-crystalline structure in the HTC process. HTC of biocrude for biochar production were carried out from 200–280 °C and 2.0 h. The results indicated that biocrude obtained at lower temperature is favorable for biochar production and polycondensation of sugar is the major factor in the HTC of biocrude. The biochar obtained from the HTC of biocrude has a uniform particle size filled with globular carbon microspheres.

Acknowledgments: Authors acknowledge financial supports provided by the National Natural Science Foundation of China (21406255), the Shanghai Science and Technology Committee (16dz1207200) and the Youth Innovation Promotion Association CAS (2015231).

Author Contributions: Xin Huang and Lingzhao Kong conceived and designed the experiments; Chang Liu performed the experiments; Chang Liu and Lingzhao Kong analyzed the data; Chang Liu and Xin Huang contributed reagents/materials/analysis tools; Lingzhao Kong wrote the paper.

Conflicts of Interest: The authors declare no conflict of interest.

References

- Matsumura, Y.; Sasaki, M.; Okuda, K. Supercritical water treatment of biomass for energy and material recovery. *Combust. Sci. Technol.* **2006**, *178*, 509–536. [[CrossRef](#)]
- Lee, I.; Kimm, M.; Ihm, S. Gasification of glucose in supercritical water. *Ind. Eng. Chem. Res.* **2002**, *41*, 1182–1188. [[CrossRef](#)]
- Motonobu, G.; Ryusaku, O.; Tsutomu, H. Hydrothermal conversion of municipal organic waste into resources. *Bioresour. Technol.* **2004**, *93*, 279–284.
- Kong, L.Z.; Li, G.M.; Wang, H. Hydrothermal catalytic conversion of biomass for lactic acid production. *J. Chem. Technol. Biotechnol.* **2008**, *83*, 383–388. [[CrossRef](#)]
- Selhan, K.; Thallada, B.; Akinori, M. Low-temperature catalytic hydrothermal treatment of wood biomass: Analysis of liquid products. *Chem. Eng. J.* **2005**, *108*, 127–133.
- Sevilla, M.; Macia-Agullo, J.A.; Fuertes, A.B. Hydrothermal carbonization of biomass as a route for the sequestration of CO₂: Chemical and structural properties of the carbonized products. *Biomass Bioenergy* **2011**, *35*, 3152–3159. [[CrossRef](#)]
- Liu, W.J.; Zeng, F.X.; Jiang, H. Preparation of high adsorption capacity biochars from waste biomass. *Biomass Bioenergy* **2011**, *102*, 8247–8252.
- Libra, J.A.; Ro, K.S.; Kamann, C. Hydrothermal carbonization of biomass residuals: A comparative review of the chemistry, processes and applications of wet and dry pyrolysis. *Biofuels* **2011**, *2*, 89–124. [[CrossRef](#)]
- Gupta, R.B.; Kumar, S.; Kong, L.Z. Biomass to Biochar Conversion in Subcritical Water. U.S. Patent 8,637,718 B2, 8 January 2014.
- Sevilla, M.; Fuertes, A.B. The production of carbon materials by hydrothermal carbonization of cellulose. *Carbon* **2009**, *47*, 2281–2289. [[CrossRef](#)]
- Sevilla, M.; Fuertes, A.B. Chemical and structural properties of carbonaceous products obtained by hydrothermal carbonization of saccharides. *Chem. A Eur. J.* **2009**, *15*, 4195–4203. [[CrossRef](#)] [[PubMed](#)]
- Titirici, M.M.; Thomas, A.; Antonietti, M. Back in the black: Hydrothermal carbonization of plant material as an efficient chemical process to treat the CO₂ problem? *New J. Chem.* **2007**, *31*, 787–788. [[CrossRef](#)]
- Phillip, E. Organic chemical reactions in supercritical water. *Chem. Rev.* **1999**, *99*, 603–621.
- Hu, B.; Yu, S.H.; Wang, K.; Liu, L.; Xu, X.W. Functional carbonaceous materials from hydrothermal carbonization of biomass: An effective chemical process. *Dalton Trans.* **2008**, *6*, 5414–5423. [[CrossRef](#)] [[PubMed](#)]
- Laginhas, C.; Valente Nabais, J.M.; Titirici, M.M. Activated carbons with high nitrogen content by a combination of hydrothermal carbonization with activation. *Microporous Mesoporous Mater.* **2016**, *226*, 125–132. [[CrossRef](#)]
- Kumar, S.; Loganathan, V.A.; Gupta, R.B.; Barnett, M.O. An Assessment of U(VI) removal from groundwater using biochar produced from hydrothermal carbonization. *J. Environ. Manag.* **2011**, *92*, 2504–2512. [[CrossRef](#)] [[PubMed](#)]
- Gao, P.; Zhou, Y.Y.; Meng, F.; Zhang, Y.H.; Liu, Z.H.; Zhang, W.Q.; Xue, G. Preparation and characterization of hydrochar from waste eucalyptus bark by hydrothermal carbonization. *Energy* **2016**, *97*, 238–245. [[CrossRef](#)]
- Nizamuddin, S.; Mubarak, N.M.; Jayakumar, N.S.; Sahu, J.N.; Ganeshan, P. Chemical, dielectric and structural characterization of optimized hydrochar produced from hydrothermal carbonization of palm shell. *Fuel* **2016**, *163*, 88–97. [[CrossRef](#)]
- Liu, Z.G.; Zhang, F.S. Removal of copper (II) and phenol from aqueous solution using porous carbons derived from hydrothermal chars. *Desalination* **2011**, *267*, 101–106. [[CrossRef](#)]
- Watanabe, M.; Sato, T.; Inomata, H.; Smith, R.L., Jr.; Arai, K., Jr.; Kruse, A.; Dinjus, E. Chemical reactions of C₁ compounds in near-critical and supercritical water. *Chem. Rev.* **2004**, *104*, 5803–5821.
- Savova, D.; Apak, E.; Ekinci, E.; Yardim, F.; Petrov, N.; Budanova, T.; Razvigorova, M.; Minkova, V. Biomass conversion to carbon adsorbents and gas. *Biomass Bioenergy* **2011**, *21*, 133–142. [[CrossRef](#)]
- Kong, L.Z.; Miao, P.J.; Qin, J.G. Characteristics and pyrolysis dynamic behaviors of hydrothermally treated micro crystalline cellulose. *J. Anal. Appl. Pyrolysis* **2013**, *100*, 67–74. [[CrossRef](#)]
- Sakanishi, K.; Ikeyama, N.; Sakaki, T. Comparison of the hydrothermal decomposition reactivities of chitin and cellulose. *Ind. Eng. Chem. Res.* **1999**, *38*, 2177–2181. [[CrossRef](#)]
- Kong, L.Z.; Li, G.M.; He, W.Z. Reutilization disposal of sawdust and maize straw by hydrothermal reaction. *Energy Sources Part A* **2009**, *31*, 876–887. [[CrossRef](#)]

25. Biagini, E.; Barontini, F.; Tognotti, L. Devolatilization of biomass fuels and biomass components studied by TG/FTIR technique. *Ind. Eng. Chem. Res.* **2006**, *45*, 4486–4493. [[CrossRef](#)]
26. Kobayashi, N.; Okada, N.; Hirakawa, A.; Sato, T.; Kobayashi, J.; Hatano, S.; Itay, Y.; Mori, S. Characteristics of solid residues obtained from hot-compressed-water treatment of woody biomass. *Ind. Eng. Chem. Res.* **2009**, *48*, 373–379. [[CrossRef](#)]
27. Zhu, N.Y.; Yan, T.M.; Qiao, J. Adsorption of arsenic, phosphorus and chromium by bismuth impregnated biochar: Adsorption mechanism and depleted adsorbent utilization. *Chemosphere* **2016**, *164*, 32–40. [[CrossRef](#)] [[PubMed](#)]
28. Kumar, S.; Kothari, U.; Lee, Y.Y.; Gupta, R.B. Hydrothermal pretreatment of switchgrass and corn stover for production of ethanol and carbon microspheres. *Biomass Bioenergy* **2011**, *35*, 956–968. [[CrossRef](#)]



© 2017 by the authors. Licensee MDPI, Basel, Switzerland. This article is an open access article distributed under the terms and conditions of the Creative Commons Attribution (CC BY) license (<http://creativecommons.org/licenses/by/4.0/>).

Article

Gasification under CO₂-Steam Mixture: Kinetic Model Study Based on Shared Active Sites

Xia Liu [†], Juntao Wei [†], Wei Huo and Guangsuo Yu ^{*}

Key Laboratory of Coal Gasification and Energy Chemical Engineering of Ministry of Education, East China University of Science and Technology, Shanghai 200237, China; lxia@ecust.edu.cn (X.L.); icct-wjt@foxmail.com (J.W.); howell26@sina.com (W.H.)

* Correspondence: gsyu@ecust.edu.cn; Tel.: +86-21-64252974

† These authors contributed equally to this work.

Received: 16 October 2017; Accepted: 15 November 2017; Published: 17 November 2017

Abstract: In this work, char gasification of two coals (i.e., Shenuf bituminous coal and Zunyi anthracite) and a petroleum coke under a steam and CO₂ mixture (steam/CO₂ partial pressures, 0.025–0.075 MPa; total pressures, 0.100 MPa) and CO₂/steam chemisorption of char samples were conducted in a Thermogravimetric Analyzer (TGA). Two conventional kinetic models exhibited difficulties in exactly fitting the experimental data of char–steam–CO₂ gasification. Hence, a modified model based on Langmuir–Hinshelwood model and assuming that char–CO₂ and char–steam reactions partially shared active sites was proposed and had indicated high accuracy for estimating the interactions in char–steam–CO₂ reaction. Moreover, it was found that two new model parameters (respectively characterized as the amount ratio of shared active sites to total active sites in char–CO₂ and char–steam reactions) in the modified model hardly varied with gasification conditions, and the results of chemisorption indicate that these two new model parameters mainly depended on the carbon active sites in char samples.

Keywords: gasification; kinetic model; active site; chemisorption

1. Introduction

Gasification is an important technology for the clean and efficient utilization of coal, petroleum coke, and other solid fuels, and is available for large-scale industry due to its high efficiency, high production intensity, and near-zero pollution emission [1,2]. Fundamental research of gasification processes identified the rate of char gasification as a significant factor controlling gasification behaviors. This was mainly attributed to the relatively slow kinetics of char–CO₂ reactions and char–steam reactions under gasification conditions [3]. Therefore, it is important to make a clear understanding of the gasification kinetics of char–CO₂ and char–steam.

Many researchers [4–7] have developed reaction models of char–CO₂ and char–steam respectively to determine their reaction rates. Moreover, the kinetics of char–CO₂ gasification and char–steam gasification have also been studied in detail [8–11]. However, these models and studies, carried out in the system with a sole gasifying agent, could hardly be applied in systems where char–CO₂ and char–steam reactions occur simultaneously. Under realistic gasification conditions, chars are reacted with the gasifying agent mixtures consisting of steam and CO₂. Therefore, the researchers in [12] investigated the gasification reactivities of metallurgical coke in a mixture of steam and CO₂, but it was hard to analyze the intrinsic char–CO₂–steam reaction because the particle size of the tested samples was large (3–6 mm), which resulted in the effect of internal diffusion. Muhlen et al. [13] have also studied the mechanism of coal char gasification under a mixture of steam and CO₂, and the proposed empirical approach could well describe the effect of the carbon conversion degree on the gasification rate.

Recently, some researchers [14–18] came to investigate interactions in the char–CO₂–steam reaction using the Langmuir–Hinshelwood (L–H) model based on the theory of absorption and desorption. Roberts and Harris [14] found that char–CO₂ and char–steam reactions occur at the common active sites and indicated that steam and CO₂ competed for active sites of chars. However, some other researchers proposed an opposite view. Both Huang et al. [15] and Everson et al. [16] thought that the char–CO₂ reaction and char–steam reaction proceeded at separate active sites and the overall gasification rate should be equal to the sum of the char–CO₂ reaction rate and the char–steam reaction rate. Li et al. [17] also pointed out that the reaction mechanism of lignite char gasification was in accordance with the separate reactive site reaction mechanism under lower gasification pressures, whereas it was superior to the common reactive site reaction mechanism when gasification pressures further increased. On the other hand, Chen et al. [18] found that the overall gasification rate is not equal to the sum of the char–CO₂ reaction rate and char–steam reaction rate, but there was no evidence proving that the two gasifying agents competed for active sites. An L–H model with two dimensionless parameters was proposed by Umemoto et al. [19] to evaluate the rate of char–CO₂–steam gasification, and could estimate interactions more accurately than other models. However, the mechanism of the two proposed parameters is unclear.

Accordingly, a modified kinetic model based on the concept of active sites was proposed in this study to evaluate the interaction in char–CO₂–steam gasification, and it was validated by char–CO₂–steam gasification experiments of carbonaceous materials (two coals of different ranks and a petroleum coke) using a Thermogravimetric Analyzer (TGA). Additionally, CO₂ and steam chemisorption of chars were also conducted in a TGA to measure chemisorption quantities so as to explore the correlation between kinetic parameters of the modified model and chemisorption quantities. This work can provide not only theoretical basis for simulation but also scientific basis for gasification industry.

2. Materials and Methods

2.1. Char Preparation

Two typical gasification coals (Shenfu bituminous coal (SF) and Zunyi anthracite (ZY) from China) and a petroleum coke (PC) from Sinopec Shanghai Gaoqiao Petrochemical Co., Ltd. (Shanghai, China) were chosen as raw materials in this study. During char preparation, all pulverized raw samples were heated at 25 °C/min to 850 °C and held 30 min under the high purity nitrogen atmosphere in a fixed bed reactor. After devolatilization, the prepared chars with particle sizes of <40 µm were used for further analysis. The proximate analysis, ultimate analysis, and specific surface area of char samples are listed in Table 1.

Table 1. Properties of tested char samples.

Samples	Proximate Analysis/d, %			Ultimate Analysis/daf, %				Specific Surface Area/m ² ·g ⁻¹	
	VM	FC	A	C	H	N	S		
SF char	8.60	81.33	10.07	95.96	1.02	1.40	0.40	1.22	2.05
ZY char	5.50	73.48	21.02	96.11	0.95	1.68	1.04	0.22	1.52
PC char	4.11	90.86	5.03	95.95	0.73	1.19	2.08	0.05	0.41

SF-Shenfu bituminous coal; ZY-Zunyi anthracite; PC-petroleum coke; VM-volatile matter; FC-fixed carbon; A-ash; d-dry basis; daf-dry and ash free basis.

2.2. Isothermal Gasification Tests

The tests of isothermal char gasification were carried out using a TGA (NETZSCH STA449-F3). In all cases, approximately 5 mg of char particles was placed in an alumina crucible and heated at 25 °C/min to the prescribed temperature (850–950 °C) under high purity nitrogen atmosphere (80 mL/min). Then, nitrogen was switched to gasifying agents to initiate the isothermal gasification.

In char gasification tests, nitrogen was used to adjust the concentration of the gasifying agents. For char gasification with sole gasifying agent (steam or CO_2), the partial pressures of the gasifying agents varied from 0.025 to 0.100 MPa. For char gasification with a mixture of steam and CO_2 , the partial pressures of steam and CO_2 varied from 0.025 to 0.075 MPa, and the total pressure was always 0.100 MPa. The effects of external and internal diffusion were eliminated by previous tests [20].

The carbon conversion was expressed by the following equation [21]:

$$x = \frac{w_0 - w_t}{w_0 - w_{ash}} \quad (1)$$

where w_0 is the initial mass of char (wt. %); w_t is the sample mass at gasification time of t (wt. %); and w_{ash} is the final sample mass at the end of gasification.

Gasification rate was defined as following:

$$r = -\frac{1}{w_0 - w_{ash}} \frac{dw}{dt} = \frac{dx}{dt} \quad (2)$$

2.3. $\text{CO}_2/\text{Steam Chemisorption}$

CO_2/steam chemisorption of chars was fulfilled by TGA, and the test procedures have been reported in previous literature [22–24]. Approximately 15 mg of char particles was first heated at 25 °C/min to 850 °C and then held for 30 min under a continuous high purity nitrogen flow, in order to remove any impurity which could be adsorbed during CO_2 or steam chemisorption. Then, the temperature was decreased to 300 °C and stabilized for 10 min. Whereafter, nitrogen was switched to pure CO_2 or steam to start the chemisorption test. After another 30 min of adsorption, pure CO_2 or steam was finally switched to high purity nitrogen, and the char samples were degassed for 30 min, in order to remove all weakly chemisorbed CO_2 or steam molecules. The flow rates of steam, CO_2 , and high-purity nitrogen were all set as 80 mL/min.

As a representative, the steam chemisorption curve of PC char is shown in Figure 1. Three sets of chemisorption data can be observed in Figure 1. The first one is the total quantity of chemisorption (C_t). The second one is the quantity of weak chemisorption (C_w). The weak chemisorption of steam or CO_2 was desorbed from char surface during the process of degassing. The last one is the quantity of strong chemisorption (C_s). Strong chemisorption of steam or CO_2 still stayed on the surface of the char after degassing.

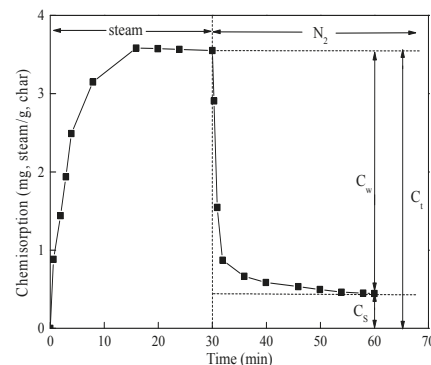


Figure 1. Steam chemisorption of petroleum coke (PC) char.

3. Results and Discussion

3.1. Choice of Kinetic Model of Char–CO₂–Steam Gasification

The mechanism of the char–CO₂ reaction is widely accepted by following description:



Based on the Langmuir–Hinshelwood (L–H) model derived from the theory of absorption and desorption, the char–CO₂ reaction rate can be expressed as Equation (5):

$$r_{CO_2} = \frac{k_1 P_{CO_2}}{1 + (k_2/k_3)P_{CO_2} + (k_1/k_3)P_{CO}} \quad (5)$$

The equation can also be written as:

$$r_{CO_2} = \frac{K_a P_{CO_2}}{1 + K_b P_{CO_2} + K_c P_{CO}} \quad (6)$$

Here, K_a , K_b , and K_c can be defined as following:

$$K_i = A_i e^{-\frac{E_i}{RT}} \quad (7)$$

According to Equation (5), $E_a = E_1$, $E_b = E_2 - E_3$, $E_c = E_1 - E_3$, $A_a = A_1$, $A_b = A_2/A_3$, $A_c = A_1/A_3$. Similarly, the char–steam reaction rate can be expressed as Equation (8):

$$r_{steam} = \frac{K_d P_{H_2O}}{1 + K_e P_{H_2O} + K_f P_{H_2}} \quad (8)$$

In this study, chars were gasified with a steam–CO₂ mixture, so the mechanism of the char–steam–CO₂ reaction should be defined. Interactions in a char–steam–CO₂ reaction have been studied recently [14,16,19], and there were two kinds of mechanisms accepted by researchers. The first assumed that char–CO₂ and char–steam reactions occur at separate active sites (Model A in Figure 2a). Based on this assumption, the overall reaction rate was equal to the sum of rates of these two reactions and can be described as following:

$$r = \frac{K_a P_{CO_2}}{1 + K_b P_{CO_2} + K_c P_{CO}} + \frac{K_d P_{H_2O}}{1 + K_e P_{H_2O} + K_f P_{H_2}} \quad (9)$$

The second mechanism assumed that these two reactions occur at common active sites (Model B in Figure 2b). This means that these two reactions compete for the same active sites, so the overall reaction rate was slower than the sum of reaction rates of these two reactions and can be described as following:

$$r = \frac{K_a P_{CO_2} + K_d P_{H_2O}}{1 + K_b P_{CO_2} + K_c P_{CO} + K_e P_{H_2O} + K_f P_{H_2}} \quad (10)$$

In general, a CO₂ molecule can enter into pores with sizes larger than 1.5 nm, while a steam molecule can enter into pores with sizes larger than 0.6 nm. This led to a phenomenon where some active sites existed in pores with sizes smaller than 1.5 nm and could only be occupied by steam molecules. In addition, the catalytic effect of the inherent mineral on the char–CO₂ reaction was quite different from that on the char–steam reaction [25]. Based on these reasons, it was conjectured that

char–CO₂ and char–steam reactions may share active sites partially, and the modified model was proposed as shown in Figure 2c. Some new parameters were introduced to quantify the amount of shared active sites for char–steam and char–CO₂ reactions. They were defined as following:

$$a = \frac{n_{share}}{n_{CO_2}} \quad (11)$$

$$b = \frac{n_{share}}{n_{steam}} \quad (12)$$

Here, a and b are dimensionless parameters, representing the ratio of the amount of shared active sites to the total amount of active sites for the char–CO₂ reaction and char–steam reaction, respectively. n_{share} is the amount of shared active sites for the char–steam and char–CO₂ reactions. n_{CO_2} and n_{steam} represent the total amount of active sites for the char–CO₂ reaction and char–steam reaction, respectively.

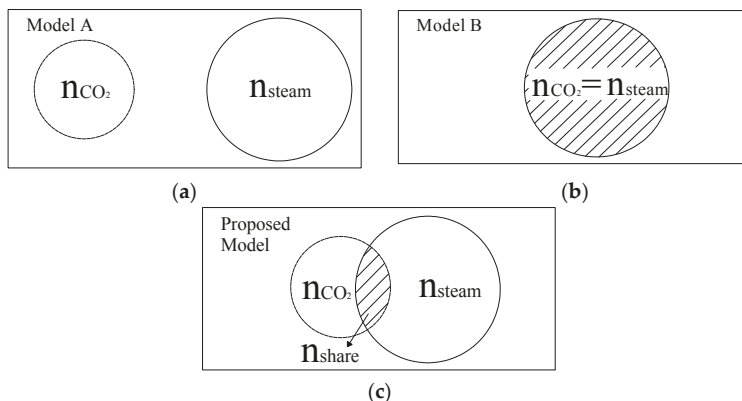


Figure 2. Models of char–CO₂–steam gasification: (a) Model A; (b) Model B; (c) Modified model.

Based on the assumption and these parameters, the overall reaction rate of the char–steam–CO₂ reaction can be derived as:

$$r = \frac{(1-a)K_a P_{CO_2}}{1 + K_b P_{CO_2} + K_c P_{CO}} + \frac{(1-b)K_d P_{H_2O}}{1 + K_e P_{H_2O} + K_f P_{H_2}} + \frac{aK_a P_{CO_2} + bK_d P_{H_2O}}{1 + K_b P_{CO_2} + K_c P_{CO} + K_e P_{H_2O} + K_f P_{H_2}} \quad (13)$$

It was noteworthy that the proposed model (Equation (13)) was the same as Model A (Equation (9)) in the case of $a = b = 0$ ($n_{share} = 0$), while the proposed model was the same as Model B (Equation (10)) in the case of $a = b = 1$ ($n_{share} = n_{CO_2} = n_{steam}$).

3.2. Validation of the Modified Model

3.2.1. Kinetic Parameters of Char Gasification with Sole Gasifying Agent

In this study, the initial gasification rate (r_0) was used as a representative. The concentrations or partial pressures of H₂ and CO were very low and can be neglected at the initial stage of gasification. Therefore, P_{H_2} and P_{CO} were not shown in this study.

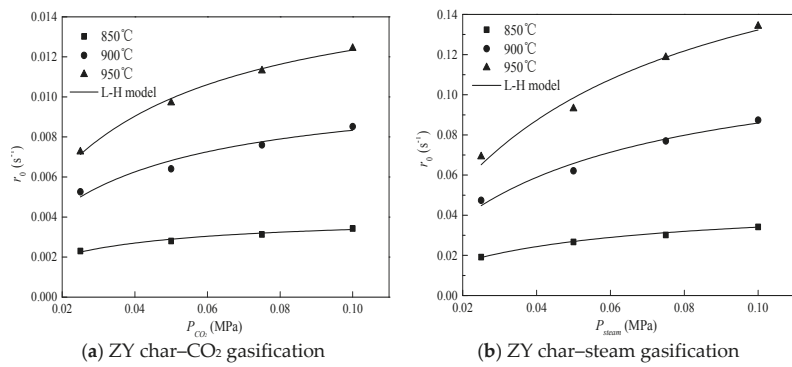


Figure 3. Effect of steam–CO₂ partial pressure on gasification rate.

Figure 3 shows the initial rate of ZY char gasification with a sole gasifying agent as a function of the partial pressure of the gasifying agent (steam/CO₂) and gasification temperature. It was evident that the initial gasification rate of ZY char depended strongly on temperature and steam/CO₂ partial pressure. The initial gasification rate of ZY char increased as the temperature and steam/CO₂ partial pressure increased. Moreover, it is shown in Figure 3 that the L-H model (the fitted line) fitted the experimental data well. In addition, the rate of steam gasification was faster than that of CO₂ gasification when the gasification temperature was fixed. These phenomena were also observed for the other two chars. The kinetic parameters (K_i , A_i , E_i) were determined by the L-H model and the results are listed in Table 2. The activation energies of tested char samples were similar to those reported in the literature [15,16].

Table 2. Kinetic parameters of char–CO₂ and char–steam reactions.

K_i	SF Char		ZY Char		PC Char	
	A_i	E_i (kJ/mol)	A_i	E_i (kJ/mol)	A_i	E_i (kJ/mol)
K_a	2.02×10^7	161.9	1.69×10^4	105.4	1.28×10^6	149.8
K_b	9.50×10^{-3}	-78.6	0.14	-54.3	4.88	-32.0
K_d	4.78×10^6	131.1	6.07×10^7	165.0	1.08×10^7	168.6
K_e	0.21	-51.3	0.11	-52.0	1.90×10^{-4}	-101.1

3.2.2. Kinetic Parameters of Char Gasification with Gasifying Agent Mixture

Initial rates of SF char gasification with a mixture of steam and CO₂ are presented in Figure 4.

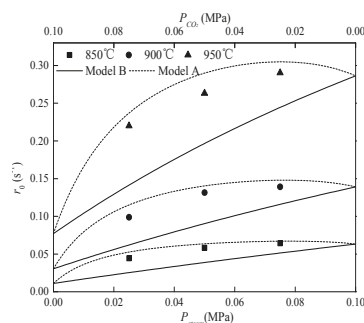


Figure 4. Comparison of experimental data and two conventional models.

In each experiment, the total system pressure was 0.100 MPa. The initial gasification rate of SF char increased as steam partial pressure increased or as CO₂ partial pressure decreased. In addition, the measured gasification rates were always a little lower than the gasification rates predicted by Model A and much higher than the gasification rates predicted by Model B. This means that char–CO₂ and char–steam reactions neither absolutely occur at separate active sites nor absolutely occur at common active sites. Thus, it can be inferred that char–CO₂ and char–steam reactions share active sites partially.

In order to evaluate the interactions by the char–CO₂–steam reaction accurately, the modified model was employed. Comparisons between experimental data and predictions by the modified model are shown in Figure 5.

For these three chars, the good agreement between experimental data and predictions confirmed the validity of the modified model. Parameters [a,b] were obtained by the fitting results and were equal to [0.47,0.25], [0.83,0.21], and [1.00,0.15] for SF char, ZY char, and PC char, respectively. The results shows that parameters [a,b] were constants and hardly varied with gasification temperature. For PC char, parameter a was equal to 1, but parameter b was not. This means that all active sites for char–CO₂ gasification were shared by steam gasification, but many active sites for char–steam gasification were not shared by CO₂ gasification. It is also noteworthy that the value of parameter a was always higher than that of parameter b for each char. It can be inferred that the total amount of active sites for steam gasification was larger than that for CO₂ gasification, based on the assumption of Equations (11) and (12). This result can also explain why rates of steam gasification were always faster than those of CO₂ gasification.

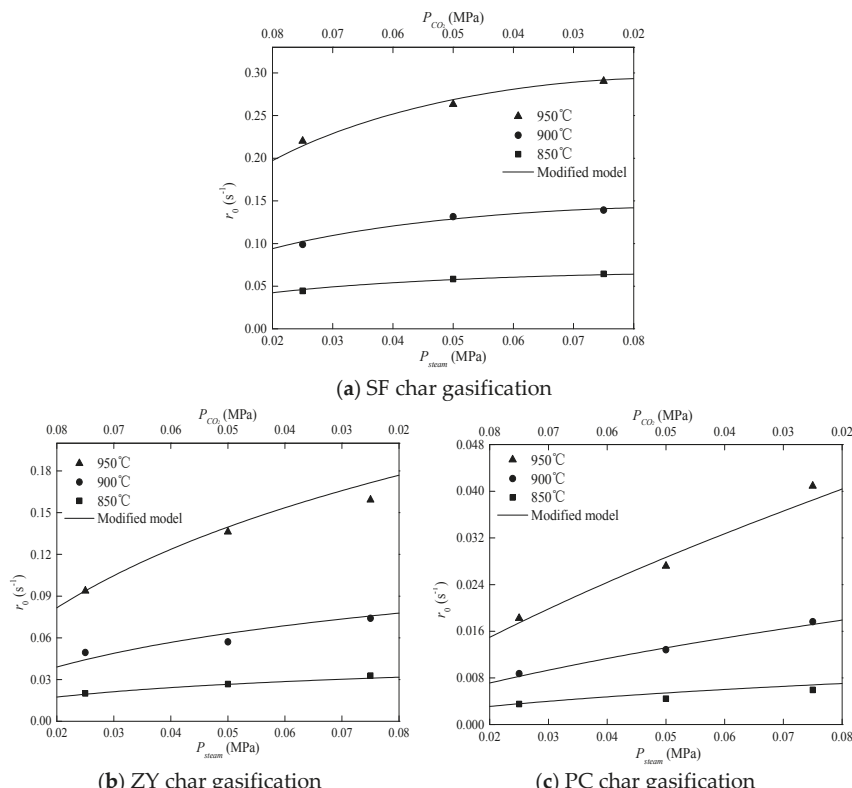


Figure 5. Comparison of experimental data and the modified model.

3.3. Correlations between Chemisorption Quantity and Model Parameters [a,b]

Indeed, active sites play a pivotal role in gasification [26,27], so an experimental method of chemisorption was proposed to quantity the amount of active sites in previous work [23]. Molina et al. [23] found that C_w was related to the presence of the organic components (carbon active sites) of the char, and C_s was related to the presence of the inorganic matter (catalytic active sites) of the char. As shown in Figure 1, C_w , C_s , and C_t can be obtained by the chemisorption experiment. Table 3 lists the chemisorption parameters of the tested chars. For each char, the value of C_s was higher than that of C_w for CO_2 chemisorption, and the opposite trend was observed for steam chemisorption. It was indicated that the catalytic (mineral) matter possessed strong ability to withhold CO_2 molecules. In addition, for all these chars, the values of C_t and C_w for steam chemisorption were always higher than those for CO_2 chemisorption. This means that the total quantity of active sites and the quantity of carbon active sites for char–steam reactions were always more than those for char– CO_2 reactions. This result was in accordance with the result obtained by the modified model.

Table 3. Chemisorption parameters of tested chars.

Samples	CO ₂ Chemisorption			Steam Chemisorption			$C_w(\text{H}_2\text{O})/C_w(\text{CO}_2)$	$C_s(\text{H}_2\text{O})/C_s(\text{CO}_2)$	$C_t(\text{H}_2\text{O})/C_t(\text{CO}_2)$
	C_w	C_s	C_t	C_w	C_s	C_t			
SF char	1.127	1.298	2.425	2.069	0.463	2.531	1.84	0.36	1.04
ZY char	0.979	3.646	4.625	4.295	0.567	4.862	4.39	0.16	1.05
PC char	0.506	1.735	2.241	3.556	0.446	4.002	7.03	0.28	1.78

In order to further study the correlation between chemisorption quantity and parameters [a,b], an equation was derived from the assumption of Equations (11) and (12). It can be expressed by following.

$$n_{share} = bn_{steam} = an_{\text{CO}_2} \Rightarrow \frac{n_{steam}}{n_{\text{CO}_2}} = \frac{a}{b} \quad (14)$$

According to this equation, the ratio of the total amount of active sites for steam gasification to that for CO_2 gasification can be calculated. The ratio values for SF char, ZY char, and PC char were 1.88, 3.95, and 6.67, respectively. The ratio of C_w of steam chemisorption to that of CO_2 chemisorption can also be seen in Table 3. The result shows that values of $C_w(\text{H}_2\text{O})/C_w(\text{CO}_2)$ for SF char, ZY char, and PC char were 1.84, 4.39, and 7.03, respectively. These values were nearly the same as the values of a/b . However, the values of $C_s(\text{H}_2\text{O})/C_s(\text{CO}_2)$ or $C_t(\text{H}_2\text{O})/C_t(\text{CO}_2)$ were absolutely not equal to those of a/b . This phenomenon indicates that parameters [a,b] depended on the presence of the organic components (carbon active sites) of the char and showed little relationship with others factors, including the gasification process and conditions. Based on the principle of gasification, all reactions were initiated at the carbon surface. In addition, carbon active sites consisted of three aspects: nascent sites attached to the aromatic clusters, carbon atoms bonded to heteroatoms, and the edge carbon atoms [24], which were all chemically unstable and could easily be reacted with gasifying agents. This indicates that the gasifying agents can easily occupy the carbon active sites and react with the char on the carbon active sites. Hence, it was concluded that the kinetic parameters [a,b] mainly depended on the carbon active sites of the char. Moreover, the results also validate the modified model proposed in this study.

4. Conclusions

The gasification of three different chars under a mixture of steam and CO_2 was carried out using a TGA. Initial gasification rates of these three chars all increased as steam partial pressure increased or as CO_2 partial pressure decreased. Two conventional gasification models were used to fit the experimental data but showed great difficulties in exactly describing the interactions in the

char–steam–CO₂ reaction. A modified model was proposed based on shared active sites and can exactly predict the gasification rates of these three char gasification with a mixture of steam and CO₂. The results indicate that char–CO₂ and char–steam reactions shared active sites partially and also show that two new parameters in the modified model were constants and did not vary with gasification conditions. In addition, the results from chemisorption tests show that these two parameters just depended on the carbon active sites of the char and thus validated the modified model.

Acknowledgments: This work has been supported by the National Natural Science Foundation of China (21376081; 21676091).

Author Contributions: Xia Liu and Juntao Wei designed the experiments and prepared the manuscript; Wei Huo performed the experiments and analyzed the data; Guangsuo Yu led the project and research.

Conflicts of Interest: The authors declare no conflict of interest.

Nomenclature

A_i	frequency factor for L–H model, s ⁻¹ MPa ⁻¹ ($i = a,d$), MPa ⁻¹ ($i = b,c,e,f$)
A	parameter for the modified model, dimensionless
b	parameter for the modified model, dimensionless
C_s	the quantity of strong chemisorption, mg/mg-char
C_t	the total quantity of chemisorption, mg/mg-char
C_w	the quantity of weak chemisorption, mg/mg-char
E_i	activation energy for L–H model, kJ/mol
K_i	adsorption constant for L–H model, s ⁻¹ MPa ⁻¹ ($i = a,d$), MPa ⁻¹ ($i = b,c,e,f$)
n_{CO_2}	the total amount of active sites for char–CO ₂ reaction
n_{share}	the amount of shared active sites for char–steam and char–CO ₂ reactions
n_{steam}	the total amount of active sites for char–steam reaction
P	the partial pressure of H ₂ /CO/steam/CO ₂ , MPa
r_0	initial gasification rate, s ⁻¹
T	the thermodynamic temperature, K
w_0	the initial mass of char, wt. %
w_{ash}	the sample mass at the end of char gasification, wt. %
w_t	the sample mass at the gasification time of t, wt. %
x	carbon conversion

References

1. Kumar, A.; Jones, D.D.; Hanna, M.A. Thermochemical biomass gasification: A review of the current status of the technology. *Energies* **2009**, *2*, 556–581. [[CrossRef](#)]
2. Zaccariello, L.; Mastellone, M.L. Fluidized-bed gasification of plastic waste, wood, and their blends with coal. *Energies* **2015**, *8*, 8052–8068. [[CrossRef](#)]
3. Roberts, D.G.; Hodge, E.M.; Harris, D.J.; Stubington, J.F. Kinetics of Char Gasification with CO₂ under Regime II Conditions: Effects of Temperature, Reactant, and Total Pressure. *Energy Fuels* **2010**, *24*, 5300–5308. [[CrossRef](#)]
4. Bhatia, S.K.; Perlmutter, D.D. A random pore model for fluid-solid reactions: I. Isothermal, kinetic control. *AIChE J.* **1980**, *26*, 379–385. [[CrossRef](#)]
5. Bhatia, S.K.; Perlmutter, D.D. A random pore model for fluid-solid reactions: II. Diffusion and transport effects. *AIChE J.* **1981**, *27*, 247–254. [[CrossRef](#)]
6. Gavals, G.R. A random capillary model with application to char gasification at chemically controlled rates. *AIChE J.* **1980**, *26*, 577–585. [[CrossRef](#)]
7. Wen, C.Y. Noncatalytic heterogeneous solid-fluid reaction models. *Ind. Eng. Chem.* **1968**, *60*, 34–54. [[CrossRef](#)]
8. Bliek, A.; Lont, J.C.; Van Swaaij, W.P.M. Gasification of coal-derived chars in synthesis gas mixtures under intraparticle mass-transfer-controlled conditions. *Chem. Eng. Sci.* **1986**, *41*, 1895–1909. [[CrossRef](#)]
9. Kirtania, K.; Joshua, J.; Kassim, M.A.; Bhattacharya, S. Comparison of CO₂ and steam gasification reactivity of algal and woody biomass chars. *Fuel Process. Technol.* **2014**, *117*, 44–52. [[CrossRef](#)]

10. Ren, L.; Yang, J.; Gao, F.; Yan, J. Laboratory study on gasification reactivity of coals and petcoke in CO₂/steam at high temperatures. *Energy Fuels* **2013**, *27*, 5054–5068. [[CrossRef](#)]
11. Jayaraman, K.; Gökpal, I.; Jeyakumar, S. Estimation of synergistic effects of CO₂ in high ash coal-char steam gasification. *Appl. Therm. Eng.* **2017**, *110*, 991–998. [[CrossRef](#)]
12. Koba, K.; Ida, S. Gasification reactivities of metallurgical cokes with carbon dioxide, steam and their mixtures. *Fuel* **1980**, *59*, 59–63. [[CrossRef](#)]
13. Muhlen, H.J.; Van Heek, K.H.; Juntgen, H. Kinetic studies of steam gasification of char in the presence of H₂, CO₂ and CO. *Fuel* **1985**, *64*, 944–949. [[CrossRef](#)]
14. Roberts, D.G.; Harris, D.J. Char gasification in the mixtures of CO₂ and H₂O: Competition and inhibition. *Fuel* **2007**, *86*, 2672–2678. [[CrossRef](#)]
15. Huang, Z.M.; Zhang, J.S.; Zhao, Y.; Zhang, H.; Yue, G.X.; Suda, T.; Narukawa, M. Kinetic studies of char gasification by steam and CO₂ in the presence of H₂ and CO. *Fuel Process. Technol.* **2010**, *91*, 843–847. [[CrossRef](#)]
16. Everson, R.C.; Neomagus, H.W.J.P.; Kasaini, H.; Njapha, D. Reaction kinetics of pulverized coal-chars derived from inertinite-rich coal discards: Gasification with carbon dioxide and steam. *Fuel* **2006**, *85*, 1076–1082. [[CrossRef](#)]
17. Li, F.H.; Yan, Q.X.; Huang, J.J.; Zhao, J.T.; Fang, Y.T.; Wang, J.F. Lignite-char gasification mechanism in mixed atmospheres of steam and CO₂ at different pressures. *Fuel Process. Technol.* **2015**, *138*, 555–563. [[CrossRef](#)]
18. Chen, C.; Wang, J.; Liu, W.; Zhang, S.; Yin, J.S.; Luo, G.Q.; Yao, H. Effect of pyrolysis conditions on the char gasification with the mixtures of CO₂ and H₂O. *Proc. Combust. Inst.* **2013**, *34*, 2453–2460. [[CrossRef](#)]
19. Umemoto, S.; Kajitani, S.; Hara, S. Modeling of coal char gasification in coexistence of CO₂ and H₂O considering sharing of active sites. *Fuel* **2013**, *103*, 14–21. [[CrossRef](#)]
20. Wei, J.T.; Guo, Q.H.; Ding, L.; Yoshikawa, K.; Yu, G.S. Synergy mechanism analysis of petroleum coke and municipal solid waste (MSW)-derived hydrochar co-gasification. *Appl. Energy* **2017**, *206*, 1354–1363. [[CrossRef](#)]
21. Guizani, C.; Jeguirim, M.; Valin, S.; Limousy, L.; Salvador, S. Biomass chars: The effects of pyrolysis conditions on their morphology, structure, chemical properties and reactivity. *Energies* **2017**, *10*, 796. [[CrossRef](#)]
22. Jing, X.L.; Wang, Z.Q.; Zhang, Q.; Yu, Z.L.; Li, C.Y.; Huang, J.J.; Fang, Y.T. Evaluation of CO₂ gasification reactivity of different coal rank chars by physicochemical properties. *Energy Fuels* **2013**, *27*, 7287–7293. [[CrossRef](#)]
23. Molina, A.; Montoya, A.; Mondragon, F. CO₂ strong chemisorption as an estimate of coal char gasification reactivity. *Fuel* **1999**, *78*, 971–977. [[CrossRef](#)]
24. Xu, K.; Hu, S.; Su, S.; Xu, C.F.; Sun, L.S.; Shuai, C.; Jiang, L.; Xiang, J. Study on char surface active sites and their relationship to gasification reactivity. *Energy Fuels* **2013**, *27*, 118–125. [[CrossRef](#)]
25. Takarada, T.; Ida, N.; Hioki, A.; Kanbara, S.; Yamamoto, M.; Kato, K. Estimation of gasification of coal chars in steam-nitrogen and carbon dioxide-nitrogen atmospheres. *J. Fuel Soc. Jpn.* **1988**, *67*, 1061–1069. [[CrossRef](#)]
26. Huttinger, K.J.; Nill, J.S. A method for the determination of active sites and true activation energies in carbon gasification: (II) Experimental results. *Carbon* **1990**, *4*, 457–465. [[CrossRef](#)]
27. Miura, K.; Hashimoto, K.; Silveston, P.L. Factors affecting the reactivity of coal chars during gasification, and indexes representing reactivity. *Fuel* **1989**, *68*, 1461–1475. [[CrossRef](#)]



© 2017 by the authors. Licensee MDPI, Basel, Switzerland. This article is an open access article distributed under the terms and conditions of the Creative Commons Attribution (CC BY) license (<http://creativecommons.org/licenses/by/4.0/>).

Article

Energy Recovery Efficiency of Poultry Slaughterhouse Sludge Cake by Hydrothermal Carbonization

Seung-Yong Oh and Young-Man Yoon *

Biogas Research Center, Hankyong National University, 327 Jungang-ro, Anseong-si, Gyeonggi-do 17579, Korea; yong8109@hanmail.net

* Correspondence: yyman@hknu.ac.kr; Tel.: +82-31-670-5665

Received: 11 October 2017; Accepted: 13 November 2017; Published: 16 November 2017

Abstract: Hydrothermal carbonization (HTC) is a promising technology used for bioenergy conversion from bio-wastes such as sewage sludge, livestock manure, and food waste. To determine the optimum HTC reaction temperature in maximizing the gross energy recovery efficiency of poultry slaughterhouse sludge cake, a pilot-scale HTC reactor was designed and operated under reaction temperatures of 170, 180, 190, 200 and 220 °C. During the HTC reaction, the gross energy recovery efficiency was determined based on the calorific value of the HTC-biochar and ultimate methane potential of the HTC-hydrolysate. The poultry slaughterhouse sludge cake was assessed as a useful source for the bioenergy conversion with a high calorific value of approximately 27.7 MJ/kg. The calorific values of the HTC-biochar increased from 29.6 MJ/kg to 31.3 MJ/kg in accordance with the change in the reaction temperature from 170 °C to 220 °C. The ultimate methane potential of the HTC-hydrolysate was 0.222, 0.242, 0.237, 0.228 and 0.197 Nm³/kg-COD_{added} for the reaction temperatures of 170, 180, 190, 200 and 220 °C, respectively. The potential energy of feedstock was 4.541 MJ/kg. The total gross energy recovery (GER_{total}) was 4318 MJ/kg, of which the maximum value in the HTC reaction temperature was attained at 180 °C. Thus, the optimum temperature of the HTC reaction was 180 °C with a maximum GER_{total} efficiency of 95.1%.

Keywords: hydrothermal carbonization; anaerobic digestion; poultry slaughterhouse; sludge cake; energy recovery efficiency

1. Introduction

In Korea, meat consumption (e.g., beef, pork, and poultry) has steeply increased, with food consumption patterns changing with economic growth. In particular, the poultry industry has been growing about 5% each year since 2000, and 993 million poultry heads were slaughtered in 2016. Due to the growth of the poultry industry, several environmental problems have occurred relating to the disposal of wastewater treatment sludge and various poultry processing residues (e.g., blood, feathers, bones) generated from the poultry slaughterhouse [1]. In general, poultry processing residues can be utilized as feedstock for animal feed or compost. However, sludge cake containing moisture above 80% is disposed of after incineration due to the prohibition of direct landfill and ocean disposal, although a high amount of drying energy is needed for the incineration of sludge cake [2]. Nowadays, the interest in energy conversion of sludge waste is increasing due to high sludge disposal costs and limited alternative disposal methods. Poultry slaughterhouses sludge cake is characterized by a high solid content that is composed of protein and fat [3–5]. Hence, sludge cake is considered an effective substrate for anaerobic digestion. However, it is difficult to be fed into conventional anaerobic digesters due to its high solid content [5]. Also, high ammonium nitrogen produced from protein degradation and long chain fatty acids from fat degradation can cause inhibition during the anaerobic digestion process [6].

For these reasons, hydrothermal carbonization (HTC) has recently emerged as an alternative technology for the energy conversion of the slaughterhouse sludge cake. HTC technology is a thermo-chemical process converting biomass to a coal-like material with higher carbon content [7,8]. The energy conversion of biomass by HTC technology has several advantages compared to common biological technology, such as anaerobic digestion. The HTC process requires a short operational time within hours, unlike that of biological processes that require 10 days or more [9]. In addition, waste biomass containing toxic substances cannot be biologically converted to bioenergy, and problems related to hygiene can be of concern when the byproducts generated from biological processing are further utilized. However, the high operational temperatures of the HTC process can decompose potentially toxic organic contaminants and sterilize pathogens. Because of these advantages, HTC technology could be a promising technology for the treatment of waste biomass such as sewage sludge, livestock manure, and food waste [10–12].

The HTC process is mainly composed of a relatively simple closed vessel reactor, containing the wet biomass. The HTC reactor is heated to 170–250 °C and maintained at the saturated vapor pressure that is formed in accordance with the given reaction temperature. During the HTC reaction of wet biomass, the oxygen and hydrogen content of feeding material is reduced, and the solid phase (biochar), the liquid phase (hydrothermal hydrolysate) and a small amount of gas (mainly carbon dioxide) are produced [13,14]. These products are attained by mechanisms including hydrolysis, dehydration, decarboxylation, polymerization and aromatization [8,15]. The solid phase, referred as biochar, can be easily separated due its dewatering property, and utilized as a solid fuel of high calorific value. The hydrothermal hydrolysate generated after the HTC processing requires further treatment since it contains a high amount of soluble organic material and ammonium nitrogen. Recently, anaerobic digestion is preferred for the treatment of hydrothermal hydrolysate in terms of energy recovery efficiency from biomass. In particular, for the HTC reaction, organic matter is solubilized by the hydrolysis reaction and the efficiency of anaerobic digestion can be improved [16,17]. The HTC technology has been studied for a wide range of biomass feedstocks, mainly focusing on herbal and woody biomasses with high contents of lignin, cellulose and hemicellulose, generated from the agricultural sector [13,18,19]. In the case of poultry slaughterhouse sludge cake mainly composed of protein and fat, the HTC process was not so widely investigated, but several studies focused on the properties of solid product, energy recovery rate, biochar yields and its combustion characteristic for slaughterhouse sludge cake. In particular, these studies have only focused on the determination of HTC reaction conditions for the energy recovery and their impacts on the quality of final product (HTC-biochar) without considering the appropriate treatment methods on the HTC-hydrolysate generated as the byproduct during the HTC reaction of sludge cake.

This research was focused on the assessment of total energy recovery from the HTC-biochar and HTC-hydrolysate generated from the HTC reaction with slaughterhouse sludge cake. The goal of this study was to determine the optimum HTC reaction temperature in maximizing the gross energy recovery efficiency from poultry slaughterhouse sludge cake in order to improve the operational efficiency of the HTC process. For this purpose, the energy conversion processes of HTC and anaerobic digestion were proposed. The gross energy recovery efficiency was determined based on the calorific value of the HTC-biochar and ultimate methane potential of the HTC-hydrolysate during the HTC reaction of poultry slaughterhouse sludge cake.

2. Materials and Methods

2.1. Materials

A sludge cake was collected from the wastewater treatment plant at the poultry slaughterhouse facility (Jincheon, South Korea), which has a slaughtering capacity of 300,000 heads per day. A total of 1500 m³/day wastewater is generated and treated by the activated sludge process, and approximately 30 ton of sludge cake is generated daily.

2.2. Proposed Energy Conversion System

The energy conversion system proposed in this study is shown in Figure 1. The activated sludge generated from the wastewater treatment plant of the poultry slaughterhouse is dewatered using solid/liquid separation equipment (a filter press) and sludge cake is fed into the HTC reactor. During the HTC reaction, the organic solid of the sludge cake is fixed as the carbonized solid of high carbon content and solubilized as a lower molecular compound at the same time. Thereafter, the effluent of the HTC reactor is separated into liquid and solid fractions using filter pressing. The solid fraction (HTC-biochar) is utilized as solid fuel for the incineration boiler, and the liquid fraction (HTC-hydrolysate), with its high soluble organic and nitrogen contents, is used for the high performance anaerobic digester. Lastly, digestate discharged from the anaerobic digester is treated at the wastewater treatment plant. This system is able to simultaneously produce solid fuel and biogas through the stepwise process of thermochemical decomposition and biological degradation of organic solid waste.

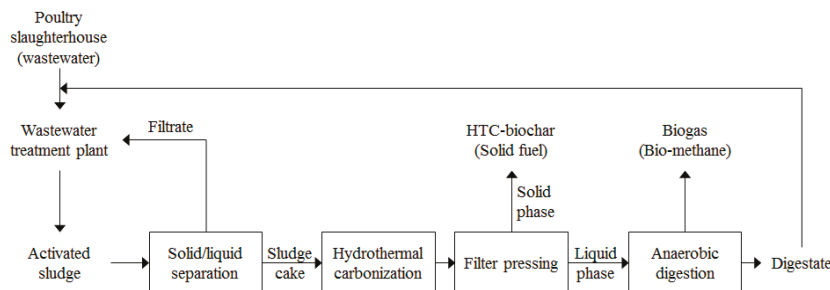


Figure 1. Scheme of the HTC (Hydrothermal carbonization) system for the energy conversion of sludge cake generated at the poultry slaughterhouse wastewater treatment plant.

2.3. Hydrothermal Carbonization

In order to assess the energy yield from the production of the HTC-biochar for several HTC reaction temperatures, a batch-type HTC reactor was designed for the thermochemical treatment of sludge cake (Figure 2). The HTC reactor is a closed system with no potential heat loss via vaporization and condensation loss. The designed HTC reactor has a working volume of 1.5 kg and is equipped with electric heater, temperature sensor, and pressure gauge. The reactor was equipped with a heating coil. A temperature sensor and pressure gauge were inserted into the reactor to monitor inner temperature and a saturated vapor pressure during the HTC reaction. For the HTC reaction test, 1.5 kg of sludge cake was directly placed without additional processing water and covered with an airtight sealant. Setting temperatures were 170, 180, 190, 200 and 220 °C. When each temperature was reached to the set point, each HTC reactor was maintained at the isothermal condition for 60 min. The inner vapor pressures were then maintained at 1.05 MPa at 170 °C, 1.18 MPa at 180 °C, 1.42 MPa at 190 °C, 1.78 MPa at 200 °C, and 2.51 MPa at 220 °C. At the end of the HTC reaction, the reactor was cooled to room temperature using a chiller. The effluent of the HTC reactor was separated into HTC-biochar and HTC-hydrolysate using a filter press. A weight loss of 5–10% occurred due to moisture absorption into the filtering cloth. However, for the theoretical valuation, moisture loss was included in the HTC-hydrolysate.

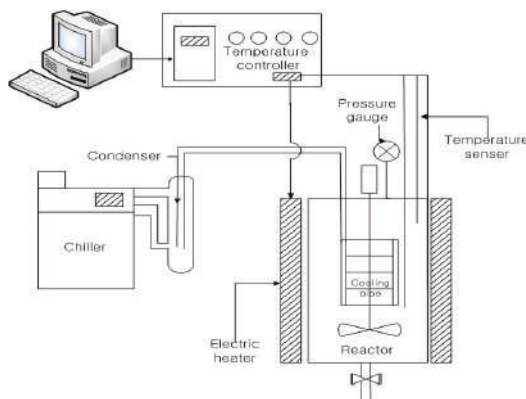


Figure 2. Schematic diagram of the lab-scale HTC batch reactor.

2.4. Methane Production Potential of HTC-Hydrolysate

To assess methane production of the HTC-hydrolysate, a batch type anaerobic reactor was operated under mesophilic conditions (38°C). Anaerobic inoculum in pig slurry was collected from a farm-scale anaerobic digester located in Anseong city, South Korea. The chemical properties of the inoculum are shown in Table 1.

Table 1. Chemical characteristics of inoculum used in the methane potential assay of HTC-hydrolysate.

Sample	pH (-)	TS ¹ (wt. %, w.b. ⁵)	VS ² (wt. %, w.b.)	COD _{Cr} ³ (g/L)	TN ⁴ (wt. %, w.b.)	NH ₄ ⁺ -N (wt. %, w.b.)	Alkalinity (g/L as CaCO ₃)
Inoculum	8.2 (0.0) ⁶	2.6 (0.0)	1.4 (0.0)	25.2 (0.1)	0.4 (0.0)	0.3 (0.0)	19.2 (0.3)

¹ Total solid, ² Volatile solid, ³ Total chemical oxygen demand, ⁴ Total nitrogen, ⁵ Wet basis, ⁶ Standard deviation ($n = 3$).

In order to remove any remaining biodegradable fraction, the inoculum for methane production potential analysis of the HTC-hydrolysate was kept under the mesophilic condition at 38°C for one week. The ratio of substrate to inoculum in all anaerobic batch reactors was equal to 0.3 (g-VS_{substrate}/g-VS_{inoculum}). A working volume for anaerobic batch fermentation was 80 mL of a 160 mL serum bottle. The head space of the serum bottle was filled with N₂ gas and sealed with a butyl rubber stopper. The anaerobic batch reactors for each sample and blank were incubated for up to 96 days in the convection incubator and manually mixed each day during the fermentation period. Methane production potential was calculated as the chemical oxygen demand (COD) content. Methane production potentials of the samples were corrected from the blank value and calibration was done under standard temperature and pressure (STP) conditions. To interpret the progress of cumulative methane production, the parallel first-order kinetic model Equation (1) was employed to fit the cumulative methane production data as in the following equation [20,21].

$$B_t = B_u \left\{ 1 - f_e e^{-k_1 t} - (1 - f_e) e^{-k_2 t} \right\} \quad (1)$$

where B_t (mL) is the amount of methane production at time t , B_u (mL) is the amount of ultimate methane production, f_e (%), g/g) is the organic distribution constant for two first-order kinetics, and k_1 and k_2 are the kinetic constants in the parallel first-order kinetics. This model considers that the degradation of organic matter is carried out in two stages. In addition, f_e distributes the characteristics of the two types of substrates with different reaction rates under anaerobic conditions, and k_1 and k_2 indicate the first-order kinetics constants for the first and the second organic degradation stages.

The degree of COD degradation (COD_{deg}) of the HTC-hydrolysate was defined as the amount of methane produced during the anaerobic fermentation of the HTC-hydrolysate for the theoretical methane potential, as shown in Equation (2) [22].

$$\text{COD}_{\text{deg}} = \frac{V_{\text{biogas}} \times C_{\text{methane}}}{320 \times m_{\text{substrate}} \times \text{COD}_{\text{substrate}}} \times 100 \quad (2)$$

where V_{biogas} is the volume of biogas (mL/day in STP), C_{methane} is the concentration of methane (%), $m_{\text{substrate}}$ is the amount of substrate added to the anaerobic reactor (mL), $\text{COD}_{\text{substrate}}$ is the COD of the substrate (g/mL), and 320 (mL/g-COD_{added} in STP) is the theoretical biochemical methane potential under practical conditions assuming that about 10% of COD added to the anaerobic reactor is consumed in the reformation of biomass.

2.5. Analysis

Total solids (TS), volatile solids (VS), pH, chemical oxygen demand (COD_{Cr}), total nitrogen (TN), ammonium nitrogen ($\text{NH}_4^+ \text{-N}$) and alkalinity were determined based on standard methods [23]. Volatile fatty acid (VFA) concentrations were measured using a gas chromatograph (GC2010, Shimazhu Scientific Instrument, Inc., Columbia, MD, USA) equipped with a flame ionization detector with an automatic sampler. This chemical analysis was performed in three replicates. Element composition (C, H, N, O, S) was determined using an element analyzer (EA1108, Thermo Finnigan LLC, San Jose, CA, USA). The higher heating value (HHV) was measured by the Bomb calorimeter (AC-350, LECO Corporation, St. Joseph, MI, USA) for a dry sample. In the anaerobic batch reactor experiment, total gas production was measured daily for the first five days and then every two or three days, followed by the displacement of acidified brine solution in a burette and recording the volume of displaced solution after correcting for atmospheric pressure [24]. To investigate the gas composition, the CH_4 and CO_2 concentrations in the gas samples were determined using a gas chromatograph (Clarus 680, PerkinElmer, Inc., Waltham, MA, USA) equipped with a thermal conductivity detector and a HayeSepQ packed column (CRS, Inc., Louisville, KY, USA). The column was operated with helium carrier gas at a constant flow rate of 5 mL/min. The set temperatures of the injector, the oven, and the detector were 150 °C, 90 °C and 150 °C, respectively.

2.6. Efficiency Parameters

The energy recovery by the HTC was assessed using gross energy recovery GER, Equation (3), that was presented as the calorific value of the product (biochar and methane) by HHV. Net energy recovery NER, Equation (4), was calculated by subtracting the thermal energy consumed during the HTC reaction and the drying energy of HTC-biochar. The GER efficiency, Equation (6), of the product was estimated as the ratio of the GER_{product} of the product and the gross energy potential GEP_{feedstock}, Equation (5), estimated from the HHV of the dried sludge cake. NER efficiency, Equation (7), was calculated using the ratio between the NER_{product} and GEP_{feedstock}.

$$\text{GER}_{\text{product}} = \text{HHV of product} \quad (3)$$

$$\text{NER}_{\text{product}} = \text{GER}_{\text{product}} - \text{Thermal energy}_{\text{HTC}} - \text{Drying energy}_{\text{biochar}} \quad (4)$$

$$\text{GEP}_{\text{feedstock}} = \text{HHV of feedstock} \quad (5)$$

$$\text{GER}_{\text{product}} \text{ efficiency} (\%) = \frac{\text{GER}_{\text{product}} (\text{MJ})}{\text{GEP}_{\text{feedstock}} (\text{MJ})} \times 100 \quad (6)$$

$$\text{NER}_{\text{product}} \text{ efficiency} (\%) = \frac{\text{NER}_{\text{product}} (\text{MJ})}{\text{GEP}_{\text{feedstock}} (\text{MJ})} \times 100 \quad (7)$$

3. Results and Discussion

3.1. Physicochemical Properties of Sludge Cake

The physicochemical characteristics of the sludge cake generated from the slaughterhouse wastewater treatment plant are shown in Table 2. The physicochemical properties of the sludge cake used in this study were typically different from those of the reported agricultural biomass, such as corn silage, dry straw, cabbage residue, poultry manure, and bedding material. These types of agricultural biomass have a carbon content of 40.7–46.9% and oxygen content of 30.1–44.4%, and calorific values lie between the ranges of 17.8–19.6 MJ/kg [25]. The sludge cake used in this study showed a higher carbon content and lower oxygen content compared to the reported agricultural biomass. In addition, the calorific value was much higher than the reported agricultural biomass.

Table 2. Physicochemical properties of raw sludge cake.

Parameters	Sludge Cake
C	61.9
H	7.2
O	5.3
Elemental composition (wt. %, d.b. ¹)	N 6.5 S 0.0
Ash	19.1
pH (-)	7.1 (0.0) ⁸
TS ² (wt. %, w.b. ³)	16.4 (0.4)
VS ⁴ (wt. %, w.b.)	13.9 (0.1)
VS/TS (%)	84.8 (0.1)
COD _{Cr} ⁵ (g/L)	208.2 (30.4)
TN ⁶ (wt. %, w.b.)	11.0 (0.3)
NH ₄ ⁺ -N (wt. %, w.b.)	2.6 (0.2)
Calorific value ⁷ (MJ/kg, d.b.)	27.7 (1.1)

¹ Dry basis, ² Total solid, ³ Wet basis, ⁴ Volatile solid, ⁵ Total chemical oxygen demand, ⁶ Total nitrogen, ⁷ Calorific value by higher heating value, ⁸ Standard deviation (n = 3).

3.2. Physicochemical Properties of HTC-Biochar and HTC-Hydrolysate

Table 3 shows the physicochemical properties of the products (HTC-biochar) from the HTC reaction. Output yields on a wet basis ranged from 23.8% to 37.7%, showing a decreasing trend as the reaction temperature increased. Solid yields on a dry basis showed a similar trend and the yields were 75.9%, 73.5%, 72.4%, 69.6% and 66.8% at 170, 180, 190, 200 and 220 °C, respectively. TS contents increased from 33.0% to 46.1%, and the ratios of VS to TS decreased from 88.2% to 85.7% with increase in the reaction temperature. These results imply that the rise of the reaction temperature caused an increase in the dewater ability of the product. The O/C atomic ratios of the HTC-biochar did not show any significant changes between 170–200 °C, and fell to 0.06 for the reaction temperature of 220 °C. The H/C atomic ratios decreased from 1.87 to 1.70 with the increase of reaction temperature. The HTC process has similar reaction characteristics as the slow pyrolysis, which is characterized by gradual heating over a wide range of temperatures to produce biochar [26]. The yield and characteristics of pyrolysis products are influenced by different factors, including biomass feedstock and pyrolysis operating parameters (solid residence time, vapor residence time, temperature, heating rate, and carrier gas flow rate). Biochars, which are produced at a slow pyrolysis rate of forest residues, switchgrass, and the solid fraction of pig manure, have elemental characteristics with an O/C ratio between 0.1 and 0.3 and H/C ratio between 0.5 and 0.9 [27]. The calorific values obtained were 29.6, 30.1, 30.2, 30.8 and 31.3 MJ/kg for the reaction temperatures of 170, 180, 190, 200 and 220 °C, respectively, and the energy densification increased from 1.07 for 170 °C to 1.13 for 220 °C. These increased calorific values improve the quality of the HTC-biochar as biofuel. Generally, this effect can be attributed to reaction mechanisms, including hydrolysis, dehydration, decarboxylation [8,15]. The hydrolysis reaction can

convert macro-molecules, such as proteins and lipids, to smaller molecules, and the decarboxylation and dehydration reactions that release H₂O and CO₂ improve the fuel properties of the HTC-biochar [28–30]. According to Qian et al. [31], those calorific values of HTC-biochar are comparable to high quality coal, which typically has a calorific value of 25–35 MJ/kg. Anderson et al. [32] also reported that biochars derived from woody plants had higher calorific values. In a recent study, bamboo sawdust biochar pyrolysis at 500 °C had a high calorific value of 32.4 MJ/kg [33], which was comparable to the calorific value (31.2 MJ/kg for 220 °C) of HTC-biochar in this study. Therefore, the HTC technique is effective in creating a high quality biochar from sludge cake at lower temperatures as compared to lignocellulosic feedstocks. The physicochemical properties of HTC-hydrolysate are shown in Table 4. The output yields of the HTC-hydrolysate were 62.3%, 69.5%, 69.0%, 74.6% and 76.2% for the reaction temperatures of 170, 180, 190, 200 and 220 °C, respectively. The COD content of the HTC-hydrolysate was in the range of 97.9–103.4 g/L. The alkalinity decreased from 9.5 g/L to 8.6 g/L for the reaction temperatures between 170–180 °C and increased to 12.1 g/L for the reaction temperature of 220 °C. Essentially, the HTC reaction is a simultaneous reaction of hydrolysis and carbonization [34]. Therefore, the COD contained in the HTC-hydrolysate may be composed of a soluble substance caused by the hydrolysis reaction during the HTC reaction [35]. The physicochemical properties of HTC-hydrolysate obtained from sludge cake are typically characterized by a high moisture content over 90% compared to the bio oil produced by pyrolysis of lignocellulosic feedstocks with less than 10% moisture content [36]. The high moisture content of HTC-hydrolysate is primarily affected by the moisture content of feedstock, which attenuates the severity of thermo-chemical reaction.

Table 3. Physicochemical properties of HTC-biochar produced at different HTC reaction temperatures.

Parameters	HTC Reaction Temperatures				
	170 °C	180 °C	190 °C	200 °C	220 °C
Output yield ¹ (wt. %, w.b.)	37.7 (0.1) ¹⁰	30.5 (0.1)	31.0 (0.1)	25.4 (0.1)	23.8 (0.1)
Solid yield ³ (wt. %, d.b. ⁴)	75.9 (0.2)	73.5 (0.2)	72.4 (0.2)	69.6 (0.2)	66.8 (0.3)
C	59.9	58.9	57.9	59.2	60.8
H	9.4	8.9	8.4	8.6	8.7
Elemental composition (wt. %, d.b.)	O	7.0	6.2	6.9	6.7
	N	4.1	3.9	4.4	3.7
	S	0.0	0.0	0.0	0.0
	Ash	19.6	22.1	22.4	21.8
Atomic ratio (-)	O/C	0.09	0.08	0.09	0.09
	H/C	1.87	1.81	1.73	1.70
pH (-)		6.2 (0.0)	5.9 (0.0)	5.6 (0.0)	6.0 (0.0)
TS ⁵ (wt. %, w.b.)		33.0 (0.7)	39.5 (0.1)	38.3 (0.1)	44.8 (0.7)
VS ⁶ (wt. %, w.b.)		29.1 (0.8)	34.5 (0.0)	33.5 (0.0)	39.0 (0.5)
VS/TS (%)		88.2 (0.5)	87.4 (0.3)	87.4 (0.2)	87.0 (0.1)
TN ⁷ (g/kg)		14.0 (0.7)	11.5 (0.7)	10.5 (0.5)	12.0 (1.6)
NH ₄ ⁺ -N (g/kg)		3.2 (0.1)	3.2 (0.3)	3.8 (0.2)	3.6 (0.1)
Calorific value ⁸ (MJ/kg, d.b.)		29.6 (0.4)	30.1 (0.1)	30.2 (0.2)	30.8 (0.1)
Energy densification ⁹		1.07 (0.02)	1.09 (0.01)	1.09 (0.01)	1.11 (0.00)
					1.13 (0.01)

¹ Mass of output/mass of feedstock, ² Wet basis, ³ Mass of solid in product/mass of solid in feedstock, ⁴ Dry basis, ⁵ Total solid, ⁶ Volatile solid, ⁷ Total nitrogen, ⁸ Calorific value by higher heating value, ⁹ Calorific value of product/calorific value of feedstock, ¹⁰ Standard deviation (n = 3).

Table 4. Physicochemical properties of HTC-hydrolysate produced at different HTC reaction temperature.

Parameters	HTC Reaction Temperatures				
	170 °C	180 °C	190 °C	200 °C	220 °C
Product yield ¹ (wt. %, w.b. ²)	62.3 (0.1) ⁸	69.5 (0.2)	69.0 (0.2)	74.6 (0.2)	76.2 (0.4)
pH	6.2 (0.0)	5.9 (0.0)	5.6 (0.0)	6.0 (0.0)	6.1 (0.0)
TS ³ (wt. %, w.b.)	6.1 (0.1)	6.6 (0.1)	6.2 (0.01)	6.9 (0.1)	7.2 (0.2)

Table 4. Cont.

Parameters	HTC Reaction Temperatures				
	170 °C	180 °C	190 °C	200 °C	220 °C
VS ⁴ (wt. %, w.b.)	5.9 (0.1)	6.3 (0.1)	6.0 (0.0)	6.7 (0.1)	6.9 (0.1)
VS/TS (%)	96.7 (0.1)	95.5 (0.2)	96.8 (0.2)	97.1 (0.0)	95.8 (0.9)
TN ⁵ (g/L)	9.7 (0.5)	10.5 (0.8)	9.8 (0.3)	10.9 (0.5)	11.5 (0.5)
NH ₄ ⁺ -N (g/L)	3.2 (0.5)	2.9 (0.0)	3.3 (0.0)	3.5 (0.3)	5.3 (0.1)
COD _{Cr} ⁶ (g/L)	99.3 (1.6)	103.4 (1.3)	101.1 (3.7)	103.0 (1.6)	97.9 (1.9)
VFAs ⁷ (mg/L)	188.2 (3.3)	195.7 (2.2)	204.3 (1.5)	191.4 (5.1)	251.6 (2.7)
Alkalinity (g/L)	9.5 (0.0)	9.1 (0.0)	8.6 (0.0)	9.6 (0.4)	12.1 (0.3)

¹ Mass of output/mass of feedstock, ² Wet basis, ³ Total solid, ⁴ Volatile solid, ⁵ Total nitrogen, ⁶ Chemical oxygen demand, ⁷ Volatile fatty acids, ⁸ Standard deviation (n = 3).

3.3. Methane Production Potential of HTC-Hydrolysate

The cumulative methane production of HTC-hydrolysate in each batch anaerobic reactor and the optimization curves fitted by the parallel first order kinetics model are presented in Figure 3. The model parameters and ultimate methane yield are shown in Table 5. In the anaerobic digestion of the HTC-hydrolysate, the degradation of substrate began immediately with the start of anaerobic digestion, with no inhibitory effects observed. Methane production increased steeply for 15 days, and thereafter, showed a slow increase. The cumulative methane production curves were well explained by the parallel first-order kinetics model. The ultimate methane potentials (B_u) of the HTC-hydrolysate were 0.222, 0.242, 0.237, 0.228 and 0.197 Nm³/kg-COD_{added} for the reaction temperatures of 170, 180, 190, 200 and 220 °C, respectively. The COD_{deg} were 70.6%, 75.6%, 74.7%, 72.8% and 62.8% for the reaction temperatures of 170, 180, 190, 200 and 220 °C, respectively. In the anaerobic digestion of the HTC-hydrolysate, there was significant relationship between the COD_{deg} and ultimate methane yields. The highest B_u and COD_{deg} were obtained at the reaction temperature of 180 °C, while the highest reaction temperature (220 °C) caused the lowest B_u and COD_{deg}. In addition, the organic distribution constants (f_e) decreased from 0.927 to 0.717 as the reaction temperature increased. These results indicated that the degraded fractions of organic matter decreased according to the increase of the reaction temperature during the first anaerobic degradation stage. These results are in agreement with Mottet et al. [37]. They reported that the methane yield increased to 0.215 Nm³/kg-COD_{added} with a COD degradability of 56% in the thermal hydrolysis of 165 °C, while the methane yield decreased to 0.142 Nm³/kg-COD_{added} with a COD degradability of 41% in the thermal hydrolysis of 220 °C. These results, along with the reduced methane yield and COD degradability at high thermal reaction temperatures, can be attributed to the Maillard reactions, in which carbohydrates react with amino acids to form melanoidines with a low biodegradability [38,39]. Such a recalcitrant compound is not always generated under conditions of high-temperatures and pressure, while a rapid increase in temperatures within the HTC reactor can more strongly affect the degree of generation of the recalcitrant compound [2].

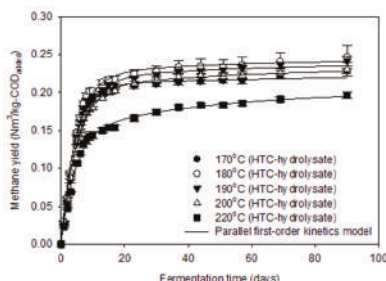


Figure 3. Cumulative methane production and optimization curves based on the parallel first-order kinetics model in the anaerobic digestion of HTC-hydrolysate (vertical bars denote standard deviations).

Table 5. Ultimate methane potential and model parameters based on the parallel first-order kinetics model.

Parameters	HTC Reaction Temperatures				
	170 °C	180 °C	190 °C	200 °C	220 °C
B _u ¹ (Nm ³ /kg-COD _{added})	0.222	0.242	0.237	0.228	0.197
f _e ² (-)	0.927	0.903	0.903	0.873	0.717
k ₁ ³ (1/day)	0.228	0.215	0.190	0.203	0.230
k ₂ ³ (1/day)	0.011	0.028	0.019	0.020	0.024
COD _{Deg} ⁴ (%)	70.6	75.6	74.7	72.8	62.8

¹ Ultimate methane yield, ² Organic distribution constant in the parallel first-order kinetics, ³ Kinetic constants in the parallel first order kinetics, ⁴ Degree of COD degradation.

3.4. Energy Recovery Efficiency

The gross energy recovery (GER) efficiency is shown in Table 6. The potential energy (GEP_{feedstock}) of 1 kg feedstock was 4.541 MJ/kg as HHV. The solid products (i.e., HTC-biochar) produced from 1 kg feedstock were 0.125, 0.121, 0.119, 0.114 and 0.110 kg, and the recovered energy values (GER_{biochar}) from each solid products were 3.689, 3.627, 3.583, 3.516 and 3.432 MJ/kg_{input} for the reaction temperatures of 170, 180, 190, 200 and 220 °C, respectively. The GER_{biochar} efficiencies of the HTC-biochar lie in the range of 75.6–81.2% and decreased with the increase in reaction temperature. Meanwhile, the methane yields produced by the HTC-hydrolysate were 12.0, 15.2, 14.5, 15.3 and 12.9 NL (Volume in STP condition), and the recovered energy values (GER_{methane}) were 0.546, 0.691, 0.657, 0.696 and 0.584 MJ/kg_{input} for the reaction temperatures of 170, 180, 190, 200 and 220 °C, respectively. The GER_{methane} efficiencies ranged from 12.0% to 15.3%. Therefore, the highest GER_{total} was 4.318 MJ/kg at 180 °C, the lowest value was 4.016 MJ/kg at 220 °C and the optimum HTC reaction temperature for maximizing GER_{total} efficiency was 180 °C, which maximized GER_{total} efficiency by 95.1%. The optimum HTC reaction conditions appear to be the net result of two competing mechanisms from the solubilizing transformation of the refractory particulate organics to degradable particulate organic and the stabilizing transformation of soluble organics to undefined refractory compounds [34]. Therefore, further studies concerned with the structural characteristics of the HTC-biochar and the relative biodegradability of the HTC-hydrolysate inherent in structural characteristics are needed to elucidate the optimum conditions of the HTC reaction. Rodríguez-Abalde et al. [3] and Salminen et al. [4] reported methane potentials of 0.46–0.58 Nm³/kg-VS_{added} and 0.60 Nm³/kg-VS_{added} in the anaerobic digestion of poultry slaughterhouse sludge waste, respectively. These values were estimated to be equivalent to 2.776–3.503 MJ/kg_{input} and 3.625 MJ/kg_{input}. Comparing the results of this study, the GER efficiency of the HTC system was much higher than the anaerobic digestion efficiency, suggesting that the GER efficiency of the sludge cake can be improved by adopting HTC technology. However, the results of this study did not take into account the energy consumed during the operation of the HTC reactor and anaerobic digester and only assessed the GER efficiency from the input biomass. Therefore, in order to evaluate the energy conversion efficiency of the sludge cake in terms of commercialization, further work on the net energy balance of the HTC system, considering consumed energy (such as electric power etc.) in the HTC process operation, is needed.

Table 7 shows NER efficiency for the case of direct utilization (e.g., solid fuel) of the sludge cake by simple drying and for the other case of energy conversion by the HTC process. In the case of direct utilization as solid fuel, the drying energy of 1.885 MJ/kg-sludge cake for the solid fuel production was estimated to be physically consumed, considering moisture vaporizing energy (2.255 MJ/kg-moisture). Therefore, the NER and NER efficiency by the simple drying of sludge were assessed as 2.656 MJ/kg_{input} and 58.5%, respectively. In the case of the HTC process, thermal energy for the HTC reaction was estimated to be 0.183 MJ/kg/kg_{input} on the basis of the reported thermal energy of 0.31 kWh/kg-feedstock [40] consumed in the HTC operation, and the drying energy of the HTC-biochar was calculated as 0.416 MJ/kg_{input}. The NER and NER efficiency were calculated as

3.628 MJ and 79.9%, respectively, during energy conversion from the HTC process. Therefore, the HTC technique was assessed to be more efficient than solid fuel production by simple drying of the sludge cake. These results were physically reasonable as a high amount of energy was consumed for the drying of moist sludge cakes with the moisture content above 80%.

Table 6. Gross energy recovery efficiency of sludge cakes in the poultry slaughterhouse with the HTC system.

Parameters	Sludge Cake	HTC Reaction Temperature (°C)				
		170	180	190	200	220
Feedstock	Solid product (kg/kg _{input})	0.164	-	-	-	-
	GEP _{feedstock} ¹ (MJ/kg _{input})	4.541	-	-	-	-
HTC-biochar	Solid product (kg/kg _{input})	-	0.125	0.121	0.119	0.114
	GER _{biochar} ² (MJ/kg _{input})	-	3.689	3.627	3.583	3.516
	GER _{biochar} efficiency ³ (%)	-	81.2	79.9	78.9	77.4
HTC-hydrolysate	Methane yield (NL/kg _{input})	-	12.0	15.2	14.5	15.3
	GER _{methane} ⁴ (MJ/kg _{input})	-	0.546	0.691	0.657	0.696
	GER _{methane} efficiency ⁵ (%)	-	12.0	15.2	14.5	15.3
GER _{total} ⁶ (MJ/kg _{input})		-	4.234	4.318	4.240	4.212
GER _{total} efficiency ⁷ (%)		-	93.2	95.1	93.4	92.7
						88.5

¹ Gross energy potential: calorific value as the HHV of sludge cake, ² Gross energy recovery: calorific value as HHV × solid product of HTC-biochar, ³ GER_{biochar}/GEP_{feedstock} × 100, ⁴ Gross energy recovery: methane yield × HHV of methane, ⁵ GER_{methane}/GEP_{feedstock} × 100, ⁶ Total GER: GER_{biochar} + GER_{methane}, ⁷ GER_{total}/GEP_{feedstock} × 100.

Table 7. Net energy recovery efficiency of sludge cakes in the poultry slaughterhouse with the HTC system.

Parameters	Sludge Cake (Simple Drying)	HTC (180 °C)	
		Biochar	Hydrolysate
Input and output (kg)	1.000	0.305	0.695
Moisture content (kg)	0.836	0.185	-
HTC thermal energy ¹ (MJ/kg _{input})	-	-	0.183
Drying energy ² (MJ/kg _{input})	1.885	0.416	-
GER ³ (MJ/kg _{input})	4.541	3.627	0.691
NER ⁴ (MJ/kg _{input})	2.656	-	3.628
NER efficiency ⁵ (%)	58.5	79.9	-

¹ Thermal energy consumed in the HTC reaction (specific thermal energy consumption = 0.31 kWh/kg_{feedstock} [40]),

² Drying energy consumed for the solid fuel production (2.255 MJ/kg-moisture), ³ Gross energy recovery as HHV,

⁴ Net energy recovery: GER-HTC thermal energy-Drying energy, ⁵ NER/GER of sludge cake × 100.

4. Conclusions

The sludge cake generated from the wastewater treatment plant of the poultry slaughterhouse was a useful source for bioenergy conversion due its high calorific value of approximately 27.7 MJ/kg. The solid yield of the HTC-biochar decreased from 75.9% to 66.8% with the increase of reaction temperature from 170 °C to 220 °C, while the calorific values increased from 29.6 MJ/kg to 31.3 MJ/kg, and the energy densification increased from 1.07 to 1.13. The output yields of the HTC-hydrolysate increased from 62.3% to 76.2% with the rise of the reaction temperature from 170 °C to 220 °C, and the COD contents of the HTC-hydrolysate were in the range of 97.9 and 103.4 g/L. The B_u of the HTC-hydrolysate increased from 0.222 Nm³/kg-COD_{added} to 0.242 Nm³/kg-COD_{added} with the increase of reaction temperature from 170 °C to 180 °C, and decreased to 0.197 Nm³/kg-COD_{added} until 220 °C, in analysis based on the parallel first-order kinetics model. The potential energy of feedstock (1 kg) was 4.541 MJ/kg. The GER_{biochar} efficiencies of the HTC-biochar from the sludge

decreased from 81.2% to 75.6% with the increase of reaction temperature. The GER_{methane} efficiencies were calculated as 12.0, 15.2, 14.5, 15.3 and 12.9 for the reaction temperatures of 170, 180, 090, 200 and 220 °C, respectively. Consequently, the GER_{total} peaked at 4318 MJ/kg for the reaction temperature of 180 °C, and exhibited its lowest value (4016 MJ/kg) for the reaction temperature of 220 °C. Therefore, the optimum HTC reaction temperature for maximizing GER efficiency was 180 °C, and the maximum gross energy recovery efficiency was 95.1%. Also, NER efficiency at the production of solid fuel by simple drying was 58.5% (NER-solid fuel = 2656 MJ/kg_{input}) and NER efficiency at the energy conversion by the HTC process was 79.9% (NER-HTC = 3628 MJ/kg_{input}). These results suggested that the GER and NER efficiencies from the HTC system are much higher than those of the direct utilization of the sludge cake by simple drying and the GER and NER efficiencies of the sludge cake can be improved by adopting HTC technology.

Acknowledgments: This research was supported by a grant (17IFIP-B113506-02) from the development of plant program funded by the Ministry of Land, Infrastructure and Transport of Korean government.

Author Contributions: Seung-Yong Oh and Young-Man Yoon conceived and designed the experiments; Seung-Yong Oh performed the experiments; Young-Man Yoon analyzed the data; Young-Man Yoon wrote the paper.

Conflicts of Interest: The authors declare no conflict of interest. The funding sponsors had no role in the design of the study; in the collection, analysis, or interpretation of data; in the writing of the manuscript, nor in the decision to publish the results.

References

1. Jeon, Y.-W.; Kang, J.-W.; Kim, H.; Yoon, Y.-M.; Lee, D.-H. Unit mass estimation and characterization of litter generated in the broiler house and slaughter house. *Int. Biodeterior. Biodegrad.* **2013**, *85*, 592–597. [[CrossRef](#)]
2. Kim, S.-H.; Kim, H.; Kim, C.-H.; Yoon, Y.-M. Effect of the pretreatment by thermal hydrolysis on biochemical methane potential of piggery sludge. *Korean J. Soil Sci. Fertil.* **2012**, *45*, 524–531. [[CrossRef](#)]
3. Rodríguez-Abalde, A.; Fernández, B.; Silvestre, G.; Flotats, X. Effects of thermal pre-treatments on solid slaughterhouse waste methane potential. *Waste Manag.* **2011**, *31*, 1488–1493. [[CrossRef](#)] [[PubMed](#)]
4. Salminen, E.; Einola, J.; Rintala, J. The methane production of poultry slaughtering residues and effects of pre-treatments on the methane production of poultry feather. *Environ. Technol.* **2003**, *24*, 1079–1086. [[CrossRef](#)] [[PubMed](#)]
5. Salminen, E.; Rintala, J. Anaerobic digestion of organic solid poultry slaughterhouse waste—A review. *Bioresour. Technol.* **2002**, *83*, 13–26. [[CrossRef](#)]
6. Angelidaki, I.; Ahring, B. Thermophilic anaerobic digestion of livestock waste: The effect of ammonia. *Appl. Microbiol. Biotechnol.* **1993**, *38*, 560–564. [[CrossRef](#)]
7. Kleinert, M.; Wittmann, T. Carbonisation of biomass using hydrothermal approach: State-of-the-art and recent developments. In Proceedings of the 17th European Biomass Conference and Exhibition, Hamburg, Germany, 29 June–3 July 2009.
8. Funke, A.; Ziegler, F. Hydrothermal carbonization of biomass: A summary and discussion of chemical mechanisms for process engineering. *Biofuels Bioprod. Bioref.* **2010**, *4*, 160–177. [[CrossRef](#)]
9. Titirici, M.-M.; Thomas, A.; Antonietti, M. Back in the black: Hydrothermal carbonization of plant material as an efficient chemical process to treat the co 2 problem? *New J. Chem.* **2007**, *31*, 787–789. [[CrossRef](#)]
10. Libra, J.A.; Ro, K.S.; Kamann, C.; Funke, A.; Berge, N.D.; Neubauer, Y.; Titirici, M.-M.; Fühner, C.; Bens, O.; Kern, J. Hydrothermal carbonization of biomass residuals: A comparative review of the chemistry, processes and applications of wet and dry pyrolysis. *Biofuels* **2011**, *2*, 71–106. [[CrossRef](#)]
11. Liu, Z.; Quek, A.; Hoekman, S.K.; Balasubramanian, R. Production of solid biochar fuel from waste biomass by hydrothermal carbonization. *Fuel* **2013**, *103*, 943–949. [[CrossRef](#)]
12. Manara, P.; Zabaniotou, A. Towards sewage sludge based biofuels via thermochemical conversion—A review. *Renew. Sustain. Energy Rev.* **2012**, *16*, 2566–2582. [[CrossRef](#)]
13. Basso, D.; Patuzzi, F.; Castello, D.; Baratieri, M.; Rada, E.C.; Weiss-Hortala, E.; Fiori, L. Agro-industrial waste to solid biofuel through hydrothermal carbonization. *Waste Manag.* **2016**, *47*, 114–121. [[CrossRef](#)] [[PubMed](#)]

14. Kim, D.; Yoshikawa, K.; Park, K. Characteristics of biochar obtained by hydrothermal carbonization of cellulose for renewable energy. *Energies* **2015**, *8*, 14040–14048. [[CrossRef](#)]
15. Hoekman, S.K.; Broch, A.; Robbins, C. Hydrothermal carbonization (htc) of lignocellulosic biomass. *Energy Fuels* **2011**, *25*, 1802–1810. [[CrossRef](#)]
16. Ramke, H.-G.; Blöhse, D.; Lehmann, H.-J.; Fettig, J. Hydrothermal carbonization of organic waste. In Proceedings of the Twelfth International Waste Management and Landfill Symposium, Sardinia, Italy, 5–9 October 2009.
17. Costa, J.C.; Barbosa, S.G.; Alves, M.M.; Sousa, D.Z. Thermochemical pre- and biological co-treatments to improve hydrolysis and methane production from poultry litter. *Bioresour. Technol.* **2012**, *111*, 141–147. [[CrossRef](#)] [[PubMed](#)]
18. Mäkelä, M.; Kwong, C.W.; Broström, M.; Yoshikawa, K. Hydrothermal treatment of grape marc for solid fuel applications. *Energy Convers. Manag.* **2017**, *145*, 371–377. [[CrossRef](#)]
19. Volpe, M.; Fiori, L. From olive waste to solid biofuel through hydrothermal carbonisation: The role of temperature and solid load on secondary char formation and hydrochar energy properties. *J. Anal. Appl. Pyrolysis* **2017**, *124*, 63–72. [[CrossRef](#)]
20. Rao, M.; Singh, S. Bioenergy conversion studies of organic fraction of msw: Kinetic studies and gas yield–organic loading relationships for process optimisation. *Bioresour. Technol.* **2004**, *95*, 173–185. [[CrossRef](#)] [[PubMed](#)]
21. Oh, S.Y.; Yoon, Y.M. Assessment of methane potential in hydro-thermal carbonization reaction of organic sludge using parallel first order kinetics. *Korean J. Environ. Agric.* **2016**, *35*, 128–136. [[CrossRef](#)]
22. VDI Standard. *VDI 4630: Fermentation of Organic Materials—Characterization of the Substrate, Sampling, Collection of Material Data, Fermentation Tests*; VDI: Düsseldorf, Germany, 2006; Volume 92.
23. Association, A.P.H.; Water Environment Federation (1998). *Standard Methods for the Examination of Water and Wastewater*; American Public Health Association: Washington, DC, USA; American Water Works Association: Denver, CO, USA; Water Environment Federation: Alexandria, VA, USA, 1994.
24. Beuvink, J.; Spoelstra, S.; Hogendorp, R. An automated method for measuring time-course of gas production of feed-stuffs incubated with buffered rumen fluid. *Neth. J. Agric. Sci.* **1992**, *40*, 401.
25. Oliveira, I.; Blöhse, D.; Ramke, H.-G. Hydrothermal carbonization of agricultural residues. *Bioresour. Technol.* **2013**, *142*, 138–146. [[CrossRef](#)] [[PubMed](#)]
26. Ronse, F.; van Hecke, S.; Dickinson, D.; Prins, W. Production and characterization of slow pyrolysis biochar: Influence of feedstock type and pyrolysis conditions. *GCB Bioenergy* **2013**, *5*, 104–115. [[CrossRef](#)]
27. Brassard, P.; Godbout, S.; Raghavan, V.; Palacios, J.; Grenier, M.; Zegan, D. The production of engineered biochars in a vertical auger pyrolysis reactor for carbon sequestration. *Energies* **2017**, *10*, 288. [[CrossRef](#)]
28. Byrappa, K.; Adschari, T. Hydrothermal technology for nanotechnology. *Prog. Cryst. Growth Charact. Mater.* **2007**, *53*, 117–166. [[CrossRef](#)]
29. Sevilla, M.; Fuentes, A.B. The production of carbon materials by hydrothermal carbonization of cellulose. *Carbon* **2009**, *47*, 2281–2289. [[CrossRef](#)]
30. Quitain, A.T.; Faisal, M.; Kang, K.; Daimon, H.; Fujie, K. Low-molecular-weight carboxylic acids produced from hydrothermal treatment of organic wastes. *J. Hazard. Mater.* **2002**, *93*, 209–220. [[CrossRef](#)]
31. Qian, K.; Kumar, A.; Patil, K.; Bellmer, D.; Wang, D.; Yuan, W.; Huhnke, R. Effects of biomass feedstocks and gasification conditions on the physicochemical properties of char. *Energies* **2013**, *6*. [[CrossRef](#)]
32. Anderson, N.; Jones, J.; Page-Dumroese, D.; McCollum, D.; Baker, S.; Loeffler, D.; Chung, W. A comparison of producer gas, biochar, and activated carbon from two distributed scale thermochemical conversion systems used to process forest biomass. *Energies* **2013**, *6*, 164–183. [[CrossRef](#)]
33. Yang, X.; Wang, H.; Strong, P.; Xu, S.; Liu, S.; Lu, K.; Sheng, K.; Guo, J.; Che, L.; He, L.; et al. Thermal properties of biochars derived from waste biomass generated by agricultural and forestry sectors. *Energies* **2017**, *10*, 469. [[CrossRef](#)]
34. Stuckey, D.C.; McCarty, P.L. The effect of thermal pretreatment on the anaerobic biodegradability and toxicity of waste activated sludge. *Water Res.* **1984**, *18*, 1343–1353. [[CrossRef](#)]
35. Kim, D.; Lee, K.; Park, K.Y. Hydrothermal carbonization of anaerobically digested sludge for solid fuel production and energy recovery. *Fuel* **2014**, *130*, 120–125. [[CrossRef](#)]
36. Jahirul, M.; Rasul, M.; Chowdhury, A.; Ashwath, N. Biofuels production through biomass pyrolysis—A technological review. *Energies* **2012**, *5*, 4952–5001. [[CrossRef](#)]

37. Mottet, A.; Steyer, J.; Déléris, S.; Vedrenne, F.; Chauzy, J.; Carrère, H. Kinetics of thermophilic batch anaerobic digestion of thermal hydrolysed waste activated sludge. *Biochem. Eng. J.* **2009**, *46*, 169–175. [[CrossRef](#)]
38. Martins, S.I.; Jongen, W.M.; Van Boekel, M.A. A review of maillard reaction in food and implications to kinetic modelling. *Trends Food Sci. Technol.* **2000**, *11*, 364–373. [[CrossRef](#)]
39. Bougrier, C.; Delgenes, J.P.; Carrère, H. Effects of thermal treatments on five different waste activated sludge samples solubilisation, physical properties and anaerobic digestion. *Chem. Eng. J.* **2008**, *139*, 236–244. [[CrossRef](#)]
40. Lucian, M.; Fiori, L. Hydrothermal carbonization of waste biomass: Process design, modeling, energy efficiency and cost analysis. *Energies* **2017**, *10*, 211. [[CrossRef](#)]



© 2017 by the authors. Licensee MDPI, Basel, Switzerland. This article is an open access article distributed under the terms and conditions of the Creative Commons Attribution (CC BY) license (<http://creativecommons.org/licenses/by/4.0/>).

Article

Chemical Characteristics and NaCl Component Behavior of Biochar Derived from the Salty Food Waste by Water Flushing

Ye-Eun Lee ^{1,2}, Jun-Ho Jo ¹, I-Tae Kim ¹ and Yeong-Seok Yoo ^{1,2,*}

¹ Division of Environment and Plant Engineering, Korea Institute of Civil Engineering and Building Technology 283, Goyang-daero, Ilsanseo-gu, Goyang-si, Gyeonggi-do 10223, Korea; yeeunlee@kict.re.kr (Y.-E.L.); junkr@kict.re.kr (J.-H.J.); itkim@kict.re.kr (I.-T.K.)

² Department of Construction Environment Engineering, University of Science and Technology, 217, Gajeong-ro, Yuseong-gu, Daejeon KS015, Korea

* Correspondence: ysyoo@kict.re.kr; Tel.: +82-31-910-0298; Fax: +82-31-910-0288

Received: 21 August 2017; Accepted: 30 September 2017; Published: 10 October 2017

Abstract: Biochar is the product of the pyrolysis of organic materials in a reduced state. In recent years, biochar has received attention due to its applicability to organic waste management, thereby leading to active research on biochar. However, there have been few studies using food waste. In particular, the most significant difference between food waste and other organic waste is the high salinity of food waste. Therefore, in this paper, we compare the chemical characteristics of biochar produced using food waste containing low- and high-concentration salt and biochar flushed with water to remove the concentrated salt. In addition, we clarify the salt component behavior of biochar. Peak analysis of XRD confirms that it is difficult to find salt crystals in flushed char since salt remains in the form of crystals when salty food waste is pyrolyzed washed away after water flushing. In addition, the Cl content significantly decreased to 1–2% after flushing, similar to that of Cl content in the standard, non-salted food waste char. On the other hand, a significant amount of Na was found in pyrolyzed char even after flushing resulting from a phenomenon in which salt is dissolved in water while flushing and Na ions are adsorbed. FT-IR analysis showed that salt in waste affects the binding of aromatic carbons to compounds in the pyrolysis process. The NMR spectroscopy demonstrated that the aromatic carbon content, which indicates the stability of biochar, is not influenced by the salt content and increases with increasing pyrolysis temperature.

Keywords: salty food waste; FT-IR; pyrolysis; biochar; NaCl

1. Introduction

The process of dealing with food waste affects climate change by emitting large amounts of greenhouse gases such as methane and carbon dioxide [1]. The Food and Agriculture Organization has reported that one-third of the produced food in the world is thrown away annually [2]. As a result, a new alternative is needed to deal with the vast amounts of food waste.

Biochar is the product that results from the pyrolysis of organic materials in a reduced state. It is distinguished from charcoal by its usage as a soil amendment [3]. Biochar can be produced from a variety of materials including wood, agricultural waste, and livestock waste [4]. Biochar also reduces the release of organic carbon into the air in the form of carbon dioxide by resisting microbial degradation [5,6]. It also helps to prevent climate change by reducing the emission of greenhouse gases such as nitrogen oxides from the soil and methane [7]. Mitchell et al. [8] studied the characteristics of biochar from pyrolyzed lignocellulosic municipal waste, and Prakongkep et al. [9] compared and analyzed 14 types of tropical plant-waste-derived biochar. In addition, Kwapiński et al. [10]

analyzed the temperature-related characteristics of biochar generated from pyrolyzing miscanthus, pine, and willow as a waste management method. They analyzed the characteristics of biochar as a soil amendment and fertilizer. Most studies on biochar have used wood or vegetable raw materials; few have used salty food wastes as raw materials.

As the applicability of biochar to organic waste management has received attention, various studies have been done on its chemical [11] and physical characteristics [12], and its effect on soil [13]. The major difference between other organic materials and biochar is the large proportion of aromatic carbon [14]. Secondly, biochar consists mostly of immobile carbon and nitrogen that microorganisms cannot use as energy sources, thereby having chemical stability (ASTM standard methodology) [15]. In addition, the difference involves cation exchange capacity (CEC) of biochar resulting from the surface charge. Pyrolysis condition is an important factor in determining the physicochemical characteristics of biochar [16]. Hossain et al. [17] revealed that the composition and chemical structure of biochar changed according to the pyrolysis temperature by pyrolyzing the sewage sludge at 300–700 °C. Cantrell et al. [18] showed that the source type could alter the physicochemical characteristics by pyrolyzing five types of manure at 350 and 700 °C.

The major difference between municipal waste (organic waste), such as sewage sludge, livestock waste, and agricultural by-products, and food waste is its high salinity [19,20]. The high salt content of food waste is a major obstacle to recycling and treating food waste. Therefore, we investigate the effect of salt on the conversion into biochar by analyzing the characteristics of pyrolyzed char according to salt content. In this paper, the chemical characteristics of biochar produced using food waste containing low- and high-concentration salt and biochar flushed with water to remove the concentrated salt are compared and analyzed. In addition, the salt component behavior of biochar is clarified.

2. Experimental

2.1. Raw Material

The food waste samples were prepared as shown in Table 1 according to the composition of the standard sample, which is the average food waste composition ratio as determined by the Ministry of Environment of Korea [21]. Food wastes were classified into grains, vegetables, fruits, and meat and fish, and the composition ratios were set to 16%, 51%, 14%, and 19%, respectively, using 10 kinds of materials. The food samples were dried at 80 °C for 48 h and then ground into powder form. NaCl solution was added such that the NaCl contents relative to the dry weight of the food samples became 1%, 3%, and 5%. The samples were then dried again.

Table 1. The standard food waste sample.

Classification	Composition Ratio (wt %)	Methods of Food Ingredient Processing	
		Food Ingredients	Processing Method
Grains	16	Rice (16)	
		Napa cabbage (9)	Cutting width less than 100 mm.
Vegetables	51	Potato (20)	
		Onion (20)	Chop into 5 mm size pieces.
Fruits	14	Daikon (2)	
		Apple (7)	Split into 8 pieces in lengthwise.
Meat and Fish	19	Mandarin/Orange (7)	
		Meat (4)	Cutting width around 3 cm.
		Fish (12)	Split into 4 pieces.
		Egg shell (3)	
Total	100	100	

2.2. Experimental Methods

Dry food samples containing 1%, 3%, and 5% NaCl were pyrolyzed in a pyrolysis reactor of 300 °C, 400 °C, and 500 °C. They were pyrolyzed for 1 h and 30 min, and 10 L/min nitrogen gas was continuously injected. Figure 1 shows the schematic diagram of the pyrolysis apparatus used in this experiment, which consisted of a nitrogen inlet, specimen vat, sample chamber, furnace, a cooling device, and gas combustion device. The total dimensions of pyrolysis reactor are 150 cm * 180 cm * 50 cm and the cooler temperature is maintained at 10 °C. The specimen vat size is 4.5 cm * 5 cm * 20 cm (H * W * D) and only two specimen vat put in the reactor. Feed weight is 100 g each specimen vat. Nitrogen gas was injected 10 min before the samples were added to prevent oxidation of the samples. The temperature in the furnace increased to the target temperature of 300 °C, 400 °C, and 500 °C, and the samples in the sample chamber were then added. The mass yield of biochar at each temperature is 0.56, 0.38, and 0.32 as the pyrolysis temperature increases 300 to 500 °C, and the biochar yields are decreased as the pyrolysis temperature increases [22].

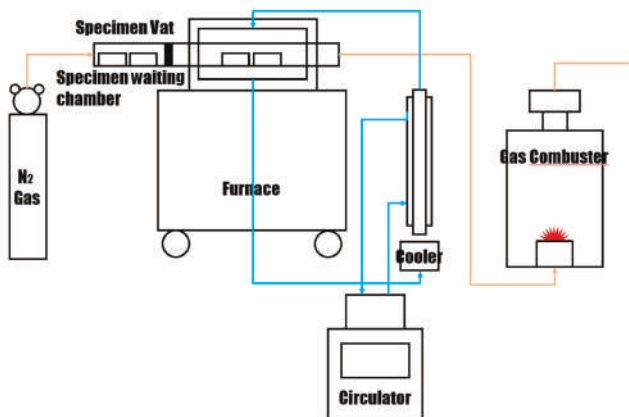


Figure 1. The schematic diagram of the pyrolysis apparatus.

After pyrolysis, the samples were removed, cooled to room temperature, weighed, and ground. They were flushed by stirring 30 g of char in 300 mL of distilled water at a ratio of 1:10 for 30 min. The flushed char was then separated using a filter paper and dried again at 80 °C for 24 h before being stored.

2.3. Analytical Methods

2.3.1. Characterization

A FLASH EA1112 instrument (Thermo Electron, Waltham, MA, USA) was used for the elementary analysis (C, H, S, N) of the salty food waste derived biochar. Oxygen is obtained by difference assuming the sum of C, H, S, N, O, Ash, and NaCl is 100%. In general, either Na or Cl is measured to determine the salt content. However, one study reported a phenomenon in which Na and Cl are independently volatilized in the pyrolysis process of saline-containing fossil fuel [23]. Therefore, both the Na and Cl contents were measured independently. Na content was measured using Agilent 5100 ICP-OES (Agilent Technologies, Santa Clara, CA, USA). Cl was carbonized after mixing 2.5–5 g samples with the milk of lime and drying. 1–2 drops of potassium chromate were added to the sample, which was filtrated after adding water and shaking. The solution was titrated with silver nitrate solution [24]. To measure Cation exchange capacity (CEC) values, 5 g of the sample was then placed in a 100 mL Erlenmeyer flask, and 50 mL of 1 M NH₄OA_c solution was added [25]. The sample was

then shaken for 30 min, filtered, and diluted. The CEC was measured using Agilent 5100 ICP-OES (Agilent Technologies). The Na, K, Mg, and Ca contents were calculated by converting the measured absorbance value (ppm) using the Brown's simplified method.

2.3.2. X-ray Diffraction Spectroscopy

X-ray diffraction (XRD) analysis was carried out to determine the structure of salt in the salty food waste derived-biochar and the change in the molecular structure both before and after flushing. The analytical equipment used was DMAX 2500 (Rigaku, Tokyo, Japan), and the X-ray generator had specifications of 18 kW and 60 kV/300 mA. The 2θ range of the recorded sample was 10–90°.

2.3.3. FT-IR

The infrared spectroscopic analysis was conducted to investigate the effect of salt in salty food waste on the biochars during pyrolysis and its effect on flushing. A VERTEX 80V (Bruker Optics, Ettlingen, Germany) device was used, and infrared rays of 400–4000 nm wavelength were transmitted to determine the characteristics. A transmission analysis was conducted using KBr powder.

2.3.4. NMR

The structure was analyzed using solid-state magic angle spinning ^{13}C NMR analysis to confirm the formation of aromatic carbons, which indicate the stability of the biochar. A DIGITAL AVANCE III 400 MHz (Bruker Biospin AG, Fällanden, Switzerland) was used with a 4 mm probe.

3. Results and Discussion

3.1. Chemical Composition of Salty Food-Waste-Derived Biochar

Table 2 shows the elementary analysis of the salty food waste derived biochar and Na and Cl contents. After flushing, the Cl content decreased to the Cl content in the STD sample, non-salted food waste sample. On the other hand, the Na content significantly increased after flushing compared to the Na content in the STD sample, non-salted food waste sample.

Table 2. The chemical compositions and atomic ratios of biochar produced by salty food waste.

Sample ID	Component, wt %							Atomic Ratio		
	C	H	N	O	Na	Cl	Ash	C/N	H/C	O/C
Dry	51.46	13.22	3.14	32.18	-	-	-	16.38	0.257	0.63
300 °C_STD	60.97	5.37	5.28	23.66	1.21	1.56	4.72	11.55	0.088	0.39
300 °C_1%_B	60.18	5.32	5.29	25.88	3.08	3.17	3.33	11.38	0.088	0.43
300 °C_1%_A	61.70	5.59	5.24	25.19	2.02	1.51	2.28	11.77	0.091	0.41
300 °C_3%_B	58.96	5.17	5.09	22.53	6.63	6.26	8.25	11.58	0.088	0.38
300 °C_3%_A	63.21	5.46	5.16	24.34	2.67	1.50	1.83	12.25	0.086	0.39
300 °C_5%_B	57.29	5.04	4.98	20.83	9.30	8.74	11.86	11.5	0.088	0.36
300 °C_5%_A	62.08	5.81	5.42	23.03	2.62	1.50	3.66	11.45	0.094	0.37
400 °C_STD	64.69	3.64	5.09	17.82	1.92	1.90	8.76	12.71	0.056	0.28
400 °C_1%_B	63.27	3.60	5.38	17.98	4.74	4.18	9.77	11.76	0.057	0.28
400 °C_1%_A	68.71	4.28	5.04	17.60	4.01	1.20	4.37	13.63	0.062	0.26
400 °C_3%_B	57.85	3.24	4.16	21.08	9.22	8.25	13.67	13.91	0.056	0.36
400 °C_3%_A	65.43	3.70	5.26	20.94	3.43	1.19	4.67	12.44	0.057	0.32
400 °C_5%_B	56.15	3.20	3.99	18.74	16.53	12.66	17.92	14.07	0.057	0.33
400 °C_5%_A	68.43	4.34	4.51	19.47	4.64	1.36	3.25	15.17	0.063	0.28
500 °C_STD	70.11	2.81	5.23	8.83	0.51	0.90	13.02	13.41	0.04	0.13
500 °C_1%_B	68.82	2.71	5.22	10.45	3.98	3.74	12.80	13.18	0.039	0.15
500 °C_1%_A	72.07	2.93	5.13	9.43	3.43	1.03	10.44	14.05	0.041	0.13
500 °C_3%_B	65.72	2.69	4.63	10.33	9.65	9.42	16.63	14.19	0.041	0.16
500 °C_3%_A	72.10	2.98	5.13	11.32	5.14	1.49	8.47	14.05	0.041	0.16
500 °C_5%_B	61.78	2.43	4.44	10.50	15.56	13.80	20.85	13.91	0.039	0.17
500 °C_5%_A	73.28	2.92	4.92	11.80	5.35	1.45	7.08	14.89	0.04	0.16

Carbon content increased with the pyrolysis temperature, and there was a difference in the content before and after flushing that resulted from a slight increase in the carbon content relative to the total weight since salt was discharged while flushing.

Hydrogen content decreased as the pyrolysis temperature increased, and there was a difference in the content before and after flushing that resulted from increased relative weight since salt was discharged while flushing, as with carbon.

Nitrogen content did not show any tendency to increase or decrease according to the pyrolysis temperature. However, the nitrogen content of the biochar having 1% salt content decreased after flushing, while the nitrogen contents of the chars having 3% and 5% salt content increased after flushing.

The higher the pyrolysis temperature and the higher the salt content, the lower the O/C ratio, which indicates the stability of biochar [26]. There was a difference before and after flushing, but this phenomenon may have been caused by changes in salt content before and after flushing. When the O/C ratio is 0.2 or less, the half-life of biochar is estimated to be 1000 years or more. When the O/C ratio is 0.2–0.6, the half-life is estimated to be 100–1000 years [27]. The H/C ratio decreased as the pyrolysis temperature increased. There was an obvious difference according to pyrolysis temperature, but there was no difference according to the salt content. The Lower values of H/C and O/C at higher pyrolysis temperatures indicate a stable biochar with a low content of O-based functional groups by demethylation and decarboxylation [28].

A C/N ratio of 12:1 is the most favored for increasing the nitrogen pool plants can use, and a C/N ratio of 20:1 is used for soil conditioners, fertilizers and compost [29]. As the pyrolysis temperature increases, the C/N ratio increases [30]. The experimental result showed that the ratio increased and the ratio was 11–15, which is suitable for use in the soil when the temperature increased from 300 to 500 °C.

H/C, O/C, and C/N values are influenced by pyrolysis temperature, and the content of salt appears to have no noticeable effect on the chemical composition.

The CEC of salty food waste biochars varies depending on raw materials and pyrolysis conditions. Some studies have reported that the CEC value increases as the pyrolysis temperature increase from 300 to 500 °C in relation to the carboxyl groups on the biochar surface [31–33]. Table 3 shows that as the pyrolysis temperature increased from 300 to 400 °C, the CEC value increased, peaked at 400 °C, and decreased again at 500 °C. CEC is determined by substitution sites, O-based functional groups such as –OH or –COOH that are made by decarboxylation and deformation as the pyrolysis temperature. Although, further study is needed to specify the required energy for deformation to contain high CEC, it is reliable trend similar to Wu et al.'s study result [32]. These results may relate to specific surface area. Focusing on O-based functional groups, 300 °C should indicate highest CEC value. But in case of this, complex action between functional group and specific surface area, may be acted on the explanation of this phenomenon. O-based functional groups are decreased gradually as the pyrolysis temperature increases. Specific surface area is increased as the pyrolysis temperature increases [34]. At 300 °C, there could be more O based functional groups but there is lower specific surface area. Overall, the surface area of pyrolyzed char at 300 °C, including O-based functional groups, may be smaller than at 400 °C. About this assumption, further study is needed.

Table 3. CEC of salty food waste derived-biochar before and after flushing.

Sample ID	CEC (cmol/kg)	Extractable Cations (cmolc/kg)			
		Ca	K	Mg	Na
300 °C_STD	25.57	0.39	12.68	0.34	5.56
300 °C_1%_B	22.20	0.29	7.77	0.12	6.99
300 °C_1%_A	18.14	0.45	4.95	0.15	4.67
300 °C_3%_B	22.42	0.17	4.06	0.06	11.08
300 °C_3%_A	20.35	0.47	3.99	0.16	8.04
300 °C_5%_B	110.71	0.35	16.59	0.24	86.26
300 °C_5%_A	22.67	0.58	3.89	0.22	10.07
400 °C_STD	62.94	1.10	44.07	1.37	14.21
400 °C_1%_B	120.39	1.19	62.59	1.15	49.98
400 °C_1%_A	36.65	0.90	18.00	0.64	12.71
400 °C_3%_B	163.48	0.96	52.17	1.23	108.91
400 °C_3%_A	52.60	1.30	16.17	1.00	24.68
400 °C_5%_B	250.72	0.65	53.19	1.29	185.03
400 °C_5%_A	39.46	1.06	9.90	0.86	22.80
500 °C_STD	54.91	0.89	60.38	1.58	1.07
500 °C_1%_B	75.22	0.83	62.37	1.10	14.88
500 °C_1%_A	24.79	1.07	18.23	0.68	7.67
500 °C_3%_B	156.81	0.76	67.59	1.22	92.30
500 °C_3%_A	18.90	1.29	10.63	1.00	9.27
500 °C_5%_B	262.08	0.63	73.55	1.31	189.90
500 °C_5%_A	24.86	1.34	10.29	1.07	14.58

STD: Standard food waste biochar sample without NaCl. A: Salty food waste derived biochar after flushing. B: Salty food waste derived biochar before flushing.

Compared to the CEC value of the char unaffected by salt, the measured CEC value was higher before flushing and lower after flushing. This may have been the result of the phenomenon in which ionized Na^+ is adsorbed on the biochar surface during the flushing. VAN ZWIETEN et al. [35] showed that the application of biochar in a ferrosol significantly increased CEC of soil. In other words, the pyrolyzed salty food waste biochar is able to hold many cations which are nutritional content used by plants and helps the soil fertility improvement.

The extractable values of Na and K were much higher than those of other elements and significantly decreased after flushing. However, the extractable value of Ca increased after flushing. The value of Mg also increased in the case of 1% and 3% at 300 °C. This phenomenon will be discussed in relation to the result of Fourier transform infrared spectroscopy (FT-IR).

The CEC of soil is an important criterion for determining the ability of plants to retain the cations they use. Sandy soil, with its low organic content, has a CEC value of less than 3 cmolc/kg, but heavy clay soil or soil with a high organic content has a CEC value higher than 20 cmolc/kg [36]. Every sample except post-flushing samples (300 °C, 1%; 500 °C, 3%) obtained values higher than 20 cmolc/kg; therefore, it is expected that they are able to be used as soil conditioners.

3.2. XRD Analysis of Salty Food-Waste-Derived Biochar

Figures 2–5 show the XRD results of salty food waste chars before and after flushing according to the pyrolysis temperature, as well as those of NaCl. The crystalline form of NaCl has peaked at 32°, 45.5°, 56.5°, 66°, 75°, and 84° (2θ). When comparing these peaks with the XRD peaks of the salty food waste biochar, the graph before flushing clearly shows the NaCl peaks. On the other hand, the graph after flushing shows that the peaks of NaCl become blurred, and the peaks show a similar tendency to the peaks of standard food waste biochars containing no salt.

In other words, even after carbonization, NaCl remains in the form of crystals. However, after flushing, the remaining NaCl has washed away, and the peaks resemble those of the standard state.

The peak near 23° (2θ) corresponds to the diffuse graphite [37,38]. As the pyrolysis temperature increases, the peak shifts from 20° to 25° (2θ). This means that cellulose crystallinity decreases and turbostratic crystallinity increases [39].

As the pyrolysis temperature increases from 300°C to 500°C , the peak intensity near 28° (2θ) increases. This peak confirms the presence of calcite [40], and the sharper the peak, the better the calcite crystallization.

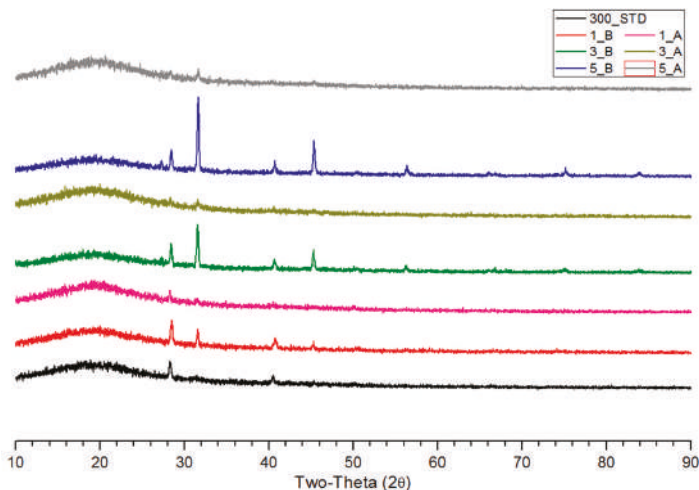


Figure 2. The XRD result of biochar pyrolyzed at 300°C before and after flushing.

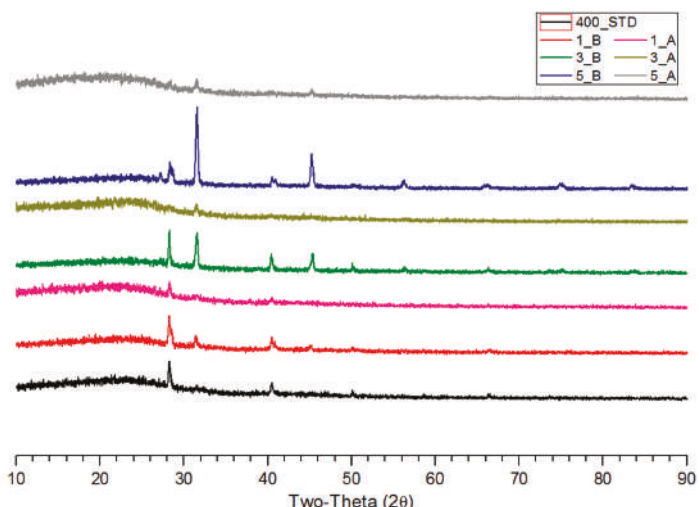


Figure 3. The XRD result of biochar pyrolyzed at 400°C before and after flushing.

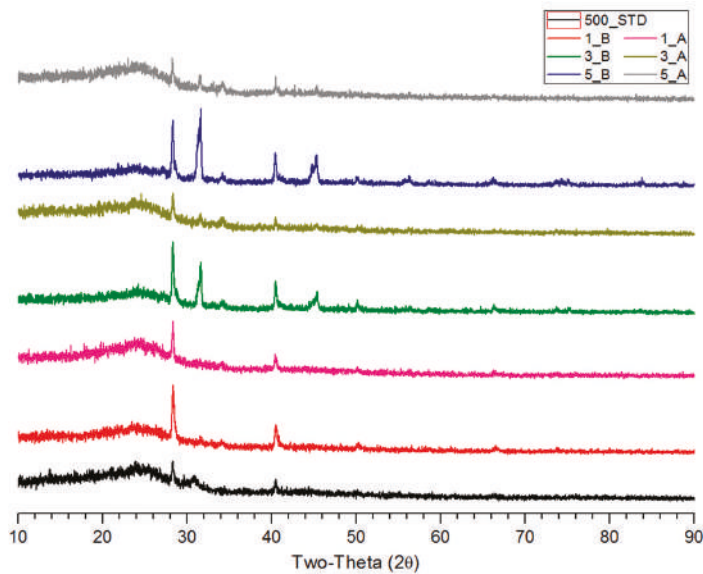


Figure 4. The XRD result of biochar pyrolyzed at 500 °C before and after flushing.

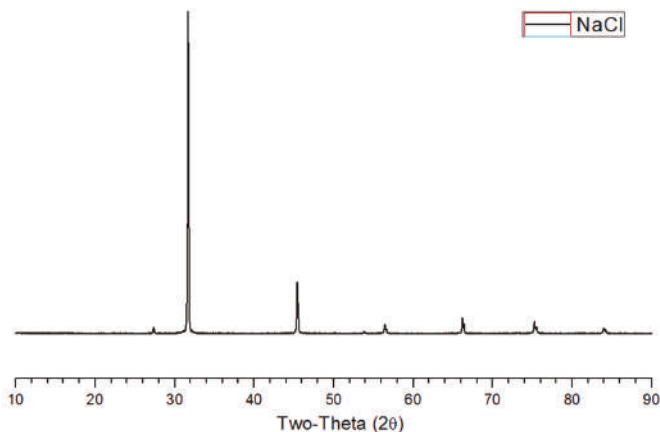


Figure 5. The XRD result of NaCl.

3.3. FT-IR Analysis of Salty Food-Waste-Derived Biochar

Figures 6–8, which show the FT-IR results for salty food waste biochars before and after flushing according to pyrolysis temperature, illustrate that the tendency varies significantly depending on the pyrolysis temperature.

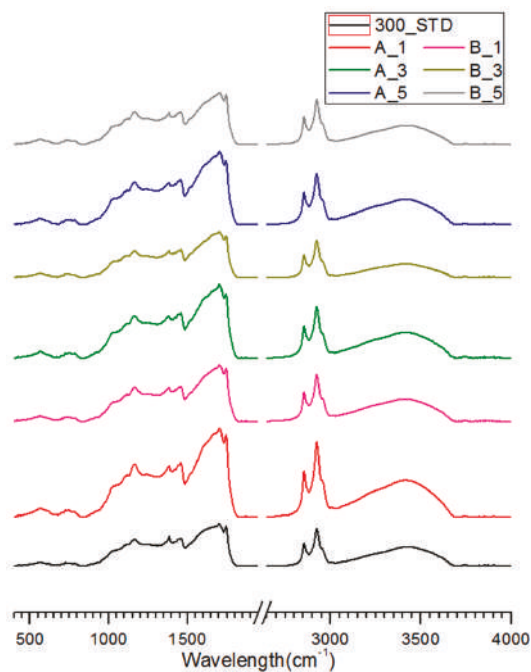


Figure 6. The FT-IR result of biochar pyrolyzed at 300 °C before and after flushing.

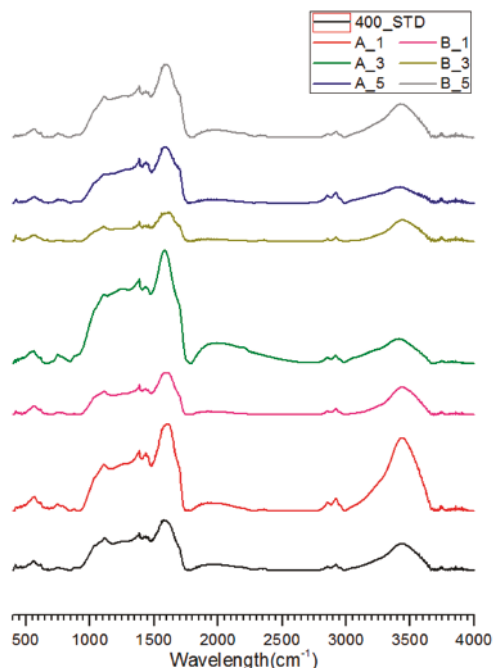


Figure 7. The FT-IR result of biochar pyrolyzed at 400 °C before and after flushing.

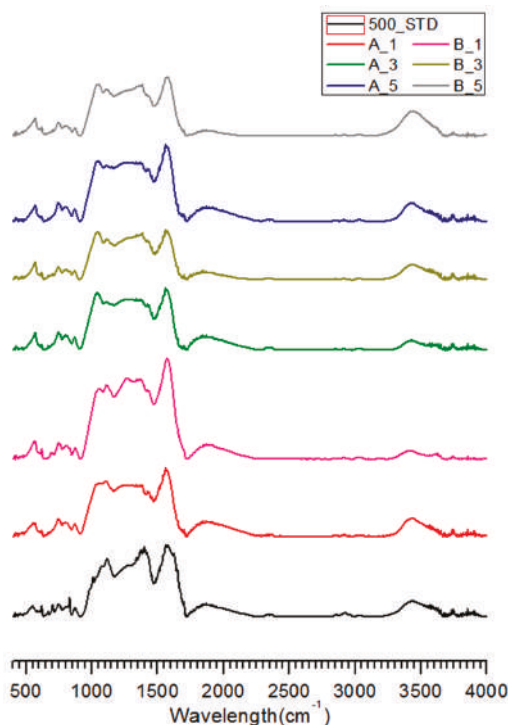


Figure 8. The FT-IR result of biochar pyrolyzed at 500 °C before and after flushing.

Carboxylic (COOH) bonds have a peak of 1700 cm^{-1} and are associated with CEC capability [41,42]. The peak near 1700 cm^{-1} that appeared clearly at $300\text{ }^{\circ}\text{C}$ and $400\text{ }^{\circ}\text{C}$ had almost disappeared at $500\text{ }^{\circ}\text{C}$. Decarboxylation occurred as the pyrolysis temperature increased, thereby decreasing the CEC value.

The peak near $1420\text{--}1440\text{ cm}^{-1}$ increased after flushing. This peak indicates a carboxylate anion [43]. It seems that NaCl is ionized while flushing and Na ions bind to the carboxylate anion, thereby intensifying the peak. The CEC values of Na and K were lower after flushing because Na was already bound, decreasing the capacity to exchange monovalent cations.

The distinctive peak change at $2800\text{--}3000\text{ cm}^{-1}$ indicates a change in aliphatic C-H, and the peak at $3600\text{--}3200\text{ cm}^{-1}$ reveals O-H hydroxyl groups [41,44]. As the pyrolysis temperature increased, the peak of the aliphatic C-H that was clear at $300\text{ }^{\circ}\text{C}$ sharply decreased. The intensity of the peak was insignificant at $500\text{ }^{\circ}\text{C}$. The peak intensity of hydroxyl groups also gradually weakened. According to the elemental analysis, this demethylation phenomenon may have caused the decreased C/H ratio as the pyrolysis temperature increased.

The peak of aromatic C-H at $700\text{--}900\text{ cm}^{-1}$ [32,39] and the aromatic skeletal vibration peak at $1515\text{--}1590\text{ cm}^{-1}$ [42,45] became clearly visible and increased in intensity as the temperature increased from $300\text{ }^{\circ}\text{C}$ to $500\text{ }^{\circ}\text{C}$. This confirms that aromatization occurred as the pyrolysis temperature and stability of biochar increased.

There were differences between the standard peak without any salt and the peak of pyrolyzed carbide containing salt. The peak shift from 550 cm^{-1} to 570 cm^{-1} was clearly shown as the pyrolysis temperature increased and salt content was higher. The peak near $550\text{--}600\text{ cm}^{-1}$ indicates C=O deformation of aromatic ketone [46]. Porchelvi and Muthu [47] investigated that the 552 cm^{-1} peak

results from SO_2 bound to deformed aromatic ketone and found that the 560 cm^{-1} peak appears due to cyano bound to a deformed aromatic ketone. In other words, a higher salt content induces more bonding of a specific compound to the aromatic ketone deformed in the pyrolysis process. More research is necessary for compounds that show a peak at about 570 cm^{-1} . In addition, the peak at 700 cm^{-1} appears in the standard without salt, while the peak is weak or does not appear at all in the presence of salt. This peak indicates the rocking vibration and binding of CH_2 with asymmetric deformation of aromatic ketone [47]. When salt is present, this bond is not induced. Thus, the salt contained in the food wastes affects the aromatic carbon in various biochar structures during the pyrolysis process.

Additionally, the peak at 520 cm^{-1} , which indicates the bonding of C-Cl [47], is not shown regardless of the pyrolysis temperature and salt content. This result demonstrates that the NaCl does not affect the biochar structure in the discrete state as Na^+ and Cl^- .

3.4. NMR Analysis of Salty Food Waste Derived Biochar

Figures 9–11 show the solid-state ^{13}C -NMR spectra. Although there is an apparent difference in the spectra according to the pyrolysis temperature, the peak shift by and influence of salt are negligible.

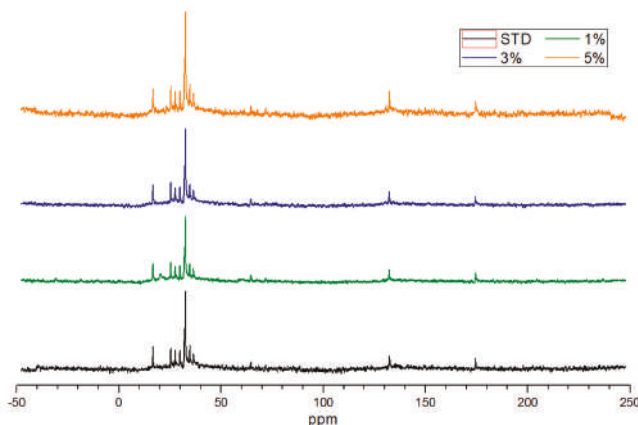


Figure 9. The NMR result of biochar pyrolyzed at $300\text{ }^\circ\text{C}$ before and after flushing.

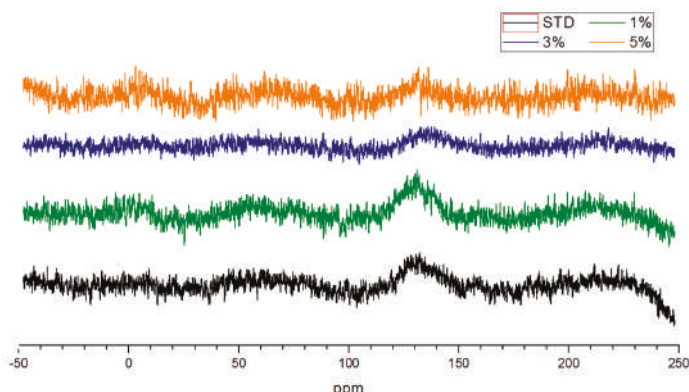


Figure 10. The NMR result of biochar pyrolyzed at $400\text{ }^\circ\text{C}$ before and after flushing.

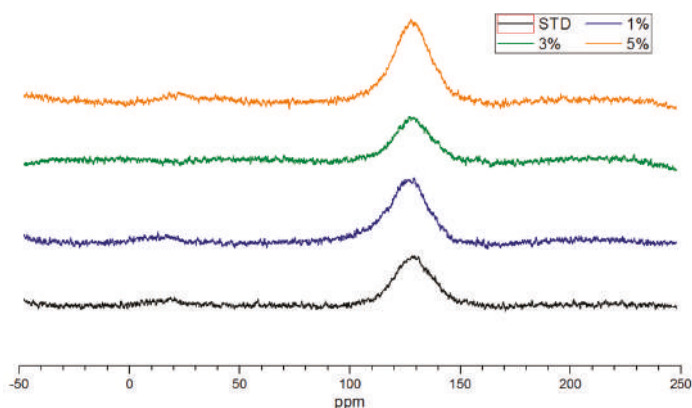


Figure 11. The NMR result of biochar pyrolyzed at 500 °C before and after flushing.

The peaks at 300 °C are shown at 16.5, 25–35, 64.5, 132, and 174.5 ppm, while broad peaks are seen from 128–132 ppm at 400 °C. At 500 °C, a weak peak is shown from 18–27 ppm and the distinct peak are seen from 110–150 ppm. The peak near 15 ppm represents CH₃ carbon, while the peak near 30–65 ppm indicates CH₂ carbon [48]. The aromatic C peak is shown narrowly around 130 ppm and also appears broadly in the range of 90–160 ppm [49,50]. The peak at 160–200 ppm means carboxylic or ketone C=O [41,50].

At 300 °C, significant amounts of CH₃ and CH₂ are present and form the main peak, while aromatic C is insufficient until demethylation occurs. As the pyrolysis temperature increases to 400 °C, sufficient dehydration occurs, and aromatic C is formed. At 500 °C, clearly visible aromatic C indicates the stabilized biochar.

4. Conclusions

In this paper, we analyzed the characteristics of pyrolyzed char according to salt content and temperature (300 °C to 500 °C) in order to determine the effect of salt on conversion into biochar. After flushing, NaCl that remains in crystalline form is washed away under all conditions, and some of Na ions that were washed off and ionized in water are adsorbed again. The pyrolysis temperature is a more important parameter than salt content for the biochar characteristics. As the charring temperature increases, salty food waste became a more stable biochar with lower H/C and O/C values and higher C/N values and aromatic carbon content. Salt content affects aromatic ketone bonding. The higher content of salt in food waste induces more bonding of a specific compound to the aromatic ketones formed in the pyrolysis process. Flushed salty food waste biochar could be recommended as a soil amendment, further studies are needed about the effect of aromatic ketone formation on the soil.

Acknowledgments: This study was supported by the major project (2017-0509) of the Korea Institute of Civil engineering and building Technology (KICT).

Author Contributions: Jun-Ho Jo and Yeong-Seok Yoo designed the experiment devices; Yeong-Seok Yoo and I-Tae Kim contributed to the analysis of experimental results; Ye-Eun Lee performed the experiments, analyzed the data, and wrote the paper.

Conflicts of Interest: The authors declare no conflict of interest.

References

1. Hall, K.D.; Guo, J.; Dore, M.; Chow, C.C. The progressive increase of food waste in America and its environmental impact. *PLoS ONE* **2009**, *4*, e7940. [[CrossRef](#)] [[PubMed](#)]

2. Venkat, K. The climate change and economic impacts of food waste in the United States. *Int. J. Food Syst. Dyn.* **2011**, *2*, 431–446.
3. Lehmann, J.; Joseph, S. Biochar for environmental management: An introduction. In *Biochar for Environmental Management: Science and Technology*; Lehmann, J., Joseph, S., Eds.; Earthscan: London, UK, 2009.
4. Ioannidou, O.; Zabaniotou, A. Agricultural residues as precursors for activated carbon production—A review. *Renew. Sustain. Energy Rev.* **2007**, *11*, 1966–2005. [[CrossRef](#)]
5. Lehmann, J. A handful of carbon. *Nature* **2007**, *447*, 143–144. [[CrossRef](#)] [[PubMed](#)]
6. Brassard, P.; Godbout, S.; Raghavan, V.G.S.; Palacios, J.H.; Grenier, M.; Zegan, D. The production of engineered biochars in a vertical auger pyrolysis reactor for carbon sequestration. *Energies* **2017**, *10*, 288. [[CrossRef](#)]
7. Taghizadeh-Toosi, A.; Clough, T.J.; Condrong, L.M.; Sherlock, R.R.; Anderson, C.R.; Craigie, R.A. Biochar incorporation into pasture soil suppresses in situ nitrous oxide emissions from ruminant urine patches. *J. Environ. Qual.* **2011**, *40*, 468–476. [[CrossRef](#)] [[PubMed](#)]
8. Mitchell, P.J.; Dalley, T.S.L.; Helleur, R.J. Preliminary laboratory production and characterization of biochars from lignocellulosic municipal waste. *J. Anal. Appl. Pyrolysis* **2013**, *99*, 71–78. [[CrossRef](#)]
9. Prakongkep, N.; Gilkes, R.J.; Wiriyakitnateekul, W. Forms and solubility of plant nutrient elements in tropical plant waste biochars. *J. Plant Nutr. Soil Sci.* **2015**, *178*, 732–740. [[CrossRef](#)]
10. Kwapinski, W.; Byrne, C.M.P.; Kryachko, E.; Wolfram, P.; Adley, C.; Leahy, J.J.; Novotny, E.H.; Hayes, M.H.B. Biochar from biomass and waste. *Waste Biomass Valoriz.* **2010**, *1*, 177–189. [[CrossRef](#)]
11. Nguyen, B.T.; Lehmann, J.; Hockaday, W.C.; Joseph, S.; Masiello, C.A. Temperature sensitivity of black carbon decomposition and oxidation. *Environ. Sci. Technol.* **2010**, *44*, 3324–3331. [[CrossRef](#)] [[PubMed](#)]
12. Downie, A.; Alan, C.; Paul, M. Physical properties of biochar. In *Biochar for Environmental Management: Science and Technology*; Earthscan: London, UK, 2009.
13. Jin, H. Characterization of Microbial Life Colonizing Biochar and Biochar-Amended Soils. Ph.D. Thesis, Cornell University, Ithaca, NY, USA, 2010.
14. Lehmann, J.; Rillig, M.C.; Thies, J.; Masiello, C.A.; Hockaday, W.C.; Crowley, D. Biochar effects on soil biota—A review. *Soil Biol. Biochem.* **2011**, *43*, 1812–1836. [[CrossRef](#)]
15. Deenik, J.L.; McClellan, T.; Uehara, G.; Antal, M.J.; Campbell, S. Charcoal volatile matter content influences plant growth and soil nitrogen transformations. *Soil Sci. Soc. Am. J.* **2010**, *74*, 1259–1270. [[CrossRef](#)]
16. Guizani, C.; Jeguirim, M.; Valin, S.; Limousy, L.; Salvador, S. Biomass Chars: The Effects of Pyrolysis Conditions on Their Morphology, Structure, Chemical Properties and Reactivity. *Energies* **2017**, *10*, 796. [[CrossRef](#)]
17. Hossain, M.K.; Strezov, V.; Chan, K.Y.; Ziolkowski, A.; Nelsona, P.F. Influence of pyrolysis temperature on production and nutrient properties of wastewater sludge biochar. *J. Environ. Manag.* **2011**, *92*, 223–228. [[CrossRef](#)] [[PubMed](#)]
18. Cantrell, K.B.; Hunt, P.G.; Uchimiya, M.; Novak, J.M.; Ro, K.S. Impact of pyrolysis temperature and manure source on physicochemical characteristics of biochar. *Bioresour. Technol.* **2012**, *107*, 419–428. [[CrossRef](#)] [[PubMed](#)]
19. Wang, X.; Selvam, A.; Chan, M.; Wong, J.W.C. Nitrogen conservation and acidity control during food wastes composting through struvite formation. *Bioresour. Technol.* **2013**, *147*, 17–22. [[CrossRef](#)] [[PubMed](#)]
20. Chan, M.T.; Selvam, A.; Wong, J.W.C. Reducing nitrogen loss and salinity during ‘struvite’ food waste composting by zeolite amendment. *Bioresour. Technol.* **2016**, *200*, 838–844. [[CrossRef](#)] [[PubMed](#)]
21. Ministry of Environment (MOE). *A Study on Food Waste Reduction Equipment Guidelines and Quality Standard P*; Ministry of Environment: Sejong City, Korea, 2009.
22. Yang, X.; Wang, H.; Strong, P.J.; Xu, S.; Liu, S.; Lu, K.; Sheng, K.; Guo, J.; Che, L.; He, L.; et al. Thermal Properties of Biochars Derived from Waste Biomass Generated by Agricultural and Forestry Sectors. *Energies* **2017**, *10*, 469. [[CrossRef](#)]
23. Quyn, D.M.; Wu, H.; Li, C.-Z. Volatilisation and catalytic effects of alkali and alkaline earth metallic species during the pyrolysis and gasification of Victorian brown coal. Part I. Volatilisation of Na and Cl from a set of NaCl-loaded samples. *Fuel* **2002**, *81*, 143–149. [[CrossRef](#)]
24. Korea Rural Development Administration, National Academy of Agricultural Science. *A Method of Inspection of Physical and Chemical Fertilizers*; Rural Development Administration: Jeonju-si, Korea, 2016.

25. Korea Rural Development Administration, National Academy of Agricultural Science. *Methods of Soil Chemical Analysis*; Rural Development Administration: Jeonju-si, Korea, 2010.
26. Zambon, I.; Colosimo, F.; Monarca, D.; Cecchini, M.; Gallucci, F.; Proto, A.R.; Lord, R.; Colantoni, A. An innovative agro-forestry supply chain for residual biomass: Physicochemical characterisation of biochar from olive and hazelnut pellets. *Energies* **2016**, *9*, 526. [[CrossRef](#)]
27. Spokas, K.A. Review of the stability of biochar in soils: Predictability of O:C molar ratios. *Carbon Manag.* **2010**, *1*, 289–303. [[CrossRef](#)]
28. Mukome, F.N.D.; Zhang, X.; Silva, L.C.R.; Six, J.; Parikh, S.J. Use of chemical and physical characteristics to investigate trends in biochar feedstocks. *J. Agric. Food Chem.* **2013**, *61*, 2196–2204. [[CrossRef](#)] [[PubMed](#)]
29. Mukome, F.N.D.; Parikh, S.J. Chemical, Physical, and Surface characterization of Biochar. In *Biochar: Production, Characterization, and Applications*; CRC Press: Boca Raton, FL, USA, 2015.
30. Ok, Y.S.; Uchimiya, S.M.; Chang, S.X.; Bolan, N. (Eds.) *Biochar: Production, Characterization, and Applications*; CRC Press: Boca Raton, FL, USA, 2015.
31. Yuan, J.-H.; Xu, R.-K.; Zhang, H. The forms of alkalis in the biochar produced from crop residues at different temperatures. *Bioresour. Technol.* **2011**, *102*, 3488–3497. [[CrossRef](#)] [[PubMed](#)]
32. Wu, W.; Yang, M.; Feng, Q.; McGrouther, K.; Wang, H.; Lu, H.; Chen, Y. Chemical characterization of rice straw-derived biochar for soil amendment. *Biomass Bioenergy* **2012**, *47*, 268–276. [[CrossRef](#)]
33. Sohi, S.P.; Krull, E.; Lopez-Capel, E.; Bol, R. A review of biochar and its use and function in soil. *Adv. Agron.* **2010**, *105*, 47–82.
34. Zhao, S.-X.; Ta, N.; Wang, X.-D. Effect of Temperature on the Structural and Physicochemical Properties of Biochar with Apple Tree Branches as Feedstock Material. *Energies* **2017**, *10*, 1293. [[CrossRef](#)]
35. Van Zwieten, L.; Kimber, S.; Morris, S.; Chan, K.Y.; Downie, A.; Rust, J.; Joseph, S.; Cowie, A. Effects of biochar from slow pyrolysis of papermill waste on agronomic performance and soil fertility. *Plant Soil* **2010**, *327*, 235–246. [[CrossRef](#)]
36. Ketterings, Q.; Reid, S.; Rao, R. *Cornell University Agronomy Fact Sheet #22: Cation Exchange Capacity (CEC)*; Cornell University: Ithaca, NY, USA, 2007.
37. Bourke, J.; Manley-Harris, M.; Fushimi, C.; Dowaki, K.; Nunoura, T.; Antal, M.J., Jr. Do all carbonized charcoals have the same chemical structure? 2. A model of the chemical structure of carbonized charcoal. *Ind. Eng. Chem. Res.* **2007**, *46*, 5954–5967. [[CrossRef](#)]
38. Guerrero, M.; Ruiz, M.P.; Millera, Á.; Alzueta, M.U.; Bilbao, R. Characterization of biomass chars formed under different devolatilization conditions: Differences between rice husk and eucalyptus. *Energy Fuels* **2008**, *22*, 1275–1284. [[CrossRef](#)]
39. Keiluweit, M.; Nico, P.S.; Johnson, M.G.; Kleber, M. Dynamic molecular structure of plant biomass-derived black carbon (biochar). *Environ. Sci. Technol.* **2010**, *44*, 1247–1253. [[CrossRef](#)] [[PubMed](#)]
40. Herbert, L.; Hosek, I.; Kripalani, R. *The Characterization and Comparison of Biochar Produced from a Decentralized Reactor Using Forced Air and Natural Draft Pyrolysis*; California Polytechnic State University: San Luis Obispo, CA, USA, 2012.
41. Cheng, C.-H.; Lehmann, J.; Thies, J.E.; Burton, S.D.; Engelhardb, M.H. Oxidation of black carbon by biotic and abiotic processes. *Org. Geochem.* **2006**, *37*, 1477–1488. [[CrossRef](#)]
42. Boeriu, C.G.; Bravo, D.; Gosselink, R.J.A.; van Dam, J.E.G. Characterisation of structure-dependent functional properties of lignin with infrared spectroscopy. *Ind. Crop. Prod.* **2004**, *20*, 205–218. [[CrossRef](#)]
43. Kačuráková, M.; Wilson, R.H. Developments in mid-infrared FT-IR spectroscopy of selected carbohydrates. *Carbohydr. Polym.* **2001**, *44*, 291–303. [[CrossRef](#)]
44. Lammers, K.; Arbuckle-Keil, G.; Dighton, J. FT-IR study of the changes in carbohydrate chemistry of three New Jersey pine barrens leaf litters during simulated control burning. *Soil Biol. Biochem.* **2009**, *41*, 340–347. [[CrossRef](#)]
45. Kubo, S.; Kadla, J.F. Hydrogen bonding in lignin: A Fourier transform infrared model compound study. *Biomacromolecules* **2005**, *6*, 2815–2821. [[CrossRef](#)] [[PubMed](#)]
46. Parimala, K.; Balachandran, V. Structural study, NCA, FT-IR, FT-Raman spectral investigations, NBO analysis and thermodynamic properties of 2', 4'-difluoroacetophenone by HF and DFT calculations. *Spectrochim. Acta Part A Mol. Biomol. Spectrosc.* **2013**, *110*, 269–284. [[CrossRef](#)] [[PubMed](#)]

47. Porchelvi, E.E.; Muthu, S. The spectroscopic (FT-IR, FT-Raman and NMR), NCA, Fukui function analysis first order hyperpolarizability, TGA of 6-chloro-3, 4dihydro-2H-1, 2, 4-benzothiazine-7-sulphonamide1, 1-dioxide by ab initio HF and Density Functional method. *Spectrochim. Acta Part A Mol. Biomol. Spectrosc.* **2014**, *123*, 230–240. [[CrossRef](#)] [[PubMed](#)]
48. Mcbeath, A.V.; Smernik, R.J.; Krull, E.S.; Lehmann, J. The influence of feedstock and production temperature on biochar carbon chemistry: A solid-state ^{13}C NMR study. *Biomass Bioenergy* **2014**, *60*, 121–129. [[CrossRef](#)]
49. Knicker, H.; Hilscher, A.; González-Vila, F.J.; Almendros, G. A new conceptual model for the structural properties of char produced during vegetation fires. *Org. Geochem.* **2008**, *39*, 935–939. [[CrossRef](#)]
50. Brewer, C.E.; Unger, R.; Schmidt-Rohr, K.; Brown, R.C. Criteria to select biochars for field studies based on biochar chemical properties. *BioEnergy Res.* **2011**, *4*, 312–323. [[CrossRef](#)]



© 2017 by the authors. Licensee MDPI, Basel, Switzerland. This article is an open access article distributed under the terms and conditions of the Creative Commons Attribution (CC BY) license (<http://creativecommons.org/licenses/by/4.0/>).

Article

Experimental Model Development of Oxygen-Enriched Combustion Kinetics on Porous Coal Char and Non-Porous Graphite

Gyeong-Min Kim ^{1,†}, Jong-Pil Kim ^{1,†}, Kevin Yohanes Lisandy ¹ and Chung-Hwan Jeon ^{1,2,*}

¹ School of Mechanical Engineering, Pusan National University, Busan 46241, Korea; Energy_min@pusan.ac.kr (G.-M.K.); kjfeel@pusan.ac.kr (J.-P.K.); Kevinlie23@pusan.ac.kr (K.Y.L.)

² Pusan Clean Coal Center, Pusan National University, Busan 46241, Korea

* Correspondence: chjeon@pusan.ac.kr; Tel.: +82-51-510-3051; Fax: +82-51-510-5236

† These authors contributed equally to the work.

Received: 28 August 2017; Accepted: 15 September 2017; Published: 18 September 2017

Abstract: The effect of oxygen-enriched air on low-rank coal char combustion was experimentally investigated. In this work, a coal-heating reactor equipped with a platinum wire mesh in the reaction chamber was used to analyze the combustion temperature, reaction time, and reaction kinetics. Increasing the oxygen content of the primary combustion air increased the combustion temperature and decreased the reaction time. As the oxygen content increased from 21% to 30%, the average temperature increased by 47.72 K at a setup temperature of 1673 K, and the reaction time decreased by 30.22% at the same temperature. The graphite sample exhibited similar trends in temperature and reaction time, although the degree of change was smaller because the pores produced during char devolatilization expanded the active surface available for oxidation of the char sample. A mathematical model was used to define the intrinsic kinetics of the reaction. As the oxygen content increased from 21% to 30%, the reaction rate of the low-rank coal char increased. These results were also compared with those of the graphite sample.

Keywords: combustion; oxygen enrichment; low-rank coal char; char oxidation; reaction kinetics

1. Introduction

Coal is used to generate electricity in coal-fired power plants, despite it being an old technology, due to its abundance and low cost. However, almost half of reserves in the world are low-rank coal, and there is a policy burden due to the high price of high-rank coal. Therefore, in recent years several efforts have been made to develop technologies for utilizing the relatively inexpensive low-rank coal [1,2].

Drying and dewatering technologies for low-rank coal have been reported by many researchers. Both evaporative drying technologies such as rotary drying, fluidized-bed drying, and hot-oil-immersion drying, and non-evaporative drying technologies, such as the hydrothermal dewatering, mechanical/thermal dewatering, and solvent extraction have been studied to enable the utilization of low-rank coal as a high-efficiency energy resource [3]. Various reaction models have been suggested to improve the combustion of low-rank coal [4,5]. A wire-heating reactor was used to measure the temperature of low-rank coal char, and a spot-ignition model was suggested for the evaluation of the intrinsic reaction kinetics and the prediction of the ignition temperature [6]. A pressurized wire-heating reactor was also used to predict the gasification kinetics of low-rank coal char in a CO₂ atmosphere. The study indicated that the reaction kinetics were affected by elevated pressure (up to 30 atm) and high temperature (up to 1723 K) [7]. However, single particle measurements of coal char ignition temperature or gasification reaction kinetics cannot provide small

particle size char measurements (e.g., 75–90 μm); therefore, a method utilizing wire-mesh was used in this study. A pressurized wire-mesh reactor was also utilized in several studies for measuring the kinetics of different gasification reactions (e.g., reactions with O_2 , CO_2 , and H_2O) [3,6,7]. An attempt was made to study the use of sodium ions as an effective catalyst for the gasification of low-rank coal. The experimental results showed that the heat treatment of low-rank coal can thermochemically affect the gasification rate via carbon conversion [8].

On the other hand, oxy-fuel and oxygen-enriched combustion of pulverized coal have been studied in order to improve the efficiency while reducing emissions in coal-fired power plants. Several studies on oxy-fuel combustion have found it to be a promising technology for capturing CO_2 from power plants. The researchers reported combustion fundamentals and modeling under oxy-fuel conditions, including the combustion physics and chemistry [9]. In addition, the effect of the CO_2 gasification reaction on coal char combustion under oxy-fuel conditions was simulated. The results showed that the gasification reaction was affected by both the char burnout time and the relative carbon consumption [10]. Oxygen-enriched combustion, which enhances the energy efficiency and reduces emissions, has also been reported by many researchers as an emerging technology for more efficient power generation [11,12]. The combustion kinetics of coal chars in an oxygen-enriched atmosphere were studied [13–15]. The results showed that under these conditions, the char combustion temperature increased and the char burnout time was reduced [15]. Natural gas combustion systems can also use oxygen-enriched air. In order to investigate the heating rate, emissions, temperature distributions, and fuel consumption in a system with extra oxygen content, 21–30% excess oxygen was used in a gas-fired burner [16]. The effect of oxygen content in a biomass-fueled burner was also investigated. The results showed improvements in flame shape, emission reduction, and burnout for oxygen-enriched combustion using biomass as the fuel [17]. The oxygen enrichment of co-fired blended coal and biomass was studied, with experimental tests on NO_x and SO_x emissions and burnout in atmospheres enriched with 25–30% oxygen being conducted [18].

This study focused on the effect of oxygen-enriched air on combustion when utilizing low-rank coal as an energy source. Experiments on the combustion temperature and the reaction time were conducted using a coal-heating reactor equipped with a platinum wire mesh in the reaction chamber when the oxygen content of the primary combustion air was increased from 21% to 30%. The well-established random pore model (RPM) was proposed several decades ago by Gavalas, Bhatia, and Perlmuter [19–21]. However, the work of Lisandy et al. showed that in some applications, especially when modeling the development of low-rank coal char reaction rates, significant deviations from this model were observed [22–24]. Based on these studies, the reaction kinetics of low-rank coal char under oxygen-enriched combustion conditions were analyzed. A mathematical model was established incorporating experimental thermogravimetric analysis data. The results of the analysis and experiments were compared with those obtained for graphite, which has a poor pore structure.

2. Experimental Methods

2.1. Sample Preparation

Coal particle reactions in conventional coal-fired boilers can generally be divided into two concepts: coal devolatilization and char oxidation [25]. During the devolatilization of raw coal, most of the moisture and volatile matter in the coal are removed, and the remaining particles, referred to as char, are then employed in oxidization or combustion with oxygen at sufficiently high temperatures (1100–1400 $^{\circ}\text{C}$). This study focused on char combustion at high temperatures. Coal char production for the experiment was performed using the following process.

Raw low-rank coal (Indonesian sub-bituminous coal, Figure 1a, was dried for 1 day at 45 $^{\circ}\text{C}$. The sample powder used as fuel had particle sizes of 75–90 μm . After drying, the sample was heated to 1000 $^{\circ}\text{C}$ at a heating rate of 10 $^{\circ}\text{C}/\text{min}$ in a thermogravimetric analyzer (TGA701, LECO Co., St. Joseph, MI, USA) under a nitrogen atmosphere. Figure 1a,b show the differences between the morphologies of

the coal before and after the char production process [26]. As can be seen in Figure 1b, some pores developed in the char due to the removal of moisture and volatile matter. Figure 1c shows graphite powder with particles in the range of 75–90 µm to allow for a comparison with the characteristics of the char. Table 1 summarizes the results of the proximate and ultimate analyses of the raw coal, char, and graphite.

The initial specific surface area of the char was measured by the Brunauer-Emmett-Teller (BET) method using a Micromeritics ASAP 2020 device. The morphologies of the coal samples were examined by scanning electron microscopy (SEM, S3500N, Hitachi, Tokyo, Japan).

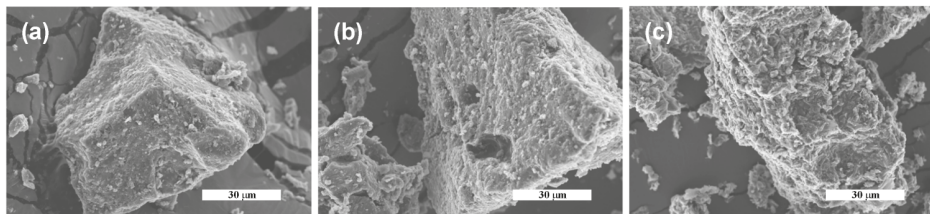


Figure 1. Scanning electron microscopy images of samples for oxygen-enriched combustion: (a) raw coal, (b) char, and (c) graphite.

Table 1. Proximate and ultimate analyses of samples.

Samples	Proximate Analysis (wt %, ad)				Ultimate Analysis (wt %, daf)				
	Moisture	Volatile Matter (daf)	Ash (dry)	Fixed Carbon (daf)	C	H	N	O	S
Raw low-rank coal	14.55	37.20	6.51	41.74	65.45	5.35	0.46	27.07	1.67
Low-rank coal char	1.84	2.16	9.15	86.85	93.26	0.23	0.42	5.78	0.31
Graphite	0.05	1.74	0.0	98.21	99.12	0.81	0.0	0.0	0.06

ad: air-dry basis; daf: dry and ash-free basis; Oxygen by difference.

2.2. Coal Heating Reactor

The experimental setup of the coal-heating reactor for the proposed oxygen-enriched combustion is shown in Figure 2 [27]. The heating reactor can be used for combustion under high-temperature conditions of up to 1750 K. A Pt wire mesh in the chamber was used to generate heat using a direct current (DC) electrical power supply (OPE-18100S, 4.7 kW, ODA Technologies Co., Ltd., Incheon, Korea) that was controlled using computer software. In this study, the temperatures used for coal heating were measured as 1373, 1473, 1573, and 1673 K.

The Pt mesh (99.9% purity) had a wire diameter of 0.04 mm, and the wire interval was 75 µm. In order to obtain the combustion temperature and reaction time, a thermocouple was located at the center of the Pt mesh.

Coal char samples were loaded onto the wire mesh in a thin layer configuration, as shown in Figure 2a. Figure 2b shows the heating state, in which the Pt mesh was heated in the coal-heating reactor. The primary reactant gas was introduced to the chamber during combustion from the atmosphere or from a mixed gas tank for the 21% and 30% oxygen conditions, respectively, and was released back into the atmosphere after combustion.

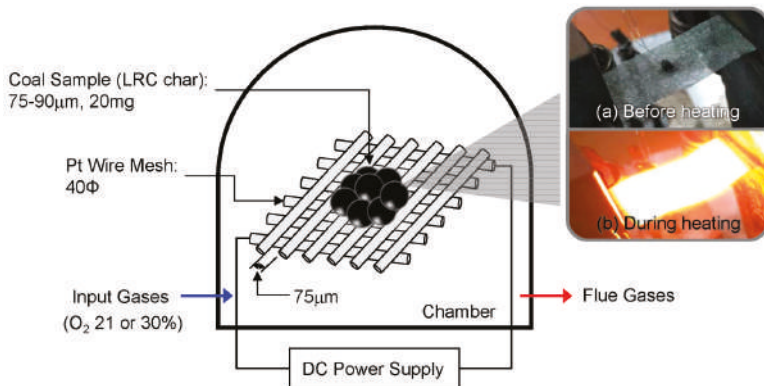


Figure 2. Schematic of the coal heating reactor. The photographs on the right show the system (a) before heating and (b) during heating.

2.3. Numerical Methods for Kinetics

In this study, a mathematical model was suggested for the calculation of the reaction kinetics of coal char combustion with an oxygen content of 21–30% after devolatilization. The carbon conversion ratio can be expressed as:

$$x = \frac{m_0 - m_t}{m_0 - m_{ash}} \quad (1)$$

where m_0 is the initial mass of the coal char, m_t is the mass of the coal char at time t , and m_{ash} is the mass of the ash content.

The apparent reaction rate (R_{app}) is expressed as:

$$R_{app} = \frac{dx}{dt} \quad (2)$$

where R_{app} is the change of carbon conversion over time.

The random pore model (RPM) is widely used to simulate changes in the micropore structure of coal char. However, when considering most low-rank coal or biomass, the random pore model does not fit well with observations. In order to achieve more accurate pore development modeling and reaction rate correlations, the Flexibility-Enhanced Random Pore Model (FERPM) proposed by Lisandy et al. was used in this study [22]. During the coal char oxidation reaction, the loss of coal char occurs rapidly. Thus, the micropore structure of the coal char also changes rapidly. In order to calculate the pore development (S_g), the RPM and FERPM were both used in this study, and they are shown below:

$$\frac{dx}{dt} = k_{RPM}(1-x)\sqrt{1-\psi_{RPM}\ln(1-x)} \quad (3)$$

$$\frac{dx}{dt} = k_{FERPM} \left[(1-x)^a \sqrt{1-\psi_{FERPM}\ln(1-x)} \tanh(cx) + (1-x)^b \right] \quad (4)$$

where k_{RPM} and k_{FERPM} are the initial reaction rates as a function of the temperature, and ψ_{RPM} and ψ_{FERPM} are the structural parameters. a , b and c are extra parameters for improving the accuracy of the prediction.

In order to determine the intrinsic reaction rate of the coal char oxidation (R_{in} , g/cm²·s), an n th-order rate equation was used. The n th-order rate equation of the global reaction can be expressed in its Arrhenius form as:

$$R_{in} = A_{in} \exp\left(-\frac{E_{in}}{R_u T_p}\right) P_{O_2,\infty}^n \quad (5)$$

where A_{in} is the intrinsic pre-exponential factor, E_{in} is the intrinsic activation energy, R_u is the universal gas constant, T_p is the coal char particle temperature, $P_{O_2,\infty}$ is the partial pressure of oxygen in the ambient atmosphere, and n is the reaction order, which was derived from the experimental results. This equation is defined by the reaction order and two Arrhenius parameters, A_{in} and E_{in} .

In order to analyze the oxidation of the coal char, the effect of the internal and external effectiveness factors should be considered. The apparent reaction rate is then expressed as [28]:

$$R_{app} = \eta_{in}\eta_{ex}S_gR_{in} \quad (6)$$

The internal effectiveness factor can be defined by the Thiele modulus (ϕ), which was developed to determine the relationship between the diffusion and the reaction rate in a microporous structure [29,30]:

$$\eta_{in} = \frac{1}{\phi} \left(\frac{1}{\tanh(3\phi)} - \frac{1}{3\phi} \right) \quad (7)$$

$$\phi = \frac{d_p}{2} \sqrt{\frac{(n+1)\nu S_g \rho_p k_{in} R_u T_p P_{O_2,S}^{n-1}}{2D_{eff,O_2}}} \quad (8)$$

where d_p is the diameter of the coal char, ν is the stoichiometric coefficient (i.e., 0.0833 moles of O_2 consumed per gram of reacted carbon), ρ_p is the apparent density, and D_{eff,O_2} is the effective O_2 diffusion coefficient in the coal char surface.

D_{eff,O_2} is calculated as:

$$D_{eff,O_2} = \frac{\varepsilon}{\tau} D \quad (9)$$

where ε is the porosity, D is the diffusivity, and τ is the tortuosity coefficient of the coal char pore, and its value is assumed to 1.414 [31]. The diffusivity, D , is calculated:

$$D = \frac{1}{\frac{1}{D_{AB}} + \frac{1}{D_k}} \quad (10)$$

where D_{AB} is the binary diffusivity and D_k is the Knudsen diffusivity, which is the diffusion that occurs when the diameter of the pore is comparable to or smaller than the mean free path of the gas particles involved. These diffusivities are expressed as [29–31]:

$$D_k = 4580 d_{pore} \sqrt{\frac{T_p}{M_A}} \quad (11)$$

$$D_{AB} = \frac{0.02628 T^{3/2}}{M_{AB}^{1/2} \sigma_{AB}^2 \Omega_{AB} P} \quad (12)$$

where d_{pore} is the diameter of the coal char pore, M_A is the molar mass, M_{AB} is the mixed molar mass of A and B, σ_{AB} is the particle collision diameter, Ω_{AB} is the collision integral, and P is the total pressure of the system.

The external effectiveness factor (η_{ex}) is an expression of gas transport to the boundary layer, which is the ratio of the partial pressure of the particle surface to the ambient atmosphere surrounding the coal char particle, and is expressed as:

$$\eta_{ex} = \frac{P_{O_2,S}}{P_{O_2,\infty}} \quad (13)$$

The kinetic coefficients of the reaction can be considered by the linear regression method as follows:

$$R_{app} = \eta_{in}\eta_{ex}^n S_g A_{in} \exp\left(-\frac{E_{in}}{R_u T_p}\right) P_{O_2,\infty}^n \quad (14)$$

$$\ln\left(\frac{R_{app}}{\eta_{in}\eta_{ex}^n P_{O_2,\infty}^n}\right) = \ln A_{in} S_g - \frac{E_{in}}{R_u T_p} \quad (15)$$

$$\ln(R_{app}) = n \ln(\eta_{ex} P_{O_2,\infty}) + \ln\left\{\eta_{in} S_g A_{in} \exp\left(-\frac{E_{in}}{R_u T_p}\right)\right\} \quad (16)$$

3. Results and Discussion

3.1. Combustion Temperature and Reaction Time

Table 2 shows the variations in combustion temperature and reaction time for low-rank coal char and graphite when the oxygen content of the primary combustion air in the coal-heating reactor was increased from 21% to 30%. The experimental data are the mean value from 10 of replicate experiments and measurements. The setup temperature, or the combustion temperature during char oxidation, was set to four values. Most of the results shown in Table 2 show more significant reaction time reductions in the lower temperature region (e.g., a 35–38% reaction time reduction at a setup temperature of 1373 K, as compared to a 28–30% reduction at a setup temperature of 1673 K). These results suggest that improved reaction rates can be achieved at lower combustion temperatures.

Table 2. Combustion temperatures and reaction time variations for oxygen-enriched combustion.

Samples	Low-Rank Coal Char				Graphite			
	O ₂ 21% (N ₂ Balance)		O ₂ 30% (N ₂ Balance)		O ₂ 21% (N ₂ Balance)		O ₂ 30% (N ₂ Balance)	
Setup Temperature (K)	Maximum Temperature (K)	Reaction Time (s)						
1373	1411.34	2.6	1420.37	1.6	1393.71	4.4	1415.30	2.88
1473	1514.68	1.98	1532.83	1.35	1525.65	2.5	1539.83	1.68
1573	1619.17	1.7	1658.47	1.15	1616.79	1.8	1654.08	1.25
1673	1721.69	1.43	1769.41	1	1705.29	1.37	1764.35	0.98

In the case of low-rank coal char at a setup temperature of 1373 K, the difference between the maximum temperatures for oxygen contents of 21% and 30% was 9 K. When the setup temperature was increased, this temperature difference tended to increase. The difference between the maximum temperatures was 47 K at a setup temperature of 1673 K.

In comparison, graphite exhibited an identical trend to that of the low-rank coal char. In the case of graphite at a setup temperature of 1373 K, the difference between the maximum temperatures for oxygen contents of 21% and 30% was 21 K. Additionally, it exhibited an increase in maximum temperature of 59.06 K at a setup temperature of 1673 K.

The results suggest that low-rank coal char developed a surface pore structure during the devolatilization process, and that this pore structure contributed to the combustion reaction by increasing the surface area. On the other hand, graphite, which has a carbon content of 99.21%, had a poor pore structure. It therefore exhibited a slow reaction at relatively low setup temperature. However, a higher environmental temperature resulted in a more effective surface for combustion, with the oxidation reaction occurring so rapidly at the particle surface that the oxidation gas could not diffuse through the pores. For this reason, the reaction time for graphite became similar to that of low-rank coal char at temperatures around 1673 K.

3.2. Reaction Kinetics

The surface area of coal char as calculated by RPM and FERPM can be expressed as follows:

$$S_{g,RPM} = S_0(1-x)\sqrt{1 - \psi_{RPM} \ln(1-x)} \quad (17)$$

$$S_{g,FERPM} = S_0[(1-x)^a \sqrt{1 - \psi_{FERPM} \ln(1-x)} \tanh(cx) + (1-x)^b] \quad (18)$$

An experiment was performed during thermogravimetric analysis (TGA) in order to define the structural parameters ψ_{RPM} and ψ_{FERPM} . Samples of 15 mg of coal char or graphite were heated to 1273 K at a ramp rate of 20 K/min under a N₂ atmosphere. After remaining isothermal at 1273 K for 10 min, the gas was changed to air and the samples were reacted isothermally at 1273 K for 30 min. The structural parameters ψ_{RPM} and ψ_{FERPM} were obtained by fitting the TGA analyses with the RPM and FERPM, as shown in Figures 3 and 4. As discussed previously, the surface areas S_g determined in Figures 3 and 4 shows that graphite had almost no microporous structure when compared to the low-rank coal char. Moreover, the FERPM was calculated using a correction function with the optimal values of the pore development model during coal combustion, including gasification. The correlation coefficient between the experimental and fitting results using the RPM was 0.6532 for low-rank coal char, while the value for graphite was 0.8376. The FERPM led to much higher correlation coefficients, with the value for low-rank coal char being 0.9956, and that for graphite being 0.9980. The improvement in the fitting correlation would be very helpful for modeling purposes as predictions that are more accurate can be made using the revised model. Table 3 summarizes the calculated structural parameters (ψ) and initial particle surface areas (S_0) of low-rank coal char and graphite. The structural parameter of low-rank coal char shows a good agreement with the prediction obtained by using the equation proposed by the literature [22], which predicts that the coal with a fixed carbon content of 42% should have a structural parameter about 0.46. However, the results for graphite, which has a carbon content of 98%, did not agree with the value provided by FERPM equation, which predicted a structural parameter of around 1. This may be due to the different fuel types used in the literature, which predicted structural changes for the thermal coal. This means that graphite was not considered in the range of fuel types used by the literature.

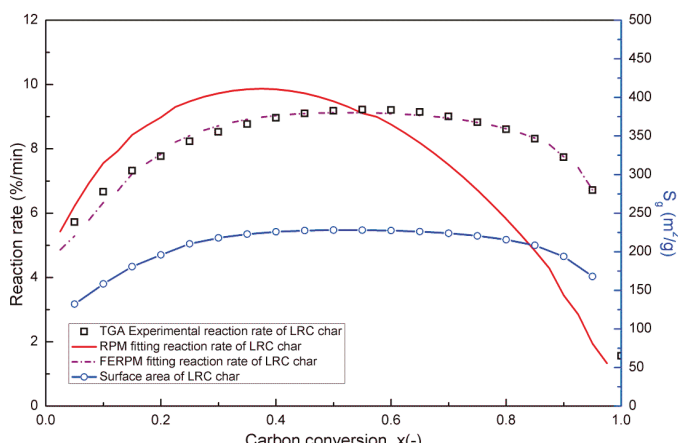


Figure 3. Char oxidation reaction rates and surface areas (S_g) for the carbon conversion of low-rank coal char as calculated by the random pore model (RPM) and Flexibility-Enhanced Random Pore Model (FERPM) using thermogravimetric analyzer (TGA) apparatus.

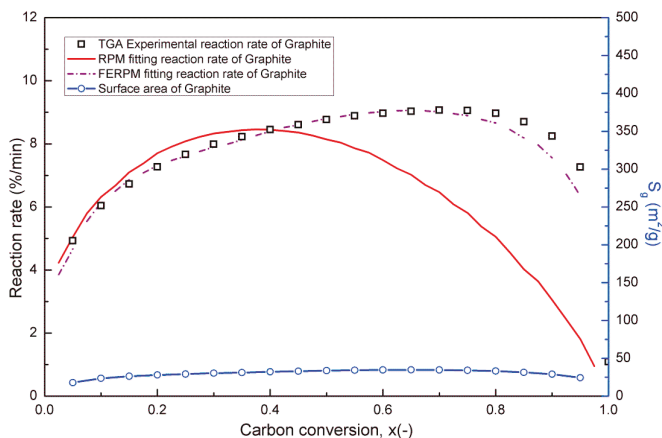


Figure 4. Oxidation reaction rates and surface areas (S_g) for the carbon conversion of graphite as calculated by the RPM and FERPM using TGA apparatus.

Table 3. Calculated structural parameters (ψ), FERPM parameters, and initial particle surface areas (S_0) of low-rank coal char and graphite.

Samples	Low-Rank Coal Char	Graphite
Structural parameter (ψ_{RPM})	23.63	32.99
Structural parameter (ψ_{FERPM})	6.81	17.43
FERPM parameter (a)	0.38	0.46
FERPM parameter (b)	2.40	6.63
FERPM parameter (c)	5.53	12.34
Initial particle surface area (S_0) (BET Ar adsorption, m^2/g)	113.4201	12.8004

The coal char surface area (S_g) was used to determine the intrinsic reaction rate, as discussed in Equation (5). The reaction order (n) can be calculated by linearly fitting the natural logarithm value of the $\eta_{ex} P_{O_2,\infty}$ and R_{app} , as described in Equation (16), with the calculated reaction order for low-rank coal char being 0.51 and the value for graphite being 0.73. The calculated reaction order results are presented in Figure 5.

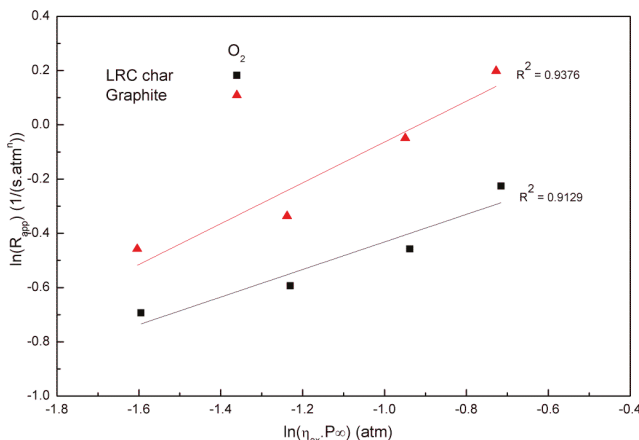


Figure 5. n th order Arrhenius plots for low-rank coal char and graphite.

In order to allow for a comparison of the reaction rate constants when considering oxygen diffusion, the apparent and intrinsic kinetics are shown in Figures 6 and 7, and Table 4, calculated by the linear regression method using Equation (15). From an Arrhenius plot, $\ln k$ versus $1/T$, a linear relationship is obtained and according to Equation (15), the activation energy and the pre-exponential factor can be calculated. The results imply that the intrinsic and apparent reaction kinetics considered both internal and external effectiveness factors at ambient oxygen concentrations of 21% and 30% as the temperature increased. Low-rank coal char and graphite both showed more significant differences between their intrinsic and apparent reaction kinetics at increased temperatures. Moreover, the results suggest that the samples were diffusion controlled, with the effectiveness factors shown in Figures 8 and 9 providing evidence to support this conclusion. To evaluate the effectiveness factors obtained from the intrinsic reaction rates at high a temperature, the external effectiveness factor decreased from 1 to 0.95, with graphite being slightly more affected by the external effectiveness factor. Meanwhile, the internal effectiveness factors decreased significantly as the temperature dropped. This implies that the reaction rates of the two samples were controlled by diffusion at high temperatures [6].

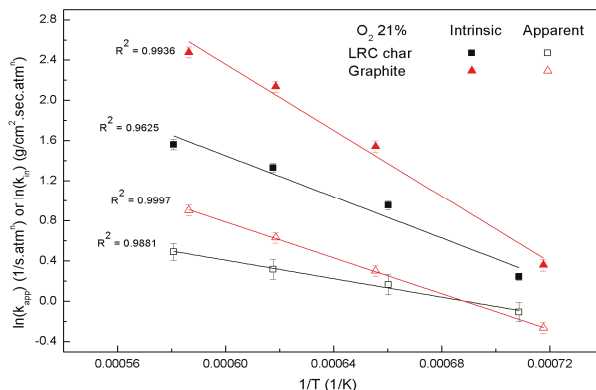


Figure 6. Comparison of reaction rate constants when considering oxygen diffusion at an ambient oxygen concentration of 21%.

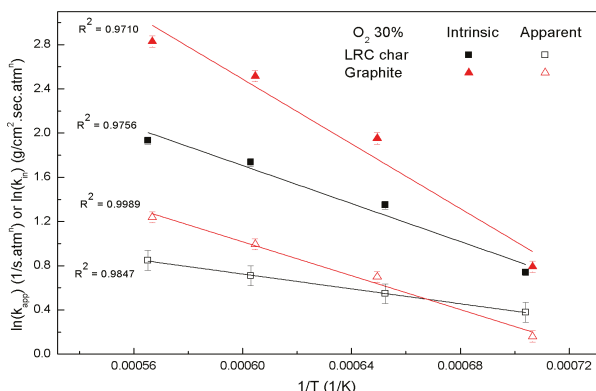


Figure 7. Comparison of reaction rate constants when considering oxygen diffusion at an ambient oxygen concentration of 30%.

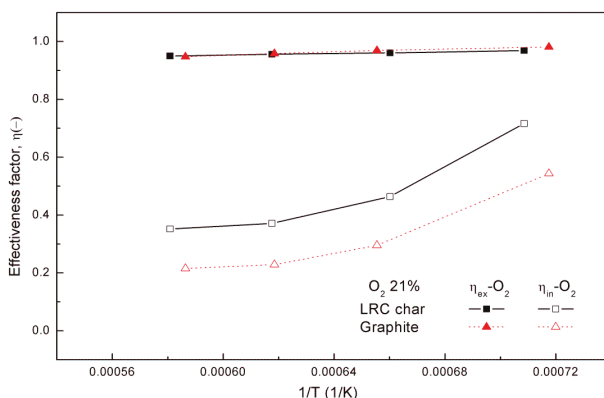


Figure 8. Effectiveness factors as a function of particle temperature at an ambient oxygen concentration of 21%.

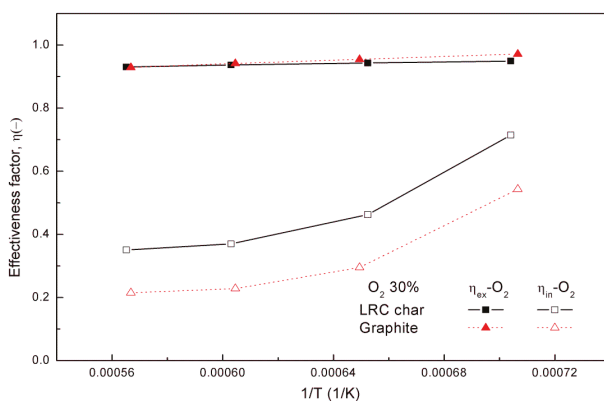


Figure 9. Effectiveness factors as a function of particle temperature at an ambient oxygen concentration of 30%.

Table 4. Linear regression results for the intrinsic reaction rates expressed as n th-order Arrhenius equations.

Samples	Low-Rank Coal Char		Graphite		
	O_2 21% (N ₂ Balance)	O_2 30% (N ₂ Balance)	O_2 21% (N ₂ Balance)	O_2 30% (N ₂ Balance)	
Reaction order, (-)	0.5081		0.7295		
Apparent kinetics	E_a (kJ/mol) A (1/s·atm ⁿ)	38.1 1.031×10^{-5}	27.9 6.81×10^{-6}	74.1 1.363×10^{-3}	63.7 8.105×10^{-4}
Intrinsic kinetics	E_a (kJ/mol) A (g/cm ² ·s·atm ⁿ)	85.5 8.956×10^{-4}	71.4 4.186×10^{-4}	136.6 5.954×10^{-1}	121.7 2.315×10^{-1}

It is apparent from the plots and the table that increasing the amount of oxygen in the atmosphere increased the burning rate in the char kinetics, in spite of the faster char combustion rates. The absolute values of the slopes of Figures 6 and 7 give the activation energies, E , and the intercepts with the y-axis provide the natural logarithms of the pre-exponential factors, A .

In order to define the intrinsic kinetics of the reaction, a mathematical model was used. The activation energy of the low-rank coal char sample reacted at an O₂ concentration of 21% was 85.5 kJ/mol, and the pre-exponential factor was 8.956×10^{-4} g/cm²·s·atmⁿ, whereas the low-rank coal char sample reacted at an O₂ concentration of 30% had an activation energy of 71.4 kJ/mol and a pre-exponential factor of 4.186×10^{-4} g/cm²·s·atmⁿ. Similarly, the activation energy of the graphite sample reacted at an O₂ concentration of 21% was 136.6 kJ/mol, and the pre-exponential factor was 5.954×10^{-1} g/cm²·s·atmⁿ, whereas the graphite sample reacted at an O₂ concentration of 30% had an activation energy of 121.7 kJ/mol and a pre-exponential factor of 2.315×10^{-1} g/cm²·s·atmⁿ. Based on these results, it can be seen that increasing the oxygen concentration in combustion promoted the char reaction rate and lowered the activation energy. The intrinsic kinetics derived from the mathematical model showed the same trend as the experimental results. As the oxygen content increased, the reaction rates of both the coal char and the graphite sample increased. Thus, oxygen-enriched combustion could help to enlarge fuel range utilization so that low-rank coal, which is hardly used in coal-fired boilers, can be used as a more common fuel.

4. Conclusions

A coal-heating reactor was utilized for oxygen-enriched combustion with oxygen concentrations of 21–30%. It consisted of a Pt wire mesh for generating heat from a DC power supply and a setup temperature controller. Low-rank coal char samples (75–90 µm) produced from pyrolysis of the raw coal were used as fuel for char oxidation, and the experimental results were compared with those obtained by using graphite with a carbon content of 99.12 wt %.

As the oxygen content in the reactor atmosphere was increased from 21% to 30%, the combustion temperature of the low-rank coal char increased by 47.72 K at a setup temperature of 1673 K, whereas the reaction time decreased by 30.22% at the same temperature. The graphite sample exhibited similar trends in combustion temperature and reaction time. This suggests that the difference between the temperature changes of the two samples at a low temperature was caused by the development of a microporous structure during the initial stage of combustion. A numerical model was chosen for calculating the reaction kinetics of the coal char in the presence of an oxygen content of 21–30%.

The structural parameters used in the fitting of the low-rank coal experiment result in a good agreement between the FERPM and predictions from previous work. However, in the case of graphite, a parameter outside of the predicted range was observed. This shows that the application of the prediction model proposed in the previous work to a wider range of fuel types is improper, despite the good agreement between the result and the model when using a prediction of the fitting parameter outside of the usual range.

The activation energy of the low-rank coal char sample when reacted in an atmosphere with an oxygen content of 21% was 85.5 kJ/mol, and the pre-exponential factor was 8.956×10^{-4} g/cm²·s·atmⁿ. The low-rank coal char sample reacted at 30% oxygen content and had an activation energy of 71.4 kJ/mol and a pre-exponential factor of 4.186×10^{-4} g/cm²·s·atmⁿ. The value of the activation energy was reduced at 30% oxygen content. Therefore, it is apparent that the reactivity of the low-rank coal char improved in a 30% oxygen atmosphere when compared to its reactivity in a 21% oxygen atmosphere. Furthermore, the graphite sample exhibited the same trend as was seen for the experimental results for the low-rank coal char.

Acknowledgments: This work was supported by the Power Generation & Electricity Delivery Core Technology Program of the Korea Institute of Energy Technology Evaluation and Planning (KETEP), and was granted financial resources from the Ministry of Trade, Industry & Energy, Korea (No. 20131010101810).

Author Contributions: C.-H.J., J.-P.K. and G.-M.K. conceived and designed the experiments; G.-M.K. and J.-P.K. performed the experiments; G.-M.K., J.-P.K. and K.Y.L. analyzed the data; G.-M.K., J.-P.K. and C.-H.J. wrote the paper.

Conflicts of Interest: The authors declare no conflict of interest.

Nomenclature

A_{int}	intrinsic pre-exponential factor ($\text{g}/\text{cm}^2 \cdot \text{s}$)
C	reaction rate constant ($1/\text{s}$)
D	diffusion constant (cm^2/s)
D_{AB}	molecular diffusion coefficient (cm^2/s)
D_{eff,O_2}	effective O_2 diffusion coefficient (cm^2/s)
d_p	diameter (cm)
d_{pore}	pore diameter (cm)
E_{int}	intrinsic activation energy (kJ/mol)
k_{app}	apparent rate constant ($1/\text{s}$)
k_{int}	Intrinsic rate constant ($\text{g}/\text{cm}^2 \cdot \text{s} \cdot \text{atm}$)
m	mass (g)
m_{ash}	ash mass (g)
m_0	initial mass of char (g)
m_t	mass of char at the time (g)
M	molecular mass (g/mol)
M_{AB}	mixed molar mass of A and B (g/mol)
n	Reaction order
P	pressure (atm)
$P_{O_2,S}$	partial pressure of O_2 with at the external particle surface (atm)
$P_{O_2,\infty}$	partial pressure of O_2 in the ambient atmosphere (atm)
R_{app}	apparent reaction rate ($1/\text{s}$)
R_{int}	intrinsic reaction rate ($1/\text{s}$)
R_u	gas constant ($8.314 \times 10^{-3} \text{ KJ}/(\text{mol} \cdot \text{K}) = 82.057 \text{ atm}/(\text{cm}^3 \cdot \text{mol} \cdot \text{K})$)
S_g	surface area (cm^2/g)
T_p	particle temperature (K)
x	carbon conversion (g/g)

Greek Symbols

ε	char particle porosity
Φ	Thiele modulus
η_{ex}	external effectiveness factor for gas transport in the boundary layer
η_{in}	internal effectiveness factor
ν	stoichiometric coefficient
τ	tortuosity factor of the pore (=1.414)
ρ_p	apparent density (g/cm^3)

References

1. Tchapda, A.H.; Pisupati, S.V. A Review of Thermal Co-Conversion of Coal and Biomass/Waste. *Energies* **2014**, *7*, 1098–1148. [[CrossRef](#)]
2. Wang, P.; Means, N.; Shekhawat, D.; Berry, D.; Massoudi, M. Chemical-Looping Combustion and Gasification of Coals and Oxygen Carrier Development: A Brief Review. *Energies* **2015**, *8*, 10605–10635. [[CrossRef](#)]
3. Rao, Z.; Zhao, Y.; Huang, C.; Duan, C. Recent developments in drying and dewatering for low rank coals. *Prog. Energy Combust. Sci.* **2015**, *46*, 1–11. [[CrossRef](#)]
4. Hwang, M.; Song, E.; Song, J. One-Dimensional Modeling of an Entrained Coal Gasification Process Using Kinetic Parameters. *Energies* **2016**, *9*, 99. [[CrossRef](#)]
5. Wang, H.; Zhang, J.; Wang, G.; Zhao, D.; Guo, J.; Song, T. Research on the Combustion Characteristics and Kinetic Analysis of the Recycling Dust for a COREX Furnace. *Energies* **2017**, *10*, 255. [[CrossRef](#)]
6. Kim, R.G.; Jeon, C.H. Intrinsic reaction kinetics of coal char combustion by direct measurement of ignition temperature. *Appl. Therm. Eng.* **2014**, *63*, 565–576. [[CrossRef](#)]
7. Kim, R.G.; Hwang, C.W.; Jeon, C.H. Kinetics of coal char gasification with CO_2 : Impact of internal/external diffusion at high temperature and elevated pressure. *Appl. Energy* **2014**, *129*, 299–307. [[CrossRef](#)]

8. Zhang, D.K.; Poeze, A. Variation of sodium forms and char reactivity during gasification of a South Australian low-rank coal. *Proc. Combust. Inst.* **2000**, *28*, 2337–2344. [[CrossRef](#)]
9. Yin, C.; Yan, J. Oxy-fuel combustion of pulverized fuels: Combustion fundamentals and modeling. *Appl. Energy* **2016**, *162*, 742–762. [[CrossRef](#)]
10. Kim, D.H.; Choi, S.M.; Shaddix, C.R.; Geier, M. Effect of CO₂ gasification reaction on char particle combustion in oxy-fuel conditions. *Fuel* **2014**, *120*, 130–140. [[CrossRef](#)]
11. Daood, S.S.; Javed, M.T.; Gibbs, B.M.; Nimmo, W. NO_x control in coal combustion by combining biomass co-firing, oxygen enrichment and SNCR. *Fuel* **2013**, *105*, 283–292. [[CrossRef](#)]
12. Boushaki, T.; Merlo, N.; Chauveau, C.; Gökalp, I. Study of pollutant emissions and dynamics of non-premixed turbulent oxygen enriched flames from a swirl burner. *Prog. Combust. Inst.* **2017**, *36*, 3959–3968. [[CrossRef](#)]
13. Aziz, M.; Budianto, D.; Oda, T. Computational Fluid Dynamic Analysis of Co-Firing of Palm Kernel Shell and Coal. *Energies* **2016**, *9*, 137. [[CrossRef](#)]
14. Li, J.; Huang, H.; Huhtaoli; Osaka, Y.; Bai, Y.; Kobayashi, N.; Chen, Y. Combustion and Heat Release Characteristics of Biogas under Hydrogen- and Oxygen-Enriched Condition. *Energies* **2017**, *10*, 1200. [[CrossRef](#)]
15. Murphy, J.J.; Shaddix, C.R. Combustion kinetics of coal chars in oxygen-enriched environments. *Combust. Flame* **2006**, *144*, 710–729. [[CrossRef](#)]
16. Wu, K.K.; Chang, Y.C.; Chen, C.H.; Chen, Y.D. High-efficiency combustion of natural gas with 21–30% oxygen-enriched air. *Fuel* **2010**, *89*, 2455–2462. [[CrossRef](#)]
17. Thornock, J.; Tovar, D.; Tree, D.R.; Xue, Y.; Tsiaiva, R. Radiative intensity, no emissions, and burnout for oxygen enriched biomass combustion. *Proc. Combust. Inst.* **2015**, *35*, 2777–2784. [[CrossRef](#)]
18. Pawlak-Kruczek, H.; Ostrycharczyk, M.; Czerep, M.; Baranowski, M.; Zgora, J. Examinations of the process of hard coal and biomass blend combustion in OEA (oxygen enriched atmosphere). *Energy* **2015**, *92*, 40–46. [[CrossRef](#)]
19. Gavalas, G.R. A random capillary model with application to char gasification at chemically controlled rates. *AIChE J.* **1980**, *26*, 577–585. [[CrossRef](#)]
20. Bhatia, S.K.; Perlmutter, D.D. A random pore model for fluid-solid reactions: I. Isothermal, kinetic control. *AIChE J.* **1980**, *26*, 379–386. [[CrossRef](#)]
21. Bhatia, S.K.; Perlmutter, D.D. A random pore model for fluid-solid reactions: II. Diffusion and transport effects. *AIChE J.* **1981**, *27*, 247–254. [[CrossRef](#)]
22. Lisandy, K.Y.; Kim, G.M.; Kim, J.H.; Kim, G.B.; Jeon, C.H. Enhanced Accuracy of the Reaction Rate Prediction Model for Carbonaceous Solid Fuel Combustion. *Energy Fuels* **2017**, *31*, 5135–5144. [[CrossRef](#)]
23. Lisandy, K.Y.; Kim, J.W.; Lim, H.; Kim, S.M.; Jeon, C.H. Prediction of unburned carbon and NO formation from low-rank coal during pulverized coal combustion: Experiments and numerical simulation. *Fuel* **2016**, *185*, 478–490. [[CrossRef](#)]
24. Lisandy, K.Y.; Kim, R.G.; Hwang, C.W.; Jeon, C.H. Sensitivity test of low rank Indonesian coal utilization using steady state and dynamic simulations of entrained-type gasifier. *Appl. Therm. Eng.* **2016**, *102*, 1433–1450. [[CrossRef](#)]
25. Smoot, L.D.; Smith, P.J. *Coal Combustion and Gasification*; Plenum Press: New York, NY, USA, 1979.
26. Guizani, C.; Jeguirim, M.; Valin, S.; Limousy, L.; Salvador, S. Biomass Chars: The Effects of Pyrolysis Conditions on Their Morphology, Structure, Chemical Properties and Reactivity. *Energies* **2017**, *10*, 796. [[CrossRef](#)]
27. Anthony, D.B.; Howard, J.B.; Hottel, H.C.; Meissner, H.P. Rapid devolatilization of pulverized coal. *Symp. Int. Combust. Proc.* **1975**, *15*, 1303–1317. [[CrossRef](#)]
28. Song, J.H.; Jeon, C.H.; Boehman, A.L. Impacts of Oxygen Diffusion on the Combustion Rate of In-Bed Soot Particles. *Energy Fuels* **2010**, *24*, 2418–2428. [[CrossRef](#)]
29. Liu, G.; Wu, H.; Gupta, R.P.; Lucas, J.A.; Tate, A.G.; Wall, T.F. Modeling the fragmentation of non-uniform porous char particles during pulverized coal combustion. *Fuel* **2000**, *79*, 627–633. [[CrossRef](#)]

30. Kajitani, S.; Suzuki, N.; Ashizawa, M.; Hara, S. CO₂ gasification rate analysis of coal char in entrained flow coal gasifier. *Fuel* **2006**, *85*, 163–169. [[CrossRef](#)]
31. Laurendeau, N.M. Heterogeneous kinetics of coal char gasification and combustion. *Prog. Energy Combust. Sci.* **1978**, *4*, 221–270. [[CrossRef](#)]



© 2017 by the authors. Licensee MDPI, Basel, Switzerland. This article is an open access article distributed under the terms and conditions of the Creative Commons Attribution (CC BY) license (<http://creativecommons.org/licenses/by/4.0/>).

Article

Biomass Production from Crops Residues: Ranking of Agro-Energy Regions

Christina Moulogianni and Thomas Bournaris *

Department of Agricultural Economics, Aristotle University of Thessaloniki, Thessaloniki 541 24, Greece; kristin@agro.auth.gr

* Correspondence: tbournar@agro.auth.gr; Tel.: +30-231-0998423

Academic Editor: Mejdi Jeguirim

Received: 4 July 2017; Accepted: 20 July 2017; Published: 22 July 2017

Abstract: The aim of the paper is to rank the agro-energy regions according to their potentials of biomass production in the Region of Central Macedonia (RCM). For this reason, a model of Multi-Criteria Analysis (MCDA) is developed with the ELimination and Et Choix Traduisant la REalite (ELECTRE) III method, with the construction of outranking relations. The aim is to compare in a comprehensive way each pair of action, in our case the agro-energy regions of the RCM, in order to satisfy the main goal which is to rank the seven regions as regards their biomass production. The final goal is to select the optimal crop plan as a pilot case for biomass production in the region. In the case of ELECTRE III multicriteria model, we used several conflicting criteria such as the farm income, the biomass production from crop residues, the variable costs, and the production of thermal energy and electrical energy. Alongside a technical and economic analysis of the study area is conducted for the existent crop plans of each agro-energy region. The results show that agro-energy regions with cereals and arable crops have better results than regions with fruit trees and other crops.

Keywords: biomass production; multicriteria model; ELECTRE III

1. Introduction

The E.U. Common Agricultural Policy (CAP) has set a series of environmental measures known as Agrienvironmental Schemes. Farmers must meet the conditions set by these measures in order to be eligible for subsidies for their cultivated crops. The new CAP framework for the 2014–2020 programming period reinforces the environmental conservation agenda [1]. According to Vlontzos et al. [1] these policy interventions impact both the energy and environmental efficiency of the primary sectors of E.U. member states. Also, one of the main objectives of the Horizon 2020 program is the creation of competitive industries based on sustainable technologies [2]. The contribution of biomass utilization industries from agricultural residues and in particular in Southern Europe has been presented in several research papers [3,4]. In this way farmers have an incentive to keep agricultural residues, a new form of bio-energy and agro-energy regions grow, diminishing the effects of climate change and creating a sustainable economic model [5].

According to the E.U. Biomass Policy and Action Plan [6] “biomass is essential for environmental and competitiveness reasons”. On the other hand the European Parliament has adopted the statement that “biomass has many advantages over conventional energy sources, as well as over some other renewable energy forms”. These advantages can be summarized, in the “low costs, less dependence on short-term weather changes, promotion of regional economic structures and provision of alternative sources of income for farmers”. For these reasons Rosillo-Calle argues that biomass production is of high importance for rural areas and especially for overall rural development [7].

According to Best [8] “agro-energy refers to the energy function of agriculture, which can make significant contributions to achieving social and environmental sustainability at local, national, regional and global levels”. This goal can be achieved by using agricultural and livestock resources worldwide and many new technologies in order to transform the traditional uses of these resources into modern forms of energy [8].

Based on the European energy policy axis [9] and the late development of renewable energy sources in Greece, the region of Macedonia is the best example to examine the creation of agro-energy regions. It is assumed that the exploitation of agricultural and forest residues has only positive impact in terms of jobs creation and the generated thermal and electrical energy [10]. Also, the utilization of energy crops and the production of biofuels, has an overall positive impact worldwide [11]. Greece depends heavily on imported forms of fossil fuels, but has high renewable energy production capacity and has set high goals. The objectives of Greece for producing final energy from renewable sources (any form) amount to 20% of total production by 2020 [12].

The main goal of this paper is to rank the agro-energy regions of the Region of Central Macedonia in Northern Greece. This can be achieved by calculating a number of indicators for biomass and bio-energy production from agricultural residues. By implementing an ELECTRE III multicriteria model, we will rank the seven agro-energy regions (Thessaloniki, Imathia, Kilkis, Pella, Pieria, Serres and Chalkidiki) with a set of criteria regarding economic and environmental aspects. In the next steps, ELECTRE III multicriteria model will compare in a comprehensive way each pair of indicators and will rank them with the use of the conflicting criteria. The three of them are economic criteria (gross margin, income and variable cost) and the rest are environmental criteria (biomass production, production of thermal energy, production of electrical energy). The final result will be the ranking of the seven agro-energy regions according to their potential production of biomass from agricultural crop residues.

First, the methodology of the ELECTRE III multicriteria model is presented with all the necessary mathematical equations. The section also includes the presentation of the case study area and the calculation of the main environmental and economic indicators that will be used as criteria for ranking the agro-energy regions of the Central Macedonia. The following section presents the results of the analysis from the implementation of the ELECTRE III multicriteria model. The final section contains the concluding remarks.

2. Methodology

2.1. Multicriteria Methods for Biomass Production

Many mathematical programming models of the decision-making process of farmers have been applied in several studies found in the literature. Examples are the multicriteria model for the assessment of rural development plans in Greece [13], the model for rural households to measure the effects of the Common Agricultural Policy (CAP) in three Southern European countries [14], and similar examples are the work of Xu et al. [15], Valiakos and Siskos [16] and Prišenek et al. [17]. The use of multicriteria models for ranking regions is also very common in the literature [18,19]. On the other hand, many methodologies have been successfully applied for the biomass production in farm level such as Haas et al. [20], Brentrup et al. [21], Pulighe et al. [22], Neri et al. [23], Blengini and Busto [24], Yu and Tao [25], Castillo-Villar et al. [26] and Fedele et al. [27].

This study will develop an ELECTRE III mathematical programming model for ranking the agro-energy regions of the region of Central Macedonia. The ELECTRE III multicriteria model will be used for the first time for ranking agro-energy regions focusing on biomass production. The great advantage of the methodology is that the results are presented clearly, facilitating the rational discussion of the results and the policy makers. The existent crop plans play a vital role in policy for biomass exploitation, especially in a sensitive environmental area since a large part of Central Macedonia consists of the Network areas Natura 2000. Therefore, this methodology is the most appropriate supportive tool for the ranking of the potentials of agro-energy regions and their combinations. Also,

the ELECTRE III multicriteria model has not been implemented anywhere in Greece for the analysis of biomass production.

2.2. The ELimination and Et Choix Traduisant la REalite (ELECTRE III) Multicriteria Method

ELECTRE III is a well-known multicriteria method widely chosen in the international literature [28,29]. This method requires the determination of prices of three thresholds of the criteria which are used as the indifference threshold, preference threshold and the veto threshold [30]. These allow the uncertainties of the evaluation criteria, be integrated into a decision-making process [31]. The ELECTRE III multicriteria model is used in solving multi-criteria decision-making problems in order to determine the best alternative to a given problem using the multi-criteria analysis [32]. The only reason that this method could be meaningless is the lack of available weights of the criteria and/or the accurate and complete information in minimum preference limits [31]. In this study a number of g_j , criteria (indicators in our case), where $j = 1, 2, \dots, r$ and a group of alternative scenarios (agro-energy regions in our case) are considered. Between the two scenarios a and b there is a possibility to have the following relationships and opposite [30]:

- aPb: The a is strongly preferred to b , where $g(a) - g(b) > p$
- aQb: The a is meager preferred to b , where $q < g(a) - g(b) \leq p$
- aIb: Indifference between a and b , when $|g(a) - g(b)| \leq q$

where p is the preference threshold and q the indifference threshold. The prices for p and q are set by the decision makers [30].

For the implementation of the ELECTRE III multicriteria model we introduce the relation with IPS = aSb symbolism, indicating that scenario a , is at least as good as b . In order to examine the aSb statement introduces the following principles according to Buchaman et al. [33]:

- Agreement Principle: Applies aSb for the majority of the criteria.
- Principle of non-discrepancy: From all the criteria under which it accepted the statement contains no criterion on which this statement is strongly rejected.

The aSjb symbol indicates that scenario a is at least as good as b relative to the j criterion. In order the criterion j to be considered in accordance with the aSb statement should apply aSjb, i.e., $g_j(a) \geq g_j(b) - q_j$. Respectively the criterion j is in disagreement with the statement aSb when applicable bPja, i.e., $g_j(b) \geq g_j(a) - p_j$.

In general, the purpose of the method is defined as the ranking of alternative scenarios considering [34]:

- The indifference and preference thresholds for each criterion.
- The criteria weights.
- The difficulties that may arise from comparing two scenarios, the first is significantly better than the second relative to a subset of criteria but inferior compared with the total evaluation.

Multicriteria evaluation of the potentials of biomass production of the agro-energy regions of Central Macedonia consists a problem which is formulated by using a set of alternatives (a, b, c, d, e, f, g) and a set of criteria (c1, c2, c3, c4, c5, c6). The evaluation of criterion j for alternative A is described as $c_j(A)$. The approach adopted in the framework of this analysis uses a ranking scheme following ELECTRE III principles, based on binary outranking relations in two major concepts; "Concordance" (c_j) when alternative a outranks alternative b if a sufficient majority of criteria are in favour of alternative a and "Non-Discordance" (d_j) when the concordance condition holds, none of the criteria in the minority should be opposed too strongly to the outranking of b by a . The assertion that a outranks b is characterized by a credibility index which permits knowing the true degree of this assertion [35]. To compare a pair of alternatives (a, b) for each criterion, the assertion " a outranks b " is

evaluated with the help of pseudo-criteria. As already discussed, the pseudo-criterion is built with two thresholds, namely indifference (q_j) and preference (p_j), for which the following apply [30]:

- When $c_j(a) - c_j(b) \leq q_j$, the non-difference between alternatives a and b for the specific criterion j under study is identified. In this case $c_j(a,b) = 0$.
- When $c_j(a) - V_j(b) > p_j$, then a is strictly preferred to b for criterion j . In this case $c_j(a,b) = 1$.

For a criterion j and a pair of alternatives (a,b) , the concordance index is defined as follows [30]:

$$c_j(a,b) = \begin{cases} 1 & g_j(b) - g_j(a) \leq q_j \\ 0 & g_j(b) - g_j(a) \geq p_j \\ \frac{p_j + g_j(a) - g_j(b)}{p_j - q_j} & q_j \leq g_j(b) - g_j(a) \leq p_j \end{cases}$$

A global concordance index $C_{a,b}$ for each pair of alternatives (a,b) , is computed with the concordance index c_j (A, B) of each criterion j [30]:

$$C(a,b) = \frac{1}{\sum_{j=1}^r k_j} \sum_{j=1}^r k_j c_j(a,b)$$

where k_j is the weight of criterion j .

As already mentioned, a discordance index $d_j(a,b)$ is also taken into consideration for all pairs of alternatives and each criterion j . Discordance index (d_j) is evaluated with the help of pseudo-criteria with a veto threshold (v_j), which represents the maximum difference $c_j(a) - c_j(b)$ acceptable to not reject the assertion “ a outranks b ”, as follows [30]:

$$d_j(a,b) = \begin{cases} 0 & g_j(b) - g_j(a) \leq p_j \\ 1 & g_j(b) - g_j(a) \geq v_j \\ \frac{g_j(b) - g_j(a) - p_j}{v_j - p_j} & p_j \leq g_j(b) - g_j(a) \leq v_j \end{cases}$$

The index of credibility $S(a,b)$ of the assertion “ a outranks b ” is defined as follows [30]:

$$S(a,b) = \begin{cases} C(a,b) & d_j(a,b) \leq C(a,b) \quad \forall j \\ & d_j(a,b) \geq C(a,b) \\ C(a,b) \cdot \prod_{j \in J(a,b)} \frac{1-d_j(a,b)}{1-C(a,b)} & J(a,b) : d_j(a,b) > C(a,b) \end{cases}$$

In the case that a veto threshold is exceeded for at least one of the selected criteria, the credibility index is null. In other words, the assertion “ a outranks b ” is rejected. As regards the ranking procedure of all available location alternatives A_j , two complete pre-orders are constructed through a descending and an ascending distillation procedure [30]. In a nutshell, descending distillation refers to the ranking from the best available alternative to the worst, while ascending distillation refers to the ranking from the worst available alternative to the best [36,37]. As a last step of the developed methodology, sensitivity analysis is available, since parameter values in real life applications originate from estimations which are sometimes more or less reliable (weighting factors, thresholds, criteria qualitative values etc.) [30].

The next step is to rank the scenarios according to the reliability table. Originally there are formed two rankings $Z1$ and $Z2$, one ascending and one descending preference respectively and from their combination we end up in the final standings $Z = Z1 \cap Z2$ [30].

At this point the constant λ is inserted, which is the highest reliability panel $\lambda = \max S(a,b)$ and is defined as s reliability value (λ), such as to remain only the values $S(a,b)$ gene is greater than $\lambda - s(\lambda)$. The reliability value, like boundaries p_j, q_j, v_j above, determined by the decision-maker. We then apply [30]:

$$T(a,b) = \begin{cases} 1 & S(a,b) > \lambda - s(\lambda) \\ 0 & S(a,b) < \lambda - s(\lambda) \end{cases}$$

From the implementation of the last function derived the final scoreboard under which rankings will be achieved. For the implementation of the ELECTRE III multicriteria model, the “demo” version of the software developed by the French university “LAMSADE Paris-Dauphine” was used [38]

2.3. Case Study Area and Criteria

2.3.1. Case Study Area

The case study area in this study is the Region of Central Macedonia (RCM). The RCM is divided into seven regional units, namely Chalkidiki, Imathia, Kilkis, Pella, Pieria, Serres and Thessaloniki. These regional units are considered as the agro-energy regions of the study. According to the biomass potential maps of the National Information System for Energy, the region of Central Macedonia has the largest reserves of biomass from agricultural residues of all Greece. All the appropriate technical and economic data of the total number of the agricultural holdings, collected from the General Directorate of Rural Economy and Veterinary and the Hellenic Statistical Authority. The data refers to the year of 2013. Crop plans of the agro-energy regions of the RCM are presented in Table 1.

Table 1. Crop plans of the agro-energy regions of the RCM.

Crops	Chalkidiki	Imathia	Kilkis	Pella	Pieria	Serres	Thessaloniki
Alfalfa		5548	4408.7	5518.7	3394.6	10,175.7	
Apples		2614					
Apricots				1628.7			
Barley	4265.8	1493.5	3549.8	4064	2425.4	7825	5324.8
Cherries				7825.1			
Cotton		16,354.4	6814.1	11,204.8	4614.8	14,816.2	10,348.6
Hard Wheat	16,218	4842	38,247.8	5933.5	9498.7	33,527	30,848.1
Kiwi					3218.4		
Maize		5998.3	3394.9	8498.7	1754.5	24,135	2994.8
Nectarines		3914		2948.5			
Oats	3214.2						
Olive Trees	30,847				3214.8	4623	2418.7
Peaches		18,235.7		15,898.7			
Rapeseed						2145	
Rice		1624			987.5	3104.5	17,994.5
Set Aside	11,922.9	2778.4	9909.9	4998.3	4358.4	8245.8	8494.5
Soft Wheat	3654.1	1598.4	22,246.3	4134.8	7914.8	11,924.5	21,911.2
Sunflower	1658.1		2158.9			10,748.5	5284.5
Tobacco					4888.8	2245	
Vetch	2549.1						
Total	30,847	65,000.7	90,730.4	72,653.8	46,270.7	133,515.2	105,619.7

2.3.2. Criteria

The selected criteria for the implementation of the ranking methodolodoy were three economic criteria (gross margin, income and variable cost) and three environmental criteria (biomass production, production of thermal energy, production of electrical energy). The criteria are calculated by multiplying the total land (ha) of each crop in the agro-energy district with the values of each indicator separately. A short description of the criteria is presented below.

Gross Margin

Gross margin is calculated by subtracting from income the variable cost of each crop of the agro energy region.

Income

It was computed by the simple combination of yields (kg/ha), and prices (€/ha), plus subsidies where applicable for each crop of the agro-energy region.

Variable Cost

In order to calculate variable cost all the agricultural inputs are summarized (seeds, fertilizers, chemicals, machinery, labour and the cost of water etc. (€/ha)).

Biomass Production

Based on the literature and taking into account newer research efforts [39] in the same direction [5] the agricultural residues from larger crops per area and yield in tons per hectare are calculated and are presented in Table 2.

Table 2. Biomass production (tn/ha) from crops residues for the main crops of the Region of Central Macedonia.

Crops	Residues Type	Output of Residues (tn/ha)	Humidity %	Biomass (tn/ha)
Alfalfa	Straw	3	0.15	2.6
Apples	Pruning	2.4	0.40	1.4
Apricots	Pruning	1.6	0.40	1
Barley	Straw	2.7	0.15	2.3
Cherries	Pruning	2.5	0.40	1.5
Cotton	Straw and shell (overground)	4.2	0.40	2.5
Cotton	Straw and shell (root)	1.3	0.56	0.6
Hard Wheat	Straw	1.6	0.15	1.4
Kiwi	Pruning	1.6	0.35	1
Maize	Stalks and cobs	10.5	0.55	4.7
Nectarines	Pruning	2.9	0.40	1.7
Olive Trees	Pruning	1.7	0.50	0.9
Peaches	Pruning	2.9	0.40	1.7
Rapeseed	Straw	4	0.53	1.9
Rice	Straw	3.8	0.25	2.9
Set Aside	Not applied			
Soft Wheat	Straw	2.5	0.15	2.1
Sunflower	Stalks	4	0.40	2.4
Tobacco	Stalks	2.2	0.85	0.3

Production of Thermal and Electrical Energy

In order to calculate the production of thermal and electrical energy for crops, the Lower Heating Values (LHV) were considered [40,41]. In the final stage of calculating the production of thermal and electrical energy using the following formulas respectively:

$$\text{Production of Thermal energy (MJ)}: 0.9 \times \text{Biomass (kg)} \times \text{LHV(MJ/kg)}$$

$$\text{Production of Electrical energy (MJ)}: 0.2 \times \text{Biomass (kg)} \times \text{LHV(MJ/kg)}$$

3. Results and Discussion

The following section includes the calculation of the indicators which are used as criteria in the ELECTRE III model (Table 3). It also includes the ranking of the seven agro-energy regions of the Central Macedonia after the implementation of the ELECTRE III multicriteria model.

Table 3. Calculation of the six criteria for ELECTRE III model.

Alternatives Agro-Energy Regions	Criteria					
	Gross Margin (€)	Income (€)	Variable Cost (€)	Biomass Production	Production of Thermal Energy (MJ)	Production of Electrical Energy (MJ)
Imathia	82,639,292.18	210,811,094.64	128,171,802.46	153,941.88	2,565,940,026.60	570,208,894.80
Thessaloniki	54,904,658.03	119,336,134.20	64,431,476.17	213,695.21	3,140,541,839.70	697,898,186.60
Kilkis	48,153,421.10	87,650,548.66	39,497,127.56	160,925.00	2,383,266,261.96	529,614,724.88
Pella	174,610,011.65	317,328,408.48	142,718,396.83	161,579.45	2,686,299,186.15	596,955,374.70
Pieria	50,209,550.87	104,365,027.78	54,155,476.91	77,115.67	1,175,256,301.05	261,168,066.90
Serres	80,164,854.89	178,619,541.72	98,454,686.83	318,397.21	4,837,020,975.00	1,074,893,550.00
Chalkidiki	56,526,005.64	135,930,670.10	79,404,664.46	77,969.21	1,275,268,402.80	283,392,978.40

From Table 3 we can conclude that Serres agro-energy region has the highest potential values for biomass production. The second region is Thessaloniki, followed by Pella, Kilkis and Imathia. The agro-energy regions of Chalkidiki and Pieria are the two with the lowest biomass production potentials. The crop plans of Serres and Thessaloniki mainly include arable crops and cereals which have mainly straw as output residues and high biomass values. The crop plans of Pella and Imathia include mainly fruit trees which produce high pruning values but with low output residues. Finally, the regions of Chalkidiki and Pieria have mixed crop plans with olive trees and arable crops. From these results we can conclude that the variety of crops in the existent crop plans is one of the most important factors as regards the biomass production potentials. Thus, agro-energy units with crops with high agricultural output residues have better results as regards the biomass production and in the production of thermal and electrical energy. As regards the comparison between the economic indicators and the biomass production potential we can conclude that biomass production hasn't any relation to the economic results. Agro-energy regions with high values of gross margin such as Pella and Imathia present the lowest biomass production potentials in comparison with the agro-energy regions of Serres and Thessaloniki.

Ranking

The ranking of the agro-energy regions of the Region of Central Macedonia was performed using the ELECTRE III multicriteria model. The criteria (gross margin, income and variable cost, biomass production, production of thermal energy, production of electrical energy) were used to describe the characteristics of each agro-energy region of the Region of Central Macedonia as regards the economic and environmental aspects. Some of these criteria are conflicting, which is important for the implementation of the ELECTRE III model.

For the implementation of the ELECTRE III multicriteria model, it is necessary a set of weights for every criterion in our research. For this reason, a group of experts (including policy makers from the Ministry of Rural Development and Food, the General Directorate of Rural and Veterinary Economy, farmers and researchers) were interviewed. For the definition of the criterias' weights, a questionnaire administered through personal meetings was used. The results of the questions as regards the weights of each criterion are presented in Table 4.

Table 4. Weights of each criterion.

Criteria	Weights (%)
Gross Margin (€)	7.70
Income (€)	7.70
Variable Cost (€)	7.70
Biomass Production	35.10
Production of Thermal Energy (MJ)	22.20
Production of Electrical Energy (MJ)	19.60
Total	100

The ELECTRE III multicriteria model was implemented using the “demo” version of a software developed by the French university “LAMSADE Paris-Dauphine” [38]. Each agro-energy region of the region of Central Macedonia was assigned a unique alphanumeric code for software use. The alphanumeric codes were:

- A0001: Agro-energy Region of Imathia
- A0002: Agro-energy Region of Thessaloniki
- A0003: Agro-energy Region of Kilkis
- A0004: Agro-energy Region of Pella
- A0005: Agro-energy Region of Pieria
- A0006: Agro-energy Region of Serres
- A0007: Agro-energy Region of Chalkidiki

The credibility matrix of the ELECTRE III multicriteria models for the agro-energy regions was (Table 5):

Table 5. Credibility Matrix.

Codes	A0001	A0002	A0003	A0004	A0005	A0006	A0007
A0001	1	0.15	0.92	0.85	0.92	0.15	0.92
A0002	0.85	1	0.92	0.85	0.95	0.077	0.98
A0003	0.81	0.15	1	0.67	0.98	0.077	0.9
A0004	0.92	0.22	0.92	1	0.92	0.15	0.92
A0005	0.077	0.21	0.15	0.077	1	0.077	0.92
A0006	0.92	0.92	0.92	0.85	0.92	1	0.92
A0007	0.077	0.15	0.15	0.077	0.92	0.077	1

The concordance matrix of the ELECTRE III multicriteria models for the agro-energy regions was (Table 6):

Table 6. Concordance Matrix.

Codes	A0001	A0002	A0003	A0004	A0005	A0006	A0007
A0001	1	0.15	0.92	0.85	0.92	0.15	0.92
A0002	0.85	1	0.92	0.85	0.95	0.077	0.98
A0003	0.81	0.15	1	0.67	0.98	0.077	0.9
A0004	0.92	0.22	0.92	1	0.92	0.15	0.92
A0005	0.077	0.21	0.15	0.077	1	0.077	0.92
A0006	0.92	0.92	0.92	0.85	0.92	1	0.92
A0007	0.077	0.15	0.15	0.077	0.92	0.077	1

After the implementation of the ELECTRE III multicriteria model, the following ranking emerged for the agro-energy regions of the Region of Central Macedonia where:

$$A0006 > A0002 > A0004 > A0001 > A0003 > A0005 \text{ and } A0007$$

The final ranking of the alternatives (agro-energy regions) presented in the next table (Table 7):

Table 7. Final ranking of the seven agro-energy regions of the RCM.

Ranking	Code	Agro-Energy Region
1	A0006	Serres
2	A0002	Thessaloniki
3	A0004	Pella
4	A0001	Imathia
5	A0003	Kilkis
6	A0005 and A0007	Pieria and Chalkidiki

From the table above, we can observe that as regards the biomass production potentials in the Central Macedonia region, the agro-energy region of Serres has the first position, followed by the agro-energy region of Thessaloniki. The third position is held by the agro-energy region of Pella, followed by the agro-energy region of Imathia. In fifth position we have the agro-energy region of Kilkis. The agro-energy regions of Pieria and Chalkidiki share the final position.

From the results we can conclude that the size of the agro-energy region was an important factor. The crop plan of the agro-energy region of Serres seems to have the best mix of crops that produce biomass. The crop plan includes mainly arable crops and cereals as described in the previous section. The second crop plan, of Thessaloniki, seems to have a similar crop mix as the agro-energy region of Serres. The following crop plans of Pella and Imathia mainly comprise fruit trees.

The next figure (Figure 1) shows the ascending and descending distillations of the optimal agro-energy region which in our case is Serres, for biomass production.

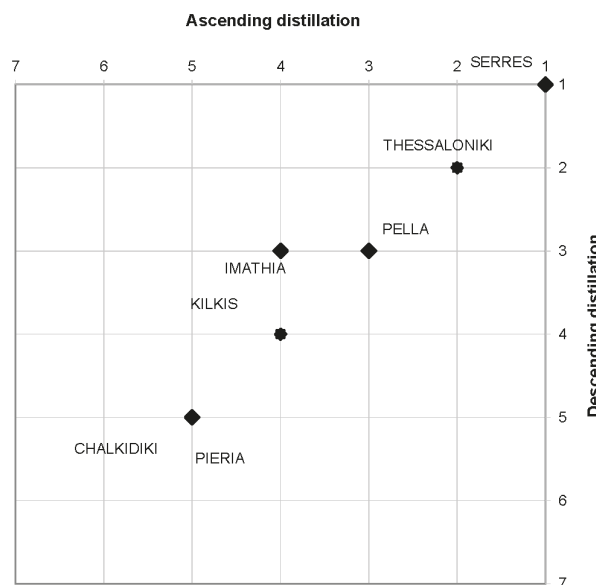


Figure 1. Ascending and descending distillations of the optimal agro-energy region for the biomass production.

4. Conclusions

The main aim of this research was to rank the agro-energy regions in Central Macedonia as regards their potential for biomass production from agricultural residues. For this purpose six main indicators were calculated (gross margin (€), farm income (€), variable costs (€), biomass production (tn), production of thermal energy (mj), production of electrical energy (mj),) for the seven agro-energy regions of the region. These indicators were used as criteria in a multicriteria analysis model. The multicriteria analysis model was developed using the ELECTRE III method. This model was used to rank the crop plans of the seven agro-energy regions under the eight criteria that we have selected. The research also examined the thermal and electrical energy in MWh produced by the biomass from agricultural residues. The results showed that the agro-energy region of Serres had the optimal crop plan for biomass production in the region, followed by the agro-energy region of Thessaloniki. These agro-energy regions had crop plans that included cereals (hard and soft wheat), maize, cotton and rice which are crops that produce high levels of biomass. The next crop plans were the crop plans from the agro-energy regions of Pella and Imathia. These crop plans included fruit

trees crops such as peaches and cherries which can produce high levels of residues from their pruning. From the above we can conclude that the biomass production in the region of Central Macedonia can be increased if the farmers were to turn to crop plans that include cultivation options like those of the agro-energy regions of Serres and Thessaloniki. Also, in the multicriteria ELECTRE III model we used criteria such as gross margin and variable costs that are basic criteria in the farmers' decision-making process when they select the crops that they will cultivate. On the other hand, as we know, their decisions do not include the biomass production. The multicriteria analysis managed to include these conflicting selection criteria in the model and the results of the ELECTRE III ranking proposed the optimal crop plans that the farmers can use and the policy makers can suggest.

The main policy message from this study is that the creation of agro-energy districts with the use of the proposed crop plans can lead to an increase in farm income and promote sustainable development for rural areas using agricultural residues for biomass production both for economic and environmental reasons. The proposed crop plans could be an important tool for the local and regional authorities, since they integrate the farmers' desire for profits and the social concerns about environmental issues. The ELECTRE III multicriteria model could be further improved in order to include more economic, environmental and social criteria that affect the biomass production. We postulate that in the future biomass production from agricultural residues will be one of the main criteria for farmers in their crop selection decision-making process. We can suggest that policy makers should encourage public and private investments in the production of energy from biomass and the creation of agro-energy districts in order to achieve better income for farmers and more sustainable development for rural areas.

Acknowledgments: Christina Moulogianni is supported by the State Scholarships Foundation (IKY) "IKY Fellowships of Excellence for Postgraduate Studies in Greece-Siemens Program".

Author Contributions: The paper was a collaborative effort between the authors. The authors contributed collectively to the theoretical analysis and manuscript preparation.

Conflicts of Interest: The authors declare no conflict of interest.

References

1. Vlontzos, G.; Niavis, S.; Manos, B. A DEA approach for estimating the agricultural energy and environmental efficiency of EU countries. *Renew. Sustain. Energy Rev.* **2014**, *40*, 91–96. [[CrossRef](#)]
2. European Commission. *Horizon 2020. Work Programme 2016–2017. 9. Food Security, Sustainable Agriculture and Forestry, Marine and Maritime and Inland Water Research and the Bioeconomy*; European Commission: Brussels, Belgium, 2015.
3. Fantozzi, F.; Bartocci, P.; D'Alessandro, B.; Arampatzis, S.; Manos, B. Public-private partnerships value in bioenergy projects: Economic feasibility analysis based on two case studies. *Biomass Bioenergy* **2014**, *66*, 387–397. [[CrossRef](#)]
4. Manos, B.; Partalidou, M.; Fantozzi, F.; Arampatzis, S.; Papadopoulou, O. Agro-energy districts contributing to environmental and social sustainability in rural areas: Evaluation of a local public-private partnership scheme in Greece. *Renew. Sustain. Energy Rev.* **2014**, *29*, 85–95. [[CrossRef](#)]
5. Tziolas, E.; Manos, B.; Bournaris, T. Planning of agro-energy districts for optimum farm income and biomass energy from crops residues. *Oper. Res.* **2017**, *17*, 535–546. [[CrossRef](#)]
6. European Commission (EC). *Biomass Action Plan*; European Commission: Brussels, Belgium, 2005.
7. Rosillo-Calle, F. The Role of Biomass Energy in Rural Development. Available online: http://www.proceedings.scielo.br/scielo.php?pid=msc00000002200000010002&script=sci_arttext (accessed on 10 February 2017).
8. Best, G. *Agro-Energy: A New Function of Agriculture*; Latin America Thematic Network on Bioenergy (LAMNET): Morelia, Mexico, 2003.
9. European Commission (EC). *A Strategy for Competitive, Sustainable and Secure Energy*; Energy 2020; European Commission: Brussels, Belgium, 2010.
10. Nishiguchi, S.; Tabata, T. Assessment of social, economic, and environmental aspects of woody biomass energy utilization: Direct burning and wood pellets. *Renew. Sustain. Energy Rev.* **2016**, *57*, 1279–1286. [[CrossRef](#)]

11. Bassegio, D.; Zanotto, M.D.; Santos, R.F.; Werncke, I.; Dias, P.P.; Olivo, M. Oilseed crop crambe as a source of renewable energy in Brazil. *Renew. Sustain. Energy Rev.* **2016**, *66*, 311–321. [[CrossRef](#)]
12. REN21. *Renewable Energy Policy Network for the 21st Century*; REN21: Paris, France, 2016.
13. Bournaris, T.; Moulogianni, C.; Manos, B. A multicriteria model for the assessment of rural development plans in Greece. *Land Use Policy* **2014**, *38*, 1–8. [[CrossRef](#)]
14. Manos, B.; Bournaris, T.; Chatzinikolaou, P.; Berbel, J.; Nikolov, D. Effects of CAP policy on farm household behaviour and social sustainability. *Land Use Policy* **2013**, *31*, 166–181. [[CrossRef](#)]
15. Xu, J.; Chang, S.; Yuan, Z.; Jiang, Y.; Liu, S.; Li, W.; Ma, L. Regionalized Techno-Economic Assessment and Policy Analysis for Biomass Molded Fuel in China. *Energies* **2015**, *8*, 13846–13863. [[CrossRef](#)]
16. Valiakos, A.; Siskos, Y. Multicriteria decision support for the evaluation of agricultural units in Greece. *Oper. Res.* **2015**, *15*, 379–393. [[CrossRef](#)]
17. Prišenek, J.; Turk, J.; Rozman, Č.; Borec, A.; Zrakić, M.; Pažek, K. Advantages of combining linear programming and weighted goal programming for agriculture application. *Oper. Res.* **2014**, *14*, 253–260. [[CrossRef](#)]
18. Koutroumanidis, T.; Papathanasiou, J.; Manos, B. A multicriteria analysis of productivity of agricultural regions of Greece. *Oper. Res.* **2002**, *2*, 339–346. [[CrossRef](#)]
19. Chatzinikolaou, P.; Bournaris, T.; Kiomourtzi, F.; Moulogianni, C.; Manos, B. Classification and ranking rural areas in Greece based on technical, economic and social indicators of the agricultural holdings. *Int. J. Bus. Innov. Res.* **2015**, *9*, 455–469. [[CrossRef](#)]
20. Haas, G.; Wetterich, F.; Geier, U. Life Cycle Assessment Framework in Agriculture on the Farm Level. *Int. J. Life Cycle Assess.* **2000**, *5*, 345–348. [[CrossRef](#)]
21. Breintrup, F.; Kusters, J.; Kuhlmann, H.; Lammel, J. Application of the Life Cycle Assessment methodology to agricultural production: an example of sugar beet production with different forms of nitrogen fertilisers. *Eur. J. Agron.* **2001**, *14*, 221–233. [[CrossRef](#)]
22. Pulighe, G.; Bonati, G.; Fabiani, S.; Barsali, T.; Lupia, F.; Vanino, S.; Nino, P.; Arca, P.; Roggero, P. Assessment of the Agronomic Feasibility of Bioenergy Crop Cultivation on Marginal and Polluted Land: A GIS-Based Suitability Study from the Sulcis Area, Italy. *Energies* **2016**, *9*. [[CrossRef](#)]
23. Neri, E.; Cespi, D.; Setti, L.; Gombi, E.; Bernardi, E.; Vassura, I.; Passarini, F. Biomass Residues to Renewable Energy: A Life Cycle Perspective Applied at a Local Scale. *Energies* **2016**, *9*. [[CrossRef](#)]
24. Blengini, G.A.; Busto, M. The life cycle of rice: LCA of alternative agri-food chain management systems in Vercelli (Italy). *J. Environ. Manag.* **2009**, *90*, 1512–1522. [[CrossRef](#)] [[PubMed](#)]
25. Yu, S.; Tao, J. Economic, energy and environmental evaluations of biomass-based fuel ethanol projects based on life cycle assessment and simulation. *Appl. Energy* **2009**, *86* (Suppl. S1), S178–S188. [[CrossRef](#)]
26. Castillo-Villar, K.; Minor-Popocat, H.; Webb, E. Quantifying the Impact of Feedstock Quality on the Design of Bioenergy Supply Chain Networks. *Energies* **2016**, *9*. [[CrossRef](#)]
27. Fedele, A.; Mazzi, A.; Niero, M.; Zuliani, F.; Scipioni, A. Can the Life Cycle Assessment methodology be adopted to support a single farm on its environmental impacts forecast evaluation between conventional and organic production? An Italian case study. *J. Clean. Prod.* **2014**, *69*, 49–59. [[CrossRef](#)]
28. Fagioli, F.F.; Rocchi, L.; Paolotti, L.; Slowiński, R.; Boggia, A. From the farm to the agri-food system: A multiple criteria framework to evaluate extended multi-functional value. *Ecol. Indic.* **2017**, *79*, 91–102. [[CrossRef](#)]
29. Micale, R.; Gialanza, A.; Russo, G.; La Scalia, G. Selection of a sustainable functional pasta enriched with Opuntia using ELECTRE III methodology. *Sustainability* **2017**, *9*. [[CrossRef](#)]
30. Banias, G.; Achillas, C.; Vlachokostas, C.; Moussiopoulos, N.; Tarsenis, S. Assessing multiple criteria for the optimal location of a construction and demolition waste management facility. *Build. Environ.* **2010**, *45*, 2317–2326. [[CrossRef](#)]
31. Banias, G. Development of a System for the Optimal Construction and Demolition Waste Management. Ph.D. Thesis, Aristotle University of Thessaloniki, Thessaloniki, Greece, 2009.
32. Wang, X.; Triantaphyllou, E. Ranking irregularities when evaluating alternatives by using some ELECTRE methods. *Omega* **2008**, *36*, 45–63. [[CrossRef](#)]
33. Buchanan, J.T.; Sheppard, P.J.; Vanderpooten, D. *Project Ranking Using ELECTRE III*; Department of Management Systems, University of Waikato: Hamilton, New Zealand, 1999.

34. Roy, B.; Présent, M.; Silhol, D. A programming method for determining which Paris metro stations should be renovated. *Eur. J. Oper. Res.* **1986**, *24*, 318–334. [[CrossRef](#)]
35. Roussat, N.; Dujet, C.; Méhu, J. Choosing a sustainable demolition waste management strategy using multicriteria decision analysis. *Waste Manag.* **2009**, *29*, 12–20. [[CrossRef](#)] [[PubMed](#)]
36. Roy, B.; Bouyssou, D. *Aide Multicritére la Decision: Methods et Cas*; Economica: Paris, France, 1993.
37. Maystre, L.Y.; Pictet, J.; Simos, J.; Roy, B. *Méthodes Multicritères ELECTRE: Description, Conseils Pratiques et cas D'application à la Gestion Environnementale*; Presses Polytechniques et Universitaires Romandes: Lausanne, Switzerland, 1994.
38. LAMSADE ELECTRE III e IV Software Official Webpage. Available online: <https://www.lamsade.dauphine.fr/spip.php?rubrique64&lang=en> (accessed on 15 December 2016).
39. Zambon, I.; Colosimo, F.; Monarca, D.; Cecchini, M.; Gallucci, F.; Proto, A.; Lord, R.; Colantoni, A. An Innovative Agro-Forestry Supply Chain for Residual Biomass: Physicochemical Characterisation of Biochar from Olive and Hazelnut Pellets. *Energies* **2016**, *9*, 9. [[CrossRef](#)]
40. Di Blasi, C.; Tanzi, V.; Lanzetta, M. A study on the production of agricultural residues in Italy. *Biomass Bioenergy* **1997**, *12*, 321–331. [[CrossRef](#)]
41. Menconi, M.E.; Chiappini, M.; Grohmann, D. Implementation of a genetic algorithm for energy design optimization of livestock housing using a dynamic thermal simulator. *J. Agric. Eng.* **2013**, *44*, 191–196. [[CrossRef](#)]



© 2017 by the authors. Licensee MDPI, Basel, Switzerland. This article is an open access article distributed under the terms and conditions of the Creative Commons Attribution (CC BY) license (<http://creativecommons.org/licenses/by/4.0/>).

MDPI
St. Alban-Anlage 66
4052 Basel
Switzerland
Tel. +41 61 683 77 34
Fax +41 61 302 89 18
www.mdpi.com

Energies Editorial Office
E-mail: energies@mdpi.com
www.mdpi.com/journal/energies



MDPI
St. Alban-Anlage 66
4052 Basel
Switzerland

Tel: +41 61 683 77 34
Fax: +41 61 302 89 18
www.mdpi.com



ISBN 978-3-03921-663-5